ISSN ...

IOP Conference Series

Materials Science and Engineering

16 International Scientific-Technical Conference
"Dynamics of Technical Systems"

517

VOLUME

1
S

EDITOR
Lukyanov Aleksandr Dmitrievich
Scientific Secretary of the Conference
Candidate of Engineering Science, Associate Professor
(Don State Technical University, Rostov-on-Don, Russia)

The open access journal for conference proceedings

iopscience.org/

IOP Publishing

XVI International scientific-technical conference
"Dynamics of technical systems" (DTS-2020)
is a traditional scientific conference. It brings together scientists and experts of technical universities engaged in the development of fundamental and applied aspects of the engineering sciences. The conference was holding every 2 years in one of the leading universities of the country until 2008, among which were: Lobachevsky State University of Nizhni Novgorod, Yuri Gagarin State Technical University of Saratov, Tula State University, Don State Technical University, and others.

The Conference will aim to exchange experience and identifying the state-of-art scientific developments in the study of technical and technological systems, covering the fundamentals of mechanics, dynamics and tribology, and also problems of non-linear dynamics and synergy in the technical systems, the problems of mechanics of heterogeneous and composite materials, as well as the fundamentals of system analysis, mathematical modelling and information processing.

The main direction of the Conference is to further integrate the efforts of scientists, engineers and designers to create, implement, and industrial applications of recent advances in science and high technologies at the enterprises of various branches of mechanical engineering, including MIC enterprises and other industries.

The conference was organized with the financial support
of the Russian Foundation for Basic Research, grant No. 20-08-22022

This collection of conference proceedings contains materials presented in the section №2 "Non-linear Dynamics and Applied Synergetics in technical systems"

Organizing Committee

Chairman:
Meskhi Besarion Chohoevich
Rector of Don State Technical University,
Professor, Doctor of Engineering Science
(Don State Technical University, Rostov-on-Don, Russia)

Deputy Chairman of the Org Committee:
Lukyanov Aleksandr Dmitrievich
Scientific Secretary of the Conference
Candidate of Engineering Science, Associate Professor
(Don State Technical University, Rostov-on-Don, Russia)

Polushkin Oleg Olegovich
Pro-Rector for Research and Innovation Activities
Candidate of Engineering Science, Associate Professor
(Don State Technical University, Rostov-on-Don, Russia)

Shvedova Svetlana Viktorovna
Pro-rector of International Activities
Candidate of Pedagogical Sciences, Associate Professor
(Don State Technical University, Rostov-on-Don, Russia)

Lebedenko Vyacheslav Georgiyevich
Pro-rector of Administrative and Maintenance Work
Candidate of Engineering Science, Associate Professor
(Don State Technical University, Rostov-on-Don, Russia)

Mozgovoy Andrey Vladimirovich
Pro-rector of General Matters
Candidate of Engineering Science, Associate Professor
(Don State Technical University, Rostov-on-Don, Russia)

Program Committee

Chairmans (Co-Chairs):
Tamarkin Michael Arkadevich
Doctor of Engineering Science, Professor
(Don State Technical University, Rostov-on-Don, Russia)

Zakovorotny Vilor Lavrent'evich
Doctor of Engineering Science, Professor
(Don State Technical University, Rostov-on-Don, Russia)

Varavka Valeriy Nikolaevich
Doctor of Engineering Science, Professor
(Don State Technical University, Rostov-on-Don, Russia)

Marchuk Vladimir Ivanovich
Doctor of Engineering Science, Professor
(Don State Technical University, Rostov-on-Don, Russia)

Deputy Chairman of the Program Committee:
Minkin Maxim Sergeevich
Head of Department of Scientific Research, Candidate of Engineering Science
(Don State Technical University, Rostov-on-Don, Russia)

Editor

Reviewers

Improving the lubricating properties of transmission oils by activating the processes of boundary films formation

A G Ponomarenko[1], T G Boiko[2], A A Bicherov[1], A V Bicherov[1], T A Shiryaeva[3] and D V Kulemzin[2]

[1]Southern Federal University, Rostov-on-Don, Russia
[2]Rostov State Transport University, Rostov-on-Don, Russia
[3]Don-Invec LTD, Rostov-on-Don, Russia

Abstract. The properties of the boundary lubricating films determine the performance of friction units, which is most important in the event of a loss of lubricant. It has been found that when sunflower oil is added to mineral transmission oil, strong boundary layers are formed during friction. These layers reduce wear and friction. Vegetable oils with the lowest iodine value have the best antiwear properties. The additional introduction of the product of the interaction of rosin with copper (II) hydroxide into the transmission oil makes it possible to form lubricating structured layers that improve the tribotechnical properties.

1. Introduction

One of the most important properties of oils is their ability to form lubricating films on friction surfaces. The ordered arrangement of molecules is one of the main reasons for the decrease in friction [1]. High lubricity is provided when shear is localized completely or in large part in the polymolecular boundary layer, in which the shear resistance is minimal and wear is practically absent [2-4].

Usually wear occurs when the thickness of the liquid film becomes less than the average height of the peaks of the sliding surface roughness, that is, under boundary lubrication conditions. The high viscosity of gear oils prevents the oil film from squeezing out of the engagement area of the gears, allowing metal parts to be divided. In case of loss of lubrication, the bearing capacity of the surface layer is set only by boundary films [5].

We have found that sunflower oil is capable of forming strong boundary films on the metal surface under friction [6]. The formation of such films significantly reduces the coefficient of friction and increases the maximum carrying capacity of the oil. This allows the use of lubricants based on sunflower oil in heavily loaded tribosystems [7].

In this work, we studied ways to improve the performance properties of SAE85W90 oil by modifying it with vegetable oils and an additive - the product of the interaction of rosin with copper (II) hydroxide. The aim of the work was to find the composition of the transmission oil that ensures the formation of strong boundary lubricating films.

2. Materials and methods

To determine the tribological characteristics of lubricants, a four-ball friction machine was used. The friction force was measured with a DEPZ-1D-0,1R-1 dynamometer with an accuracy of 0,01 N. The initial load on the lever was 98 N, then after 20 minutes it increased to 196 N, after another 20 minutes

- to 294 N. After the experiment, the measurement was carried out the diameters of the wear scars of the balls using an optical microscope.

The kinetic patterns of changes in chemical bonds in the surface antifriction film were studied by IR ATR spectroscopy on a Nicolet 380 spectrometer.

The presence of the film on the friction surface was confirmed with a Zeiss EVO-18 MA scanning electron microscope (SEM) equipped with BSD and SE sensors. The accelerating voltage ranged from 5 to 15 kV. The film is an insulator, and therefore, its presence on the metal is clearly visible. For SEM study of the friction surfaces, excess lubricant was removed with a solvent (nefras).

The tribotechnical properties of SAE85W90 mineral oil, vegetable oils - sunflower, mustard, linseed, camelina, palm oils were studied.

3. Results and discussion

Tribograms of mineral and vegetable oils differ significantly from each other, Figure 1.

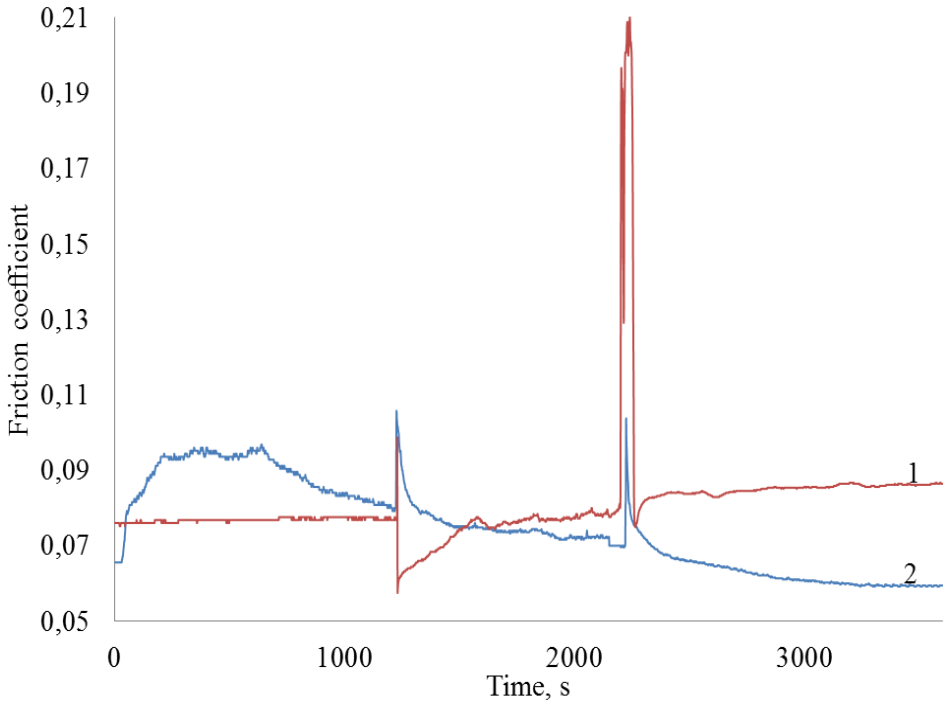

Figure 1. Tribograms of SAE85W90 (1) and sunflower (2) oils

On the tribogram of sunflower oil, at each step of increasing the load, a sharp increase in the friction coefficient is observed, and then its gradual decrease with subsequent stabilization (Figure 1). Gear oil is characterized by an increase in the friction coefficient over time at each load.

The dependence of the wear scar diameter on the concentration of sunflower oil in SAE85W90 is shown in Figure 2.

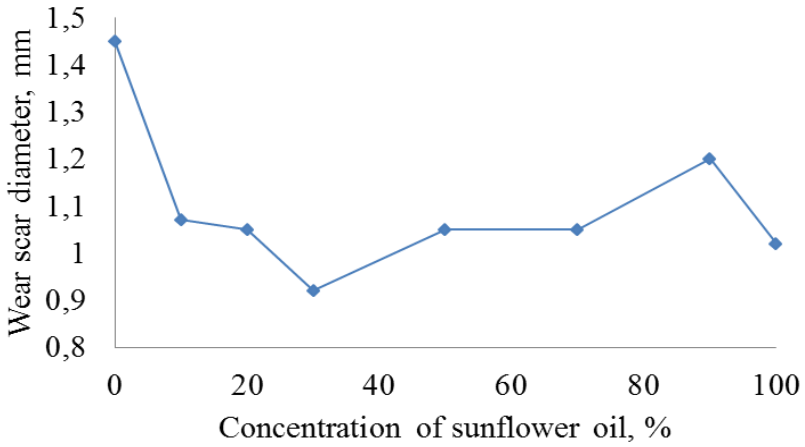

Figure 2. Effect of sunflower oil additives on antiwear properties of SAE85W90 oil

The data obtained can be explained by the fact that the addition of up to 30% sunflower oil makes it possible to activate the processes of formation of surface films. This results in a 35% reduction in wear. At high concentrations of vegetable oil, the viscosity of the transmission oil decreases, which negatively affects its tribotechnical properties.

Reducing the wear scar diameter during friction in a lubricant containing 70% of transmission oil and 30% of the sunflower oil medium is associated with the formation of boundary lubricating films, which are detected by instrumental methods, figure 3.

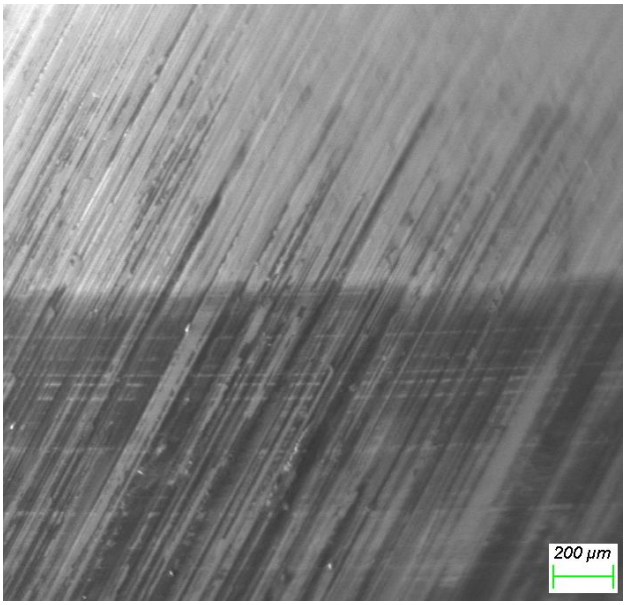

Figure 3. SEM image of a boundary film formed in a lubricant containing 70% transmission oil and 30% sunflower oil

Study of the friction surface by ATR IR spectroscopy, Figure 4, made it possible to identify the groups of atoms forming the boundary film.

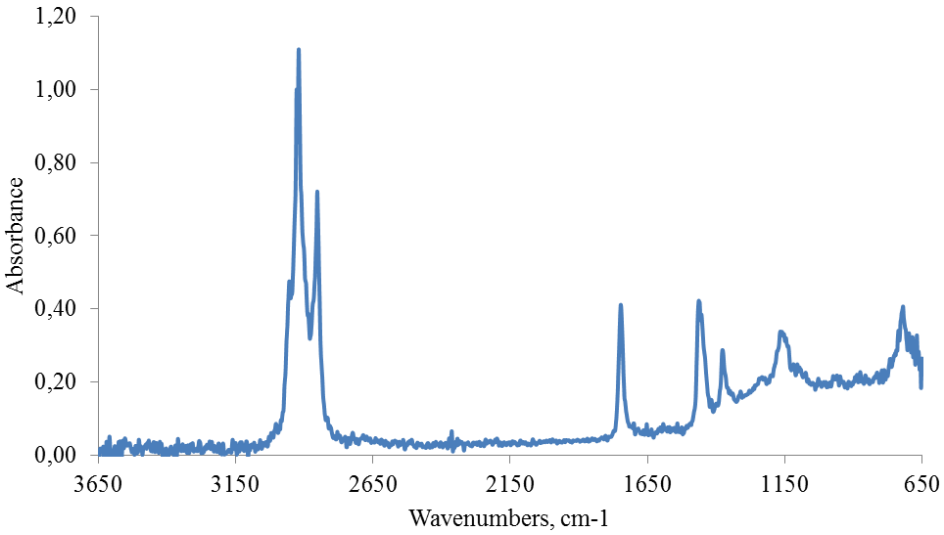

Figure 4. IR spectrum of the surface formed by friction in a lubricant containing 70% transmission oil and 30% sunflower oil

The film contains absorption peaks 2953,8; 2927,1; 2919,6; 2852,1 cm^{-1} corresponding to stretching vibrations of CH bonds; 1747,1 cm^{-1} - stretching vibrations of C=O bonds; 1463,0; 1377,0; 1233,0 cm^{-1} - bending vibrations of CH_2 and CH_3 groups; 1166,4; 1104,5 cm^{-1} - stretching vibrations of C-O bonds of esters; 720,0 cm^{-1} - bending vibrations of CH_2 groups. The form of the spectrum corresponds to the surface films formed by friction with sunflower oil [6].

It has been proven that the mechanism of action of vegetable oils as additives is associated with the formation of tribopolymer films that reduce the coefficient of friction and protect against wear.

The next step in our research was to study the effect of the chemical composition of vegetable oils on their tribotechnical properties. All vegetable oils, by their chemical nature, are esters of glycerol and higher carboxylic acids. The physicochemical and tribotechnical properties of vegetable oils depend on the structure of alkyl radicals of carboxylic acids, and, in particular, on the number and mutual arrangement of unsaturated C=C bonds in the hydrocarbon skeleton. The quantitative measure of the content of unsaturated bonds is the iodine value. A comparison of the tribological properties of oils with their iodine value is shown in Table 1.

Table 1. Results of tribological tests of the mineral oil and vegetable oils

Lubricant	Friction coefficient, at different load on the lever (N)			Wear scar diameter, mm	Iodine value
	98	196	294		
SAE 85W90 mineral oil	0,13	0,13	0,17	1,45	0
Sunflower oil	0,08	0,07	0,06	1,02	132
Mustard oil	0,15	0,14	0,16	1,24	102
Linseed oil	0,09	0,14	0,16	1,17	181
Camelina oil	0,13	0,14	0,13	1,37	142
Palm oil	0,08	0,07	0,05	0,7	54

Analysis of the data obtained shows that with an increase in the iodine value, the diameter of the wear scar tends to increase. Palm oil exhibits the best antiwear properties with a minimum iodine value of 54.

High lubricity can be achieved when a liquid crystal structure of lubricating layers is formed in the friction zone [8-10]. In this regard, it is promising to study substances capable of forming epitropic structured layers. It has been shown [11-13] that the addition of liquid-crystal type cholesterol compounds to the lubricant leads to the formation of structured layers on the friction surfaces that significantly improve the antifriction properties of oils. The disadvantage of such additives is their high cost.

The product of the interaction of rosin with freshly precipitated copper (II) hydroxide (Additive) was studied as an additive that forms structured layers. The main component of rosin is resin acids, whose copper salts are structurally similar to cholesteryl esters. Due to the specific structural features of these compounds, it can be expected that they will create surfaces with a high orientation in the process of friction, which can provide an improvement in the lubricating properties and performance of the boundary layers. In addition, abietic acid, the main component of resin acids, contains a 1, 3-butadiene fragment in its molecule, which is capable of participating in the formation of a three-dimensional network structure. This structure, like a sponge, can be filled with oil molecules and provide an additional decrease in the coefficient of friction [14]. The results of tribological tests of various compositions of transmission oils containing sunflower oil and an Additive are shown in Table 2.

Table 2. Results of tribological tests of transmission oils

Lubricant	Friction coefficient, at different load on the lever (N)			Wear scar diameter, mm	Specific load, MPa
	98	196	294		
70% SAE85W90 + 30% Sunflower oil	0,09	0,10	0,07	1,23	21,05
70% SAE85W90 + 29,9% Sunflower oil +0,1% Additive	0,08	0,08	0,07	1,10	26,32
70% SAE85W90 + 29,5% Sunflower oil +0,5% Additive	0,07	0,08	0,07	0,78	52,45
70% SAE85W90 + 29% Sunflower oil +1,0% Additive	0,07	0,07	0,07	0,77	53,72

Comparison of the data in Table 2 shows that the introduction of the Additive increases both the antiwear and loading properties of the oil. Thus, the Additive promotes the formation of boundary lubricating layers.

4. Conclusion

It is shown that when sunflower oil is added to mineral transmission oil, strong boundary lubricating films are formed during friction.

The addition of the product of the interaction of rosin with copper (II) hydroxide to the transmission oil allows the formation of structured boundary films that reduce friction.

5. Acknowledgments

Research was financially supported by the Ministry of Science and Higher Education of the Russian Federation (State assignment in the field of scientific activity, Southern Federal University, 2020, project №FENW-2020-0031 (0852-2020-0031). The study of boundary films by ATR IR spectroscopy

and SEM was carried out by T.G. Boiko with financial support from the Russian Science Foundation (project No. 18-19-00292).

References

[1] Lin J, Wang L and Chen G 2011 Modification of graphene platelets and their tribological properties as a lubricant additive *Tribology Letters* **41** pp 209-15
[2] Wazynska B, Okowiak J, Kolacz S and Malysa A 2008 Tribological properties of parafine oil doped with liquid crystalline mezogenes *Opto-electronics review* **16** pp 267-70
[3] Amann T, Dold C and Kailer A 2013 Complex fluids in tribology to reduce friction: mesogenic fluids, ionic liquids and ionic liquid crystals *Tribology International* **65** pp 3-12
[4] Iglesias P, Bermúdez M D, Carrion F J and Martinez-Nicolas M 2004 Friction and wear of aluminium–steel contacts lubricated with ordered fluids-neutral and ionic liquid crystals as oil additives *Wear* **256** pp 386-92
[5] Mohamed Faruck A A, Hsu C-J, Doerr N, Weigand M and Gachot C 2020 How lubricant formulations and properties influence the performance of rotorcraft transmissions under loss of lubrication conditions *Tribology International* **151** p 106390
[6] Boiko M V, Kolesnikov I V, Boiko T G and Bicherov A A 2019 Kinetics of antifriction film formation in sunflower oil *Journal of Friction and Wear* **40** pp 532-35
[7] Boiko M and Lebedinsky K 2015 Biodegradable lubricant for railway transport *Transport Problems* **10** pp 99-105
[8] Wazynska B and Okowiak J A 2006 Tribological properties of nematic and smectic liquid c rystalline mixtures used as lubricants *Tribology Letters* **24** pp 1-5
[9] Shen M, Luo J, Wen S and Yao J 2001 Nano-tribological properties and mechanisms of the liquid crystal as an additive *Chinese Science Bulletin* **46** pp 1227-32
[10] Xu F, Matsumoto K and Hagiwara R 2010 Effects of alkyl chain length on properties of 1-alkyl-3-methylimidazolium fluorohydrogenate ionic liquid crystals *Chem. Eur. J.* **16** pp 12970-76
[11] Boiko M V, Sychev A P and Kolesnikov I V 2020 Investigations of antifriction films formation in dioctyl sebacate medium with cholesteryl esters *Lecture Notes in Mechanical Engineering* pp 1035-41
[12] Ermakov S F and Myshkin N K 2018 Tribological properties of liquid-crystal nanomaterials *Springer Series in Materials Science* **267** pp 143-86
[13] Kolesnikov V I, Ermakov S F, Shershnev E B and Sychev A P 2019 Structurally induced lubricity of liquid crystal cholesterol nanomaterials in the friction of metals *Doklady Physics* **64** pp 356-59
[14] Ponomarenko A G, Boiko M V, Kalmykova A G, Boiko T G, Shiryaeva T A and Burlov A S 2016 Tribochemical processes in engine oil with copper nanoparticles and azomethine ligand *Journal of Friction and Wear* **37** pp 435-40

Simulation of Oscillation Frequency Effects on Complex Shape Part Milling

A S Yamnikov and M N Bogomolov

Dept. of Manufacturing Technology, Tula State University Tula, Russia

Abstract. The study shows that auto-oscillations occur even at low-speed turning. The paper includes a literature review revealing the reasons for machining vibrations. It is difficult to analytically describe the physical processes in the cutting area, so we used simulation. Moreover, milling is the most difficult process to describe and research. The variable magnitudes/directions of the cutting forces resulting in extra auto-oscillations make the analysis even more complex. It is shown that reducing the cutting speed leads to lower vibrations, and to lower output, higher rigidity, and damping capacity. It is important to know the natural frequency of the workpiece to choose the right cutting mode. The finite element method and SoldWorks CAD models were used for simulating the complex shape part dynamic behavior. We found out that the workpiece natural frequency is 6.5 times higher than the forced oscillation frequency.

1. Introduction

Cutting oscillations occur even in turning leading to lower part quality [1-3]. Methods to stabilize and control the cutting process are intensively studied [4, 5]. The available papers do not offer an analytical definition or the cutting process since the chip material is in its boundary state. So, most researchers apply numerical simulation of the physical phenomena in the cutting area [5-14]. The most complex process is milling because the magnitude and direction of the cutting forces oscillate systematically, so forced oscillation complement the auto-oscillations [8, 9]. Reduced cutting modes, higher rigidity and damping capacity can reduce cutting vibrations. Moreover, it can be achieved by changing the workpiece location and using vibration-resistant cutters [3-14].

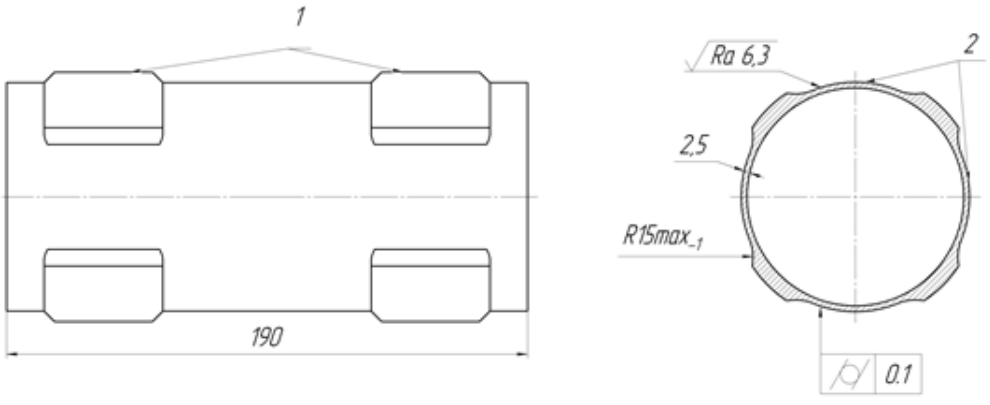

Figure 1. Shaped sleeve

Another interference factor affecting thin-walled sleeve milling is the periodical variations of the cutting force magnitude and direction [13, 14]. Moreover, re-machining a workpiece with cutting traces produces a regenerative effect that boosts the oscillations.

Figure 1 shows a shaped sleeve used as an example. The wall thickness is 2.5 mm. The upper surface has two steps 1. Eight fillets 2, Rmax15-1 radius are to be machined. The surface 2 roughness should be Ra 6.3 and the cylindricity deviation should be 0.1 mm.

The workpiece is a 121×7 tube, GOST 8732-78 made of steel grade 30 (GOST 1050-88.) Such a configuration (large sleeve size to the wall thickness ratio) reduces the machining rigidity. It is another factor inducing vibrations [3-5, 13, 14]. That is why the non-rigid sleeve milling results in intense oscillations.

"In serial production at SPLAV Corp., the tube workpiece is milled by the RBH BCF3028S32-160 ball cutters with the ZCET 150CE replaceable inserts. The equipment is the Akira seiki performa v4 xp4-axis machining center. The workpiece was clearance-placed onto the rigid mandrel. The arbor was clamped into the dividing head of the 4th machine axis. A washer, a nut and a stud screwed into the rigid mandrel were used for clamping. The cutting mode was: cutting speed V = 282.6 m/min, milling RPM n = 3,000 min-1, feed Smin = 450 mm/min, cutting depth t = 2.5 mm, milling width B = 3 mm" [3]. Correspondingly, the mill tooth impact frequency was ω = (2×3,000): 60 = 300 Hz.

2. Theoretical background

It is important to know the natural frequency of the workpiece to choose the right cutting mode. The finite element method (FEM) was used for the complex shape part dynamic modeling [10-14].

According to the FEM concept, the workpiece is divided into elements that form its finite element model. Refer to Figure 2.

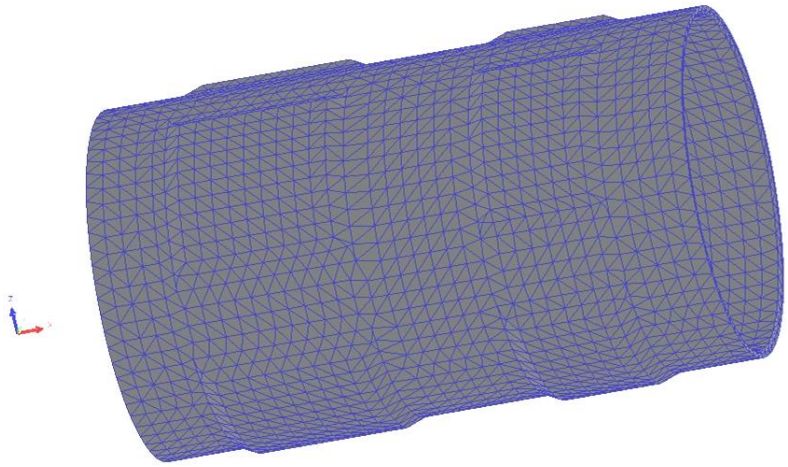

Figure 2. A cylinder model and its partitioning into finite elements

A finite element model of the part was made in the SolidWorks CAD software. The key finite element motion displacement equation can be expressed as matrices [15]:

$$m^e \ddot{q}_e + c^e q_e + k^e q_e = f^e \quad (1)$$

Where $m^e = \int_v [N]^r \rho [N] dv$ is the finite elements mass matrix; $c^e = \int_v [N]^r c [N] dv$ is the finite element damping matrix; κ^e is the finite element rigidity matrix; f^e is the finite element nodal force vector; q^e is the finite element nodal displacement vector; [N] are the finite element shape functions; ρ is the density; c is the damping coefficient.

By summing up the contributions of each finite element we obtained a system of differential linear motion equations relative to the nodal displacement vector of the entire finite element model:

$$M_d \ddot{q} + C_d \dot{q} + K_d q = F \quad (2)$$

where q is the finite element model nodal displacement vector; F is the nodal force vector; M_d is the mass matrix, C_d is the damping matrix; K_d is the structural rigidity [15].

3. Solution

A law of mechanics is: "A body disturbed from its rest position tends to vibrate at certain frequencies called natural, or resonant frequencies. For each natural frequency, the body takes a certain shape called mode shape. Frequency analysis calculates the natural frequencies and the associated mode shapes."

We used the frequency analysis to estimate the part deformation at its natural frequencies, and the fraction of the part mass associated with these frequencies. The total effective mass in each direction can also be estimated. Refer to Table 1 for the frequency analysis results. The table lists mass contribution coefficients for the global X-Y-Z directions normalized to the total mass. The use of sections to divide the text of the paper is optional and left as a decision for the author. Where the author wishes to divide the paper into sections the formatting shown in table 2 should be used.

Table 1. Mass contribution coefficients for the global directions

Mode No.	Frequency (Hz)	X axis %	Y axis %	Z axis %
1	1,059.8	0	0	0
2	1,203.5	0	0	0
3	**1,963.4**	**0**	**19**	**52**
4	**1,963.6**	**0**	**52**	**19**
5	2,228.7	0	0	0
6	2,231.2	0	0	0
Total effective mass, %			71	71

The results show that the mode No. 3 at 1 963.4 Hz along the Z-axis is the most destructive one: 52% of the part mass is affected (refer to Figure 3).

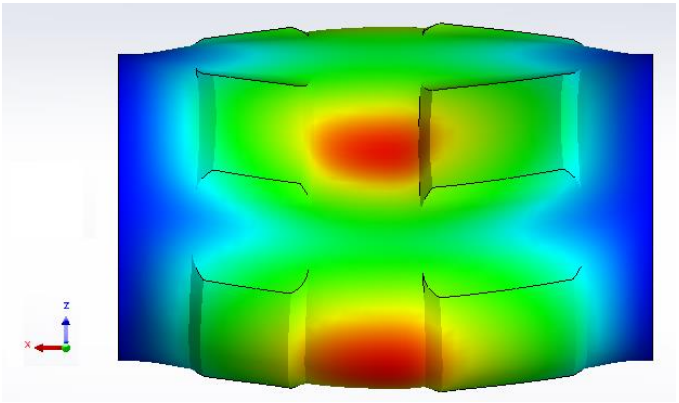

Figure 3. Stress distribution curve for mode No.3

For the Y axis the most dangerous is mode No. 4 at 1,963.6 Hz: 52% of the part mass is affected (refer to Figure 4).

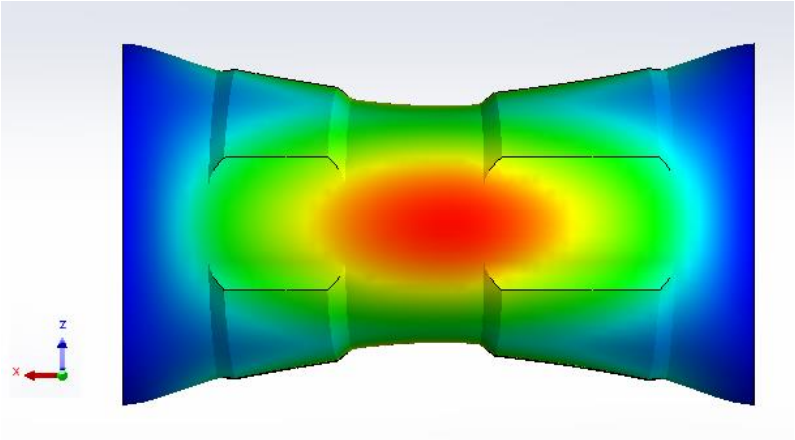

Figure 4. Stress distribution curve for mode No.4

We can claim that central portion of the part is most vulnerable to deformations and vibrations.

4. Conclusion

The resonance oscillation frequencies along the Y and Z axis are almost equal because the material and the wall thickness distribution are nearly identical in two mutually perpendicular directions (ref. to Figure 1).

Natural frequencies of a specific workpiece are 6.5 times higher than the forcing dynamic load oscillation frequency, so no resonance can occur.

Acknowledgments

The reported study was funded by RFBR according to the research project «Postgraduate» №20-38-90248-RFBR.

References

[1] Lazarev G. Metal Cutting Stability. Moscow: *Vysshaia Shkola Publishing*, 1973. 184 p.

[2] Amosov V. Scragan Turning: Accuracy, *Vibrations, and Surface Finish* [in Russian] Moscow, Leningrad. MASHGIZ Publishing. 1958. 91 p.

[3] Leontiev B.V., Leontieva A.N. Cutting Process Management to Remove Vibrations (Far East Federal University Vladivostok, 2012), pp. 159-162.

[4] Kuznetsov V., Yamnikova O. *Machining System Stability for Threading with Multi-Cutter Heads* [in Russian] // STIN Journal, 2004. No. 2 Pp. 12-14

[5] Bykov G.T. *Vibrational stability in turning thin-walled pipe by multicutter heads* / G.T. Bykov, A.S. Yamnikov, O.A. Yamnikova, etc.// Russian Engineering Research. 2010. V. 30. No 3. Pp. 296-299.

[6] Kalinski K., Mazur M., Galewski M. *High speed milling vibration surveillance with the use of the map of optimal spindle speeds* // Proceedings of the 8th International Conference on High Speed Machining, 2010. ENIM, Metz, France. Pp. 300-305.

[7] Wu D.W. Comprehensive *Dynamic Cutting Force Model and Its Application to Wave-Removing Processes* // Journal of Engineering for Industry. 1989. No 2. Pp. 155-164.

[8] Yamnikova O. A *Simulation Model of a Non-Rigid Shaft Oscillations under Cutting* // STIN Journal, Moscow: 2003, No. 1, pp. 18-21

[9] Zagórski I., Kulisz M., Semeniuk A., Malec A. *Artificial neural network modelling of vibration in the milling of AZ91D alloy*. Advances in Science and Technology // Research Journal. Sep. 2017. Vol. 11, Issue 3. Pp. 261-269. DOI: 10.12913/22998624/76546

[10] Comak A., Budak E. *Modeling dynamics and stability of variable pitch and helix milling tools for development of a design method to maximize chatter stability*// Precision Engineering, 2017, 47, 459-468.

[11] Yamnikov A.S., Chuprikov A.O. *Chucks for Thin-Walled Blanks* // Russian Engineering Research. Vol. 35 No. 11 2015, Pp. 838-840.

[12] Voronov S., Kiselev I. Identification of the Cutting Forces *Coefficients via Milling Process Simulation* // Proceedings of the ASME 2011 International Design Engineering Technical Conference and Computer and Information in Engineering Conference IDETC/CIE, USA. 2011. V 1. P. 127-133.

[13] Yamnikov A., Bogomolov M. *High Vibration Stability Centering Mandrel for the Thin Walled Sleeves* // Ferrous Metals, No. 5, 2019. Pp. 52-57

[14] Bogomolov M., Chuprikov A., Yamnikov A. Mandrel for Fixing Thin-Wall Cylindrical Workpieces // Russian Federation Patent No. 2688019, B23B31/40. Published on May 17, 2019 No. 14.

[15] Zenkevich O. *The Finite-Element Method in Engineering*. Moscow: MIR Publishing. 1975. 541 p. ing the last numbered section of the paper.

Assessment of the mechanical properties of welded joints after wave strain hardening

A V Kirichek[1,*], S V Barinov[2], S A Silantyev[2], A V Aborkin[3] and A V Yashin[2]

[1]Bryansk State Technical University, Bryansk, Russia
[2]Murom Institute (branch) of Vladimir State University, Murom, Russia
[3]Vladimir State University, Vladimir, Russia

*Corresponding author: avk@tu-bryansk.ru

Abstract. The purpose of this work is to establish the relationship between the modes of wave strain hardening (WSH) and changes in the ultimate strength, microhardness, impact strength of welded joints. The need for these studies is associated with the prevention of destruction of welded joints with the help of their subsequent WSH. The uniqueness of the WSH method lies in the wave loading of the processed material by shock pulses with a given duty cycle, energy and duration. This makes it possible to increase microhardness and form compressive residual stresses at a depth of more than 10 mm, which makes the use of the method promising for increasing the strength of welded seams. These studies have not previously been conducted. Materials 10ХСНД, 30ХГСА and 40Х were taken as objects of research, from which important welded products are often made in industry. As a result of the research, based on the conditions for increasing the strength of welded joints of the selected materials, rational modes of strengthening and the direction of processing have been determined.

1. Introduction

Welding is one of the most common technological processes for assembling products of varying complexity, such as body elements, pipelines, pressure vessels, etc. In this case, the share of destruction of welded structures is approximately 30% of the total number of reasons for their failures [1]. Prevention of destruction of welded joints is an urgent task for modern mechanical engineering. The requirements for the strength of the weld are such that it should not be lower than that of the base metal. To increase metal strength in the heat-affected zone and reduce the residual stresses both in the base metal and in welds, various technological methods such as heat treatment, aging, surface plastic deformation (SPD), etc. are used [2-7].

The use of traditional methods to improve the strength properties of the heat-affected zone - heat treatment and aging is characterized by significant time and energy costs and has certain limitations associated with the overall dimensions of the processed product.

Among the SPD methods, for the treatment of welded joints and near-weld zones, ultrasonic and vibro-shock treatment, rolling, etc. are used [13-20].

A fairly effective method for processing welded joints and near-weld zones, in order to increase their strength properties, is the SPD method - wave strain hardening (WSH). This method, due to a number of additional design and technological parameters, makes it possible to act on the surface to be hardened with controlled shock pulses and to form in it the required hardness distribution at a depth of 15 mm and create compressive residual stresses [8-12]. However, studies on the use of WSH, to

increase the strength properties, were carried out only in fragments, using welded samples made from 09Г2С steel.

The purpose of this work is to study the influence of WSH modes on the mechanical properties of welded products.

2. Research methodology

As a material for research, we used steel widely used in industry for the manufacture of welded products, such as: 10ХСНД, 30ХГСА and 40Х. Workpieces with dimensions of 600 * 100 * 7 mm were made from each material and then welded into a plate of 600 * 200 * 7 mm. Welding was carried out in a semi-automatic mode.

To prepare for WSH, the leg of the welded seams was cut off to the height of the protrusion above the plane of the plate of 0.1 mm. Strengthening by a deformation wave was carried out with an energy of 150 J with a shock frequency of 10 Hz and with modes corresponding to a change in the overlap coefficient K: 0; 0.3 and 0.6. The overlap coefficient K is a value that makes it possible to evaluate the uniformity of overlapping of the plastic imprints of the tool impacts during WSH. The range of change for K is from 0 to 1: at K = 0, the prints do not overlap, the edges of the prints border each other; at K = 1, there is a complete overlap of prints [8-12]. A rod roller with a diameter of 10 mm and a width of 40 mm was used as a tool for strengthening.

In order to identify the most effective direction of hardening, WSH of the welded seams was carried out both in the longitudinal and transverse directions relative to the axis of the welded joint (figure 1).

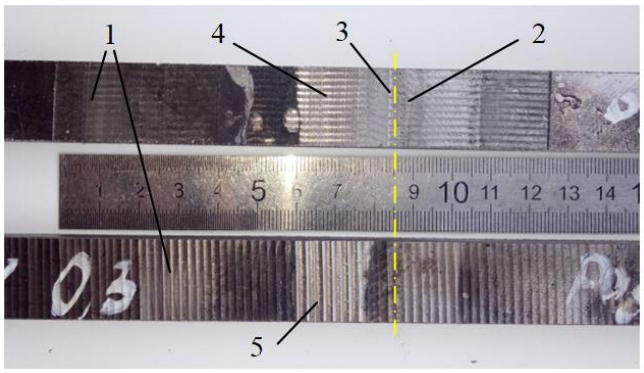

Figure 1. Welded joints: 1) samples with welded joints; 2) area of the welded joint; 3) axis of the welded joint; 4) direction of longitudinal strengthening of the welded joint; 5) the direction of the transverse hardening of the welded joint.

After WSH, samples for research were cut out of the welded plates on a band saw:

1) microhardness maps in the welded product;
2) strength properties of welded joints by static tensile strength test;
3) impact strength.

To study the microhardness map after different modes of WSH, hardened samples were cut along the weld axis. Microhardness studies were carried out using a KB 30S hardness tester. Static tensile resistance tests were carried out on a WDW-100E universal electromechanical computer-controlled machine. The determination of the values of the impact strength of the material was carried out on an impact driver.

3. Investigation of the influence of WSH modes on the mechanical properties of welded joints

The values of microhardness, strength, impact toughness obtained as a result of research at various modes of WSH are shown in figure 2-4.

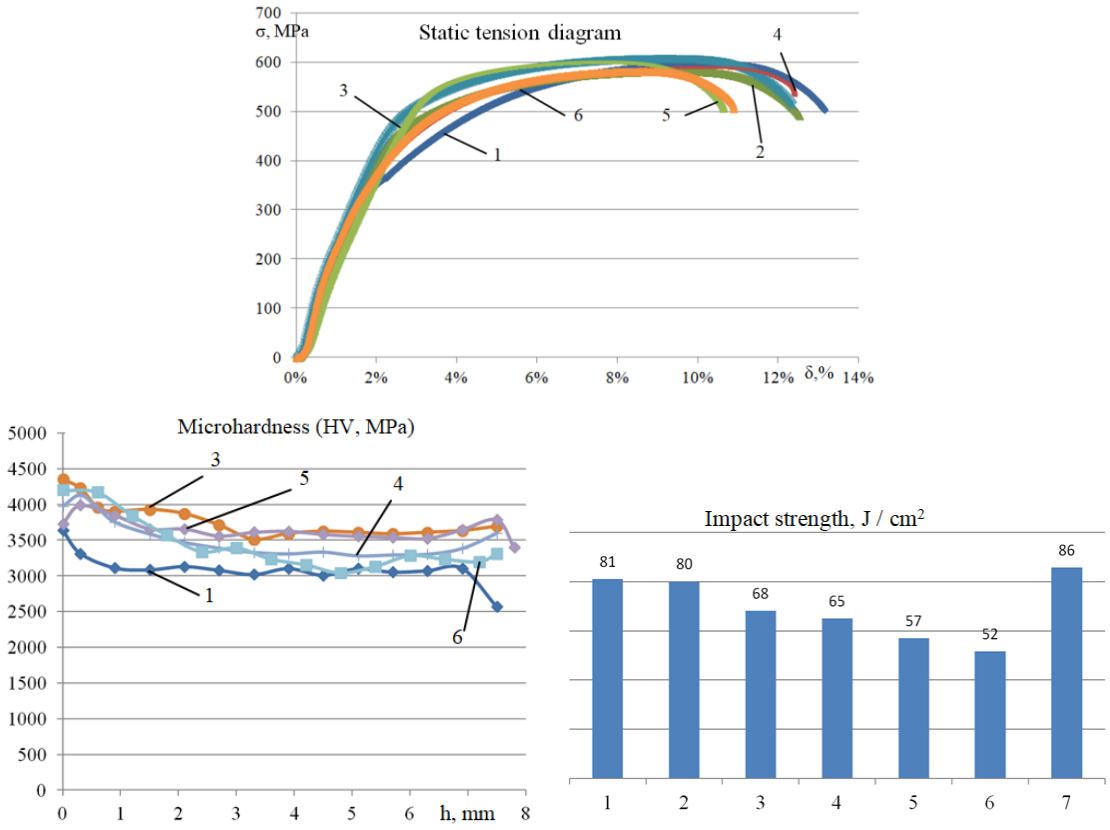

Figure 2. Change in ultimate strength, microhardness and impact toughness of welded seams made of 40X steel as a result of WSH: 1) unselected seam; 2) K=0 transverse hardening of the seam; 3) K=0.3 transverse hardening of the seam; 4) K=0.3 longitudinal hardening of the seam 5) K=0.6 transverse hardening of the seam; 6) K=0.6 longitudinal strengthening of the seam; 7) initial material.

Thus, with WSH of the welded seams of the 40X steel plate, based on the analysis of the obtained tensile diagram (figure 2), it was possible to establish that, in general, strengthening led to a significant increase in the yield strength and the tensile strength. With transverse hardening with K = 0.3, it was possible to increase the ultimate strength by 3% while maintaining the plasticity at the level of that of the unhardened welded joint material. An increase in the yield point and ultimate strength, without a significant decrease in the plasticity of the material, has a positive effect on the performance properties of the part, including the fatigue resistance.

WSH of plates made of steel 40X led to strengthening of the weld along its entire thickness. Thus, the transverse strengthening of the welded seam with K = 0.3 and K = 0.6 led to an increase in microhardness, on average over the entire thickness of the welded seam and the heat-affected zone, by 21 and 16.5%, respectively. Longitudinal hardening of the weld area led to an increase in microhardness only by 13 and 9.5%, respectively, at K = 0.3 and K = 0.6.

The impact toughness of the welded joint formed in 40X steel decreased by 5.8%. WSH with K = 0 practically does not change the impact toughness of unreinforced weld material. WSH with K = 0.3 is accompanied by a decrease in impact toughness upon strengthening in the transverse direction by 21%, and upon strengthening in the longitudinal direction - by 24%. WSH with K = 0.6 is accompanied by a decrease in impact toughness with strengthening in the transverse direction by 33.7%, and with strengthening in the longitudinal direction - by 39.5%.

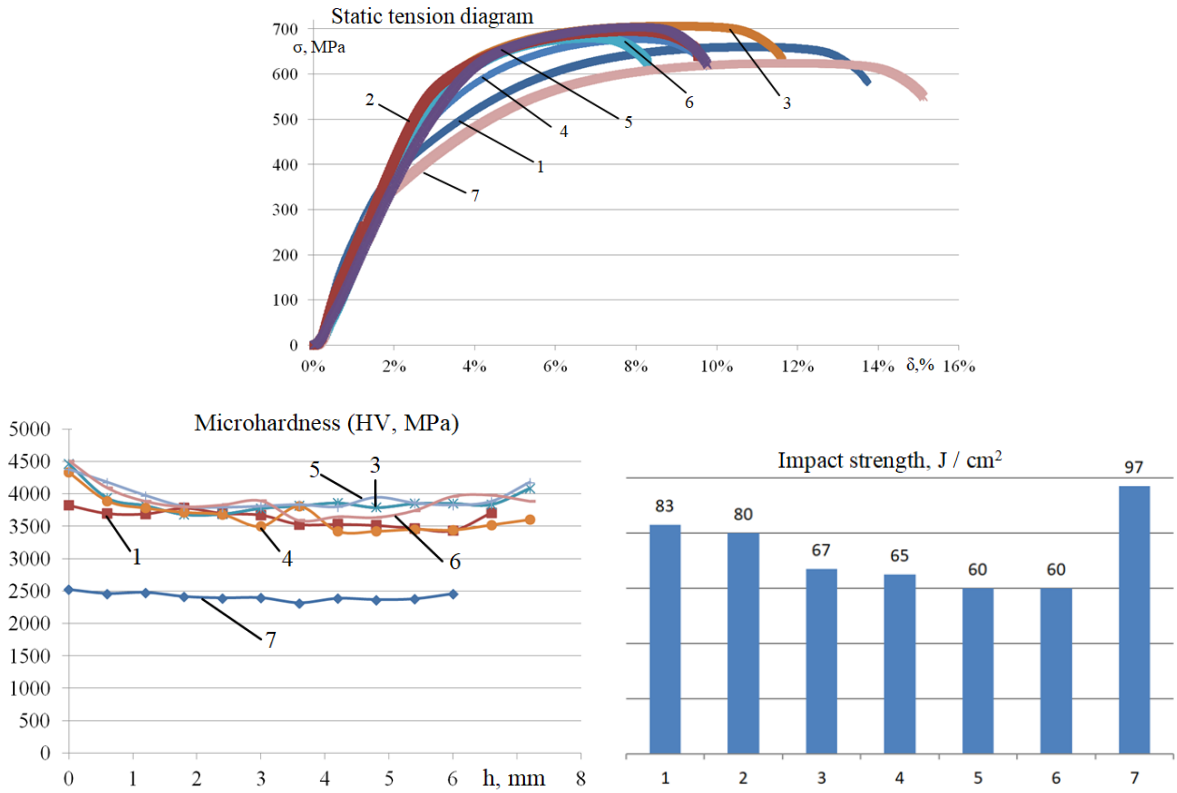

Figure 3. Changes in microhardness, ultimate strength and impact toughness of welded joints made from 30 ХГСА steel as a result of WSH: 1) unselected seam; 2) K=0 transverse hardening of the seam; 3) K=0.3 transverse hardening of the seam; 4) K=0.3 longitudinal hardening of the seam; 5) K=0.6 transverse hardening of the seam; 6) K=0.6 longitudinal strengthening of the seam; 7) initial material.

When welding plates made of 30 ХГСА steel, an increase in the microhardness of the welded seam by 50% compared to the parent metal was established (Fig. 3), which introduces serious restrictions on the possibility of a welded product hardening using WSH.

Thus, the WSH of a welded seam with K = 0 led to an increase in its microhardness by only 7% in comparison with an unreinforced seam. When hardening with K = 0.3 in the transverse direction, the microhardness increased by 7.1%, and in the longitudinal direction by 4%. Hardening with K = 0.6 in the transverse direction led to an increase in microhardness by 8.1%, and in the longitudinal direction by 6.9%.

As a result of the analysis of the static tension diagram, it was found that the ultimate strength of the welded joint material is 5.7% higher than that of the initial material. WSH of the weld with K = 0 led to an increase in the ultimate strength by 5.1%, with a decrease in the ductility of the material by 38.1%, compared with an unreinforced weld. WSH with K = 0.3 in the transverse direction is accompanied by an increase in the ultimate strength by 7% in comparison with unreinforced material, and hardening in the longitudinal direction is accompanied by an increase in the ultimate strength by only 2.4%. At the same time, plasticity decreases by 22.7 and 38.1%, respectively. WSH with K = 0.6 in the transverse direction is accompanied by an increase in the ultimate strength by 6.6%, and in hardening in the longitudinal direction - by an increase in the ultimate strength by 3% The value of plasticity decreased by 38.1 and 54.5%, respectively.

Due to the formation of a welded seam in 30 ХГСА steel impact strength decreased by 14.4%. Hardening with K = 0 practically did not change the impact strength in comparison with an unreinforced weld. WSH with K = 0.3 is accompanied by a decrease in impact strength upon strengthening in the transverse direction by 19.2%, and upon strengthening in the longitudinal

direction - by 21.6%. Treatment with K = 0.6 leads to a decrease in impact strength during hardening in the transverse and longitudinal directions by 27.7%.

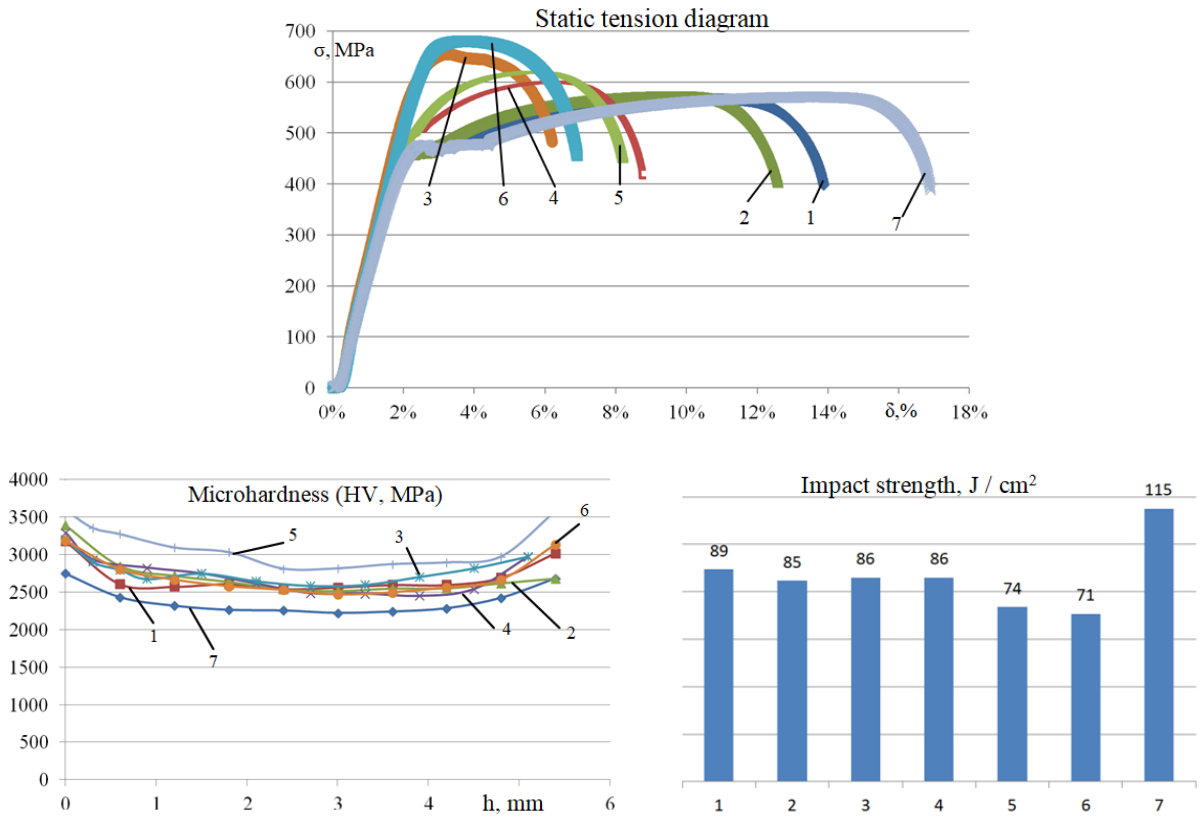

Figure 4. Changes in microhardness, ultimate strength and impact toughness of welded joints made from 10 ХСНД steel as a result of WSH: 1) unselected seam; 2) K=0 transverse hardening of the seam; 3) K=0.3 transverse hardening of the seam; 4) K=0.3 longitudinal hardening of the seam; 5) K=0.6 transverse hardening of the seam; 6) K=0.6 longitudinal strengthening of the seam; 7) initial material.

The microhardness of the material of the welded joints of plates made of 10 ХСНД steel is by 13% higher in comparison with the initial material. WSH with K = 0 leads to an increase in the microhardness of the weld by 4.2%. Strengthening in the transverse direction with K = 0.3 is accompanied by an increase in microhardness on average over the thickness of the weld and the heat-affected zone by 5.4%. WSH in the longitudinal direction with K = 0.3 provides an increase in the microhardness of the material by 4.2%. WSH in the transverse direction with K = 0.6 provides an increase in microhardness by 14.5%, and in the longitudinal direction - by 2.7%.

As a result of testing the samples under static tension, it was found that when compared with the original material, the presence of a weld did not affect the value of the ultimate strength, but the ductility decreased by 19%. Strengthening with K = 0 did not change the ultimate strength, and the ductility decreased by 12.5%. With WSH with K = 0.3 in the transverse direction, an increase by 15.3% in the ultimate strength was established, and in the longitudinal direction - by 5.8%. Compared with an unreinforced weld, the plasticity in the transverse and longitudinal directions decreased by 64.8 and 43%, respectively due to WSH. Strengthening with K = 0.6 in the transverse direction made it possible to increase the ultimate strength by 20%, and in the longitudinal direction by 9%. At the same time, the plasticity decreased by 58.5 and 49%, respectively.

Impact strength, due to the formation of a weld in 10 ХСНД steel, decreased by 22.6%. Hardening with K = 0 had little effect on the change in impact strength; in comparison with an unreinforced weld, it decreased by 4.5%. WSH with K = 0.3 reduces the impact strength during hardening in the transverse and longitudinal directions by 3.3%. WSH with K = 0.6 leads to a decrease in impact strength during hardening in the transverse direction by 16.8%, and in the longitudinal direction by 20.2%.

4. Conclusion

1. A significant influence of the direction of WSH processing of the welded joint on its microhardness, strength and impact strength has been established. The best complex of the above listed properties is provided by WSH with transverse hardening of welded joints, which is associated with the peculiarities of the implementation of the WSH process and the geometric parameters of the weld.

2. It has been established that with the WSH of welded seams of plates made of 40X steel, the rational mode is transverse strengthening of welded seams with an overlap coefficient K = 0.3, which ensures 21% increase in microhardness over the entire section of the welded seam, and preserves its plasticity at the level of unreinforced welded joint material.

3. It has been established that the rational modes for strengthening welds made of 30 ХГСА steel are those that provide hardening in the transverse direction with K = 0.3 and K = 0.6. This makes it possible to increase microhardness by 7-8% and the ultimate strength by 6.6-7%. It should be taken into account that hardening with K = 0.6 in comparison with K = 0.3 is accompanied by a more significant decrease in plasticity - by 40%.

4. It has been established that WSH of welded joints made of 10 ХСНД steel can significantly increase their ultimate strength. So, in the case of the longitudinal direction of hardening with K = 0.3 and K = 0.6, the ultimate strength increases by 15-20%, which is accompanied by a 58-64% decrease in plasticity. The optimal mode of WSH of welded joints on products made of 10 ХСНД steel is hardening in the transverse direction with K = 0.3, which provides an increase of 5.8% in ultimate strength, 5.4% of microhardness with a decrease in plasticity by 43%.

Acknowledgments

The research has been performed with the assistance of the Russian Foundation for Basic Researches No. 18-38-20066.

References

[1] Shinkarev A S 2010 *Improvement of the quality of the surface layer of welded seams based on the improvement of ultrasonic shock treatment Diss. ... Cand. tech. sciences.* 146 p.

[2] Kryukov S A, Tkach M A 2017 *Procedia Engineering* **206** pp. 200-203

[3] Shumyacher V M, Bochkarev P U, Slavin A V 2017 *Procedia Engineering* **206** pp.232-235

[4] Yang L, Wang D, Guo Y 2018 *Tribology International* **123** pp.180-190

[5] Babichev A P, Shudaley S N 2012 *Vibration Mechanical Chemistry in Processes of Finishing – Hardening Working and Coatings of Machinery* (Rostov-on-Don: Don State Technical University Publishing House) p 354

[6] Smolentsev V P 2000 *Handbook of technological-engineering* (Moscow) p 264

[7] Babichev A P, Babichev I A 2008 *Fundamentals of Vibration Techniques* (Rostov-on-Don:Don State Technical University Publishing House) p 694

[8] Kirichek A V, Barinov S V, Yashin A V 2017 *IV International Technology Forum"Innovations. Technology. Production*" (RGATU n.a. P.A. Solovyov) **2** (41) pp. 147-149

[9] Kirichek A V, Soloviev D L and Lazutkin A G 2004 *Technology and equipment of static-pulse processing by surface plastic deformation* (Moscow: Engineering)

[10] Kirichek A V, Barinov S V, Ryzhkova M N, Yashin A V 2019 *CEUR Workshop Proceedings* **2485** pp. 265-267

[11] Kirichek A V, Barinov S V, Yashin A V 2019 *MATEC Web of Conferences* **297** 05012

[12] Kirichek A V, Barinov S V, Aborkin A V, Yashin A V 2018 *IOP Conf. Series: Mater. Science and Eng.* **327** 042011
[13] Vasiliev K V, Vill V I, Volchenko V N, and others 1978-1979 *Welding in mechanical engineering: Handbook in 4 volumes.* (Moscow: Mechanical Engineering)
[14] Porowski J S, O'Donnell W J, et al. 1990 *Nuclear Engineering and Design* **124**, pp. 91-100
[15] Eremjants V E, Niu V V 2016 *Modern problems of theory of mashines* **4(1)** pp. 123-127
[16] Eremyants V E, Niu V V 2016 Journal of Advanced Research in Technical Science **2** pp. 20-24
[17] Zaides S A, Kuang L Kh 2019 *IOP Conference Series: Materials Science and Engineering* **632(1)** 012115
[18] Melnik Y, Zaides S, Bobrovskij N, Cuong N, Levitskih O, Salov P and Lukyanov A 2019 *IOP Conference Series: Earth and Environmental Science* **315** 052080
[19] Lebedev V A, Ahmad E D, Sanamyan G V, Bagdasaryan T M 2019 *AIP Conference Proceedings* **2188 (1)** 020008
[20] Lebedev V A, Shishkina A P, Davydova I V, Morozova A V 2018 *IOP Conference Series: Materials Science and Engineering* **327** 042061

Regularities of technological inheritance in the categories of loading programs

V Yu Blumenstein, A A Krechetov

Department of Mechanical Engineering Technology, T.F. Gorbachev Kuzbass State Technical University, Kemerovo, Russia

Abstract. The paper presents an approach to describing technological inheritance as a pattern of changing loading programs under the influence of the loading history of the metal of the surface layer at the previous stages of processing. The loading program represents the regularity of the accumulation of deformation under conditions of a change in the stress state in the process of deformation and determines the regularities of the accumulation of metal damage during the processing and operation of the product. The proposed approach makes it possible to assess the accumulation of deformation and damage to the metal of the surface layer at all stages of the product life cycle.

1. Introduction

The increasing requirements for the durability of machine parts, including those operating under conditions of application of cyclic loads, require continuous improvement of methods and technologies, including hardening processing. In this case, the parameters of the quality of the surface layer after machining are important, including the parameters of the microstructure, roughness, hardening, residual stresses, etc. Ensuring the optimal ratio of these parameters requires the development of a methodology for predicting their formation at the processing stages and manifestation at the operation stage. This is possible based on taking into account subtle physical phenomena and evaluating the plastic flow of the surface layer material when exposed to cutting or deforming tools. In this case, it is important to transfer properties from previous operations to subsequent ones, i.e. accounting for technological inheritance (TI). This research area has been developed quite intensively over the past 50 years [1-3].

Further research and considering of TI made it possible to analyze various designs, technologies and manufactures of products from various materials at various stages of the life cycle. Therefore, the authors [4] investigated the surface quality and fatigue strength of structural titanium alloys. The regularities of the technological inheritance of such material properties as strain hardening, residual stresses, fatigue strength, etc. were established. The results made it possible to determine a process that is beneficial from the standpoint of fatigue strength and efficiency. In the work [5] it is shown that the physical integration of reproductive information, as well as sensory abilities in relation to the loads on the components during their life cycle should be implemented in the component itself. Technological inheritance was taken into account in the study of technological processes for the production of metal products in the form of a sequence of macroscopic, microscopic and submicroscopic transformations, typical for the initiated structure [6].

The method of nanostructuring deformation was used, which allowed the authors to formulate the foundations of a strategy for evaluating various multi-stage materials developing processes to achieve the required set of properties. Technological heredity in the form of a multilevel hierarchical system is used to describe the production of products from polymer composite materials (PCM) [7]. In this case,

products can be represented using graph theory, a distinctive feature of which is the implicit representation of the input-and-output relationship. The technological interrelationships of all individual transitions and operations are identified, which can contribute to either an increase or decrease in the performance characteristics of products.

The authors [8-9] propose to use the paradigm of technological inheritance to control production and use of components, analyze and use the collected data in the development of the next generation of a component, and to obtain an optimized structure. This approach allows you to create new generations of products based on the life cycle data of previous generations, which are more adapted to the new requirements of the actual environment. A.G. Korchunov [10] proposes a formalized concept of technological heredity in relation to quality control in equipment manufacturing processes; at the same time, TI is described using fuzzy models based on the theory of fuzzy sets. The article [11] is devoted to the influence of TI stress-strain state on the accuracy and dimensional stability of non-rigid parts such as shafts, which made it possible to determine the negative inherited factors and improve the process of manufacturing non-rigid shafts. A.N. Ovseenko performed an analysis of the quality of the surface layer of parts of low rigidity, taking into account the influence of TI [12]. The revealed regularities of TI made it possible to form the quality of the surface layer of parts, optimal from the point of view of fatigue life, at the stage of its technological design by performing a rational sequence of finishing and hardening, and thermal operations [13]. Some authors [14] believe that it is expedient to describe TI of the operational properties in the processes of manufacturing parts by a graph reflecting the transmission coefficients and the mutual influence of physical-and-mechanical and geometric parameters. The research made it possible to develop methods of technological management and control of the inheritance of the operational properties of parts, including measurements of the physical, mechanical and geometric parameters of the material and surface for the most critical parts. The work [15] shows the rational influence of TI in the processes of manufacturing and restoration of the rods and journals of the crankshaft. Based on the research results, it was recommended to monitor and control the plasma metallization operation to ensure stable hardness and thickness of the coating; to regulate the depth of cut and the feed of the grinding wheel with a uniform allowance at the final machining operations. The TI analysis during the restoration of the working surfaces of the crankshafts and camshafts of the engines made it possible to revise the sequence of technological transitions and regulate technological influences [16]. In [17], it was shown that the purposeful formation of the surface layer, taking into account TI, is one of the most important tasks of the technological process of manufacturing parts with nano- and submicrocrystalline structure.

Within the framework of this study, the apparatus of mechanics of deformable bodies was used to describe the state of the metal of the surface layer at the stages of the part's life cycle, including cutting, surface plastic deformation (SPD), and operational fatigue loading. This description is based on the concept of continuous accumulation of deformations and exhaustion of the plasticity margin of the metal of the surface layer of the part under the influence of loading programs at the stages of cutting, surface plastic deformation and operational fatigue loading [18-20].

When solving the problems of mechanics, the initial characteristics of the metal include hardening curve $\sigma_s = \sigma_s(\Lambda)$, limiting plasticity curve $\Lambda_p = \Lambda_p(\Pi)$, loading program as $\Lambda = \Lambda(\Pi)$, degree of depletion of the plasticity margin $\Psi = 0$ in the initial unhardened state, and the diagram of cyclic crack resistance $V = V(K)$, where σ_s – flow limit; Λ – shear strain rate; Λ_p – limiting shear strain rate for a given indicator of the stress state diagram Π; K – stress intensity factor; V – fatigue crack growth rate.

2. Loading programs at the stages of the life cycle

As noted, for a quantitative assessment of the loading history (technological inheritance), it was proposed to use the concept of the LP. The loading program describes the accumulation of deformations under the conditions of a changing stress state of the metal of the surface layer in the plastic deformation site at each stage of loading. Thus, the loading program reveals the physical laws of the formation of the surface layer. The convenience of its use in the theory of technological inheritance lies in the fact that it has a serious scientific basis, based on the fundamental section of physics – continuum mechanics; it

has a technological meaning, since it is completely determined by technological factors; it does not contradict the existing engineering parameters of the state of the surface layer, since the degree of deformation Λ has a relationship with hardness, and the stress state indicator Π – with residual stresses; it can be used for each operation (loading stage), including mechanical tooling and subsequent operational loading, which made it possible to perform an end-to-end analysis of all stages of processing and operation of parts from a single methodological standpoint; it has a clear connection with the degree of depletion of the plasticity of the metal.

In accordance with the established regularities, when developing a generalized model of LP, it was taken:

- the metal is in its original state (not hardened);
- the loading program consists of three stages of quasi-monotonic deformation at the stages of cutting and SPD, and *n* stages at the step of fatigue loading (where *n* is the number of loading cycles);
- the accumulation of deformations in the deformation site (at each stage) occurs continuously;
- the loading program at each next stage starts from some previously accumulated deformation value;
- the change in the sign of deformation at the boundaries of the stages occurs abruptly, respectively, the numerical values of the scheme indicator change abruptly;
- the type of LP at each next stage of loading is determined by the history of loading.

For example, for the stages of cutting and SPD, the generalized model of the loading program at three stages of quasi-monotonic deformation is as follows:

$$\Lambda_i = \frac{1}{\sigma_\Pi \sqrt{2\pi}} e^{-\frac{(\Pi_i - \Pi_j)^2}{2\sigma_\Pi^2}}, \tag{1}$$

where Λ_i and Π_i – respectively, the initial (current) values of the degree of shear strain and the scheme indicator at the stages of quasi-monotonic deformation; Λ_j и Π_j – respectively, the final values of the degree of shear strain and the indicator of the scheme at the stages of quasi-monotonic deformation; σ_Π^2 – variance of the scheme indicator. Initial state for unhardened metal $\Lambda_0 = 0$ and Π_0. Further adopted:

for the first quasi-monotonic stage:

$$\begin{cases} \Lambda_{|\,i=1} = 0 \\ \Pi_{|\,i=1} = -0{,}577 \\ \Lambda_{|\,j=1} = \Lambda_1 \\ \Pi_{|\,j=1} = \Pi_1 \end{cases}, \tag{2}$$

for the second quasi-monotonic stage:

$$\begin{cases} \Lambda_{|\,i=2} = \Lambda_1 \\ \Pi_{|\,i=2} = \Pi_1 \\ \Lambda_{|\,j=2} = \Lambda_1 + \Lambda_2 \\ \Pi_{|\,j=2} = \Pi_2 \end{cases}, \tag{3}$$

for the third quasi-monotonic stage:

$$\begin{cases} \Lambda_{|\,i=3} = \Lambda_1 + \Lambda_2 \\ \Pi_{|\,i=3} = \Pi_2 \\ \Lambda_{|\,j=3} = \Lambda_1 + \Lambda_2 + \Lambda_3 \\ \Pi_{|\,j=3} = -0{,}577 \end{cases}, \tag{4}$$

where indices 1, 2, and 3 refer to the corresponding quasi-monotonic stage.

The initial values of the scheme exponent and the shear strain rate certainly depend on the loading history and may differ from those accepted. Then the loading program of the first stage starts from a certain accumulated value of the shear strain rate. In accordance with this type of description, between the first and second stages, there is an abrupt change in the indicator of the stress state, which reflects a violation of the monotony of the process. As you can see, the loading program for each next stage starts with the scheme exponent corresponding to the end of the previous stage, and the deformation – from the previously accumulated level. As a result, deformation accumulates at the end of the second stage $(\Lambda_1 + \Lambda_2)$, and the third – $(\Lambda_1 + \Lambda_2 + \Lambda_3)$.

The starting value of the scheme exponent at the first stage and the finishing value at the third stage are taken equal to $\Pi = -0{,}577$. This corresponds to the concept of the beginning and end of the plastic flow of metal in a plastic deformation site, which is a characteristic of the beginning of plastic flow of material under conditions of simple compression. Depending on the type of the problem of mechanics being solved, these values may differ from those adopted in the proposed models.

The paper establishes the numerical values of the circuit indicators at the start and finish, as well as the dispersion of the scheme exponent at the corresponding stages of the loading program.

An analytical description of the loading program at the stage of fatigue loading is obtained; the numerical value of the scheme exponent is determined by the combined action of the tensors of the external load and residual stresses. In each cycle, there are several sections of quasi-monotonic deformation. Therefore, the loading program at the stage of cyclic life consists of a set of programs for loading the metal of the surface layer of the part in each cycle of fatigue loading. At the start of fatigue loading, only residual stresses act, during loading – residual and external cyclic stresses, and at the finish – only cyclic stresses. This is due to the gradual relaxation of residual stresses as deformations accumulate and the plasticity margin is depleted.

Different loading histories lead to different configurations of loading programs, which means different curvature of the lines, the slope of these lines to the coordinate axes, the range of values of the scheme exponent and the degree of deformation in each cycle.

Thus, the stage under consideration ends with the accumulation of the limiting deformation Λ_p, complete relaxation of residual stresses and complete depletion of the plasticity margin, i.e. $\Psi = 1$. This state corresponds to the first signs of material discontinuity in the form of defects with a size of (0.02-0.2) mm. The appearance of these visible defects means the beginning of a new stage – the stage of cyclic crack resistance, which means the work of a part with a crack.

The paper provides the analytical description of the loading programs for this stage in the categories of cyclic crack resistance diagrams in the form of $V = V(K)$.

3. Technological inheritance in the categories of loading programs

Based on the studies performed, the following possible options for taking into account the loading history (technological inheritance) in the categories of loading programs can be proposed.

The general description of the manifestation of heredity in the formation of the loading program of the *n*-th stage in the presence of *n* previous stages of loading is presented in the form:

$$LP_n = f_n\left(LP_{n-1}\left(LP_{n-2}\left(LP_{n-3}\ldots(LP_1)\right)\right)\right). \tag{5}$$

In other words, the loading program at a given quasi-monotonic stage is determined not only by the nature of the effect and accumulation of deformation at a given time, but by the entire history of the change in the function of the shear strain rate from the indicator of the stress state diagram.

It can be stated that LP_n is a functional from the load history described in the categories of loading programs, i.e.:

$$LP_n = F\Big|_{i=1}^{i=n-1}(LP)_i. \quad (6)$$

Studies have shown that the “older” the history, the less the influence of this loading history on the character of deformation accumulation and depletion of the plasticity margin at a given quasi-monotonic stage of loading. In this case, the peculiarity is that the loading program and the nature of the depletion of the plasticity margin at the previous loading stage have the greatest influence on the accumulation of deformations and the depletion of the plasticity margin at this stage. The role of more "ancient" stages is reduced to the influence of the total (accumulated) deformation and the degree of depletion of the plasticity margin on the formation of loading programs.

Let us formulate the general rules of technological inheritance using the concept of loading programs.

1. Technological inheritance is manifested in the formation of hereditary deformation sites at each stage of loading.

2. Technological inheritance manifests itself in the formation of hereditary loading programs depending on hereditary deformation sites, which act as a set of initial and boundary conditions in solving problems of deformation mechanics (Fig. 1).

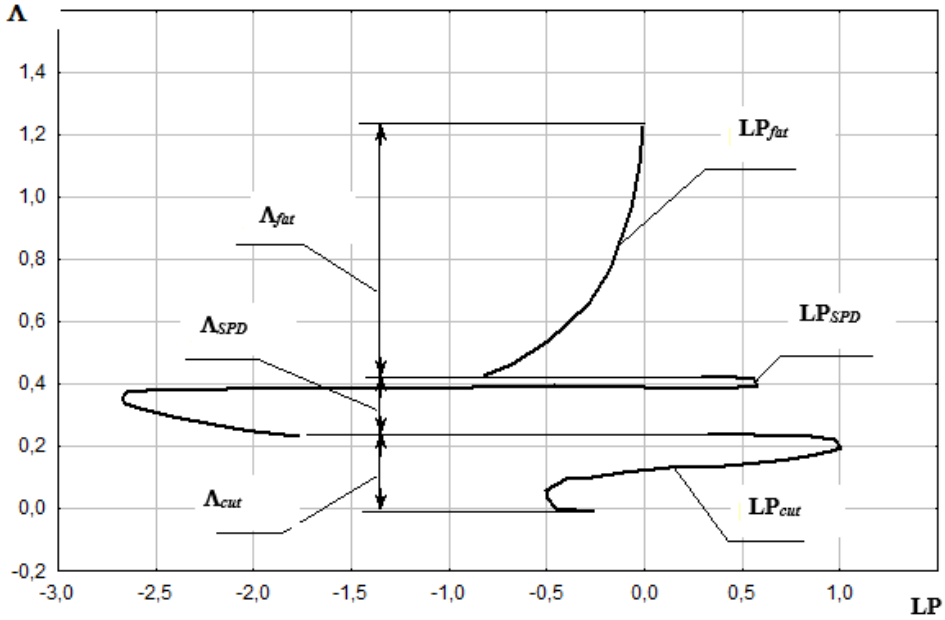

Figure 1. Loading programs for cutting stages, SPD and fatigue loading

3. The history of loading is described in program categories in the previous stages of loading.

4. Technological inheritance at each subsequent stage manifests itself through the transformation of loading programs in comparison with loading programs for a material that does not have a similar deformation history.

5. The inherited loading program "decays" in accordance with the exponential hereditary law, which manifests itself in the displacement of the LP to the region of more "rigid" loading schemes.

6. Each stage (and step) is characterized by its own rate of deformation accumulation in unreinforced material.

7. The rate of accumulation of deformations at each subsequent stage of loading "decays" (decreases) in accordance with the exponential hereditary law.

8. The set of analytical expressions for the LP rates at the previous stages constitute the core of the hereditary type functional (HTF) at this stage of loading in the categories of loading programs or the rate of depletion of the plasticity margin.

9. The influence of the change rate in LP on the HTF at the early stages is significantly lower than at the previous stage.

10. Residual stress state hereditarily depends on the total (accumulated) values of the degree of deformation and the rate of depletion of the plasticity margin.

Technological inheritance in a mechanical interpretation is the interaction of various sequential loading programs with a decreasing deformation site, when the accumulation of defects at each subsequent stage occurs under conditions of more severe loading schemes than at the previous one.

The history of deformation development is a general property described in the chronology of loading programs for the metal of the surface layer of the product.

Technological inheritance is a regularity that characterizes the ability of previous loading programs to influence the formation of loading programs at subsequent stages, and being a consequence of a certain history of loading the metal of the surface layer of the product.

Acknowledgments

The reported study was funded by RFBR, project number 20-08-00587.

References

[1] Yashchericyn P. I., Ryzhov E. V., Averchenkov V. I. (1977) *Technological inheritance in mechanical engineering* (Minsk: Nayka and tehnika) p. 256

[2] Dalsky A. M. (1975) *Technological reliability of high-precision parts of machinery* (Moscow: Mashinostroyeniye) p. 223

[3] Vasiliev A. S., Dalsky A.M., Klimenko S. A. et al. (2003) *Technological bases of machine quality management* (Moscow: Mashinostroyeniye) p. 256

[4] Grechishnikov V.A., Pautov G.A., Yurasov S.Yu., Yurasova O.I. (2017) Technological Inheritance in the Machining of Titanium Russian Engineering Research, Vol. 37, No. 3, p. 270–272.

[5] Roland Lachmayera, Iryna Mozgovaa, Wilfried Reimcheb, Frank Colditzc, Gregor Mrozb, Philipp Gottwalda (2014) Technical Inheritance: A Concept to Adapt the Evolution of Nature to Product Engineering. Procedia Technology, 15, p. 178 – 187 doi:10.1016/j.protcy.2014.09.070

[6] Korchunov Aleksey, Polyakova Marina, Gulin Aleksandr, Konstantinov Dmitriy (2014) Technological Inherited Connections in Continuous Method of Deformational Nanostructuring. Applied Mechanics and Materials Vol. 555, p. 401-405 doi:10.4028/www.scientific.net/AMM.555.401

[7] N.I. Baurova, V.A. Zorin, V.M. Prikhod'ko (2018) Graph Representation of Technological Inheritance in Structures Made of Polymer-Composite Materials. Polymer Science, Series D, Vol. 11, No. 2, pp. 225–229

[8] Lachmayer R., Mozgova I., Gottwald P. (2015) Formulation of Paradigm of Technical Inheritance, Proceedings of the 20th International Conference on Engineering Design (ICED15), July 27-30, 2015, Milan, Italy, Vol. 8, p. 271-278

[9] Philipp Wolniaka, Iryna Mozgovaa, Roland Lachmayera (2018) Concept for the Implementation of a Scaling Strategy into the Paradigm of Technical Inheritance. Procedia Manufacturing, 24, p. 80–85

[10] A.G. Korchunov (2009) Quality control of hardware products based on the use of fuzzy models to describe technological inheritance. Metallurgist, 53 (5), p. 290-295 doi:10.1007/s11015-009-9176-6

[11] G. V. Muratkin, V. A. Sarafanova. (2020) Influence of technological heredity of the stress-strain state on the accuracy of non-rigid parts. Problemy mashinostroeniya i nadezhnosti mashin, 1, p. 56–64

[12] Ovseenko A. N. (2011) Technological heredity, residual stresses and deformations of low-hard parts such as discs. Izvestiya vuzov. Severo-Kavkazskij region. Tekhnicheskie nauki, 1. p. 93-98
[13] Usoltseva I. I. (2010) Surface layer engineering and technological inheritance. Izvestiya Samarskogo nauchnogo centra Rossijskoj akademii nauk, T. 12, Vol. 4(3), p. 698-701.
[14] M. L. Kheifets, A. S. Vasiliev, S. A. Klimenko, L. Tanovich (2014) Technological inheritance of a set of operational parameters for the quality of material and surface of a part. Technologes of informations are in education, science and production, 2(7), p. 29-37.
[15] M. V. Podosetnikov, S. V. Semenov, G. B. Prement, V. A. Gaiko. (2015) Comparative analysis of technological inheritance of operational quality parameters in the production and restoration of the crankshaft. News of the national Academy of Sciences of Belarus. Series of physical and technical Sciences, 3, p. 23-30.
[16] M. L. Heifetz, N. L. Gretsky, G. B. Prement/ (2019) Technological inheritance of operational quality parameters in the life cycle of internal combustion engine parts. High-tech technologies in mechanical engineering, 7, p. 35-42.
[17] A. A. Simonova, N. V. Verezub. (2013) Technological inheritance of the nanocrystalline state of the surface layer of products at the stages of the life cycle. High technologies in Mechanical Engineering, 1 (23), p. 176-179.
[18] Blumenstein V.Yu., Smelyanskiy V.M. (2007) *Mechanics of technological inheritance during treatment and operation of machine parts* (Moscow: Mashinostroyeniye-1,) p 400
[19] Chizhik S. A. et al. (2019) *Quality assurance of products in technological complexes* (Minsk: Belarusian science) 248 p.
[20] Blumenstein V. (2015) *Mechanics of technological inheritance* (International journal for science and innovations for the industry. Innovations in discrete productions) Issue 2 (Sofia) p 18-21.

Study of the parameters of the pure iron structure after surface plastic deformation treatment with a complex-profile tool

V Yu Blumenstein, K S Mitrofanova

T.F. Gorbachev Kuzbass State Technical University, Department of mechanical engineering technology, Kemerovo, Russia

Abstract. The structure of pure iron after surface plastic deformation (SPD) by a multiradius roller (MR-roller) was studied using optical microscopy (OM) and atomic force microscopy (AFM). An optical microscope of reflected light is used to study the size and uniformity of grains and subgrains (*Neophot-21*). The fine structure of the sample surface was studied using an atomic force microscope (*Solver PH47-PRO*) contact method. The paper shows changes in the deformation relief of the material after processing with an MR-roller.

1. Introduction

Currently, a number of studies have proved the possibility of grinding the structure using surface plastic deformation (SPD) methods [1-7].

Thus, in the study [8], the possibility of grinding the structure was first discoveredbearing steel *100Cr6*after diamondburnishing. Klassen N. V., Kobelev N. P. and co-authors [9] showed the possibility of creating a gradient nanostructure using ball rolling (Ø3 mm). At the same time, as the depth increases even by 2-3 micrometers, the grain size increases several times. A team of authors [10] investigated the mechanical properties of alloy samples *PbTe*under torsion conditions with high hydrostatic pressure. A decrease in the grain size to 300 nm was found, which led to significant strain hardening without failure; this is evidenced by the results of nano - and microhardness tests.

Previously, metal studies were conducted after processing SPD with a multiradius roller (MR- roller) [11-13] and a number of effects that positively affect the mechanical characteristics are established: increasing microhardness; reducing roughness; implementing a loading scheme, according to which an intense hydrostatic pressure is created in the surface layer of the material, and others. However, the characteristics of the structure were not sufficiently studied.

One of the informative methods for studying the structure of materials on submicron spatial scales after various processing methods is atomic force microscopy (AFM) [14-22].

In this regard, the aim of the work is to study the elements of the material structure after processing the SPD with an MR-roller.

2. Materials and methods

Experimental studies consisted in processing a sample of pure iron with an MR-roller Ø 60 mm (fig.1, a) in the next mode: running-in force$P$=2700 H; traverse feeding$S$=0,07mm/ rpm; speed$n$=630 rpm/min. The multiradius roller has the shape of a working surface profile in the form of a combination of sequentially arranged deforming elements (DE) with radii of constant value located relative to each other with some displacement in the radial and axial directions: $Rpr1 = 1$ mmwith interference

$h_{d1} = 0{,}05$ mm;$R_{pr2} = 1$ mmwith interference$h_{d2} = 0{,}072$ mm; $R_{pr3} = 1$ mmwith interference $h_{d3} = 0{,}076$ mm;$R_{pr4} = 0{,}3$ mm with interference$h_{d4} = 0{,}099$ mm(fig.1, b) [23].

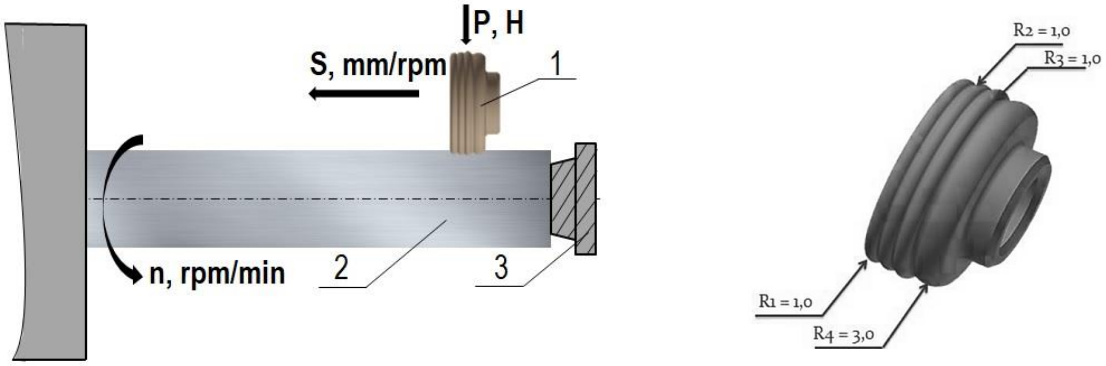

a) b)

Figure 1. Scheme SPD by MR-roller: a) Scheme of the machining process on a numerical control lathe (NCL), 1 – MR-roller, 2 – work piece, 3 – pressure center; b) General view of the working part MR-roller

After rolling the MR-roller, the metallographic section was prepared for optical (OM) and atomic force microscopy (AFM). Any defects were not allowed on the surface of metallographic sections.

The parameters of the structure of the studied sections, namely, grain and subgrain sizes and their homogeneity, were determined using a reflected light optical microscope "Neophot-21" at magnifications of 200 and 500 microns. The thin structure of the surface of the sections was studied using an atomic force microscope Solver PH47-PRO. To study the deformation relief of the surface, the "Contact Mismatch Method" mode was used» (*DFL*). The contact method is intended for more accurate detection of the deformation relief of cross-sections of sections by AFM method. The combination of contact mode with DFL allowed us to get additional information about the surface topography. The essence of the method is that during the scanning process, the current value of the signal associated with the cantilever bend is a signal of mismatch in the feedback circuit and contains additional information about the surface relief. This signal is used for a more accurate reproduction of the relief. During the scanning process, the adjusted speed of processing the mismatch signal was set so that the system worked out relatively smooth terrain features quickly enough and at the same time was slow enough to work out steeper sections. As a result, the mismatch signal weakly displays smooth terrain features (grains) and displays sharp roughness (inclusions and grain boundaries) with high contrast.

It should be noted that the working area of the cantilever of the device has dimensions of ~ 10 nm, and the characteristic distance between the probe and the sample surface in an atomic force microscope is 0.1-10 nm in order of magnitude. Thus, the use of V-shaped NSG10 (NT-DMT) cantilevers with a resonant frequency of 240 kHz and pyramidal probes, which have a ratio of the probe height to the base width of 3:1, the radius of the rounded end is less than 10 nm, the ratio of the probe height to the base width of 1:1, and the radius of the rounded end is less than 50 nm, allowed us to obtain a surface topography with a fairly high resolution.

The size of the scanning area during the study of the deformation relief varied from 25 to 50 microns, depending on the size of the object under study. The image of the surface within one scan was built line by line along 255 lines and remained constant for all subsequent images.

3. Results and discussion

Metallographic analysis showed that from the edge of the free surface (0.01-0.02 mm), an intensely deformed layer with a depth of 150 microns was detected (fig. 2-3). The average grain size in this area was ~ 20-25 microns: horizontally 2 ±1.5 microns, vertically ~ 20 ± 5 microns.

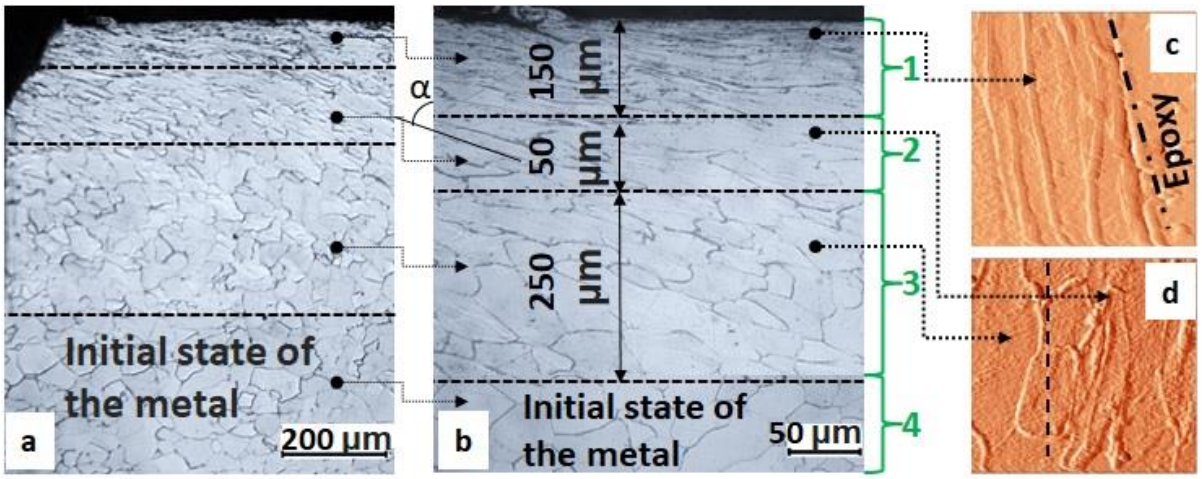

Figure 2. The structure of sample No. 1 after the SPD MR-roller (force of 2700 H):a – on an optical microscope, magnification of 200 times; b) on an optical microscope, magnification of 500 times, with sections: 1-intensely deformed layer (150 microns); 2-deformed layer (50 microns); 3-transition layer between the deformed and initial state (250 microns); 4-undeformed layer (initial state of pure iron); c, d – 2Dscan image of the deformed surface (AFM).

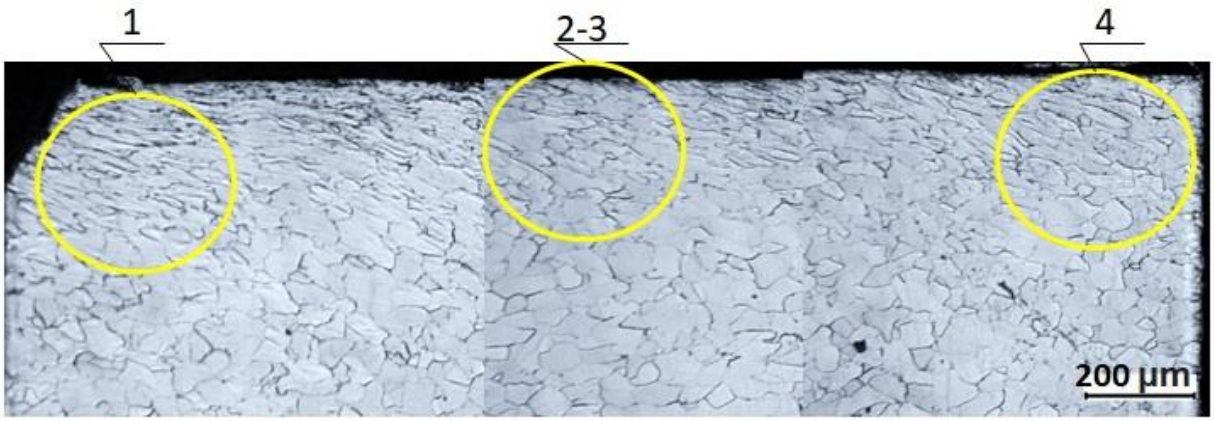

Figure 3. The structure of sample No. 1 after the SPD MR-roller, OM- images, zoom x200 microns. Areas of OM and AFM studies: 1 – hardened layer (left edge), 2-3 – hardened layer (center), 4 – hardened layer (right edge), 5 – non-hardened layer (middle of the sample)

Figures (2 in and 4) show that the grains are thin, but strongly elongated along the direction of metal flow, and in some places repeat the undulating contour of the working part of the MR-roller.

At a depth of 150 microns from the free edge of the surface, you can observe a deformed layer (50 microns deep), in which the grains are slightly less elongated in the direction of the metal flow and slightly enlarged. The average grain size was ~ 23-25 microns: horizontally 4 ±1.1 microns, vertically ~ 23 ± 1.8 microns.

At a depth of 200 microns from the free edge of the surface, a transition layer was found between the deformed and initial state (depth of 250 microns), in which the size of the deformed ferritic grain can be increased. The average grain size in this area was ~ 25-30 microns: horizontally 5 ±2.3 microns, vertically ~ 25 ± 3 microns.

The dimensions of the structure elements were taken from an atomic force microscope using the profilogram method (Fig. 4). the size of the studied area was 25 × 25 microns.

The height of the grain boundaries at point # 1 (Fig. 3) varies from 0.01 microns to 0.08 microns, and the width varies from 0.05 microns to 0.5 microns. The height of inclusions (chromium carbides) at point # 1 varies from 0.011 to 0.45 microns, and the width varies from 0.09 to 5 microns. The height of the grain boundaries at point 2-3 (fig. 3) varies from 0.01 to 0.015 microns, and the width varies from 0.5 to 1 microns.

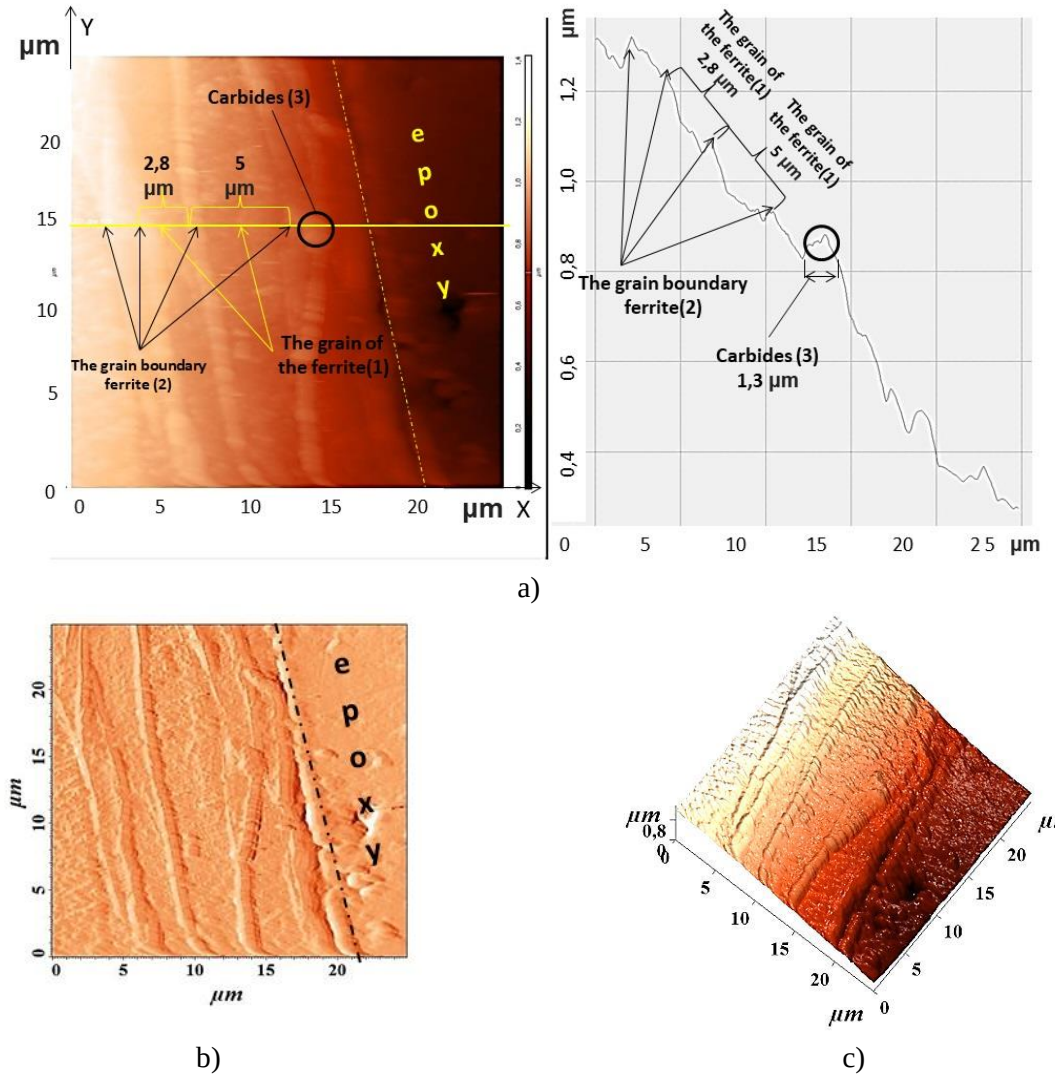

Figure 4. Scan images of the structure and topography of the Armco-iron surface:
a) 2D scan-image with a profilogram of the structure; b) 2D scan-image of the surface of the structure;
c) 3D scan-image of the surface relief

The height of inclusions (chromium carbides) at point # 2-3 varies from 0.04 to 0.8 microns, the width varies from 0.4 to 1 microns. The height of the grain boundaries at point # 4 (fig. 3) varies from

0.012 to 0.08 microns, and the width-from 0.04 to 0.5 microns. The height of inclusions (chromium carbides) at point # 4 varies from 0.04 to 0.8 microns, and the width – from 0.2 to 1 microns.

OM and AFM studies showed that a deformed layer up to 250 microns deep was detected from the edge of the free surface (0.01-0.02 mm). Figure 5 shows a graph of grain size distribution.

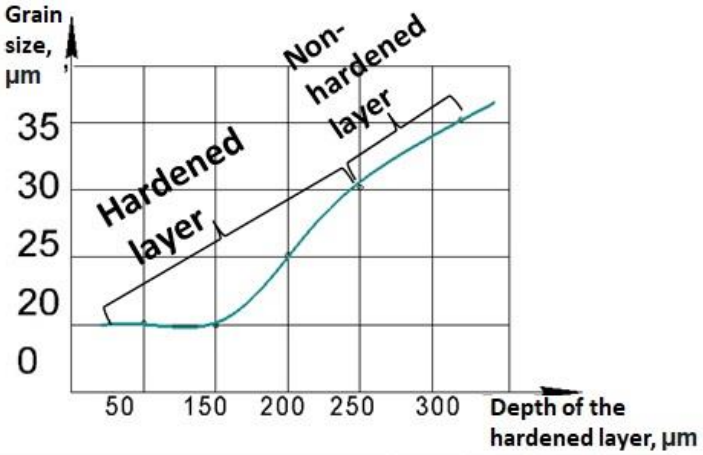

Depth of the deformed layer, μm	150	200	250	300
Minimum grain size, μm	20	21	25	34

Figure 5.Graph of grain size distribution over the depth of the hardened layer

4. Conclusion

The distinctive features of grains in the hardened region are their "elongated" shape in the direction of the MR-roller feed (the direction of the main deformation) and curved grain boundaries.

The authors believe that the identified effects will favorably affect the macromechanical characteristics of the hardened metal.

Acknowledgments

The research was carried out with the financial support of the RFFI in the framework of scientific project No. 20-08-00587.

References

[1] Pu Z., Song G.L., Yang S. 2012 *Grain refined and basal textured surface produced by burnishing for improved corrosion performance of AZ31B Mg alloy (*Corrosion Science. *Vol. 57)* p. 192-201.

[2] Priyadarsinia Ch., Venkata Ramanab V.S.N. et al. 2019 *Review on Ball, Roller, Low Plasticity Burnishing Process* (Materials Today: Proceedings 18) p. 5087–5099.

[3] Lowa K.O., Wongb K.J. 2011 *Influence of ball burnishing on surface quality and tribological characteristics of polymers under dry sliding conditions* (Tribology International. Vol. 44, Iss. 2) p. 144-153.

[4] Zhao J., Xia W., Li N., Li F. 2014 *A gradient nano/micro-structured surface layer on copper induced by severe plasticity roller burnishing* (Trans. Nonferrous Met. Soc. China.Vol. 24) p.441-448.

[5] Zaydes S.A., Hin Nguyen V. 2016 *Evaluation of surface layer quality in reversible surface plastic deformation* (Proceedings of Irkutsk State Technical University. no.6 (113)) c.34-40.

[6] Kuznetsova V.P., Tarasovc S.Yu., Dmitrievc A.I. 2015 *Nanostructuring burnishing and subsurface shear instability* (Journal of Materials Processing Technology. Vol. 217) p. 327-335

[7] Klassen N. V., Kobelev N. P. et al. 2017 *Ultrasound: problems, developments, prospects. Materials of the international scientific conference*. 18-20.
[8] Marcus L. I. and Smelyanskiy, V. M., 1971 Diamond smoothing (Moscow: NII-car industry). 117.
[9] Klassen N. V., Kobelev N. P. et al. 2017 Features of gradient nanostructures formed by deformation (Minsk: FTI NAS of Belarus. Modern methods and technologies for creating and processing materials: Collection of scientific papers In 3 books 1.) 111-121 p.
[10] Santamaría, J.A., Alkorta, J. et al. 2014 *Mechanical properties of PBTE processed by HPT (high-pressure torsion)* (Materials Science and Technology Conference and Exhibition, MS and T 2013, 4) p. 2623-2629.
[11] Blumenshtein, V. Yu., Kukareko V. A. et al. 2018 Study of the quality of the surface layer during processing with a multiradius deforming tool (Kemerovo: KuzSTU. Strengthening technologies and functional coatings in mechanical engineering. Proceedings of the IV all-Russian youth scientific and practical school with international participation.) 1-4 p.
[12] Mitrofanova K. S., Blumenshtein V. Yu. 2020 Study of the influence of technological factors of the process of surface plastic deformation with a complex-profile tool on the quality of the surface layer (Moscow: Innovative mechanical engineering publishing house. Strengthening technologies and coatings. V. 16. N. 2 (182)) 68-74 p.
[13] Mitrofanova K.S. 2020 *Study of Surface Layer Hardening after Treatment Complex Tool* (Switzerland:Trans Tech Publications Ltd. SolidStatePhenomena. Vol.303) p. 89-96.
[14] Danilenko N. I., Podrezov Yu. N. et al. 2014 creating a gradient structure under surface intensive plastic deformation (Ukraine: Ukrnii at. Technological system.Issue 1) pp. 31-38.
[15] Eremin E. N., Filippov Yu. O. et al. 2011 Investigation of the structure of the ZHS6U alloy by atomic force microscopy (Omsk scientific Bulletin. Mechanical engineering and machine science.Number 1 (97)) p .24-29.
[16] Shlyakhova G. V., Zuev L. B., Popova E. A. 2018 Estimation of structural parameters of carbon steel by AFM methods (Bulletin of Tambov University. Series: Naturalandtechnical Sciences, Vol. 23, no. 123, pp. 581-584.
[17] Zuev L.B., Shlyakhova G.V., Barannikova S.A., Kolosov S.*V. 2013* Microstructure of the elements of a superconducting alloy Nb-Ti cable (Russian metallurgy (Metally).Vol. 2013. № 3) p. 229-234.
[18] Morales-Rivas L., González-Orive A. et al. *2015 Nanomechanical characterization of nanostructured bainitic steel: Peak Force Microscopy and Nanoindentation with AFM* (Scientific Reports. vol. 5. num. 17164) p.1-16.
[19] Jelita Rydela J., Vegterb R.H. et al. 2016 *Tribochemistry of bearing steels: A new AFM methodto study the material–tribofilm correlation* (Tribology International. Vol. 98.) p. 74-81.
[20] Furustiga J., Dobrydenb I. et al. 2016 *The measurement of wear using AFM and wear interpretation usinga contact mechanics coupled wear model* (Wear. Vol. 350–351) p. 74-81.
[21] Morales-Rivas L., González-Orive A. and all. *2015 Nanomechanical characterization of nanostructured bainitic steel: Peak Force Microscopy and Nanoindentation with AFM* (Scientific Reports. vol. 5. num. 17164) p.1-16.
[22] Jäger J., Moosburger-Will J. et al. 2013 *Determination of nano-roughness of carbon fibers by atomic force microscopy* (Journal of Materials Science. Vol. 48) p. 6803–6810.
[23] Li R., Li Z., Pambou E. et al. 2018 *Determination of PMMA Residues on a Chemical-Vapor-Deposited Monolayer of Graphene by Neutron Reflection and Atomic Force Microscopy* (Langmuir. ACS Publications. Vol.34 (5)) p. 1827-1833.
[24] Patent RU N. 2557377. Multiradius rolling roller: Pat.no. 2557377 ROS. Federation. No. 2013135797/02; application 20.07.20153; publ. 27.05.2016, Byul. no. 27 (II CH.). 6 P.

Alignment the controlled trajectories of the machine's executive elements with the properties of the cutting system

V L Zakovorotny, V E Gvindjiliya

Don State Technical University, Rostov-on-Don Russia

Abstract. The article considers the task of alignment of trajectories of machine executive elements set by CNC-system with evolutionarily changing properties of the cutting process in such a way that minimize the wear intensity. Consequently not position optimizes in the space of the technological regimes but its trajectories are harmonized with changes of the properties of the manufacturing process. The definition of trajectories is considered from the point of view of synergetic mutually agreed interaction of external control and internal dynamic of the cutting system.

The study of alignment is performed on the basis of constructing mathematical models of a controlled dynamic system and performing digital experiments for a cutting system, the parameters of which and tool wear depend on the phase trajectory of the power of irreversible energy transformations in the cutting zone. Based on the research, new directions for improving the efficiency of cutting processes on CNC machines are proposed, which allow increasing the productivity of the cutting process without changing the requirements for the quality of manufacturing parts.

1. Introduction

After the publication of works on the synergy of interaction of systems with different environments [1,2] many issues of improving machine processing began to use the system-synergetic paradigm [3, 4]. It is uses to optimize of cutting process [5-14] take into account wear intensity of tools that is increment of wear along path. This is due to the fact that all the main characteristics of the process change with development of wear, including the quality indicators of parts. Therefore, the study of the influence of processing conditions, properties of tool materials, the lubricating and cooling medium, technological modes, tool geometry, vibrations, etc. on wear has been the subject of numerous studies [3-9]. It is show that the properties of the soldered zones change fundamentally, in which new dissipative structures are formed as power irreversible transformation increases. In particular, it is proved that when the speed increases, there is an optimal value at which the wear intensity is minimal. In this case, there is a transition from the prevailing adhesive to diffusion wear. This transition corresponds to a defined power of irreversible energy transformations, which is estimated by temperature during cutting. Therefore, article presents proven hypotheses about the existence of an optimal cutting temperature in which the wear intensity is minimal [15 - 18]. It is show that tool wear and indicators of the quality of manufacturing parts depend on the dynamics of the cutting process [19 - 29]. Moreover, the dynamic properties of the manufacturing process have the property of evolutionary changes [30 - 35]. Moreover, the evolution depends on the phase trajectory of the power of irreversible energy transformations in the cutting zone for perfect work. One of the manifestations of evolution is the development of tool wear [34, 35]. The improving the processing efficiency on the machines is the next step aimed at improving

the processing efficiency on the machines is to align the CNC program of the machine with the evolutionarily changing dynamic cutting system. The solution to this issue is discussed in the article.

2. Link between external control and internal dynamic of cutting system.

At first, the concept of the cutting system is described. Following coordinates of state and control are introduced (fig. 1).

1) Trajectories of executive elements of machines (TEEM) are set CNC-program and considered in the article as a control: $\mathbf{l} = \{l_1(t), l_2(t), l_3(t)\}^T \in \mathfrak{R}_{\mathbf{l}}^{(3)}$ and $\mathbf{V} = \{V_1(t), V_2(t), V_3(t)\}^T \in \mathfrak{R}_{\mathbf{l}}^{(3)}$. For turning machine these are trajectories of the cross-section $l_1(t)$ and longitudinal $l_2(t)$ calipers and the rotation of the spindle $l_3(t)$. Derivatives $\mathbf{dl/dt} = \mathbf{V}$ are the speeds of executive elements. The link of $V_3(t) = \pi D\Omega$ (Ω - cyclic frequency) is obvious. The phase trajectories $\mathbf{V}_{\mathbf{\Phi}} = \{V_1(l_1), V_2(l_2), V_3(l_3)\}^T$ correspond to vectors $\mathbf{l}$ and $\mathbf{V}$. For instance, the trajectory of speed of the longitudinal caliper V_2 along the axes l_2 is desired phase trajectory. Modern machines ensure with high accuracy correspond of the programmed trajectories to the real ones within the bandwidth of the servomotors.

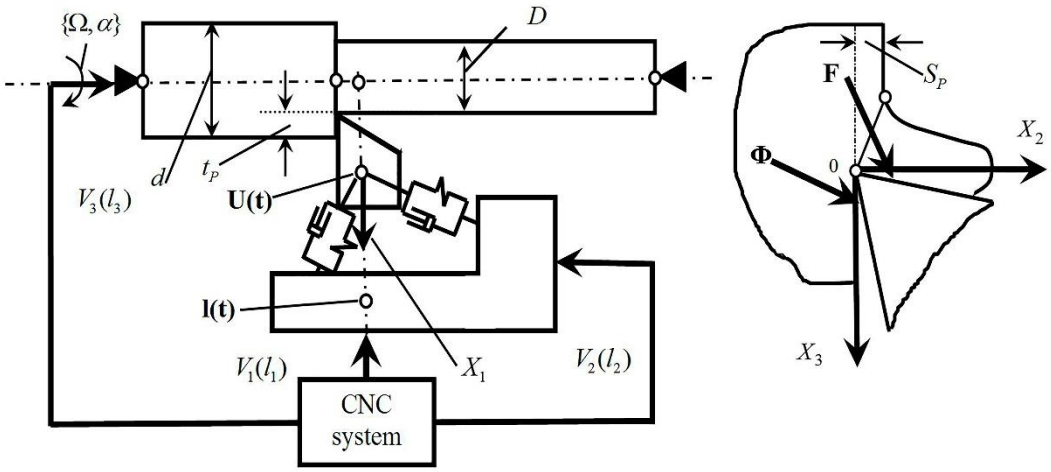

Figure 1. Scheme of controlled dynamic cutting system

2) The space of elastic deformation $\mathbf{X} = \{X_1(t), X_2(t), X_3(t)\}^T \in \mathfrak{R}_{\mathbf{X}}^{(3)}$. The tool deformations are considered in movable coordinates system $\mathbf{l}$ and relative to the machine carrier. Following the previously justified provisions, the dynamic subsystem of the tool in the movable coordinate system is represented as [35] (fig. 1)

$$\mathbf{m}\frac{\mathbf{d}^2\mathbf{X}}{\mathbf{dt}^2} + \mathbf{h}\frac{\mathbf{dX}}{\mathbf{dt}} + \mathbf{cX} = \mathbf{F}_{\mathbf{\Sigma}} \qquad (1)$$

where $\mathbf{m} = [m_{s,k}]$, $m_{s,k} = m, npu: s = k,\ m_{s,k} = 0, npu: s \neq k,\quad s,k = 1,2,3$ in kgf^2/mm, $\mathbf{h} = [h_{s,k}]$ in kgf/mm, $\mathbf{c} = [c_{s,k}]$, $s,k = 1,2,3$ в kg/mm - are symmetrical, positively definite matrices of inertial, speeds and elastic coefficients; $\mathbf{F}_{\mathbf{\Sigma}} = \{F_{\Sigma,1}, F_{\Sigma,2}, F_{\Sigma,3}\}^T \in \mathfrak{R}_{\mathbf{X}}^{(3)}$ - cutting force are represented in coordinates of state and control, allowing relate elastic deformation with $\mathbf{X}$ parameters of interacting subsystem and vectors $\mathbf{l}$ and $\mathbf{V}$. The force $\mathbf{F}_{\mathbf{\Sigma}}$ is presented as sum $\mathbf{F}_{\mathbf{\Sigma}} = \mathbf{F} + \mathbf{\Phi}$. There $\mathbf{F} = \{F_1, F_2, F_3\}^T \in \mathfrak{R}_{\mathbf{X}}^{(3)}$ and $\mathbf{\Phi} = \{\Phi_1, \Phi_2, \Phi_3\}^T \in \mathfrak{R}_{\mathbf{X}}^{(3)}$ is forces acting on the front and back face of the tool (fig.1). Following properties are taken into account for $\mathbf{F}$:

- $Mod[\mathbf{F}]$ depends on the area of the cut layer S;
- proportional coefficient ρ between $Mod[\mathbf{F}] = F_0$ and area S decrease in the medium speed range when the speed increases;
- lag of forces F_0 in relation to the variations of the area S is taken into account;
- orientation of forces in space with small variations $\mathbf{X}$ is represented by angular coefficients that is $\mathbf{F(t)} = F_0(t)\{\chi_1, \chi_2, \chi_3\}^T$. Then

$$T_0 dF_0 / dt + F_0 = \rho\{1 + \mu \exp[-\alpha(V_3 - dX_3 / dt)]\} t_P(t) S_P(t) \tag{2}$$

where T_0 - the time constant of chip formation $[\sec]$; ρ - pressure chips in the region of small velocities kg/mm^2; μ - dimensionless coefficient; α - coefficient that determines the decrease in forces as the speed increases.

Forces $\mathbf{\Phi}$ in the areas of contact of the back faces of the tool with the workpiece, disproportionately increase as they approach to the workpiece. Convergence is determined by changing the angles between the back faces (main $\beta_{\Sigma,2}(t)$ и auxiliary $\beta_{\Sigma,1}(t)$) the direction of the cutting speed. Back angle $\beta_{\Sigma,i}(t), i = 1,2$

$$\beta_{\Sigma,i}(t) = \beta_i + \Delta\beta_i(t), \quad i = 1,2, \tag{3}$$

where β_i - back angle of the tool in static; $\Delta\beta_i = arctg[V_2(t)/V_3(t)]$ - angle variations due to changes in $\mathbf{V}$ and $\mathbf{X}$. Value β_i and the radius at the top of the tool change due to the development of wear w. In addition, the dependence of the coefficient of friction on the speed is taken into account. Fair enough then

$$\begin{cases} \Phi_1 = \rho_0\{\int_{t-T}^{t} [V_2 - dX_2/dt]dt\} \exp[\alpha_1 \beta_{\Sigma,1}(t)]; \\ \Phi_2 = \rho_0[t_P^{(0)} - X_1(t)] \exp[\alpha_2 \beta_{\Sigma,2}(t)]; \Phi_3 = k_T[\Phi_1 + \Phi_2], \end{cases} \tag{4}$$

where α_1, α_2 - growth factors; ρ_0 - parameter that makes sense of stiffness; $k_T = k_T[1 + \mu_1 \exp(-\alpha_T V_3)]$ - coefficient of friction.

The vector of shape-generating movements $\mathbf{U(t)} = \{U_1, U_2, U_3\}^T \in \Re_{\mathbf{l}}^{(3)}$, which differs from TEEM in the values of elastic deformations $\mathbf{U(t)} = \mathbf{l(t)} - \mathbf{X(t)}$ is considered and also the relationship between $\mathbf{U(t)}$, $\mathbf{l(t)}$, $\mathbf{X(t)}$ and technological modes (5) is determined

$$t_P(t) = \int_0^t V_1(\xi)d\xi - X_1(t); S_P(t) = \int_{t-T}^{t} \{V_2(\xi) - v_2(\xi)\}d\xi; V_3(t) = \pi D\Omega - dX_3/dt; \mathbf{U(t)} = \mathbf{l(t)} - \mathbf{X(t)}, \tag{5}$$

where $t_P(t)$, $S_P(t)$, $V_P(t)$ - depth, feed and cutting speed; $T = (\Omega)^{-1}$ - part turnaround time. It follows from (5) that for longitudinal turning $\int_0^t V_1(\xi)d\xi = t_P^{(0)} = const$. The feed change function $S_P(t)$ is related to the feed speed and speed of deformation $v_2(t)$ by an integral operator whose integration time depends on the spindle speed.

Cutting has evolutionary properties manifesting in changing the parameters of dynamic coupling, in the development of tool wear, in changing the output characteristics of processing. Moreover, the driving force of these changes is the power of irreversible transformations in the cutting zone. Previously, methods allowing model evolution based on analysis $N(t)$ are developed. It relies on the Volterra integral equation of the second kind to calculate the reduced power $N^{(\Pi)}(t)$, in the function of which the wear rate changes [30 - 35]

$$N^{(\Pi)}(t) = \{N(t) + \eta \int_0^t W(t-\xi)N(\xi)d\xi\}, \quad v_w = \Phi(N^{(\Pi)}) \tag{6}$$

where η - coefficient $\left[\sec^{-1}\right]$; $W(t-\varsigma)$ - dimensionless core that simulates the dynamics of physical interactions that determine the wear rate v_w. If v_w is set, then $v_w^{(l)} = \partial w / \partial l$ and w wear are determined

$$v_w^{(l)} = v_w / (V_\Sigma),\ w(t) = \int_0^t v_w(\xi)d\xi \tag{7}$$

where $V_\Sigma = Mod[d\mathbf{L}^{(\Phi)} / dt]$ - projection of the total speed on the direction of travel.

Trajectories $w(t)$ correspond to trajectory of parameters system.

These models allow, first, to find out the dependence $\mathbf{U(t)}$ on $\mathbf{V_\Phi}$, $\mathbf{V}$ and $\mathbf{l}$. Secondly, to determine the change of the system dynamic and its evolution depending on the TEEM. Many of these issues were discussed earlier [20 - 23]. Current task is to alignment the external control is set by $\mathbf{V_\Phi}$, $\mathbf{V}$ and $\mathbf{l}$ and with the evolutionarily changing dynamic cutting system.

3. Optimal alignment strategy

The purpose of the cutting process is to produce a batch of parts of a requirement quality while minimizing the costs involved. One of the ways to achieve this goal is to alignment the TEEM $\mathbf{V_\Phi}$, $\mathbf{V}$ and $\mathbf{l}$ with the dynamic properties of the cutting process. For this, the state vector of the process $\mathbf{Q} = \{Q_1, Q_2, ...Q_n\}^T \in \Re_Q^n$, as well as the set of acceptable variations of its components $\mathbf{Q^{(0)}} = \{Q_1^{(0)}, Q_2^{(0)}, ...Q_n^{(0)}\}^T$ are introduced. The components of the vector $\mathbf{Q}$ are the assessment of condition process and the quality parameters of details are presented in the coordinate condition. The most important ones are highlighted below.

1) The first group of components $\mathbf{Q}$ describes the state of the processing process. Limited the most important characteristic of the power of irreversible energy transformations in the integration zone of the tool face and the workpiece Q_1 and used the known ideas about the existence of a power at which the wear intensity is minimal. Based on (4), the power $N_\Phi(t)$ and work $A_\Phi(t)$ in the contact area of the back face are calculated

$$N_\Phi(t) = \Phi_2(t)[V_2 - \frac{d(X_2)}{dt}] + k_T\Phi_2(t)[V_3 - \frac{d(X_3)}{dt}]\ ,\ A_\Phi(t) = \int_0^t N_\Phi(t)dt \tag{8}$$

Taken into account the forces caused by elastic deformations accumulated in the cutting zone during the transition of the processed material through the top of the cutting blade, and their power $N_F(t)$, that is

$$N_F(t) = k_F F_0(t)[V_3(t) - dX_3 / dt], \quad N(t) = N_F(t) + N_\Phi(t), \quad A(t) = A_F(t) + A_\Phi(t), \tag{9}$$

where k_F - transformation coefficient; $N(t)$, $A(t)$ - summary power and work. It is considered related to the contact length of the cutting blade with the workpiece. It follows from (8) and (9) that the conditions that minimize the intensity of wear depend on the speed and forces in the direction of speed.

2) The second group of vector $\mathbf{Q}$ components determines the parameters of accuracy and manufacturing quality. To do this, we can use the methods are developed by us for reconstructing the geometric topology of the surface is formed by cutting [31, 32]. Based on the topology using different functionals, adopted in engineering practice evaluation of the geometry of the microrelief, waviness are determined. In the article two estimates are considered:

$$Q_2(t) = \frac{1}{T^{(0)}} \int_{t-T^{(0)}}^{t} X_1(\xi) d\xi \; - \tag{10}$$

moving average in the time window $T^{(0)}$ of the deviation of the part radius from the set point of the tool tip in the machine bases;

$$Q_3(t) = \frac{1}{T^{(0)}} \int_{t-T^{(0)}}^{t} \{Q_2(\xi) - X_1(\xi)\}^2 d\xi \; - \tag{11}$$

moving average of the dispersion estimation of the microrelief.

The General algorithm for optimal alignment is represented below.

1. The surface length ΔL of each of the n same-type parts to be processed is set. Then the total length of the cutting surface of n parts whose parameters meet the quality requirements: $L = n\Delta L$.

2. For ΔL there is a set $\mathbf{V^{(i)}(\Delta L)} = \{V_1^{(i)}, V_2^{(i)}, V_3^{(i)}\}^T \in \mathfrak{R}_1^{(3)}$, $i = 1,2,...n$, which represents as piecewise constant approximation of the trajectories $\mathbf{V_\Phi}$.

3. For each ΔL, select $\mathbf{V^{(i)}(\Delta L)}$ meeting the conditions

$$\tilde{N}^{(i)} = \frac{1}{\Delta L} \int_0^{\Delta L} N^{(i)}(\xi) d\xi \Rightarrow N^{(onm.)} \text{ with } \mathbf{V_\Phi^{(i)}} \in \mathbf{V_\Phi^{(0)}}, L = n\Delta L = \max, \mathbf{Q} \in \mathbf{Q}^{(0)}, \tag{12}$$

where $N^{(onm.)}$ - the power value in the integration zone of the tool face and the workpiece, at which the tool wear intensity is minimal; $\mathbf{V_\Phi^{(0)}} = \{V_1(l_1), V_2(l_2), V_3(l_3)\}^T$ - the set of acceptable variations of TEEM. It is determined by the kinematic relations between the speeds of the Executive elements are dictated by the requirements of cutting kinematics and the restrictions on the trajectory are determined by the properties of the drives. It is clear from (12) that in order to determine the optimal conditions, the TEEM must change as the work progresses. As a result, we get their optimal trajectories are adapted to the evolutionary changes in the dynamic cutting system.

4. Instance of alignment the CNC-program with the dynamic properties of the cutting process. The example of the effectiveness of alignment TEEM with an evolutionarily changing dynamic system of turning a shaft made of austenitic steel is shown below. Turning by perishable plates of company SANDVIK Coromant, hard alloys GC2015, plates form - «W». Tool geometry: $\alpha = 2^0$; $\gamma = 6^0$; $\varphi = 90^0$. The axes of the ellipsoid of rigidity coincide with the axes of space $\mathfrak{R}^{(3)}$. Parameters of the tool subsystem: $m = \lfloor m_{s,k} \rfloor, m_{s,s} = m_0$, ; $h = \lfloor h_{s,k} \rfloor, h_{s,s} = h_0, \; m_{s,k} = h_{s,k} = 0, \; npu: s \neq k \; s,k = 1,2,3$; $h_0 = 5{,}0 \; кг \cdot с / мм$; $m_0 = 0{,}025 кг \cdot с^2 / мм$. The dynamic link parameters are shown in table.1. The parameters of the integral operator are shown in table 2. All parameters are given for a cutting speed of 1.2 m/s. In the future, the parameters varied.

Table 1. Parameters of dynamic link of the cutting process

$\rho, kg/mm^2$	$\alpha = \alpha_T, f/m$	$\mu = \mu_1$	$\rho_0, kg/mm$	k, mm^{-1}	$\alpha_1 = \alpha_2, rad^{-1}$	k_T
500	2,0	0,5	50,0	5×10-3	20	0,2

Table 2. Parameters change of the integral equation when variation of cutting speed

Speed, m/s	$T_1, [s]$	$T_2, [s]$	$\eta, [s^{-1}]$	$\eta_1, [kg^{-1}]$	$\eta_2, [kg^{-1}]$
1,2	13	30	0,5	8×10-6	3×10-6

Instances of evolutionary trajectories are shown in the fig.2. When processing in constant modes, there is usually a dynamic bifurcation of properties. As shown earlier [35], bifurcations of attractive sets of deformations are observed (an asymptotically stable point is transformed into a limit cycle and then chaotic dynamics is formed in the system). It is possible to improve the dynamic properties of the system based on the choice of parameters of the tool subsystem (compare the trajectories "1" and " 2 " in figure 2). Stability is lost in fig. 2, " 2 " – shows an example of forming a limit cycle. This significantly increases the work and power in the area of the intergrade of the back face of the tool with the workpiece (fig. 2, "3" shows an example of the formation of cyclic forces acting on the back face of the tool). According to our data when stability is lost the average power of irreversible transformations of the energy of the mechanical system supplied to cutting increases in all cases, so the necessary condition for optimal tool wear resistance is the asymptotic stability of the trajectories at all stages of evolution. In addition, due to the formation, for example, of a stable limit cycle (fig. 2, "2, 3"), a dynamic displacement of the equilibrium point Δ is formed in the system, which changes during the evolution of the system. The equilibrium point also shifts in the case of asymptotic stability of the evolutionary trajectory (Fig. 2 "4") due to an increase in all parameters depending on the volume of plastic deformation associated with the evolution of wear. The loss of stability as the cutting speed increases is determined based on a compromise between the two mechanisms. On the one hand, as the cutting speed increases the parameter T_0 from (2) decreases and, consequently, the stability margin increases. On the other hand, parametric self-excitation is observed due to an increase in the spindle speed.

Researches show that value of the cutting speed complying with maximum margin of stability, usually corresponds to the minimum intensity of tool wear. Examples show that the cutting system is characterized by the fact that all its main output characteristics change without external interference but due to irreversible transformations of the energy introduced into the cutting zone. The irreversibility of transformations determines the irreversibility of evolutionary changes in the properties of the system. For example, it is not possible to restore the geometry of a worn tool spontaneously, just as it is not possible to reverse changes in dynamic coupling parameters. In this regard, there is a work value after which at least one of the components of the vector $\mathbf{Q}$ achieves its terminal value $\mathbf{Q}^{(0)}$. Once achieved $\mathbf{Q}^{(0)}$, the tool system of the machine must be reconfigured. In our example, to provide $Q_2 \le Q_2^{(0)}$ and $Q_3 \le Q_3^{(0)}$, it is necessary to reduce the area of the cut layer, that is the amount of feed, in the course of evolution.

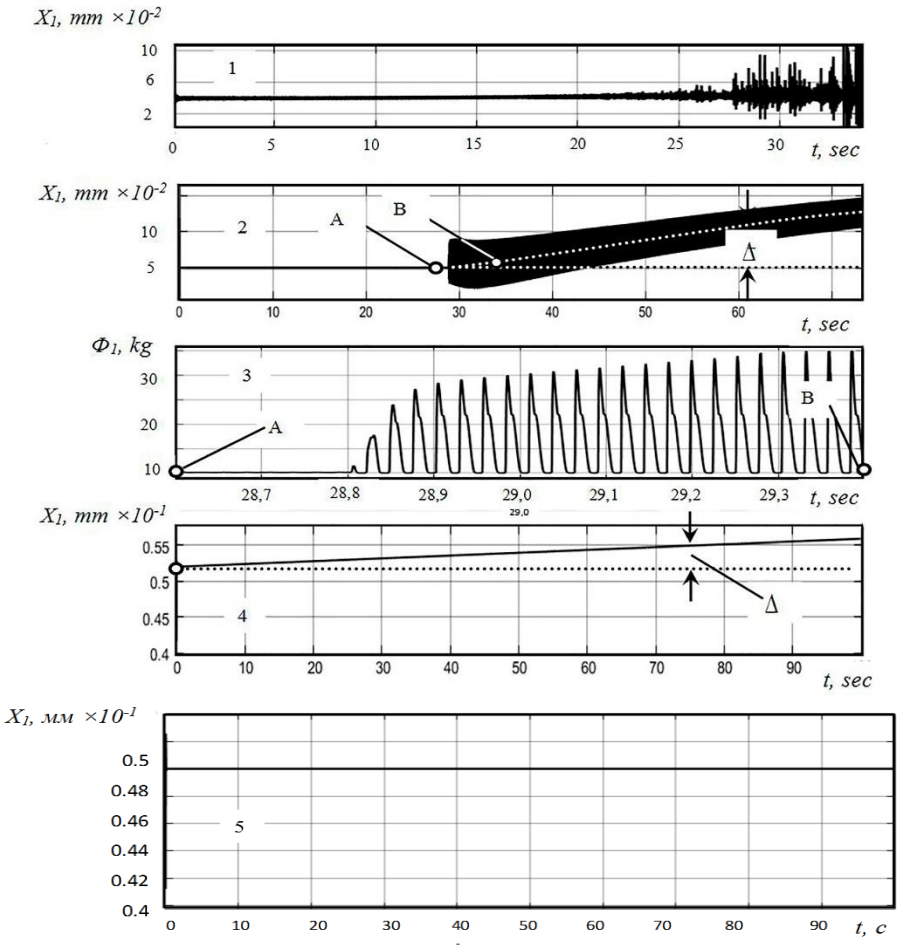

Figure 2. An example of changes of the trajectory of the deformation displacement in the direction of X_1 and force Φ_1. **1**- constant cutting conditions: $S_P^{(0)} = 0{,}1mm$, $V_3^{(0)} = 1{,}2m/s$, the stiffness parameters $c_{1,0} = 3000\,kg/mm$, $c_{2,0} = 1000\,kg/mm$, $c_{3,0} = 600\,kg/mm$. 2 - constant cutting conditions: $S_P^{(0)} = 0{,}1\,mm$, $V_3^{(0)} = 1{,}2\,m/s$, the stiffness parameters $c_{1,0} = 3000\,kg/mm$, $c_{2,0} = 2000\,kg/mm$, $c_{3,0} = 1000\,kg/mm$. 3 – a fragment of the strength Φ_1 in section formation of a limit the formation of the limit cycle (section A-B) for the curve 2. 4 - the trajectory with the modes corresponding to paragraph 2, but with a cutting speed 1,6 m/s. 5 - in contrast to 4 it is further reduced $S_P(l)$

In this section, we analyze the effectiveness of control algorithms (fig. 3). Path $L = \max$ is passed by the tool under the condition $\mathbf{Q} \in \mathbf{Q}^{(0)}$ that there is an optimality condition. Therefore the concept of critical wear is replaced by the concept of the terminal state of the cutting system. Three algorithms of alignment of CNC-program with dynamic properties of cutting process during the evolution are considered.

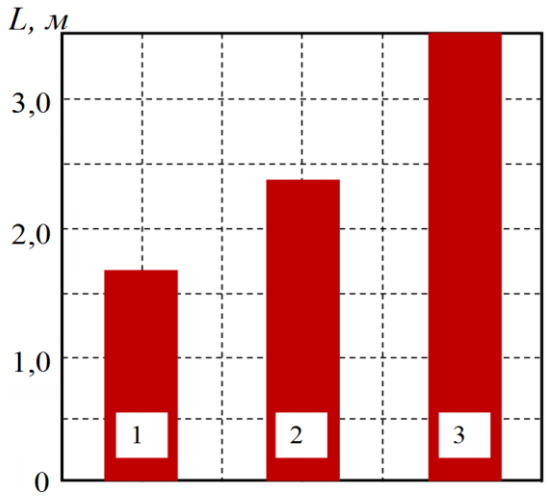

Figure 3. Compare of effectiveness of algorithms

The first algorithms. The cutting speed and the feed speed corresponding to cutting speed remain constant and equal $S_P^{(0)} = 0{,}1mm$, $V_3^{(0)} = 1{,}2\ m/s$. Second algorithm. The cutting speed decreases linearly from a value $V_3^{(0)} = 1{,}4\ m/s$ to $V_3^{(0)} = 0{,}9\ m/s$, and the feed remains constant $S_P^{(0)} = 0{,}1\ mm$. Third algorithm. The cutting speed decreases linearly from a value $V_3^{(0)} = 1{,}4\ m/s$ to $V_3^{(0)} = 0{,}9\ m/s$, and the feed also decreases from $S_P^{(0)} = 0{,}1\ mm$ to $S_P^{(0)} = 0{,}05\ mm$. The results of algorithms based on the adjustment of all components of the vector to the processing conditions that change in the course of evolution are shown in fig. 3 and allow to increase the number of processed parts without changing the tool system by a factor of (1.5 – 2.0).

5. Conclusion

The evolution of the properties of a dynamic cutting system depends on its initial parameters and uncontrolled disturbances depending on the accuracy of the machine and its current state. Depending on the initial parameters in the course of evolution depending on the phase trajectory of the power of irreversible transformations for perfect work, the output characteristics of processing change, considered in the unity of the geometric quality of the surface formed by cutting and the intensity of tool wear. This unity characterizes the state vector of the process. Its components can reach their limit value (the limit set) in the course of evolution. Moreover, the limit set, as a rule, does not correspond to the maximum wear of the tool. The parameters of the dynamic connection is formed by cutting depend not only on the properties of interacting subsystems, such as tool geometry, but to a greater extent on the technological modes are set by the machine's TEEM, in particular, the CNC program. Therefore, when designing technological manufacturing process, including the CNC program, it is necessary to alignment the trajectories are set by the external control with the dynamics of the system that characterizes the internal control. The solution to this problem allowing to increase the processing efficiency, is nothing other than providing a condition for interaction between external and internal controls, that it is known in synergetic.

The study was funded by RFBR according to the research project № 19-08-00022.

References

[1] Haken H 2006 *Information and Self-Organization* Amsterdam, Macroscopic Approach to Complex Systems, p 251, ISSN: 0172-7389

[2] Prigogine I, George C 1983 *The Second Law as a Selection Principle: The Microscopic Theory of Dissipative Processes in Quantum Systems* Proceedings of the National Academy of Sciences, 80, pp 4590-4594 doi: 10.1073 / pnas.80.14.4590

[3] Zakovorotnyj V L, Shapovalov V V 2005 *Dinamika transportnyh tribosistem [Dynamics of transport tribosystem]* Sborka v mashinostroe-nii, priborostroenii = Assembly in machine-building, instrument-making, 12, pp 19-24

[4] Ryzhkin A A 2019 *Sinergetika iznashivaniya instrumental'nyh materialov pri lezvijnoj obrabotke* [Synergetics of tool wear in blade processing]. Rostov-on-Don, Don state technical University Publ. p 289, ISBN 978-5-7890-1669-5

[5] Starkov V K 2009 *Fizika i optimizaciya rezaniya materialov* [*The Physics and optimization of cutting of materials]* Moscow, Mashinostroenie Publ. p 640, ISBN 978-5-94275-460-0
[6] Makarov A D 1976 *Optimizaciya processov rezaniya [Optimization of cutting processes]*. Moscow, Mashinostroenie Publ. p 278
[7] Vasin S A, Vereshchaka A S, Kushner V S 2001 *Rezanie metallov: termomekhanicheskij podhod k sisteme vzaimosvyazej pri rezanii [Metal cutting: a thermomechanical approach to the system of interrelations in cutting]*. Moscow, Bauman Moscow state technical University Publ. p 447
[8] Ostafiev V A 1976 *Fizicheskie osnovy processa rezaniya metallov [Physical basis of the metal cutting process]*. Vyscha SHKOLA Publ. p 136
[9] Migranov M SH 2006 *Issledovaniya iznashivaniya instrumental'nyh materialov i pokrytij s pozicij termodinamiki i samoorganizacii [Research of wear of tool materials and coatings from the positions of thermodynamics and self-organization]* Izvestiya vuzov. Mashinostroenie = University news. Engineering, 11, pp 65 – 71
[10] Gomez-Solano J R 2015 *Non-equilibrium work distribution for interacting colloidal particles under friction* New J.Phes., 045026, pp 1 – 13 doi: 10.1088 / 1367-2630 / 17/4/045026
[11] Banjac M 2014 *Friction and Wear Processes Thermodynamic Approach* Tribology in Industre, 36, 4, pp 341-347
[12] Abdel-Aal H A 2013 *Thermodynamic modelling of wear* Encyclopedia of Tribology, pp 3622-3636
[13] Duyun T A, Grinek A V, Rybak L A 2014 *Methodology of manufacturing process design, providing quality parameters and minimal costs* World Applied Sciences Journal, 30 (8), pp 958-963 doi: 10.5829 / idosi.wasj.2014.30.08.14120
[14] Mukherjee I, Ray P K 2006 A review of optimization techniques in metal cutting processes // Computers and Industrial Engineering, 50, 2, pp 15-34
[15] Karimov I G 2012 *Vliyanie temperatury rezaniya na energeticheskie parametry kontakta instrumenta s detal'yu [Influence of the cutting temperature on the energy parameters of the tool contact with the part]* Vestnik UGATU = UGATU Bulletin, 16, 44(49), pp 85 – 89
[16] Postnov V V, Shafikov A A 2012 *Razrabotka evolyucionnoj modeli iznashivaniya rezhushchego instrumenta dlya upravleniya processom obrabotki [Development of an evolutionary model of cutting tool wear to control the processing process]* Vestnik UGATU = UGATU Bulletin, 11, 2 (29), pp 139 – 146
[17] *Sposob opredeleniya optimal'noj skorosti rezaniya v processe metalloobrabotki* [Method for determining the optimal cutting speed in the process of Metalworking] Rassian patent: RU 2538750C2 from 23.05.2013 / Kozochkin M P , Fedorov S V , Tereshin M V
[18] Zariktuev V C 2009 *Avtomatizaciya processov na osnove polozheniya ob optimal'noj temperature rezaniya [Automatization of process based on concept of optimal cutting temperature]* Vestnik UGATU = UGATU Bulletin, 12, 4, pp 14 – 19
[19] Kudinov V A 1967 *Dinamika stankov [Dynamics of machine tools]*. Moscow, Mechanical engineering Publ., p 326
[20] Voronov S A, Kiselev I A 2017 *Nelinejnye zadachi dinamiki processov rezaniya [Nonlinear problems of cutting process dynamics]*. Mechanical engineering and engineering education, 2 (51), pp 9-23
[21] Gouskov A M, Voronov S A, Paris H, Batzer S A 2002 *Nonlinear dynamics of a machining system with two interdependent delays* Commun. Nonlin. Sci. Numer. Simul, 7, pp 207–221
[22] Warminski J, Litak G, Cartmell M P, Khanin R, Wiercigroch M 2003 *Approximate analytical solutions for primary chatter in the non-linear metal cutting model* Journal of Sound and Vibration, 259 (4), pp 917–933, doi: /10.1006/jsvi.2002.5129
[23] Stepan G, Insperge T, Szalai R 2005 *Delay, Parametric excitation, and the nonlinear dynamics of cutting processes* International Journal of Bifurcation and Chaos, 15, no 9, pp 2783–2798, doi: 10.1142/S0218127405013642

[24] Balachandran B 2001 *Nonlinear dynamics of milling process* Philosophical Transactions of The Royal Society A Mathematical Physical and Engineering Sciences, 359(1781), pp 793–819, doi: /10.1098/rsta.2000.0755
[25] Corpus W T, Endres W J 2004 *Added stability lobes in machining processes that exhibit periodic time variation – Part 1: An analytical solution* Journal of Manufacturing Science and Engineering, 126, pp 467-474, doi: 10.1115/1.1765137
[26] Peigne G, Paris H, Brissaud D, Gouskov A 2004 *Impact of the cutting dynamics ofsmall radial immersion milling operations on machined surface roughness* International journal machine tools manufacture, 44, pp 1133-1142, doi: 10.1016/j.ijmachtools.2004.04.012
[27] Szalai R, Stepan G, Hogan S J 2004 *Global dynamics of low immersion high-speed milling* Chaos, 14, pp 1069-1077, doi: /10.1063/1.1807395
[28] Hasnul H 2011 *The Parametric Effect and Optimization on JIS S45C Steel Turning* International Journal of Engineering Science and Technology, 3, no 5, pp 4479-4487
[29] Rusinek R, Wiercigroch M, Wahi P 2014 *Influence of tool flank forces on complex dynamics of a cutting process* International Journal of Bifurcation and Chaos, 24 (9), pp 189-201, doi: 10.1142/S0218127414501156
[30] Zakovorotny V L, Gvindjiliya V E 2019 *Evolution of the dynamic cutting system with irreversible energy transformation in the machining zone* Russian Engineering Research, 39, no, 5. pp 423-430
[31] Zakovorotny V L, Gvindjiliya V E 2018 *Influence of spindle wobble in turning on the workpiece's surface topology* Russian Engineering Research, 38, 10, pp 818-823
[32] Zakovorotny V L, Gvindjiliya V E 2018 *Influence of spindle wobble in a lathe on the tools deformational-displacement trajectory* Russian Engineering Research, 38, 8, pp 623-631
[33] Zakovorotnyj V L, Gvindzhiliya V E 2018 *Bifurkacii prityagivayushchih mnozhestv deformacionnyh smeshche-nij rezhushchego instrumenta v hode evolyucii svojstv processa obrabotki [Bifurcations of attracting sets of deformation spaces of a cutting tool during the evolution of processing properties]* Izvestiya vysshih uchebnyh zavede-nij. Prikladnaya nelinejnaya dinamika = Proceedings of higher educational institutions. Applied nonlinear dynamics, 26, 5, pp 20-38. doi: /10.18500/0869-6632-2018-26-5-20-38
[34] Zakovorotnyj V L, Gvindzhiliya V E 2019 *Zavisimost' iznashivaniya instrumenta i parametrov kachestva formiruemoj rezaniem poverhnosti ot dinamicheskih harakteristik [Dependence of tool wear and quality parameters of the surface formed by cutting on dynamic characteristics]* Obrabotka metallov (tekhnologiya, obo-rudovanie, instrumenty) = Metal Processing (technology, equipment, tools), 21, 4, pp31-46, doi: /10.17212/1994-6309-2019-21.4-31-46
[35] Zakovorotnyj V L, Gvindzhiliya V E 2020 *Svyaz' samoorganizacii dinamicheskoj sistemy rezaniya s izna-shivaniem instrumenta [Connection of self-organization of the dynamic cutting system with tool wear]* Izvestiya vuzov. Prikladnaya nelinejnaya dinamika = University news. Applied nonlinear dynamics, 28, 1, pp 46-61, doi: /10.18500/0869-6632-2020-28-1-46-61

Identification of optimal switching coordinates of processing cycles on metal cutting machines

V L Zakovorotny, V E Gvindjiliya

Don State Technical University, Rostov-on-Don, Russia

Abstract. The traditional algorithm of replacing tools and readjusting tool subsystems bases on determining the critical wear of the tool where the evaluation for example bases on statistical characteristics of the development of wear. Many methods for diagnosing are developed, including those based on observing the dynamic properties of the cutting process. As a rule, these methods use information about the evolutionary rearrangement of process properties as the wear develops. In recent years, algorithms for changing the programmed trajectories of the machine's Executive elements in accordance with the evolutionarily changing properties of the cutting system were used to improve efficiency. In this case, for example, the cutting speed is characterized by a certain optimal trajectory, and it decreases as wear develops. Therefore, there is a problem of determining the coordinates of the tool replacement by the criterion of the minimum cost of production. In this case, between the switching of cycles, the trajectory of speed of the cutting path is maintained such that the power of irreversible transformations of the applied energy in the cutting zone remains optimal and corresponding to the minimization of the wear intensity. Cycle switching coordinates should be selected based on the criterion of minimizing the reduced cost of manufacturing a batch of parts. The article is devoted to the definition of these coordinates.

1. Introduction

The synergetic approach to the analysis of complex systems [1-5], including the systems such as metal-cutting machines, led to the formation of new views on the optimization of cutting processes. It was shown that the cutting process is a complex dynamic system [5], in which it is necessary to analyze external disturbances, controls in the form of the trajectories of the Executive elements of the machine set by the CNC program, and the evolutionary restructuring of properties. It is the evolution depending on the phase trajectory of the power of irreversible transformations of the energy supplied to cutting for perfect work, that causes the development of tool wear and changes in the output properties of processing [9 - 22]. It is shown [13-18] that when the speed increases, there is an optimal value for it, at which the wear intensity is minimal. There is a transition from the prevailing adhesive to diffusion wear. This transition corresponds to a well-defined power of irreversible energy transformations, which is estimated by temperature during cutting. Therefore, hypotheses about the existence of an optimal cutting temperature at which the wear intensity is minimal have been put forward and are confirmed by practice [17, 18]. It is proposed to choose the cutting speed such that in the zones of contact of the tool faces with the workpiece, the optimal value of the power of irreversible energy transformations is maintained [5]. In this case, the cutting speed and the corresponding speed of the caliper must be reduced indefinitely. This is due to the peculiarities of the system's evolution [19-22] In this regard, there is a problem of determining such coordinates of switching processing cycles, in which the cost of

manufacturing a batch of parts is minimal. The purpose of the article is to develop mathematical techniques and techniques to determine these coordinates.

2. Mathematic description

Given: the general cutting path L, which is determined by the sum of the processed surfaces of parts (Fig. 1). Thus, the path L is equivalent to a batch of parts. The task of determining the coordinates of tool replacement $l^{(i)}$ along the trajectory "l" is considered ($l^{(1)} = l_1, l^{(2)} = l_1 + l_2, l^{(3)} = l_1 + l_2 + l_3, \ldots$ $l^{(n-1)} = L - l_n$), at which the cost of manufacturing a batch of parts is minimal.

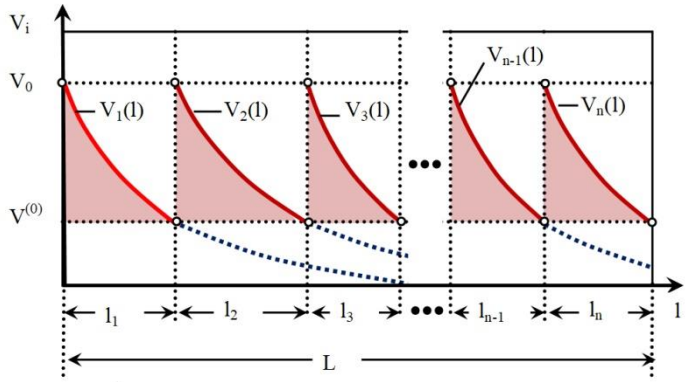

Figure 1. Scheme of determining switching coordinates of processing cycles

These coordinates are called switching coordinates of processing cycles by analogy of the switching coordinates in optimal fast-action systems [23-26]. The speed trajectory Vi (l) along the path is calculated in such a way that the intensity of tool wear within the speed is minimal. The trajectory calculation method is based on the hypothesis that the wear intensity relates to the power of irreversible energy transformations. The optimal power corresponds to the optimal temperature – the area of conversation from the prevailing adhesive to diffusion wear of the tool [5]. Consequently, the functions for changing the cutting speed along the path $V_i(l)$ and the total cutting path are set (fig. 1), i.e.

$$L = \sum_{i=1}^{i=n} l_i \tag{1}$$

Expenditure "$З$" on the manufacturing of batch of parts with set speed $V_i(l)$ is

$$З = c_1 \sum_{i=1}^{i=n} \int_0^{l_i} \frac{d\xi}{V_i(\xi)} + (n-1)c_2 \tag{2}$$

where c_1 is the cost of the machine minute $[rub/\min]$; c_2 - the cost of replacing the tool with its installation and configuration. The solution of the problem is reduced to calculating l_i when $З \Rightarrow \min$

3. Necessary optimality conditions

The irreversibility of the energy conversion leads to the fact that the cutting speed is a monotonously decreasing function where the tool wear is minimal. In this case, the optimal coordinates correspond to equal cutting speeds. Moreover, these speeds are equal for different functions of changing the cutting speed. This statement is discussed below.

In the solving of the problem the number of switching n are fixed, the coordinates of the switch are determined for given «n» и «L» subject to (2) $\Im(l_1,l_2,...l_n)=\sum_{i=1}^{i=nl_i}\int_0\frac{d\xi}{V_i(\xi)}=\min$ and implementation of requirement (1). Obviously, the problem of determining the optimal coordinates does not make sense if the condition (1) isn't imposed and «n» isn't fixed. If $\Im(l_1,l_2,...l_n)=\Im_i$ is fixed, then the resulting surface may intersect with a hyperplane $L(l_1,l_2,...l_n)=\sum_{i=1}^{i=n}l_i$ (fig. 2). If $\Im_i$ reduces, then the lines of intersection of the surface $\Im_i(l_1,l_2,...l_n)$ with the hyperplane represent convex closed trajectories that degenerate into a point $\Im_0(l_1,l_2,...l_n)$ whose coordinates are the optimal coordinates for switching cycles. Moreover, the surfaces $\Im_i(l_1,l_2,...l_n)$ are convex as the work is performed, wear only increases. This is the optimal point at which the hypersurface $\Im(l_1,l_2,...l_n)$ touches the hyperplane $L(l_1,l_2,...l_n)$. Therefore, it is true for this point $\Im_0(l_1,l_2,...l_n)$

$$\partial\Im(l_1,l_2,...l_n)/\partial l_i\equiv\partial L(l_1,l_2,...l_n)/\partial l_i \tag{3}$$

From this it follows

$$V_i(l_i)=V_s(l_s),\quad i,s\Rightarrow 1,2,3...n. \tag{4}$$

Condition (4) allows significantly simplifying the calculation of optimal coordinates, as well as physically implementing a control system providing an optimality condition. Moreover, this condition takes into account the physical and economic requirements for optimality.

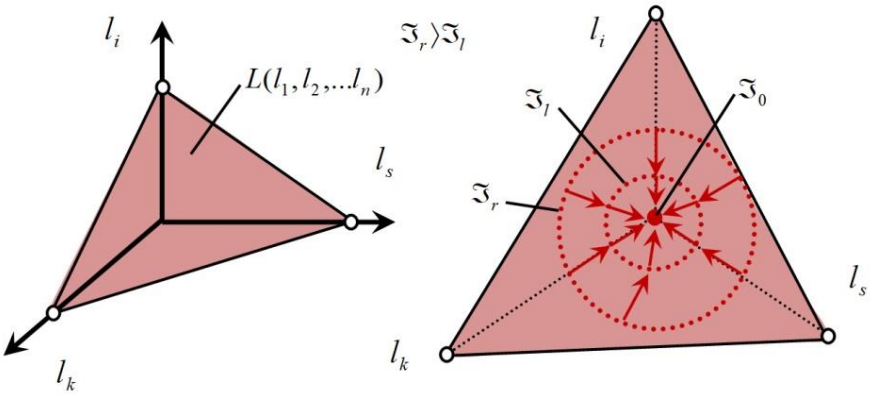

Figure 2. The intersection of a hyperplane $L(l_1,l_2,...l_n)$ and a hypersurface $\Im(l_1,l_2,...l_n)$

The optimality condition is considered sufficient if additionally n is defined from (2) for which $3\Rightarrow\min$. Previously [13-18] an approximation of the speed change along the cutting path was proposed in the form of an exponential function

$$V^{(i)}(l_i)=V_0\exp[-\alpha_i l_i], \tag{5}$$

where V_0 - initial speed value $[m/\sec]$; α_i - parameter $\left[\min^{-1}\right]$.

It is shown that the trajectories (5) determined by the evolutionary properties of the dynamic cutting system are sensitive to small variations in the initial parameters of the system and to uncontrolled perturbations, for example, beats [11]. Therefore, if the initial speed is constant, the parameters α_i and

length l_i may vary. The proved condition (4) and the function (5) are taken into account, then the length l_i of each segment "$n-1$" is

$$l_i = \frac{\alpha_i L}{\sum\limits_{s=1}^{s=n} \alpha_s}. \tag{6}$$

4. Instance of determining the optimal coordinates for switching processing cycles

The instance of the effectiveness of the method for selecting the speed trajectories and switching processing cycles is considered for longitudinal turning of the shaft D=8.0 mm made of steel 08H15N24V4TR non-sharpenable plates of the firm SANDVIK Coromant hard alloy GC2015, the shape of the plate - "W". The length of the longitudinal turning section is 38.0 mm. The output program accepted for calculations is 100 parts. The averaged approximations of the change in the cutting speed along the path $V(l) = V_0 \exp[-\alpha l]$ is used, that is

$$3 = \frac{c_1 n}{V_0} \int_0^l \exp[\alpha \xi] d\xi + c_2 (n-1). \tag{7}$$

Cost parameters c_1, c_2 are accepted in conventional units of cost per unit of time. For this case the dependences of cost effectiveness on n are shown in the fig. 3. The cost of the tool change operation and its installation and configuration fundamentally affect the efficiency of choosing the optimal coordinates for switching processing cycles. If this operation is equal to zero in cost terms, then it is optimal $n \to \infty$. As the cost c_2 increases, the number of switches decreases. In analysis, it is usually n not an integer, so it is natural to take the optimal number of switches as the nearest integer value. In addition, it is necessary the path corresponding to the switch align with the length of the tool vertex movement when processing a specific part. The presented mathematical instrumentarium, the proven optimal conditions and developed methodology allow to effectively solve this problem.

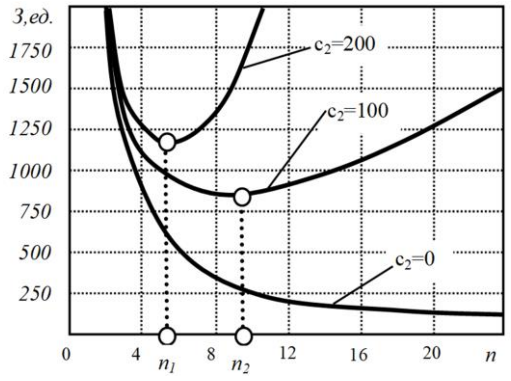

Figure 3. Changes to the optimal number of switches

5. Conclusion

Modern ideas about optimal processing on machines are based not on the definition of constant technological modes, but on their trajectory along the cutting path. These trajectories determine the alignment of evolutionary changes in the properties of the cutting process with the CNC program, which characterizes the external control. At the same time, it is necessary to determine such points in the tool path that the cost of processing a batch of parts is minimal. The given mathematical tools, proven optimality conditions and the developed methodology allow us to effectively solve this problem. Its use is not limited to managing processing processes. It is equally valid for a set of controlled discrete-continuous systems.

The study was funded by RFBR according to the research project №20-38-90074.

References

[1] Haken H 2006 *Information and Self-Organization* Amsterdam, Macroscopic Approach to Complex Systems, p 251, ISSN: 0172-7389

[2] Prigogine I, George C 1983 *The Second Law as a Selection Principle: The Microscopic Theory of Dissipative Processes in Quantum Systems* Proceedings of the National Academy of Sciences, 80, pp 4590-4594 doi: 10.1073 / pnas.80.14.4590

[3] Kolesnikov A A 2007 *Prikladnaya sinergetika: osnovy sistemnogo sinteza prikladnaya sinergetika: osnovy sistemnogo siteza [Applied synergetics: fundamentals of system synthesis applied synergetics: fundamentals of system synthesis]*. Rostov-on-don, SFU publishing house, p 384

[4] Zakovorotnyj V L, Shapovalov V V 2005 *Dinamika transportnyh tribosistem [Dynamics of transport tribosystem]* Sborka v mashinostroe-nii, priborostroenii = Assembly in machine-building, instrument-making, 12, pp 19-24

[5] Ryzhkin A A 2019 *Sinergetika iznashivaniya instrumental'nyh materialov pri lezvijnoj obrabotke* [Synergetics of tool wear in blade processing]. Rostov-on-Don, Don state technical University Publ., p 289, ISBN 978-5-7890-1669-5

[6] Migranov M SH 2006 *Issledovaniya iznashivaniya instrumental'nyh materialov i pokrytij s pozicij termodinamiki i samoorganizacii [Research of wear of tool materials and coatings from the positions of thermodynamics and self-organization]* Izvestiya vuzov. Mashinostroenie = University news. Engineering, 11, pp 65 - 71

[7] Karimov I G 2012 *Vliyanie temperatury rezaniya na energeticheskie parametry kontakta instrumenta s detal'yu [Influence of the cutting temperature on the energy parameters of the tool contact with the part]* Vestnik UGATU = UGATU Bulletin, 16, 44(49), pp 85 – 89

[8] Gomez-Solano J R 2015 *Non-equilibrium work distribution for interacting colloidal particles under friction* New J.Phes., 045026, pp 1 – 13 doi: 10.1088 / 1367-2630 / 17/4/045026

[9] Banjac M 2014 *Friction and Wear Processes Thermodynamic Approach* Tribology in Industre, 36, 4, pp 341-347

[10] Abdel-Aal H A 2013 *Thermodynamic modelling of wear* Encyclopedia of Tribology, pp 3622-3636

[11] Duyun T A, Grinek A V, Rybak L A 2014 *Methodology of manufacturing process design, providing quality parameters and minimal costs* World Applied Sciences Journal, 30 (8), pp 958-963 doi: 10.5829 / idosi.wasj.2014.30.08.14120

[12] Mukherjee I, Ray P K 2006 A review of optimization techniques in metal cutting processes // Computers and Industrial Engineering, 50, 2, pp 15-34

[13] *Sposob opredeleniya optimal'noj skorosti rezaniya v processe metalloobrabotki* [Method for determining the optimal cutting speed in the process of Metalworking] Rassian patent: RU 2538750C2 from 23.05.2013 / Kozochkin M P , Fedorov S V , Tereshin M V

[14] Zariktuev V C 2009 *Avtomatizaciya processov na osnove polozheniya ob optimal'noj temperature rezaniya [Automatization of process based on concept of optimal cutting temperature]* Vestnik UGATU = UGATU Bulletin, 12, 4, pp 14 – 19

[15] Begic-Hajdarevic D 2014 *Experimental study on the high speed machining of hardened steel* Procedia Engineering, 69, pp 291-295 doi: /10.1016/j.proeng.2014.02.234

[16] Blau P 2015 *Flushing strategies for high performance, efficient and environmentally friendly cutting* Procedia CIRP, 26, pp 361-366 doi: /10.1016/j.procir.2014.07.058

[17] Chin C H 2013 *The effect of surface roughness of end-mills on optimal cutting performance for high-speed machining* Journal of Mechanical Engineering, 52 (2), pp 124-134 doi: 10.5545/sv-jme.2012.677

[18] Kant G 2014 *Prediction and optimization of machining parameters for minimization power consumption and surface roughness in machining* Journal of Cleaner Production, 83, pp 151-164 doi: 10.1016 / j.jclepro.2014.07.073

[19] Zakovorotny V L, Gvindjiliya V E 2018 *Influence of spindle wobble in a lathe on the tools deformational-displacement trajectory* Russian Engineering Research, 38, 8, pp 623-631
[20] Zakovorotny V L, Gvindjiliya V E 2019 *Evolution of the dynamic cutting system with irreversible energy transformation in the machining zone* Russian Engineering Research, 39, no, 5. pp 423-430
[21] Zakovorotnyj V L, Gvindzhiliya V E 2018 *Bifurkacii prityagivayushchih mnozhestv deformacionnyh smeshche-nij rezhushchego instrumenta v hode evolyucii svojstv processa obrabotki [Bifurcations of attracting sets of deformation spaces of a cutting tool during the evolution of processing properties]* Izvestiya vysshih uchebnyh zavede-nij. Prikladnaya nelinejnaya dinamika = Proceedings of higher educational institutions. Applied nonlinear dynamics, 26, 5, pp 20-38. doi: /10.18500/0869-6632-2018-26-5-20-38
[22] Zakovorotnyj V L, Gvindzhiliya V E 2020 *Svyaz' samoorganizacii dinamicheskoj sistemy rezaniya s izna-shivaniem instrumenta [Connection of self-organization of the dynamic cutting system with tool wear]* Izvestiya vuzov. Prikladnaya nelinejnaya dinamika = University news. Applied nonlinear dynamics, 28, 1, pp 46-61, doi: /10.18500/0869-6632-2020-28-1-46-61
[23] Pontryagin L S, boltyansky V G, Gamkrelidze R V, Mishchenko E F 1969 *Matematicheskaya teoriya optimal'nyh processov* [Mathematical theory of optimal processes]. Moscow, Nauka Publ., p 384
[24] Boltyanskij V G 1961 Modelirovanie linejnyh optimal'nyh bystrodejstvij pri pomoshchi relejnyh skhem [Modeling of linear optimal speeds using relay circuits]. DAN SSSR Publ., 139, 2, pp 19-22
[25] Bellman R 1960 *Dinamicheskoe programmirovanie [Dynamic programming]*. Moscow, Publishing house of foreign literature = Izdatelstvo inostrannoj literatury, p 423
[26] Bellman R, Gliksberg I, Gross O 1962 *Nekotorye voprosy matematiche-skoj teorii processov upravleniya [Some questions of the mathematical theory of control processes]*. Moscow, Publishing house of foreign literature = Izdatelstvo inostrannoj literatury, p 363

Synergetic synthesis of aggregated discrete regulators for induction motors

G Veselov[1], **I Kondratiev**[2], **V Semenov**[1]

[1] Southern Federal University, Rostov-on-Don, Russia
[2] Queensland University

e-mail: gev@sfedu.ru, igor.kondratiev@qut.edu.su, vsemenov@sfedu.ru

Abstract. The paper presents the method of synergetic synthesis of a nonlinear discrete control system for induction motors. The proposed approach is based on using the methods of the synergetic control theory and nonlinear mathematical models of induction motors. This approach allows to create nonlinear closed-loop piecewise-continuous control systems which guarantee the asymptotic stability of the controlled induction motors, accomplishment of the determined technological and electromagnetic invariants and selective invariance to the unknown external disturbances acting on the system. The invariance of the designed systems is ensured due to the usage of a dynamic discrete regulator which increases the astatism of the synthesized system.

1. Introduction

Induction (or asynchronous) motors (IM) is a very popular and perspective solution for the modern complex technical systems with mechanical energy generation subsystems. IMs are one of the simplest, most reliable and most economically effective motors. They are commonly used in the systems where regulation of the rotation frequency and turning angle over a wide range is not required. However, the design of IMs is associated with some typical difficulties. This type of motors is one of the most complex electromechanical highly dynamic objects from the control point of view. Its exceptional difficulty is due to the fact that the precise mathematical models of IMs are high-dimensional and highly nonlinear. Effective functioning of IMs requires control over several interrelated coordinates — rotation frequency, angular position, torque, flux, current, etc.

That is why, the scalar control methods have become the most widespread solution for IMs. In these methods, one of the essentially independent control channels (e.g. the stator's voltage amplitude) is assumed to be dependent on another control — the source voltage frequency [1, 2, 3]. Then, the control law is synthesized using simplified linearized models, which don't reflect the physical processes accurately enough. Moreover, these methods of synthesis are based upon the principles of "compensation" of the model's nonlinearities (or even completely ignoring them), separation of the control channels, neutralization of cross-connections, etc. Naturally, such methods impose significant restrictions upon such important qualitative characteristics of IMs as the stability region, regulation range, mechanical characteristics, etc. All this eventually leads to the ineffective exploitation of the wide technological capabilities of IMs.

At the modern stage of development of the theory and practical applications of IMs, the further performance improvement is only possible if the nonlinear interconnections in the AC machines are taken into account via using vector control synthesis techniques. The vector control methods [4, 5] allow to achieve a significant improvement in the IMs' functioning. A big breakthrough in the IM control

systems design occurred with the progress of the sliding mode control methods [6, 7, 8]. It is important to mention that one of the intrinsic problems of vector control systems is the difficulties in gaining accurate information about the instantaneous values of the IM states. This problem led to the development of the methods which use the IM states estimates [9, 10, 11, 12].

The cornerstone problem on the way to improving the IMs performance is the formulation of the full dynamical model of the controlled IM, which would take into account its nonlinear properties. It should also have such a structure which would best reflect the identity of the basic processes of all types of AC machines and at the same time identify specific properties for each of these types. The theory of such synthesis, which would remove any restrictions on the dimensionality and nonlinearity of the controlled object, was developed in the frame of synergetic control theory [13, 14]. Consequently, there appeared opportunities for development and realization of more effective nonlinear vector control laws in the controlled IMs. In [15, 16], the methods of synergetic synthesis of continuous vector control systems for IMs were presented, including the design of sensorless systems [17]. However, considering that modern systems rely on digital tools, we propose to apply the method of Analytical Design of Aggregated Discrete Regulators (ADADR) [18, 19] to the problem of IM vector nonlinear control systems design.

2. Mathematical model and IM invariants

The IMs are modelled as systems of nonlinear differential equations in one of the following reference frames:

- stator oriented stationary reference frame α, β;
- rotor oriented rotationary reference frame d, q;
- rotor flux oriented rotationary reference frame x, y.

The most popular choice for the basis vector of IM control systems is the rotor flux linkage oriented vector, i.e. x, y reference frame model [5]:

$$\begin{aligned} J\frac{\mathrm{d}\omega_r}{\mathrm{d}t} &= \frac{m}{2}pk_r\psi_r i_{sy} - M_c; \\ \frac{\mathrm{d}\psi_r}{dt} &= r_r k_r i_{sx} - \frac{1}{T_r}\psi_r; \\ \frac{\mathrm{d}i_{sy}}{\mathrm{d}t} &= -\frac{1}{T_s^*}i_{sy} - \omega_\psi i_{sx} - \frac{pk_r}{L_s^*}\omega_r\psi_r + \frac{1}{L_s^*}u_{sy}; \\ \frac{\mathrm{d}i_{sx}}{\mathrm{d}t} &= -\frac{1}{T_s^*}i_{sx} + \omega_\psi i_{sy} + \frac{k_r}{T_r L_s^*}\psi_r + \frac{1}{L_s^*}u_{sx}. \end{aligned} \quad (1)$$

where u_{sx}, u_{sy} are the stator voltage projections to the x and y axes of the rotationary reference frame; i_{sx}, i_{sy} are the stator current projections to the axes; ψ_r — absolute value of the resulting rotor flux vector; ω_r — rotor's angular velocity; ω_ψ — rotor flux rotation frequency; $k_r = \frac{L_m}{Lr}$ — rotor's electromagnetic link coefficient; r_s, r_r — active resistances of the stator and rotor wirings; L_s, L_r — full inductances of the stator and rotor wirings; L_m — mutual inductance between stator and rotor; $L_s^* = L_s - L_m k_r$, $r_s^* = r_s + r_r k_r^2$ — transformed inductance and resistance of the stator; $T_r = \frac{L_r}{r_r}$, $T_S^* = \frac{L_s^*}{r_s^*}$ — time constants of the stator and rotor; p is the number of the pole pairs; J — moment of inertia; m — the number of the motor phases; M_c — moment of resistance of the IM's shaft load. We assume that the variables related to the rotor wiring (such as the power sources' voltages, currents and fluxes) as well as the rotor wiring parameters are taken with respect to the number of the stator wiring coils. Besides, we add the static equation to the equation (1):

$$\psi_r(\omega_\psi - p\omega_r) = k_r r_r i_{sy}. \quad (2)$$

We consider the model (1), (2) with the following commonplace assumptions:

- the parameters of the rotor and stator wirings are the same, and the system of the phase voltages is symmetric;
- the magnetic cores are not saturated;
- the air gap between the moving parts is uniform;
- the magnetomotive force in the air gap is sinusoidal;
- the effect of the steel wearout as well as the skin effect in IM are neglected;
- both IM parts have identical distributions of the wirings.

To solve the control synthesis problem, we present new applied methods of control design, which are based on the principles of the synergetic control theory. The control criteria (or the design goals) in this theory are expressed as a corresponding system of invariants. These invariants act as control goals, and either the execution of a given control task is insured on the invariants or some given energetic relations (physical, chemical, etc.) are maintained. The synergetic synthesis procedure consists of finding the control laws such that the invariants are fulfilled.

Two main groups of possible IM invariants can be distinguished [15, 16] — ***technological and electromagnetic***. The form of a ***technological*** invariant is defined by a given practical task solved by the IM included to some technological process. It characterizes the desired dynamic or static state of the controlled variables — rotation frequency, turning angle or torque. By example, for the task of rotation frequency stabilization, the technological invariant is $\omega_r = \omega_{r0}$.

A particular interest lies in the invariants related to the constant motor flux — ***electromagnetic invariants***. The idea of stabilization of the IM magnetic state is widespread in the well known frequancy control laws for IMs, and it has a significant practical importance. These electromagnetic invariants include:

$\psi_s = \text{const}$ — constant stator flux linkage;

$\psi_r = \text{const}$ — constant rotor flux linkage;

$\Phi = \text{const}$ — constant combined flux linkage.

The choice of the invariant set is an important step in the process of solving the synergetic IM control synthesis problem. This set must correspond to the designer's goals for the mechanical, electromagnetic and other properties of the IM and to satisfy the requirements of the given task. The number of invariants is defined by the number of control channels. Thus, for the two-channel amplitude-frequency IM control, it is possible to form a set consisting of two invariants.

It is worth noting that in the synthesis of vector control laws with synergetic approach (i.e. using the technological and electromagnetic invariants), it is not even necessary to use the terms of amplitude and frequency of the source currents and voltages, which are customary for the theory of IM frequency control. In order to fully reflect the dynamic and static states of the IM, it is sufficient to define the desired rotation frequency of the shaft as a technological invariant, as well as the value characterizing the state of the IM's magnetic circuit, e.g. the rotor flux linkage, as an electromagnetic invariant. In this case, the control goal is to maintain the given rotation frequency with the optimal state of the IM's magnetic circuit. Depending on the invariant set, one can come up with other types of controlled IMs.

3. Synergetic synthesis of discrete vector regulators for IMs

We address the problem of synthesis of a discrete regulator which stabilizes the IM's shaft rotation frequency and the rotor flux linkage. For that purpose, we formulate an extended model of synergetic synthesis [19] taking into account the technological and electromagnetic invariants:

$$\begin{aligned} \frac{\mathrm{d}\mathbf{v}}{\mathrm{d}t} &= \mathbf{Q}\mathbf{x} - \mathbf{L}\mathbf{g}; \\ \frac{\mathrm{d}\mathbf{x}}{\mathrm{d}t} &= \mathbf{A}(\mathbf{x})\mathbf{x} + \mathbf{B}\mathbf{u} - \mathbf{C}\mathbf{v}, \end{aligned} \tag{3}$$

where $\mathbf{x} = |\omega_r \quad \psi_r \quad i_{sy} \quad i_{sx}|^T$ — vector of the object's phase coordinates; $\mathbf{v} = \begin{vmatrix} z_1 \\ z_2 \end{vmatrix}$ — vector of the regulator's state coordinates; $\mathbf{u} = \begin{vmatrix} u_1 \\ u_2 \end{vmatrix}$ — control vector; $\mathbf{g} = \begin{vmatrix} \omega_{r0} \\ \psi_{r0} \end{vmatrix}$ — vector of the desired values of the control variables;

$$\mathbf{L} = \begin{vmatrix} \eta_1 & 0 \\ 0 & \eta_2 \end{vmatrix};$$

$$\mathbf{A} = \begin{vmatrix} 0 & 0 & \frac{mpk_r}{2J}\psi_r & 0 \\ 0 & -\frac{1}{T_r} & 0 & r_r k_r \\ -pi_{sx} & -\frac{pk_r}{L_s^*}\omega_r & -\frac{1}{T_s^*} & -k_r r_r \frac{i_{sx}}{\psi_r} \\ pi_{sy} & \frac{k_r}{T_r L_s^*} & k_r r_r \frac{i_{sy}}{\psi_r} & -\frac{1}{T_s^*} \end{vmatrix};$$

$$\mathbf{B} = \begin{vmatrix} 0 & 0 \\ 0 & 0 \\ 0 & \frac{K_C}{L_s^*} \\ \frac{K_C}{L_s^*} & 0 \end{vmatrix}; \mathbf{Q} = \begin{vmatrix} \eta_1 & 0 & 0 & 0 \\ 0 & \eta_2 & 0 & 0 \end{vmatrix}; \mathbf{C} = \begin{vmatrix} 1 & 0 \\ 0 & 1 \\ 0 & 0 \\ 0 & 0 \end{vmatrix}.$$

Now, we apply the Euler approximation to the equations (3), which results in the discrete model of synergetic synthesis:

$$\begin{aligned} \mathbf{v}[k+1] &= \mathbf{S}\mathbf{x}[k] - \mathbf{W}\mathbf{g}[k]; \\ \mathbf{x}[k+1] &= \mathbf{F}(\mathbf{x}[k])\mathbf{x}[k] + \mathbf{D}\mathbf{u}[k] - \mathbf{H}\mathbf{v}[k], \end{aligned} \tag{4}$$

where $\mathbf{F} = \mathbf{I}^4 + T_0\mathbf{A}$; T_0 — discretization step in time; $\mathbf{I}^4$ — unit matrix of dimensionality 4×4; $\mathbf{D} = T_0\mathbf{B}$; $\mathrm{H} = T_0\mathbf{C}$; $\mathbf{S} = T_0\mathbf{Q}$; $\mathbf{W} = T_0\mathbf{L}$. Following to the next step of the ADADR, we now introduce the first set of macrovariables:

$$\boldsymbol{\psi}_1[k] = \mathbf{P}(\check{\mathrm{x}}[k] + \boldsymbol{\varphi}_1[k]) \tag{5}$$

where $\boldsymbol{\psi}_1[k] = \begin{vmatrix} \psi_{1,1}[k] \\ \psi_{1,2}[k] \end{vmatrix}$; $\check{\mathbf{x}}[k] = \begin{vmatrix} i_{sy}[k] \\ i_{sx}[k] \end{vmatrix}$; $\boldsymbol{\varphi}_1[k] = \begin{vmatrix} \varphi_{1,1}[k] \\ \varphi_{1,2}[k] \end{vmatrix}$ — vector of the internal controls; $\mathbf{P} = \| p_{ij} \|$ — numeric invertible matrix $i, j = 1,2$.

The parallel set of macrovariables (5) must satisfy the solution $\boldsymbol{\psi}_1[k] = 0$ of the vector equation:

$$\boldsymbol{\psi}_1[k+1] + \boldsymbol{\Lambda}_1\boldsymbol{\psi}_1[k] = 0, \tag{6}$$

where $\boldsymbol{\Lambda}_1 = \begin{vmatrix} \lambda_{1,1} & 0 \\ 0 & \lambda_{1,2} \end{vmatrix}$. To assure the asymptotical stability of the solution for the equation(6), the following conditions are necessary:

$$|\lambda_{1,1}| < 1, \; |\lambda_{1,2}| < 1. \tag{7}$$

After the transients $\boldsymbol{\psi}_1[k] = 0$, for which the process speed is defined as $\lambda_{1,1}$ and $\lambda_{1,2}$, are finished, the dynamic decomposition of the closed-loop system occurs:

$$\begin{aligned} \mathbf{v}[k+1] &= \bar{\mathbf{S}}\bar{\mathbf{x}}[k] - \mathbf{W}\mathrm{g}[k]; \\ \bar{\mathbf{x}}[k+1] &= \bar{\mathbf{F}}\bar{\mathbf{x}}[k] - \bar{\mathbf{D}}\boldsymbol{\varphi}_1[k] - \bar{\mathbf{H}}\mathbf{v}[k], \end{aligned} \tag{8}$$

where $\bar{\mathbf{x}}[k] = |\omega_r \quad \psi_r|^T$ — the decomposed state vector; $\bar{\mathbf{F}} = \begin{vmatrix} 1 & 0 \\ 0 & 1 - \frac{T_0}{T_r} \end{vmatrix}$; $\bar{\mathbf{D}} = \begin{vmatrix} 0 & T_0 \frac{mpk_r}{2J} \psi_r[k] \\ r_r k_r T_0 & 0 \end{vmatrix}$; $\bar{\mathbf{H}} = \begin{vmatrix} T_0 & 0 \\ 0 & T_0 \end{vmatrix}$; $\bar{\mathbf{S}} = \begin{vmatrix} T_0\eta_1 & 0 \\ 0 & T_0\eta_2 \end{vmatrix}$.

For the decomposed model (8), we introduce the second set of macrovariables

$$\boldsymbol{\psi}_2[k] = \bar{\mathbf{x}}[k] + \mathbf{K}\mathbf{v}[k], \tag{9}$$

where $\boldsymbol{\psi}_2[k] = \begin{vmatrix} \psi_{2,1}[k] \\ \psi_{2,2}[k] \end{vmatrix}$; $\mathbf{K} = \begin{vmatrix} \gamma_1 & 0 \\ 0 & \gamma_2 \end{vmatrix}$.

From the combined solution (9), the functional equation

$$\boldsymbol{\psi}_2[k+1] + \boldsymbol{\Lambda}_2 \boldsymbol{\psi}_2[k] = 0 \tag{10}$$

and the decomposed model (8), we find the expressions for the internal equations:

$$\varphi_1[k] = (\bar{\mathbf{D}})^{-1}\{(\bar{\mathbf{F}} + \boldsymbol{\Lambda}_2 + \mathbf{K}\bar{\mathbf{S}})\bar{\mathbf{x}}[k] + (\boldsymbol{\Lambda}_2\mathbf{K} - \bar{\mathbf{H}})\mathbf{v}[k] - \mathbf{K}\mathbf{W}\mathbf{g}[k]\}, \tag{11}$$

where $\boldsymbol{\Lambda}_2 = \begin{vmatrix} \lambda_{2,1} & 0 \\ 0 & \lambda_{2,2} \end{vmatrix}$, $|\lambda_{2,1}| < 1$, $|\lambda_{2,2}| < 1$. We transform the equation (11) as

$$\boldsymbol{\varphi}_1[k] = \hat{\mathbf{R}}(\bar{\mathbf{x}}[k])\bar{\mathbf{x}}[k] + \bar{\mathbf{R}}(\bar{\mathbf{x}}[k])\mathbf{v}[k] - \tilde{\mathbf{R}}(\bar{\mathbf{x}}[k])\mathbf{g}[k], \tag{12}$$

where $\hat{\mathbf{R}} = (\bar{\mathbf{D}})^{-1}(\bar{\mathbf{F}} + \boldsymbol{\Lambda}_2 + \mathbf{K}\bar{\mathbf{S}})$; $\bar{\mathbf{R}} = (\bar{\mathbf{D}})^{-1}(\boldsymbol{\Lambda}_2\mathbf{K} - \bar{\mathbf{H}})$; $\tilde{\mathbf{R}} = (\bar{\mathbf{D}})^{-1}\mathbf{K}\mathbf{W}$.

We find the vector control law for the rotation frequency of the IM's shaft by solving the combined equations (5), (6) while taking into account the mathematical model of the synthesis (4)

$$\mathbf{u}[k] = -(\mathbf{P}\check{\mathbf{D}})^{-1}\{\mathbf{P}\check{\mathbf{F}}(\mathbf{x}[k])\mathbf{x}[k] + \boldsymbol{\Lambda}_1\mathbf{P}(\check{\mathbf{x}}[k] + \boldsymbol{\varphi}_1[k]) + \mathbf{P}\boldsymbol{\varphi}_1[k+1]\}, \tag{13}$$

where $\check{\mathbf{D}} = \begin{vmatrix} 0 & T_0 \frac{K_C}{L_S^*} \\ T_0 \frac{K_C}{L_S^*} & 0 \end{vmatrix}$; $\check{\mathbf{F}} = \begin{vmatrix} -T_0 p i_{sx} & -\frac{pk_r T_0}{L_S^*}\omega_r & 1 - \frac{T_0}{T_S^*} & -k_r r_r T_0 \frac{i_{sx}}{\psi_r} \\ T_0 p i_{sy} & \frac{T_0 k_r}{T_r L_S^*} & k_r r_r T_0 \frac{i_{sy}}{\psi_r} & 1 - \frac{T_0}{T_S^*} \end{vmatrix}$.

We obtain the final solution for the IM's control law by substituting (12) to (13):

$$\begin{aligned} &\mathbf{v}[k+1] = \mathbf{S}\mathbf{x}[k] - \mathbf{W}\mathbf{g}[k]; \\ &\mathbf{u}[k] = \hat{\mathbf{L}}(\mathbf{x}[k])\mathbf{x}[k] + \bar{\mathbf{L}}(\mathbf{x}[k])\mathbf{v}[k] - \tilde{\mathbf{L}}(\mathbf{x}[k])\mathbf{g}[k], \end{aligned} \tag{14}$$

where $\mathbf{R}_1 = \begin{vmatrix} \mathbf{O}_2 & \vdots & \mathbf{O}_2 \\ \cdots & \cdots & \cdots \\ \mathbf{O}_2 & \vdots & \bar{\mathbf{R}}_1 \end{vmatrix}$; $\mathbf{R}_2 = \begin{vmatrix} \mathbf{O}_2 & \vdots & \mathbf{O}_2 \\ \cdots & \cdots & \cdots \\ \bar{\mathbf{R}}_2 & \vdots & \mathbf{O}_2 \end{vmatrix}$; $\mathbf{O}^2 = \begin{vmatrix} 0 & 0 \\ 0 & 0 \end{vmatrix}$;

$\hat{\mathbf{L}} = -\left(\mathbf{P}\check{\mathbf{D}}\right)^{-1}\left\{\mathbf{P}\left(\check{\mathbf{F}}(\mathbf{x}[k]) + \bar{\mathbf{R}}(\mathbf{x}[k+1])|_{\mathbf{x}[k+1]=\mathbf{F}(\mathbf{x}[k])\mathbf{x}[k]+\mathbf{D}\mathbf{u}[k]-\mathbf{H}\mathbf{v}[k]}\mathbf{S}\right) + \mathbf{R}_1 + \mathbf{R}_2\right\}$;

$\bar{\mathbf{R}}_1 = \boldsymbol{\Lambda}_1\mathbf{P} - \mathbf{P}\hat{\mathbf{R}}(\mathbf{x}[k+1])|_{\mathbf{x}[k+1]=\mathbf{F}(\mathbf{x}[k])\mathbf{x}[k]+\mathbf{D}\mathbf{u}[k]-\mathbf{H}\mathbf{v}[k]}\bar{\mathbf{D}}$;

$\bar{\mathbf{R}}_2 = \boldsymbol{\Lambda}_1\mathbf{P}\hat{\mathbf{R}}(\mathbf{x}[k]) + \mathbf{P}\hat{\mathbf{R}}(\mathbf{x}[k+1])|_{\mathbf{x}[k+1]=\mathbf{F}(\mathbf{x}[k])\mathbf{x}[k]+\mathbf{D}\mathbf{u}[k]-\mathbf{H}\mathbf{v}[k]}\bar{\mathbf{F}}$;

$\bar{\mathbf{L}} = -\left(\mathbf{P}\check{\mathbf{D}}\right)^{-1}\left\{\boldsymbol{\Lambda}_1\mathbf{P}\bar{\mathbf{R}}(\mathbf{x}[k]) - \mathbf{P}\hat{\mathbf{R}}(\mathbf{x}[k+1])|_{\mathbf{x}[k+1]=\mathbf{F}(\mathbf{x}[k])\mathbf{x}[k]+\mathbf{D}\mathbf{u}[k]-\mathbf{H}\mathbf{v}[k]}\bar{\mathbf{H}}\right\}$;

$\tilde{\mathbf{L}} = -\left(\mathbf{P}\check{\mathbf{D}}\right)^{-1}\left\{\boldsymbol{\Lambda}_1\mathbf{P}\tilde{\mathbf{R}}(\mathbf{x}[k]) + \mathbf{P}\bar{\mathbf{R}}(\mathbf{x}[k+1])|_{\mathbf{x}[k+1]=\mathbf{F}(\mathbf{x}[k])\mathbf{x}[k]+\mathbf{D}\mathbf{u}[k]-\mathbf{H}\mathbf{v}[k]}\mathbf{W} + \right.$

$\left. + \mathbf{P}\bar{\mathbf{R}}(\mathbf{x}[k+1])|_{\mathbf{x}[k+1]=\mathbf{F}(\mathbf{x}[k])\mathbf{x}[k]+\mathbf{D}\mathbf{u}[k]-\mathbf{H}\mathbf{v}[k]}\right\}$;

The results of the modelling for the synthesized discrete-continuous control system (1), (2), (14) are shown in the figures 1 and 2. For the modelling, we set the IM's parameters as follows: $r_s = 0{,}03\text{Om}$, $r_r = 0{,}0172\text{Om}$, $L_m = 0{,}0154\text{H}$, $m = 3$, $p = 2$, $L_s = L_r = 0{,}0158\text{H}$, $J = 0{,}968\text{kg}\cdot\text{m}^2$ and the regulator parameters: $p_{11} = 1$; $p_{12} = 2$; $p_{21} = 3$; $p_{22} = 4$; $\omega_{r0} = 150\text{rad/s}$; $\psi_{r0} = 0{,}987\text{Wb}$; $\eta_1 = \eta_2 = 10$; $\gamma_1 = \gamma_2 = 2$; $\lambda_{1,1} = \lambda_{1,2} = \lambda_{2,1} = \lambda_{2,2} = -0{,}9$; $T_0 = 0{,}001\text{s}$ and for the case of unknown external disturbance $M_c = \mu\omega_r - M_{c0}$, where $\mu = 0{,}5\text{N}\cdot\text{m}\cdot\text{s/rad}$;

$$M_{c0} = \begin{cases} 400\text{N}\cdot\text{m}, & \text{for } t < 0{,}7; \\ 1000\text{N}\cdot\text{m}, & \text{for } 0{,}7 \le t < 1{,}5; \\ 100\text{N}\cdot\text{m}, & \text{for } t \ge 1{,}5. \end{cases}$$

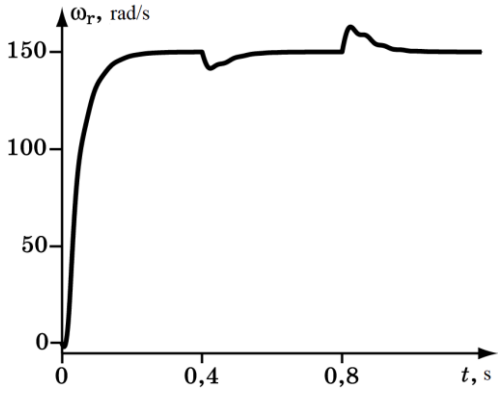

Figure 1. Rotation frequency of the shaft in a system with unknown external disturbance

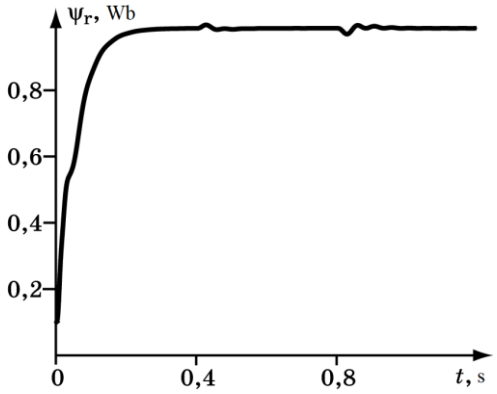

Figure 2. Rotor flux linkage in a system with unknown external disturbance

The figure 3 shows the phase portrait of the system with $M_c = \mu\omega_r - M_{c0}$, where $\mu = 0{,}5\text{N}\cdot\text{m}\cdot\text{s/rad}$, $M_{c0} = 400\text{N}\cdot\text{m}$.

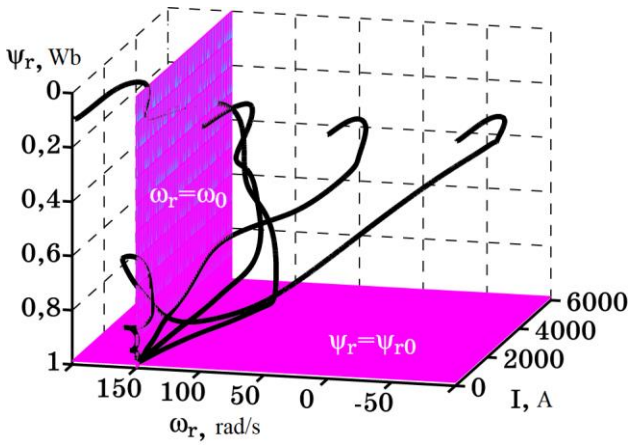

Figure 3. Phase portrait of the synthesized piecewise-continuous control system

The modelling results of the closed-loop discrete-continuous IM control system (1), (2), (14) demonstrate its high precision in the sustaining of the required values of the output variables. In other words, it satisfies the introduced invariant set $\omega_r = \omega_{r0}$, $\psi_r = \psi_{r0}$, it is invariant to unknown external disturbances, and it is asymptotically stable in the whole range of the phase coordinates.

The figures 4 and 5 show the test results for different types of disturbances:

- for the curves I $M_c = \mu\omega_r + M_{c0} sign\omega_r$, $\mu = 0{,}5$ N·m·s/rad, $M_{c0} = 200$ N·m;
- for the curves II $M_c = \mu\omega_r + \xi\omega_r|\omega_r| + M_{c0}$, $\mu = 0{,}5$ N·m·s/rad, $M_{c0} = 200$ N·m, $\xi = 0{,}2$ N·m·s^2/rad^2;
- for the curves III $M_c = \mu\omega_r + \alpha\omega_r^3 + M_{c0}$, $\mu = 0{,}5$ N·m·s/rad, $M_{c0} = 200$ N·m, $\alpha = 0{,}0025$ N·m·s^3/rad^3.

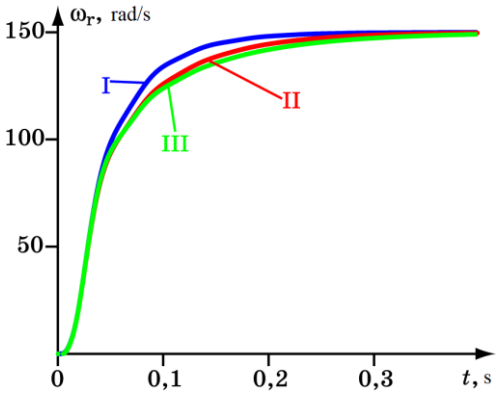

Figure 4. Rotation frequency of the shaft in a system with different types of external disturbances

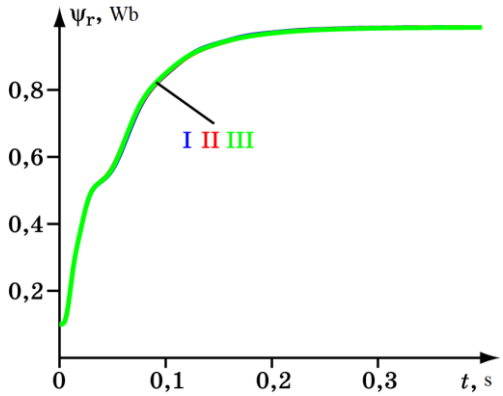

Figure 5. Rotor flux linkage in a system with different types of external disturbances

The figures (6), (7) demonstrate the modelling results of the closed-loop discrete-continuous IM control system (1), (2), (14) when varying the wiring parameters:

- figure I nominal object parameters;
- figure II — rotor resistance is two times bigger than nominal;
- figure III — rotor resistance is two times smaller than nominal;
- figure IV — stator resistance is two times bigger than nominal;
- figure V — stator resistance is two times smaller than nominal;

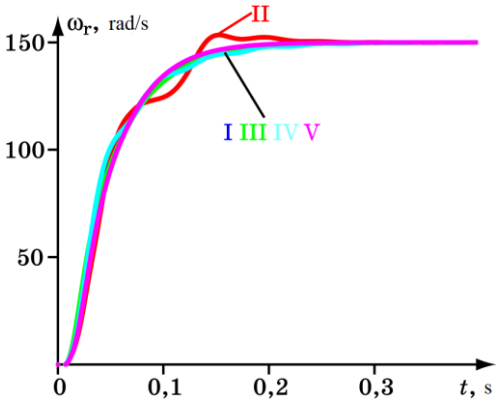

Figure 6. Rotation frequency of the shaft in a system with varying parameters of the IM wirings

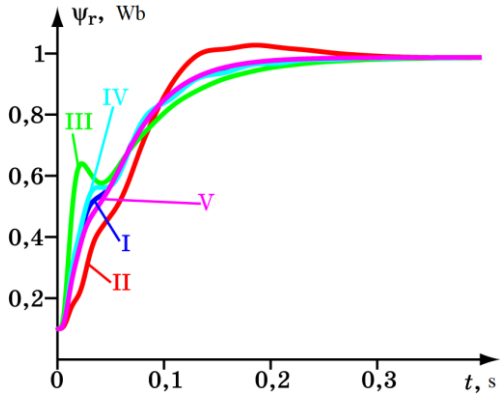

Figure 7. Rotor flux linkage in a system with varying parameters of the IM wirings

The numerical modelling results show that the synthesized discrete regulator (14) makes the closed-loop system invariant to the external disturbances and robust to the parameter changes.

4. Conclusion

We presented the method of synergetic synthesis of discrete-continuous control systems for torque generation in induction motors. The synthesis makes use of the exhaustive mathematical description of the electromechanical energy transformation in IMs. The methodology of synergetic synthesis applied to the design of IM control systems allows to synthesize highly effective control laws which assure such important properties as asymptotic stability in relation to the desired stationary or dynamic equilibrium, invariance to the unknown external disturbances and parametric robustness of transients.

The use of the synergetic control systems for torque generators in complex hierarchical structures allows to maintain precise accomplishment of the tasks from the higher levels, and thus, guarantees effective functioning of the systems and achievement of the global control goals.

Acknowledgment

This work was supported by the Russian Foundation for Basic Research, project no. 19-07-00645-A.

References

[1] Buja G S, Kazmierkowski M P 2004 *Direct Torque Control of PWM Inverter-Fed AC Motors – A Survey*. IEEE Transactions on Industrial Electronics, 51(4), 744–757.

[2] Abdulrazzak J A et al. 2017 *Speed control of three phase induction motor by v/f method with arduino Uno*. Int. Journal of Engineering Research and Application, ISSN : 2248-9622, Vol. 7, Issue 12, Part -5, pp.62-66.

[3] Shilpa V K, Keswani R A 2013 *Speed control of three phase induction motor by v/f method for batching motion system*. International Journal of Engineering Research and Applications, ISSN: 2248-9622, Vol. 3, Issue 2, pp.1732-1736.

[4] Blaschke F 1972 *The principle of field orientation as applied to the new transvector closed loop control system in a PWM inverter induction motor drive*. Siemens Rev., vol. 39, no. 5, pp. 217–220.

[5] Vas P 1990 *Vector Control of AC Machines*. Oxford University Press: New York, NY, USA.

[6] Young K D, Utkin V I, Ozguner U 1999 *A control engineer's guide to sliding mode control*. IEEE Transactions on Control Systems Technology, 7(3), 328–342.

[7] Panchade V M et. al. 2013 *A survey on sliding mode control strategies for induction motors*. Annual Reviews in Control, 37(2), 289–307.

[8] Tarchała G, Orłowska-Kowalska T 2020 *Discrete Sliding Mode Speed Control of Induction Motor Using Time-Varying Switching Line*. Electronics, 9(1), 185.

[9] Vas P 1998 *Sensorless Vector and Direct Torque Control*. London, U.K.: Oxford Univ. Press.

[10] Wang F et. al. 2018 *Advanced Control Strategies of Induction Machine: Field Oriented Control, Direct Torque Control and Model Predictive Control*. Energies, 11(1), 120.

[11] Luo Y C, Tsai C L 2018 *Speed estimation vector-controlled induction motor drive based on fuzzy logic control flux estimator*. Journal of Low Frequency Noise, Vibration and Active Control.

[12] Gou L 2019 *Integral Sliding Mode Control for Starting Speed Sensorless Controlled Induction Motor in the Rotating Condition*. IEEE Transactions on Power Electronics, 1–1.

[13] Kolesnikov A A 2014 *Introduction of synergetic control*. Proceedings of the American Control Conference, pp. 3013-3016.

[14] Kolesnikov A A 2003 *The cognitive potential of synergetics*. Vestnik Rossijkoj Akademii Nauk, 73(8), pp. 727-735.

[15] Veselov G E, Popov A N, Radionov I A 2014 *Synergetic control of asynchronous electric traction drives of locomotives*. Journal of Computer and Systems Sciences International, 53(4), pp. 587-600.

[16] Kolesnikov A A, Veselov G E 2006 *Synergetic control of nonlinear electric drives. III. Vector control of induction motors*. Izvestiya vysshih uchebnyh zavedeniy. Electromekhanika, 2, pp. 25-36.

[17] Radionov I A, Mushenko A S 2018 *Estimation of components of rotor flux linkage vector for asynchronous electric drive*. 2018 International Russian Automation Conference, RusAutoCon.
[18] Veselov G E 1997 *Alalytic design of aggregated discrete regulators based on the sequence of invariant manifolds*. Ozvestiya TRTU. № 1 (4). pp. 64-70.
[19] Kolesnikov A A, Veselov G E, et. al. 2000 *Modern applied control theory: Synergetic approach in the control theory*. Taganrog, Izdatelstvo TRTU, part II.

Vibration dynamics and cutting process temperature at various stages of forming the wear of the cutting wedge

V P Lapshin, I A Turkin

Don State Technical University, Rostov-on-Don, Russia

Abstract. On today, there is no single and consistent mathematical model describing the complex connectivity of the metal cutting process. Therefore, the article proposes new approach based on the formation of feedback connecting subsystems describing the power, thermal and vibration reactions from the cutting process. The purpose of the work: By forming a consistent model of connections between subsystems describing the power, thermal and vibration reactions from the cutting process to the shaping movements of the tool, you can obtain a description of the mechanism of self-organization of the cutting process in the process of evolutionary changes of the tool. The resulting mechanism is needed to search for some mode of operation of the cutting system, in which further wear of the cutting wedge, cutting force, temperature in the cutting zone and vibration of the tool can be stabilized. Research methods: For processing and analysis of the obtained data, a Matlab package of mathematical programs was used, in which a subprogram was developed that allows a series of numerical experiments. The main conclusion on the work is the provision put forward by us on the self-organization of the cutting system, through the process of evolution of the instrument.

1. Introduction

In many ways, the modern base of metal cutting machines in its scientific and engineering complexity is not inferior to such an industry as astronautics. In metalworking today, the digital approach to the control and control of processing processes is most fully implemented, which is explained by the wide implementation of digital control systems (sensors) and data processing systems received from them. This approach makes it possible to use more complex models in the analysis of the cutting process on a particular machine than previously used. Here, a promising direction of quality control of the processing process is rapidly developing vibration monitoring and vibration diagnostics systems [1-5]. It is therefore an object to describe the relationship of vibrations measured during cutting with non-measurable but of engineering interest characteristics such as force reaction and temperature in the contact zone of the tool and the workpiece.

In the modern representation of vibrations arising during cutting, it is customary to divide them into three components: free vibrations, forced vibrations and self-excited oscillations [6]. Free oscillations are related to the quality of the cutting system and are a reaction to changes in the processing process, forced oscillations are due to external actions, such as, for example, beats in the bearings of the spindle assembly, vibrations of the machine body or beats in the IWP. To combat free and forced vibrations, many engineering methods have been developed today, but with self-excited oscillations that can extract energy from the interaction that arises in the cutting zone of unambiguous engineering solutions today. This makes the topic of self-excited oscillations in cutting very popular in modern scientific research [7-11]. However, in these works, the main emphasis is on assessing the effect on the oscillation of the tool, the so-called regenerative effect. For the first time, the regeneration of oscillations in metal

processing on metal cutting machines was investigated by Hahn R.S., Tobias S.A. and Merritt H.E. [12-14]. The works of these authors are the fundamental basis underlying the analysis of the dynamics of regenerative vibrations of the tool during cutting. Many works note the possibility of establishing the chaotic nature of instrument vibrations during vibration regeneration [15-18]. In these works, it is indicated that the main factor affecting the regenerative effect is the so-called time delay, which determines the dynamics of the process of regenerating the tool oscillations.

In the Russian scientific journalism devoted to self-excited oscillations (vibrations) of the instrument in metal cutting, the issues of estimation of the effect of cutting on the "trace" on the dynamics of vibrations of the instrument are considered indirectly, more attention is paid to the construction and analysis of models describing the interconnected dynamics of the processing process [19-21]. For example, in our previously published works [22-25], the analysis of the dynamics of the deformation vibrations of the tool is carried out on the basis of the connectivity, through the force reaction, of this deformation movement with the cutting elements of the NC system of the machine. In this case, the dynamic effects that occur during the simulation, in our opinion, more accurately reflect the nature of the interaction between the subsystems of the cutting control system in the contact area of the tool and the workpiece. In the fundamental works of leading Soviet and Russian scientists studying the vibrational dynamics of the cutting process [26-30], it is noted that in the cutting process, in addition to feedback on the cutting force, which takes into account the regeneration of vibrations during cutting along the "trace," thermodynamic feedback is formed, which is also associated with the vibration activity of the instrument and wear of the cutting wedge [26-30]. Thus, in the actual process of processing, there is a rather complex interaction involving the formation of a plurality of interconnected feedback.

2. Research methodology and simulation results

When presenting wear in the coordinates of the state, we rely on the connection of wear and work with the power of irreversible transformations of the supplied energy in the cutting zone. Fundamentally, the change in wear depending on irreversible transformations is disclosed in the works of A. L. Bershadsky, Kostetsky B.I., Ryzhkin A.A., etc. [30].

The reason for evolutionary transformations is related to the power and operation of the cutting forces, that is, the energy of irreversible transformations in the processing zone. Thus, all the parameters characterizing the cutting process and the manufacturing quality of the part are not only interconnected, but also have one nature of change - this is the trajectory of the power of irreversible transformations in perfect work. To simulate evolutionary changes in this case, it is necessary to use Volterre integral operators of the second kind, having the following structure [25]:

$$h_3 = k\int_0^A w(t-\xi)\cdot N(\xi)d\xi \tag{1}$$

where $w(t-\xi)$ is the core of the integral operator, is the phase trajectory of the power of irreversible transformations by perfect work, and A- the work of cutting forces. However, as follows from the structure of the operator, wear depends on the fluidity of irreversible transformations and its prehistory, which is taken into account by the core of the integral operator (see expression 1). The tool wear process is always bi-directional in nature, one of the directions of which is oriented towards the treatment of the cutting wedge to the cutting process, as a result of which we observe, the process of forming the tool contact area along the back face, through which the temperature field and the force reaction are stabilized, described by us in previous sections. The second direction is related to the growth of degrading features of the wear process, which subsequently lead to a significant change in cutting properties and properties. If N (t) is not equal to N0 = const, then we can assume that the measured or calculated discrete values of power N0, N1, ..., Nn-1, due to the smallness of ΔA = Ak-Ak-1, are close to constant or constant, then we can obtain an approximating discrete sum describing the integral operator (2):

$$h_3 = \frac{\beta_1}{\alpha_1}[-N_0 e^{-\alpha_1 A} - (N_1 - N_0)e^{\alpha_1(A_1 - A)} - (N_2 - N_1)e^{\alpha_1(A_2 - A)} - .... - (N_{n-1} - N_{n-2})e^{\alpha_1(A_{n-1} - A)} + N_{n-1}] +$$

$$+ \frac{\beta_2}{\alpha_2}[N_0 e^{\alpha_2 A} + (N_1 - N_0)e^{-\alpha_2(A - A_1)} + (N_2 - N_1)e^{-\alpha_2(A - A_2)} + ... + (N_{n-1} - N_{n-2})e^{-\alpha_2(A - A_{n-1})} - N_{n-1}] \quad (2)$$

The expression (2) can be modeled using the Matlab/Simulink package of mathematical programs. When modeling the expression (2), we will use some of the workpieces we obtained earlier in the previous section, and consider the option of increasing the wear of the cutting wedge for the case of a low-oscillation processing process, when the secondary regeneration of oscillations is small and for the case of a high-oscillation cutting process, when the regenerative effect forms the vibrations of the tool along the entire path passed by it during cutting. To do this, as part of the model presented in the previous section, we will introduce an additional unit for calculating tool wear on the rear gras. The results of the simulation of the system taking into account this unit are shown in the figures below. Figure 1 shows the results of the simulation of the cutting force.

The power response from the processing process is quite large, this increase was made by us specifically in order to accelerate the process of wear growth, the results of which are shown in Figure 1.

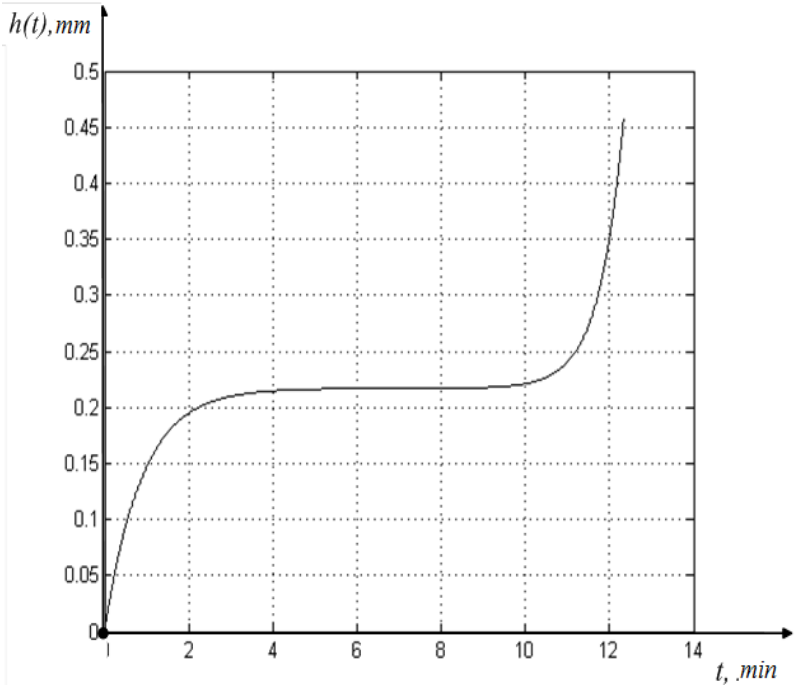

Figure 1. Wear Curve Plot

As can be seen from Figure 2, the wear curve that we obtained for the specified case of simulating the cutting control system is similar to the one obtained experimentally, however, the area of stabilizing the wear characteristic is more pronounced here, as well as not less than the time of increasing critical wear. For subsequent modeling, it is of interest to consider separately the process of tapping described by the first part of the discretely equation (5) and the increase in the process of degradation of the cutting wedge of the in-tool, the second part of the discrete sum presented in the expression (5). Figure 2 shows the simulation of the curve reflecting the tool run-in.

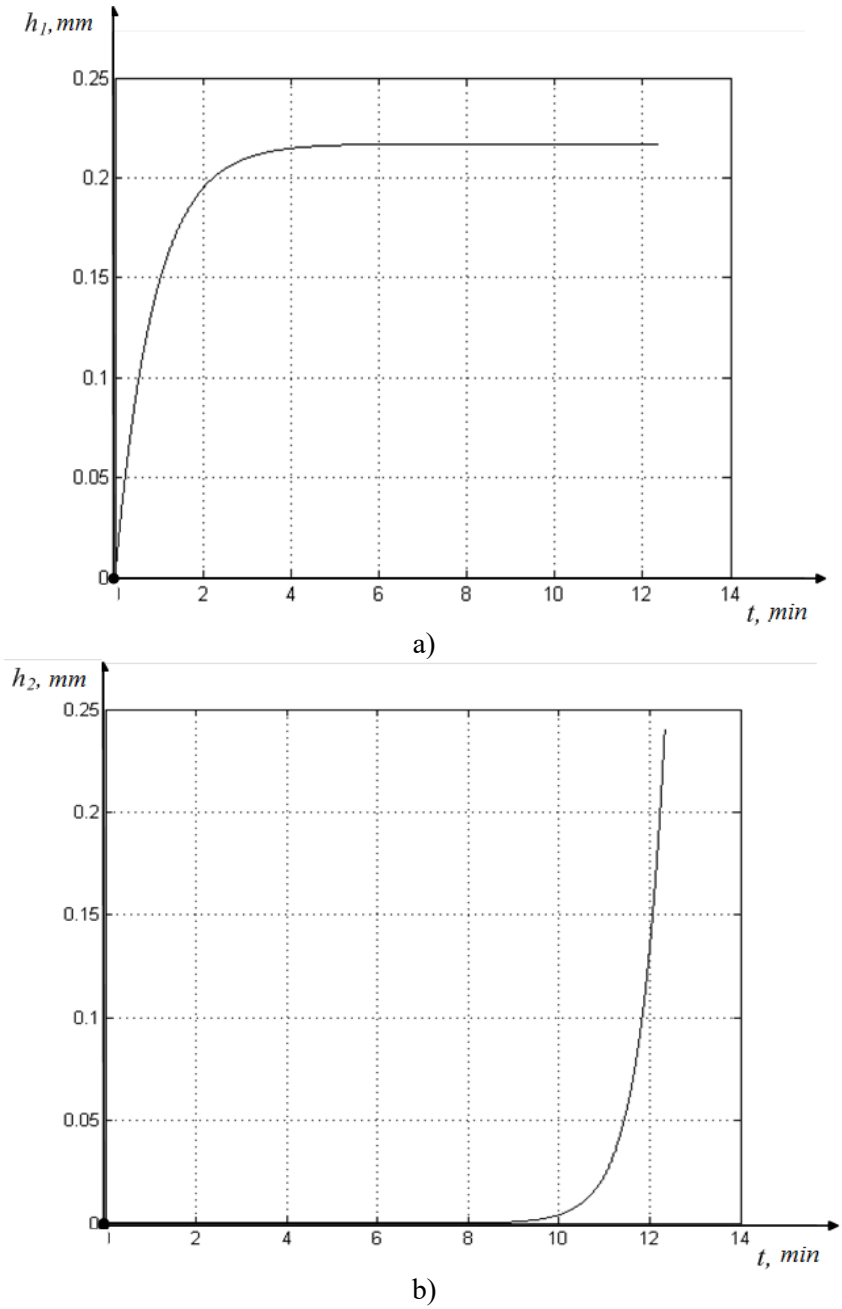

Figure 2. a) Diagram of the wear and tear run-in curve, b) Wear Tool Degradation Curve Graph

As can be seen from Figure 2 b), the degradation of the tool begins to have a significant effect on the wear curve only after 9 minute of processing. The curve reflecting the process of degradation of the cutting wedge is different from zero and up to this minute, but its growth here is not very large, nor is its effect on the entire wear curve up to 10 seconds of the cutting process great.

Only one question of interest is whether tool vibrations will be taken into account in the in-run and degradation curves of the cutting wedge when modeling wear using the Volterr operator. To answer this question, we simulate the Volterra operator with various types of vibration signals, which we will relatively evaluate using the vibration signal value module. This is due to the fact that direct integration of the complex cutting speed signal, which has a periodic part in its composition, will lead to the fact

that the integral of the periodic component over the observation period will be zero. To numerically estimate the instrument vibration signal, we used the following integral index:

$$VA = \sqrt{(\int_0^{T_v} \frac{dx(t)}{dt}^2 dt)} \tag{3}$$

where $x(t)$ - the vibration signal itself, and T_v - the signal observation period.

To simplify our reasoning, we assume that we are talking about a scalar case of cutting, in which the cutting force is constant, and the speed of relative movement of the tool along the workpiece is the sum of the cutting speed and deformation vibrations of the tool. This allows us to describe the power of irreversible transformations as the product of the cutting force (F) on the sum of the cutting speed (V) and the speed of the deformation movements of the tool (dx/dt), or in the form of an expression:

$$M(t) = F(V - \frac{dx(t)}{dt}) \tag{4}$$

The operation of the cutting force in this case is conveniently modeled using the following expression:

$$A(t) = F(Vt + VA) \tag{5}$$

When modelling, we will use the initial data obtained by us earlier in experiments on a lathe, where the cutting speed V = 2620 mm/s, the cutting force F = 45 N., the amplitude of the tool vibration speed in the cutting direction was 50-200 mm/s, the oscillation frequency was about 2000 Hz. Consider two extreme cases, in the first we take two extreme cases, the case with an amplitude of oscillations of 50 mm/s and the case of oscillations of 200 mm/s. As can be seen from Figure 5, the energy growth of the vibration signal reflecting the dynamics of the deformation movement of the tool was 4 times with 50 mm/s in Figure 4 a), up to 200 mm/s in Figure 4 b). Results of simulation of in-run and degradation curves taking into account accepted two versions of tool vibrations in cutting direction are given in Figure 3.

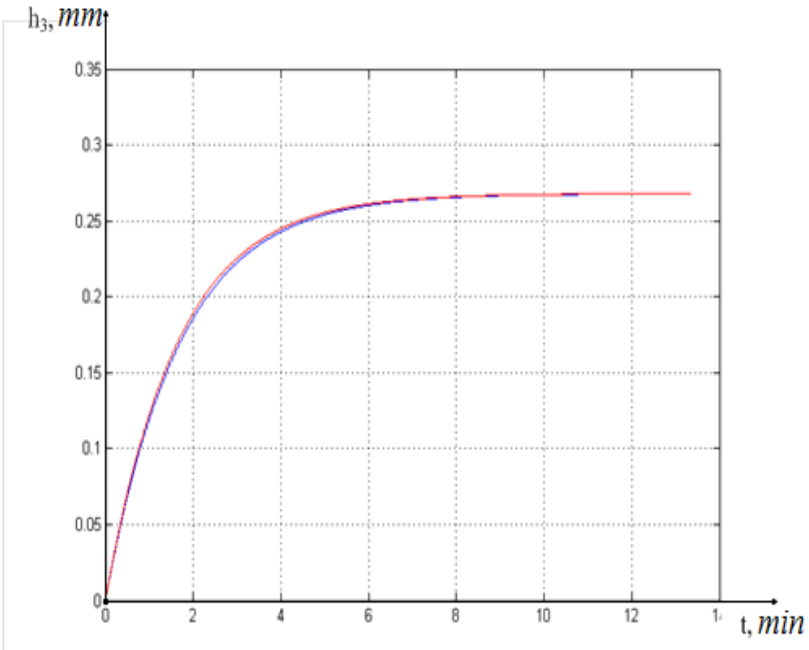

a)

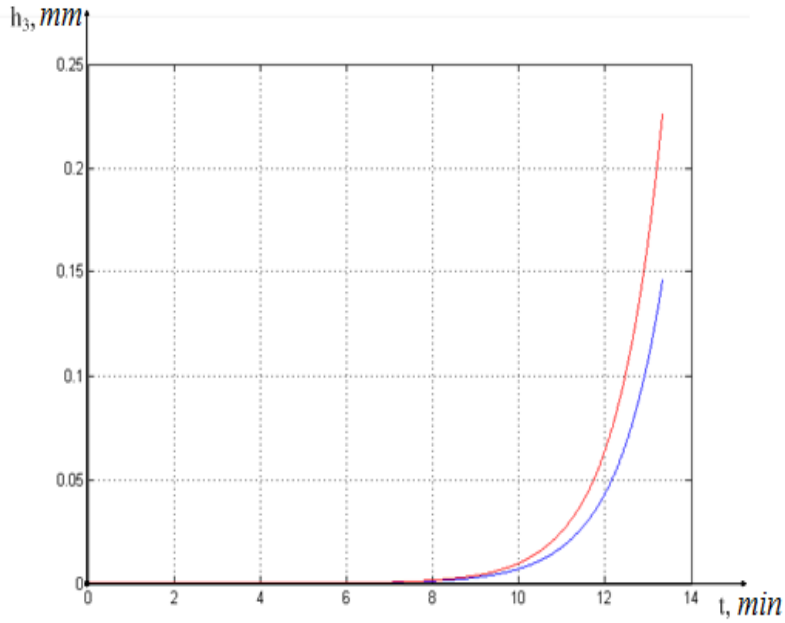

b)

Figure 3. Simulation results: (a) run-in graphs, (b) cutting wedge degradation plot

As can be seen from Figure 3, changes in the curve reflecting the wear of the in-tool appear only in part of the degradation characteristic (see Figure 3 (b)) and almost do not appear in the run-in curve (see Figure 3 (a)). Note that in both characteristics, red, a characteristic associated with a more amplitude version of the instrument vibrations is shown.

The force that determines the reaction on the back face will remain unchanged, and the decomposition coefficients will be made dependent on the degree of degradation of the h_3^d instrument. According to our research presented in the second section, the greatest impact of the degradation of the cutting wedge has on the components of the cutting forces Px, Py. We take as a hypothesis the following mathematical description of the dependence of decomposition coefficients:

$$\begin{aligned} \chi_1 &= \chi_1^{\,0} + a_1 h_3^d \\ \chi_2 &= \chi_2^{\,0} + a_2 h_3^d \\ \chi_3 &= \sqrt{\chi_1^{\,2} + \chi_2^{\,2}} \end{aligned} \tag{6}$$

wherein a1 and a2 are coefficients linking the restructuring of the power response to the shaping movements of the tool when the cutting wedge is degraded. According to our experiments, the components of the cutting forces when the wear on the back face changes from zero to about 0.42 mm, increase along the x coordinate by 125%, along the y coordinate by 65%, and along the z coordinate by 36%. This makes it possible to make the assumption of pre-ascendancy a1 over a2 almost twice, we accept in the future that a1 = 1 over a2 = 0.5. Given this, we assume that the model of the dynamics of the deformation movement of the tool will take the following form:

$$
\begin{aligned}
m\frac{d^2x}{dt^2} + h_{11}\frac{dx}{dt} + h_{12}\frac{dy}{dt} + h_{13}\frac{dz}{dt} + c_{11}x + c_{12}y + c_{13}z = \chi_1 F + \Phi_1 \\
m\frac{d^2y}{dt^2} + h_{21}\frac{dx}{dt} + h_{22}\frac{dy}{dt} + h_{23}\frac{dz}{dt} + c_{21}x + c_{22}y + c_{23}z = \chi_2 F + \Phi_2 \\
m\frac{d^2z}{dt^2} + h_{31}\frac{dx}{dt} + h_{32}\frac{dy}{dt} + h_{33}\frac{dz}{dt} + c_{31}x + c_{32}y + c_{33}z = \chi_3 F + \Phi_3
\end{aligned} \quad (7)
$$

To analyze the effect of the restructuring of the power reaction associated with the degradation of the cutting wedge on the static of the processing process, we assume that the forces formed on the back face of the tool are zero, in this case the static equations take the form:

$$
\begin{aligned}
c_{11}x + (c_{12} + \chi_1\rho)y + c_{13}z = \chi_1 F \\
c_{21}x + (c_{22} + \chi_2\rho)y + c_{23}z = \chi_2 F \\
c_{31}x + (c_{32} + \chi_3\rho)y + c_{33}z = \chi_3 F
\end{aligned} \quad (8)
$$

As can be seen from the expression (11), the stiffness matrix of the tool under cutting conditions becomes skew-symmetric, which suggests that the presence of circulating forces will be observed in the system. However, this effect will be present in the cutting system regardless of the wear of the cutting wedge, it is of interest that it will occur during the restructuring of the power reaction during the degradation of the cutting wedge. To analyze the effect of cutting wedge degradation, consider three variants h_3^d, the first $h_3^d = 0$, the second $h_3^d = 0.1$, the third $h_3^d = 0.2$, values of matrix coefficients $c = \begin{bmatrix} 1390 & 190 & 165 \\ 190 & 795 & 150 \\ 165 & 150 & 970 \end{bmatrix} kg/mm$. Orientation factors: $\chi_1 = 0{,}3369$, $\chi_2 = 0{,}48$, $\chi_3 = 0{,}81$. Process modes: depth $t_P = 2mm$, feed $S = 0{,}1mm$, spindle $n = 1000$ rpm, $\rho = 400kg/mm^2$, radius of machined part $R = 50mm$. That is, consider the case given in the previous section, when the total cutting force was approximately equal to 50 H. Based on these data, the values of the forces that prevent the shaping movements of the tool for the case $h_3^d = 0$ will be:

$$
\begin{aligned}
Fx_0 = 16 \\
Fy_0 = 24 \\
Fz_0 = 40
\end{aligned} \quad (9)
$$

The stationary values of the strain coordinates for this case are shown below:

$$
\begin{aligned}
x_0 = 0.0047 \\
y_0 = 0.022 \\
z_0 = 0.0376
\end{aligned} \quad (10)
$$

For the case of the non-zero value of the degradation of the cutting wedge, that is, when $h_3^d = 0.1$, the values of the forces that prevent the forming movements of the tool are given below:

$$
\begin{aligned}
Fx_0 = 21.85 \\
Fy_0 = 26.5 \\
Fz_0 = 36.34
\end{aligned} \quad (11)
$$

As can be seen from expression 11, at this level of degradation of the cutting wedge, the force component directed along the feed axis has increased most, and the cutting force itself has even decreased slightly. In the real case of cutting, the cutting force will not decrease, but even increase due to the effect of the growth of friction forces on the back face. The values of the orientation coefficients of the resistance forces for this case of wear were:

$$\begin{aligned} \chi_1 &= 0.437 \\ \chi_2 &= 0.53 \\ \chi_3 &= 0.7267 \end{aligned} \tag{12}$$

As seen in comparison with the previous version of the orientation forces, there is a decrease in the effect of the coefficient associated with the main motion direction. The equilibrium values of the coordinates of the state of the de-formation movement system of the tool are given below:

$$\begin{aligned} x_0 &= 0.0085 \\ y_0 &= 0.0253 \\ z_0 &= 0.0321 \end{aligned} \tag{13}$$

The next version of wear of the tool will be the value of the degradation component in h_3^d=0.2, the results of modeling the distribution of the cutting force along the deformation axes are given in the system (17).

$$\begin{aligned} Fx_0 &= 26.85 \\ Fy_0 &= 29 \\ Fz_0 &= 30.63 \end{aligned} \tag{14}$$

As can be seen from the expression (17), the trend we noted above is also executed here. The orientation coefficient values are as follows:

$$\begin{aligned} \chi_1 &= 0.537 \\ \chi_2 &= 0.58 \\ \chi_3 &= 0.6185 \end{aligned} \tag{15}$$

The corresponding equilibrium values of the deformation coordinates for this case are given in the system (19):

$$\begin{aligned} x_0 &= 0.0126 \\ y_0 &= 0.0288 \\ z_0 &= 0.0250 \end{aligned} \tag{16}$$

Further degradation of the cutting wedge leads to a critical restructuring of the cutting system in the space of deformation movements of the tool, and, for example, with h_3^d=0.39, the equilibrium values of the deformation coordinates will be:

$$\begin{aligned} x_0 &= 0.0213 \\ y_0 &= 0.0379 \\ z_0 &= -0.003 \end{aligned} \tag{17}$$

As can be seen from the expression (17), with such wear of the tool, the cutting wedge is literally drawn into the cutting zone, which is unacceptable from the point of view of processing. A similar

situation is also possible with improper sharpening of the cutting wedge. In this case, cutting becomes impossible and the tool must break.

To analyze the effect of cutting wedge degradation on the dynamics of the cutting process, consider this system in the version of equations (17), but under the condition of zero values of the forces formed on the back face of the tool (0).

The simulation results for case h_3^d=0.1and n = 880 are shown in Figure 4.

As can be seen from Figure 5, in comparison with Figure 3, as a result of the resulting degradation of the cutting wedge, the cutting system lost stability, given the above stated conditions of the experiment, this loss of stability is associated precisely with the restructuring of the power reaction. Results of simulation of cutting system with degradation value h_3^d = 0.2 and n = 880 are given in Figure 5.

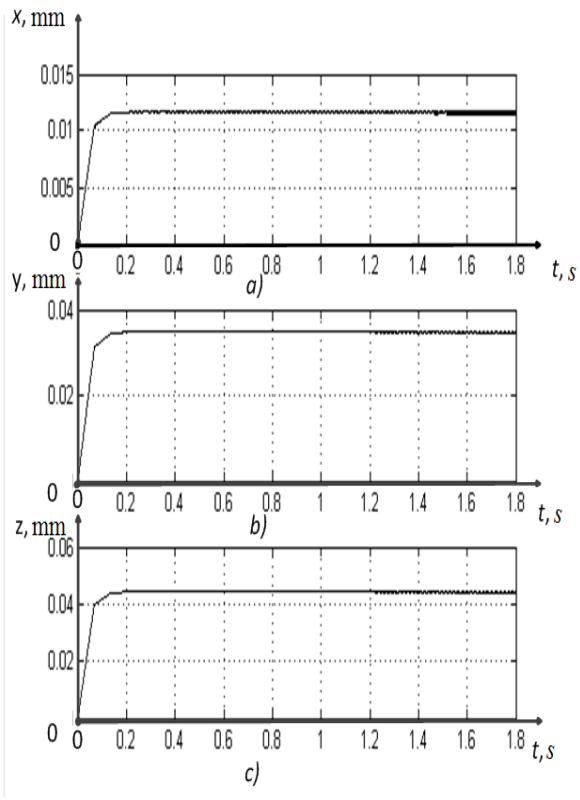

Figure 4. Simulation results - tool strain coordinates at h_3^d = 0.1

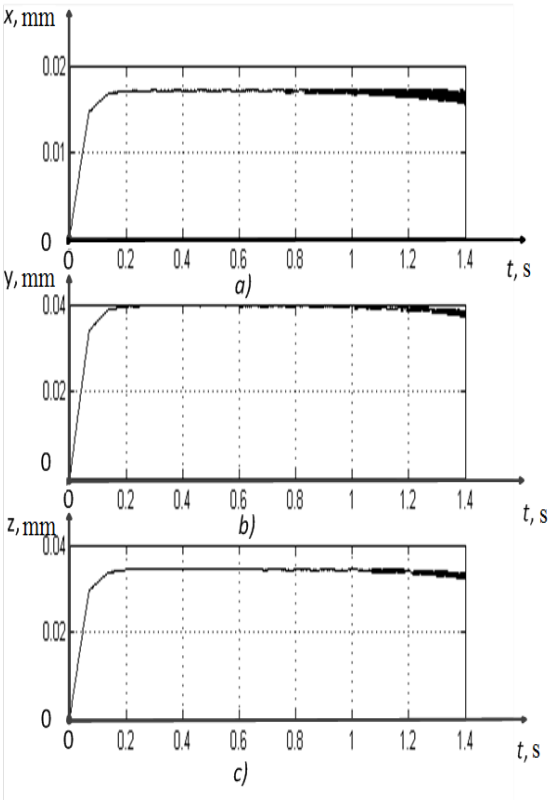

Figure 5. Simulation results - tool strain coordinates at h_3^d = 0.2

As can be seen from Figure 4, the system is also not stable, as in the previous case, but the process of fluctuation divergence is much faster than in the previous case.

Consider the dynamics of the vibrational motion of the cutting wedge for the case of stable system behavior, that is, at a processing speed of 1772 revolutions per minute. A variant of such treatment, in conditions of zero level of cutting wedge degradation is shown in Figure 5.

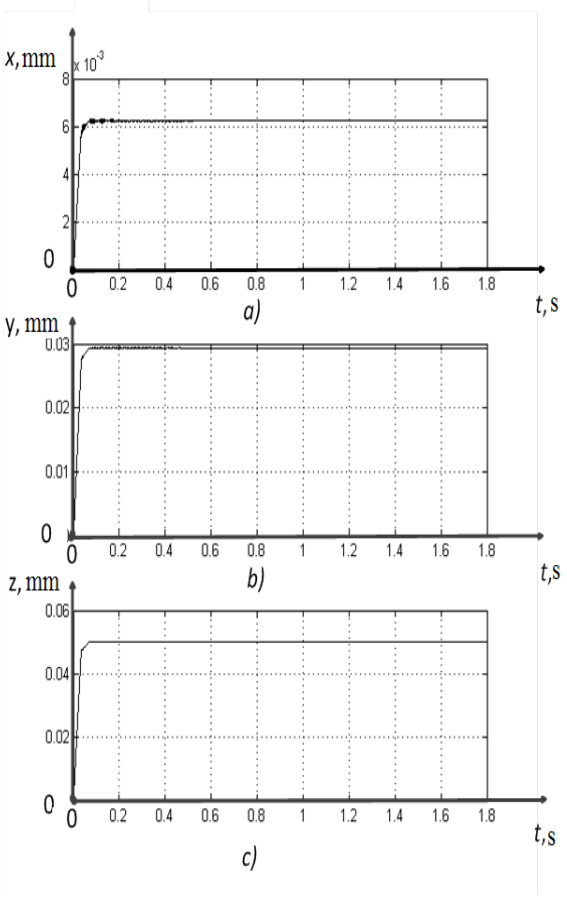

Figure 6. Simulation results - tool strain coordinates at $h_3^d = 0$

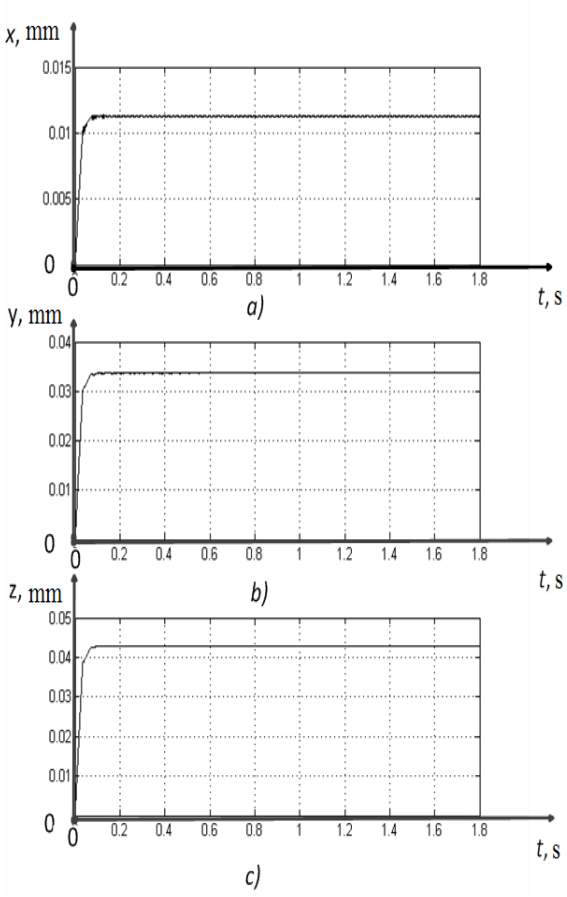

Figure 7. Simulation results - tool strain coordinates at $h_3^d = 0.1$

As shown in Figure 6 in comparison with Figure 5, there is no loss of stability in the cutting process. The vibration vibrations of the tool are resistant to this level of degradation of the cutting wedge, however, the vibrations in the feed direction are non-extinguishing, which distinguishes them quite strongly from the vibrations shown in Figure 7. The results of the modeling of the cutting system, for the case of the critical level of degradation of the cutting wedge with $h_3^d = 0.2$, are shown in Figure 8.

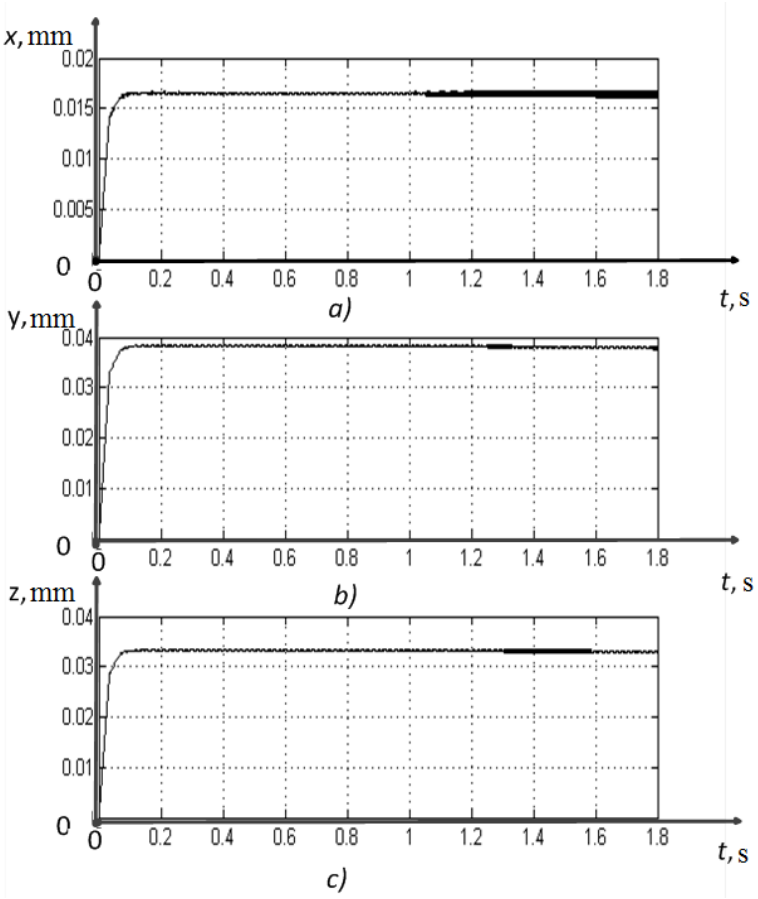

Figure 8. Simulation results - tool strain coordinates at $h_3^d = 0.2$

As shown in Figure 8, despite the fact that at a spindle speed of 1772 revolutions per minute, the regenerative effect is minimal, we observe a loss of stability by the cutting system, which is caused by the degradation of the cutting wedge.

The research allows us to form the following position: during the evolution of the tool during cutting, the formation of the contact area of the tool with the machined part, serves the purpose of self-organization of the cutting system through the formation of additional thermodynamic feedback, the stabilization of which is ensured by a certain combination of tool wear and limited vibration cutting mode. After this, the interconnectedness of the thermodynamic, power and vibration subsystems already ensures the stabilization of the wear intensity of the wired tool. In other words, during the cutting process, the cutting system tends to work the cutting wedge of the tool to reach a certain level of wear, which reduces the level of vibration activity of the tool and provides the function of thermodynamic feedback, which allows, through stabilization of the power reaction, to achieve the maximum possible decrease in the further wear intensity of the cutting wedge.

3. Discussion and conclusions

The validity of our position, in addition to the results of modeling the integral operator we obtained, is confirmed by the provision widely known from the works of A.D. Makarov on the existence of the optimal cutting mode from the point of view of ensuring the maximum resistance of the tool [28]. In his reasoning, A.D. Makarov relies on the principle of V. Reichel, which can be reduced to the statement that a certain period of resistance for a given tool-part pair corresponds to the same temperature in the contact zone of the tool and the workpiece. Based on this principle, A.D. Makarov introduces the concept

of optimal cutting temperature, which provides optimal tool resistance. However, the temperature in the contact area of the tool and the workpiece cannot be stationary, since the processing process itself is not substantially stationary. Therefore, in order to ensure that the optimum temperature is constant over a long period of the cutting process, it is necessary to provide, if not a steady state of the entire processing process, at least some quasi-stationary of this process. It is this quasi-stationary that is formed during the tool run-in and the formation of the primary wear of the cutting wedge, the stabilization of this quasi-stationary state of the cutting process occurs due to the stabilization of the cutting force, which in turn is stabilized by the temperature, which depends on the vibration activity of the tool, depending on the cutting force.

4. Acknowledgments

The study was carried out with the financial support of RFFI grant No. 19-08-00022.

References

[1] Sze S M 1969 *Physics of Semiconductor Devices* (New York: Wiley–Interscience)
[2] Dorman L I 1975 *Variations of Galactic Cosmic Rays* (Moscow: Moscow State University Press) p 103
[3] Caplar R and Kulisic P 1973 *Proc. Int. Conf. on Nuclear Physics (Munich)* vol 1 (Amsterdam: North-Holland/American Elsevier) p 517
[4] Szytula A and Leciejewicz J 1989 *Handbook on the Physics and Chemistry of Rare Earths* vol 12, ed K A Gschneidner Jr and L Erwin (Amsterdam: Elsevier) p 133
[5] Kuhn T 1998 Density matrix theory of coherent ultrafast dynamics *Theory of Transport Properties of Semiconductor Nanostructures(Electronic Materials* vol 4*)* ed E Schöll (London: Chapman and Hall) chapter 6 pp 173–214
[6] Huang, S N, Tan K K, Wong Y. S, De Silva C W, Goh H L, and Tan WW (2007). Tool wear detection and fault diagnosis based on cutting force monitoring. International Journal of Machine Tools and Manufacture, 47(3-4), 444-451.
[7] Arslan H Er, A O Orhan Sand Aslan E (2016). Tool condition monitoring in turning using statistical parameters of vibration signal. International journal of acoustics and vibration, 21(4), 371-378.
[8] Alonso F Jand Salgado D R (2005). Application of singular spectrum analysis to tool wear detection using sound signals. Proceedings of the Institution of Mechanical Engineers, Part B: Journal of Engineering Manufacture, 219(9), 703-710.
[9] DimlaSr D Eand Lister P M (2000). On-line metal cutting tool condition monitoring.: I: force and vibration analyses. International Journal of Machine Tools and Manufacture, 40(5), 739-768.
[10] Orhan S Er, A O Camuşcu N and Aslan E (2007). Tool wear evaluation by vibration analysis during end milling of AISI D3 cold work tool steel with 35 HRC hardness. NDT & E International, 40(2), 121-126.
[11] Tobias S A Machine Tools Vibrations (VibracionesenMáquinas-Herramientas) URMO, Spain (1961)
[12] Namachchivaya S et al. Spindle speed variation for the suppression of regenerative chatter //Journal of Nonlinear Science. 2003. Vol.13. №. 3. pp. 265-288.doi: 10.1007/s00332-003-0518-4
[13] Wahi P, Chatterjee A Regenerative tool chatter near a codimension 2 Hopf point using multiple scales //Nonlinear Dynamics. 2005. Vol. 40. №. 4. pp. 323-338.
[14] Stépán G, Insperger T, Szalai R Delay, parametric excitation, and the nonlinear dynamics of cutting processes //International Journal of Bifurcation and Chaos. 2005. Vol. 15. №. 09. pp. 2783-2798.doi: 10.1142/S0218127405013642
[15] Moradi H et al. Nonlinear behaviour of the regenerative chatter in turning process with a worn tool: Forced oscillation and stability analysis //Mechanism and Machine Theory. 2010. Vol. 45. №. 8. pp. 1050-1066. doi: 10.1016/j.mechmachtheory.2010.03.014

[16] Gouskov A Met al. Nonlinear dynamics of a machining system with two interdependent delays //Communications in Nonlinear Science and Numerical Simulation. 2002. Vol. 7. №. 4. pp. 207-221.doi: /10.1016/S1007-5704(02)00014-X
[17] Hahn R S On the Theory of Regenerative Chatter in Precision Grinding Operation // Transactions of American Society of Mechanical Engineers. 1954. Vol. 76. P. 356 – 260.
[18] Tobias S A and Fishwick W Theory of regenerative machine tool chatter //The engineer. 1958. Vol. 205. №. 7. pp. 199-203.
[19] Merritt H E Theory of self-excited machine-tool chatter: Contribution to machine-tool chatter research. 1965. №1. pp. 447-454. doi: 10.1115/1.3670861
[20] Grabec I Chaos generated by the cutting process // Physics Letter A. 1986. Vol. 117, N 8. P. 384 – 386. doi: 10.1016/0375-9601(86)90003-4.
[21] Balachandran B Nonlinear dynamics of milling process // Philosophical Transactions of The Royal Society A Mathematical Physical and Engineering Sciences. 2001. Vol. 359(1781). P. 793–819.
[22] Stepan G Modelling nonlinear regenerative effects in metal cutting // Philosophical Transactions of The Royal Society a Mathematical Physical and Engineering Sciences. 2001. Vol. 359. P. 739–757. doi: 10.1098/rsta.2000.07537.
[23] Litak G Chaotic vibrations in a regenerative cutting process // Chaos Solitons & Fractals. 2002. Vol. 13. P. 1531–1535. doi: 10.1016/S0960-0779(01)00176-X.
[24] Guskov A M, Voronov S A, Kvashnin A S Influence of torsional oscillations on the process of vibration drilling//Bulletin of the Moscow State Technical University named after N.E. Bauman. Series Mechanical Engineering. 2007. №.. 1 (66). p. 3-19.
[25] Vasin S A, Vasin L A Synergistic approach to describing the nature of the emergence and development of self-oscillations during turning//Science-intensive technologies in mechanical engineering. 2012. №.. 1. p. 11-16.
[26] Voronin A A Influence of ultrasonic oscillations on the process of cutting heat-resistant alloys//Machines and tools. 1960. №.11. page 15 – 18.
[27] Zakovorotny V L, Lapshin V P, Babenko T S Assessing the Regenerative Effect Impact on the Dynamics of Deformation Movements of the Tool during Turning //Procedia Engineering. 2017. Vol. 206. pp. 68-73. doi:10.1016/j.proeng.2017.10.439
[28] Zakovorotny V L, Lukyanov A D, Gubanova A A, Khristoforova V V Bifurcation of stationary manifolds formed in the neighborhood of the equilibrium in a dynamic system of cutting // Journal of Sound and Vibration. 2016. Vol. 368. P. 174-190.doi: 10.1016/j. jsv.2016.01.020.
[29] Zakovorotny V, Lapshin V, Gvindjiliya V Tool wear due to deformation displacements during metal turning //AIP Conference Proceedings. AIP Publishing LLC, 2019. Vol. 2188. №.1. pp. 030002.
[30] Zakovorotny V L, Lapshin V P, Babenko T S Modeling of Tool Wear: Irreversible Energy Transformations //Russian Engineering Research. 2018. Vol. 38. №. 9. p. 707-708.
[31] Zharkov I G Vibrations when machining with a blade tool. L.: Engineering. 1986. 184 s.
[32] Markov A I Ultrasonic cutting of hard-to-process materials. M.: Mashinostroeniya. 168. 367 s.
[33] Zakovorotny V L, Fleck M B Dynamics of the cutting process. Synergistic approach. - Rostov N/A: Terra, 2006. 880 c. ISBN: 5-98254-055-2
[34] Ryzhkin A A,Synergetics of wear of instrumental cutting materials (triboelectric aspect). Rostov N/A: Publishing Center of DSTU. 2004. 323 sec. ISBN: 5-7890-0307-9

Conflict of interest

The authors declare that there is no conflict of interest.

Synergetic synthesis of tracking control systems

A N Popov

Southern Federal University, Taganrog, Russia

Abstract. The application of the principles and methods of the synergetic theory of control for the synthesis of automatic controllers that provide a solution to the tracking problem is considered. The study aims to develop analytical procedures for the synthesis of tracking controllers for a general class of nonlinear systems. The proposed approach is based on the idea of the current piecewise linear approximation of the input signal and the synthesis of an asymptotic observer of the slope coefficient of the approximating straight line. To confirm the theoretical conclusions, a computer simulation of the synthesized tracking system with various input signals was carried out.

1. Introduction

Tracking systems are usually allocated to a separate class of automatic control systems. Unlike the most common stabilization systems that perform the task of holding controlled variables in a given constant value, tracking systems must provide a change of the controlled variable $x^{(c)}$ in accordance with some time signal $g(t)$ received at the system input. This input signal is considered as a setting action, which is an a priori unknown function of time. The task of the tracking system is to reproduce the input signal with a given accuracy $\left|g(t) - x^{(c)}\right| \le \varepsilon$.

Currently, the design of tracking systems mainly uses the approaches of the classical theory of automatic control using a linear or linearized mathematical description of controlled processes [1] – [5]. The use of "frequency" methods of analysis and synthesis allows us to solve the tracking problem for a given order of astatism of the system by the input effect. However, this approach encounters serious methodological difficulties in those cases where the dynamics of the controlled object is substantially non-linear. The need to increase the effectiveness of linear tracking controllers determines the use of various areas of modern control theory [6] – [12]: fuzzy logic, adaptive controllers, robust controllers, H_∞ control, etc. But the general "linear" ideology remains dominant.

Synergetic control theory [13] – [15] provides effective methods for the synthesis of controllers for controlling multidimensional and nonlinear objects. At the same time, the synthesized controllers solved the problem of stabilization of the controlled variable, or the problem of generating oscillations of the controlled variable. In [16], [17], a solution to the problem of synergetic synthesis of controllers providing reproduction of a given time signal (periodic or chaotic) and involving the introduction of reference signal generators into the structure of a closed system is presented. It was believed that the characteristics of a temporary signal are a priori determined, and its dynamics can be described by the corresponding differential equations.

This article will show the use of the principles and methods of the synergetic theory of control to solve the problem of the synthesis of tracking automatic control systems in its generally accepted formulation.

2. Synthesis method

Let us formulate the problem of the synthesis of tracking controllers, assuming that the object has one control channel and it is necessary to ensure tracking of one input signal.

Let the dynamics of a controlled object be described by a system of ordinary differential equations:

$$\dot{\mathbf{x}} = \mathbf{F}(\mathbf{x}, u, g) \tag{1}$$

where $\mathbf{x}$ is the vector of system state variables, u is the control action, $g = g(t)$ is the setting action. Any continuous function with a sufficient degree of accuracy can be approximated by a polynomial. If the degree of this polynomial is equal to unity, a linear approximation takes place, which has found wide application in practice.

The reference signal in the tracking system, which is an unknown function of time, can also be considered as a linear signal with a variable slope coefficient of the approximating straight line. These considerations formed the basis for the development of the following methodology for the synergetic synthesis of tracking controllers, which is based on the principle of expanding the state space of the original system by adding differential equations of the reference time signal (a linear function of time) and uses the synthesis technique of an asymptotic observer for the slope of the approximating straight line.

If some value $g(t)$ is changed linearly in time: $g(t) = g_0 + g_1 t$ then the dynamics of this change is described by a differential equation $\dot{g} = g_1$. Then the extended system model (synthesis model) takes the following form:

$$\begin{aligned} &\dot{\mathbf{x}} = \mathbf{F}(\mathbf{x}, u), \\ &\dot{y}_1 = y_2, \\ &\dot{y}_2 = 0, \end{aligned} \tag{2}$$

where y_1 is the variable of the reference signal model, and y_2 is the variable characterizing the current value of the slope coefficient of the approximating straight line. From the last equation (2) it follows that y_2 is a piecewise constant quantity, and, therefore, is a piecewise linear function of time.

The synthesis procedure includes two stages. At the first stage, the controller is synthesized under the assumption that all the variables of model (2) are observable. On the second stage, an asymptotic observer is synthesized to evaluate the current value y_2. After that, the estimate of $\hat{y}_2$ is substituted into the synthesized control law.

Let us show the application of this technique with a simple example. We pose the problem of synthesizing a tracking controller for a nonlinear object described by the model:

$$\begin{aligned} &\dot{x}_1 = x_2, \\ &\dot{x}_2 = (u + f(x_2))a_1. \end{aligned} \tag{3}$$

Such structure is seen in the models that describe the dynamics of mechanical systems with one degree of freedom, where the variables x_1 and x_2 correspond to movement and velocity, control u means the controlling external force, and the function $f(x_1, x_2)$ characterizes the forces accompanying the movement (friction, gravity, etc.).

In this case, the extended system model takes the form:

$$\begin{aligned} &\dot{x}_1 = x_2, \\ &\dot{x}_2 = (u + f(x_1, x_2))a_1 \\ &\dot{y}_1 = y_2, \\ &\dot{y}_2 = 0. \end{aligned} \tag{4}$$

The synergetic synthesis methods are based on the idea of introducing attractive invariant manifolds $\psi_i(\mathbf{x})=0$ in the state space of a controlled system. The control law in the scalar case (one control channel) is found as a solution to a functional equation written with respect to the corresponding macro variable ψ_1. This equation is a differential equation that has asymptotic stability with respect to $\psi_1=0$. Usually, the first-order functional equation $T_1\dot{\psi}_1+\psi_1=0, T_1>0$ is used.

The controller should provide an asymptotic convergence of the controlled variable to the variable of the reference signal: $x_1 \to y_1$. Therefore, we introduce an invariant manifold

$$\psi_1 = x_2 + k(x_1 - y_1) = 0.$$

In this case, given the $\psi_1=0$, the dynamics of the controlled variable is described by a differential equation $\dot{x}_1=-k(x_1-y_1)$, which, at $k>0$, has the asymptotic stability with respect to y_1.

The control law is found as a solution to the functional equation $T_1\dot{\psi}_1+\psi_1=0$ by virtue of the equations of the model (4):

$$\begin{aligned} &T(\dot{x}_2 + k(\dot{x}_1 - \dot{y}_1)) + x_2 + k(x_1 - y_1) = 0 \Leftrightarrow \\ &\Leftrightarrow T((u + f(x_1, x_2))a_1 + k(x_2 - y_2)) + x_2 + k(x_1 - y_1) = 0 \Rightarrow \\ &\Rightarrow u = -f(x_1, x_2) - k(x_2 - y_2)/a_1 - \left(x_2 + k(x_1 - y_1)\right)/(a_1 T). \end{aligned} \tag{5}$$

For the synthesis of the observer, the method of synergetic synthesis of asymptotic observers is used [14]. The model of the extended system is represented in the vector-matrix form:

$$\begin{aligned} \dot{\mathbf{v}} &= \mathbf{g_0}(\mathbf{v}, u) + \mathbf{G_1}(\mathbf{v})\mathbf{w}; \\ \dot{\mathbf{w}} &= \mathbf{h_0}(\mathbf{v}, u) + \mathbf{H_1}(\mathbf{v})\mathbf{w}, \end{aligned}$$

where $\mathbf{v}$ is the vector of the observed variables, $\mathbf{w}$ is the vector of the observed variables.

In our case:

$\mathbf{v} = [x_1 \quad x_2 \quad y_1]^T$, $\mathbf{w} = y_2$, $\mathbf{g_0} = [x_2 \quad (u + f(x_1, x_2))a_1 \quad 0]^T$, $\mathbf{G_1} = [0 \quad 0 \quad 1]^T$, $\mathbf{h_0} = 0$, $\mathbf{H_1} = 0$.

The observer equations are found from the expression

$$\begin{aligned} \dot{\mathbf{z}} &= \mathbf{L}\mathbf{z} - \mathbf{L}\int_{\mathbf{0}}^{\mathbf{v}} \Gamma(\mathbf{v})d\mathbf{v} - \mathbf{h_0} + \Gamma(\mathbf{v})\mathbf{g_0}, \\ \hat{\mathbf{w}} &= \int_0^{\mathbf{v}} \Gamma(\mathbf{v})d\mathbf{v} - \mathbf{z}. \end{aligned} \tag{6}$$

where $\mathbf{z}$ are the observer variables, $\mathbf{L}$ is the matrix selected from the observer stability condition (in our case, it contains one element l_1, the stability condition is $l_1<0$), and the matrix $\Gamma(\mathbf{v})$ is calculated from the equation $\mathbf{H_1} - \mathbf{L} = \mathbf{\Gamma}(\mathbf{v})\mathbf{G_1}$.

By substituting the matrices and vectors into (5), we obtain the desired observer equations:

$$\dot{z}_1 = l_1 z_1 + l_1^2 y_1 \tag{7}$$

and the estimates of the slope of the approximating straight line

$$\hat{y}_2 = -l_1 y_1 - z_1 \tag{8}$$

It should be noted that equations (7), (8) are valid for any objects described by model (2).

Taking into account the assessment (8), the control law takes the final form:

$$u = -f(x_1, x_2) - k(x_2 + l_1 y_1 + z_1)/a_1 - \big(x_2 + k(x_1 - y_1)\big)/(a_1 T). \quad (9)$$

3. Computer modelling

To analyze the effectiveness of the synthesized tracking controller, computer simulation of a closed-loop system (3), (7) – (9) was carried out under various input signals. In real operating conditions, the input of the tracking system receives not the piecewise-linear reference signal y_1, but the signal $g(t)$ that varies in time in an arbitrary way. Therefore, for the correct modeling of the system, it is necessary to make a replacement of $y_1 \leftrightarrow g(t)$ in the equations (7) - (9). The function $f(x_1, x_2)$ was set as $f(x_1, x_2) = -x_2 - x_2^3$.

In the simulation, the signal $g(t)$ was defined as a piecewise continuous function of time:

$$g(t) = \begin{cases} -5 + t, \ 0 \le t < 10; \\ 1 + 0{,}5t - 0{,}1t^2, \ 10 \le t < 20; \\ 30\sin 0{,}3t, \ 20 \le t < 50; \\ 10\sin 0{,}2t - 5\cos 0{,}3t, \ 50 \le t < 100. \end{cases}$$

Figure 1 shows the transient graphs of a controlled variable and a input signal. Figure 2 shows the transient graphs of the estimation of the slope of the approximating line. It can be seen that the estimate at the first stage tends to a value of 1, which corresponds to the slope coefficient of the linear function $g(t) = -5 + t$. At the second stage, it changes linearly, which corresponds to a piecewise linear approximation of a parabolic function. At the third and fourth stages, it varies periodically, which corresponds to a periodic input signal.

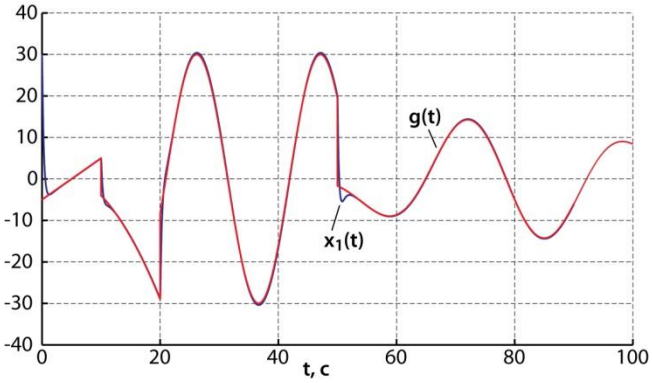

Figure 1. Transient processes of a controlled variable and an input signal in the tracking system

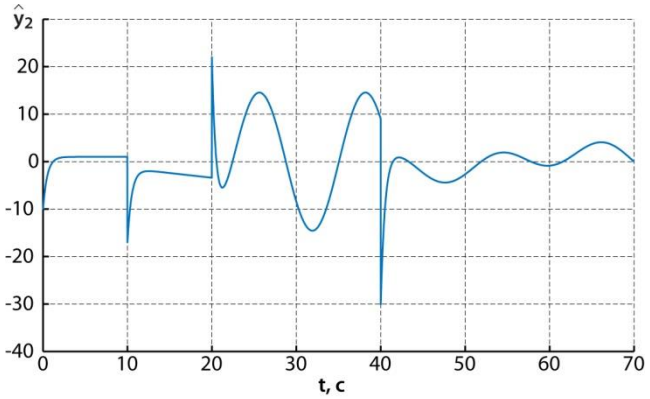

Figure 2. Transient processes of estimation of the slope of the approximating line in the tracking system

4. Conclusion

By assessing the results of computer modeling, we can conclude that the proposed approach allows us to synthesize controllers that can work out the defining influences of a general class of continuous functions of time and can serve as a theoretical basis for the design of tracking systems for controlling nonlinear dynamic objects.

5. Acknowledgments

This work was supported by the Russian Foundation for Basic Research, project no. 18-08-00924.

References

[1] Akhmetzhanov A A and Kochemasov A V 1986 *Tracking systems and regulators* (Moscow: Energoatomizdat) p 286
[2] Barsky A G 2009 *Optoelectronic Tracking Systems* (Moscow: University book) p 200
[3] Nikiforov V O Lukyanova G V 2011 The tracking system of combined control *Scientific and Technical Bulletin of the St. Petersburg State University of Information Technologies Mechanics and Optics* no 6 (76) pp 39-43
[4] Ivanchura V I Prokopyev A P 2011 Optimization of the tracking system of automatic control *Bulletin of the Siberian State Aerospace University* no 5 (38) pp 44-49
[5] Shapran A A Ustyugova A A 2013 Synthesis of a control system for a tracking drive of increased accuracy *Bulletin of the Ural State University of Railway Engineering* no 3 (19) pp 45-49
[6] Bo Xiao, Lam H K, Ge Song and Hongyi Li 2013 Output-Feedback Tracking Control for Interval Type-2 Polynomial Fuzzy-Model-Based Control Systems *IEEE Transactions on Industrial Electronics* vol 60 no 12 pp 5830-5840
[7] Chang Yeong-Chan 2010 Robust tracking control for nonlinear MIMO systems via fuzzy approaches *Automatica* vol 36 no 10 pp 1535-1545
[8] Ivanchura V I, Prokopyev A P and Emelyanov R T 2012 A model of a tracking system of automatic control with a fuzzy controller *Bulletin of the Siberian State Aerospace University* no 3 (43) pp 15-20
[9] Putov V V, Dung Ch A and Kuang F K 2018 Adaptive electromechanical tracking system with two- and three-mass nonlinear elastic objects and neurofuzzy control *News of St. Petersburg Electrotechnical University "LETI"* no 5 pp 21-24
[10] Reshetnikova G N 2006 Tracking system of adaptive control with a predictive model of lower order Bulletin of Tomsk State University no 290 pp 237-240
[11] Maltsev G N and Afonin G I 2014 Optimization of the adaptive circuit parameters of the tracking system of automatic control based on the analysis of the frequency response News of higher educational institutions. Instrument Engineering vol 57 no 7 pp 26-31

[12] Celentano L 2017 Pseudo-PID robust tracking design method for a significant class of uncertain MIMO systems *IFAC-PapersOnLine* vol 50 no 1 pp 1545–1552
[13] Kolesnikov A A 1994 *Synergetic control theory* (Moscow: Energoatomizdat) p 344
[14] *Modern applied control theory Part 2 Synergetic approach in control theory* 2000 (Taganrog: TRTU publ) p 656
[15] Kolesnikov A A 2019 *Synergetic control methods for complex systems: the theory of system synthesis* (Moscow: URSS Publ) p 244
[16] Popov A N 2012 Synergetic synthesis of regulators for the problems of generation of oscillatory modes in technical systems *News of SFedU. Technical sciences* no 4 (129) pp 156-162
[17] Popov A N 2016 Synergetic synthesis of autopilots for the formation of reference motion trajectories in the horizontal plane *Modern Science and Innovation* no 4, pp 29-36

Development of an algorithm for forming the structure of composite fiber insulation with heat-accumulating properties in clothing

I V Cherunova[1,3*], E B Stefanova [1], S Sh Tashpulatov [2]

[1] Department of Design and technology, Don State Technical University, Shakhty, Russia

[2] Department of design and technology of sewing products, Tashkent Institute of textile and light industry, Tashkent, Uzbekistan

[3] Chair of Modeling and Simulation, Rostock University, Rostock, Germany

*Corresponding author: i_sch@mail.ru

Abstract. In the article research results are presented, which aim to development of an algorithm for forming the structure of composite fiber insulation with heat-accumulating properties in clothing. The presence of heat-retaining polymer components in the structure of the fibrous composition of materials leads to its general heterogeneity. Combining such materials with traditional fibrous structures is a rather promising area, as it allows for the use of heat-retaining effect not only in thin materials, but also in voluminous thermal insulating materials. As the main core fibrous composition of materials used to study a system of combining with elements of heat-retaining components, we have selected composition of polyester fibers of various configurations and sizes. Pattern of connections between the composition of fibers and groups of materials intended for integrating with heat-retaining components, scheme for creating priority fibrous materials with heat-retaining properties, which form heat-protective textile clothing shells we have developed.

1. Introduction

Clothing heat-retaining properties are actively developing in all countries worldwide. They are of particular importance for cold-protective clothing. The presence of heat-retaining polymer components in the structure of the fibrous composition of materials leads to its general heterogeneity. This is the reason for the change in the properties of a composite material, as compared to the properties of its initial components. Special heat-retaining effects of materials are based on the phase-change properties of the integrated active polymers [1, 2]. Combining such materials with traditional fibrous structures is a rather promising area, as it allows for the use of heat-retaining effect not only in thin materials, but also in voluminous thermal insulating materials. For the purpose of a comprehensive analysis of the fibrous composition of modern textiles, we studied [3, 4] fiber classification according to [4]. Depending on their origin, textile fibers are divided into natural and chemical ones. Chemical fibers are subdivided into artificial and synthetic ones. Given the diversity of methods for obtaining primary fibers, modern

fibrous materials represent a wide range of products [5-7]. Therefore, an urgent task arises – development of an algorithm for forming the structure of composite fiber insulation with heat-accumulating properties in clothing.

2. Theoretical part

The range of natural and semi-natural insulating materials includes such fabrics as batting, sherston, and a loose variant of insulating material – feather-down mixture, which account for a much smaller share of industrial output in the total volume of the garment industry and, as a general rule, provide special properties of clothing based on the advantages of natural materials and on the absence or a small proportion of synthetic products in the clothing composition. This is important, for instance, in the production of clothing that protects against static electricity or children's clothing. In this case, additional thermic regulation properties due to integrating heat-retaining materials into the structure of the clothing pack have some limitations. Therefore, as the main core fibrous composition of materials used to study a system of combining with elements of heat-retaining components, we have selected composition of polyester fibers of various configurations and sizes.

Our analysis of lining materials showed that their main parameters should ensure their high density with a small thickness, which provides the main important properties of the inner surface layer of clothing [8] – slipping and abrasion resistance.

This problem can be solved only at the stage of primary production of fabrics using initial composite fibers with heat-retaining properties, which are directly integrated into the material structure at the stage of primary nonwoven or knitted production.

Based on the research, we have developed a pattern of connections between the composition of fibers and groups of materials intended for integrating with heat-retaining components (Fig. 1).

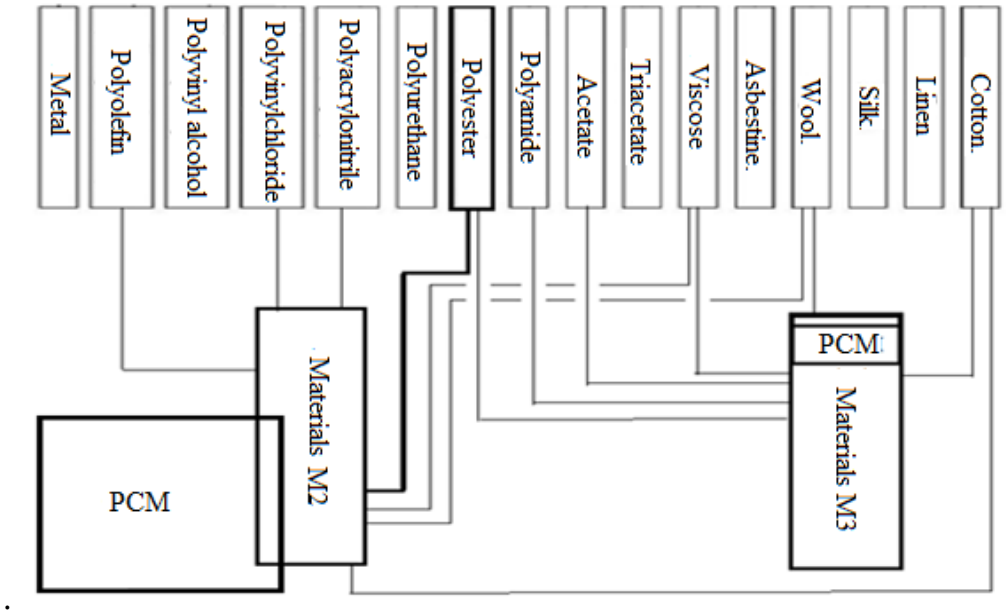

Figure 1. Block 1 "A" of the algorithm for creating the structure of composite fiber insulating materials: the connection pattern of the fibrous base and material groups of the closing heat-protective pack with heat-retaining materials

The considered fibers (in accordance with Fig.1) form the required functions in the corresponding layers of clothing.

Thus, in the corresponding material layers, different functions are provided:

M1 – the main barrier protection function against harmful environmental factors (production process and weather), preserving and maintaining the clothing shape and size;

M2 – the thermal insulation and thermoregulation function (including heat preserving);

M3 – moisture exchange, thermic regulation (including heat preserving), surface sliding.

Polymer materials with heat-retaining properties are classified based on the method of accumulating thermal energy, as well as the content of such components in the general structure of a composite material [9].

In the classification of heat-retaining materials, important characteristics of the thermal energy retaining process are as follows [10,11]:

- capacity per unit volume or weight;
- operating temperature range;
- methods of supply and extraction of heat and the corresponding temperature differences;
- temperature stratification in the accumulator;
- power required to supply and remove heat;
- volumes of structural elements related to the accumulation system;
- means for regulating heat losses by the heat accumulator;
- manufacturing and operating costs [11

There is a classification of heat-retaining materials, as shown in Fig. 2 [11, 12].

For fibrous composite materials with heat-retaining properties, the clothing industry uses heat-retaining materials (HRMs), integrated with the structure and conditions of production and operation of their main fiber systems under consideration. Encapsulated and granular materials can be compatible with fibrous structures and depend on the fiber structure, size, and connection system. As solid hydrocarbons, we can use paraffin, ceresin, wax, primary higher fatty synthetic alcohols with obtaining the stabilization temperature of +53 to +80 ℃ [13]. This temperature range, as a prerequisite for application in clothing, is typical for clothing that protects against high temperatures. The study [10,14] is devoted to the development and research of cold-protective materials, which allowed to establish the actual melting point ranges for octadecane ($C_{18}H_{38}$), nonadecane ($C_{19}H_{40}$), eicosane ($C_{20}H_{42}$), the melting point of which is set within the range of +27.6...38.6 ℃.

Among the substances and materials used as HRMs, we identified inorganic substances such as sodium thiosulfate pentahydrate ($Na_2S_2O_3 \cdot 5H_2O$), sodium sulfate decahydrate ($Na_2SO_4 \cdot 10H_2O$), sodium sulfite heptahydrate ($Na_2SO_3 \cdot 7H_2O$), sodium carbonate decahydrate ($Na_2CO_3 \cdot 10H_2O$), sodium acetate trihydrate ($Na(CH_3COO) \cdot 3H_2O$) [15], and typical paraffins [16,17].

However, the main temperature range of interest for heat accumulation in the operating mode of heat-protective clothing is within +20...+40℃ [18].

3. Practical part

Our analysis of modern developments in the creation and application of special encapsulated materials with heat-retaining properties for fibrous structures allowed us to identify a group of materials intended for integrating with textiles for clothing.

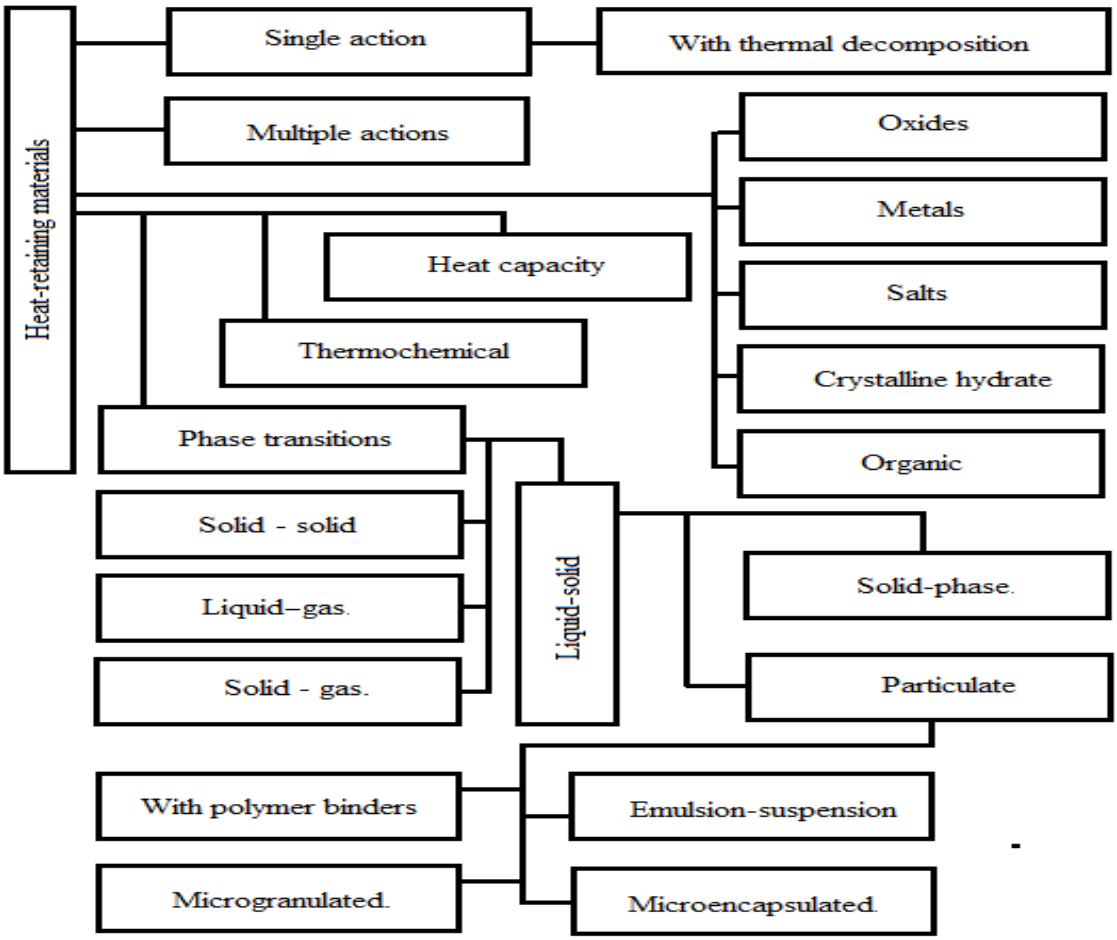

Figure 2. General classification of heat-retaining materials

For heat-protective clothing, as applicable to M3 material group, materials with heat-retaining properties can be integrated into the textile base using the method [19].

Based on this method, the most common types of textiles with heat-retaining properties have been developed, that are implemented in the form of nonwoven and knitted structures.

For voluminous heat-insulating materials of the M2 group in heat-protective clothing, it is advisable to concentrate micro-encapsulated components directly in the volume of fibers [20,21].

As a result, we obtained a variety of multicomponent fibrous integrated materials. Their basis consists of fibrous systems [22,23,24] that are typical for nonwoven voluminous textile materials, whereas integrated components are parts of heat-retaining micro-encapsulated materials of various sizes and proportions in volume.

Therefore, as a result of our studies of modern heat-retaining materials, their composition and production methods, as well as specifics of the method for integrating into textile materials, we developed a scheme for creating priority fibrous materials with heat-retaining properties, which form heat-protective textile clothing shells, as presented in Fig. 3.

Algorithm for forming the structure of composite fiber insulation with heat-accumulating properties in clothing has been developed (Fig. 4)

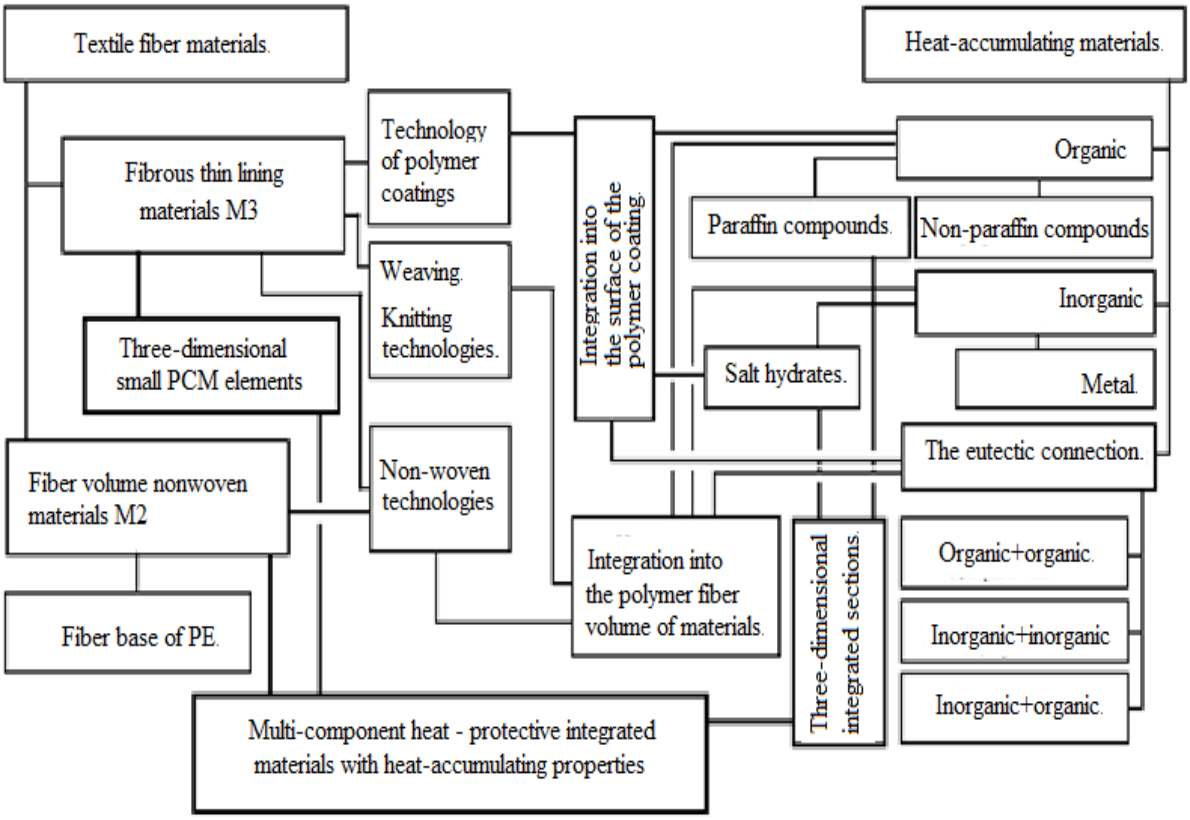

Figure 3. Block "B" of the algorithm for creating the structure of composite fibrous insulating materials: the scheme for creating priority fibrous materials with heat-retaining properties that form heat-protective textile clothing shells

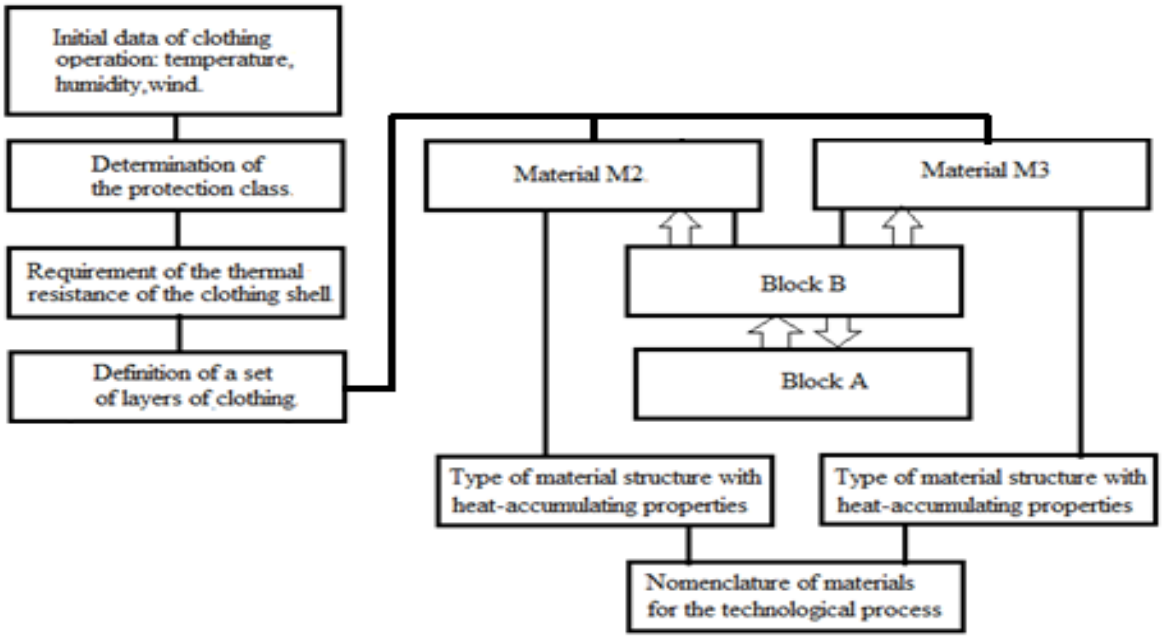

Figure 4 Algorithm for forming the structure of composite fiber insulation with heat-accumulating properties in clothing

4. Discussion and conclusions

There is a concept and algorithm for designing complex textiles. Specific behavior of textiles is explored and resolved between methods of form-finding in physical studies, spring-based modeling and simulation, and finite element analysis. The sequence of methods is predicated upon the degree of topological complexity in the material system [25]. However, such a system and such an algorithm do not allow us to solve the problem of creating a fiber insulation. In the work [26] investigated the relationships between the thermal insulation properties of the set of materials and the parameters of the particular components of sets, as well as the configuration of layers. The results obtained [26] have expanded the knowledge about the thermal properties of complex fibrous materials, but do not have a comprehensive algorithm for designing new materials.

The result is the suggested algorithm that allows to build the route for obtaining a multicomponent insulating material depending on the type and structure of the core insulating materials. The algorithm allows to immediately determine the type of process methods for producing a new multicomponent material, depending on the chemical nature of obtaining heat-retaining active components, that are integrated into new composite clothing materials.

5. Acknowledgements

The reported study was funded by RFBR, project number 19-38-90324.

References

[1] Leon-Gil A, Martinez-Flores J J, Alvarez-Quintana J 2019 A hybrid thermal diode based on phase transitionmaterials. J.Mater Sci. 54:3211–3221

[2] Dulebová L, Jachowicz T, Duleba B 2016 Propertoes and application of polimer – clay nanocomposites // Transfer inovaciíi.Vol.33. pp.132-136.

[3] Cherunov P., Cherunova I., Knyazeva S., Stenkina M., Stefanova E. , Kornev N. 2015 The Development of the Research Techniques of Structure and Properties of Composite Textile Materials when Interacting with Viscous Fractions of Hydrocarbon Compounds. Proc. of the conference on “Textile Composites and Inflatable Structures” (Structural Membranes 2015) pp.555-564.

[4] GOST R 56561-2015/ISO/TR 11827:2012 2016 Textile materials. Determining the composition. Identification of fibers. M.: STANDARTINFORM. 26p.

[5] Bontoux L, Boucher P, Scapolo F 2017 Textiles and Clothing Manufacturing: Vision for 2025 and Actions Needed. EUR 28634 EN / Luxembourg: Publications Office of the European Union. - doi:10.2760/279200.

[6] Cherunova IV, Kovaleva AA, Nazarenko EV 2020 Experimental Evaluation of Thermal Protection Properties of Volume Textile Materials. Materials Science Forum. Vol.992, pp. 916-921.

[7] Akbarov R D., Zhilisbaeva R O., Tashpulatov S Sh, Cherunova I V, Bolysbekova RT 2018 Application of composite materials for protective clothing from exposure electric fields. Izvestiya Vysshikh Uchebnykh Zavedenii, Seriya Teknologiya Tekstil'noi Promyshlennost vol.5. pp.188-192.

[8] GOST 20272-2014 2015 Lining fabrics made of chemical yarns and yarns. General specifications. Moscow: STANDARTINFORM. 24p.

[9] Pospelova I Y, Pospelova M Y, Bondarenko A S, Kornilov D A 2018 Results of thermal modeling of Smart Energy Coating with phase-transition material for independent electricity generation. IOP Conf. Series: Journal of Physics: Conf. Series 1015 (2018) 032108 doi :10.1088/1742-6596/1015/3/032108

[10] Nayak AO, Gowtham M, Vinod R, Ramkumar G 2011 Analysis of PCM Material in Thermal Energy Storage System. International Journal of Environmental Science and Development. vol. 2(6) pp.437-441.

[11] Ilyin RA, Khromykh VYu 2014 Classification of heat-accumulating materials. Proc. of the int. conference "Prospects for the development of technical Sciences". Chelyabinsk: ICRON. p. 18.
[12] An Trana N H, Kirstena M, Cherif Ch. 2019 New fibers from PCM using the conventional melt spinning process. AIP Conference Proceedings 2055, 060002. doi.org/10.1063/1.5084834 .
[13] Patent RU 2190656 C1, 2002.
[14] Cherunova I V, Stenkima M P , Cherunov P V 2017 Investigation of the structure and properties of flexible polymeric materials for integration with thin heat conductors structural membranes Proc. of the VIII Int. Conf. on Textile Composites and Inflatable Structures (STRUCTURAL MEMBRANES 2017) pp. 210-216.
[15] Aleksandrov VD, Sobol OV, Alexandrova OV, Sobolev AYu, Pokintelitsa EA, Loiko DP, Amerkhanova Sh.K. 2016 Bulletin of the Donbass national Academy of construction and architecture: Modern building materials. vol.81(117). pp.5-13.
[16] Kumar M P, Mylsamy K, Saravanakumar PT, Anandkumara R, Pranava A 2020 Experimental Study on Thermal Properties of Nano-TiO2 Embedded Paraffin (NEP) for Thermal Energy Storage Applications. January Materials today: Proc. 22:2153-2159 DOI: 10.1016/j.matpr.2020.03.282.
[17] Nayak A O, Gowtham M, Vinod R, Ramkumar G. 2011 Analysis of PCM Material in Thermal Energy Storage. International Journal of Environmental Science and Development, vol. 2(6) pp.437-441.
[18] Gould CA 2020 Thermoelectric cooling and heating of human body temperature. Journal of Physics: Conference Series 1534 012009 doi:10.1088/1742-6596/1534/1/012009.
[19] Outlast® textiles. - URL: https://www.outlast.com/.
[20] Cherunova I, Tashpulatov S, Kolesnik S. 2018 Automation of Deformed Fibrous Materials Thermal Characteristics Accounting Process in Garments Production. IEEE Xplore. DOI: 10.1109/RUSAUTOCON.2018.8501795 .
[21] Clift M J-D 2020 Fibrous Material Science: Extensive and Persistent. Fibers 8(2):16 DOI: 10.3390/fib8020016
[22] Angelova R A, Georgieva E, Markov D, Bozhkov T, Simova I, Kehaiova N, Stankov P. 2019 Estimating the Effect of Torso Clothing Insulation on Body Skin and Clothing Temperatures in a Cold Environment Using Infrared Thermography FIBRES & TEXTILES in Eastern Europe vol.26 4(130) pp.122-129. DOI: 10.5604/01.3001.0012.1323.
[23] Cherunova IV, Kolesnik SA, Kurenova SV, Eremina YuV, Merkulova AV, Cherunov PV 2015 Study of the structural and acoustic properties of clothing materials for thermal protection of human. International Journal of Applied Engineering Research. vol.10 (19). pp.40506-40512.
[24] Makowski T, Zhang C, Olah A, Piorkowska E, Baer E, Kregiel D 2018 Modification of dual-component fibrous materials with carbon nanotubes and methyltrichlorosilane. Materials & design 162 DOI: 10.1016/j.matdes.2018.11.026 .
[25] Ahlquist S, Menges A 2013 Frameworks for Computational Design of Textile Micro-Architectures and Material Behavior in Forming Complex Force-Active Structures. – Proc. of the Int. conf. „Association for Computer-Aided Design in Architecture" (ACADIA). - Cambridge, Ontario, Canada - Pp.281-292.
[26] Matusiak M 2006 Investigation of the thermal insulation properties of multilayer textiles. - Fibres and Textiles in Eastern Europe. - Vol. 14, No. 5 (59). – Pp.98-102.

Displacements of a surface of FGM-coated half-space heated in a circular area taking into account imperfect coating-substrate interface

S S Volkov

Don State Technical University, Rostov-on-Don, Russia

*e-mail: fenix_rsu@mail.ru

Abstract. The paper presents a solution to the axisymmetric problem of heating of a half-space with a functionally graded coating. The coating is assumed to be imperfectly bonding to the substrate that makes it possible to model various defects arising on the interface. The problem is reduced to solution of a dual integral equation. To solve the dual integral equation approximations for the kernel transform and all the compliance functions of a thermoelastic coated half-space was used. The solution was obtained in an analytical form. For the first time, analytical expressions are obtained for surface displacements and temperature distribution over the surface of a functionally graded coating both in the heating zone and outside it. Due to the use of the bilateral asymptotic method, the expressions are asymptotically exact for coatings of small and large relative thickness and of high accuracy for coatings of intermediate relative thickness including those constructed for complicated variation of thermoelastic properties in depth of the coating.

1. Introduction

A significant number of machine parts and structural elements are exposed to high temperatures, caused both by external sources of heating, and by heating that occurs during their operation, caused for example by friction. The effect of high temperatures on these parts can lead to their deformation and to a subsequent reduction in the service life. Therefore, when creating them, it is necessary to take into account the thermomechanical properties of materials and their possible inhomogeneity. Methods of mathematical modeling help to predict the behavior of structural elements with heterogeneous coatings applied to them. The simplest possible way to model thermoelastic contact of solids is to consider contact problems in one-dimensional formulations. Such a simplification makes it possible to study complicated conditions of a sliding contact including wear, frictional heating and dynamic effects [1 – 3]. For example, the effect of thermodynamic instability, which was found experimentally by J.R. Barber [4], was studied in details by many authors [1–3,5–7] using one-dimensional contact problems.

Two-dimensional plane and axisymmetric thermoelastic contact leads to more difficult mathematical problems. During the accurate modelling of two-dimensional thermoelastic contact one faces the necessity to solve singular integral equations and they systems. Nevertheless, a significant interest in solving quasistatic thermoelastic problems can be noted both for homogeneous and inhomogeneous materials. The surface temperature distribution and thermoelastic stress fields for materials with a functionally graded (FGM) coatings subjected to mixed Hertz pressure, tangential traction and frictional

heating were studied in [8]. Fretting normal and torsional contacts of two elastic solids with FGM coatings were studied in [9, 10]. Sliding frictional thermoelastic contact of FGM coatings was analyzed in [11,12]. Papers [13–15] addresses to the contact of FGM coated materials taking into account thermoelectroelastic coupling for piezoelectric materials. Singular integral equations and their systems arising during the process of solution in [9–15] were solved numerically. To solve thermoelastic three-dimensional contact problems authors use less accurate numerical methods [16–18] because of the increasing difficulty of the mathematical problems.

Present paper addresses to simulation of two-dimensional axisymmetric thermoelastic deformation of a FGM coating bonding to a homogeneous half-space caused by heating of a circular area of the surface. Due to the absence of the mechanical stresses on the surface of the coating the problem is reduced to a single singular integral equation using the Hankel integral transformation. The integral equation is similar to that arising for purely elastic contact problems on indentation by a flat punch which was solved previously [19, 20] using the bilateral asymptotic method [21]. Present paper addresses to the construction of analytical expressions for the displacements and temperature on the surface. The main advantages of the present results and results obtained previously by other authors are:

- distribution of displacements and temperature on the surface are constructed in analytical form;
- the results are asymptotically exact for small and large values of the characteristic geometric parameter of the problem (i.e. the results are effective for thin and thick coatings);
- the results are of high accuracy for intermediate values of the characteristic geometric parameter.

These statements are confirmed by the previously obtained results for elastic frictionless [22–24] and frictional lubricated [25, 26] contact and piezoelastic contact [27] for solids with functionally graded coatings. The results obtained by the bilateral asymptotic method was also approved using the numerical simulations [28] and nanoindentation experiments [29].

The results obtained are suitable both for the coating perfectly and imperfectly bonding to the substrate. Imperfect bonding of the coating to the substrate is used to model incomplete adhesion on the interface that can occur during various coating deposition technologies. Effect of incomplete adhesion was studied earlier in a case of torsional contact [30], indentation [31, 32], distributed forces [33] taking into account fatigue [34], wear [35] and piezoelectric effect [36].

2. Statement of the problem

We consider a thermoelastic half-space with a functionally graded thermoelastic coating of thickness H. The cylindrical coordinate system (r, φ, z) is related to the half-space so that the z axis is normal to the coating surface. The case of axial symmetry is considered, i.e. there is no dependence of the thermomechanical characteristics on the angular coordinate φ. Thermoelastic characteristics change with depth according to the following laws:

$$\{E, \nu, \lambda_T, \alpha_T\} = \begin{cases} \{E_c(z), \nu_c(z), \lambda_T^c(z), \alpha_T^c(z)\}, -H \le z \le 0, \\ \{E_s, \nu_s, \lambda_T^s, \alpha_T^s = \text{const}\}, -\infty < z < -H. \end{cases} \quad (1)$$

Here and after the indices (c) and (s) refer to the coating and substrate respectively. E is Young's modulus, ν is the Poisson's ratio, λ_T is the coefficient of thermal conductivity, α_T is the coefficient of linear thermal expansion.

Following boundary conditions are satisfied on the coating-substrate interface

$$z = -H: \begin{cases} \sigma_z^{(c)} = \sigma_z^{(s)}, \ w^{(c)} = w^{(s)}, T^{(c)} = T^{(s)} \\ \lambda_T^c(z) T'^{(c)} = \lambda_T^s T'^{(s)}, \tau_{rz}^{(c)} = \tau_{rz}^{(s)} = \dfrac{1}{\varepsilon}\left(u^{(c)} - u^{(s)} \right) \end{cases} \quad (2)$$

Here u and w are the components of the displacement vector, σ_z and τ_{rz} are the stress tensor components, and T is the temperature difference before and after deformation. The last relation in (2)

describes incomplete adhesion of the coating to the substrate, ε is the coefficient of elastic bonding, see [31, 32] for details.

Let the temperature distribution be constant on the surface of the coating $z = 0$, in some circular region of radius a, and outside this region the surface is free of stress and thermally insulated:

$$z=0:\begin{cases}\sigma_z^{(c)}=\lambda_T^c(z)T'^{(c)}=0, & r>a;\\ T^{(c)}=-T_0 & r\le a.\end{cases} \tag{3}$$

We assume that the displacements and temperature difference decay at infinity: $u, w, T \to 0$ as $z \to -\infty$.

It is required to determine the heat flux on the surface

$$\lambda_T^{(c)}(0)T'\big|_{z=0}=-q_a(r),\ r\le a, \tag{4}$$

and the distribution of normal $w(0,r)$ and radial $u(0,r)$ displacements of the coating surface.

3. Solution of the problem

The displacements, temperature and heat flux are written in the form of the integral Hankel transforms

$$u(r,z)=-\int_0^\infty \overline{u}(\alpha,z)\,\mathrm{J}_1(\alpha r)\alpha d\alpha,\quad \{w,T\}(r,z)=\int_0^\infty \{\overline{w},\overline{T}\}(\alpha,z)\,\mathrm{J}_0(\alpha r)\alpha d\alpha$$
$$q_a(r)=\int_0^\infty \overline{q}_a(\alpha)\mathrm{J}_0(\alpha r)\alpha d\alpha \tag{5}$$

The Hankel transforms of displacements and temperature on the surface can be expressed in the following form:

$$\overline{u}(\alpha,0)=-\frac{L_{13}(\alpha)\overline{q}_a(\alpha)}{\Theta_{13}^{(c)}\alpha^2},\quad \overline{w}(\alpha,0)=-\frac{L_{23}(\alpha)\overline{q}_a(\alpha)}{\Theta_{23}^{(c)}\alpha^2},\quad \overline{T}(\alpha,0)=-\frac{L_{33}(\alpha)\overline{q}_a(\alpha)}{\Theta_{33}^{(c)}\alpha} \tag{6}$$

where $\Theta_{33}^{(c)}=\lambda_T^{(c)}(0), \Theta_{23}^{(c)}=-\Theta_{13}^{(c)}=\dfrac{\lambda_T^{(c)}(0)}{(1+\nu)\alpha_T^{(c)}(0)}$ are the effective thermoelastic moduli calculated on the coating surface; functions L_{ij} are the compliance functions of the thermoelastic half-space with a coating. An algorithm of construction the compliance functions and analysis of their properties both for perfect and imperfect coating-substrate interface are described in [37] in details. Substituting (5) and (6) into equation (3) yields the dual integral equation of the problem:

$$\int_0^\infty L_{33}(\alpha\lambda)\overline{q}(\alpha)\mathrm{J}_0(\alpha r)d\alpha=\frac{\Theta_{33}^{(c)}T_0}{a},\quad r\le 1$$
$$\int_0^\infty \overline{q}(\alpha)\mathrm{J}_0(\alpha r)\alpha d\alpha=0,\quad r>1 \tag{7}$$

Following dimensionless notations were used above (the primes were omitted):

$$\{r',\lambda\}=\frac{\{r,H\}}{a},\alpha'=\alpha a,\ q(r')=q_a(r'a),L'_{kj}(\alpha)=L_{kj}\left(\frac{\alpha}{H}\right) \tag{8}$$

$\overline{q}(\alpha)$ is the Hankel transform of the function $q(r)$.

Taking into account the properties of the compliance functions which are described in [37], they are approximated by the following expressions:

$$L_{ij}(\lambda\alpha)\approx\Pi_{ij}^{+}(\lambda\alpha),\quad \Pi_{ij}^{\pm}(\lambda\alpha)=\prod_{n=1}^{N_{ij}}\frac{\left(\lambda^2\alpha^2\pm A_{ijn}^2\right)}{\left(\lambda^2\alpha^2\pm B_{ijn}^2\right)} \tag{9}$$

Using this approximation in (7) we obtain an approximated dual integral equation which was solved analytically earlier [19,20]. Its solution has the following form:

$$\bar{q}(\alpha)=\frac{2\Theta_{33}^{(s)}T_0}{\pi a}\left(\frac{\sin(\alpha)}{\alpha}+\sum_{i=1}^{N_{33}}C_{33i}\,\frac{\alpha\sin(\alpha)\cosh\left(A_{33i}\lambda^{-1}\right)+A_{33i}\lambda^{-1}\cos(\alpha)\sinh\left(A_{33i}\lambda^{-1}\right)}{\alpha^2+A_{33i}^2\lambda^{-2}}\right) \tag{10}$$

$$q(r)=\frac{2\Theta_{33}^{(s)}T_0}{\pi a}\left[\frac{1}{\sqrt{1-r^2}}+\sum_{i=1}^{N}C_{33i}\left(\frac{\cosh\left(A_{33i}\lambda^{-1}\right)}{\sqrt{1-r^2}}-\frac{A_i}{\lambda}\int_r^1\frac{\sinh\left(A_{33i}\lambda^{-1}\right)tdt}{\sqrt{t^2-r^2}}\right)\right] \tag{11}$$

where $\Theta_{33}^{(s)}=\lambda_T^{(s)},\Theta_{23}^{(s)}=-\Theta_{13}^{(s)}=\dfrac{\lambda_T^{(s)}}{(1+\nu)\alpha_T^{(s)}}$ are the effective thermoelastic moduli of the substrate; constants C_{33i} are determined from the following system of linear algebraic equations:

$$\sum_{i=1}^{N_{33}}C_{33i}\,\frac{B_{33k}\cosh(A_{33i}\lambda^{-1})+A_{33i}\sinh(A_{33i}\lambda^{-1})}{A_{33i}^2-B_{33k}^2}=\frac{1}{B_{33k}},\ k=1,2,\ldots,N_{33} \tag{12}$$

The solution is asymptotically exact for $\lambda\to 0$ and $\lambda\to\infty$ [21]. It was also obtained earlier for the similar problems [28, 38, 39] that for the intermediate values of λ the solution error is the same order of magnitude as the error of approximation of the compliance function L_{33} which can be achieved not exceeding 0.3% even for complicated laws of inhomogeneity [40].

Substituting (6) into (5) and taking into account notations (8) we obtain representations for the surface displacements and surface temperature in the form of the following quadratures:

$$\begin{aligned}
u(r,0)&=\frac{2a\Theta_{33}^{(s)}T_0}{\pi\Theta_{13}^{(c)}}\int_0^\infty\frac{L_{13}(\lambda\alpha)\bar{q}(\alpha)}{\alpha}\mathrm{J}_1(\alpha r)d\alpha,\\
w(r,0)&=-\frac{2a\Theta_{33}^{(s)}T_0}{\pi\Theta_{23}^{(c)}}\int_0^\infty\frac{L_{23}(\lambda\alpha)\bar{q}(\alpha)}{\alpha}\mathrm{J}_0(\alpha r)d\alpha,\\
T(r,0)&=-\frac{2\Theta_{33}^{(s)}T_0}{\pi\Theta_{33}^{(c)}}\int_0^\infty L_{33}(\lambda\alpha)\bar{q}(\alpha)\,\mathrm{J}_0(\alpha r)d\alpha
\end{aligned} \tag{13}$$

Taking into account (10) and using approximations (9) for all compliance functions and making analytical integration, we obtain analytical representations for the temperature and displacements valid for $r > 0$:

$$\begin{aligned}
u(r,0)=\frac{2a\Theta_{33}^{(s)}T_0}{\pi\Theta_{13}^{(c)}}\Bigg[&\Pi_{13}^{+}(0)I_{11}(r)+\sum_{n=1}^{N_{13}}P_{13n}I_{13}\left(\frac{B_{13n}}{\lambda},r\right)+\sum_{n=1}^{N_{13}}F_{13n}I_{12}\left(\frac{B_{13n}}{\lambda},r\right)+\\
&+\sum_{i=1}^{N_{33}}C_{33i}\Pi_{13}^{-}(A_{33i})\left(\cosh\left(\frac{A_{33i}}{\lambda}\right)I_{12}\left(\frac{A_{33i}}{\lambda},r\right)+\frac{A_{33i}}{\lambda}I_{13}\left(\frac{A_{33i}}{\lambda},r\right)\sinh\left(\frac{A_{33i}}{\lambda}\right)\right)\Bigg]
\end{aligned} \tag{14}$$

$$\begin{aligned}
w(r,0)=-\frac{2a\Theta_{33}^{(s)}T_0}{\pi\Theta_{23}^{(c)}}\Bigg[&\Pi_{23}^{+}(0)I_{21}(r)+\sum_{n=1}^{N_{23}}P_{23n}I_{23}\left(\frac{B_{23n}}{\lambda},r\right)+\sum_{n=1}^{N_{23}}F_{23n}I_{22}\left(\frac{B_{23n}}{\lambda},r\right)+\\
&+\sum_{i=1}^{N_{33}}C_{33i}\Pi_{23}^{-}(A_{33i})\left(\cosh\left(\frac{A_{33i}}{\lambda}\right)I_{22}\left(\frac{A_{33i}}{\lambda},r\right)+\frac{A_{33i}}{\lambda}I_{23}\left(\frac{A_{33i}}{\lambda},r\right)\sinh\left(\frac{A_{33i}}{\lambda}\right)\right)\Bigg]
\end{aligned} \tag{15}$$

$$T(r,0) = -\frac{2\Theta_{33}^{(s)} T_0}{\pi\Theta_{33}^{(c)}}\left[\Pi_{33}^{+}(0) I_{31}(r) + \sum_{n=1}^{N_{33}} P_{33n} I_{33}\left(\frac{B_{33n}}{\lambda}, r\right) + \sum_{n=1}^{N_{33}} F_{33n} I_{32}\left(\frac{B_{33n}}{\lambda}, r\right)\right] \tag{16}$$

Following notations for the functions of *r* coordinate were used above:

$$I_{11}(r) = \begin{cases} \dfrac{\pi r}{4}, & 0 < r \le 1 \\ \dfrac{r}{2}\arcsin\left(\dfrac{1}{r}\right) + \dfrac{1}{2}\sqrt{\dfrac{r^2-1}{r^2}}, & r > 1 \end{cases} \tag{17}$$

$$I_{12}(A,r) = \begin{cases} \dfrac{\pi}{2A}\exp(-A) I_1(Ar), & 0 < r \le 1 \\ \dfrac{1}{A}\left(\dfrac{\pi}{2}\exp(-A) I_1(Ar) - \dfrac{1}{r}\displaystyle\int_1^r \frac{t\sinh(A(t-1))dt}{\sqrt{r^2-t^2}}\right), & r > 1 \end{cases} \tag{18}$$

$$I_{21}(r) = \begin{cases} d_1 - \left(1 - \sqrt{1-r^2} + \ln\left(\dfrac{1+\sqrt{1-r^2}}{2}\right)\right), & 0 < r \le 1, \\ d_1 - \left(1 + \ln\left(\dfrac{r}{2}\right)\right), & r > 1 \end{cases} \tag{19}$$

$$I_{22}(A,r) = \begin{cases} \dfrac{1}{A}\left(\sinh(A) K_0(Ar) + \displaystyle\int_r^1 \frac{\sinh(A(t-1))}{\sqrt{t^2-r^2}}\right), & 0 < r \le 1, \\ \dfrac{1}{A}\sinh(A) K_0(Ar), & r > 1 \end{cases} \tag{20}$$

$$I_{23}(A,r) = \begin{cases} \dfrac{1}{A^2}\left(d_2 - \ln\left(\dfrac{1+\sqrt{1-r^2}}{2}\right) - \cosh(A) K_0(Ar) + \displaystyle\int_r^1 \frac{\cosh(A(t-1))dt}{\sqrt{t^2-r^2}}\right), & 0 < r \le 1, \\ \dfrac{1}{A^2}\left(d_2 - \ln\left(\dfrac{r}{2}\right) - \cosh(A) K_0(Ar)\right), & r > 1, \end{cases} \tag{21}$$

$$I_{31}(r) = \begin{cases} \dfrac{\pi}{2}, & 0 < r \le 1, \\ \arcsin\left(\dfrac{1}{r}\right), & r > 1 \end{cases} \tag{22}$$

$$I_{32}(A,r) = \begin{cases} \dfrac{\pi}{2}\exp(-A) I_0(Ar), & 0 < r \le 1, \\ \dfrac{\pi}{2}\exp(-A) I_0(Ar) - \displaystyle\int_1^r \frac{\cosh(A(t-1))dt}{\sqrt{r^2-t^2}}, & r > 1 \end{cases} \tag{23}$$

$$I_{33}(A,r)=\begin{cases}\dfrac{\pi}{2A}\exp(-A)I_0(Ar), & 0<r\le 1,\\ \dfrac{1}{A}\left(\dfrac{\pi}{2}\exp(-A)I_0(Ar)-\displaystyle\int_1^r\dfrac{\sinh(A(t-1))}{\sqrt{r^2-t^2}}\right), & r>1,\end{cases} \tag{24}$$

Following notations for the constants were also used:

$$\begin{aligned}P_{ijn}&=\sum_{k=1}^{N_{33}}C_{33k}\,\frac{\lambda A_{33k}\Pi_{ijn}(iB_{ijn})\sinh\left(A_{33k}\lambda^{-1}\right)}{A_{33k}{}^2-B_{ijn}{}^2},\\ F_{ijn}&=\sum_{k=1}^{N_{33}}C_{33k}\,\frac{\lambda^2\Pi_{ijn}(iB_{ijn})\cosh\left(A_{33k}\lambda^{-1}\right)}{A_{33k}^2-B_{ijn}^2}-\frac{\lambda^2\Pi_{ijn}(iB_{ijn})}{B_{ijn}^2}\end{aligned} \tag{25}$$

$$\Pi_{ijn}(\alpha)=\frac{\left(A_{ijn}^2-B_{ijn}^2\right)}{\lambda^2}\prod_{m=1,m\ne n}^{N_{ij}}\frac{\alpha^2+A_{ijm}^2}{\alpha^2+B_{ijm}^2} \tag{26}$$

$$d_1=\int_0^\infty\frac{\sin(\alpha)}{\alpha^2}\,d\alpha=\infty,\quad d_2=\int_0^\infty\frac{\cos(\alpha)d\alpha}{\alpha}=\infty \tag{27}$$

$I_0(x)$, $I_1(x)$ and $K_0(x)$, $K_1(x)$ are the modified Bessel's functions of the first and second kind.

The first terms in (14) – (16) containing I_{11}, I_{21} and I_{31} refer to the solution in the case of non-coated half-space, see results by Johnson [41]. Second and third terms containing I_{j2} and I_{j3} (j=1,2,3) correspond to the additional part caused by the coating response. It is easy to make sure by substituting the corresponding expressions in (16) that boundary condition (3) is satisfied, i.e.: $T(r,0) = -T_0$ for $r \le 1$.

As the heat is continuously transferred to the solid and the surface is assumed to be isolated everywhere outside the heated circle $r \le 1$, the displacements infinitely increases at $r \to \infty$. That is why, similar to Johnson [41] it is convenient to assume that where is a point r_0 at a distance from the heated circle where the displacements are assumed to be 0. It is the same as we consider following function to analyze the displacements of the surface:

$$w^{(s)}(r)=w(r,0)-w(r_0,0) \tag{28}$$

It is obvious that $w^{(s)}(r_0) = 0$. It makes possible to avoid the unphysical behavior related to infinite growth of displacements in the region $0 \le r \le r_0$ and helps to remove the unphysical infinite constants d_1 and d_2 from the expression for displacements.

4. Conclusion

Approximated analytical expressions for the displacements and temperature distribution of the surface of a functionally graded thermoelastic coating is constructed for a case of a local heating in a circular area. The results are suitable both for perfect and imperfect bonding of the coating to the homogeneous substrate. Analytical expressions for the displacements and temperature distribution consist of two terms: first one corresponds to the homogeneous non-coated half-space while second describe the addition caused by the coating response. Due to the fact that the problem is mathematically similar to the problems studied earlier, the obtained results possess the same properties: they are valid for arbitrary independent variation of thermoelastic properties in depth of the coating; they are asymptotically exact for relatively thin and thick coatings and have high accuracy for intermediate thickness of the coating. The expressions obtained can be also used to describe the displacements of the coating which is indented by a rigid flat punch (without heating of the surface). The results obtained can be applied to the problems

of prediction of the properties for the bulk materials or inhomogeneous coatings deposited either by means of machining processes [42] or specially designed [43,44] for engineering applications.

Acknowledgments
This work was supported by the Russian Foundation for Basic Research through grant No. 18- 07- 01177-a and Scholarship of the President of Russian Federation No. SP-3615.2018.1.

References

[1] Zelentsov V B, Mitrin B I, Lubyagin I A and Kudish I I 2018 Diagnostics of wear thermoelastic instability based on sliding contact parameter monitoring *IMA J. Appl. Math*. **84** (2) 345–65
[2] Zelentsov V B and Mitrin B I 2019 Thermoelastic instability in the quasi-static coupled thermoelasticity problem dealt with the sliding contact with frictional heating *Mech. Solids* **54** 58–69
[3] Zelentsov V B, Mitrin B I, Lubyagin I A and Aizikovich S M Thermoelastic instability in coupled thermoelastic sliding wear problem *In Advanced Materials (Cham: Springer)* **224** pp. 379–97
[4] Barber J R 1969 Thermoelastic instabilities in the sliding of conforming solids *Proc. R. Soc. Lond*. **312** 381–94.
[5] Dow T A and Burton R A 1973 The Role of Wear in the Initiation of Thermoelastic Instabilities of Rubbing Contact *J. Lubr. Technol.* **95** 71–5
[6] Afferrante L and Ciavarella M A 2007 Note on Thermoelastodynamic Instability (TEDI) for a 1D Elastic Layer: Force Control *Int. J. Sol. Struct.* **44** 1380–90
[7] Liu J, Ke L-L and Wang Y-S Frictionally excited thermoelastic dynamic instability of functionally graded materials 2019 *Acta Mech. Sinica* **35** 99–111
[8] Yang J Ke L-L and Kitipornchai S 2009 Thermo-Mechanical Analysis of an Inhomogeneous Double-Layer Coating System under Hertz Pressure and Tangential Traction *Mech. Adv. Mater. Struct.* **16** 308–18
[9] Ke L-L and Wang Y-S 2010 Fretting contact of two dissimilar elastic bodies with functionally graded coatings *Mech. Adv. Mater. Struct.* **17** 433–47
[10] Liu J, Wang Y-S and Xing Y-M 2012 Fretting contact of two elastic solids with graded coatings under torsion *Int. J. Solids Struct.* **49** 1283–93
[11] Liu J, Ke L-L and Wang Y-S 2011 Two-dimensional thermoelastic contact problem of functionally graded materials involving frictional heating *Int. J. Solids Struct.* **48** 2536–48
[12] Liu J, Ke L-L, Wang Y-S, Yang J and Alam F 2012 Thermoelastic frictional contact of functionally graded materials with arbitrarily varying properties *Int. J. Mech. Sci.* **63** 86–98
[13] Su J, Ke L-L and Wang Y-S 2016 Fretting contact of a functionally graded piezoelectric layered half-plane under a conducting punch *Smart Mater. Struct.* **25** 025014
[14] Su J, Ke L-L and Wang Y-S 2015 Two-dimensional fretting contact analysis of piezoelectric materials *Int. J. Solids Struct.* **73–74** 41–54
[15] Su J, Ke L-L, Wang Y-S and Xing Y-M 2017 Axisymmetric torsional fretting contact between a spherical punch and an FGPM coating *Appl. Math. Model.* **52** 576–89
[16] Zhang X, Liu J, Shen H and Wang Y 2019 Elastic response of coating materials in thermoelasticity: Indented by a hot punch *J. Thermal Stresses* **42** 475–89
[17] Wang T, Ma X, Wang L, Gu L, Yin L, Zhang J, Zhan L and Sun D 2018 Three-Dimensional Thermoelastic Contact Model of Coated Solids with Frictional Heat Partition Considered *Coatings* **8** 470
[18] Zhang X and Wang W J 2020 Thermoelastic contact of layered materials with interfacial imperfection *Int. J. Mech. Sci.* **186** 105904
[19] Aizikovich S M and Aleksandrov V M 1984 Axisymmetric problem of indentation of a circular die into an elastic half-space that is nonuniform with respect to depth *Mech. Sol.* **19** 73–82

[20] Vasiliev A S, Volkov S S, and Aizikovich S M 2016 Indentation of an axisymmetric punch into an elastic transversely-isotropic half-space with functionally graded transversely-isotropic coating *Mater. Phys. Mech.* **28** 11–5
[21] Aizikovich S M 1990 An asymptotic solution of a class of coupled equations *J. Appl. Math. Mech.* **54** 719–24
[22] Vasiliev A S, Volkov S S, Aizikovich S M and Mitrin B I 2017 Plane contact problem on indentation of a flat punch into a transversely-isotropic half-plane with functionally graded transversely-isotropic coating *Z. Angew. Math. Phys.* **68** doi: 10.1007/s00033-016-0746-8
[23] Vasiliev A S, Volkov S S and Aizikovich S M 2018 Approximated analytical solution of contact problem on indentation of elastic half-space with coating reinforced with inhomogeneous interlayer *Mater. Phys. Mech.* **35** 175–80
[24] Volkov S S, Litvinenko A N, Aizikovich S M, Wang Y C and Vasiliev A S 2016 Axisymmetric bending of a circular plate with stiff edge on a soft FGM layer *Struct. Eng. Mech.* **59** 227–41
[25] Kudish I I, Volkov S S, Vasiliev A S and Aizikovich S M 2017. Effectiveness of coatings with constant, linearly, and exponentially varying elastic parameters in heavily loaded line elastohydrodynamically lubricated contacts *J. Tribology* **139** 021502
[26] Kudish I I, Volkov S S, Vasiliev A S and Aizikovich S M 2018. Lubricated point heavily loaded contacts of functionally graded materials. Part 2. Lubricated contacts *Math. Mech. Solids* **23** 1081–103
[27] Vasiliev AS 2019 Penetration of a spherical conductive punch into a piezoelectric half-space with a functionally graded coating *Int. J. Eng. Sci.* **142** 230–41
[28] Vasiliev A S, Volkov S S, Sadyrin E V and Aizikovich S M 2020 Simplified Analytical Solution of the Contact Problem on Indentation of a Coated Half-Space by a Conical Punch *Mathematics* **8** 983
[29] Vasiliev A S, Sadyrin E V, Mitrin B I, Aizikovich S M and Nikolaev A L 2018 Nanoindentation of ZrN Coatings on Silicon and Copper Substrates *Russian Eng. Research* **38** 735–7
[30] Antonenko N N and Velichko I G 2014 Contact problem of torsion of a multilayer base with elastic connections between layers *J. Samara State Tech. Univ., Ser. Phys. Math. Sci.* **136** 66 – 78
[31] Aleksandrov V M and Klindukhov V V 2000 Contact problems for a two-layer elastic foundation with a nonideal mechanical bond between the layers *Izv. Ross. Akad. Nauk, Mekh. Tverd. Tela* **3** 84–92
[32] Goryacheva I G and Torskaya E V 2016 Modeling the influence of the coating deposition technology on the contact interaction characteristics *Mech. Solids* **51** 550–6
[33] Torskaya E V and Goryacheva I G 2003 The effect of interface imperfection and external loading on the axisymmetric contact with a coated solid *Wear* **254** 538–45
[34] Torskaya E V 2011 Modeling of contact-fatigue damage accumulation in a two-layer half-space with incomplete adhesion between the layers *Mech. Solids* **46** 913–21
[35] Goryacheva I G and Torskaya E V 2010 Modeling of fatigue wear of a two-layered elastic half-space in contact with periodic system of indenters *Wear* **268** 1417–22
[36] Wu Y F, Yu H Y and Chen W Q 2013 Indentation responses of piezoelectric layered half-space *Smart Mater. Struct.* **22** 1–16
[37] Volkov S S, Vasiliev A S, Aizikovich S M, Sadyrin E V 2020 Compliance functions for a thermoelastic FGM coated half-plane with incomplete adhesion between the coating and substrate *Journal of Physics: Conference Series*, **1474** 012034
[38] Volkov S S, Vasiliev A S, Aizikovich S M and Sadyrin E V 2018 Contact problem on indentation of an elastic half-plane with an inhomogeneous coating by a flat punch in the presence of tangential stresses on a surface *AIP Conference Proceedings* **1959** 070037
[39] Sadyrin E V, Vasiliev A S, Volkov S S, Mitrin B I and Aizikovich S M 2019 Simplified analytical solution of the contact problem on indentation of a coated half-space by a spherical punch *WIT Transactions on Engineering Sciences* **122** 209–21

[40] Vasiliev A S, Swain M V, Aizikovich S M and Sadyrin E V 2016 Torsion of a circular punch attached to an elastic half-space with a coating with periodically depth-varying elastic properties *Arch. Appl. Mech.* **86** 1247–54
[41] Johnson K 1985 *Contact Mechanics* (Cambridge: Cambridge University Press) p. 452
[42] Burlakova V E, Tyurin A I, Drogan E G, Sadyrin E V, Pirozhkova T S, Novikova A A and Belikova M A 2019 Mechanical Properties and Size Effects of Self-Organized Film *J. Tribology* **141** 051601
[43] Sadyrin E V, Mitrin B I, Aizikovich S M and Zubar T I 2016 Effect of temperature on the mechanical properties of multi-component Al-Mg-Si alloys during nanoindentation test *Mater. Phys. Mech* **28** 6–10
[44] Nikolaev A L, Mitrin B I, Sadyrin E V, Zelentsov V B, Aguiar A R and Aizikovich S M 2020 Mechanical Properties of Microposit S1813 Thin Layers. *In Model., Synthesis Fract. Adv. Mater. Industrial Medical Appl. (Cham: Springer)* **136** pp. 137-146

Pulsed laser deposition of Au nanoparticles on ZnO nanostructures

A L Nikolaev[1,*], A S Kamencev[2], N V Lyanguzov[2] and S M Aizikovich[1]

[1]Don State Tecnical University, Rostov-on-Don, Russia
[2]Southern Federal University, Rostov-on-Don, Russia

*e-mail: andreynicolaev@eurosites.ru

Abstract. Au nanoparticles and ultrathin gold films were obtained on the surface of thin (100 nm) ZnO films on Si (001) by pulsed laser deposition (PLD) at high argon pressure by sputtering a pure gold target with a CL3100 pulsed excimer laser (λ = 248 nm) at room temperature. The dependence of the size and distribution of nanoparticles on the argon pressure in the vacuum chamber (P_{Ar}), the power density of laser radiation (j), and the number of laser pulses (N) was investigated. Also, to obtain nanostructures, axial and non-axial deposition was used, where the substrate was located perpendicular and parallel to the plasma torch, respectively. Stable modes of obtaining gold nanoparticles with high uniformity and average size from 4 to 10 nm were demonstrated. The modes of stable and reproducible deposition of ultrathin Au films (23-42 nm) and percolation structures (18-20 nm) were also demonstrated. Thus, PLD is a reliable and flexible tool for obtaining nanoparticles and ultrathin Au films the average size and thickness of which can be predictably controlled by varying the deposition parameters. This technique is well suited for coating with gold nanoparticles the surface of nanostructured materials based on chemically active substances that are particularly sensitive to surface cleanliness, which cannot be coated by standard methods.

1. Introduction

Au nanoparticles are of great interest due to their unique physical and chemical properties. These properties and a number of dimensional physical parameters (mean free path of the charge carriers, De Broglie wavelength, etc.) depend on the size of nanoparticles and are determined by the proportion of surface atoms [1,2]. Bulk gold is inert, but exhibits pronounced chemical and catalytic activity at sizes less than 100 nm [3]. This fact makes Au nanoparticles attractive for catalysis [4-7]. Due to their optical and electrical properties, Au nanoparticles are used in the diagnosis and therapy of various diseases [8, 9, 10], enhanced Raman scattering [11], to increase the efficiency of solar cells [12], nanosensorics [13, 14], etc.

Modern methods of synthesis should ensure the obtaining of nanoparticles not only of controlled size, but also structure. At the moment, there are several methods for the stable production of Au nanoparticles, for example, the method of thermal annealing of ultrathin gold films [15], methods based on sputtering of pure gold in liquids [16], in vacuum, Turkevich method [17], variations of chemical methods based on the decomposition of metal salts [18] under the influence of ionizing radiation [19], microwave radiation [20], as well as usage of various reducing agents such as NaBH4 [21], hydrazine [22], citrate [23]. Also the biological methods based on the so-called "green approach" are known: nanoparticles are synthesized using non-toxic reducing agents [24, 25]. The methods mentioned provide consistent and stable results, but have some drawbacks. For example, to reduce the agglomeration of

nanoparticles, stabilizers are introduced into the suspension [26]; as a result, in addition to nanoparticles, a number of reaction by-products and complex compounds are formed [27]. Another drawback is rather limited lifetime of obtained suspensions. When applying nanoparticles from solutions and suspensions to the surface of chemically active nanomaterials one may encounter undesirable chemical reactions and contamination of the chemically active surface. For example, it is extremely important to the semiconductor surface to remain clean while using nanoparticles in the gas sensors based on semiconductor nanorods [28, 29]. For this reason, it is necessary to use purely physical methods for obtaining nanoparticles for some applications. In this work, Au nanoparticles were obtained by pulsed laser sputtering of a gold target in vacuum. Dependence of size and distribution of nanoparticles on the deposition parameters was shown.

2. Experimental Section

Gold was sputtered by PLD using a CL7100 KrF laser (λ = 248nm). The pulse duration was 15–20 ns and the energy of one pulse was 300 mJ. Laser radiation was focused through a transparent sapphire window onto the surface of a rotating target located inside a VCL103 vacuum chamber. A gold disc was used as a target. The vacuum chamber was evacuated to a pressure of 2.5 Pa before argon injection. Thin (100 nm) ZnO films, previously deposited on Si (001) by PLD, were used as substrates. Thin ZnO films (100 nm) on silicon were obtained by PLD with the following parameters of a pure zinc oxide target: substrate temperature 500 ^{o}C, j= 2 J/cm^2. N = 1000, oxygen pressure 2 Pa.

During deposition of nanoparticles some parameters of PLD remained unchanged, for example, j (2 or 3.7 J/cm^2), target-substrate distance (3.5 cm), preliminary vacuum (2.5 Pa), temperature (room temperature), target rotation speed (~ 90 rps). Variable parameters were P_{Ar} and the N.

Au nanoparticles were obtained by axial (Figure 1) and non-axial (Figure 2) deposition.

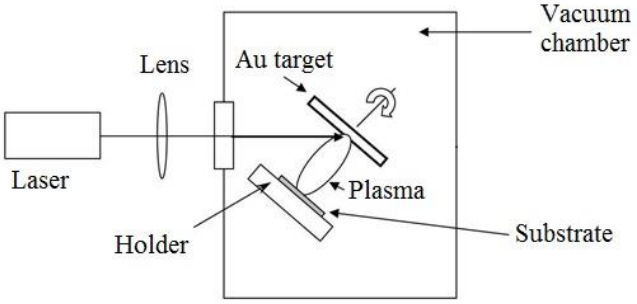

Figure 1. Schematic representation of axial PLD

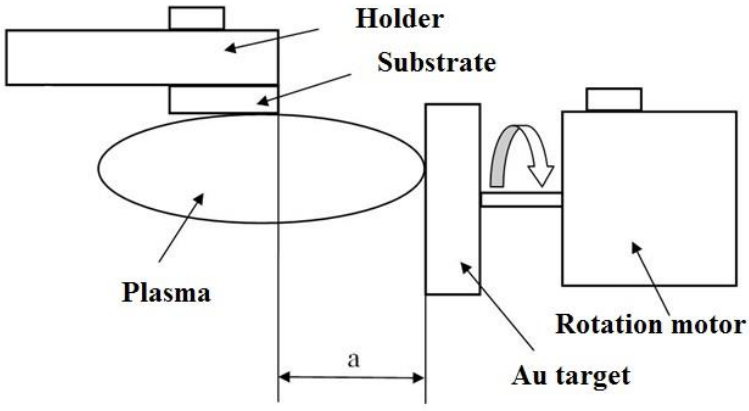

Figure 2. Schematic representation of non-axial PLD

The images of nanoparticles and ultrathin gold films were obtained using a Zeiss Supra 25 scanning electron microscope; the analysis of the obtained images and correlation with the deposition parameters were performed using the ImageJ and OriginLab software.

3. Results and discussion

A group of samples was obtained on the surface of thin zinc oxide films by PLD. Each sample was obtained with different synthesis parameters such as: N, j, and P_{Ar}. The images of the deposited nanoparticles obtained using an electron microscope (Figure 3, 4) were processed using the ImajeJ software.

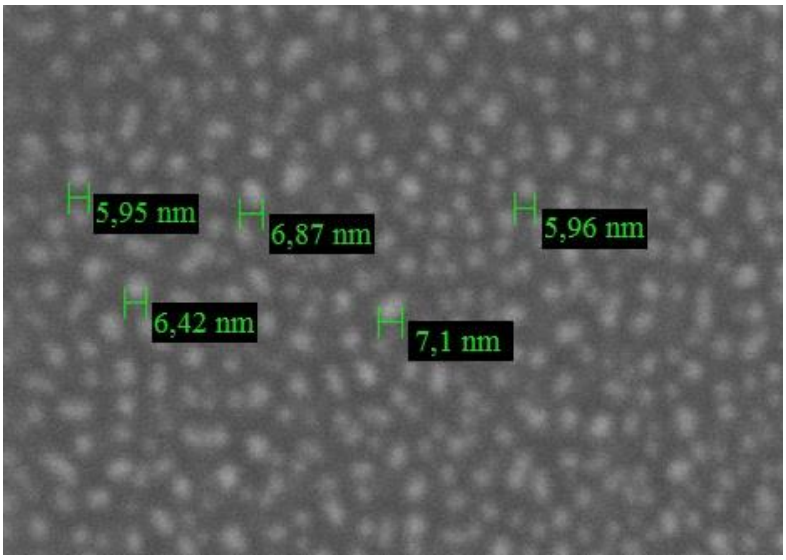

Figure 3. Au nanoparticles obtained at P_{Ar} = 70 Pa

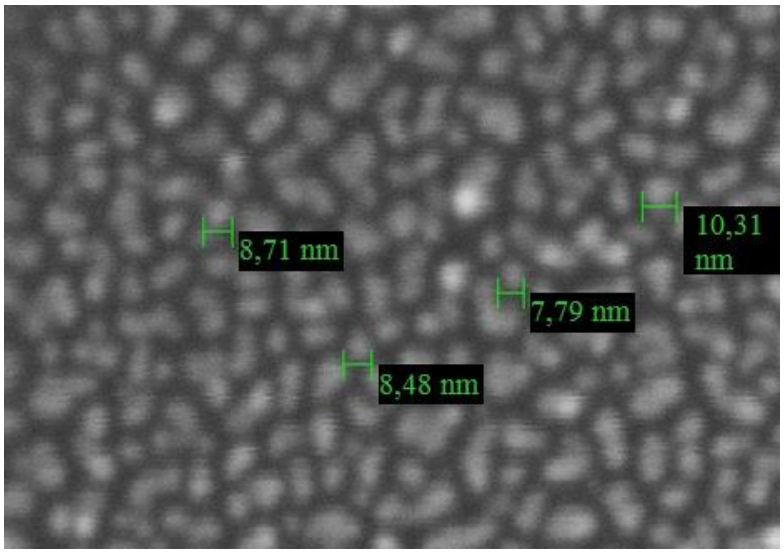

Figure 4. Au nanoparticles obtained at P_{Ar} = 100 Pa

During the processing, the total number of nanoparticles in each image and the area of each particle were obtained. To simplify the search of particle sizes, all of them were represented as spherical ones. Particles cropped by the edges of the image were excluded from the calculations. To measure thickness of the obtained ultrathin gold films (Figure 5) we used the tools of the standard Zeiss Supra 25 scanning electron microscope software.

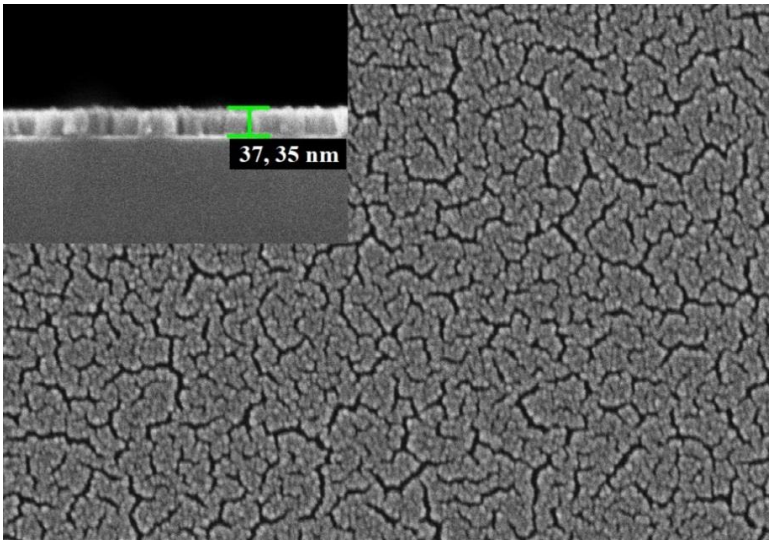

Figure 5. Ultrathin Au film

In order not to clutter up the text with a large number of figures, we will below present the information obtained in the analysis of the most interesting samples and discuss only the parameters of stable and reproducible preparation of Au nanoparticles.

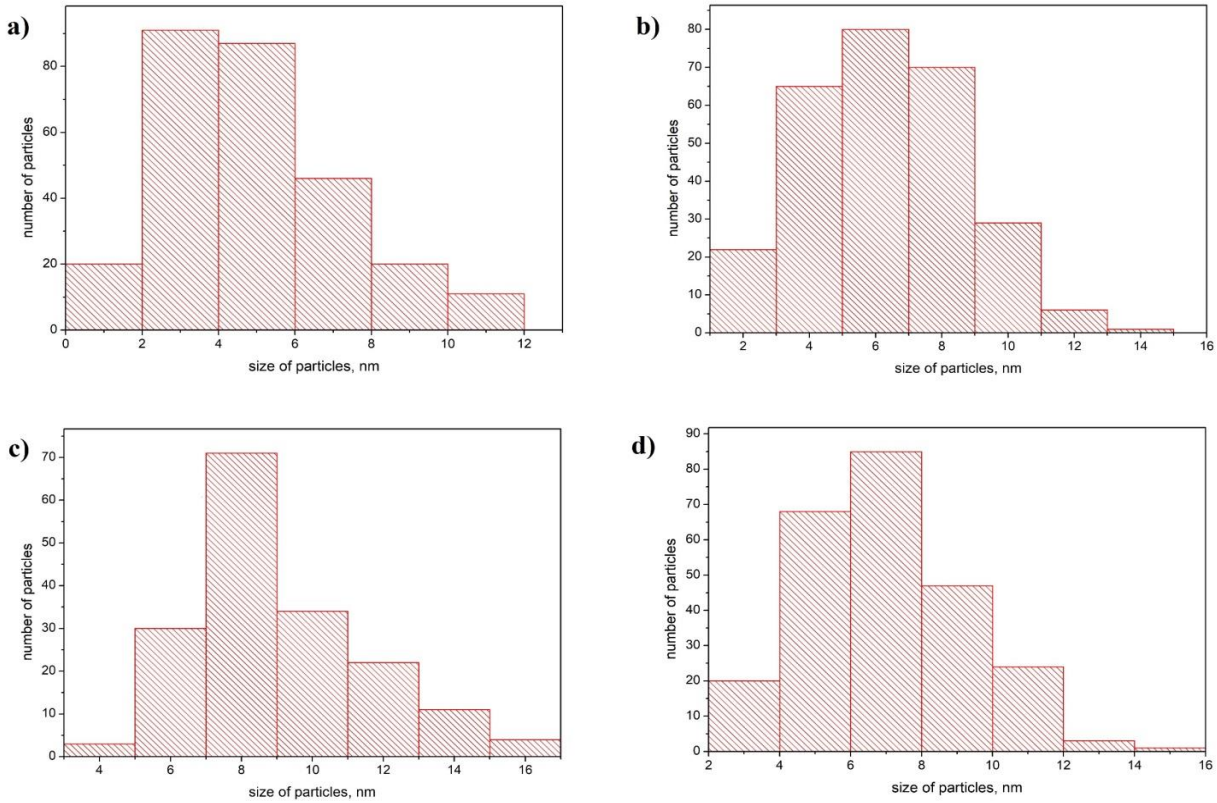

Figure 6. Size distribution of Au nanoparticles for axial PLD with the following deposition parameters: a) P_{Ar}=100 Pa, j=2 J/cm^2, N = 500; b) P_{Ar} =70 Pa, j=2 J/cm^2, N = 500; c) P_{Ar} =70 Pa, j=3.7 J/cm^2, N = 250; d) P_{Ar} =70 Pa, j=3.7 J/cm^2, N = 150

Using an axial PLD, isolated Au nanoparticles with good uniformity and high density were obtained at argon pressures of 70 and 100 Pa at j = 2 J/cm^2 and 500 pulses (Figure 6a, b), as well as at j = 3.7 J/cm^2 and an argon pressure of 70 Pa at 250 (Figure 6c) and 150 (Figure 6d) pulses. As P_{Ar} increased from 70 to 100 Pa, the nanoparticles grew larger due to their fusion with each other. When N exceeded 350 pulses, percolation structures with a thickness of 18 nm and more were formed due to more intense fusion of particles. When N exceeded 500 pulses, ultrathin Au films with a thickness of 23 nm and more were formed. When N was less than 150, the uniformity of the distribution and particle size deteriorated. The same phenomena happened at P_{Ar} above 150 Pa and below 70 Pa. The most stable and reproducible mode of Au nanoparticle deposition for axial geometry was the mode with the following parameters: P_{Ar} = 70 Pa, j = 3.7 J/cm^2, N = 250. In this mode, Au nanoparticles with an average size of 9.06 nm were reproducibly obtained, and the number of fused particles and large agglomerates was minimal. In fact, there were no gold particles larger than 12 nm on the surface of the samples. In more detail axial deposition results are shown in Table 1.

Table 1. Parameters of axial PLD with good reproducibility

Ar pressure, Pa	j, J/cm^2	Number of pulses	Size of particles/ thickness of film
70	2	500	6.28 nm
70	3.7	150	6.86 nm
70	3.7	250	9.06 nm
70	3.7	500	Percolation 18 nm
70	3.7	750	Percolation 19 nm
70	3.7	1000	film 23.87 nm
100	3.7	150	7.89 nm
100	3.7	250	8.48 nm
100	3.7	500	Percolation 18 nm
100	2	500	4.87 nm

The average particle size was found by fitting histograms in the OriginLab software using a log-normal distribution. Non-axis deposition results are shown in Table 2 in more details.

Table 2. Parameters of non-axial PLD with good reproducibility

Ar pressure, Pa	J, J/cm^2	Number of pulses	Size of particles/ thickness of film
70	3.7	1000	film 37.35 nm
70	3.7	100	4.8 nm
150	3.7	1000	film 42 nm
150	3.7	100	6.35 nm

In order not to clutter up the text, the tables demonstrate only the results that were obtained with good reproducibility. For the axial PLD geometry, it was not possible to obtain reproducible and stable results at a j = 2 J/cm^2 for N greater or less than 500 in the entire pressure range from 70 to 150 Pa. The deposition mode with increased focusing of laser radiation (j = 3.7 J/cm^2) turned out to be more stable and made it possible to reproducibly obtain Au nanoparticles at N = 150 and 250 pulses and P_{Ar} in the range from 70 Pa to 100 Pa. In this case, the dependence of the average size of nanoparticles on the number of laser pulses (Fig. 7) indicates that the growth rate of particles decreases with increasing pressure.

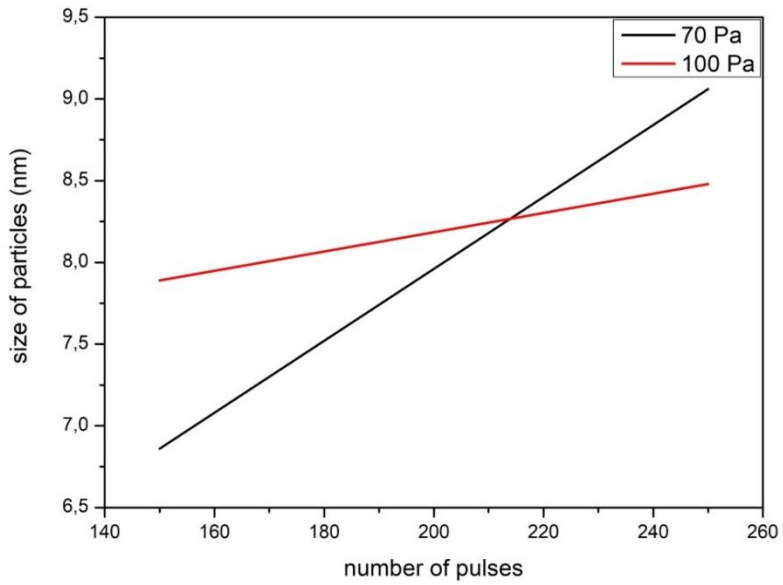

Figure 7. Dependence of the average size of Au nanoparticles on the number of laser pulses for different P_{Ar}.

Figure 8 shows the histograms of the size distribution of Au nanoparticles obtained by off-axis PLD. For this sputtering geometry, axial PLD parameters were used with the most stable and reproducible results. However, with N> 100 pulses and N <100 pulses, stable results were not obtained.

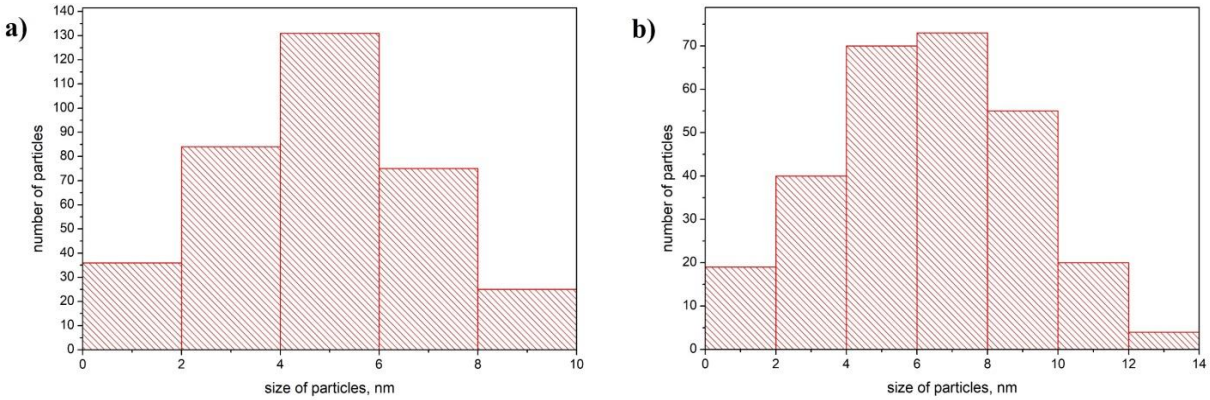

Figure 8. Size distribution of Au nanoparticles for non-axial PLD with the following deposition parameters: a) P_{Ar} =70 Pa, j=3.7 J/cm^2, N = 100; b) P_{Ar} =150 Pa, j=3.7 J/cm^2, N = 100

Also, at P_{Ar} greater than 150 Pa and less than 70 Pa, the spread of nanoparticle sizes was too large. The most uniform in size and distribution Au nanoparticles were obtained with the following deposition parameters: P_{Ar} = 70 Pa, j = 3.7 J/cm^2, N = 100. The average nanoparticle size was ~ 4.8 nm, the maximum size did not exceed 10 nm. About 80% of the particles were between 2 and 8 nm. As the argon pressure rises to 150 Pa, larger nanoparticles up to 14 nm appear, the number of particles from 2 nm to 8 nm decreases to 55%, and the average particle size increases to 6.35 nm.

Thus, PLD is a reliable tool for obtaining Au nanoparticles and ultrathin Au films. The flexibility of this method makes it possible to obtain nanoparticles of various sizes (from 4 nm to 10 nm) and distributions without heating in a high argon pressure by varying j, N, the deposition geometry, and P_{Ar}.

With PLD it is possible to coat structures with chemically active surfaces with nanoparticles when contamination and surface degradation of the active surface that occur with other application methods is critical. It is planned to assess and predict the behavior of the strength properties of such modified surfaces using the mathematical apparatus proposed by the authors in the previous works [30-33].

4. Conclusion

PLD makes it possible to obtain Au nanoparticles uniformly distributed over the substrate surface and exhibit a small scatter of sizes. The modes of stable and reproducible production of Au nanoparticles with an average size of 4 to 10 nm, ultrathin Au films with a thickness of 23 nm and percolation structures (agglomerated particles) with a thickness of 18 nm were revealed. Larger Au particles can be obtained by thermal decomposition of percolation structures and ultrathin Au films in vacuum or in argon atmosphere. The results obtained prove that by means of PLD at high argon pressure, particles of different sizes and with different distributions over the substrate surface can be obtained. Also, specific modes of obtaining structures were demonstrated and the dependences of the average size of Au nanoparticles on the PLD parameters were indicated. Thus, PLD is a reliable tool for reproducible deposition of Au nanoparticles of the required size and can be used in cases where the deposition of particles by other methods can adversely affect the properties of the objects to be coated.

Acknowledgments

A. L. Nikolaev and S. M. Aizikovich acknowledge support from the Government of Russia within grant no. 14.Z50.31.0046. A. S. Kamencev acknowledge support from the Russian Foundation for Basic Research within grant no. 20-07-00637 A.

References

[1] Sergeev G 2003 *Nanochemistry* (MGU Publishing)
[2] Lozovskii V N, Irkha V A and Lozovskii, V. S. 2011 Diffusion in quasi-one-dimensional nano- and microobjects *Technical Physics Letters* **37(11)** pp 1078-81
[3] Haruta M 2003 When gold is not noble: catalysis by nanoparticles *The chemical record* **3(2**) pp 75-87
[4] Suchomel P, Kvitek L, Prucek R, Panacek A, Halder A, Vajda S and Zboril R 2018 Simple size-controlled synthesis of Au nanoparticles and their size-dependent catalytic activity *Scientific reports* **8(1)** pp 1-11
[5] Valcárcel M and López-Lorente Á I 2014 *Gold nanoparticles in analytical chemistry* (Elsevier)
[6] Pushkariov V I, Nikolaev A L and Kaidashev E M 2015 Influence of Zn Vapor Supersaturation on Morphology and Optical Properties of ZnO Nanorods Grown by CVD Technique *Advanced materials-studies and applications* chapter 4 (New York: Nova Science Publishers) pp 51-56
[7] Zhilin D A, Pushkariov V I, Nikolaev L A, Kaidashev E M, Lyanguzov N V and Kaydashev V E 2015 Photoelectric Properties of Metal-Semiconductor-Metall Structure Based on ZnO Nanorods Designed Thermal Evaporation and Carbothermal Methods *Advanced materials-studies and applications* chapter 5 (New York: Nova Science Publishers) pp 57-64
[8] Yager P, Domingo G J and Gerdes J 2008 Point-of-care diagnostics for global health *Annual review of biomedical engineering* **10**
[9] Manju S and Sreenivasan K 2010 Functionalised nanoparticles for targeted drug delivery Biointegration of Medical Implant Materials (Woodhead Publishing) pp 267-297
[10] Chandran P R and Thomas R T 2015 Gold nanoparticles in cancer drug delivery Nanotechnology Applications for Tissue Engineering (William Andrew Publishing) pp 221-237
[11] Prakash J, Kumar V, Kroon R E, Asokan K, Rigato V, Chae K H and Swart H C 2016 Optical and surface enhanced Raman scattering properties of Au nanoparticles embedded in and located on a carbonaceous matrix *Physical Chemistry Chemical Physics* **18(4)** pp 2468-80
[12] Notarianni M, Vernon K, Chou A, Aljada M, Liu J and Motta N 2014 Plasmonic effect of gold nanoparticles in organic solar cells *Solar Energy* **106** pp 23-37

[13] Pushkariov V I, Nikolaev A L and Kaidashev E M 2014 Synthesis and characterization of ZnO nanorods obtained by catalyst-free thermal technique *Journal of Physics: Conference Series* Vol 541 No 1 p 012031
[14] Zhilin D A, Lyanguzov N V, Nikolaev L A, Pushkariov V I and Kaidashev E M 2014 Photoelectric properties of MSM structure based on ZnO nanorods, received by thermal evaporation and carbothermal syntesis *Journal of Physics: Conference Series* Vol 541 No 1 p 012038
[15] Starinskiy S V, Sulyaeva V S, Shukhov Y G, Cherkov A G, Timoshenko N I, Bulgakov A V and Safonov A I 2017 Comparison of structures of gold nanoparticles synthesized by pulsed laser ablation and magnetron sputtering *Journal of Structural Chemistry* **58(8)** pp 1581-87
[16] Hernández-Maya M, Rivera-Quintero P, Ospina R, Quintero-Orozco J H and García-Castro A C 2019 Ablation energy, water volume and ablation time: Gold nanoparticles obtained through by pulsed laser ablation in liquid *Journal of Physics: Conference Series* Vol. 1386 No 1 p 012062
[17] Turkevich J and Cooper P H J 1951 A study of the nucleation and growth process in the synthesis of colloidal gold *Discuss. Faraday Soc* **55** pp 55–75
[18] Alibart F, Pleutin S, Guérin D, Novembre C, Lenfant S, Lmimouni K, Gamrat C and Vuillaume D 2010 An Organic Nanoparticle Transistor Behaving as a Biological Spiking Synapse *Adv. Funct. Mater.* **20** pp 330–337
[19] Misra N, Biswal J, Gupta A, Sainis J K and Sabharwal S 1012 Gamma radiation induced synthesis of gold nanoparticles in aqueous polyvinyl pyrrolidone solution and its application for hydrogen peroxide estimation *Radiat. Phys. Chem.* **81** pp 195–200
[20] Gangapuram B R, Bandi R, Alle M, Dadigala R, Kotu G M and Guttena V 2018 Microwave assisted rapid green synthesis of gold nanoparticles using Annona squamosa L peel extract for the efficient catalytic reduction of organic pollutants *J. Mol. Struct.* **1167** pp 305–315
[21] Jang B and Choi Y 2012 Photosensitizer-Conjugated Gold Nanorods for Enzyme-Activatable Fluorescence Imaging and Photodynamic Therapy *Theranostics* **2** pp 190–197
[22] Turner M, Golovko V B, Vaughan O P H, Abdulkin P, Berenguer-Murcia A, Tikhov M S, Johnson B F G and Lambert R M 2008 Selective oxidation with dioxygen by gold nanoparticle catalysts derived from 55-atom clusters *Nature* **454** pp 981–983
[23] Zhao P, Li N and Astruc D 2013 State of the art in gold nanoparticle synthesis *Coord. Chem. Rev.* **257** pp 638–665
[24] Nune S K, Chanda N, Shukla R, Katti K, Kulkarni R R, Thilakavathi S, Mekapothula S, Kannan R and Katti K V 2009 Green Nanotechnology from Tea: Phytochemicals in Tea as Building Blocks for Production of Biocompatible Gold Nanoparticles *J. Mater. Chem.* **19** pp 2912–2920
[25] Freitas de Freitas L, Varca G H C, dos Santos Batista J G and Benévolo Lugão A 2018 An overview of the synthesis of gold nanoparticles using radiation technologies *Nanomaterials* **8(11)** p 939
[26] Al-Yasiri A Y, Khoobchandani M, Cutler C S, Watkinson L, Carmack T, Smith C J, Kuchuk M, Loyalka S K, Lugão A B and Katti K V 2017 Mangiferin functionalized radioactive gold nanoparticles (MGF-198AuNPs) in prostate tumor therapy: Green nanotechnology for production: In vivo tumor retention and evaluation of therapeutic efficacy *Dalt. Trans.* **46** pp 14561–71
[27] Shukla R, Nune S K, Chanda N, Katti K, Mekapothula S, Kulkarni R R, Welshons W V, Kannan R and Katti K V 2008 Soybeans as a phytochemical reservoir for the production and stabilization of biocompatible gold nanoparticles *Small* **4** pp 1425–36
[28] Nikolaev A L, Karapetyan G Y, Nesvetaev D G, Lyanguzov N V, Dneprovski V G and Kaidashev E M 2014 Preparation and investigation of ZnO nanorods array based resistive and SAW CO gas sensors *Advanced Materials* pp 27-36

[29] Nikolaev A L, Kaidashev E M and Kamencev A S 2019 Morphology and Photoluminescence of Zinc Oxide Nanorods Obtained by Carbothermal Synthesis at Different Temperatures *Advanced Materials* pp 103-113
[30] Volkov S S, Vasiliev A S, Aizikovich S M, Sadyrin E V Contact problem on indentation of an elastic half-plane with an inhomogeneous coating by a flat punch in the presence of tangential stresses on a surface 2018 *AIP Conf. Proc.* (vol. 1959) ed E Kustova, G Leonov et al (New York: AIP Publishing LLC) p 070037
[31] Sadyrin E, Swain M, Mitrin B, Rzhepakovsky I, Nikolaev A, Irkha V, Yogina D, Lyanguzov N, Maksyukov S, Aizikovich S 2020 Characterization of enamel and dentine about a white spot lesion: mechanical properties, mineral density, microstructure and molecular composition *Nanomaterials* **10** p 1889
[32] Vasiliev A S, Sadyrin E V, Mitrin B I, Aizikovich S M, Nikolaev A L 2018 Nanoindentation of ZrN Coatings on Silicon and Copper Substrates *Russ. Eng. Res*. **38** pp 735-737
[33] Sadyrin E V, Mitrin B I, Krenev L I, Nikolaev A L, Aizikovich S M Evaluation of Mechanical Properties of the Two-Layer Coating Using Nanoindentation and Mathematical Modeling 2017 *International Conference on Physics and Mechanics of New Materials and Their Applications ed* I Parinov, S-H Chang et al (Cham: Springer) pp. 495-502

Numerical modeling of hydrodynamic processes in the Taganrog Bay of the Azov Sea

A I Sukhinov[1], A E Chistyakov[1] , A V Nikitina[2,3], Y V Belova[1], I Y Kuznecova[2,3], V N Litvinov[1,4,*], and L Kravchenko[1]

[1]Don State Technical University, Rostov-on-Don, Russia
[2]Southern Federal University, Rostov-on-Don, Russia
[3]Supercomputers and Neurocomputers Research Center, Co. Ltd., Taganrog, Russia
[4]Azov-Black Sea Engineering Institute of Don State Agrarian University, Zernograd, Russia

*Corresponding author: LitvinovVN@rambler.ru

Abstract. The paper covers the development and numerical implementation of a mathematical model of hydrodynamic processes in shallow water based on modern information technology and computational methods to improve the accuracy of predictive modeling of the ecological situation using the example of the Taganrog Bay of the Azov Sea. The proposed mathematical hydrodynamics model takes into account surges, dynamically reconstructed geometry, elevation of the level and coastline, wind currents and friction against the bottom, Coriolis force, turbulent exchange, evaporation, river flow, deviation of the pressure field value from the hydrostatic approximation, the salinity and temperature impact. A discrete analogue of the mathematical model of hydrodynamics is built based on the splitting schemes for physical processes. The constructed discrete analogs possess the properties of conservatism, stability, and convergence. Numerical algorithms are also proposed for solving the arising SLAEs that improve the accuracy of predictive modeling. The practical significance of the work is that the proposed model was software implemented; the limits and prospects of its use were defined. The experimental software was designed based on a graphics accelerator for mathematical modeling of possible development scenarios of the shallow waters ecosystems, taking into account the environmental factors influence. Parallel implementation was performed using the decomposition methods for computationally labors diffusion-convection problems taking into account the CUDA architecture characteristics.

1. Introduction

The salinity of sea water, being one of the most important abiotic factors, has a significant impact on the state of the sea ecosystem. The Taganrog Bay of the Azov Sea, which is a vast zone of mixing the fresh river waters from the Don River and the salty waters from the western part of the Azov Sea, is characterized by high temporal and spatial variability of water salinity. A significant contribution to its dynamics is made by the effects of mixing of the aquatic environment caused by surges arising from the westerly wind.

Much work on the study of the hydrological regime of the Azov Sea, in particular salinity and temperature, was done by G.G. Matishov, Yu. M. Gargopa and others [1]. In work [2], it is noted that the salinity dynamics of the Azov Sea significantly depends on the inflow of saline waters from the Black Sea, river flow, and atmospheric processes that affect the balance of precipitation and moisture evaporation from the sea surface. Therefore, the Azov Sea is characterized by periods of relative desalination and salinization. Since 2007, there has been a modern period of salinization of the Azov Sea [3,4], which is associated with a decrease in the Don River flow by 35.6% compared to the period from 1998 to 2006.

Despite a significant number of publications, many effects that have a significant impact on the spatial change in the hydrodynamic processes of shallow water bodies are not taken into account in the development of mathematical models, which leads to a deterioration of the forecasts quality of changes in the studied water areas ecological situation.

In this regard, there is a need to develop a computational structure that implements parallel algorithms for modeling hydrodynamic processes for prediction changes in the environmental situation in shallow waters and coastal areas, including the movement of pollutants and sediments, organic deposits, implemented on high-performance computer systems to provide a forecast basis for sustainable development of coastal systems.

In July 2017, the staff members of the Don State Technical University, the Southern Federal University, and the Southern Scientific Center of the Russian Academy of Sciences went on an expedition to the Azov Sea aboard the Scientific Research Vessel "Deneb" (Fig. 1).

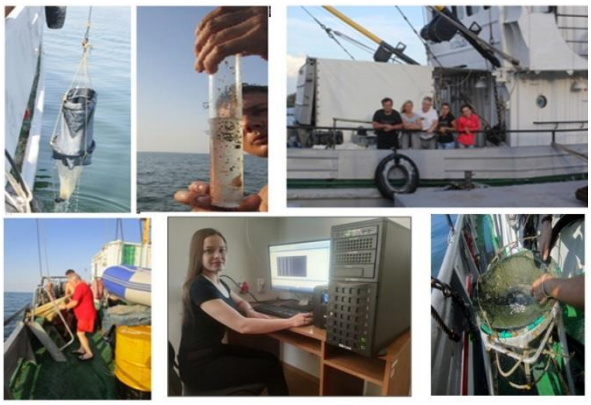

Figure 1. Expeditionary researches

Expedition data, data of the Unified state system of information on the situation in the World ocean ("USIWO") portal, for complex geoinformational analysis of spatial-temporal processes and phenomena, were used for modeling hydrobiological shallow water processes.

2. Problem statements

The developed model for calculation three-dimensional fields of water velocity vector, temperature and salinity is based on the mathematical hydrodynamic model of shallow waters, which takes into account the heat and salts transport [5,6]:

- the Navier-Stokes motion equation

$$u_t' + uu_x' + vu_y' + wu_z' = -\frac{1}{\rho}P_x' + \left(\mu u_x'\right)_x' + \left(\mu u_y'\right)_y' + \left(\nu u_z'\right)_z' + 2\Omega(v\sin\theta - w\cos\theta), \qquad (1)$$

$$v_t' + uv_x' + vv_y' + wv_z' = -\frac{1}{\rho}P_y' + \left(\mu v_x'\right)_x' + \left(\mu v_y'\right)_y' + \left(\nu v_z'\right)_z' - 2\Omega u\sin\theta, \quad (2)$$

$$w_t' + uw_x' + vw_y' + ww_z' = -\frac{1}{\rho}P_z' + \left(\mu w_x'\right)_x' + \left(\mu w_y'\right)_y' + \left(\nu w_z'\right)_z' + 2\Omega u\cos\theta + g\left(\rho_0/\rho - 1\right), \quad (3)$$

- the continuity equation in the case of variable density

$$\rho_t' + (\rho u)_x' + (\rho v)_y' + (\rho w)_z' = 0, \quad (4)$$

- the heat transport equation

$$T_t' + uT_x' + vT_y' + wT_z' = \left(\mu T_x'\right)_x' + \left(\mu T_y'\right)_y' + \left(\nu T_z'\right)_z' + f_T, \quad (5)$$

- the salt transport equation

$$S_t' + uS_x' + vS_y' + wS_z' = \left(\mu S_x'\right)_x' + \left(\mu S_y'\right)_y' + \left(\nu S_z'\right)_z' + f_S, \quad (6)$$

where $\mathbf{V} = \{u, v, w\}$ are components of velocity vector; P is the full hydrodynamic pressure; ρ is the water density; μ, ν are horizontal and vertical components of the turbulent exchange coefficient; $\mathbf{\Omega} = \Omega \cdot \left(\cos\theta \cdot \mathbf{j} + \sin\theta \cdot \mathbf{k}\right)$ is the angular velocity of the Earth rotation; θ is the latitude of the region; g is the gravity acceleration; f_T, f_S are sources of heat and salt (located on the border of the region), T is the water temperature, S is the water salinity.

Two components are conditionally distinguished from the total hydrodynamic pressure – the pressure of the liquid column and the hydrodynamic part [6,7]:

$$P(x, y, z, t) = p(x, y, z, t) + \rho_0 gz, \quad (7)$$

where p is the hydrostatic pressure of the unperturbed fluid; ρ_0 is the fresh water density under normal conditions.

State equation for density:

$$\rho = \rho + \rho_0, \quad (8)$$

where ρ_0 is the fresh water density under normal conditions; ρ is determined by the equation recommended by UNESCO:

$$\rho = \rho_w + (8.24493\cdot10^{-1} - 4.0899\cdot10^{-3}T + 7.6438\cdot10^{-5}T^2 - 8.2467\cdot10^{-7}T^3 + 5.3875\cdot10^{-9}T^4)S + \\ + (-5.72466\cdot10^{-3} + 1.0227\cdot10^{-4}T - 1.6546\cdot10^{-6}T^2)S^{3/2} + 4.8314\cdot10^{-4}S^2, \quad (9)$$

where ρ_w is the fresh water density, specified by a polynomial [8]:

$$\rho_w = 999.842594 + 6.793952\cdot10^{-2}T - 9.095290\cdot10^{-3}T^2 + \\ + 1.001685\cdot10^{-4}T^3 - 1.120083\cdot10^{-6}T^4 + 6.536332\cdot10^{-9}T^5. \quad (10)$$

Equation (9) is applicable for salinity in the range from 0 to 42 ‰ and temperature from -2 to 40 °C.

The system of equations (1–6) is considered under the following boundary conditions [9–11]:

- at the input:

$$\mathbf{V} = \mathbf{V}_0,\ P_{\mathbf{n}}' = 0,\ T = T_1,\ S = S_1 \quad (11)$$

- the bottom boundary:

$$\rho_v \mu \left(\mathbf{V}_{\boldsymbol{\tau}}\right)_{\mathbf{n}}' = -\boldsymbol{\tau},\ \mathbf{V}_{\mathbf{n}} = 0,\ P_{\mathbf{n}}' = 0,\ T_{\mathbf{n}}' = 0,\ S_{\mathbf{n}}' = 0,\ f_T = 0,\ f_S = 0, \quad (12)$$

- the lateral boundary:

$$\left(\mathbf{V}_{\boldsymbol{\tau}}\right)_{\mathbf{n}}' = 0,\ \mathbf{V}_{\mathbf{n}}' = 0,\ P_{\mathbf{n}}' = 0,\ T_{\mathbf{n}}' = 0,\ S_{\mathbf{n}}' = 0,\ f_T = 0,\ f_S = 0, \quad (13)$$

- the upper boundary:

$$\rho_v \mu \left(\mathbf{V}_\tau\right)'_{\mathbf{n}} = -\boldsymbol{\tau}, w(x,y,t) = -\omega - P_t'/\rho g, P'_{\mathbf{n}} = 0,\ T'_{\mathbf{n}} = 0,$$
$$S'_{\mathbf{n}} = 0,\ f_T = k\left(T_a - T\right),\ f_S = \frac{h_\omega}{h_z - h_\omega} S, \tag{14}$$

- at the output (Kerch Strait):

$$P'_{\mathbf{n}} = 0, \mathbf{V}'_{\mathbf{n}} = 0, T'_{\mathbf{n}} = 0,\ S'_{\mathbf{n}} = 0,\ f_T = 0,\ f_S = 0, \tag{15}$$

where ω is the liquid evaporation rate; $\mathbf{n}$ is the outer normal vector to the boundary of the computational domain; $\mathbf{V}_{\mathbf{n}}$, $\mathbf{V}_{\boldsymbol{\tau}}$ are normal and tangential components of the velocity vector; $\boldsymbol{\tau} = \left\{\tau_x, \tau_y, \tau_z\right\}$ is the tangential stress vector; ρ is the water density; ρ_v is the sediment density; T_a is the atmospheric temperature, k is the heat transport coefficient between the atmosphere and water environment.

Components of tangential stress for free surface: $\boldsymbol{\tau} = \rho_a C d_s |\mathbf{w}| \mathbf{w}$, where $\mathbf{w}$ is the wind velocity vector relative to water; ρ_a is the atmosphere density; $Cd_s = 0.0026$ is the dimensionless coefficient of surface resistance, which depends on the wind velocity, is considered in the range 0.0016–0.0032 [12].

Tangential stress for the bottom $\boldsymbol{\tau} = \rho C d_b |\mathbf{V}| \mathbf{V}$, where $Cd_b = gk^2 / h^{1/3}$; $k = 0.025$ is a group roughness coefficient in the Manning formula, is considered in the range 0.025–0.2; $h = H + \eta$ is the water depth; H is the depth of undisturbed surface; η is the height of free surface relative to the geoid (sea level).

The system of equations (1–6) is considered under the following initial conditions:

$$\mathbf{V} = \mathbf{V}_0, T = T_0, S = S_0, \tag{16}$$

where $\mathbf{V}_0$, T_0 and S_0 are predefined functions.

3. Model discretization

According to the pressure correction method, the original model of hydrodynamics is divided into three subproblems [13–15]. The first subproblem is represented by the diffusion-convection-reaction equation, used for calculation the components of velocity vector field on the intermediate layer in time:

$$\frac{\tilde{u} - u}{\tau} + u\bar{u}'_x + v\bar{u}'_y + w\bar{u}'_z = \left(\mu\bar{u}'_x\right)'_x + \left(\mu\bar{u}'_y\right)'_y + \left(\nu\bar{u}'_z\right)'_z + 2\Omega(v\sin\theta - w\cos\theta),$$
$$\frac{\tilde{v} - v}{\tau} + u\bar{v}'_x + v\bar{v}'_y + w\bar{v}'_z = \left(\mu\bar{v}'_x\right)'_x + \left(\mu\bar{v}'_y\right)'_y + \left(\nu\bar{v}'_z\right)'_z - 2\Omega u\sin\theta, \tag{17}$$
$$\frac{\tilde{w} - w}{\tau} + u\bar{w}'_x + v\bar{w}'_y + w\bar{w}'_z = \left(\mu\bar{w}'_x\right)'_x + \left(\mu\bar{w}'_y\right)'_y + \left(\nu\bar{w}'_z\right)'_z + 2\Omega u\cos\theta + g\left(\frac{\rho_0}{\rho} - 1\right).$$

Note that the term $g\left(\rho_0 / \rho - 1\right)$ describes the buoyancy (the Archimedes' Power). Numerous experiments on simulation of the water environment transport in shallow waters such as the Azov Sea have shown that this term makes a minor contribution to the solution of the problem and can be ignored. Schemes with weights are used to approximate the diffusion-convection-reaction equation in time. Here $\bar{u} = \sigma\tilde{u} + (1-\sigma)u$, $\sigma \in [0,1]$ is the weight of the scheme.

The calculation of the pressure distribution (the second subproblem) is based on the Poisson equation:

$$p''_{xx} + p''_{yy} + p''_{zz} = \frac{\hat{\rho} - \rho}{\tau^2} + \frac{\left(\hat{\rho}\tilde{u}\right)'_x}{\tau} + \frac{\left(\hat{\rho}\tilde{v}\right)'_y}{\tau} + \frac{\left(\hat{\rho}\tilde{w}\right)'_z}{\tau}. \tag{18}$$

The value of the velocity field at the upper boundary (water surface) is defined as $w = -\omega - p'_t / \rho g$. As an initial approximation for this problem, a simplified hydrostatic model of the water environment transport

was used, which significantly reduces the calculation time. The third subproblem allows us to use explicit formulas to determine the velocity distribution on the next layer in time:

$$\frac{\hat{u}-\tilde{u}}{\tau}=-\frac{1}{\hat{\rho}}p'_x,\ \frac{\hat{v}-\tilde{v}}{\tau}=-\frac{1}{\hat{\rho}}p'_y,\ \frac{\hat{w}-\tilde{w}}{\tau}=-\frac{1}{\rho}p'_z, \tag{19}$$

where τ is the step along the time coordinate; u is the value of the velocity vector field on the previous layer in time; $\tilde{u}$ is the value of the velocity field on the intermediate layer in time; $\hat{u}$ is the value of the velocity field on the current layer in time.

The computational domain is inscribed in a parallelepiped. A uniform grid is introduced for software implementation of the three-dimensional mathematical model of hydrodynamics. $o_{i,j,k}$ is the "fullness" of the cell (i,j,k). The degree of cell occupancy is defined by the pressure of water column at the cell bottom. In general, the degree of cell occupancy is calculated based on the expression [8]:

$$o_{i,j,k}=\frac{P_{i,j,k}+P_{i-1,j,k}+P_{i,j-1,k}+P_{i-1,j-1,k}}{4\rho g h_z}. \tag{20}$$

The approximation of calculation problem the velocity field of water environment by spatial variables is based on the balance method taking into account the filling coefficients of control domains.

The grid equations were obtained as a result of finite-difference approximations of problem (1) – (16) using a scheme with weights [16]. A modified alternating triangular method (MATM) [17 – 19] and the domain decomposition by the *k*-means algorithm [20,21] were used for the solution of the problem (1) – (16).

4. Features of software implementation

For the numerical implementation of the proposed mathematical model, we developed parallel algorithms that will be adapted for hybrid computer systems using the NVIDIA CUDA architecture which will be used for mathematical modeling of described problems and to design high-performance information systems.

One of the most important tasks of the stable functioning of such systems is to ensure automatic adjustment of the threshold parameters of the simulation, such as the dimension of the SLAE, since the lack of RAM or video memory leads to a significant decrease in performance or an abnormal termination of the application. In order to implement the algorithm that solves the described problem, a software module for collecting information on the performance of a hybrid computing system has been developed (Fig. 2).

Computer modeling of the set tasks, while meeting the requirements for the accuracy and speed of calculation, requires large computing resources that are not always available in production conditions and in the event of emergency situations that require immediate organizational and managerial decisions in order to eliminate them. To increase the efficiency of using available technical means, the architecture of an information system for supporting scientific research is proposed, which can function under conditions of using heterogeneous computing environments.

The system is based on the requirement to use free software as much as possible in order to minimize capital and operating costs. It is proposed to use CentOS 7 as the main operating system with the nginx http-server installed, MariaDB database management system and .NET Core 3.1 platform installed. The application software of the system is developed in the form of a server part, implemented in the form of an ASP .NET Core MVC / Blazor web application, and a client part, which is a set of services installed on all involved computers. The interaction between these system components is provided through the use of gRPC.

The server part provides the solution to the following tasks:

- management of system user accounts, including the assignment of roles;
- configuration management of available computing resources;
- managing the process of uploading modeling tasks to the server in the form of rpm packages;
- management of the monitoring service for performed tasks.

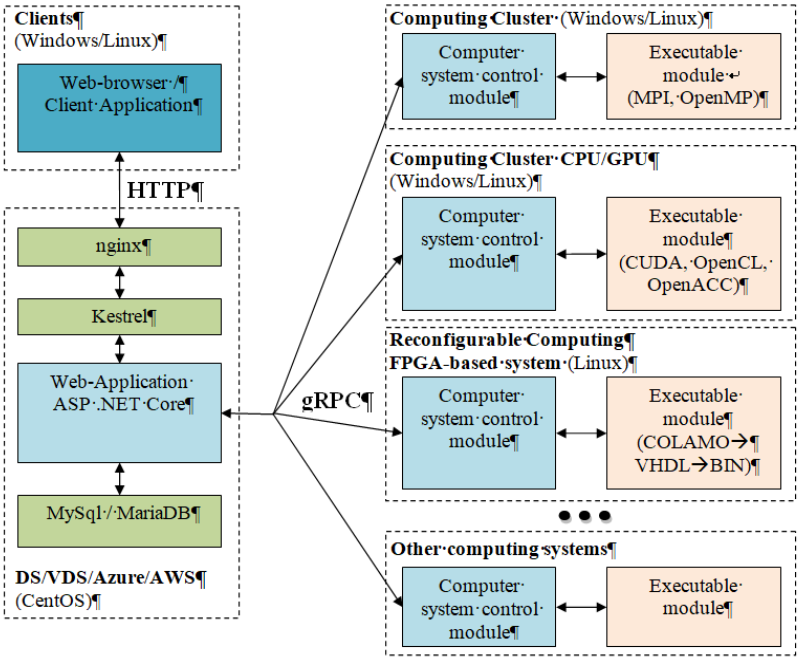

Figure 2. Generalized system diagram

Management of the development process of system and application software is carried out using the Git version control system. Developers are working with the system code base on their workstations, where local repositories of system components projects are deployed, synchronized with a remote repository accessible through a web service based on the Git version control system.

Management of the processes of deployment, configuration and operation of the system is performed by the administrator using any available SSH client, for example, ssh for the Linux console terminal or Bitvise SSH Client for Windows (Fig. 3).

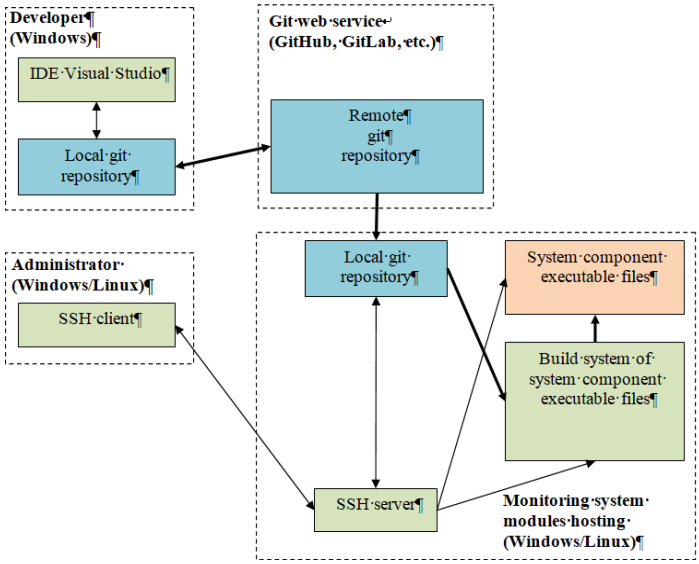

Figure 3. System development process control diagram

A distinctive feature of the development is the use of an algorithm for preliminary estimation of the time spent on executing the task based on the data of preliminary testing of the performance of the hardware platform. When the computer control module is launched, it checks for the presence of the performance.xml file. In the absence of a file, performance tests are performed, which are a number of problems for solving SLAEs with different parameters, and their results are written to a file. For the test system Windows 10 (x64), CUDA Toolkit v10.0.130, Intel Core i5-6600 3.3 GHz processor, 32 GB DDR4 RAM, NVIDIA GeForce GTX 750 Ti 2GB video adapter (640 CUDA cores) using NVIDIA CUDA technology, obtained the results shown in Figures 4 and 5.

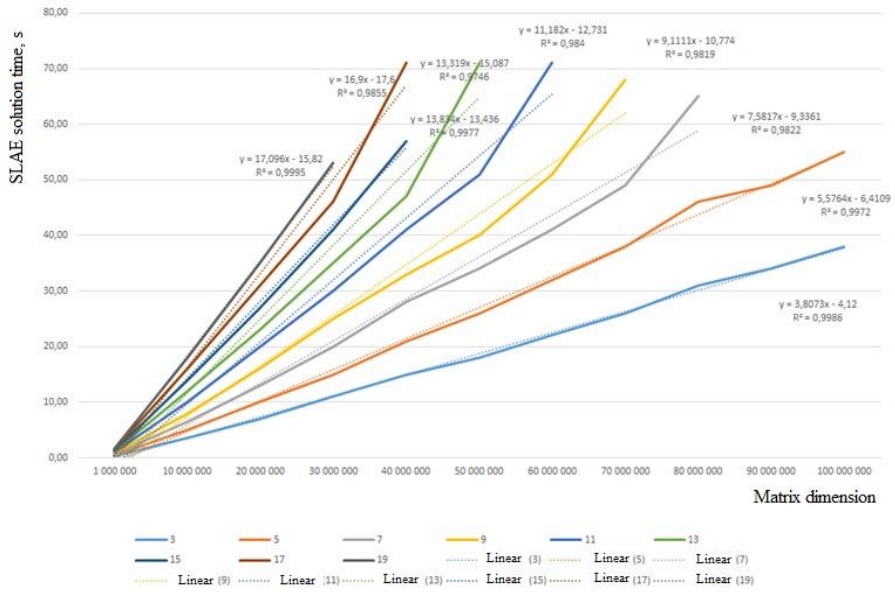

Figure 4. Graph of SLAE solution time dependence on the order of a square matrix

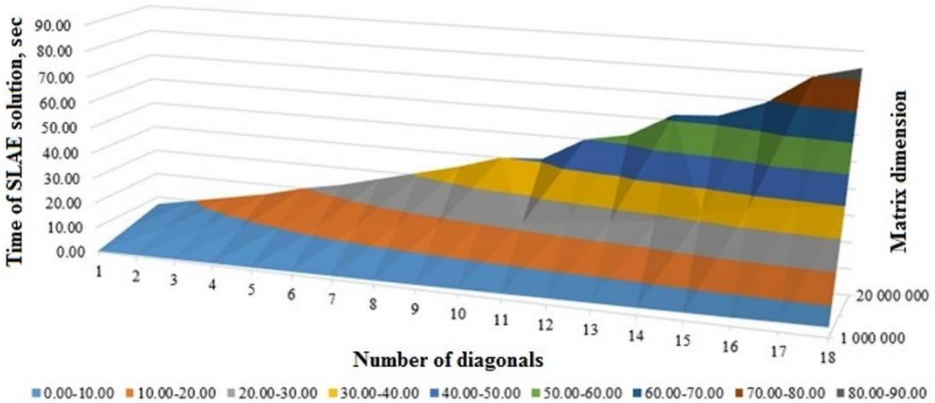

Figure 5. Test system performance study results

The obtained data on the performance parameters are then used by the control modules of the computing system in the process of controlling the process of placing the computational problem in the queue based on the algorithm shown in Figure 6.

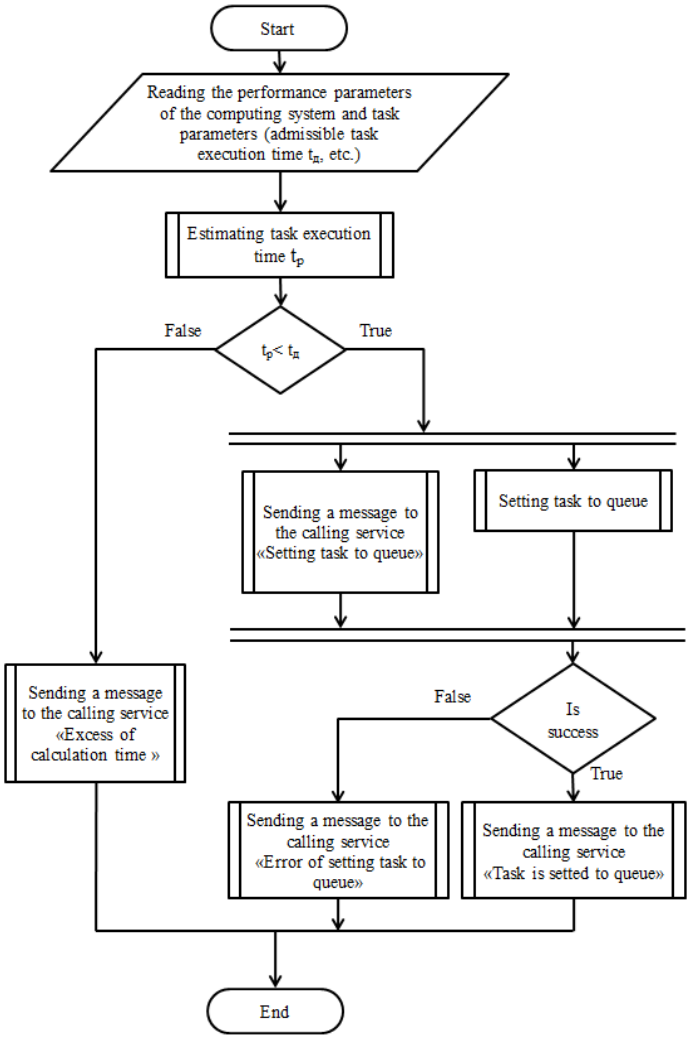

Figure 6. Algorithm for managing the process of placing a computational problem in the queue

5. Results of experimental researches

For numerical solution of proposed mathematical model (1) – (16), we developed adapted for hybrid computer systems parallel algorithms which use the NVIDIA CUDA architecture.

The program is designed to build turbulent flows of an incompressible velocity field of the aquatic environment on grids with high resolution. This program is used to calculate transport of heat and salts and takes into account the velocity field of the aquatic environment. The program takes into account such physical parameters as: surges, dynamically reconstructed geometry, elevation of the level and coastline, wind currents and friction against the bottom, Coriolis force, turbulent exchange, evaporation, river flow, deviation of the pressure field value from the hydrostatic approximation. The program provides the following functions:

- calculation of the velocity field without taking into account pressure based on (17);
- calculation of hydrodynamic pressure based on (18);
- calculation of a three-dimensional velocity field taking into account pressure based on (19);

- calculation of transport of heat and salts.

The criterion for checking the adequacy of the developed models was the error estimation with simultaneous consideration of the field data from the available n measurements: $\delta = \sqrt{\left(\sum_{k=1}^{n} q_{k\,nat} - q_k\right)^2} \Big/ \sqrt{\sum_{k=1}^{n} q^2{}_{k\,nat}}$, where $q_{k\,nat}$ is the value of the calculated function obtained using field measurements; q_k is the value of the grid function, calculated by simulation.

The salinity and temperature fields reconstructed from cartographic information are taken as input data for the hydrodynamic model when calculating the transport of heat and salts. The data of long-term observations and satellite images were taken in the form of images, from which, after applying the recognition algorithm, the salinity and temperature isolines were obtained. The reconstructed salinity and temperature fields were obtained using an interpolation algorithm based on high-order approximation schemes (Fig. 7). These fields are smoother functions for approximating functional dependencies describing the salinity and temperature fields, and can increase the accuracy of hydrodynamic calculations [5,22].

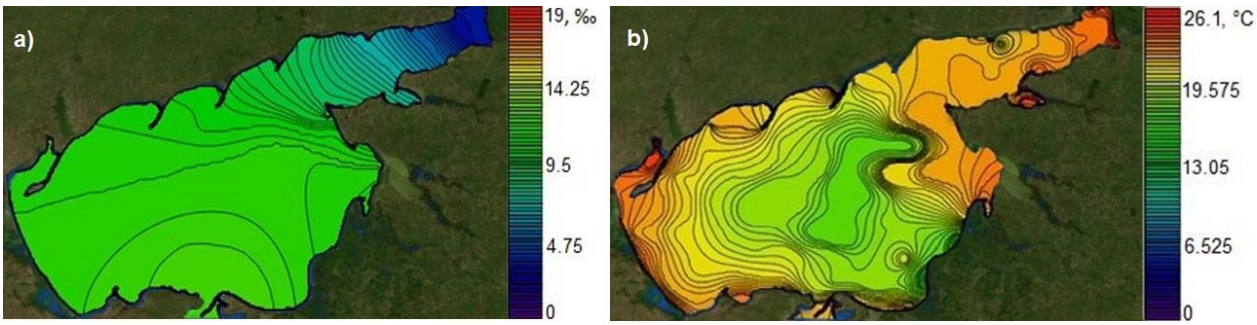

Figure 7. Images of reconstructed salinity and temperature fields

As a result of the research, a software was developed to more accurately describe hydrodynamic processes, salts and heat transport in shallow waters, such as the Azov Sea, with complex spatial structures of currents in the conditions of reducing freshwater flow of the Don river, increasing the flow of highly saline waters of Sivash lake and filtering the waters of salt lakes in the North-East of Crimea. Software implementation of mathematical models takes into account the Coriolis force, wind currents and bottom friction, turbulent exchange, evaporation, river flows, as well as the complex geometry of the bottom and coastline. The computational domain corresponds to the physical dimensions of the Azov Sea: the length is 355 km; the width is 233 km; the horizontal step is 1000 m. The time interval is 30 days. Results of numerical simulation of water environment transport in the Azov Sea water area based on the developed software complex are given in Fig. 8.

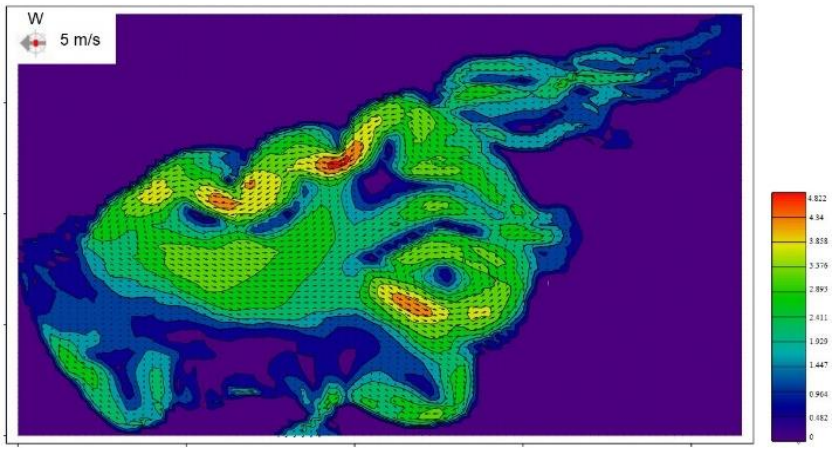

Figure 8. Results of mathematical modeling the water environment transport (barotropic flows)

Conclusion

The proposed 3D hydrodynamic model of shallow waters allows us to obtain three-dimensional fields of the water flow velocity vector, pressure, sea water density, salinity, and temperature. The geometry of water bottom has a great influence on the flow fields in hydrodynamics models of shallow water. Results of expedition measurements were used at developing hydrodynamic models of shallow waters. Measurements of water flow velocities were performed and based on the ADCP probe, which measures instantaneous values of the vertical profile of the velocity vector. The following parameters were specified at device setting: the vertical step is 10 cm; the number of vertical measurements is 128; the measurement frequency is 1 s. The Kalman filter algorithm was used to filter field data. Simulation results and field measurements of the vertical turbulent exchange coefficient at various water horizons were compared; based on it, we concluded that the calculation results of turbulent processes in shallow waters based on the Smagorinsky subgrid turbulence model are best consistent with the field data.

Acknowledgment

The reported study was funded by RFBR according to the research project No. 19-07-00623.

References

[1] G. Matishov, Y. Gargopa, S. Berdnikov, and S. Jenuk, Regularities of ecosystem processes in the Sea of Azov, Southern Science Centre of the Russian Academy of Science, Moskow, 2006, 304 p.

[2] G. Matishov, D. Matishov, Y. Gargopa, L. Dashkevich, S. Berdnikov, O. Baranova, I. Smolyar. 2006. Climatic Atlas of the Sea of Azov 2006. G. Matishov, S. Levitus, Ed., NOAA Atlas NESDIS 59, U.S. Government Printing Office, Washington, D.C., 103 pp.

[3] Dubinina V.G., Zhukova S.V. “Assessment of the possible consequences of the construction of the Bagaevsky hydroelectric complex for the ecosystem of the Lower Don” in Fish industry, vol. 4, 2016, pp. 20-30.

[4] Kuropatkin A.P., Shishkin V.M., Burlachko D.S., Karmanov V.G., Zhukova S.V., Podmareva T.I., Fomenko I.F., and Lutynskaya L.A. “Modern and prospective changes in the salinity of the Sea of Azov” in Environmental protection in the oil and gas complex, vol. 11, 2015, pp. 7-16.

[5] Sukhinov, A.I., Belova, Y.V., Filina, A.A. Parallel implementation of substance transport problems for restoration the salinity field based on schemes of high order of accuracy // CEUR Workshop Proceedings. – 2019. –Vol. 2500.

[6] G. I. Marchuk and B. A. Kagan, Dynamics of oceans tides, Moscow: Hydrometeoizdat, 1983, 359 p.

[7] G. G. Matishov and V. G. Ilyichev, “On optimal exploitation of water resources. The concept of domestic prices” in Reports of the Academy of Science, vol. 406, no. 2., 2006, pp. 249–251.
[8] A. V. Nikitina, A. I. Sukhinov, G. A. Ugolnitsky, A. B. Usov, A. E. Chistyakov, M. V. Puchkin and I. S. Semenov, “Optimal control of sustainable development in the biological rehabilitation of the Azov Sea” in Mathematical Models and Computer Simulations, vol.9, 2017, pp. 101–107.
[9] O. M. Belotserkovsky, A. M. Oparin and V.M. Chechetkin, Turbulence. New approaches, Moscow: Nauka, 2003, 286 p.
[10] V. A. Gushchin, A. I. Sukhinov, A. V. Nikitina, A. E. Chistyakov and A. A. Semenyakina, “A Model of Transport and Transformation of Biogenic Elements in the Coastal System and Its Numerical Implementation” in Computational Mathematics and Mathematical Physics”, vol. 58, 2018, pp. 1316–1333.
[11] A. I. Sukhinov, A. E. Chistyakov, A. V. Shishenya and E.F. Timofeeva, “Predictive modeling of coastal hydrophysical processes in multiple-processor systems based on explicit schemes” in Mathematical Models and Computer Simulations, vol. 10(5), 2018, pp. 648–658.
[12] A. I. Sukhinov, D. Khachunts and A. E. Chistyakov, “A mathematical model of pollutant propagation in near-ground atmospheric layer of a coastal region and its software implementation” in Computational Mathematics and Mathematical Physics, vol. 55, 2015, pp. 1216–1231.
[13] P. Marchesiello, J. C. Mc.Williams and A. Shchepetkin, “Open boundary conditions for long-term integration of regional oceanic models” in Oceanic Modelling Journal, vol. 3, 2001, pp. 1–20.
[14] N. E. Wolzinger, K. A. Cleany and E. N. Pelinovsky, Long-wave dynamics of the coastal zone, Moskow: Hydrometeoizdat, 1989, 271 p.
[15] A. A. Androsov and N. E. Wolzinger, The straits of the world ocean: a General approach to modelling, Saint Petersburg: Nauka, 2005, 171 p.
[16] E. Alekseenko, B. Roux, A.I. Sukhinov, R. Kotarba and D. Fougere, “Coastal hydrodynamics in a windy lagoon” in Computers and Fluids, vol. 77, 2013, pp. 24–35.
[17] A. A. Samarskii and P. N. Vabishchevich, Numerical methods for solving convection-diffusion problems, Moscow: URSS, 2009, 248 p.
[18] A. N. Konovalov, “Method of rapid descent with adaptive alternately-triangular recondition” in Differential equations, vol. 40, no. 7, 2004, pp. 953–963.
[19] E. Alekseenko, B. Roux et al, “Coastal hydrodynamics in a windy lagoon”, Computers and Fluids, **77**, 24–35 (2013). DOI: 10.1016/j.compfluid.2013.02.003
[20] A. I. Sukhinov, A. E. Chistyakov, A. V. Shishenya, “Error estimate for diffusion equations solved by schemes with weights”, Mathematical Models and Computer Simulations, **6:3**, 324–331 (2014). DOI: 10.1134/S2070048214030120
[21] A. I.Sukhinov, A. E. Chistyakov, E. V. Alekseenko, “Numerical realization of the three-dimensional model of hydrodynamics for shallow water basins on a high-performance system”, Mathematical Models and Computer Simulations, **3:5,** 562-574 (2011). DOI: 10.1134/S2070048211050115
[22] State Research Center “Planeta”, http://planet.iitp.ru/english/index_eng.htm

Application of FPGA technologies for modeling hydrophysical processes in reservoirs with complex bottom topography

A L Leontyev[1,2,3,*], M I Chumak[1,4], A V Nikitina[1,2,3], I V Chumak[5]

[1] Scientific and Technological University "Sirius", Sochi, Russia
[2] Southern Federal University, Rostov-on-Don, Russia
[3] Supercomputers and Neurocomputers Research Center, Co. Ltd., Taganrog, Russia
[4] Don State Technical University, Rostov-on-Don, Russia
[5] Department Institute of Technology of the Don State Technical University, Azov, Russia

*E-mail: Leontyev_Anton@mail.ru

Abstract. The article is devoted to the development and research of methods for accelerating calculations and processing input data for mathematical modeling of hydrodynamic processes in reservoirs with complex bottom geometry. The mathematical model of hydrodynamics considers: microturbulent diffusion; the influence of salinity and temperature. To increase the speed of calculations, it is proposed to transfer part of the computational load to reconfigurable computing systems (RVS). The paper also proposes an algorithm for adding input data by analyzing the existing database of environmental data, which was successfully verified analytically. The practical significance of the work is that a hardware implementation of the IP core was proposed, which allows solving systems of linear algebraic equations that arise when sampling the model of hydrodynamics of the Caspian Sea. It is experimentally established that the resulting implementation is characterized by low power consumption and is capable of processing large-dimensional matrices. The prospects of using the proposed algorithm are determined.

1. Introduction

To predict the situation of waters with complex bottom geometry, mathematical models are constructed, considering the unique features of the researched water object – climatic factors and hydrodynamic regimes. Among the papers of Russian scientists devoted to the research and forecast of aquatic ecosystems can be identified the papers of Marchuk G.I., Matishov G.G., Sukhinov A.I., etc. [1-8] The development of models, software and information systems for monitoring and forecasting the situation of water ecosystems is performed by leading foreign research centers and organizations such as Sweden's Meteorelogical and Hydrological Institute, Center for Water Research, National Oceanic and Atmospheric Administration, Centre for Ecology and Hydrology [9-14].

Many approaches are used to model spatially inhomogeneous three-dimensional Hydrophysics processes in reservoirs with complex bottom topography. The most acceptable of them is the modeling of hydrodynamic processes of a reservoir as a single body of water. It is known that this approach increases the computational complexity of algorithms and increases the time spent.

Another problem is the lack of sufficient input data. For example, a three-dimensional digital map was developed for the Caspian Sea, including 2.5 billion nodal points, while existing databases on

hydrometeorological characteristics have coarser measurement grids and do not allow modeling with the required accuracy (figure 1).

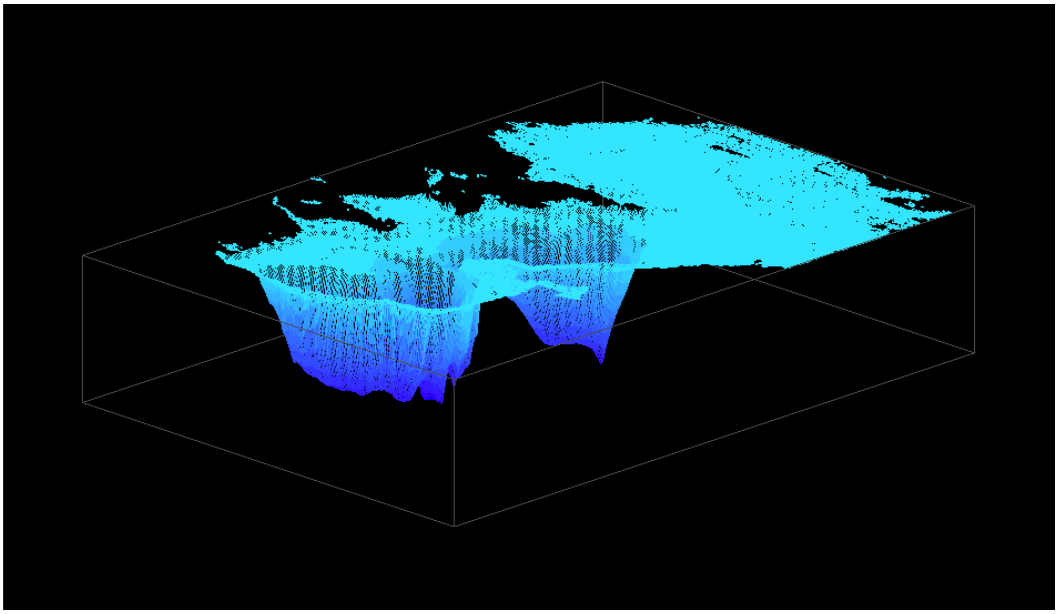

Figure 1. Three-dimensional map of the Caspian Sea

Problems that arise can be solved by using reconfigurable computing systems. A high degree of parallelization allows you to process databases at high speed and analyze multiple indicators in near-real-time mode.

2. Statement of the problem the hydrodynamics of the Caspian Sea

One of the computationally labor-intensive tasks is the model of hydrodynamics of the Caspian Sea:

$$u_t' + uu_x' + vu_y' + wu_z' = -\frac{1}{\rho}P_x' + \left(\mu u_x'\right)_x' + \left(\mu u_y'\right)_y' + \left(\nu u_z'\right)_z' + 2\Omega(v\sin\vartheta - w\cos\vartheta), \quad (1)$$

$$v_t' + uv_x' + vv_y' + wv_z' = -\frac{1}{\rho}P_y' + \left(\mu v_x'\right)_x' + \left(\mu v_y'\right)_y' + \left(\nu v_z'\right)_z' + 2\Omega u\sin\vartheta, \quad (2)$$

$$w_t' + uw_x' + vw_y' + ww_z' = -\frac{1}{\rho}P_z' + \left(\mu w_x'\right)_x' + \left(\mu w_y'\right)_y' + \left(\nu w_z'\right)_z' + 2\Omega u\cos\vartheta + g, \quad (3)$$

$$\rho_t' + (\rho u)_x' + (\rho v)_y' + (\rho w)_z' = 0, \quad (4)$$

$$T_t' + uT_x' + vT_y' + wT_z' = (\mu T_x')_x' + (\mu T_y')_y' + (\nu T_z')_z' + f_T, \quad (5)$$

$$S_t' + uS_x' + vS_y' + wS_z' = (\mu S_x')_x' + (\mu S_y')_y' + (\nu S_z')_z' + f_S, \quad (6)$$

where t is a time; $\mathbf{V} = \{u, v, w\}$ is the velocity vector of the water flow; P is full hydrodynamic pressure; T, S are water temperature and salinity; ρ is density of water; μ, ν are horizontal and vertical diffusion coefficients, respectively [15]; $\mathbf{\Omega} = \Omega(\cos\vartheta\mathbf{j} + \sin\vartheta\mathbf{k})$ is angular velocity of the Earth's rotation; ϑ is the latitude of the place; g is acceleration of gravity; f_T, f_S are sources of heat and salt (located on the border of the region). In this case, two components are conditionally distinguished from the total hydrodynamic pressure: the pressure function of the liquid column and the hydrodynamic part [16]

$$P(x, y, z, t) = p(x, y, z, t) + \rho_0 gz,$$

where p is the hydrostatic pressure of the unperturbed fluid, ρ_0 is fresh water density under normal conditions (at 20 °C); the water density is determined by the formula:

$$\rho = \tilde{\rho} + \rho_0,$$

where ρ_0 is fresh water density under normal conditions, $\tilde{\rho}$ determined by the equation recommended by UNESCO:

$$\tilde{\rho} = \tilde{\rho}_w + (8.24493 \cdot 10^{-1} - 4.0899 \cdot 10^{-3} T + 7.6438 \cdot 10^{-5} T^2 - 8.2467 \cdot 10^{-7} T^3 + 5.3875 \cdot 10^{-9} T^4) S +$$
$$+(-5.72466 \cdot 10^{-3} + 1.0227 \cdot 10^{-4} T - 1.6546 \cdot 10^{-6} T^2) S^{3/2} + 4.8314 \cdot 10^{-4} S^2,$$

where $\tilde{\rho}_w$ is the density of fresh water is specified by the polynomial:

$$\tilde{\rho}_w = 999.842594 + 6.793952 \cdot 10^{-2} T - 9.09529 \cdot 10^{-3} T^2 + 1.001685 \cdot 10^{-4} T^3 - 1.120083 \cdot 10^{-6} T^4 + 6.536332 \cdot 10^{-9} T^5.$$

Add the boundary conditions to the system (1) – (6).

At the bottom:

$$\rho_v \mu (\mathbf{V}_\tau)_\mathbf{n}' = -\tau, \mathbf{V}_\mathbf{n} = 0, P_\mathbf{n}' = 0, T_\mathbf{n}' = 0, S_\mathbf{n}' = 0, f_T = 0, f_S = 0.$$

On the side surface:

$$(\mathbf{V}_\tau)_\mathbf{n}' = 0, \mathbf{V}_\mathbf{n} = 0, P_\mathbf{n}' = 0, T_\mathbf{n}' = 0, S_\mathbf{n}' = 0, f_T = 0, f_S = 0.$$

On the upper border:

$$\rho_v \mu (\mathbf{V}_\tau)_\mathbf{n}' = -\tau, w = -\omega - \frac{P_t'}{\rho g}, P_\mathbf{n}' = 0, T_\mathbf{n}' = 0, S_\mathbf{n}' = 0, f_T = k_T (T_a - T), f_S = \frac{\omega}{h_z - h_\omega} S.$$

Here ω is the rate of evaporation of liquid; $\mathbf{V}_\mathbf{n}, \mathbf{V}_\tau$ are normal and tangential components of the water flow velocity vector; ρ is density of the water environment; ρ_v is the density of the suspended impurities; T_a is atmospheric temperature; k_T is heat transfer coefficient between the atmosphere and the water environment; h_z is depth step; $h_\omega = \omega\tau$ is the thickness of the liquid layer that evaporates over time τ; $\boldsymbol{\tau} = \{\tau_x, \tau_y, \tau_z\}$ is the tangential stress vector, which is calculated using the formulas: for a free surface $\boldsymbol{\tau} = \rho_a C d_S |\mathbf{w}| \mathbf{w}$, where $\mathbf{w}$ is wind speed vector relative to water, ρ_a is atmospheric density, Cd_S is a dimensionless coefficient of surface resistance that depends on wind speed and is in the range of 0.0016–0.0032 [17]; for the bottom $\boldsymbol{\tau} = \rho C d_b |\mathbf{V}| \mathbf{V}$, where $Cd_b = g k_R^{\,2} / h^{1/3}$, at the same time k_R is the group roughness coefficient in the manning formula (varies in the range 0.025-0.2), $h = H + \eta$ is water depth, H is the depth of the undisturbed surface, η is surface height relative to the geoid.

3. Methods of accelerating the calculations using FPGA technology

Modern technologies can be used to solve the problems that arise when solving the described problem. Methods related to parallelization of algorithms for solving tasks at the software and hardware levels are developed to increase the speed of calculations. Among the high-speed equipment used for solving model problems of hydrodynamics, it is necessary to single out supercomputers built on the basis of programmable logic integrated circuits (FPGAs), the main advantage of which is a high degree of parallelization. The time of processes occurring in the water area of a reservoir is comparable to the time of modeling these processes on conventional computers. In the process of discretization of a model problem of the form (1) – (6), a system of linear algebraic equations of large dimension arises, the solution of which requires large computational costs.

To optimize calculations, we developed a library element-the IP-core for organizing the computational process using the algorithm of an alternately triangular method for solving grid equations that arise during the discretization of model hydrophysics problems for the self-adjoint case [18].

The IP core was implemented using the following algorithm.

Algorithm 1. Solving a system of grid equations

1. Arrays are Formed for the input values of the SLA.
2. Is filling the arrays with data from files.
3. Constants are used for the calculations.
4. A library element is Connected that implements the square root calculation operation.
5. Arrays of initial values for variables are Formed.
6. Enter the condition of the calculations when you change the time signal on the rising edge.
7. Start of the cycle of comparing the maximum discrepancy and the maximum error value.
8. Calculation of the vector of residuals and its norms on the input values.
9. Calculation of the amendment.
10. The iteration counter is being built up.
11. End of the cycle of comparing the maximum discrepancy with the maximum error value.
12. Creating an array of SLOUGH solutions and writing it to a file.

The implementation of this algorithm on the xc7vx485tffg1157-1 FPGA of the seventh series used in the "Taigeta" RVS (figure 2) uses a small part of the available resources (table 1) with the power consumption shown in table 2.

Figure 2. "Taigeta" computing block.

Table 1. Resources involved in implementation

Resource	Utilization	Available	Utilization %
LUT	3721	303600	1.23
FF	127	607200	0.02
DSP	27	2800	0.96
IO	33	600	5.50
BUFG	1	32	3.12

Table 2. Power consumption

Total On-Chip Power	0.258 W
Junction Temperature	25.4 °C
Thermal Margin	59.6 °C (41.1 W)
Power supplied to off-chip devices	0 W
Confidence level	Medium

Methods based on interpolation or the use of neural networks to assimilate satellite sensing data can be used to address the problem of data scarcity. Currently, existing databases are not being updated as actively and regularly, and satellite data does not provide all the necessary input data for predictive modeling.

Within the framework of this research, an algorithm for expanding input data databases for predictive modeling of hydrophysical processes has been developed the main idea of this method is to find unknown characteristics based on retrospective data correlated with SPZ data.

Algorithm 2. Forecast of ecosystem development based on the observation model

1. Gathering information from public databases (DB).
2. Acquisition and processing of neural network is not less than two consecutive data packets of the SPZ.
3. Determine the gradients of characteristics obtained during data processing in the previous step for each node point.
4. Search for the most similar to the received retrospective data.
5. The definition of missing for the simulation of the characteristics of brute force.
6. Predictive modeling of hydrodynamic processes of a reservoir.
7. Determining the error of modeling the main calculation functions.
8. If the modeling error is more than 15%, we recalculate the gradients of the obtained characteristics considering the data received during the execution of points 4)-7) of this algorithm, otherwise we update the database.

In [19] it is proved that points 4) and 5) are solved most effectively using FPGA technologies. The solution of the problem from point 6) of this algorithm for a given prediction time is described in [20].

4. Conclusion

An algorithm for implementing the alternately triangular SLOUGH solution method for the self-adjoint case is proposed. it is used for solving the problem of distribution of the density of sea water in the Caspian Sea. The application of this algorithm will allow modeling the processes of hydrodynamics and biological kinetics occurring in reservoirs with complex bathymetry in conditions of lack of input data with minimal time costs and error values. Presents data on the results of the modeling involved in the implementation of resource and power consumption.

In the future, it is planned to develop an IP core that implements a modified alternating-triangular method for solving large-dimensional slows for the non-self-adjoint case and its application in solving problems of Hydrophysics and biological kinetics in a mode close to real-time.

Acknowledgments

The reported study was funded by RFBR, project number 19-31-51017.

References

[1] Marchuk G I and Kagan B A 1983 *Dynamics of oceans tides* (Moscow: Hydrometeoizdat)

[2] Wolzinger N E, Cleany K A and Pelinovsky E N 1989 *Long-wave dynamics of the coastal zone* (Moskow: Hydrometeoizdat)

[3] Oliger J and Sundstorm A 1978 Theoretical and practical aspects of some initial boundary-value problems in fluid dynamica *SIAM Journal on Applied Mathematics* **35** 419–45

[4] Marchesiello P, Mc Williams J C and Shchepetkin A 2001 Open boundary conditions for long-term integration of regional oceanic models *Oceanic Modelling Journal* **3** 1–20

[5] Androsov A A and Wolzinger N E 2005 *The straits of the world ocean: a General approach to modelling* (Saint Petersburg: Nauka)

[6] Sukhinov A., Chistyakov A., Nikitina A., Semenyakina A., Korovin I., Schaefer G. 2016 Modelling of oil spill spread *Electronics and Vision* pp 1134–1139

[7] Gushchin V.A., Sukhinov A.I., Nikitina A.V., Chistyakov A.E., Semenyakina A.A. 2018 A Model of Transport and Transformation of Biogenic Elements in the Coastal System and Its Numerical Implementation *Computational Mathematics and Mathematical Physics* vol 58 pp 1316–1333.

[8] Sukhinov A.I., Khachunts D.S., Chistyakov A.E. 2015 A mathematical model of pollutant propagation in near-ground atmospheric layer of a coastal region and its software implementation *Computational Mathematics and Mathematical Physics* vol 55 pp 1216–1231.

[9] Tran J.K. 2008 A predator-prey functional response incorporating indirect interference and depletion *Verh. Internat. Verein. Limnol* vol 30 pp 302–305

[10] Alekseenko E, Roux B, Sukhinov A I, Kotarba R and Fougere D 2013 Coastal hydrodynamics in a windy lagoon *Computers and Fluids* vol 77 pp 24–35

[11] Sukhinov A.I., Nikitina A.V., Semenyakina A.A. Chistyakov, A.E. 2016 Complex of models, explicit regularized schemes of high-order of accuracy and applications for predictive modeling of after-math of emergency oil spill *CEUR Workshop Proceedings* vol 1576 pp 308–319.

[12] Arkhipov B., Solbakov V., Solov'ev M. et al. 2013 Ecological modeling and Lagrangian approach *Open Mathematics* vol 11 pp 734–745.

[13] Kabanikhin S.I., Krivorot'ko O.I. 2016 A numerical algorithm for computing tsunami wave amplitudes *Numerical analysis and applications* vol 9 pp 118–128

[14] Kalenchuk-Porkhanova A.A. 2019 Modeling flow states in water bodies *Cybernetics and systems analysis* vol 4 pp 683–691.

[15] Sukhinov A.I., Chistyakov A.E., Shishenya A.V., Timofeeva E.F. 2018 Predictive Modeling of Coastal Hydrophysical Processes in Multiple-Processor Systems Based on Explicit Schemes *Mathematical Models and Computer Simulations* vol 10 pp 648–658.

[16] Sukhinov A.I., Chistyakov A.E., Protsenko E.A., Sidoryakina V.V., Protsenko S.V. 2020 Accounting Method of Filling Cells for the Solution of Hydrodynamics Problems with a Complex Geometry of the Computational Domain *Mathematical Models and Computer Simulations* vol 12 pp 232–245.

[17] Gushchin V.A., Sukhinov A.I., Nikitina A.V., Chistyakov A.E., Semenyakina A.A. 2018 A Model of Transport and Transformation of Biogenic Elements in the Coastal System and Its Numerical Implementation *Computational Mathematics and Mathematical Physics* vol 58 pp 1316-1333.

[18] Nikitina A.V., Sukhinov A.I., Ugolnitsky G.A., Usov A.B., Chistyakov A.E., Puchkin M.V., Semenov I.S. 2017 Optimal control of sustainable development in the biological rehabilitation of the Azov Sea *Mathematical Models and Computer Simulations* vol 9 pp 101–107.

[19] Abakumov A.I., Izrailsky Y.G. 2017 Stabilizing role of the fish population structure in terms of fisheries impacts in a random environment *Computer Research and Modeling* vol 9 pp 609–620.

[20] Vinberg G.G. 1983 Biological productivity of waters *Ecology* vol 3 pp 3–12.

Use of modern technologies in assessing the stability and vulnerability analysis of information technology systems

A L Leontyev[1,2,3,*], **M I Chumak**[1,4], **I V Chumak**[5]

[1] Scientific and Technological University "Sirius", Sochi, Russia
[2] Southern Federal University, Rostov-on-Don, Russia
[3] Supercomputers and Neurocomputers Research Center, Co. Ltd., Taganrog, Russia
[4] Don State Technical University, Rostov-on-Don, Russia
[5] Department Institute of Technology of the Don State Technical University, Azov, Russia

*E-mail: Leontyev_Anton@mail.ru

Abstract. The paper is devoted to the study of the possibility of applying the main methods of assessing the reliability of information technology systems, including a review of existing developments in this field and analysis of the basic principles of testing systems. Special attention is paid to methods for evaluating the reliability of software. This paper describes the main steps that should be taken by an attacker in a cyber-attack. Methods of vulnerability detection using graph theory are considered and methods of their elimination are shown. The possibility of using neural networks for traffic analysis in order to detect signatures is considered. The mechanism of DDoS attacks is considered and the main mechanisms of protection against them are analyzed. Mechanisms for changing the topology of information technology systems through the use of graph theory were tested on decentralized systems and showed a significant increase in the system's resistance to unauthorized access. Mechanisms to prevent DDoS attacks through the use of neural networks allowed real-time tracking of unwanted content and reduced the time required to update databases of malicious signatures.

1. Introduction

The development and testing of information systems have been actively developing in recent decades. However, despite progress in this area, the information regularly appears about global data leaks and the failure of expensive equipment. Information technology systems constantly interact with information resources on the Internet, and may also be subject to adverse environmental influences, which under certain conditions can disrupt the stability of the system and as a result leads to loss of control over equipment or data. Here, sustainability is an integral property that includes the reliability of data storage, the survivability of the system, and its security. The development of software tools allows attackers to find vulnerabilities in information systems much faster and with a higher probability of success. The means of introducing malware into information systems are being improved, and decentralization and increased complexity in the connections between individual parts of the systems themselves lead to a decrease in the level of security.

In the works of Matveevsky V.R., the analytical dependencies of the failure rate on time for the distribution of Strett D. U. and Weibull V. are considered [1]. Polovko A.M. and Gurova S.V. investigate reliability indicators of non-redundant recoverable systems [2]. The manual describes the structural and

logical analysis of technical systems in order to assess the impact of each element on the performance of the system as a whole [3]. The paper by Romanyuk S.G. describes the possibility of applying a probabilistic approach to the reliability problem in the analysis of the technical system under study. The work of Graham B., Leroux P.N., and Landry T. is devoted to the static and dynamic analysis of software code for various defects and weaknesses. With such a wide variety of information on this topic, the consensus on methods for assessing the stability of information systems remains unformed.

2. Assessment of the reliability of information technology systems

The complexity of evaluating information technology systems (ITS) consists of two criteria. The first is the reliability of the technical part of the system, i.e. the hardware part. Since this area has been actively developing over a fairly long period of time, most of the system vulnerabilities are eliminated at the design stage. Another factor is the unreliability of the software, which is due to its increased complexity relative to the hardware, as well as its uniqueness and speed of obsolescence. Thus, the estimation of reliability is based on the theory of reliability of technical systems, based on which it is proposed to separate models associated with the probabilistic distribution of errors, the model allows to obtain acceptable results of the assessment, not considering the reliability of the instrument and assessment models FOR considering the complexity. Among the analytical methods for evaluating the reliability of information technology systems, there are continuous and discrete dynamic evaluation models, as well as static models.

2.1. Continuous dynamic models for reliability estimation

In such models, testing is performed without correcting errors. This type of model includes the Jelinski-Moranda model and the Markov transition probability model. The Jelinski-Moranda model assumes that the time between system failures is distributed exponentially, provided that the failure rate of the program is proportional to the number of errors remaining in the program [4-5].

Thus, under this assumption the probability of software uptime is defined as a function of time t_i, detections i errors counted from the moment of detection $(i-1)$ error:

$$P(t_i) = e^{-\lambda_i t_i}, \tag{1}$$

where λ_i is failure rate,

$$\lambda_i = C_D(N-(i-1)), \tag{2}$$

here C_D is coefficient of proportionality; N is initial number of errors.

The main advantage of the model is the simplicity of calculations, but if the parameter is incorrectly defined N the failure rate of the program becomes negative, which leads to meaningless results. A more important factor is that this theory assumes that no new errors are introduced when the detected errors are corrected, which is almost never done during software development.

The Markov model [6-7] is used to estimate the likely number of errors that will be corrected in a given time, considering the preliminary modeling of the intensity of errors that occur l and the adopted error correction system. m. Under this model it is possible to obtain information about the readiness $A(t)$ and reliability $R(t)$ software. So, the system is ready for time $t>0$ defined by the equation:

$$A(t) = \sum_{k=0}^{\infty} P_{n-k}(t), \tag{3}$$

here P_{n-k} is the probability of a system's transition from state n to state k, independent of the previous and subsequent states of the system.

The reliability of the system is determined by the expression

$$R_k(\tau) = e^{-\lambda_k t}, \quad 0 \le \tau \le T_{k+1}, \quad k = 0,1,2,\ldots. \tag{4}$$

Within this model, there are a number of limitations: all errors are considered random and do not consider the generated consequences, the intensity of occurrence and correction of errors is constant, and the time to change the state of the system is infinitely short. The practice of using this model shows

that the intensity of error correction is delayed in relation to their detection, which makes the process difficult.

On the other hand, the use of this model assumes the presence of pre-accumulated experience, which will allow you to systematize error data and improve the accuracy of analysis when using data from previous modeling.

2.2. Discrete dynamic models for evaluating ITS reliability

In such models, when a failure occurs in the system, all errors are found and eliminated. Classical models of this type are the Schumann and Musa models [8-10].

The Musa model assumes an assessment of software reliability at the operational stage. With the total testing time T and the number of failures during testing n, this model allows you to determine the average time to failure:

$$\tau = \tau_0 \left(\frac{CT}{n\tau_0} \right), \tag{5}$$

here τ_0 is average time to failure before testing; C is a coefficient that reflects the compaction of the test time compared to the actual operating time.

The parameter τ_0 can be defined as

$$\tau_0 = \frac{1}{NKf}, \tag{6}$$

here N is the initial number of errors in the software (can be obtained from other models); K is error rate; f is averaged values of the execution speed of a single program operator.

As the main drawback of this model, it should be noted that it is necessary to perform calculations using a different model (definition N), which increases the time cost. However, this model does not need to fix failure points, since errors are registered and can be corrected after software testing is completed.

The Schumann model involves step-by-step testing with different sets of test data. While testing is underway, errors are only registered. When the tests are completed, all registered errors are corrected, the test data sets are corrected, and the test is repeated. It is assumed that no new errors are made during the correction, and the intensity of error detection is proportional to the number of remaining errors.

At the i testing stage, the Schumann reliability function is described as:

$$R_i(t) = e^{-\lambda_i t}, \tag{7}$$

here $\lambda_i = (N - n_{i-1})C$; N is initial number of errors in the software; $N - n_{i-1}$ is number of errors remaining by the beginning of the i stage; C is coefficient of proportionality:

$$C = \sum_{i=1}^{k} \frac{m_i}{N - n_{i-1}} \Big/ \sum_{i=1}^{k} t_i, \tag{8}$$

where m_i is number of errors detected over time t_i.

The advantage of this model is that it does not require additional calculations based on third-party models, while the obvious disadvantage is the assumption that there are no new errors when correcting the detected ones.

2.3. Static models of reliability assessment

Among the static models for evaluating the reliability of systems, which differ from others by not considering the time of error occurrence, there are classical models: mills and Nelson, Corcoran and Monte Carlo [11-13].

The mills model is based on the fact that a number of known errors are previously introduced into the software. At the same time, the testing specialist does not know the number and nature of errors made, which creates equal probability conditions for finding errors.

After testing, when n real and m artificial errors are detected, you can determine the initial number of errors in the program N:

$$N = nM/m, \tag{9}$$

where M is number of pre-entered errors.

Then the calculated value is checked N. It is assumed that the program initially had K errors and the program is tested before all M errors are detected. The probability that the program initially had K errors is calculated from the ratio:

$$p = \begin{cases} 0, if\ n > K, \\ M/(M + K + 1), if\ n \le K. \end{cases} \tag{10}$$

If not all previously M entered errors are detected, but m only some of them, then the ratio is used:

$$p = \begin{cases} 0, if\ n > K, \\ C_S^{m-1} / C_{S+K+1}^{K+m}, if\ n \le K. \end{cases} \tag{11}$$

where C_n^m – число сочетаний из n элементов по m элементам.

This model uses a fairly simple mathematical apparatus, but errors are made in the software, which is a poorly formalized process, and an arbitrary assumption of the K value is a subjective factor.

The Corcoran model assumes that the software has multiple sources of software failures. The model argument is the number of programs runs, and the software reliability score is expressed as follows:

$$R(n) = \frac{n^+}{n} + \sum_{i=1}^{k} \delta_i \frac{n_{\bar{i}} - 1}{n}, \tag{12}$$

here n^+ is number of successful software runs; $n_{\bar{i}}$ is number of detected i type errors that are likely to be resolved p_i; δ_i is the coefficient is determined as:

$$\delta_i = \begin{cases} p_i, if\ n_{\bar{i}} > 0, \\ 0, if\ n_{\bar{i}} = 0. \end{cases} \tag{13}$$

This model considers the existence of several types of errors in the software, which is an extremely positive factor. The disadvantage of the model is the need to determine the probability of sampling data from the required area.

The Nelson model was developed with the basic properties of machine programs in mind. The model is based on software properties, and it allows development by detailed description of other aspects of reliability, and, therefore, can be used to calculate the reliability of software throughout the life cycle of an information technology system.

In this model, it is assumed that the program input data is divided into disjoint areas $Z_i, i = 1, 2, \ldots, k.$ It is assumed that a set of data from the area Z_i is likely to be selected p_i. The value p_i is determined based on statistics of input data in real-world software conditions.

If by the time the reliability of the software was evaluated, n_i software runs were performed on data sets from the Z_i area, n_i^- of which ended in failure, then the software reliability is evaluated using the formula:

$$R = 1 - \sum_{i=1}^{k} \frac{n_i^-}{n_i} p_i. \tag{14}$$

The main advantage of this model is its focus on determining the reliability of software without interacting with the theory of hardware reliability, which allows us to apply this model at all stages of the software lifecycle. On the other hand, this model does not provide significant results at the initial stage of software development, as it requires a large number of runs to build an objective assessment.

3. Analysis of the vulnerability of ITS

Vulnerability analysis refers to the process of searching for threats and potential ways to implement them, as well as the models of attackers involved in these processes.

The presence of vulnerabilities has a negative impact on the scope of ITS application and causes rejection by users, among other things, the risks of disclosure of confidential information increase. Threat sources can be intentional or accidental, as well as caused by natural or man-made factors. For each threat, there is a list of vulnerabilities that allow it to be implemented, as well as a variety of methods to identify and combat them.

3.1. The application of graph theory

To detect vulnerabilities in complex decentralized systems, it is best to use graph theory. If you represent system elements as separate vertexes, you can get the topology of ITS or the interaction of several systems (figure 1).

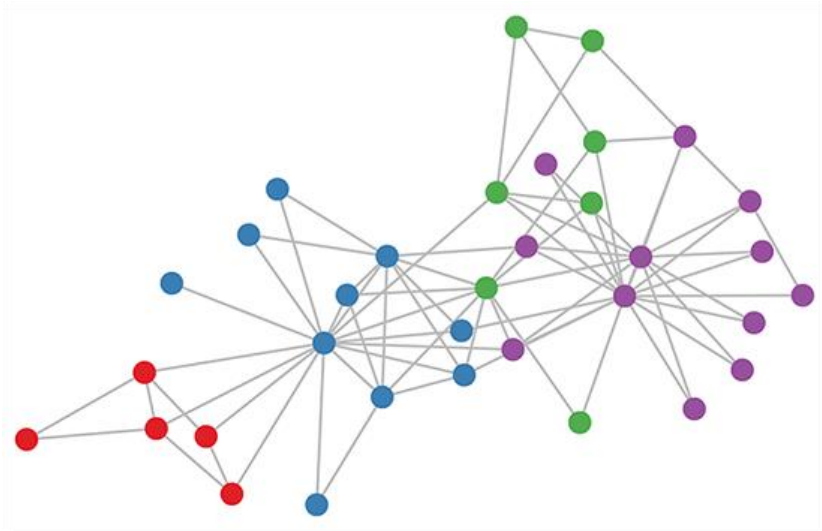

Figure 1. Topology of interaction of elements of several ITS

In addition to direct attacks, attackers can resort to indirect attacks, in which case the attack is not the system itself, but a less secure system that interacts with the main target of the attacker. In this case, the goal of the attack is to find the minimum path of traversing the graph before getting access to the files of interest. To implement security tools in this case, you need to solve the problem of finding a click in an undirected graph. In this case, the application of methods of protection against such attacks consists in a preliminary analysis of vulnerabilities, that is, it is necessary to conduct a simulation of the attack. This method is good because it allows you to find possible threats from the first stages of system design.

To minimize the possibilities of exploiting vulnerabilities of topology you can create multiple false peaks that you will pass on useless information. This method requires additional hardware costs, but can be extremely effective, especially if the transmitted data is subject to encryption.

Another, more effective method of countering this threat is to deliberately minimize the path to the intended target of the attacker, while complicating the security system. In this case, it is assumed that when analyzing the topology, the attacker will find the minimum path, but then will not be able to use it either for delivering malicious software or for hacking.

Incorrect topology analysis can make an attack very difficult or impossible. If the topology analysis uses several systems and it is impossible to identify all possible attack paths due to the size of the system, then you can embed additional vertexes-detectors. The essence of these types of vertexes is that at a certain stage, information gets to an independent evaluation, automated or manual, depending on the type of system. In practice, each of these vertexes assumes the definition of a separate type of threat,

which allows you to differentiate the levels of access to information and its forwarding, which in turn leads to minimizing user errors.

Thus, the use of graph theory allows you to: monitor intersystem security; track the shortest ways to bypass the system; fix potentially dangerous data transfer paths within the system; check the system at all stages of development and for all elements of the system, in order to minimize risks; assess the possibility of security violations due to the human factor.

The main disadvantages of this method in modern conditions are the high growth rate of information technology systems and the high complexity of the mathematical apparatus. Based on this, graph theory is most often used in the design of individual elements of the topology of interaction of system elements. Most often, it focuses on creating false vertexes that give the appearance of a highly complex data network.

3.2. Application of neural networks

Currently, additional tools such as antivirus programs, firewalls, and security scanners are usually used to ensure the security of information. Not enough attention is paid to software security. Analytical reports of major companies in the field of software information security show that the number of vulnerabilities detected in software has increased significantly in recent years.

To increase the efficiency of signature detection, it is rational to use neural networks. The activation function can be different and is generally written as:

$$y = f(s). \tag{15}$$

The network itself consists of layers of neurons. Usually, the neurons of one layer are not connected to each other, and their outputs are inputs for the neurons of the next layer [14-17]. Starting from the need to identify the specified constructs, to train a neural network, it is necessary to use the method of reverse error propagation, which is aimed at minimizing the difference between the actual and expected outputs of the network by changing the weights of synapses. If there are pairs of input data and output images $((\bar{x}_1, \bar{t}_1), (\bar{x}_2, \bar{t}_2), ..., (\bar{x}_P, \bar{t}_P))$, $\bar{x}_P = (x_1^P, x_2^P, ..., x_n^P)$, $\bar{t}_P = (t_1^P, t_2^P, ..., t_m^P)$, the value that characterizes the discrepancy between the actual output and the expected one is determined by the expression:

$$E = \frac{1}{2} \sum_P \sum_k (t_k^P - y_k^P)^2. \tag{16}$$

Here t_k^P is the k value in the P output image; y_k^P is k the value in the actual output data when the P input image is fed to the input $\bar{x}_P$ $(k = 1, 2, ..., m)$. Thus, all sets of input signals are first passed through the network, receiving a set of output signals, and then the discrepancy value is calculated.

Improved safety due to faster signature detection could not provide a complete security system. The main part of the largest cyber-attacks is called DDoS attacks. A DDoS attack is a simultaneous attack from a large number of computing devices connected to a single information technology system in order to disable the system. All methods of detecting attacks can be divided into two large categories. These are methods for detecting anomalies and methods for fixing abuse.

Activities aimed at detecting abuse are based on creating templates and finding signs of known attacks. The main advantage of this method is that it practically eliminates false positives. The disadvantage of this method is the inability to detect attacks that are not built into the system. As a result, it is necessary to maintain and regularly update a large database containing each attack and all its possible variants [18].

A more flexible method is the detection of abnormal activity, which allows you to detect unknown attacks, but can often lead to false positives. To detect an attack, you must compare the current values of the activity characteristics with the standard values, and in case of any deviation from the standard behavior, you must consider this situation as a violation. Data averaged over a sufficiently long period of time (from one day to several months) is considered normal [18].

Examples of abnormal behavior include a large number of connections over a short period of time or high CPU usage. It should also be understood that abnormal behavior should not always be considered an attack. Thus, the attack does not consist of a large number of responses to the station activity request from the network management system. A fairly rare update of the database with normal behavior characteristics allows attackers to adapt their behavior to the requirements of the system for detecting abnormal activity, which perceives it as a legal user [18].

The main mechanisms for preventing DDoS attacks are shown in table I. All methods of protection against DDoS attacks are divided into two blocks: methods that precede the start of the attack, aimed at preventing the very fact of the attack, and methods of active counteraction and weakening the results of the attack, which are used immediately after the start of the attack [19]. Methods to prevent attacks include organizational and legal measures.

Table 1. Comparative analysis of the main protection mechanisms

Criterion / method	State analysis	Neural network	Expert system	Signature-based methods	Statistical technology
The observation level	Network, OS, apps	Network, OS	Network, OS	Network, OS, apps	Network, OS
Anomalies	-	+	+	-	+
Corrupt practices	+	+	+	+	-
Verifiability	+	-	+	+	-
Adaptivity	-	+	+	-	+
Stability	+	-	+	+	-
Computational complexity	Low	Average	High	Low	Average

If the attack still took place, then after the start of the attack, you must take active measures to counter the attack as soon as possible. The most important of these measures are increasing resources and filtering traffic.

Resource growth is preceded by a detailed analysis of server and network segment usage to identify bottlenecks. If, for example, the server occupies a significant part of the communication channel during normal operation, it can be assumed that an attacker can completely fill the channel with malicious requests in the event of an attack. In this case, it is advisable to increase the bandwidth of the communication channel in advance [20].

4. Evaluation of the survivability of ITS

When forming fault tolerance strategies, you need to define a set of States of the $S^{(f)} = \{s_v^{(f)}\}$ system in which it is necessary to counteract threats to health, as well as set options for distributing functions between functional components of the information technology system in the States of the set $S^{(f)}$. This strategy is aimed at fully compensating for the envisaged functional failures and ensuring the performance of systems in these cases.

Creating survivability strategies for each state of a set of $S^{(f)}$ you need to further develop solutions related to the system functions: whether to narrow the set of functions that together make up the purpose of functioning; how to do it; whether to simplify the algorithm for implementing functions, etc.Опишем варианты решения относительно цели функционирования системы в условиях наличия нежелательных влияний может быть одним из таких:

- many functions of the system cannot be changed, all functions must be used, possibly with less efficiency or with poor quality, that is, in any state of the $S^{(f)}$, the condition must be met:

$$\prod_{i \in I} x(f_i) = 1,\ x(f_i) = \begin{cases} 1, \text{ if executed } f_i; \\ 0, \text{ if not executed } f_i. \end{cases} \quad (15)$$

- in any state of the $S^{(f)}$, some subset of functions that implement the purpose of the information system functioning must be performed F^*

$$\prod_{f_i \in F^*} x(f_i) = 1. \quad (16)$$

The set of F^* functions depends on the state of the system and the set conditions for functional survivability. In an arbitrary state from $S^{(f)}$, the system must provide at least one function from the set of F^*

$$\sum_{i \in I} x(f_i) \geq 1. \quad (17)$$

The functional viability of an information system depends on the pre-defined purpose of its functioning. The functional viability of different information systems can only be compared if they have the same functioning goals. The assessment of the survivability of the same information system may change if the purpose of operation changes. At the same time, the parameters that determine the conditions of their operability have as significant an impact on the quantitative indicators of the survivability of information systems as the purpose of their functioning.

5. Conclusion

The article discusses methods for assessing the reliability of information technology systems, describes various types of vulnerabilities that the information technology system is exposed to. The main steps that should be taken by an attacker during a cyber-attack are shown. Methods of vulnerability detection using graph theory are considered and methods of their elimination are shown.

The necessity of using neural networks in traffic analysis in order to detect signatures is justified. The mechanism of DDoS attacks is analyzed and methods of their prevention are shown. The analysis of the main mechanisms of protection against DDoS attacks is carried out.

Acknowledgments

The reported study was funded by RFBR, project number 19-31-51017.

References

[1] Matveevsky V R 2002 *Reliability of technical systems: textbook* (Moscow: Moscow State Institute of Electronics and Mathematics)

[2] Polovko A M and Gurov S V 2006 *Fundamentals of reliability theory: workshop* (St. Petersburg: BHV-Petersburg)

[3] Vikharev S M and Barinov A A 2007 *Reliability of automated systems: textbook* (Kostroma: KSTU publishing House)

[4] Yamada S. 2002 Software Reliability Models *Stochastic Models in Reliability and Maintenance* pp 253–280.

[5] Peña E.A., Hollander M. 2004 Models for Recurrent Events in Reliability and Survival Analysis. *Mathematical Reliability: An Expository Perspective. International Series in Operations Research & Management Science* vol 67 pp 105–123.

[6] Afanasyeva L.G., Tkachenko A. 2016 On the Convergence Rate for Queueing and Reliability Models Described by Regenerative Processes *Journal of Mathematical Sciences* vol 218 pp 119–136.

[7] Rahmoune F., Aïssani D. 2014 Quantitative Stability Estimates in Queues with Server Vacation *Journal of Mathematical Sciences* vol 200 pp 480–485.
[8] Polovko A M and Gurov S V 2006 *Fundamentals of reliability theory* (St. Petersburg: BHV-Petersburg)
[9] Mazzola G. et al. 2020 Software Tools and Hardware Options *The Future of Music* pp 35–80.
[10] Ceschia S., Schaerf A. 2013 Local search for a multi-drop multi-container loading problem *Journal of Heuristics* vol 19 pp 275–294.
[11] Vasilenko N V and Makarov V A 2004 Model of software compaction *Bulletin of the Novgorod state University* Vol 28 p 126–132.
[12] Murgu A., Postlethwaite I., Gu D., Edwards C. 2010 Topology Information Control in Feedback Based Reconfiguration Processes *Dynamics of Information Systems* pp 101–124.
[13] Zeng Z., Wen M., Kang R. 2013 Belief reliability: a new metrics for products' reliability *Fuzzy Optimization and Decision Making* vol 12 pp 15–27.
[14] Kalan R 2001 *Basic concepts of neural networks* (Moscow: Williams)
[15] Nalini D.N., Singh K.J., De T. 2018 ICMP-DDoS Attack Detection Using Clustering-Based Neural Network Techniques *Operations Research and Optimization* vol 225 pp 211-225.
[16] Ahmed M., Naser M.A., Hu J. 2016 A survey of network anomaly detection techniques *Journal of Network and Computer Applications* vol 60 pp 19–31.
[17] Sun Y., Guo L., Li Y., Xu L., Wang Y. 2020 Semi-supervised Deep Learning for Network Anomaly Detection *Algorithms and Architectures for Parallel Processing* vol 11945 pp 383–390.
[18] Lukatsky A V 2003 *Detection of attacks* (St. Petersburg: BHV-Petersburg)
[19] Ternovoy O S 2016 Methods and means of early detection and counteraction to threats of information security violations in DDOS attacks: (dissertation for the degree of candidate of technical Sciences) (Barnaul)
[20] Tarasov Ya V 2014 Method for detecting low-intensity DDOS attacks based on a hybrid neural network, infrastructure *News of the southern Federal University. Technical Sciences* Vol 8 p 47–87.

Software development for calculating the polluted by suspension and other impurities zones volumes on the basis of graphics accelerator

A Ev. Chistyakov [1,2], A V Strazhko[1,2], A M Atayan[1, 2,*], S V Protsenko[1, 2]

[1] Don State Technical University, Rostov-on-Don, Russia
[2] University of Science and Technology «Sirius», Sochi, Russia

*Corresponding author: atayan24@mail.ru

Abstract. Software package construction for a distributed solution of the matter transfer problem in a reservoir is the aim of the work. The software package consists of several components that use different methods of interaction. The solution study posed by various methods and comparison of their performance is carried out. An algorithm for parallel solution on a graphics accelerator controlled by the CUDA system has been developed. A comparative analysis of the algorithms operation on CPU and GPU is carried out. The software implementation of the components included in the complex is described; the main classes and implemented methods are documented.

1. Introduction

Matter transfer mathematical modeling makes it possible to study the dynamics and trend of phenomena occurring in shallow water bodies and river systems [1]. It becomes possible to predict the anthropogenic interference consequences in the aquatic ecosystem.

The algorithms and programs development is necessary for the hydrodynamics model problems numerical implementation in coastal systems, including channel processes in river sections with the channel and floodplain complex morphometry [2]. This makes it possible to solve an important scientific and practical problem of assessing the planned technological facilities construction impact on the flooding of floodplain areas and the river bed erosion.

Abrasion is a result of the impact of channel flows destruction process. It is one of the factors that negatively affect the operation of the coast, various types of coastal structures and engineering equipment near river ports. The aquatic environment continuous movement leads to irreversible consequences, for example, to changes in the bottom topography, which occurs as a result of bottom sediments rise and transfer. Thus, the task of protecting the river systems coast infrastructure is important and urgent. It is necessary to build port and berthing facilities for the needs of the population of most settlements located on the banks of rivers. The construction and installation of coastal protection structures is an expensive and technically complex undertaking. One of the effective tools for analyzing and predicting the state of river systems is numerical modeling, which includes algorithms and programs development [3]. An important problem related to the river systems ecology is forecasting the spread of pollutants in the air and water environments.

The conducted research considers individual phenomena and does not cover them in a complex in the field of mathematical modeling of the processes of movement of pollutants in river systems, as well as in the development of numerical methods for solving problems [4-6]. It is necessary to develop and theoretically study new algorithms and programs for solving model problems, including the equations of aero- and hydrodynamics, satisfying the basic laws of conservation of matter, taking into account the multicomponent nature of the medium [7-8].

Currently, there is no universal method for constructing optimal three-dimensional computational grids [9]. Methods for constructing 3D unstructured grids for solving problems with discontinuous coefficients are described in detail in [10-12]. In [13-15], it was proposed to use the grid-characteristic method to solve this class of problems.

Since the tasks under consideration are complex and require large computing power, it is much more efficient to use parallel algorithms to perform calculations in the case of using a large amount of data. One of the ways to parallelize computations is to use CUDA technology, which allows to implement computations on a graphics accelerator.

2. Discrete mathematical model

The transfer problem is considered, it can be represented by the diffusion-convection equation [16]:

$$c'_t + uc'_x + vc'_y = (\mu c'_x)'_x + (\mu c'_y)'_y + f \tag{1}$$

with boundary conditions:

$$c'_n(x, y, t) = \alpha_n c + \beta_n, \tag{2}$$

where u,v are the components of the velocity vector, μ is the turbulent exchange coefficient, f is the function describing the intensity and distribution of sources.

The calculated area is inscribed in a rectangle. For the discrete mathematical model numerical implementation of the problem, a uniform grid is introduced [17]:

$$\begin{gathered} w_h = \{t^n = n\tau, x_i = ih, y_j = jh_y : n = \overline{0, N_t}, i = \overline{0, N_x} : \\ N_t\tau = \mathrm{T}, \mathrm{N}_x h_x = l_x, N_y h_y = l_y\}, \end{gathered} \tag{3}$$

where τ is the time step; h_x, h_y are space steps; l_x, l_y are the computational domain characteristic dimensions; N_x, N_y are boundaries in space; N_t is the upper time limit.

To approximate Eq. (1) in the time coordinate, we use schemes with weights

$$\frac{\hat{c} - c}{\tau} + u\bar{c}'_x + v\bar{c}'_y = (\mu\bar{c}'_x)'_x + (\mu\bar{c}'_y)'_y + f \tag{4}$$

where $c, \hat{c}$ are the values of the unknown function on n and $n+1$ time layers; $\bar{c} = \sigma\hat{c} + (1-\sigma)c, \sigma \in [0,1]$ is the weight of the scheme.

Discrete analogs of the convective and diffusion transfer operators in the case of partial fullness of the computational cells take the form:

$$
\begin{aligned}
&(q_0)_{i,j}\frac{\hat{c}_{i,j}-c_{i,j}}{\tau}+(q_1)_{i,j}u_{i+1/2,j}\frac{\overline{c}_{i+1,j}-\overline{c}_{i,j}}{2h_x}+(q_2)_{i,j}u_{i-1/2,j}\frac{\overline{c}_{i,j}-\overline{c}_{i-1,j}}{2h_x}+\\
&+(q_3)_{i,j}v_{i,j+1/2}\frac{\overline{c}_{i,j+1}-\overline{c}_{i,j}}{2h_y}+(q_4)_{i,j}v_{i,j-1/2}\frac{\overline{c}_{i,j}-\overline{c}_{i,j-1}}{2h_y}=(q_1)_{i,j}\mu_{i+1/2,j}\frac{\overline{c}_{i+1,j}-\overline{c}_{i,j}}{h_x^2}-\\
&-(q_2)_{i,j}\mu_{i-1/2,j}\frac{\overline{c}_{i,j}-\overline{c}_{i-1,j}}{h_x^2}-\left|(q_1)_{i,j}-(q_2)_{i,j}\right|\mu_{i,j}\frac{\alpha_x\overline{c}_{i,j}+\beta_x}{h_x^2}+(q_3)_{i,j}\mu_{i,j+1/2}\frac{\overline{c}_{i,j+1}-\overline{c}_{i,j}}{h_y^2}-\\
&-(q_4)_{i,j}\mu_{i,j-1/2}\frac{\overline{c}_{i,j}-\overline{c}_{i,j-1}}{h_y^2}-\left|(q_3)_{i,j}-(q_4)_{i,j}\right|\mu_{i,j}\frac{\alpha_y\overline{c}_{i,j}+\beta_y}{h_y^2}+(q_0)_{i,j}f_{i,j}
\end{aligned}
\tag{5}
$$

where $q_i, i=0..4$ are the control volumes fullness coefficients [2].

Discrete analogue (5) of equation (1) describes not only the change in the impurity concentration due to boundary sources, but also the complex geometry of the computational domain.

3. Development of algorithms for solving the transfer problem based on CPU and GPU

Parallel algorithm that implements the transfer problem (1), (2) based on a graphics accelerator controlled by the CUDA system [18] is presented in this paper, the results of the algorithm are compared with the classical implementation on the CPU. The data on the computational grids and the running time of the software components are presented in tables 1 and 2.

Table 1. Results of the CUDA algorithm

№	1	2	3	4	5	6	7	8	9
Nx	10	20	50	100	200	500	1000	1000	1000
Ny	10	20	50	100	200	500	1000	1000	1000
T	1	2	5	10	50	50	100	500	1000
Time (sec)	0,065	0,072	0,102	0,092	0,412	1,570	10,957	79,292	134,51

Table 2. Results of the CPU algorithm

№	1	2	3	4	5	6	7	8	9
Nx	10	20	50	100	200	500	1000	1000	1000
Ny	10	20	50	100	200	500	1000	1000	1000
T	1	2	5	10	50	50	100	500	1000
Time (sec)	0,002	0,004	0,02	0,15	4,22	37,78	273,05	1413,97	2721,85

Figure 1 shows the operation time dependence graph on the grid size for evaluating the algorithms on the CPU and GPU operation. Similar graph using a logarithmic scale is shown for clarity. Numbers 1-9 mark the computational experiments on the abscissa axis, carried out on various computational grids described earlier in tables 1 and 2. The operating times of the software components for the CPU and GPU are marked on the ordinate axis in seconds.

CUDA is ineffective for small grids (up to 100x100 computational nodes), according to figure 1. CPU reaches its maximum acceleration on 100x100 computational nodes, according to table 2, which allows the GPU to be used where the CPU is not so good. Using CUDA reduces the computation time by an order of magnitude in the case of large grids (1000x1000 computational nodes). The maximum value of the ratio of the running time of the algorithm that implements the set task of transferring matter in a

shallow reservoir on a graphics accelerator (GPU) to the running time of a similar algorithm on the central processing unit (CPU) was 24.92, which is achieved on a 1000x1000 grid size.

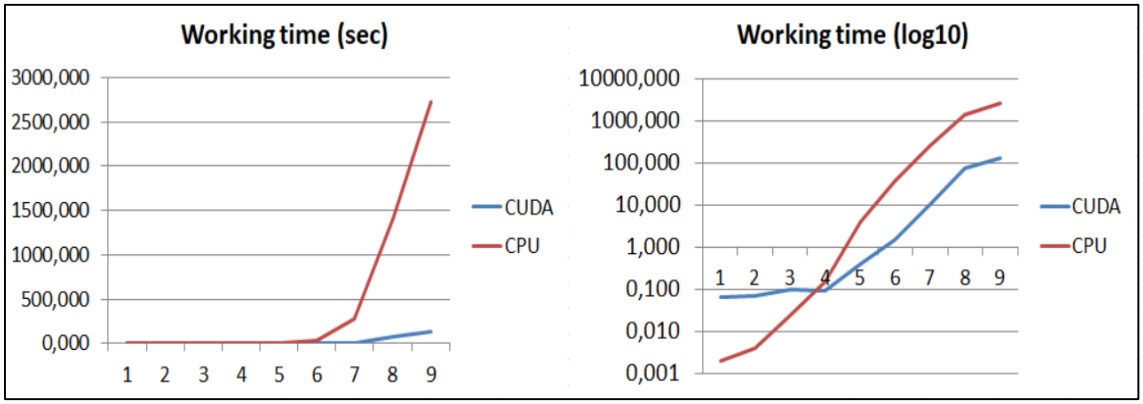

Figure 1. Software components operating time based on CPU and GPU

4. Software implementation

When solving the problem of transferring substances (1), (2), when the input data of the source function is selected using the developed software package, an image of the contour graph representing the source function appears on the right panel. When all the necessary parameters are loaded and the «START» button is pressed, the calculation of the assigned task begins, as evidenced by the entry in the table of running tasks. Figure 2 shows the information about the launched task.

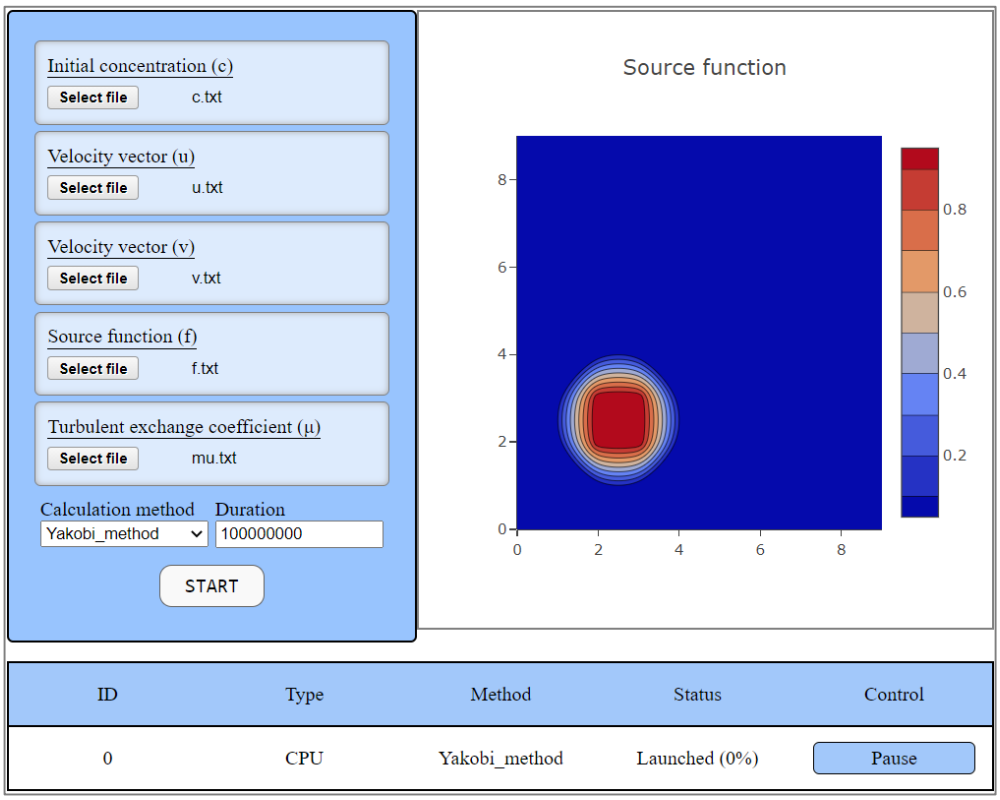

Figure 2. Displaying task status

It is possible to suspend a task after it has started. In this case, the calculator will save the state in the storage and it will be possible to resume the task later. Figure 3 shows the panel's response to pressing the «Pause» button.

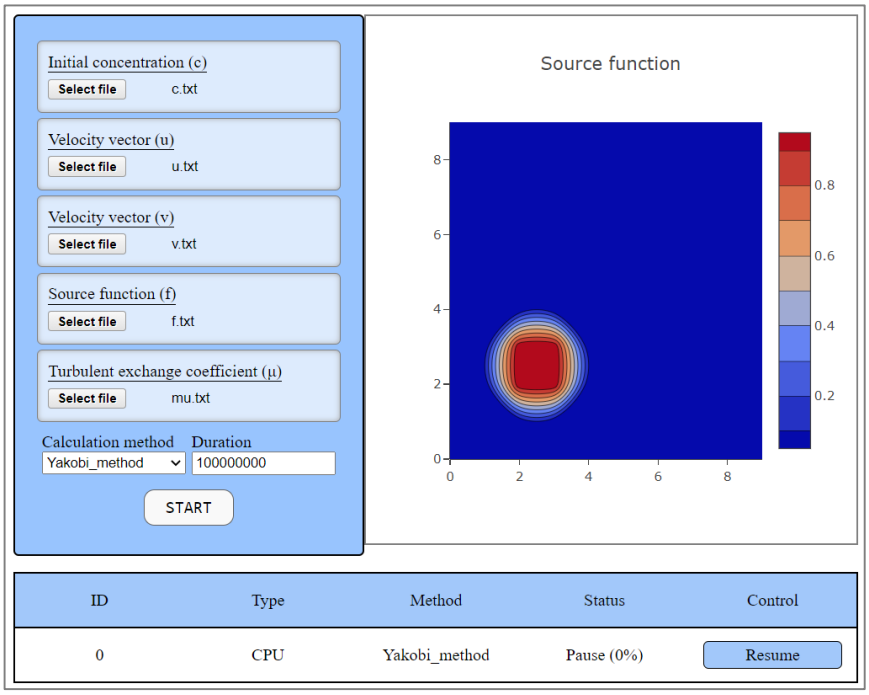

Figure 3. Task in the «Pause» status

After the task has been suspended, it is possible to continue the work of the software component by pressing the «Resume» button. Figure 4 shows the result of pressing the button.

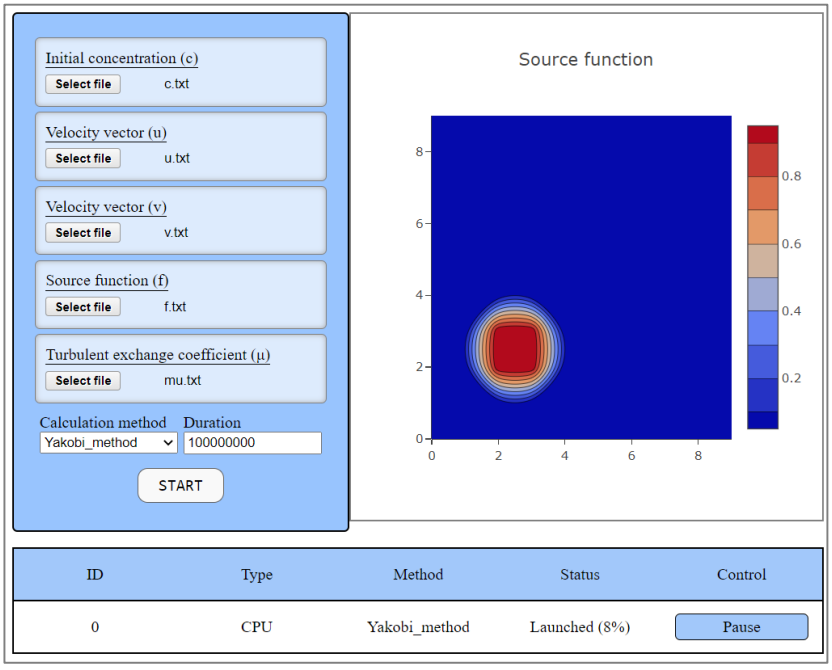

Figure 4. Resumed task

The next stage is waiting for the completion of the program component and viewing the results. When the task is completed, the status changes to «Completed». Figure 5 shows ehe completed task.

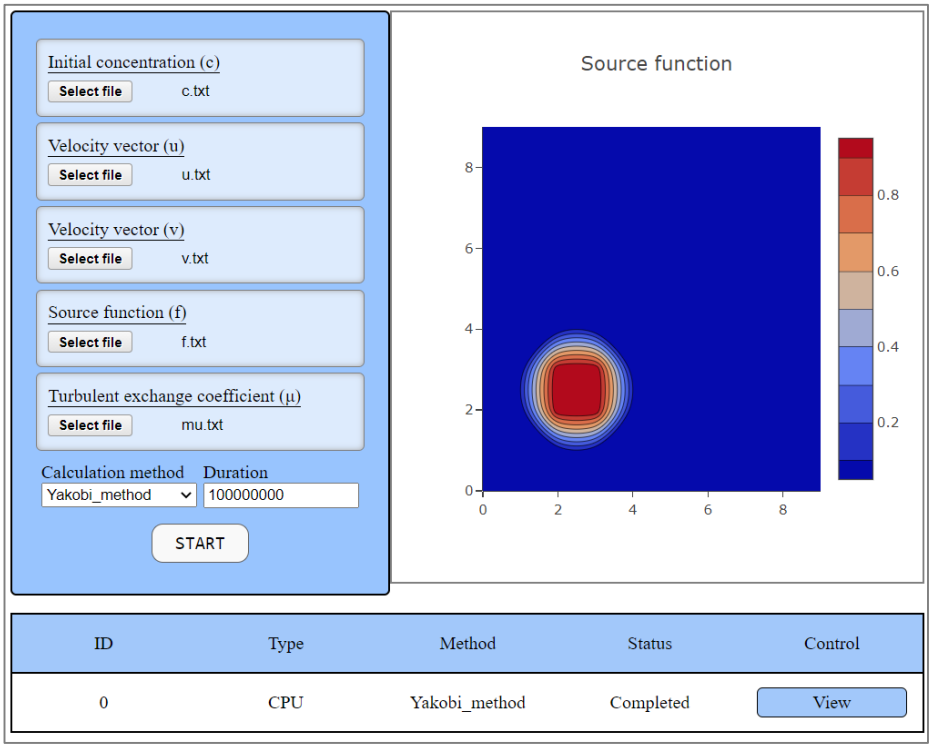

Figure 5. Completed task

When you click the «View» button, window with the result view of the program module in a graphical representation opens, and download the result as a text file. Figure 6 shows the result of clicking «View» button.

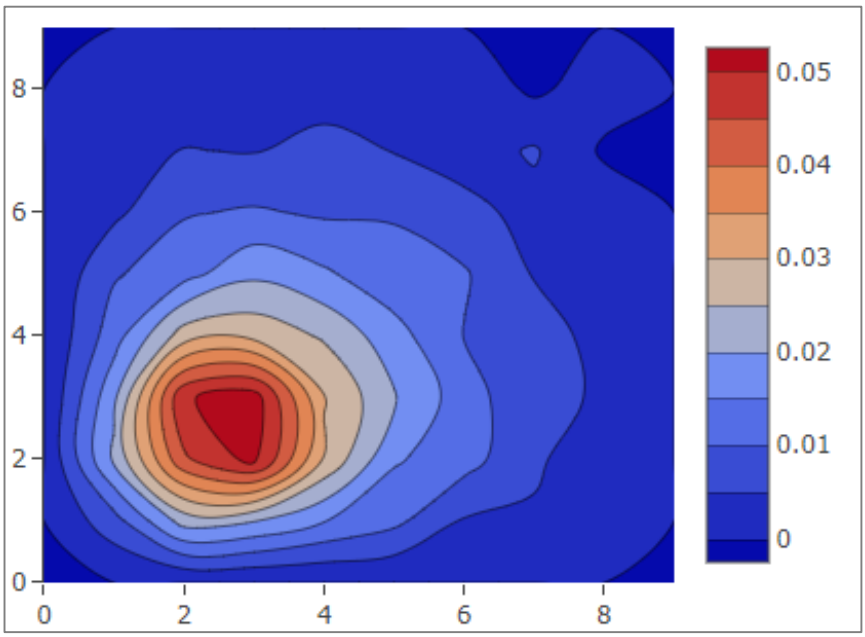

Figure 6. The algorithm result

The «Save as file» button allows you to load a file with the results of calculations. Table 1 shows the contents of the loaded file.

Table 1. The result file content

	X1	X2	X3	X4	X5	X6	X7	X8	X9	X10
Y1	0	0	0	0	0	0	0	0	0	0
Y2	0	0.007891	0.022129	0.020214	0.015181	0.01128	0.004511	0.004543	0.001249	0
Y3	0	0.020942	0.044146	0.051694	0.029435	0.015595	0.012113	0.005559	0.002768	0
Y4	0	0.018931	0.049487	0.052433	0.030232	0.020525	0.012237	0.006177	0.004505	0
Y5	0	0.012748	0.027527	0.028419	0.024343	0.016913	0.009832	0.009109	0.001787	0
Y6	0	0.00944	0.013235	0.019048	0.015776	0.011665	0.010528	0.004581	0.003588	0
Y7	0	0.003928	0.009577	0.010572	0.009328	0.0096	0.006565	0.003376	0.003207	0
Y8	0	0.002681	0.005221	0.004688	0.007556	0.004782	0.002792	0.005524	-0.000754	0
Y9	0	0.001425	0.00136	0.0039	0.001606	0.002635	0.003315	-0.000883	0.002459	0
Y10	0	0	0	0	0	0	0	0	0	0

The main functions of the developed software package, the functions of starting the calculation of the problem, viewing the results are tested in operation. The developed software is efficient, as evidenced by test calculations.

5. Conclusions

Much attention is paid to the study of transfer processes in practice. The processes taking place on the coastal areas with the adjacent water area often lead to a change in the shape of the bottom and the coastline. During the movement of sediments, three stages can be distinguished: the involvement of sediments from bottom sediments into movement, the movement of sediments, and the transition of moving sediments into bottom sediments. Building a general model of the movement of matter is a complex process. First, the individual process components are simulated. Then several models are combined into one.

In this work, software package focused on a graphics accelerator was implemented. The complex makes it possible to calculate the transfer problem in a shallow water body on various computational grids. The parallel algorithm implemented in the software package, oriented to the graphics accelerator, can significantly reduce the operating time of the software package with a large amount of input data. The presented complex is a distributed system with centralized control. It can be used to study aquatic ecosystems, assess the technogenic impact on them.

Acknowledgments

The reported study was funded by RFBR, project number 19-31-51017

References

[1] Tishkin V. F., Gasilov V. A., Zmitrenko N. V., Kuchugov P. A., M. E. Ladonkina, Yu. A. Poveschenko 2020 *Modern methods of mathematical modeling of the development of hydrodynamic instabilities and turbulent mixing* (Matem. Mod) 32:8 pp 57–90

[2] Sukhinov A.I., Chistyakov A.E., Protsenko E.A., Sidoryakina V.V., Protsenko S.V. 2020 *Accounting Method of Filling Cells for the Solution of Hydrodynamics Problems with a Complex Geometry of the Computational Domain* (Mathematical Models and Computer Simulations 12(2)) pp 232-245 DOI: 10.1134/S2070048220020155

[3] Sukhinov A.I., Chistyakov A.E., Shishenya A.V., Timofeeva E.F. 2018 *Predictive Modeling of Coastal Hydrophysical Processes in Multiple-Processor Systems Based on Explicit Schemes* (Mathematical Models and Computer Simulations 10(5)) pp 648-658 DOI 10.1134/S2070048218050125

[4] Gushchin V.A., Sukhinov A.I., Nikitina A.V., Chistyakov A.E., Semenyakina A.A. 2018 *A Model of Transport and Transformation of Biogenic Elements in the Coastal System and Its*

Numerical Implementation (Computational Mathematics and Mathematical Physics, 58 (8)) pp 1316-1333 DOI: 10.1134/S0965542518080092

[5] Sukhinov A.I., Khachunts D.S., Chistyakov A.E. 2015 *A mathematical model of pollutant propagation in near-ground atmospheric layer of a coastal region and its software implementation* (Computational Mathematics and Mathematical Physics 55 (7)) pp 1216-1231 DOI: 10.1134/S096554251507012X

[6] Sukhinov A.I., Nikitina A.V., Semenyakina A.A., Chistyakov A.E. 2016 *Complex of models, explicit regularized schemes of high-order of accuracy and applications for predictive modeling of after-math of emergency oil spill* (CEUR Workshop Proceedings 1576) pp 308-319

[7] Chetverushkin B. N., Saveliev A. V., Saveliev V. I. 2018 *A quasi-gasdynamic model for the description of magnetogasdynamic phenomena* (Comput. Math. Math. Phys., 58:8) pp 1384–1394

[8] Chetverushkin B. N. 2013 Resolution limits of continuous media models and their mathematical formulations (Math. Models Comput. Simul. 5:3) pp 266–279

[9] Vabishchevich P. N. , Samarskii A. A. 2002 *Monotone finite-difference schemes on triangular grids for convection-diffusion problems* (Comput. Math. Math. Phys. 42:9) pp 1317–1330

[10] Krasnov M.M., Kuchugov P.A., Ladonkina M.E., Tishkin V.F. 2017 *Discontinuous Galerkin method on three-dimensional tetrahedral grids: Using the operator programming method* (Mathematical Models and Computer Simulations Vol. 9) Is. 5 pp 529–543

[11] Milyukova O. Yu., Tishkin V. F. 2016 *A multigrid method for a heat equation with discontinuous coefficients with a special choice of grids* (Mathematical Models and Computer Simulations, Vol. 8) Is. 2 pp 118–128.

[12] Gasilov V. A., Gasilova I. V., Klochkova L. V., Poveshchenko Yu. A., Tishkin V. F. 2015 *Difference schemes based on the support operator method for fluids dynamics problems in a collector containing gas hydrates* (Computational Mathematics and Mathematical Physics, Vol. 55), Is. 8 pp 1310–1323

[13] Vasyukov A. V., Petrov I. B. 2018 *Grid-characteristic method on tetrahedral unstructured meshes with large topological inhomogeneities* (Comput. Math. Math. Phys. 58:8) pp 1259–1269

[14] Petrov I. B., Favorskaya A. V., Khokhlov N. I. 2017 *Grid-characteristic method on embedded hierarchical grids and its application in the study of seismic waves* (Comput. Math. Math. Phys. 57:11) pp 1771–1777

[15] Golubev V. I., Petrov I. B., Khokhlov N. I. 2016 *Compact grid-characteristic schemes of higher orders for 3D linear transport equation* (Math. Models Comput. Simul. 8:5) pp 577–584

[16] Sukhinov A., Chistyakov A., Nikitina A., Semenyakina A., Korovin I., Schaefer G. 2016 *Modelling of oil spill spread* (5th International Conference on Informatics, Electronics and Vision, ICIEV) pp 1134-1139 DOI: 10.1109/ICIEV.2016.7760176

[17] Khokhlov N. I., Petrov I. B. 2019 *Application of the grid-characteristic method for solving the problems of the propagation of dynamic wave disturbances in high-performance computing systems* (Proceedings of ISP RAS 31:6) pp 237–252

[18] CUDA Toolkit Documentation 2020 https://docs.nvidia.com/cuda/

Wave hydrodynamics discrete models construction and research

A I Sukhinov[1], A E Chistyakov[1], E A Protsenko[2], V V Sidoryakina[2], S V Protsenko[1, 2,*]

[1] Don State Technical University, Rostov-on-Don, Russia
[2] Taganrog Institute, named after A.P. Chekhov – branch of Rostov State University of Economics, Taganrog, Russia

*Corresponding author: rab55555@rambler.ru

Abstract. Analysis of the existing methods and tools for predictive modeling of hydrodynamics suggests the need to develop discrete analogs of the constructed models that have the properties of conservatism, stability and convergence, as well as algorithms for their solution, providing an increase in the accuracy of predictive modeling. In this work, a continuous three-dimensional mathematical model of the hydrodynamics of shallow water bodies is considered, and its discretization is carried out. To solve the problem of hydrodynamics, the method of correction to pressure in the case of variable density was used. When constructing discrete mathematical models of hydrodynamics, the filling of the control cells was taken into account, which made it possible to increase the real accuracy of the solution in the case of a complex geometry of the investigated area by improving the approximation of the boundary. The preservation of the flow at the discrete level of the developed hydrodynamic model, as well as the absence of non-conservative dissipative terms obtained as a result of the discretization of the system of equations, is proved.

1. Statement of 3D wave hydrodynamics problem

3B mathematical model of the wave hydrodynamics of a shallow water body includes [6-8]:

– equations of motion (Navier-Stokes):

$$u_t' + uu_x' + vu_y' + wu_z' = -\frac{1}{\rho} p'_x + \left(\mu u_x'\right)_x' + \left(\mu u_y'\right)_y' + \left(\nu u_z'\right)_z',$$

$$v_t' + uv_x' + vv_y' + wv_z' = -\frac{1}{\rho} p'_y + \left(\mu v_x'\right)_x' + \left(\mu v_y'\right)_y' + \left(\nu v_z'\right)_z', \quad (1)$$

$$w_t' + uw_x' + vw_y' + ww_z' = -\frac{1}{\rho} p'_z + \left(\mu w_x'\right)_x' + \left(\mu w_y'\right)_y' + \left(\nu w_z'\right)_z' + g;$$

– continuity equation:

$$\rho_t' + \left(\rho u\right)_x' + \left(\rho v\right)_y' + \left(\rho w\right)_z' = 0, \quad (2)$$

where $\mathbf{V}=\{u,v,w\}$ is the water flow of shallow water body velocity vector; ρ is the aquatic environment density ; p is the hydrodynamic pressure; g is the gravitational acceleration; μ, ν are turbulent exchange coefficients in the horizontal and vertical directions; n is the normal vector to the surface describing the boundary of the computational domain.

Add boundary conditions to system (1)-(2):

– entrance (left border): $\mathbf{V}=\mathbf{V}_0,\ p'_{\mathbf{n}}=0,$

– bottom border: $\rho\mu\left(\mathbf{V}_{\boldsymbol{\tau}}\right)'_{\mathbf{n}}=-\boldsymbol{\tau},\ \mathbf{V}_{\mathbf{n}}=0,\ p'_{\mathbf{n}}=0,$

– lateral border: $\left(\mathbf{V}_{\boldsymbol{\tau}}\right)'_{\mathbf{n}}=0,\ \mathbf{V}_{\mathbf{n}}=0,\ p'_{\mathbf{n}}=0,$

– upper border: $\rho\mu\left(\mathbf{V}_{\boldsymbol{\tau}}\right)'_{\mathbf{n}}=-\boldsymbol{\tau},\ w=-\omega-p'_t/\rho\mathrm{g},\ p'_{\mathbf{n}}=0,$ (3)

– surface of the structure: $\rho\mu\left(\mathbf{V}_{\boldsymbol{\tau}}\right)'_{\mathbf{n}}=-\boldsymbol{\tau}, w=0,\ p'_{\mathbf{n}}=0,$

where ω is the liquid evaporation intensity, $\mathbf{V}_{\mathbf{n}}, \mathbf{V}_{\boldsymbol{\tau}}$ are the velocity vector normal and tangential component, $\boldsymbol{\tau}=\{\tau_x,\tau_y,\tau_z\}$ is the tangential stress vector [1-3]. $\boldsymbol{\tau}=\rho_a Cd_s|\mathbf{w}|\mathbf{w}$ is the tangential stress vector for free surface, $Cd_s=0{,}0026$, $\mathbf{w}$ is the wind velocity relative to water, ρ_a is the atmosphere density, Cd_s is the dimensionless surface resistance coefficient, which depends on wind speed [4]. $\boldsymbol{\tau}=\rho Cd_b|\mathbf{V}|\mathbf{V}$ is the tangential stress vector for the bottom, which takes into account the water movement, $Cd_b=gk^2/h^{1/3}$, where $k=0.04$ is the group roughness coefficient, considered in the range of 0.025 – 0.2; h=H+η is the water area depth, [m]; H is the undisturbed surface depth, [m]; η is the free surface elevation relative to the sea level, [m].

The following approximation allows to build non-uniform in depth vertical turbulent exchange coefficient on the basis of measured water flow velocity pulsations [5]:

$$\nu=C_s^2\Delta^2\frac{1}{2}\sqrt{\left(\frac{\partial\overline{U}}{\partial z}\right)^2+\left(\frac{\partial\overline{V}}{\partial z}\right)^2}, \tag{4}$$

where C_s is the dimensionless empirical constant; Δ is the characteristic grid scale; $\overline{U},\overline{V}$ are the time-averaged ripple water flow velocity components in the horizontal direction.

2. Discrete hydrodynamics model

The computational domain inscribed in a parallelepiped. For the numerical realization of the discrete mathematical model of the hydrodynamic problem posed, a uniform grid is introduced:

$$\overline{w}_h=\Big\{t^n=n\tau, x_i=ih_x, y_j=jh_y, z_k=kh_z;\ n=\overline{0..N_t}, i=\overline{0..N_x}, j=\overline{0..N_y}, k=\overline{0..N_z};$$
$$N_t\tau=T, N_xh_x=l_x, N_yh_y=l_y, N_zh_z=l_z\Big\},$$

where τ is the time step, h_x, h_y h_z are space steps, N_t is the time layers number, T is the upper bound on the time coordinate, N_x, N_y N_z are the nodes number by spatial coordinates, l_x, l_y l_z are the boundaries along the parallelepiped in the direction of the axes Ox, Oy and Oz accordingly.

The variant of the correction to pressure method in the case of a variable density was used to solve the hydrodynamic problem [6-8]:

$$\frac{\tilde{u}-u}{\tau}+u\overline{u}'_x+v\overline{u}'_y+w\overline{u}'_z=\left(\mu\overline{u}'_x\right)'_x+\left(\mu\overline{u}'_y\right)'_y+\left(\nu\overline{u}'_z\right)'_z,$$

$$\frac{\tilde{v}-v}{\tau}+u\bar{v}'_x+v\bar{v}'_y+w\bar{v}'_z=\left(\mu\bar{v}'_x\right)'_x+\left(\mu\bar{v}'_y\right)'_y+\left(\nu\bar{v}'_z\right)'_z,$$
$$\frac{\tilde{w}-w}{\tau}+u\bar{w}'_x+v\bar{w}'_y+w\bar{w}'_z=\left(\mu\bar{w}'_x\right)'_x+\left(\mu\bar{w}'_y\right)'_y+\left(\nu\bar{w}'_z\right)'_z+g, \quad (5)$$
$$p''_{xx}+p''_{yy}+p''_{zz}=\frac{\hat{\rho}-\rho}{\tau^2}+\frac{\left(\hat{\rho}\tilde{u}\right)'_x}{\tau}+\frac{\left(\hat{\rho}\tilde{v}\right)'_y}{\tau}+\frac{\left(\hat{\rho}\tilde{w}\right)'_z}{\tau},$$
$$\frac{\hat{u}-\tilde{u}}{\tau}=-\frac{1}{\rho}\hat{p}'_x,\ \frac{\hat{v}-\tilde{v}}{\tau}=-\frac{1}{\rho}\hat{p}'_y,\ \frac{\hat{w}-\tilde{w}}{\tau}=-\frac{1}{\rho}\hat{p}'_z,$$

where $V=\{u,v,w\}$ are the velocity vector components, $\{\hat{u},\hat{v},\hat{w}\},\{\tilde{u},\tilde{v},\tilde{w}\}$ are the velocity vector fields components on the «new» and intermediate time layers, respectively, $\bar{u}=(\tilde{u}+u)/2$, $\hat{\rho}$ and ρ are the aqueous medium density distribution on the new and previous time layers, respectively.

Through $o_{i,j,k}$ marked the volume of fluid (VOF) of the cell (i,j,k) [9-10]. VOF is determined by the pressure of the liquid column inside this cell. If the average pressure at the nodes that belong to the vertices of the cell in question is greater than the pressure of the liquid column inside the cell, then the cell is considered to be full $(o_{i,j,k}=1)$. In the general case, VOF can be calculated by the following formula:

$$o_{i,j,k}=\frac{p_{i,j,k}+p_{i-1,j,k}+p_{i,j-1,k}+p_{i-1,j-1,k}}{4\rho g h_z}. \quad (6)$$

We introduce the coefficients q_0, q_1, q_2, q_3, q_4, q_5, q_6, describing VOF of regions located in the vicinity of the cell. The value q_0 characterizes the VOF of the area

$$D_0:\{x\in(x_{i-1},x_{i+1}),\ y\in(y_{j-1},y_{j+1}),\ z\in(z_{k-1},z_{k+1})\},$$
$$q_1-D_1=D_0\cap\{x>x_i\},\ q_2-D_2=D_0\cap\{x<x_i\},\ q_3-D_3=D_0\cap\{y>y_j\},$$
$$q_4-D_4=D_0\cap\{y<y_j\},\ q_5-D_5=D_0\cap\{z>z_k\},\ q_6-D_6=D_0\cap\{z<z_k\}.$$

The filled parts of the regions D_m will be called Ω_m, where $m=\overline{0..6}$. In accordance with this, the coefficients q_m can be calculated using the formulas:

$$(q_m)_{i,j,k}=\frac{S_{\Omega_m}}{S_{D_m}},\qquad (q_1)_{i,j,k}=\frac{o_{i+1,j,k}+o_{i+1,j+1,k}+o_{i+1,j,k+1}+o_{i+1,j+1,k+1}}{4},$$
$$(q_2)_{i,j,k}=\frac{o_{i,j,k}+o_{i,j+1,k}+o_{i,j,k+1}+o_{i,j+1,k+1}}{4},\ (q_3)_{i,j,k}=\frac{o_{i+1,j+1,k}+o_{i,j+1,k}+o_{i+1,j+1,k+1}+o_{i,j+1,k+1}}{4},$$
$$(q_4)_{i,j,k}=\frac{o_{i,j,k}+o_{i+1,j,k}+o_{i,j,k+1}+o_{i+1,j,k+1}}{4},\ (q_5)_{i,j,k}=\frac{o_{i,j,k+1}+o_{i+1,j,k+1}+o_{i+1,j+1,k+1}+o_{i,j+1,k+1}}{4},$$
$$(q_6)_{i,j,k}=\frac{o_{i,j,k}+o_{i+1,j,k}+o_{i+1,j+1,k}+o_{i,j+1,k}}{4},\ (q_0)_{i,j,k}=\frac{1}{2}\left((q_1)_{i,j,k}+(q_2)_{i,j,k}\right).$$

In the case of boundary conditions of the third kind $c'_n(x,y,t)=\alpha_n c+\beta_n$, the discrete analogues of the convective uc'_x and diffusion $\left(\mu c'_x\right)'_x$ transfer operators, taking into account the VOF, can be written in the following form [11, 12]:

$$(q_0)_i\,uc'_x\ \square\ (q_1)_i\,u_{i+1/2}\frac{c_{i+1}-c_i}{2h_x}+(q_2)_i\,u_{i-1/2}\frac{c_i-c_{i-1}}{2h_x},$$

$$(q_0)_i(\mu c_x')'_x \approx (q_1)_i \mu_{i+1/2} \frac{c_{i+1}-c_i}{h_x^2} - (q_2)_i \mu_{i-1/2} \frac{c_i - c_{i-1}}{h_x^2} - \left|(q_1)_i - (q_2)_i\right| \mu_i \frac{\alpha_x c_i + \beta_x}{h_x}.$$

Similarly, approximations for the remaining coordinate directions will be recorded. The error in approximating the mathematical model is equal to $O\left(\tau + \|h\|^2\right)$, where $\|h\| = \sqrt{h_x^2 + h_y^2 + h_z^2}$. The conservation of the flow at the discrete level of the developed hydrodynamic model is proved, as well as the absence of non-conservative dissipative terms obtained as a result of discretization of the system of equations. A sufficient condition for the stability [13] and monotony of the developed model is determined on the basis of the maximum principle [14], with constraints on the step with respect to the spatial coordinates: $h_x < |2\mu / u|$, $h_y < |2\mu / v|$, $h_z < |2\nu / w|$ or $\mathrm{Re} \le 2N$, where $\mathrm{Re} = |V| \cdot l / \mu$ is the Reynolds number [10], l is the characteristic size of the region $N = \max\{N_x, N_y, N_z\}$. Discrete analogs of the system of equations (5) are solved by an adaptive modified alternating-triangular method of variational type [15].

3. 3D aquatic environment movement discrete model's conservatism

Let's check the 3D aquatic environment movement discrete model's flow. Let's write down the grid equation for calculating the pressure:

$$\begin{aligned}
&(q_1)_{i,j,k} \frac{\hat{p}_{i+1,j,k} - \hat{p}_{i,j,k}}{h_x^2} - (q_2)_{i,j,k} \frac{\hat{p}_{i,j,k} - \hat{p}_{i-1,j,k}}{h_x^2} + (q_3)_{i,j,k} \frac{\hat{p}_{i,j+1,k} - \hat{p}_{i,j,k}}{h_y^2} - \\
&-(q_4)_{i,j,k} \frac{\hat{p}_{i,j,k} - \hat{p}_{i,j-1,k}}{h_y^2} + (q_5)_{i,j,k} \frac{\hat{p}_{i,j,k+1} - \hat{p}_{i,j,k}}{h_z^2} - (q_6)_{i,j,k} \frac{\hat{p}_{i,j,k} - \hat{p}_{i,j,k-1}}{h_z^2} + \\
&+\left((q_5)_{i,j,k} - (q_6)_{i,j,k}\right) H\left((q_5)_{i,j,k} - (q_6)_{i,j,k}\right)\left(\frac{\hat{p}_{i,j,k} - p_{i,j,k}}{\tau^2 h_z g} + \frac{\omega \hat{\rho}_{i,j,k}}{\tau h_z}\right) = \\
&= (q_0)_{i,j,k} \frac{\hat{\rho}_{i,j,k} - \rho_{i,j,k}}{\tau^2} + \frac{(q_1)_{i,j,k}(\hat{\rho}\tilde{u})_{i+1/2,j,k} - (q_2)_{i,j,k}(\hat{\rho}\tilde{u})_{i-1/2,j,k}}{\tau h_x} + \\
&+\frac{(q_3)_{i,j,k}(\hat{\rho}\tilde{v})_{i,j+1/2,k} - (q_4)_{i,j,k}(\hat{\rho}\tilde{v})_{i,j-1/2,k}}{\tau h_y} + \frac{(q_5)_{i,j,k}(\hat{\rho}\tilde{v})_{i,j,k+1/2} - (q_6)_{i,j,k}(\hat{\rho}\tilde{v})_{i,j,k-1/2}}{\tau h_z} + \\
&+\left(\frac{(q_2)_{i,j,k} - (q_1)_{i,j,k}}{\tau h_x}(\hat{\rho}\tilde{u})_{i,j,k} + \frac{(q_4)_{i,j,k} - (q_3)_{i,j,k}}{\tau h_y}(\hat{\rho}\tilde{v})_{i,j,k}\right) m_{i,j,k},
\end{aligned} \tag{7}$$

where $(\hat{\rho}\tilde{u})_{i+1/2,j,k} = \left(\hat{\rho}_{i+1,j,k}\tilde{u}_{i+1,j,k} + \hat{\rho}_{i,j,k}\tilde{u}_{i,j,k}\right)/2$, p is the pressure excess over the hydrostatic pressure of the undisturbed liquid; ω is the liquid evaporation intensity; $m_{i,j,k}$ is the boundary condition mask.

Let sum up equation (7) over the domain D: $i \in [1, N_x - 1]$, $j \in [1, N_y - 1]$, $k \in [1, N_z - 1]$:

$$\sum_D (q_1)_{i,j,k} \frac{\hat{p}_{i+1,j,k} - \hat{p}_{i,j,k}}{h_x^2} - \sum_D (q_2)_{i,j,k} \frac{\hat{p}_{i,j,k} - \hat{p}_{i-1,j,k}}{h_x^2} + \sum_D (q_3)_{i,j,k} \frac{\hat{p}_{i,j+1,k} - \hat{p}_{i,j,k}}{h_y^2} - \tag{8}$$

$$-\sum_D (q_4)_{i,j,k}\frac{\hat{p}_{i,j,k}-\hat{p}_{i,j-1,k}}{h_y^2}+\sum_D (q_5)_{i,j,k}\frac{\hat{p}_{i,j,k+1}-\hat{p}_{i,j,k}}{h_z^2}-\sum_D (q_6)_{i,j,k}\frac{\hat{p}_{i,j,k}-\hat{p}_{i,j,k-1}}{h_z^2}+$$

$$+\sum_D \Big((q_5)_{i,j,k}-(q_6)_{i,j,k}\Big)H\Big((q_5)_{i,j,k}-(q_6)_{i,j,k}\Big)\left(\frac{\hat{p}_{i,j,k}-p_{i,j,k}}{\tau^2 h_z g}+\frac{\omega\hat{\rho}_{i,j,k}}{\tau h_z}\right)=$$

$$=\sum_D (q_0)_{i,j,k}\frac{\hat{\rho}_{i,j,k}-\rho_{i,j,k}}{\tau^2}+\sum_D\frac{(q_1)_{i,j,k}(\hat{\rho}\tilde{u})_{i+1/2,j,k}-(q_2)_{i,j,k}(\hat{\rho}\tilde{u})_{i-1/2,j,k}}{\tau h_x}+$$

$$+\sum_D\frac{(q_3)_{i,j,k}(\hat{\rho}\tilde{v})_{i,j+1/2,k}-(q_4)_{i,j,k}(\hat{\rho}\tilde{v})_{i,j-1/2,k}}{\tau h_y}+\sum_D\frac{(q_5)_{i,j,k}(\hat{\rho}\tilde{v})_{i,j,k+1/2}-(q_6)_{i,j,k}(\hat{\rho}\tilde{v})_{i,j,k-1/2}}{\tau h_z}+$$

$$+\sum_D\left(\frac{(q_2)_{i,j,k}-(q_1)_{i,j,k}}{\tau h_x}(\hat{\rho}\tilde{u})_{i,j,k}+\frac{(q_4)_{i,j,k}-(q_3)_{i,j,k}}{\tau h_y}(\hat{\rho}\tilde{v})_{i,j,k}\right)m_{i,j,k}\ .$$

Let's carry out the following transformations:

$$\sum_{i\in[1,N_x-1]}(q_1)_{i,j,k}\frac{\hat{p}_{i+1,j,k}-\hat{p}_{i,j,k}}{h_x^2}-\sum_{i\in[1,N_x-1]}(q_2)_{i,j,k}\frac{\hat{p}_{i,j,k}-\hat{p}_{i-1,j,k}}{h_x^2}=\sum_{i\in[1,N_x-1]}(q_1)_{i,j,k}\frac{\hat{p}_{i+1,j,k}-\hat{p}_{i,j,k}}{h_x^2}- \quad (9)$$

$$-\sum_{i\in[0,N_x-2]}(q_2)_{i+1,j,k}\frac{\hat{p}_{i+1,j,k}-\hat{p}_{i,j,k}}{h_x^2}=\sum_{i\in[1,N_x-1]}(q_1)_{i,j,k}\frac{\hat{p}_{i+1,j,k}-\hat{p}_{i,j,k}}{h_x^2}-\sum_{i\in[0,N_x-2]}(q_1)_{i,j,k}\frac{\hat{p}_{i+1,j,k}-\hat{p}_{i,j,k}}{h_x^2}=$$

$$=\left((q_1)_{i,j,k}\frac{\hat{p}_{i+1,j,k}-\hat{p}_{i,j,k}}{h_x^2}\right)\Bigg|_{i=N_x-1}-\left((q_1)_{i,j,k}\frac{\hat{p}_{i+1,j,k}-\hat{p}_{i,j,k}}{h_x^2}\right)\Bigg|_{i=0}=0 \text{ because } (q_1)_{i,j,k}=0\text{, at } i=0,N_x-1.$$

Let show similarly that the following expressions vanish:

$$\sum_D (q_3)_{i,j,k}\frac{\hat{p}_{i,j+1,k}-\hat{p}_{i,j,k}}{h_y^2}-\sum_D (q_4)_{i,j,k}\frac{\hat{p}_{i,j,k}-\hat{p}_{i,j-1,k}}{h_y^2}=0\,,$$

$$\sum_D (q_5)_{i,j,k}\frac{\hat{p}_{i,j,k+1}-\hat{p}_{i,j,k}}{h_z^2}-\sum_D (q_6)_{i,j,k}\frac{\hat{p}_{i,j,k}-\hat{p}_{i,j,k-1}}{h_z^2}=0\,.$$

Transform the expression:

$$\sum_{i\in[1,N_x-1]}\frac{(q_1)_{i,j,k}(\hat{\rho}\tilde{u})_{i+1/2,j,k}-(q_2)_{i,j,k}(\hat{\rho}\tilde{u})_{i-1/2,j,k}}{\tau h_x}=\sum_{i\in[1,N_x-1]}\frac{(q_1)_{i,j,k}(\hat{\rho}\tilde{u})_{i+1/2,j,k}}{\tau h_x}- \quad (10)$$

$$-\sum_{i\in[1,N_x-1]}\frac{(q_2)_{i,j,k}(\hat{\rho}\tilde{u})_{i-1/2,j,k}}{\tau h_x}=\sum_{i\in[1,N_x-1]}\frac{(q_1)_{i,j,k}(\hat{\rho}\tilde{u})_{i+1/2,j,k}}{\tau h_x}-\sum_{i\in[0,N_x-2]}\frac{(q_2)_{i+1,j,k}(\hat{\rho}\tilde{u})_{i+1/2,j,k}}{\tau h_x}=$$

$$=\sum_{i\in[1,N_x-1]}\frac{(q_1)_{i,j,k}(\hat{\rho}\tilde{u})_{i+1/2,j,k}}{\tau h_x}-\sum_{i\in[0,N_x-2]}\frac{(q_2)_{i+1,j,k}(\hat{\rho}\tilde{u})_{i+1/2,j,k}}{\tau h_x}=\sum_{i\in[1,N_x-1]}\frac{(q_1)_{i,j,k}(\hat{\rho}\tilde{u})_{i+1/2,j,k}}{\tau h_x}-$$

$$-\sum_{i\in[0,N_x-2]}\frac{(q_1)_{i,j,k}(\hat{\rho}\tilde{u})_{i+1/2,j,k}}{\tau h_x}=\sum_{i=N_x-1}\frac{(q_1)_{i,j,k}(\hat{\rho}\tilde{u})_{i+1/2,j,k}}{\tau h_x}-\sum_{i=0}\frac{(q_1)_{i,j,k}(\hat{\rho}\tilde{u})_{i+1/2,j,k}}{\tau h_x}=0\,.$$

Let show similarly that the following expressions vanish:

$$\sum_D \frac{(q_3)_{i,j,k}(\hat{\rho}\tilde{v})_{i,j+1/2,k} - (q_4)_{i,j,k}(\hat{\rho}\tilde{v})_{i,j-1/2,k}}{\tau h_y} = 0, \ \sum_D \frac{(q_5)_{i,j,k}(\hat{\rho}\tilde{v})_{i,j,k+1/2} - (q_6)_{i,j,k}(\hat{\rho}\tilde{v})_{i,j,k-1/2}}{\tau h_z} = 0.$$

Taking into account (9), (10), we write down the transformed expression (8):

$$\sum_D \left((q_5)_{i,j,k} - (q_6)_{i,j,k}\right) H\left((q_5)_{i,j,k} - (q_6)_{i,j,k}\right)\left(\frac{\hat{p}_{i,j,k} - p_{i,j,k}}{\tau^2 h_z g} + \frac{\omega\hat{\rho}_{i,j,k}}{\tau h_z}\right) = \tag{11}$$

$$= \sum_D \left(\frac{(q_2)_{i,j,k} - (q_1)_{i,j,k}}{\tau h_x}(\hat{\rho}\tilde{u})_{i,j,k} + \frac{(q_4)_{i,j,k} - (q_3)_{i,j,k}}{\tau h_y}(\hat{\rho}\tilde{v})_{i,j,k}\right) m_{i,j,k} + \sum_D (q_0)_{i,j,k}\frac{\hat{\rho}_{i,j,k} - \rho_{i,j,k}}{\tau^2}.$$

Expression (11) can be written as follows:

$$\sum_D \left((q_5)_{i,j,k} - (q_6)_{i,j,k}\right) H\left((q_5)_{i,j,k} - (q_6)_{i,j,k}\right)\left(\frac{\hat{p}_{i,j,k} - p_{i,j,k}}{\tau h_z g}\right) =$$

$$= -\sum_D \left((q_5)_{i,j,k} - (q_6)_{i,j,k}\right) H\left((q_5)_{i,j,k} - (q_6)_{i,j,k}\right)\left(\frac{\omega\hat{\rho}_{i,j,k}}{h_z}\right) + \tag{12}$$

$$+ \sum_D \left(\frac{(q_2)_{i,j,k} - (q_1)_{i,j,k}}{h_x}(\hat{\rho}\tilde{u})_{i,j,k} + \frac{(q_4)_{i,j,k} - (q_3)_{i,j,k}}{h_y}(\hat{\rho}\tilde{v})_{i,j,k}\right) m_{i,j,k} + \sum_D (q_0)_{i,j,k}\frac{\hat{\rho}_{i,j,k} - \rho_{i,j,k}}{\tau}.$$

4. Conclusions

It can be concluded that pressure is responsible for maintaining the amount of matter. The conservation of the flow, that is, the absence of non-physical sources, is also proved by a discrete mathematical model of the movement of the water medium. At the outlet boundary, the flow depends on: flow at the inlet boundary, level rise, evaporation and compressibility of the aqueous medium. Summarizing the above, we note that, as a result of checking the basic balance relations for the diffusion-convection problem, it was found that the diffusion operator is conservative, and the convection operator is conservative when the condition of incompressibility of the aqueous medium is satisfied.

5. Acknowledgments

This paper was supported by the Russian Foundation for Basic Research (RFBR) grant No. 19-01-00701.

References

[1] John M H 2019 Coastal-Trapped Waves *Encyclopedia of Ocean Sciences (Third Edition) (Academic Press)* 598–605

[2] Tang J, Lyu Y, Shen Y, Zhang M, Su M 2017 Numerical study on influences of breakwater layout on coastal waves, wave-induced currents, sediment transport and beach morphological evolution *Ocean Engineering* 141 375–387

[3] Huang B, Zhu B, Cui S, Duan L, Zhang J, 2018 Experimental and numerical modelling of wave forces on coastal bridge superstructures with box girders *Ocean Engineering* 149 53–77

[4] Ferrer M et al. 2016 A multi-region coupling scheme for compressible and incompressible flow solvers for 2-phase flow in a numerical wave tank. *Computer & Fluids* 125 116–129

[5] Martínez-Ferrer P J, Qian L, Ma Z, Causon D M, Mingham C G 2018 Improved numerical wave generation for modelling ocean and coastal engineering problems *Ocean Engineering* 152 257–272.

[6] Gushchin V.A., Sukhinov A.I., Nikitina A.V., Chistyakov A.E., Semenyakina A.A. 2018 *A Model of Transport and Transformation of Biogenic Elements in the Coastal System and Its Numerical Implementation* (Computational Mathematics and Mathematical Physics, 58 (8)) pp 1316-1333 DOI: 10.1134/S0965542518080092

[7] Sukhinov A.I., Khachunts D.S., Chistyakov A.E. 2015 *A mathematical model of pollutant propagation in near-ground atmospheric layer of a coastal region and its software implementation* (Computational Mathematics and Mathematical Physics 55 (7)) pp 1216-1231 DOI: 10.1134/S096554251507012X

[8] Sukhinov A.I., Nikitina A.V., Semenyakina A.A., Chistyakov A.E. 2016 *Complex of models, explicit regularized schemes of high-order of accuracy and applications for predictive modeling of after-math of emergency oil spill* (CEUR Workshop Proceedings 1576) pp 308-319

[9] Hirt C W, Nichols B D 1981 Volume of fluid (VOF) method for the dynamics of free boundaries. *Journal of Computational Physics* **39 (1)** 201–225

[10] Suhinov A I, Chistyakov A E, Timofeeva E F, Shishenya A V 2013 Mathematical Model Vabishchevich P. N. , Samarskii A. A. 2002 *Monotone finite-difference schemes on triangular grids for convection-diffusion problems* (Comput. Math. Math. Phys. 42:9) pp 1317–1330

[11] Krasnov M.M., Kuchugov P.A., Ladonkina M.E., Tishkin V.F. 2017 *Discontinuous Galerkin method on three-dimensional tetrahedral grids: Using the operator programming method* (Mathematical Models and Computer Simulations Vol. 9) Is. 5 pp 529–543

[12] Milyukova O. Yu., Tishkin V. F. 2016 *A multigrid method for a heat equation with discontinuous coefficients with a special choice of grids* (Mathematical Models and Computer Simulations, Vol. 8) Is. 2 pp 118–128.

[13] Gasilov V. A., Gasilova I. V., Klochkova L. V., Poveshchenko Yu. A., Tishkin V. F. 2015 *Difference schemes based on the support operator method for fluids dynamics problems in a collector containing gas hydrates* (Computational Mathematics and Mathematical Physics, Vol. 55), Is. 8 pp 1310–1323

[14] Golubev V. I., Petrov I. B., Khokhlov N. I. 2016 *Compact grid-characteristic schemes of higher orders for 3D linear transport equation* (Math. Models Comput. Simul. 8:5) pp 577–584

[15] Sukhinov A., Chistyakov A., Nikitina A., Semenyakina A., Korovin I., Schaefer G. 2016 *Modelling of oil spill spread* (5th International Conference on Informatics, Electronics and Vision, ICIEV) pp 1134-1139 DOI: 10.1109/ICIEV.2016.7760176

Synthesis of control of the aircraft angular velocities based on algorithm with a predictive model

S V Lazarenko[1,3], V N Trofimenko[1,2], A A Volkova[1], N O Kuchugura[1]

[1] Don State Technical University, Rostov-on-Don, Russia
[2] Rostov State Transport University, Rostov-on-Don, Russia
[3] Moscow State University of Technology and Management named after K.G. Razumovsky, Moscow, Russia

E-mail: lazarenkosv@icloud.com, nasty1998.nasty@mail.ru; trofimvn@mail.ru

Abstract. An urgent issue is to obtain optimal control laws for nonlinear dynamic objects. The article presents a numerical algorithm to control stabilization of the angular velocities of spacecraft with various axial moments of inertia based on optimization with respect to the Krasovsky functional using the predictive model method. The simulation results are presented. The character of the curves of angular velocity dynamics and control moments obtained in the simulation corresponds to the curves of angular velocity dynamics and control moments obtained in the simulation of control using the analytical law for an axisymmetric spacecraft, which confirms the adequacy of the synthesized algorithm.

1. Introduction

Air and space crafts belong to nonlinear dynamic systems. Linear models for control of dynamic systems are used when changes in operating conditions are small. Thus, the use of linear models for the synthesis of a craft controls in real operating conditions leads to unacceptable errors in achieved control goals. Therefore, the problem of synthesizing the control laws for nonlinear objects is relevant and scientists pay constant attention to it, for example [1-6]. A large group of optimal control synthesis algorithms is based on the dynamic programming method [7], which application is limited by the need to solve the nonlinear functional Bellman equation in partial derivatives [8].

The difficulties of synthesis based on the method of dynamic programming with minimization of classical functionals [9] can be avoided using nonclassical semidefinite functionals (functionals of "generalized work") presented in the works of Academician N.N. Krasovsky [10, 13]. The semidefiniteness of the functionals of the generalized work is due to the fact that it contains an unknown optimal control, which is determined during the synthesis.

Set of papers [6, 14, 15, 16, 17, 18, 19] presents a solution to the problem of synthesizing the optimal control of angular movement of an axisymmetric craft based on the Krasovsky functional using the predictive model method. A positive feature of the algorithms presented in these works is the analytical form of the control laws. This form of synthesized algorithms is obtained by means of analytical solutions to the fundamental matrix and to the free motion of an axisymmetric craft.

But many crafts have a shape differ from axisymmetric. Therefore, it is important to obtain the optimal control law for a non-axisymmetric craft.

This paper presents the results of synthesis and modeling the optimal control law for a non-axisymmetric spacecraft.

To synthesize the stabilization law, it is convenient to represent the craft in the form of a rigid body with the corresponding axial moments of inertia. The dynamics of the rotational motion of a rigid body is described by the following equations [11]:

$$\begin{aligned} &\dot{\omega}_1 + A_1\omega_2\omega_3 = u_1, && \omega_1(t)\Big|_{t=0} = \omega_1(0), \\ &\dot{\omega}_2 - A_2\omega_1\omega_3 = u_2, && \omega_2(t)\Big|_{t=0} = \omega_2(0), \\ &\dot{\omega}_3 + A_3\omega_1\omega_2 = u_3, && \omega_3(t)\Big|_{t=0} = \omega_3(0), \end{aligned} \tag{1}$$

where $A1 = (I_{yy} - I_{zz})/I_{xx}$, $A2 = (I_{zz} - I_{xx})/I_{yy}$, $A3 = (I_{xx} - I_{yy})/I_{zz}$ are the reduced moments of inertia with respect to the corresponding axes, I_{xx}, I_{yy}, I_{zz}, are the moments of inertia with respect to the axes x, y, z; $\omega_1, \omega_2, \omega_3$ are the angular velocities; u_1, u_2, u_3 are the reduced control moments constituting vectors ω and u respectively.

According to [14], for the Krasovsky functional

$$J = \int_{t_0}^{t_1} \Psi(\boldsymbol{\omega})dt + \frac{1}{2}\int_{t_0}^{t_1} \left(\boldsymbol{u}^T \boldsymbol{K}^{-1}\boldsymbol{u} + \boldsymbol{u_0}^T \boldsymbol{K}^{-1}\boldsymbol{u_0} \right) dt \tag{2}$$

the corresponding optimal control from the predictive model method is determined by the formula:

$$\boldsymbol{u}_0(t) = -\boldsymbol{K}\int_{t}^{t_1} \boldsymbol{G}^T(s,t)\ \frac{\partial}{\partial \boldsymbol{\omega}_m}\left(\Psi(\boldsymbol{\omega}_m, s)\right)ds,\ \ \frac{\partial}{\partial \boldsymbol{\omega}_m}\left(\Psi(\boldsymbol{\omega}_m, s)\right) = \boldsymbol{Q}\ \boldsymbol{\omega}_m(t,s), \tag{3}$$

where $\Psi(\boldsymbol{\omega}) = \boldsymbol{\omega}^T \boldsymbol{Q}\ \boldsymbol{\omega}$; $\boldsymbol{Q}, \boldsymbol{K}$ are the positive definite diagonal weight matrices; G(s, t) is the fundamental matrix determined on the free motions of system (1) from the equation

$$\frac{\partial\ \mathbf{G}(s,t)}{\partial\ s} = \mathbf{F}^*\ \mathbf{G}(s,t), \quad \mathbf{G}(s,t)\Big|_{s=t} = \begin{pmatrix} 1 & 0 & 0 \\ 0 & 1 & 0 \\ 0 & 0 & 1 \end{pmatrix}; \tag{4}$$

$\boldsymbol{\omega}_m(s) = \left[\omega_{m1},\ \omega_{m2},\ \omega_{m3}\right]^T$ is the vector of free motion, determined from the motion equations of system (5) with zero right-hand side:

$$\begin{aligned} &d\omega_{f1}/ds + A1\omega_{f2}\omega_{f3} = 0, && \omega_{f1}(s)\Big|_{s=t} = \omega_1(t), \\ &d\omega_{f2}/ds - A2\omega_{f1}\omega_{f3} = 0, && \omega_{f2}(s)\Big|_{s=t} = \omega_2(t), \\ &d\omega_{f3}/ds + A3\omega_{f1}\omega_{f2} = 0, && \omega_{f3}(s)\Big|_{s=t} = \omega_3(t). \end{aligned} \tag{5}$$

The Jacobi matrix F for system (5) can be defined by the following expression:

$$F = \begin{pmatrix} 0 & -A1\omega_3 & -A1\omega_2 \\ A2\omega_3 & 0 & A2\omega_1 \\ -A3\omega_2 & -A3\omega_1 & 0 \end{pmatrix} \tag{6}$$

The matrix equation (4) is a system of 9 first-order differential equations:

$$\frac{\partial G_{11}}{\partial s} = -A1\omega_3 G_{21} - A1\omega_2 G_{31}, \quad \frac{\partial G_{12}}{\partial s} = -A1\omega_3 G_{22} - A1\omega_2 G_{33}, \quad \frac{\partial G_{13}}{\partial s} = -A1\omega_3 G_{23} - A1\omega_2 G_{33},$$

$$\frac{\partial G_{21}}{\partial s} = A2\omega_3 G_{11} + A2\omega_1 G_{31}, \quad \frac{\partial G_{22}}{\partial s} = A2\omega_3 G_{12} + A2\omega_1 G_{32}, \quad \frac{\partial G_{23}}{\partial s} = A2\omega_3 G_{13} + A2\omega_1 G_{33}, \quad (7)$$

$$\frac{\partial G_{31}}{\partial s} = -A3\omega_2 G_{11} - A3\omega_1 G_{21}, \quad \frac{\partial G_{32}}{\partial s} = -A3\omega_2 G_{12} - A3\omega_1 G_{22}, \quad \frac{\partial G_{33}}{\partial s} = -A3\omega_2 G_{13} - A3\omega_1 G_{23},$$

Numerical integration of systems for the fundamental matrix (7) and for the free motion (5) are the basis for calculating controls in accordance with expression (3).

It should be noted that the matrix (7) for an axisymmetric craft "splits" into three independent systems of differential equations, for which analytical solutions are found in [14].

2. Simulation modeling

To check the adequacy of the synthesized algorithm, we carry out calculations for an axisymmetric spacecraft (A1=A2=1, A3=0) with initial velocities $\omega_1(0) = 2{,}5\tilde{n}^{-1}$, $\omega_2(0) = -1{,}7\tilde{n}^{-1}$, $\omega_3(0) = 1{,}2\tilde{n}^{-1}$. The dynamics of angular velocities and control moments are shown in Fig. 1 and 2.

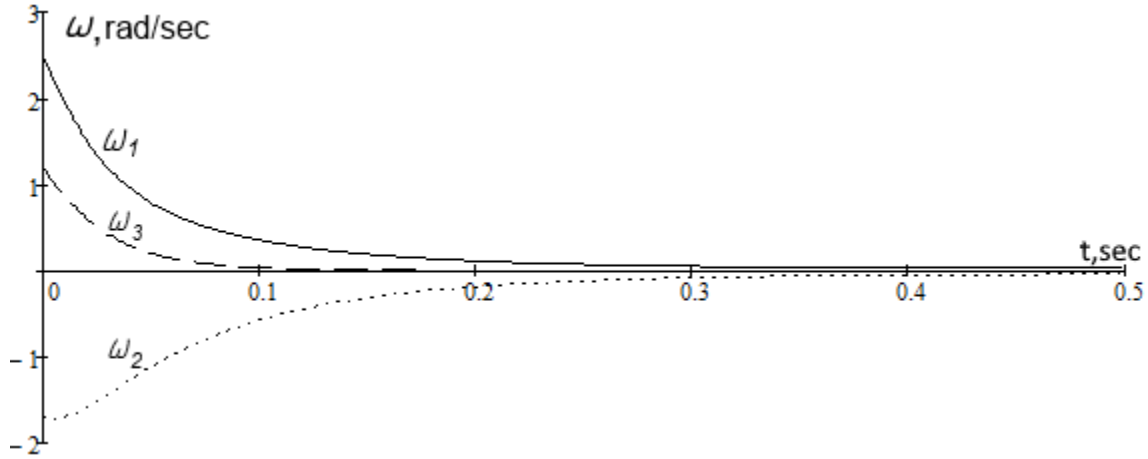

Figure 1. Graphs of changes in angular velocities

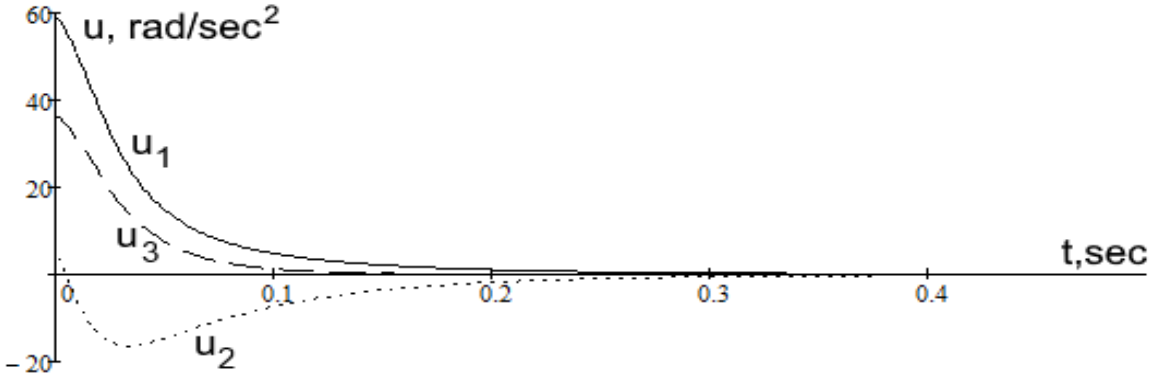

Figure 2. Graphs of changes in control action

3. Conclusion

This paper presents a numerical algorithm for angular stabilization of a non-axisymmetric craft based on a predictive model along with the results of control modeling. The nature of the curves of the dynamics of angular velocities and control moments obtained by simulating the control using the synthesized algorithm corresponds to the curves of the dynamics of angular velocities and control moments obtained by simulating the control using the analytical law for an axisymmetric craft [14], which confirms the adequacy of the synthesized algorithm.

Thus, the obtained numerical control algorithm can be implemented in a craft on-board computer to stabilize the angular velocities.

The reported study was funded by RFBR, project number 18-08-01494 A.

References

[1] Methods of the theory of optimal control in the design of technical systems: textbook / I. K. Romanov. - Moscow: Publishing house of MSTUnamedN. E. Bauman, 2017. – 150 [2] pp. with figures.

[2] Kostoglotov, A.A. Structural synthesis of discrete adaptive servo systems based on the combined maximum principle / A.A. Kostoglotov, S.V. Lazarenko, A.A. Kuznetsov, I.V. Deryabkin, V.A. Losev // Bulletin of the Don State Technical University. - 2017. - V. 17. . -No. 1 (88). - pp. 105-112.

[3] Kostoglotov, A.A. Synthesis of adaptive multi-mode controllers based on combined control of the combined maximum principle / A. A. Kostoglotov, Z.V. Lyashchenko, S.V. Lazarenko, I. V. Deryabkin, O. N. Manaenkova // Bulletin of the Rostov State Transport University. - 2016. -v. 3. - pp. 124-132.

[4] Kostoglotov A.A., TaranV.N., TrofimenkoV.N. Adaptation of control algorithms based on the methods of the predictive model and the combined maximum principle // VestnikRGUPS, 3, 2017. – pp. 134-139

[5] Kostoglotov A.A., TaranV.N., TrofimenkoV.N. Fuzzy Topological Approach to a Solid Control Task// Proceedings of the Third International Scientific Conference “Intelligent Information Technologies for Industry” (IITI’18). Volume 1. – 530 p. – P.373-381.

[6] Nikolaev N.N., Marchenko Yu.V., Filatov S.K. Research and modeling of the taxi service in small towns // International Scientific Conference «Construction and Architecture: Theory and Practice of Innovative Development» (CATPID-2019): IOP Conference Series: Materials Science and Engineering, Vol. 698, 2019. doi:10.1088/1757-899X/698/6/066027 (Kislovodsk, Russian Federation, 1–5 October 2019).

[7] Optimization methods in examples and problems Authors: BiryukovR.S., Grigorieva S.A., PavlyuchonokZ.G. Saveliev V.P. Methodological manual. - Nizhny Novgorod: Nizhny Novgorod State University, 2010. –101p.

[8] Alexandrov A. G., Krasovsky A. A. and etc. Handbook on the theory of automatic control / Ed. A. A. KrasovskyM .: Nauka, Ch. Ed. physical - mat. lit., 1987

[9] VasilievF.P. Lectures on methods for solving extreme problems. Moscow University Publishing House, 1974, 374 p.

[10] Alexandrov A. G., Krasovsky A. A. and etc. Handbook on the theory of automatic control / Ed. A. A. Krasovsky M.: Nauka. Ch. Ed. physical - mat. lit., 1987, KrasovskyA.A. Automatic flight control systems and their analytical design. M.: Nauka, 1973

[11] TikhonravovM.K., YatsunskyI.M., MaksimovG.Yu., BazhinovI.K., GurkoO.V. Fundamentals of flight theory and design elements for artificial earth satellites. M.: Mashinostroenie, 1967.

[12] Xu D., Meyer A. Modern theory of automatic control and its application. M.: Mashinostroenie, 1972.

[13] KrasovskyA.A., BukovV.N., ShendrikV.S. Universal algorithms for optimal control of continuous processes. M.: Nauka, 1977 .

[14] TaranV.N., TrofimenkoV.N. Synthesis of the optimal algorithm for angular stabilization by the predictive model method // Automation and Telemechanics. - 1997. - N5. - pp. 82-85.
[15] O.E. Maikova Suboptimal Regimes in the Fuller Problem. Proc. Steklov Inst. Math. 236, 214–217.
[16] TaranV.N., TrofimenkoV.N., TrofimenkoE.N. – Algorithm of terminal speed control of the spacecraft by the predictive model method. In the collection: Modern problems of radio electronics materials of the Third International Scientific Conference. Scientific editor: Bezuglov D.A. 2010. pp. 83-87.
[17] Yasnitskiy L.N., Gladkiy S.L., Nikitenko I.I. Possibilities and prospects of using artificial intelligence methods to solvt boundary value problems of mathematical physics in engineering practice, Neurocomputers: development, application. No. 2. . pp. 16-31. (2019)
[18] Vasiliev S.N., Kudinov Yu.I., Pashchenko F.F., Durgaryan I.S., Kelina A.Yu., Kudinov I.Yu., Pashchenko A.F. Intelligent control systems and fuzzy regulators Part II. Learning fuzzy regulators, fuzzy PID regulators, Sensors and systems. V.3 (211) pp. 3 – 12. (2017)
[19] Lon-Chen Hung, Hung-Yuan Chung Decoupled Sliding-Mode with Fuzzy-Neural Network Controller for Nonlinear Systems, International Journal of Approximate Reasoning. Issue 46. Pp. 74 – 96.

Detailing the model and objective function for the task of optimizing the power distribution process

V A Mokhov*, A N Tkachev, D V Shaykhutdinov, S S Kostinskiy and Y M Manatskov

Platov South-Russian State Polytechnic University (NPI), Novocherkassk, Russia

*e-mail: mokhov_v@mail.ru

Abstract. In this article, for the spectral expansion of periodic functions by means of a truncated segment of the Fourier series, the authors demonstrated options for their representation in the form of sets of coefficients and showed the relationship between the latter. On the basis of mathematical calculations, the authors have prepared an appropriate mechanism for organizing calculations, for which a number of linear matrix operations have been formed. The application of a new computing mechanism based on a discrete expansion of continuous periodic functions is demonstrated in detailing the problem of combinatorial optimization of the power distribution process, as well as the corresponding load model and target function.

1. Introduction

The world practice of spectral analysis and signal processing has developed quite a long time ago. It mainly relies on the use of discrete Fourier transform operators. Representation of periodic signals in the form of a set of Fourier coefficients is widely used in calculations in various subject areas [1, 2]. However, the need to develop new mechanisms for using the Fourier apparatus still remains [3, 4]. There is a need for solving the practical problem of optimizing the process of distributing electricity between single-phase consumers at the level of a transformer substation, and for detailing the corresponding load model and target function, in particular. It is important to note that the solution of the problem must be performed using binary optimization algorithms, operating in the search for solutions by variables in the form of discrete binary vectors.

We propose a corresponding solution for consideration. Section 2 describes the mechanisms of the spectral expansion of continuous periodic functions and shows the corresponding variants of linear operations. Paragraph 3 presents the formulation of the problem of optimizing the power distribution process at the level of criteria and the developed data presentation. Section 4 shows the load and objective function models for the optimization problem, detailed using the mechanisms of discrete transformation of periodic functions.

2. Discrete expansion of continuous periodic functions

Let $a = x(t)$ be a continuous periodic function with the main period T, that is $a(t + T) = x(t)$. A discrete expansion of a function $x(t)$ is its representation in the form:

$$a_n(t) = c_1 e_1(t) + c_2 e_2(t) + \cdots + c_n e_n(t) + \cdots = \sum_{k=1}^{\infty} c_k e_k(t) \quad (1)$$

In the case when $\|a - a_n\| \to 0$, where the norm is defined by the equation

$$\|a - a_n\| = \int_0^T \big(a(t) - a_n(t)\big)^2 dt,$$

usually, on the right-hand side of equality (1) we are limited to a finite number *n* of terms of the series. The resulting truncated sum of a series of the form

$$\tilde{a}(t) = \sum_{k=1}^{n} c_k e_k(t) \tag{2}$$

is taken as an approximation of the function $a(t)$, and the set of coefficients $\bar{c} = (c_1, c_2, \dots\ c_n)$ is called its spectrum over the set of functions$\{e_k(t)\}_{k=1}^{n}$.

The most common spectral decomposition of periodic functions is their representation in the form of a truncated segment of the Fourier series [5, 6] of the form:

$$\tilde{a}(t) = a_0 + \sum_{k=1}^{n} a_k \sin k\omega t + \sum_{k=1}^{n} a_{n+k} \cos k\omega t \tag{3}$$

where $\omega = 2\pi f;\ f = \frac{1}{T};$

$$a_0 = {}^{1}\!/_{T} \int_0^T x(t)dt\,;$$

$$a_k = {}^{2}\!/_{T} \int_0^T x(t) \sin k\omega t\, dt\,; \tag{4}$$

$$a_{n+k} = {}^{2}\!/_{T} \int_0^T x(t) \cos k\omega t\, dt\,;$$

$k = \overline{1, n}.$

wherein $e_1 = 1;\ e_k = \sin k\omega t;\ e_{n+k} = \cos k\omega t.$

Spectral decomposition of the form (2) can be specified differently. Let us introduce a set of functions$\{e_k(t)\}_{k=1}^{m}$, the graphs of which are shown in Figure 1.

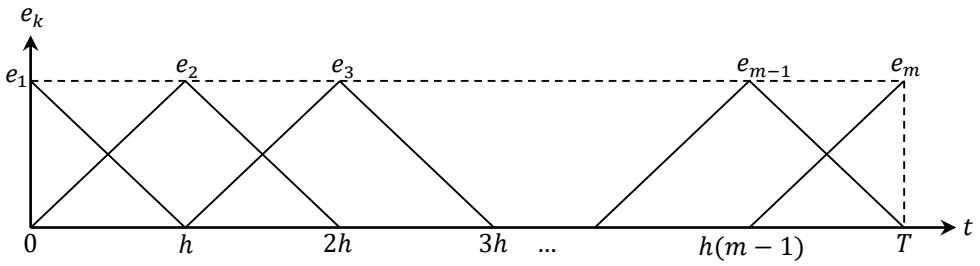

Figure 1. Function graph $e_k(t)$

The functions $e_k(t)$ on the segment $[0, T]$ are defined by equation

$$e_1(t) = \begin{cases} \dfrac{h - t}{h}, t \in [0, h]; \\ 0, \quad t \notin [0, h], \end{cases}$$

$$e_k(t) = \begin{cases} \frac{t-(k-1)h}{h}, t \in [(k-1)h, kh]; \\ \frac{(k-1)h-t}{h}, t \in [kh, (k+1)h], \end{cases} \tag{5}$$

$$e_m(t) = \begin{cases} \dfrac{t - T + h}{h}, t \in [T - h, T]; \\ 0, \quad t \notin [T - h, T], \end{cases}$$

where $h = {}^{T}\!/_{(m-1)}$.

For the system of functions (5), the segment (2) of the series can be represented as

$$\tilde{a}(t) = \sum_{k=1}^{m} b_k e_k(t), \tag{6}$$

where $b_k = e_k(t_k)$;

$t_k = (k-1)h$;

$k = \overline{1,m}$.

The operation of transition from a continuous function $x(t)$ to its scalar representation in the form of a segment of the Fourier series (3), which is specified by a set of values of the Fourier coefficients $\bar{a} = (a_0, a_1, \dots\ a_n, a_{n+1}, \dots\ a_{2n})$ in accordance with equation (4), will be denoted by S_f. In this case

$$S_f x(t) = \bar{a} \tag{7}$$

Similarly, the operation of transition from the function $x(t)$ to its expansion (6), which is formally specified by the set $\bar{b} = (b_1, b_2, \dots\ b_m)$, we will denote as S_d. In this case

$$S_d x(t) = \bar{b} \tag{8}$$

Spectral decomposition of representations (7), (8) is performed by linear operations.

Indeed, if $y(t)$ is a periodic function with Fourier coefficients (4), (6) respectively equal to $\bar{c} = (c_0, c_1, \dots\ c_n, c_{n+1}, \dots\ c_{2n})$, $\bar{d} = (d_1, d_2, \dots\ d_m)$, then

$$S_f\big(x(t) + y(t)\big) = \bar{a} + \bar{c}; \quad S_f\big(\alpha x(t)\big) = \alpha\bar{a};$$

$$S_d\big(x(t) + y(t)\big) = \bar{b} + \bar{d}; \quad S_d\big(\alpha x(t)\big) = \alpha\bar{b};$$

where α is an arbitrary number.

For a function of the form $\tilde{a}(t)$ of the form (3) the following also holds:

$$\frac{1}{2}\int_0^T \tilde{x}^2(t)dt = a_0^2 + \frac{1}{2}\sum_{k=1}^{n}(a_k^2 + a_{n+k}^2) \tag{9}$$

It must be noted that the sets of coefficients $\bar{a}$, $\bar{b}$, corresponding to transformations (7), (8) are related to each other. Indeed, using the trapezoid formula $x_k = x((k-1)h)$ in finding integrals (4), we obtain:

$$\begin{aligned}
a_0 &= \frac{h}{2}(x_1 + 2x_2 + \dots + 2x_{m-1} + x_m) = \frac{h}{2}(b_1 + 2b_2 + \dots + 2b_{m-1} + b_m);\\
a_k &= 2h(x_2 \sin k\omega h + x_3 \sin 2k\omega h + \dots + x_{m-1} \sin 2k\omega(T-h)) =\\
&= 2h(b_2 \sin k\omega h + b_3 \sin 2k\omega h + \dots + b_{m-1} \sin 2k\omega(T-h));\\
a_{h+k} &= \frac{h}{2}(x_1 + 2x_2 \cos k\omega h + \dots + 2x_{m-1} \cos 2k\omega(T-h) + x_m) =\\
&= \frac{h}{2}(b_1 + 2b_2 \cos k\omega h + \dots + 2b_{m-1} \cos 2k\omega(T-h) + b_m).
\end{aligned} \tag{10}$$

Similarly, the components of the vector $\bar{b}$ are expressed through the components of the vector $\bar{a}$. This follows formally from the congruence

$$\tilde{x}_i = a_0 + \sum_{k=1}^{n} a_k \sin k\omega t_i + \sum_{k=1}^{n} a_{n+k} \cos k\omega t_i \tag{11}$$

where $t_i = (i-1)h$;

$i = \overline{1,m}$.

From formulas (10), (11) we obtain the equalities

$$S_f x(t) = A_f \bar{b} = A_f S_d x(t);$$

$$S_d x(t) = A_d \bar{a} = A_d S_f x(t);$$

where matricesA_f, A_d are determined according to formulas (10), (11), respectively.

3. Formulation of the optimization problem for electricity distribution process

3.1. Optimization criteria

The determining criteria for solving the problem of optimizing the process of electricity distribution [7, 8] are:

1) equalization of the effective total for each of the three phases of the currents I_A, I_B, I_C of all the loads connected to them;
2) ensuring a decrease in the coefficients of nonlinear distortion of currents in the phases (Total Harmonic Distortion, THD [9, 10]), equal to

$$K_{THD} = \frac{\sqrt{I_{2_E}^2 + I_{3_E}^2 + \ldots + I_{s_E}^2}}{I_{1_E}}; \quad E = A; B; C, \tag{12}$$

where I_{1_E}, I_{2_E}, I_{3_E}, I_{s_E} are first, second, third and s-th, accordingly, the harmonics of the effective total current in the *E*-th phase.

3.2. Data representation

Let there be *p* consumers in total, the instantaneous and effective values of the load currents of which are respectively equal

$$i_q(t),\ I_q,\ q = \overline{1, p}. \tag{13}$$

To identify the connected consumers to each of the three phases A, B, C we will use a binary vector $\overline{Z}$ of dimension $3p$ of the form

$$\overline{Z} = \left(z_1, z_2, \ldots z_p, z_{p+1}, \ldots z_{2p}, z_{2p+1}, \ldots z_{3p}\right). \tag{14}$$

Vector $\overline{Z}$ has three segments of length p, corresponding to consumers and connection phases. For the *j*-го consumer, one of the values z_j, z_{p+j}, z_{2p+j} is equal to one in the segment that corresponds to the connection phase. The rest of the values are zero. With this formalization, the phase currents are

$$\begin{aligned} i_A(t) &= \textstyle\sum_{j=1}^{p} z_j\, i_j(t); \\ i_B(t) &= \textstyle\sum_{j=p+1}^{2p} z_j\, i_j(t); \\ i_C(t) &= \textstyle\sum_{j=2p+1}^{3p} z_j\, i_j(t). \end{aligned} \tag{15}$$

Factoring in the linearity of the operation S_f we obtain from (15)

$$\begin{aligned} S_f i_A(t) &= \textstyle\sum_{j=1}^{p} z_j\, S_f i_j(t); \\ S_f i_B(t) &= \textstyle\sum_{j=p+1}^{2p} z_j\, S_f i_j(t); \\ S_f i_C(t) &= \textstyle\sum_{j=2p+1}^{3p} z_j\, S_f i_j(t). \end{aligned} \tag{16}$$

It follows that the Fourier spectra of the phase currents are equal to the sum of the spectra connected to each of the phases of the load currents. This allows the objective functions to be expressed through the specified spectra of the harmonics of phase currents and variables z_j, $j = \overline{1,3p}$, which must satisfy additional conditions:

$$z_j + z_{p+j} + z_{2p+j} = 1,\ j = \overline{1, p} \tag{17}$$

Limitations (17) express the fact that each of the loads can be connected to only one phase (line). Obviously:

$$z_{2p+j} = 1-(z_j + z_{p+j}), j = \overline{1,p}, \tag{18}$$

which indicates the sufficiency of storing data on $\overline{Z}$ in the form of a vector of length $2p$: in the course of software data processing, it is necessary to store only $z_j, z_{p+j}, j = \overline{1,p}$, and the values $z_{2p+j}, j = \overline{1,p}$ can be uniquely determined based on formula (16). It is also worth noting that the described data presentation is very convenient for organizing calculations based on binary optimization algorithms.

4. Proposed solution

4.1. Detailing the load model

For each of the three phases A, B and C, the load current is

$$i_E(t), E = A; B; C \tag{19}$$

in accordance with (3) and (7) is uniquely determined by the set of values of the Fourier coefficients $\bar{a} = (a_0, a_1, \dots\ a_n, a_{n+1}, \dots\ a_{2n})$.

Let's consider $a_0, a_1, \dots\ a_n, a_{n+1}, \dots\ a_{2n}$ as random variables. In this case $i_E(t)$ is a random process, and $\bar{a} = (a_0, a_1, \dots\ a_n, a_{n+1}, \dots\ a_{2n})$ is a random vector.

To build a specific load model (19), factoring in (15), it becomes necessary to preliminary estimate the statistical parameters of the distribution $a_0, a_1, \dots\ a_n, a_{n+1}, \dots\ a_{2n}$. The solution to the estimation problem assumes the presence of γ corresponding statistical observations, for which, using (3), a statistical sample of the form

$$\begin{matrix} \bar{a}_1 \leftrightarrow \{a_{0_1}, a_{1_1}, \dots a_{n_1}, a_{n+1_1}, \dots\ a_{2n_1}\} \\ \dots \\ \bar{a}_\gamma \leftrightarrow \{a_{0_\gamma}, a_{1_\gamma}, \dots a_{n_\gamma}, a_{n+1_\gamma}, \dots\ a_{2n_\gamma}\} \end{matrix}. \tag{20}$$

The statistical estimates obtained on the basis of (20) will make it possible to determine the parameters of the distribution functions:

$$\eta_k = \mathcal{F}_k^x(\zeta_k), \quad \zeta_k \in [0; 1] \tag{21}$$

for each of the $2n$ values. Naturally, the larger the value of statistical measurements γ, the smaller the statistical error of parameter estimates (21) are.

Thus, it is possible to generate random vectors:

$$\overline{A} \leftrightarrow \{a_0, a_1, \dots\ a_n, a_{n+1}, \dots\ a_{2n}\}, \tag{22}$$

defining characteristics of load currents (13) for a given number p of individual consumers when constructing, according to the rules (14), a model of load current consumption (19), corresponding to a statistical sample (20).

4.2. Detailing the objective function

In the task of optimizing the electricity distribution process, the target function is determined based on 3 criteria [11]:

$$F(\overline{Z}, \overline{A}) = c_1 \cdot f_1 + c_2 \cdot f_2 + c_3 \cdot f_3 \to \min, \tag{23}$$

where c_1,c_2,c_3 are criteria weights $(c_1 + c_2 + c_3 \le 1)$;

f_1 is a criterion reflecting the level of asymmetry / uneven distribution of the effective values of currents in the phases (current Unbalance Factor, IUF [12, 13]**)**;

f_2 is a criterion reflecting the average estimate of the nonlinear distortion coefficients of currents in the phases (12);

f_3 is a criterion reflecting the ratio of the number of required switchings of single-phase electricity consumers between phases to their total number.

However, in practice, for the optimization algorithm to work, it is sufficient to use only two criteria out of three: f_1 и f_2. At the same time, it is logical to take the second criterion into restrictions and solve the problem in the following setting:

$$f_1(\overline{Z}, \overline{A}) \to min$$

$$f_{2,E}(\overline{Z}, \overline{A}) \leq K_{THDmax}, E = A, B, C,$$

where K_{THDmax} is the maximum permissible value of the harmonic distortion factor of currents in the phases, specified as a constant.

Using the operation on (7), the phase currents (16) obtained for each of the three phases *A*, *B*, and *C* are determined by means of the corresponding sets of Fourier coefficients:

$$S_f i_E(t) = \overline{a_E} = \left(a_{0_E}, a_{1_E}, \dots a_{n_E}, a_{n+1_E}, \dots\ a_{2n_E}\right), E = A; B; C. \quad (24)$$

Then the f_1 values will be calculated based on the formula:

$$f_1 = \frac{I_A^2 + I_B^2 + I_C^2}{\left(I_A + I_B + I_C\right)^2},$$

where, based on the formula for calculating the effective current value from the amplitude spectrum of its signal [14, 15] and by virtue of (3) and (24)

$$I_E = \sqrt{a_{0_E}^2 + \sum_{k=0}^{2n} \frac{a_{k_E}^2}{2}}, \ \ E = A; B; C,$$

Calculations of f_2 values will be performed according to formula (12), for which, due to (3) and (24)

$$I_{k_E}^2 = a_{k_E}^2 + a_{n+k_E}^2.$$

5. Results

Organization of calculations based on binary optimization algorithms requires discrete representation of variables in the appropriate format. The possibility of transition from continuous functions to their scalar representation is given by the Fourier transform. The paper exhibits variants of linear operations of such a transition as applied to a specific optimization problem from the field of electric power industry. It was found that with the described approach the Fourier spectra of the phase currents are equal to the sum of the spectra connected to each of the phases of the load currents. In turn, we were able to express the objective functions for the optimization problem through the spectra of the harmonics of the phase currents and the vector of binary variables that identify the connected consumers to each of the three phases. It has been shown that for the organization of computations it is necessary and sufficient to use a binary vector, the length of which is only twice the number of consumers.

6. Discussion

The described mechanism for organizing calculations is illustrated with examples, detailed models and objective functions in relation to the problem of optimizing the electricity distribution process. This mechanism corresponds to the rules for performing numerical calculations based on the discrete Fourier transform [16, 17] and expands the scope of their application. It is quite possible that this approach will be successfully applied to problems of another class, in which the processes occurring are also initially described by continuous periodic functions [18, 19, 20]. However, in each specific case, the expressions for the objective functions are likely to be different. The authors of the work provide an opportunity for other researchers to test the described mechanisms based on the Fourier transform for detailing their own models and target functions when solving optimization problems from other subject areas.

7. Conclusions

This work provides variants of discrete expansion of continuous periodic functions and their representation in the form of sets of Fourier coefficients. There is an obvious relationship between these concepts, which was proven by the calculations. A corresponding mechanism for organizing calculations has been prepared, for which a number of linear matrix operations has been formed.

The use of the presented computing mechanism based on the discrete expansion of continuous periodic functions made it possible to detail the problem of optimizing the process of power distribution between single-phase consumers at the level of a transformer substation in order to establish its effective solution through binary optimization algorithms. For this task, at the level of the linear matrix operations prepared by the authors, the corresponding load model and the goal function were also detailed.

Acknowledgments

The reported study was funded by RFBR according to the research project № 18-38-20188 «Development and research of tools for intellectual modeling and synthesis of electric power net-works technological processes trajectories» using equipment of shared facility «Diagnosis and energy-efficient electrical equipment» (NPI).

References

[1] Göc D 2019 *Fast Fourier Transform using compiler auto-vectorization* (Gothenburg: Sweden)

[2] White R 2020 *Chromatography/Fourier transform infrared spectroscopy and its applications* (Boca Raton: CRC press)

[3] Olver P J 2018. *Topics in Fourier Analysis: DFT & FFT, Wavelets, Laplace Transform* (Minneapolis: University of Minnesota) p 42

[4] Ren K et al. 2020 *Infrared small target detection based on non-subsampled shearlet transform and phase spectrum of quaternion Fourier transform* (Optical and Quantum Electronics) vol 52(3) p 1–15.

[5] Kohaupt L 2015 *Introduction to the discrete Fourier series considering both mathematical and engineering aspects – A linear-algebra approach* (London: Cogent Education) vol 2(1) p 1064560.

[6] Kido K 2014 *Digital Fourier analysis: fundamentals* (New York Springer–verlag New York)

[7] Mokhov V A et al. 2018 On the Task of Multi-objective Dynamic Optimization Power Losses *Energy Management of Municipal Transportation Facilities and Transport* (Springer: Cham) December pp 611–618

[8] Mokhov V A 2019 *Formation and Analysis of Target Function for Optimization of the Process of Electricity Distribution at the Transformer Substation Level* (University news. North-Caucasian region. Technical sciences series) vol 1 pp 51–56.

[9] Ingale R 2014 *Harmonic analysis using FFT and STFT* (International Journal of Signal Processing, Image Processing and Pattern Recognition) vol 7(4) pp 345-362

[10] Li P, Li R and Feng H 2018 Total harmonic distortion oriented finite control set model predictive control for single-phase inverters *Energies* (Basel: MDPI) vol 11(12) p 3467

[11] Mokhov V A et al. 2019 Optimal Control of Phase-to-Phase Switching of Single-Phase Power Consumers Based on Binary Algorithms of Agent Metaheuristics *Int. Russian Automation Conf. (RusAutoCon)* (Russia: IEEE) September pp 1–6

[12] Alsulami A et al. 2014 Balancing Asymmetrical Load Using a Static Var Compensator *Innovative Smart Grid Technologies* (Europe: IEEE/PES) pp 1–6

[13] Xu Y et al. 2017 Methodology for optimized power quality compensation in networks with electrified railways *IEEE Innovative Smart Grid Technologies-Asia* (ISGT-Asia: IEEE) December pp 1–5

[14] Nastase A S 2015 *How to derive the RMS value of pulse and square waveforms* Retrieved from: https://masteringelectronicsdesign.com/how-to-derive-the-rms-value-of-a-trapezoidal-waveform/

[15] Poomjan S et al. 2014 *Adv. Studies Theor. Phys.* vol 8.1 (Bangkok: Thailand) pp 21–25

[16] Gasquet C and Witomski P 2013. *Fourier analysis and applications: filtering, numerical computation, wavelets* (New York: Springer Science & Business Media)

[17] Garg H K 2017 *Digital signal processing algorithms: number theory, convolution, fast Fourier transforms, and applications* (London: Routledge)
[18] Guan Y et al. 2020 *Formalization of continuous Fourier transform in verifying applications for dependable cyber-physical systems* (Journal of Systems Architecture) vol 106 p 101707
[19] Zijlstra F et al. 2017 *Fast Fourier-based simulation of off-resonance artifacts in steady-state gradient echo MRI applied to metal object localization* (Magnetic resonance in medicine) vol 78(5) pp 2035–2041
[20] Rashid A and Hasan O 2016 On the formalization of Fourier transform in higher-order logic *Int. Conf. on Interactive Theorem Proving* (Springer: Cham) August pp 483–490

Intelligent Regularized Measurement Procedure Based on the Use of a Dynamic Model of the Combined Maximum Principle and the Theory of Regularization

S V Lazarenko[1,2,*], A A Kostoglotov[1,2], R Z Khayrullin[3,4] and A S Kornev[3]

[1]Don State Technical University, Rostov-on-Don, Russia
[2]Moscow State University of Technology and Management named after K.G. Razumovsky, Moscow, Russia
[3]FSBI «MSMC» of the Ministry of Defense of the Russian Federation, Mytishchi, Russia
[4]Moscow State (National Research) University of Civil Engineering, Moscow, Russia

*e-mail: lazarenkosv@icloud.com

Abstract. A method for intellectualization of measurement procedures based on step-by-step optimization procedure is developed. The procedure reduces the stochastic estimation problem to a number of deterministic problems. The goal of the first stage of optimization is the synthesis of adaptive mathematical model of the measuring process based on the combined maximum principle. In contrast to the known methods this ensures the constructiveness of its use at the next stages of optimization. The goal of the subsequent stages of optimization is to solve the estimation problem based on the regularization method of A.N. Tikhonov. The equations for the iterative measurement procedure are obtained. The structure of their state transition vector functions differs from the known equations structure. This procedure belongs to the category of intelligent measurement procedures, since it makes a targeted choice of the parameter estimation closest to the true value the under the conditions of structural uncertainty of the model of the studied object and of parametric uncertainty of the observation model.

1. Introduction

The modern development of digital technology consistently removes restrictions on the computing power of microprocessors. This fact allows us to speak of a wide intellectualization of measuring devices [1–4], which is based on the use of software-algorithmic capabilities to take into account a priori and actual data about the purposes and conditions of measurements. The relevance of the intellectualization of measurement algorithms appears in rather complex measurement problems. As an example, we can mention the problems to estimate the parameters of controlled processes based on the results of processing the measurement information, the problems to estimate the characteristics of a random process of changing the errors of measuring instruments based on the results of verification [5], and the problems to form group references using the Kalman algorithm, etc.

In the general formulation the estimation problem turns out to be extremely difficult. Therefore, at the moment, various ways to simplify it are developed. For example, it leads for random Gaussian processes to the widely used the Kalman-Bucy filter (KBF) [6]. It gives good results in case of moderate nonlinearities and low noise levels. However, in practice, external actions often do not satisfy the

Markov property; as a result, the KBF rarely provides convergent high-precision estimates of the required parameters [7–9].

It is often possible to facilitate the analysis and synthesis of real stochastic systems using an approach that consists in reducing the estimation problem to a number of deterministic problems. Of course, this approach is not universal, but it plays a very important role in systems analysis, where it is called a step-by-step synthesis procedure [10]. This is due to the fact that a wide class of problems is defined by those situations in which random disturbances are considered to be small with respect to regular unknown disturbances. This assumption allows to obtain approximations for the solution of the estimation problem as a solution to the problems of synthesis of optimal control, which imply determining controls that satisfy deterministic constraints and deliver an extremum to a given quality functional.

The trajectory obtained in this way in the first stage of optimization is traditionally called the programmed trajectory, and the synthesized system is called the model adaptive to external disturbances. To avoid the need to solve a two-point boundary value problem, it is reasonable to consider the optimal control synthesis problem as an inverse problem of dynamics and to use the combined maximum principle (CMP) to solve it [5, 11–13]. The result of its application is a model of measuring processes, adaptive to external disturbances, which satisfies the Hamilton-Ostrogradskii variational principle [14]. This allows to resolve the contradiction between the complexity and the adequacy of the model.

The subsequent stages of the proposed step-by-step optimization procedure consist in correcting deviations from the program trajectory arising because of random actions. Constructive solutions of such inverse ill-posed problems [15–17] use the idea of A.N. Tikhonov on the stabilization of deviations of the theoretical curve from the experimental using an auxiliary stabilizing functional and determining the regularization parameter based on the use of a variational selection method.

Thus, the article discusses a variant of synthesizing the intelligent measuring procedure using the methodology of the CMP and the principle of regularization by A.N. Tikhonov. The "intelligence" of the procedure [2, 4] consists in the adaptation of the measuring process model based on the CMP [18] and in the iterative process to obtain the refined values of the regularization parameter using a priori and actual data about the characteristics of the measuring process.

2. Formulation of the problem

Let the equation of state of the process under study is written as the nonstrict Langevin equation [19]

$$\dot{\mathbf{x}} = \mathbf{f}\left(\mathbf{x},\mathbf{u},t\right) + \mathbf{g}\left(\mathbf{x},t\right)\boldsymbol{\zeta}\left(t\right), \tag{1}$$

where $\mathbf{x} \in R^{2n}$ is the state vector; $\mathbf{u} \in R^{v}$ is the vector of disturbances; $\mathbf{f}\left(\mathbf{x},\mathbf{u},t\right) \in R^{2n}$ is the vector-function of state transition; $\mathbf{g}\left(\mathbf{x},t\right)$ is the matrix function, $\dim \mathbf{g} = 2n \times l$; $\boldsymbol{\zeta} \in R^{l}$ is a random process of the white noise kind with known local characteristics: $\mathbf{M}\left[\boldsymbol{\zeta}\left(t\right)\right] = 0, \quad \mathbf{M}\left[\boldsymbol{\zeta}\left(t\right)\boldsymbol{\zeta}^{\mathrm{T}}\left(t+\tau\right)\right] = \frac{1}{2}\mathbf{R}_{\zeta}\boldsymbol{\delta}\left(\tau\right)$, where $\boldsymbol{\delta}\left(t\right)$ is the vector delta function; $\mathbf{R}_{\zeta}$ is the covariance matrix.

The measurement equation has the form

$$\mathbf{y}\left(t\right) = \mathbf{H}\left(\mathbf{x},t\right) + \boldsymbol{\xi}\left(t\right), \tag{2}$$

where $\mathbf{H} \in R^{2n}$ is a known vector function; $\boldsymbol{\xi} \in R^{2n}$ is the vector of random actions on the measuring noise channel with known local characteristics: $\mathbf{M}\left[\boldsymbol{\xi}\left(t\right)\right] = 0, \quad \mathbf{M}\left[\boldsymbol{\xi}\left(t\right)\boldsymbol{\xi}^{\mathrm{T}}\left(t+\tau\right)\right] = \frac{1}{2}\mathbf{R}_{\xi}\boldsymbol{\delta}\left(\tau\right),$ where $\mathbf{R}_{\zeta}$ is the covariance matrix; *n,v,l* are corresponding dimensions.

It is assumed that the structure of the vector function $\mathbf{f}\left(\mathbf{x},\mathbf{u},t\right)$ in model (1) is a priori unknown or changes in time due to the influence of external disturbances **u**. Then the task of synthesizing the

measurement procedure consists in constructing the vector function $\mathbf{f}\left(\mathbf{x},\mathbf{u},t\right)$ with subsequent finding of the corresponding vector of state estimates $\hat{\mathbf{x}} \in R^{2n}$ from the condition of the minimum of the loss functional:

$$\left\langle J_0 \right\rangle = M\left[\left(\mathbf{x}-\hat{\mathbf{x}}\right)^T \mathbf{W}\left(\mathbf{x}-\hat{\mathbf{x}}\right) \middle| \mathbf{y} \right], \tag{3}$$

where $M\left[\cdot\right]$ – is the expectation operator; $\mathbf{W}$ – is the non-negative real weight matrix. The vector of estimates $\hat{\mathbf{x}}$ minimizes the loss functional $\left\langle J_0 \right\rangle$ and represents the conditional mathematical expectation $\hat{\mathbf{x}} = M\left[\mathbf{x}|\mathbf{y}\right]$. The estimate obtained from the minimum condition (3) corresponds to the estimate of the least squares method criterion in the case of the Gaussian probability

$$J = \int_{t_0}^{t_1} \frac{1}{2}\left(\mathbf{y}(t)-\mathbf{H}\left(\hat{\mathbf{x}}(t),t\right)\right)^T \mathbf{R}_\xi^{-1}\left(\mathbf{y}(t)-\mathbf{H}\left(\hat{\mathbf{x}}(t),t\right)\right)dt = \int_{t_0}^{t_1} \Delta dt \cdot \tag{4}$$

Along with probabilistic constraints and the requirements for the estimation system is subject to the deterministic requirements and constraints. In particular, $\mathbf{u} \in \overline{G}_u$; here $\overline{G}_u$ is a closed set of admissible disturbances, concertized in accordance with the specifics of the problem being solved.

The decomposition of the problem of synthesis of the measuring procedure (1) is carried out based on the hypothesis of the smallness of random disturbances: $\boldsymbol{\xi}\left(t\right) \equiv \mathbf{0}$ [10]. Then instead of (1) we can consider the mathematical model

$$\dot{\mathbf{x}} = \mathbf{f}\left(\mathbf{x},\mathbf{u},t\right). \tag{5}$$

In this case, the vector function $\mathbf{X}$ will no longer be a random process.

Equation (5) is obtained basis on the procedure for expanding the state space from the Lagrange equation of the second kind [5, 15]

$$\frac{d}{dt}\left(\frac{\partial T}{\partial \dot{q}_s}\right) - \frac{\partial T}{\partial q_s} = Q_s, \quad \mathbf{Q} \in \overline{G}_Q, \quad s = \overline{1,n}, \tag{6}$$

where T is the kinetic energy of the system; q_s is the generalized coordinate; $\overline{G}_Q$ is the closed set of admissible generalized forces $\mathbf{Q}$.

The hypothesis of the smallness of the perturbations does not affect the form of Eq. (2), which is represented by an additive convolution of the observed generalized coordinates and the Gaussian measurement noises.

Since $\boldsymbol{\xi}\left(t\right) \equiv \mathbf{0}$ and by virtue of the procedure for expanding the state space, functional (3) takes the form [10]

$$J_0 = \int_{t_0}^{t_1} \left(\mathbf{q}-\hat{\mathbf{q}}\right)^T \mathbf{W}\left(\mathbf{q}-\hat{\mathbf{q}}\right) dt. \tag{7}$$

The inverse problem of dynamics is posed as follows: it is required to determine the vector of generalized forces $\mathbf{Q} \in \overline{G}_Q$ as a function of the generalized coordinates and velocities, as well as the trajectory corresponding to the vector, providing minimum for (7) under constraints on the dynamics of the system following from the Hamilton-Ostrogradskii principle, which leads to (6). The solution to the inverse problem of dynamics determines the structure of the vector function $\mathbf{f}\left(\mathbf{x},\mathbf{u},t\right)$.

The goal of the subsequent optimization stages is to find the estimate $\hat{\mathbf{x}}\left(t\right)$ from the condition of the minimum of the posterior probability density $p\left(\mathbf{x}|\mathbf{y}\right)$ when the time t increases, $t \in \left[t_0, t_1\right]$.

Thus, the synthesis of measurement procedures requires to solve the particular optimization problems:

- first, it is the synthesis of an adaptive mathematical model of the measuring process. Under conditions of a priori uncertainty about generalized forces, in order to avoid the two-point boundary value problem (TPBVP) [20], we propose to use the CMP to solve the inverse problem of dynamics (6), (7) [18];
- second, it is the solution of the estimation problem (1), (4) based on the regularization method of A.N. Tikhonov.

3. The combined maximum principle

The procedure for finding the minimum of the functional (7) must be carried out taking into account the constraints in the form of the differential equations (6) that follow from the Hamilton-Ostrogradskii principle. Then we have [5, 11–14]

$$J = J_0 + \int_{t_0}^{t_1} \lambda \left[T + A \right] dt, \tag{9}$$

where λ is an indefinite Lagrange multiplier; A is the work of generalized forces.

The solution to such a problem is obtained based on the theorem of the combined maximum principle [11]: in order for the generalized force $\mathbf{Q}$ and the corresponding trajectory $\left(\mathbf{q}, \dot{\mathbf{q}}\right)$ to provide a minimum to the extended functional (9) under constraints $\mathbf{Q} \in \overline{G}_Q$, it is necessary and sufficient to fulfill the maximum condition for the function of the generalized power Φ of variables $\left(\mathbf{q}, \dot{\mathbf{q}}\right) \in R^{2n}$

$$\Phi\left(\mathbf{q}, \dot{\mathbf{q}}\right) = \max_{\mathbf{Q} \in \overline{G}_Q} \sum_{s=1}^{n} \left[\lambda Q_s - W_{ss} \left[q_s - \hat{q}_s \right] \right] \dot{\hat{q}}_s, \lambda = \text{const}.$$

From this with $T = \frac{1}{2} \dot{\mathbf{q}}^T \mathbf{A} \dot{\mathbf{q}}$ the model adaptive to external disturbances can be presented in the following form [14]:

$$\ddot{\hat{q}}_s = -\frac{1}{a_{ss}} \frac{\left| \dot{\hat{q}}_s \right| \dot{\hat{q}}_s}{\left| L_s \hat{q}_s \right|} + \frac{W_{ss}}{\lambda a_{ss}} \left[q_s - \hat{q}_s \right] = F_s + \Delta_s,$$

where $\mathbf{A}$ is the matrix of constant coefficients of inertia a_{ss}; $F_s = -\frac{1}{a_{ss}} \frac{\left| \dot{\hat{q}}_s \right| \dot{\hat{q}}_s}{\left| L_s \hat{q}_s \right|}$; $\Delta_s = \lambda^{-1} a_{ss}^{-1} W_{ss} \left[q_s - \hat{q}_s \right]$; L_s are constants [13].

The procedure for expanding the state space for the case of observing one coordinate leads to a first-order vector differential equation:

$$\dot{\mathbf{x}}(t) = \mathbf{f}(\mathbf{x}(t), t) + \mathbf{G}\boldsymbol{\eta}(t), \quad \mathbf{x}(0) = \mathbf{x}^0, \tag{10}$$

where $\mathbf{x} = \left[x_1 \quad x_2 \right]^T$, $x_1 = q, x_2 = \dot{q}$; we introduce the notation $b = a_{11}^{-1} L^{-1}$; $\mathbf{f}(\mathbf{x}(t), t) = \begin{bmatrix} x_1 \\ \dfrac{-b \left| x_2 \right| x_2}{\left| x_1 \right|} \end{bmatrix} = \mathbf{f}\left(x_1, x_2 \right)$ is a function that is continuous together with its derivatives on the sets $\{x_1>0,\ x_2>0\}$, $\{x_1>0,\ x_2<0\}$, $\{x_1>0,\ x_2=0\}$; $\mathbf{G} = \begin{bmatrix} 1 & 0 \\ 0 & a_{11}^{-1} \lambda^{-1} R_{\xi 1} \end{bmatrix}$ is the intensity of external

disturbances; $\boldsymbol{\eta}(t)=\begin{bmatrix}0\\ \lambda^{-1}a_{11}^{-1}W_{11}\left[x_1-\hat{x}_1\right]\end{bmatrix}$ are external disturbances that determine the adequacy of the constructed model (10).

4. Regularization by A.N. Tikhonov

By virtue of the continuity of the transition function $\mathbf{f}(\mathbf{x},t)$, the solutions of the equation (10) continuously depend on $\boldsymbol{\eta}(t)$ in accordance with the theorem on the continuous dependence of the solution of the differential equation on the parameters and the initial data. Therefore, the functional (4) on each solution of the system (10) continuously depends on $\boldsymbol{\eta}(t)$, $\mathrm{J}[\mathbf{x}]=\mathrm{J}[\boldsymbol{\eta}]$. It follows that the problem to determine the estimate $\hat{\mathbf{x}}(t)$ that provides the minimum (4) is equivalent to the problem of determining $\boldsymbol{\eta}^*(t)=\arg\min_{\boldsymbol{\eta}} \mathrm{J}[\boldsymbol{\eta}]$. Such a problem, according to [17], is ill-posed and refers to problems of the optimal control type. To solve it, we use the regularization method of A.N. Tikhonov [17]. When implementing the method, it is enough to construct a minimizing sequence $\{\boldsymbol{\eta}_n(t)\}$ converging to $\boldsymbol{\eta}^*(t)$. Let us consider the smoothing functional

$$\mathrm{J}^{\alpha}[\hat{\mathbf{x}},\boldsymbol{\eta}]=\mathrm{J}[\hat{\mathbf{x}}]+\alpha\Omega[\boldsymbol{\eta}],\quad \Omega[\boldsymbol{\eta}]=\frac{1}{2}\int_0^t \boldsymbol{\eta}^{\mathrm{T}}(s)\boldsymbol{\eta}(s)ds,$$

where α is a positive number. For a differentiable convex functional $\mathrm{J}^{\alpha}[\hat{\mathbf{x}},\boldsymbol{\eta}]$, the minimum is determined from the stationarity condition:

$$grad\ \ \mathrm{J}^{\alpha}[\hat{\mathbf{x}},\boldsymbol{\eta}]=0. \tag{12}$$

The expression for recording the gradient in expanded form can be represented as follows [4]:

$$grad\ \ \mathrm{J}^{\alpha}=\alpha\boldsymbol{\eta}(s)+\int_s^t \mathbf{G}^{T}(s,\tau)\mathbf{N}^{-1}\frac{\partial\mathbf{H}^{T}}{\partial\mathbf{x}}\left[\mathbf{y}-\mathbf{H}\left(\hat{\mathbf{x}}(s),\mathbf{x}_{\eta}(\tau),\tau\right)\right]d\tau, \tag{13}$$

where $\mathbf{G}^{T}(s,\tau)$ is a fundamental matrix satisfying the homogeneous linear equation $\frac{d}{d\tau}\mathbf{G}(s,\tau)=\frac{\partial\mathbf{f}}{\partial\mathbf{x}}\left(\mathbf{x}_{\eta}(\tau),\tau\right)\mathbf{G}(s,\tau)$, $\mathbf{G}(s,\tau)=\mathbf{I}$; $\mathbf{I}$ is the unity matrix, and the value of the derivative $\frac{\partial\mathbf{f}}{\partial\mathbf{x}}$ are found on the solutions of the system $\frac{d\mathbf{x}_{\eta}}{d\tau}+\mathbf{f}\left(\mathbf{x}_{\eta},\tau\right)=\boldsymbol{\eta}(\tau)$, $\tau\in[s,t]$, $\mathbf{x}_{\eta}(\tau)\big|_{\tau=s}=\hat{\mathbf{x}}(s)$. Using the stationarity condition (12), we write

$$\boldsymbol{\eta}^*(s)=\alpha^{-1}\int_s^t \mathbf{G}^{\mathrm{T}}(s,\tau)\mathbf{N}^{-1}\frac{\partial\mathbf{H}^{\mathrm{T}}}{\partial\mathbf{x}}\left[\mathbf{y}-\mathbf{H}\left(\hat{\mathbf{x}}(s),\mathbf{x}_{\eta}(\tau),\tau\right)\right]d\tau.$$

5. Iterative Intelligent Measurement Procedure

To determine the point $\left[\hat{\mathbf{x}},\boldsymbol{\eta}^*\right]$, we use the iteration method:

$$\boldsymbol{\eta}_{k+1}=\boldsymbol{\eta}_K-\alpha_K\ grad\ \ \mathrm{J}^{\alpha}\left[\hat{\mathbf{x}}_{k+1},\boldsymbol{\eta}_K\right]. \tag{14}$$

To shorten formulae, we introduce the notation $\mathbf{B}(\hat{\mathbf{x}},\tau)=\mathbf{G}^T(s,\tau)\mathbf{N}^{-1}\dfrac{\partial\mathbf{H}^T}{\partial\mathbf{x}}\left[\mathbf{y}-\mathbf{H}(\hat{\mathbf{x}},\tau)\right]$. Then, taking into account (13), the expression (14) can be represented as follows:

$$\boldsymbol{\eta}_{k+1}(s)=-\int_s^t\sum_{i=1}^{k+1}\gamma_i^K\mathbf{B}(\hat{\mathbf{x}}_i(s),\tau)d\tau,\quad \dot{\hat{\mathbf{x}}}_{k+1}+\mathbf{f}(\hat{\mathbf{x}}_{k+1},s)=\boldsymbol{\eta}_{k+1},\quad s\in[0,t],$$

where γ_i^k is determined by the rule [4]

$$\gamma_i^k=\alpha_{i-1}\left[1-\alpha_i^2\right]\cdot\ldots\cdot\left[1-\alpha_{K-1}^2\right],\qquad i=\overline{1,k}.$$

The equation for the k+1 approximation of the estimate $\hat{\mathbf{x}}_{k+1}$ has the form

$$\dot{\hat{\mathbf{x}}}_{k+1}+\mathbf{f}(\hat{\mathbf{x}}_{k+1},s)=-\int_s^t\sum_{i=1}^{k+1}\gamma_i^{k+1}\mathbf{B}(\hat{\mathbf{x}}_i(s),\tau)d\tau. \tag{15}$$

To solve the estimation problem, Eq. (15) can be reduced to the form TPBVP

$$\dot{\hat{\mathbf{x}}}_{k+1}+\mathbf{f}(\hat{\mathbf{x}}_{k+1},s)=\boldsymbol{\eta}_{k+1}(s),\dot{\boldsymbol{\eta}}_{k+1}(s)=\frac{\partial\mathbf{f}^T}{\partial\mathbf{x}}\boldsymbol{\eta}_{k+1}(s)+\sum_{i=1}^{k+1}\gamma_i^{k+1}\mathbf{b}(s,\hat{\mathbf{x}}_i(s)),$$

under the boundary conditions $\boldsymbol{\eta}_{k+1}(t)=0,\quad \hat{\mathbf{x}}_{k+1}=\mathbf{x}^0+\mathbf{P}^0\boldsymbol{\eta}_{k+1}(0)$; $\mathbf{P}^0$ is some matrix; $\mathbf{b}(s,\hat{\mathbf{x}}_i)=\mathbf{N}^{-1}\dfrac{\partial\mathbf{H}^T}{\partial\hat{\mathbf{x}}}\left[\mathbf{y}(s)-\mathbf{H}(\hat{\mathbf{x}}_i,s)\right]$. Problems of this kind are successfully solved by the R. Bellman method of "invariant immersion" [20]. Following the method [2, 4], we obtain the equations of the intelligent measuring procedure:

$$\begin{gathered}\frac{d\hat{\mathbf{x}}_1}{dt}+\mathbf{f}(\hat{\mathbf{x}}_1,t)=-\mathbf{P}_1\gamma_1^1\mathbf{b}(\hat{\mathbf{x}}_1,t),\frac{d\mathbf{P}_1}{dt}=\frac{\partial\mathbf{f}}{\partial\mathbf{x}}\mathbf{P}_1+\mathbf{P}_1\frac{\partial\mathbf{f}}{\partial\mathbf{x}}^T+\gamma_1^1\mathbf{P}_1\frac{\partial\mathbf{b}(\hat{\mathbf{x}}_1,t)}{\partial\mathbf{x}}\mathbf{P}_1+\mathbf{I},\\ \ldots\ldots\ldots\ldots\ldots\ldots\ldots\ldots\\ \frac{d\hat{\mathbf{x}}_{k+1}}{dt}+\mathbf{f}(\hat{\mathbf{x}}_{k+1},t)=-\mathbf{P}_{k+1}\sum_{i=1}^{k+1}\gamma_i^{k+1}\mathbf{b}(\hat{\mathbf{x}}_i,t),\\ \frac{d\mathbf{P}_{k+1}}{dt}=\frac{\partial\mathbf{f}}{\partial\mathbf{x}}\mathbf{P}_{k+1}+\mathbf{P}_{k+1}\frac{\partial\mathbf{f}}{\partial\mathbf{x}}^T+\gamma_{k+1}^{k+1}\mathbf{P}_{k+1}\frac{\partial\mathbf{b}(\hat{\mathbf{x}}_{k+1},t)}{\partial\mathbf{x}}\mathbf{P}_{k+1}+\mathbf{I},\end{gathered} \tag{16}$$

which differs from the known structure of the vector function $\mathbf{f}$.

The first pair of equations (16) is the extended Kalman filter with adaptation to external actions, and each subsequent estimation equation for k+1 uses the function **y** and $\hat{\mathbf{x}}_1,\ldots,\hat{\mathbf{x}}_k$ as input parameters. All the equations are identical by form; therefore, the same calculation algorithm can be used to solve them all. The well-known residual criterion [18] can be used as the criterion for exit from the recursive calculation.

6. Conclusion

The analysis of the obtained equations allows to make the following conclusions.

The reason to apply the proposed measuring procedure (16) arises when solving measuring problems under conditions of structural uncertainty of the model of the object under study and parametric uncertainty of the observation model, when it is required to increase the accuracy of the obtained estimates of the measured parameters from the results of indirect measurements.

The use of the criterion of minimum residual [18] $\delta(i)=\frac{1}{t}\int_0^t\left[y^1(s)-\hat{x}_i^1(s)\right]^2 ds$ makes it possible to complete the process of step-by-step processing of measurement data, i.e. to determine the number of the most accurate estimate of the parameter under study using the ratio $N=\arg\min_i \delta(i)$. This allows the resulting measurement procedure to be classified as "intelligent" [21, 22], or as carrying out a targeted selection of the measured parameter estimate that is the closest to the true value.

The experience of solving the ill-posed problems [2, 4, 7, 11, 12] can be used when constructing the measuring procedures of similar type under various conditions of the measurement process in order to obtain either the most accurate and stable, or the most time-efficient estimation of the measured parameters by choosing the values α_0, α_1, α_2..... This makes it possible to change the purpose of measurements, and hence the nature of the "intelligence" of the measurement procedure.

The works have been under grants RFBR No 18-01-00385 A, No. 18-08-01494 A.

References

[1] D.S. Andrashitov Synthesis of recurrent algorithms for parametric identification based on variational principles // Educational resources and technologies. 2017. v. 3 (20). pp. 48-54.

[2] Kostoglotov A.A., Kuznetsov A.A., Andrashitov D.S., Deryabkin I.V., Lazarenko S.V. Regularized iterative algorithms for processing measurement information // Herald of computer and information technologies. 2010. No. 11. pp. 3-9.

[3] Krupennikov E.A. On Estimates of the Solutions of Inverse Problems of Optimal Control. In: Bykadorov I., Strusevich V., Tchemisova T. (eds) Mathematical Optimization Theory and Operations Research. MOTOR 2019. Communications in Computer and Information Science, vol 1090. Springer, Cham. https://doi.org/10.1007/978-3-030-33394-2_39.

[4] A.A. Kostoglotov, A.A. Kuznetsov Synthesis of an intelligent measuring procedure based on the method of minimal errors // Measuring equipment. 2005. v. 7. pp. 8-13.

[5] Kostoglotov, A.A., Andrashitov, D.S., Kornev, A.S. et al. A Method for Synthesis of Algorithms to Estimate the Dynamic Error of Measurement System Software on the Basis of the Combined Maximum Principle // Measurement Technics, vol. 62. 2019. Pp. 497–502. https://doi.org/10.1007/s11018-019-01652-8/

[6] Kalman R.E. A New Approach to Linear Filtering and Prediction Problems // Trans. ASME J, Vol. 82D, 1960. pp. 34-45. http://dx.doi.org/10.1115/1.3662552.

[7] Farina A., Studer F. Digital processing of radar information. Moscow: Radio and communications, 1993. 320 pp.

[8] Singer R.A., Behnke K.W. Real-Time Tracking Filter Evaluation and Selection for Tactical Applications // IEEE Trans., Vol. AES-7, No. 1, 1971. Pp. 100-110. https://doi.org/10.1109/TAES.1971.310257.

[9] Omkar Lakshmi Jagan B., Koteswara Rao S., Jawahar A. and Karishma SK. B. Application of Bar-Shalom and Fortmann's Input Estimation for Underwater Target Tracking // Indian Journal of Science and Technology, vol 9(21). 2011. https://doi.org/10.17485/ijst/2016/v9i21/85451/.

[10] Moiseev N.N. Mathematical problems of system analysis. Moscow: Nauka, 1981. p. 488.

[11] Kostoglotov A.A., Lazarenko S.V. Synthesis of Adaptive Tracking Systems Based on the Hypothesis of Stationarity of the Hamiltonian on the Switching Hypersurface // Journal of Communications Technology and Electronics. 2017. Issue 2. Pp. 123-127. https://doi.org/10.7868/S0033849417020061.

[12] Kostoglotov A.A., Lazarenko S.V., Kuznetsov A.A., Deryabkin I.V., Losev V.A. Structural synthesis of discrete adaptive tracking systems based on the combined maximum principle // Vestnik of Don State Technical University. 2017. Issue 17. Pp. 105-112.

https://doi.org/10.23947/1992-5980-2017-17-1-105-113.
[13] Frommlet F., Nuel G. An Adaptive Ridge Procedure for L0 Regularization // PLOS ONE 11. 2016. https://doi.org/10.1371/journal.pone.0148620.
[14] Yunt K. The Hamilton Principle for Mechanical Systems with Impacts and Unilateral Constraints. In: Constanda C., Kirsch A. (eds) Integral Methods in Science and Engineering. Birkhäuser, Cham. 2015. https://doi.org/10.1007/978-3-319-16727-5_57.
[15] Sizkov V.S. Sustainable methods for processing measurement results. SPb: SpecLit, 1999. p. 240.
[16] Chen HB, Zhuang HL. A new highly anti-interference regularization method for ill-posed problems. Vibroengineering PROCEDIA [Internet]. JVE International Ltd. 2017. http://dx.doi.org/10.21595/vp.2017.19358.
[17] Alifanov A.M., Artyukhin E.A., Rumyantsev S.V. Extreme methods for solving ill-posed problems. Moscow: Nauka, 1988. p. 288.
[18] Krut'ko P.D. Algorithms of a nontraditional structure in the problems of the control of the longitudinal motion of aircraft. J. Mach. Manuf. 2010. Reliab. 39, 168–178. https://doi.org/10.3103/S1052618810020123.
[19] Van Trees G. The theory of the detection, estimation and modulation. Volume I. The theory of detection, estimation and linear modulation. Moscow: Sov. Radio, 1972. p. 744.
[20] Anna L. Balaban, Yuri A. Bakhvalov and Peter A. Denisov Review of methods for solving inverse problems in identifying permanent magnets of executive elements in dynamic devices. MATEC Web Conf., 226. 2018. https://doi.org/10.1051/matecconf/201822604022.
[21] Ferri C. Uncertainty in Measurement, Intelligent System and Computing, Yang (Cindy) Yi, IntechOpen. 2019. https://doi.org/10.5772/intechopen.89568.

Researching removal of metal from workpiece surface during centrifugal rotation processing

Nguyen Van Tho[1,2,3,*], M A Tamarkin[2], A N Soloviev[3] and E E Tishchenko[2]

[1] Faculty of Mechanical Engineering, Haiphong University, Haiphong City, Vietnam
[2] Department of Mechanical Engineering, Don State Technical University, Rostov-on-Don, Russia
[3] Department of Theoretical and Applied Mechanics, Don State Technical University, Rostov-on-Don, Russia

*e-mail: thonv@dhhp.edu.vn

Abstract. The modeling and analysis of the metal removal process at centrifugal-rotational processing (CRP) of parts in an abrasive discrete medium are considered in this article. we have developed a three-dimensional statement about contact interaction, the interaction of a single abrasive particle with a flat surface of the part is considered. Finite element models of abrasive particle and workpieces were constructed in the ANSYS package and Archard codes will be programmed to analyze the data. The relation between workpiece metal removal and parameters of contact interaction: pressure force, processing time, sliding speed — is researched, experiments were conducted on centrifugal-rotary setup and the dependence removal of metal from workpiece surface on the technological parameters was investigated. The dependences constructed in the work allow determining the rational value of parameters of the CRP when workpiece machining. Experimental results have been confirmed by simulation results. Through this research, the essential and important data-sheets will provide for the experiment works and real manufacturing. Hence, time and finance save a lot to achieving the desired surface quality.

1. Introduction

In mechanical engineering, grinding is used as the last step in surface treatment. It allows you to achieve the required accuracy, surface roughness and can be applied to materials with high strength, heat resistance and hardness [1]. Process optimization requires the development of models that improve the frictional interaction between abrasive particles and workpiece surfaces. To simulate the removal of metal from workpiece surface process, numerical methods have been developed, among which the finite element method (FEM) is the most general [2-5]. In [6], using the FEM, a thermostructural analysis was carried out and a forecast of the wear of the seal element was carried out. The work [7] is devoted to the creation of an efficient machine learning framework for local predictions of surface erosion by means of Gaussian processes. The results of real-time experimental measurements on metal removal due to sliding aluminum oxide particles are presented in [8].

This article examines the process of interaction of an abrasive particle with the surface of the workpiece in the framework of the dynamic contact problem of the theory of elasticity. The interaction of an abrasive

grain element in the form of a truncated cone and the surface of a part is investigated. The action of an abrasive particle is modeled by the introduction of the base of a truncated cone of a smaller diameter into the surface of the part, taking into account dry friction and metal removal in the contact area. As parameters of the technological process, the size of the abrasive particles, the volume of the abrasive medium, the speed of rotation of the centrifuge, and the forces of interaction are considered. The depth of removal of metal from workpiece surface is investigated depending on these parameters.

In this research, we use the following models and methods:

(i) The interaction of abrasive particles with the workpiece surface is considered within the dynamic problem of thermoplastic contact theory.

(ii) Archard model is used to model the material removal process in a dynamic contact problem

(iii) Theoretical problems are solved by the finite element method in Ansys

(iv) Experimental research of processing in centrifugal-rotary installation.

2. Problem formulation

The principle of the CRP process is shown in figure 1. The summary of the CRP method is that abrasive particles 3 and workpiece 4 are loaded into the working chamber and rotated about the vertical axis so that the entire mass of the load becomes a torus in which particles move along spiral paths.

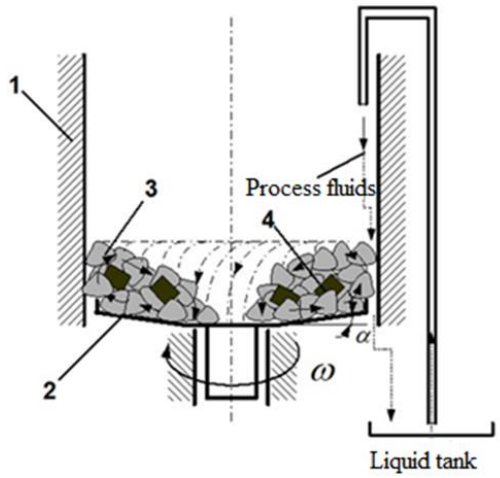

Figure 1. Centrifugal-rotary processing in abrasive medium
1 is fixed cylindrical ring; 2 is rotor; 3 is abrasive particles; 4 is workpieces

The toroidal helical flow is ensured through the design of the machine working chamber consisting of a fixed cylindrical ring 1 and a rotating bottom (rotor) 2 adjacent to it, having a common plate shape. Workpieces 4 are loaded into the working chamber with abrasive particles 3. To reduce wear, the inner surfaces of the bottom and the fixed part of the working chamber are coated with a wear-resistant material. The contacting parts of the abrasive granules have the shape of truncated cones, a diagram with the construction of a three-dimensional model of the contact interaction of an abrasive particle with a part is shown in figure 2.

Friction and removal of metals have been studied for a long time and their basis is presented in [9]. The processing process in the rotating chamber is described in the works of M.A. Tamarkin and his students and research on the features of this process are devoted to working [10, 11]. The interaction between the abrasive particle and the workpiece leads to wear and heating of the workpiece surface. Experiments and calculations

are presented in [12,13], it is known that the temperature in the processing area is not high and does not lead to changes in the surface layer structure of workpiece surface. Modeling and analysis of the material removal depth from the workpiece surface in [14-18]. In this paper, research the contact interaction of an abrasive particle sliding on workpiece surface without taking into account heating.

Figure 2. Model abrasive particles and workpiece

2.1. Mathematical model

The interaction of an abrasive particle with the workpiece surface is studied. The problem is formed in the framework of the dynamic contact problem of elastic theory, taking into account friction and metal removal in the contact area. The abrasive particle is simulated by a truncated cone, the smaller diameter part in contact with the workpiece surface. The abrasive particles are modeled by a truncated cone, in a smaller base in contact with workpiece surface. The abrasive particle is pressed onto workpiece surface by a vertical force and slides at a constant speed, modeled by a parallel rectangle that is much larger than the diameter of the contact point (figure. 3).

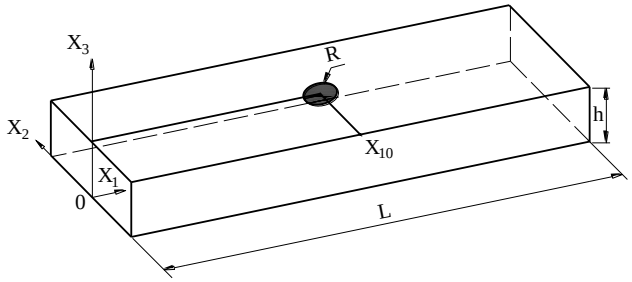

Figure 3. Diagram workpiece and flat round stamp

The problem is reduced to motion of a circular cone with constant speed $v > 0$ in the positive direction of the axis, X_1, taking into account the friction forces arising under it. Due to this interaction, the strip material is removed, the Archard model is used [19]

$$w = \frac{K}{H}\sigma_n^b v^q \tag{1}$$

where w is the displacement of contact surface points in the direction removal of metal; K is the metal removal coefficient; H is the material hardness; σ_n is the contact pressure; v is the relative sliding speed;

b, *q* parameters characterizing the power-law dependence of the metal removal depth on the contact pressure and relative velocity.

Tangential stresses on the contact surface are related to normal stresses according to Coulomb's law with a friction coefficient f. Abrasive particle 1 moves at a constant speed v along the workpiece surface. In a moving coordinate system (figure 3), wherein $X_1 \to X_1 - vt$, $X_i \to X_i$, $i = 2,3$ the complete equation following form

$$\mu u_{i,kk} + (\lambda + \mu) u_{k,ki} - v^2 \rho u_i = 0 \tag{2}$$

where λ, μ are the Lame coefficients, μ_i is the displacement vector components

The value of the force of abrasive particles on workpiece of the sliding process is related to the rotation speed of the setup ω and is determined as follows:

$$F = m\omega^2 R \tag{3}$$

where *m* is the mass of the abrasive particle, *R* is the machining radius (distance from the axis of rotation to the workpiece).

The boundary conditions correspond to the effect of uniform pressure distribution P on the round surface of the abrasive particle (figure 4), particle and workpiece in friction contact, the lower plane of the part is fixed, the remaining surfaces have no stress.

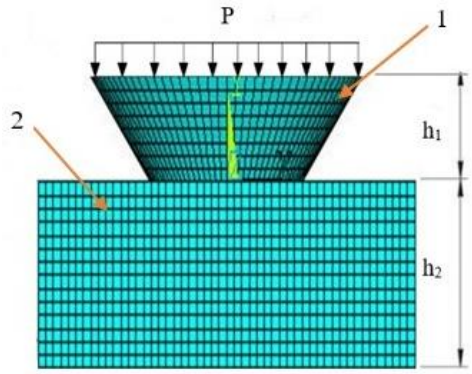

Figure 4. Design contact interaction of the abrasive particles and workpiece

Table 1 presents the parameters of the abrasive particles and workpiece.

Table 1. Model parameters abrasive particles and workpiece

№	Characteristic	Material model	
		workpiece (Steel)	abrasive particles (Corundum)
1	Young's modulus, Mpa	2 x 10^5	2 x 10^9
2	Poisson's Ratio	0.28	0.3
3	Material hardness (HB)	190	400
4	Density, kg/m^3	7850	4000

3. Finite Element Modeling in Ansys

Method for solving the second boundary value problem, finite element method and ANSYS are used, which implements the Archard metal removal model. Figure 5 shows the finite element mesh of a three-dimensional model of workpiece and abrasive particle; in the contact area, the mesh is thickened. The final elements SOLID185. CONTA174 and TARG169 are used for contact surfaces, both models are constructed using the command TB, WEAR, and the material is assigned a unique identifier ID. Activation of the generalized Archard wear model is carried in the format

TB,WEAR,MATID,,,ARCD,

where: MATID is the identification of the material associated with contact elements.

Abrasive particle 1 sliding with a constant speed v along the workpiece surface

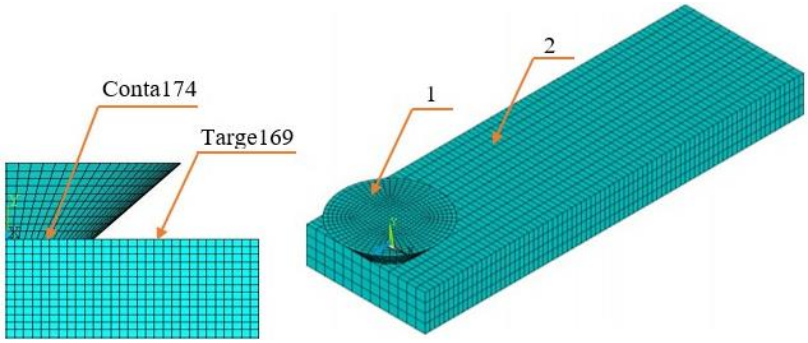

Figure 5. Finite-element partitioning in contact problem. 1 is an abrasive particle, 2 is a workpiece

4. Calculation removal of metal from the workpiece surface

Calculations are made for an abrasive particle and workpiece, the material parameters are shown in table 1. The following mechanical properties and geometric parameters are used: metal removal rate $K_d = 1.06793 \times 10^{-6}$; b=q=1.0; radius of the truncated cone $R_1 = 2\,mm$ and $R_2 = 4\,mm$, cone height $h_1 = 2\,mm$; workpiece height $h_2 = 3\,mm$, workpiece lenght $L = 30\,mm$, workpiece width $D = 5\,mm$; friction coefficient $f = 0.1$; step $t = 1s$.

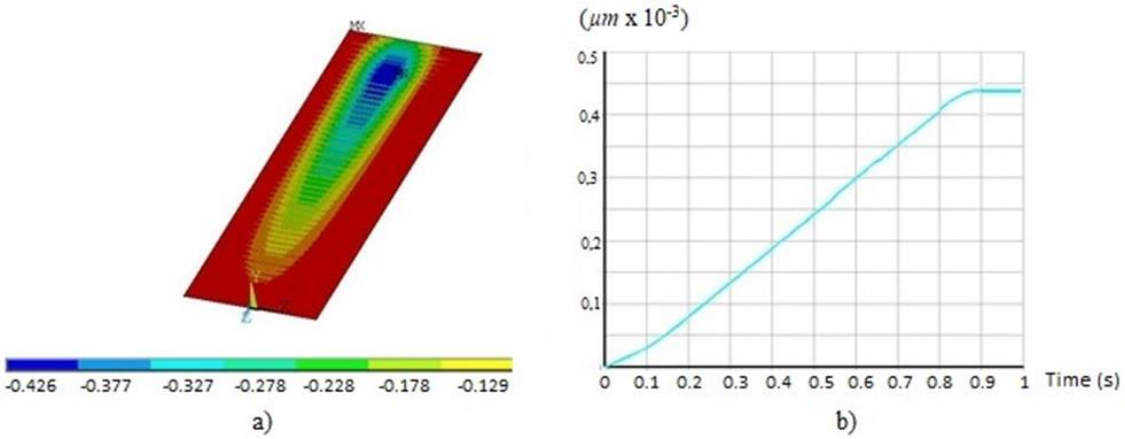

Figure 6. Distribution of removed metal (μm x 10^{-3}): a- distribution of rates for metal removal from workpiece surface, b - dependence of the maximum rate of metal removal on time

Figure 6 shows the distribution of metal removal rate from workpiece surface when abrasive particles are pressed to the workpiece by vertical pressure $P = 2.5 N / mm^2$ and slide with constant speed $v = 25 mm / s$ on the workpiece surface.

Figure 7 shows the distributions of rates for metal removal from the workpiece surface depending on rotation speed, for the values of rotation speed equal to 5; 12; 16 and 20 rp/s.

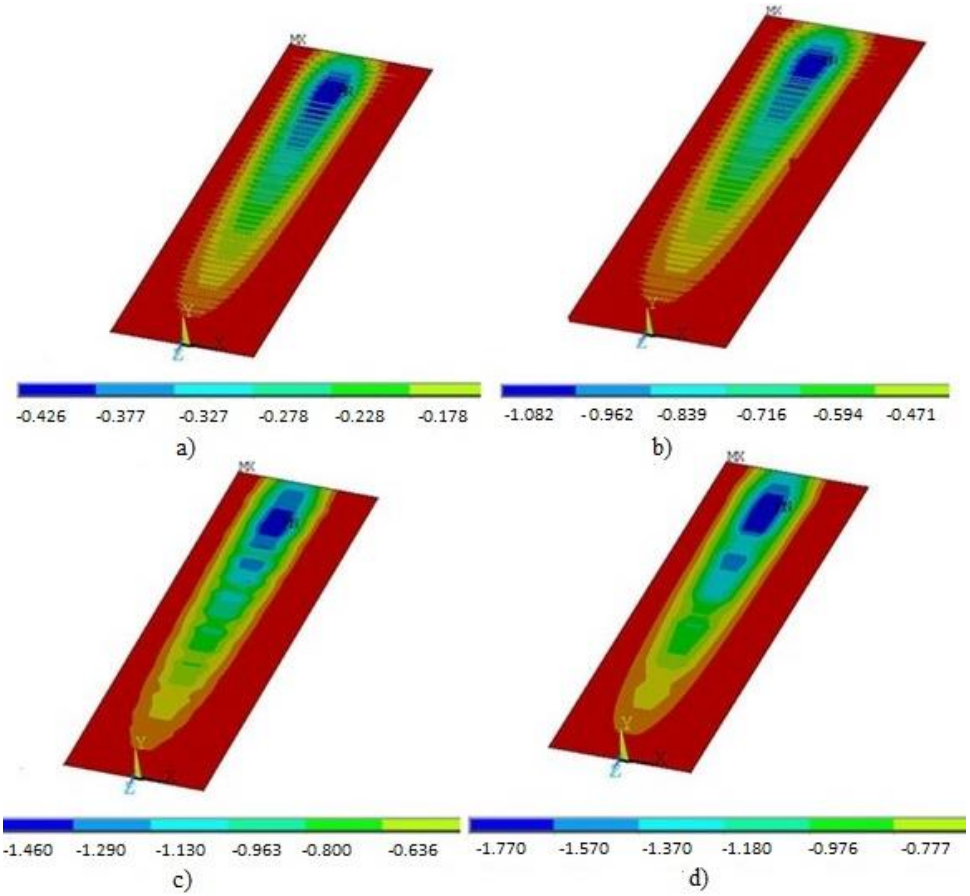

Figure 7. Distribution of metal removal rate on rotational speed (μm x 10^{-3}):
a- 5 rp/s; b- 12 rp/s; c- 16 rp/s; d- 20 rp/s

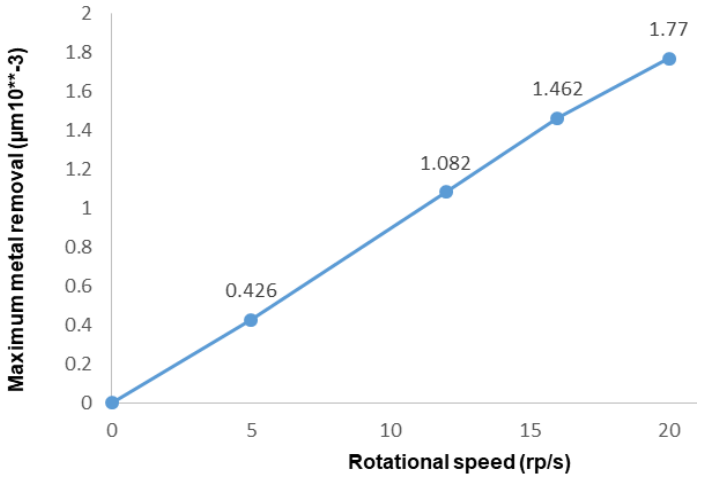

Figure 8. The maximum of metal removal rate depending on the rotation speed

Figure 9 shows the numerical results obtained by performing 4 different processing modes depending on the time. Notice that curves 1 and 2 are smooth curves and increase with time. When machining in this mode, the workpiece surface provides the best of metal removal rate and surface roughness. Curves 3 and 4 show that metal removal values increase over time, but in these modes, instability has occurred, uncontrolled metal removal rate, causing high surface roughness, the authors of [20] noted similar results.

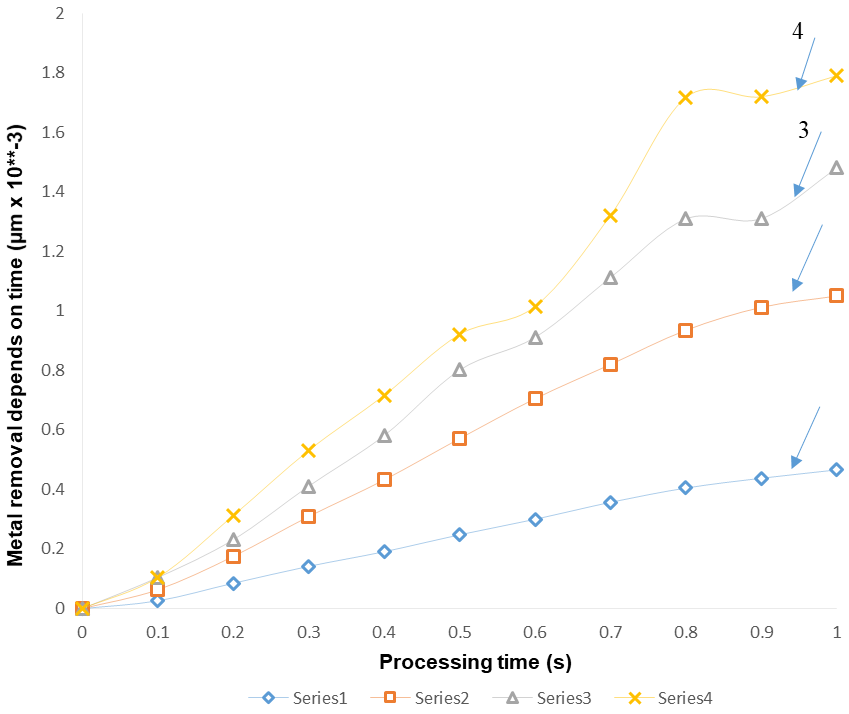

Figure 9. The metal removal rate depending on time
(Series1) 5 rp/s; (Series2) 12 rp/s; (Series3) 16 rp/s; (Series4) 20 rp/s.

Table 2 shows the dependence metal removal rate from the workpiece surface on the uniformly distributed pressure acting on the larger circle of the dead-end cone.

Table 2. Dependence metal removal from the vertical force

Vertical force F (N)	100	280	370	460
Removal of metal from the workpiece surface (μm x 10^{-3})	0.287	1.03	1.37	1.75

5. Experimental research on the CRP

Research the process removal of metal from workpiece surface, we used steel 45 cylindrical samples of size ∅ 15x20 *mm*.

The parameters of abrasive particles and workpieces are shown in Table 1. Also, 3 samples were processed, every 25 minutes, the processing is stopped, the samples are taken out of the chamber, washed, dried and weighed on the analytical balance.

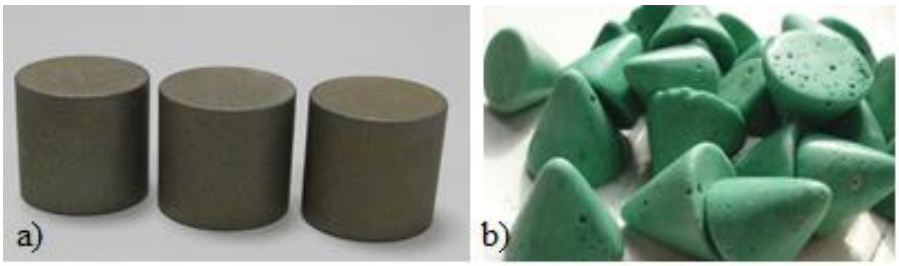

Figure 10. a - workpiece, b - abrasive particles in experiments

The following formula was used to convert to unit gam (g) between the numerical results and experimental modeling:

$$m = V\rho$$

where: m is the metal removal weight, V is the volume lost metal after the machining process ρ is the density.

Figure 11 shows the comparison between numerical simulation results and experimental research metal removal rate of workpiece from the rotation speed.

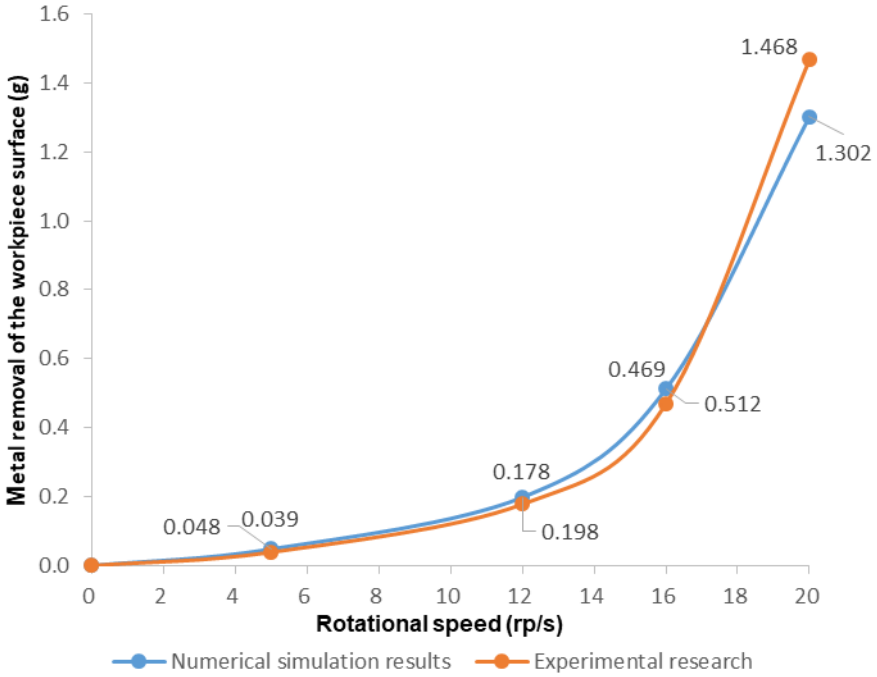

Figure 11. Compare results of numerical models and experimental research

Found that, the results obtained in experimental research are consistent with numerical simulation results.

6. Conclusion

In this research, the process of interaction of an abrasive particle moving at a constant speed with the surface of the workpiece is considered, taking into account the removal of metal in the contact area. The problem of contact interaction was solved in a three-dimensional setting. Finite element models of particles and workpiece were built in the ANSYS package.

When modeling the metal removal process, only the metal removal of the workpiece was taken into account, the abrasive particles had not wear. Calculations of the metal removal depth for various parameters of the technological process are carried out, namely: on the processing time of the workpiece at different values of the angular velocity of the rotor of the installation, the dependence of the maximum metal removal depth of the workpiece is built depending on the angular velocity of the rotor. The distributions of metal removal over the surface of workpiece are calculated. The dependence of metal removal on the force applied to the abrasive particle is investigated. The dependencies constructed in the work make it possible to determine the rational values of the parameters of the CRP process of metal parts.

Acknowledgments

Thank you to the Don State Technical University for their help in conducting experiments and to the Hai Phong University for their help in decoding them.

References

[1] Rowe W B 2014 Principles of Modern Grinding Technology *William Andrew* p 480

[2] Hegadekatte V, Huber N and Kraft O 2005 Finite element based simulation of dry sliding wear *Modelling and Simulation in Materials Science and Engineering* **13(1)** 57-75

[3] Martínez F J *et al* 2012 Finite element implementation and validation of wear modelling in sliding polymer–metal contacts *Wear* **284-285** 52-64
[4] Opoz T T and Chen X 2010 An Investigation of the Rubbing and Ploughing in Single Grain Grinding using Finite Element Method *Paper presented at the 8th international Conference on Manufacturing Research, Durham, UK*
[5] Rezaei A *et al* 2012 Adaptive finite element simulation of wear evolution in radial sliding bearings *Wear* **296** 660-671
[6] Xin L, Gaoliang P and Zhe L 2014 Prediction of seal wear with thermal structural coupled finite element method *Finite Elements in Analysis and Design* **83** 10-21
[7] Tran A *et al* 2019 A computationally efficient machine learning framework for local erosive wear predictions via nodal Gaussian processes *Wear* **422-423** 9-26
[8] Gee M and Nunn J 2017 Real time measurement of wear and surface damage in the sliding wear of alumina *Wear* **376-377** 1866-76
[9] Kragelsky I V, Dobychin M N and Kombalov V S 1982 Friction and wear *Pergamon* p 478
[10] Tamarkin M A, Tishchenko E E and Rozhnenko O A 2013 Metal Removal in the Abrasive Machining of Complex Surfaces *Russian Engineering Research* **33(5)** 25-30
[11] Nguyen V T, Soloviev A N, Tamarkin M A and Panfilov I A 2019 Finite element modeling method of centrifugal rotary processing *Applied Mechanics and Materials* **889** 140-147
[12] Nguyen V T, Soloviev A N and Tamarkin MA 2019 Finite element modeling of thermoelastic contact interaction in the abrasive surface treatment of machine components *Ecological Bulletin of Research Centers of the Black Sea Economic Cooperation* **16(1)** 51-58
[13] Pearson S R 2013 The effect of temperature on wear and friction of a high strength steel in fretting *Wear* **303** 622-631
[14] Wang G, Wang Y and Xu Z 2009 Modeling and analysis of the material removal depth for stone polishing *J. Mater. Process Tech* **209(5)** 2453-63
[15] Qi J, Zhang D, Li S, Chen B 2016 A micro-model of the material removal depth for the polishing process *J. of Engineering Manufacture* **86(9)** 2759-70
[16] Wang G, Zhou X, Yang X, Zhou H and Chen G 2015 Material removal profile for large mould polishing with coated abrasives *Int. J. Adv Manuf Technol* **80(1-4)** 625-635
[17] Bortoleto EM *et al* 2013 Experimental and numerical analysis of dry contact in the pin on disc test *Wear* **301(1)** 19-26
[18] Zhang L, Tam H, Yuan C, Chen Y, Zhou Z 2002 An investigation of material removal in polishing with fixed abrasives. *Proceedings of the Institution of Mechanical Engineers, Part B: Journal of Engineering Manufacture* **216 (1)** 103-112
[19] Arunachalam A P S and Idapalapati S 2019 Material removal analysis for compliant polishing tool using adaptive meshing technique and Archard wear model *Wear* **418-419** 140-150
[20] Suresh R *et al* 2017 Numerical simulation & experimental study of wear depth and contact pressure distribution of aluminum MMC pin on disc tribometer *J. Sci. Materials Today: Proceedings* **4** 11218–28

Modeling of carrot thin layer convective drying process

M Petković[1], V Filipović[2], I Filipović[3], A Lukyanov[4], S Studennikova[4], E A Mardasova[4]

[1] University of Kragujevac, Faculty of Agronomy, Department of Food Technology, Cara Dušana 34, Čačak, Serbia
[2] University of Novi Sad, Faculty of Technology, Department of Chemical Engineering, Bul. cara Lazara 1, Novi Sad, Serbia
[3] SP Laboratory, Industrijska 3, Bečej, Serbia
[4] Don State Technical University, square Gagarin 1, Rostov on Don, Russian Federation

Abstract. The effects of different dehydration temperature (35, 50 and 70 °C) and carrot slice thickness (3, 6, and 9 mm), at the constant (hot) air speed and mass load, on moisture ratio (*MR*) and drying ratio (*DR*) in thin layer convective drying process were investigated. The mathematical models Modified Page, Logarithmic, and Two-term models (for *MR*), and Gauss Modified model (for *DR*) were the most appropriate. Based on the obtained results for the R^2 and *RSME*, the optimal parameters for thin layer drying carrot slices in laboratory dehydrator are dehydration temperature 70 °C, and carrot slice thickness of 3 mm, with the shortest dehydration time of 4.5 hours and the maximum DR of 106.7 g/h.

1. Introduction

Carrot (*Daucus carota* L.) is an essential root vegetable, contains β-carotene and vitamin B complex, vitamins A, C and K, minerals K, Mg, P, Fe and Ca, and many aminoacids [1, 2, 3]. With a high level of phenolics, the color of the carrot shows variations, from ancient black to yellow/orange [4].

The dehydration process includes surface diffusion, liquid/vapor diffusion, and capillary diffusion within the porous region of the dehydrated material. The convective thin layer dehydration process, created by (hot) air fluctuation, is associated with simultaneous heat and mass transfer. Moisture diffuses toward the external surface from the solid sample; the vapor is transferred by convection and heat transfer by conduction [5]. Thin layer dehydration is a single layer drying process, which results in faster moisture evaporation, less nutrient loss, and more straightforward modeling. The predicted drying time of thin layer dehydration is determined by material type, (hot) airspeed, temperature, pressure, material thickness, relative humidity, the size and the shape of the material (sphere, cube, slice, etc.), total energy input, mass load and other parameters [5, 6, 7].

Modeling of thin layer dehydration (drying) process of vegetables, such as carrot, allows us to determine the optimal drying conditions for the specific material and could be described by three groups of mathematical models based on their derivation [6, 8]. The most commonly used models are the semi theoretical and empirical models, while the third group was theoretical models [9]. Semi theoretical models are described within the dehydrating temperature, relative humidity, (hot) air speed, moisture content, material thickness, and size [10].

In this study, the thin layer convective drying process of carrot slices with different thicknesses in a laboratory dryer has been investigated and mathematically modeled.

2. Materials and methods

Thin layer dehydration was conducted in the dehydrator (Colossus CSS 5330 250W, PRC) at temperatures of 35, 50, and 70 °C at atmospheric pressure, to the constant weight. Carrot (collected in the village Striža, 35350 Paraćin, Pomoravlje, Serbia 43°49'57.7"N 21°23'20.3"E) slices with different thickness (3, 6, and 9 mm) were placed in a tray of 320-mm diameter with a mass load of 3 kgm^{-2} (240 g per single tray), and an airspeed of 0,25 ms^{-1} [11, 12]. The moisture ratio (*MR*) is defined according to Eq. (1):

$$MR = \frac{M_t - M_e}{M_o - M_e} \tag{1}$$

M_t, M_o and M_e are the moisture content achieved after dehydration time t, the initial moisture content, and the equilibrium moisture content, respectively. The value of equilibrium moisture content (M_e) usually is deficient and can be deleted from Eq. (1) without a significant change in the amount of *MR*.

The drying kinetic is a change in the total mass loss of fruits ($M_{i-1} - M_i$) in the interval of time between two measurements ($t_{i-1} - t_i$) on a particular tray during the convective drying process (drying ratio, *DR*) [11, 12].

$$DR = \frac{M_{i-1} - M_i}{t_{i-1} - t_i} \tag{2}$$

Origin8 software was used when fitting basic convective drying models to the measured moisture ratios determined accordingly to the Eq. 1&2 [13]. Preliminary tests analyzed in this study proved that the best model (fitting) was obtained by many equation models (as given by Tab. 1-6). The best fitting of a specific model to the experimental data was evaluated using the coefficient of determination (R^2), and the root means square error (*RMSE*). The model fit is better if the value of R^2 is closer to 1, and the *RMSE* value is closer to 0 [11].

3. Results and Discussion

Thin layer drying kinetics (*MR*, *DR*) could be predicted by many mathematical models (Figure 1, Tables 1-6).

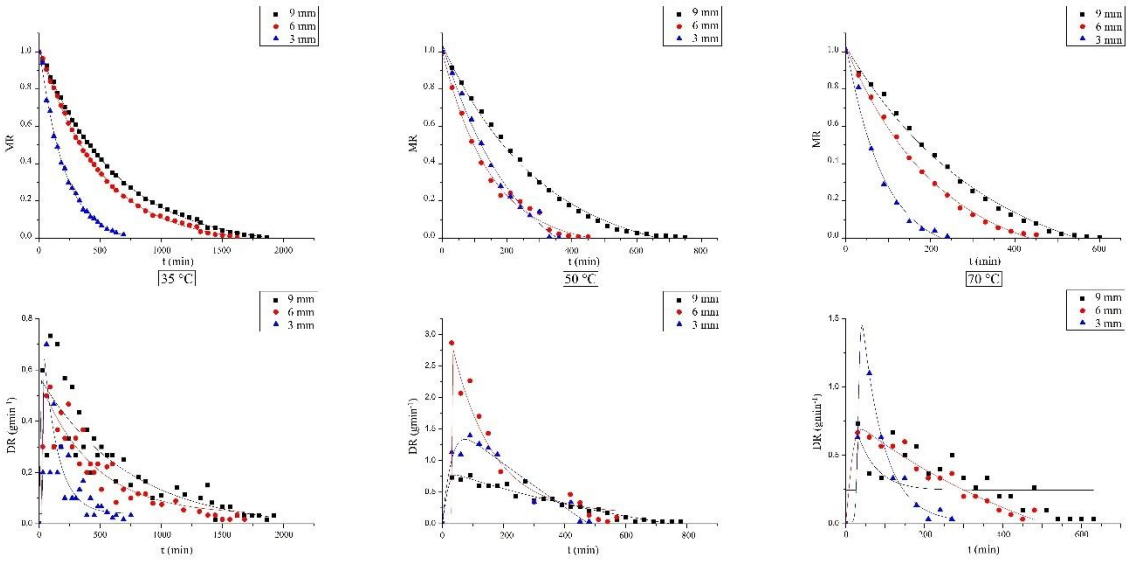

Figure 1. Effects of thin layer drying temperature and carrot slice thickness on the moisture (*MR*) and drying ratio (*DR*)

In the first (initial) stage of thin layer convective drying, it was noticed the fastest water removal, regardless of the dehydration temperature and carrot thickness (Figure 1). The second stage showed the

slower speed of water removal (*MR* curve was less steep) due to a significantly lower drying rate. All dehydration curves had the same shape, with different drying times to a constant mass. Dehydration time depended directly on the temperature of thin layer convective drying and carrot slice thickness. Thus the drying time was 12.5, 28, and 32 hours (35 °C), 8, 9.5, and 13 hours (50 °C), and 4.5, 8, and 10.5 hours (70 °C) for the carrot slice thickness 3, 6, and 9 mm, respectively. If the temperature of the drying process was increased and the carrot slice thickness was decreased, the water diffusion from the interior towards the surface of the carrot slices was faster because the partial pressure of the water vapor on the surface of the carrot slices was increased as well. Increasing the temperature of thin layer dehydration at the constant thickness, the drying time was decreased, and *DR* was increased; increasing the carrot slice thickness at constant dehydration temperature, the drying time was increased, and *DR* was decreased. The maximum *DR* was achieved in the first two hours of the drying process, regardless of the temperature and carrot slice thickness, and at a temperature of 70 °C and a carrot slice thickness of 3 mm was maximum 106.7 g/h.

All mathematical models for *MR* and *DR* were found as an appropriate model for the thin layer dehydration process. According to the R^2 and *RSME*, Modified Page, Logarithmic, and Two-term were selected as the best mathematical models for describing the *MR* (Tables 1-3) and Gauss Modified as the best mathematical model for describing the *DR* (Tables 4-6). Similar models were used to predict the drying behavior of different carrot materials (slices, pomace, etc.) [14, 15, 16]. Increasing the temperature and carrot slice thickness, drying constants:

- *k*, *a*, *b* will be decreased, except *b* which will be raised at temperature 35 °C in Modified Page model for *MR*
- *a*, *b* will be increased, and *c*, *d* will be reduced in Two-term model for *MR*
- *k*, *c* will be reduced, and *a* will be raised in Logathmic model for *MR*
- y_o, *a*, t_0 will be increased, and x_c, *w* will be reduced, except y_o will be reduced at temperature 35 °C in Gauss Modified model for *DR*

Table 1. Model of the moisture ratio (*MR*) applied to the experimental drying curves (35 °C)

		MR							
Model	*Model eguation*	*d (mm)*	*k*	*a*	*b*	*c*	*d*	R^2	*RSME*
Newton	$y=e^{-a\cdot x}$	3		0.0049				0.9944	0.0104
		6		0.0021				0.9967	0.0113
		9		0.0017				0.9963	0.0141
Henderson-Pabis	$y=a\cdot e^{-k\cdot x}$	3	0.0051	1.0371				0.9958	0.0074
		6	0.0022	1.0350				0.9981	0.0062
		9	0.0018	1.0268				0.9972	0.0106
Modified Page	$y=a\cdot e^{-k\cdot x^b}$	3	0.0036	1.0177	1.0600			0.9963	0.0063
		6	0.0013	1.0055	1.0838			0.9992	00027
		9	0.0009	0.9926	1.0949			0.9986	0.0051
Logarithmic	$y=a\cdot e^{-k\cdot x}+c$	3	0.0048	1.0493		-0.0209		0.9962	0.0065
		6	0.0020	1.0532		-0.0311		0.9992	0.0026
		9	0.0016	1.0581		-0.0513		0.9995	0.0018
Two-term	$y=a\cdot e^{-b\cdot x}+c\cdot e^{-d\cdot x}$	3		1.0272	-0.0016	-0.0182	0.0005	0.9959	0.0065
		6		1.0437	-0.0020	-0.0210	0.0002	0.9992	0.0026
		9		1.0626	-0.0047	-0.0346	0.0006	0.9995	0.0017
Midilli-Kucuk	$y=a\cdot e^{-k\cdot x^b}+c\cdot x$	3	0.0038	1.0192	1.0464	0		0.9962	0.0062
		6	0.0015	1.0102	1.0515	0		0.9993	0.0021
		9	0.0015	1.0048	1.0156	0		0.9995	0.0017
Weibull	$y=a-b\cdot e^{-k\cdot x^c}$	3	-0.0004	157.9994	156.9281	0.4472		0.9563	0.0699
		6	-0.0004	138.0355	136.9182	0.4315		0.9676	0.1018
		9	-0.0003	116.9997	115.8892	0.4495		0.9775	0.0799
Parabolic	$y=c+a\cdot x+b\cdot x^2$	3		-0.0033	0.000003	0.9542		0.9834	0.0280
		6		-0.0014	0.0000005	0.9490		0.9879	0.0391
		9		-0.0012	0.0000004	0.9455		0.9915	0.0308

MR – moisture ratio, *d* – carrot thickness, *t* – drying time, *MR* = y, *t* = x

Table 2. Model of the moisture ratio (*MR*) applied to the experimental drying curves (50 °C)

		MR							
Model	*Model eguation*	*d (mm)*	*k*	*a*	*b*	*c*	*d*	R^2	*RSME*
Newton	$y=e^{-a\cdot x}$	3		0.0066				0.9635	0.0504
		6		0.0075				0.9904	0.0135
		9		0.0041				0.9771	0.0575
Henderson-Pabis	$y=a\cdot e^{-k\cdot x}$	3	0.0071	1.0822				0.9695	0.0381
		6	0.0076	1.0153				0.9899	0.0131
		9	0.0044	1.0781				0.9827	0.0416
Modified Page	$y=a\cdot e^{-k\cdot x^b}$	3	0.0007	0.9920	1.4253			0.9926	0.0084
		6	0.0053	0.9975	1.0654			0.9902	0.0119
		9	0.0005	0.9751	1.3638			0.9982	0.0042
Logarithmic	$y=a\cdot e^{-k\cdot x}+c$	3	0.0043	1.3187		-0.2831		0.9893	0.0122
		6	0.0066	1.0450		-0.0474		0.9920	0.0096
		9	0.0033	1.1643		-0.1282		0.9957	0.0099
Two-term	$y=a\cdot e^{-b\cdot x}+c\cdot e^{-d\cdot x}$	3		15.9935	0.0027	-14.9591	0.0025	0.9886	0.0117
		6		17.0046	0.0072	-15.00169	0.0024	0.9921	0.0088
		9		20.0347	0.0021	-19.0025	0.0021	0.9966	0.0076
Midilli-Kucuk	$y=a\cdot e^{-k\cdot x^b}+c\cdot x$	3	0.0007	0.9921	1.4249	0		0.9918	0.0084
		6	0.0075	1.0169	1.0010	0		0.9883	0.0131
		9	0.0005	0.9743	1.3678	0		0.9981	0.0042
Weibull	$y=a-b\cdot e^{-k\cdot x^c}$	3	-0.0002	152.0416	150.9994	0.6606		0.9706	0.0300
		6	-0.0006	103.0431	102.0086	0.4565		0.9683	0.0357
		9	-0.0003	146.9943	145.9136	0.5133		0.9648	0.0774
Parabolic	$y=c+a\cdot x+b\cdot x^2$	3		-0.0051	0.000006	1.0247		0.9908	0.0104
		6		-0.0047	0.000005	0.9343		0.9779	0.0268
		9		-0.0029	0.000003	1.0008		0.9994	0.0014

MR – moisture ratio, *d* – carrot thickness, *t* – drying time, *MR* = y, *t* = x

Table 3. Model of the moisture ratio (*MR*) applied to the experimental drying curves (70 °C)

		MR							
Model	*Model eguation*	*d (mm)*	*k*	*a*	*b*	*c*	*d*	R^2	*RSME*
Newton	$y=e^{-a\cdot x}$	3		0.0131				0.9755	0.0256
		6		0.0060				0.9798	0.0316
		9		0.0045				0.9647	0.0749
Henderson-Pabis	$y=a\cdot e^{-k\cdot x}$	3	0.0138	1.0611				0.9773	0.0208
		6	0.0064	1.0631				0.9837	0.0238
		9	0.0048	1.0827				0.9711	0.0583
Modified Page	$y=a\cdot e^{-k\cdot x^b}$	3	0.0025	1.0113	1.3763			0.9961	0.0031
		6	0.0011	0.9835	1.3227			0.9981	0.0026
		9	0.0003	0.9624	1.4873			0.9966	0.0065
Logarithmic	$y=a\cdot e^{-k\cdot x}+c$	3	0.0113	1.1315		-0.0882		0.9827	0.0135
		6	0.0045	1.1889		-0.1651		0.9971	0.0039
		9	0.0030	1.2732		-0.2453		0.9938	0.0118
Two-term	$y=a\cdot e^{-b\cdot x}+c\cdot e^{-d\cdot x}$	3		29.0855	0.0076	-28.0437	0.0074	0.9814	0.0122
		6		16.6606	0.0029	-15.6393	0.0028	0.9976	0.0030
		9		19.9649	0.0018	-18.9388	0.0018	0.9943	0.0102
Midilli-Kucuk	$y=a\cdot e^{-k\cdot x^b}+c\cdot x$	3	0.0019	1.0082	1.4334	0		0.9958	0.0027
		6	0.0011	0.9824	1.3275	0		0.9979	0.0026
		9	0.0003	0.9610	1.4942	0		0.9964	0.0065
Weibull	$y=a-b\cdot e^{-k\cdot x^c}$	3	-0.0003	212.6791	-211.6471	0.51419		0.9219	0.0509
		6	-0.0002	145.8299	- 144.7839	0.57481		0.9747	0.0317
		9	-0.0002	134.1434	- 133.0868	0.60340		0.9745	0.0460
Parabolic	$y=c+a\cdot x+b\cdot x^2$	3		-0.0097	0.00002	1.01685		0.9878	0.0096
		6		-0.0045	0.000005	1.00254		0.9996	0.0006
		9		-0.0033	0.000003	1.01377		0.9978	0.0041

MR – moisture ratio, *d* – carrot thickness, *t* – drying time, *MR* = y, *t* = x

Table 4. Model of the drying ratio (*DR*) applied to the experimental drying curves (35 °C)

***DR* (g h^{-1})**								
Model	*Model eguation*	*d (mm)*						
			a_0	a_1	a_2	a_3	a_4	R^2
Polynomial	$y = a_0 + a_1 \cdot x + \cdots + a_{n-1} \cdot x^{n-1}$	3	0.0546	0.0089	-0.00007			0.4949
		6	0.1700	0.0033	-0.00001			0.6424
		9	0.2898	0.0021	-0.000008			0.5911
			y_0	a	x_c	w	t_0	R^2
Gauss Modified	$y = y_0 + \frac{a}{t_0} e^{\frac{1}{2}\left(\frac{\omega}{t_0}\right)^2 - \frac{x-x_c}{t_0}} \int_{-\infty}^{z} \frac{1}{\sqrt{2\pi}} e^{\frac{-y^2}{2}} dy,$ $z = \frac{x - x_c}{w} - \frac{w}{t_0}$	3	0.0387	78.7106	32.2716	3.3142	118.3559	0.7103
		6	0.0340	218.1488	29.7467	2.3008	444.0332	0.7289
		9	-0.0161	422.3769	27.1674	3.7384	722.4330	0.7248

DR – moisture ratio, *d* – carrot thickness, *t* – drying time, *DR* = y, *t* = x, *RSME* – not appropriate parameter for the functions

Table 5. Model of the drying ratio (*DR*) applied to the experimental drying curves (50 °C)

***DR* (g h^{-1})**								
Model	*Model eguation*	*d (mm)*						
			a_0	a_1	a_2	a_3	a_4	R^2
Polynomial	$y = a_0 + a_1 \cdot x + \cdots + a_{n-1} \cdot x^{n-1}$	3	0.0859	0.0349	-0.00031	0.000001		0.9065
		6	0.2532	0.0920	-0.00114	0.000005		0.7957
		9	0.1929	0.0115	-0.00008	0.0000002		0.8435
			y_0	a	x_c	w	t_0	R^2
Gauss Modified	$y = y_0 + \frac{a}{t_0} e^{\frac{1}{2}\left(\frac{\omega}{t_0}\right)^2 - \frac{x-x_c}{t_0}} \int_{-\infty}^{z} \frac{1}{\sqrt{2\pi}} e^{\frac{-y^2}{2}} dy,$ $z = \frac{x - x_c}{w} - \frac{w}{t_0}$	3	-12.8160	269.6796	64.5868	53.0170	86.4016	0.9089
		6	0.1646	357.6324	29.1649	30.0002	132.1474	0.7552
		9	-0.7165	1491.1554	1.5684	16.9588	950.6972	0.9391

DR – moisture ratio, *d* – carrot thickness, *t* – drying time, *DR* = y, *t* = x, *RSME* – not appropriate parameter for the functions

Table 6. Model of the drying ratio (*DR*) applied to the experimental drying curves (70 °C)

***DR* (g h^{-1})**								
Model	*Model eguation*	*d (mm)*						
			a_0	a_1	a_2	a_3	a_4	R^2
Polynomial	$y = a_0 + a_1 \cdot x + \cdots + a_{n-1} \cdot x^{n-1}$	3	-0.0277	0.0422	-0.0006	0,000003		0.8188
		6	0.0656	0.0209	-0.0002	0,000001		0.8834
		9	0.1488	0.0094	-0.00007	0,0000002		0.8091
			y_0	a	x_c	w	t_0	R^2
Gauss Modified	$y = y_0 + \frac{a}{t_0} e^{\frac{1}{2}\left(\frac{\omega}{t_0}\right)^2 - \frac{x-x_c}{t_0}} \int_{-\infty}^{z} \frac{1}{\sqrt{2\pi}} e^{\frac{-y^2}{2}} dy$ $z = \frac{x - x_c}{w} - \frac{w}{t_0}$	3	0.0121	100.5063	31.6404	5.0981	56.9168	0.9713
		6	-0.5949	830.2276	30.4374	15.9508	601.0380	0.9440
		9	0.2458	20.5970	29.8533	0.0249	49.7758	0.9329

DR – moisture ratio, *d* – carrot thickness, *t* – drying time, *DR* = y, *t* = x, *RSME* – not appropriate parameter for the functions.

4. Conclusions

The mathematical models Modified Page, Logarithmic, Two-term, and Gauss Modified are the most appropriate models for thin layer drying in the air temperature range of 35 °C to 70 °C, 0.25 ms^{-1} (hot) drying air speed and mass (carrot slices) load 3 kgm^{-2}. Based on the obtained results for the R^2 and *RSME*, the optimal parameters for thin layer drying carrot slices in laboratory dehydrator are dehydration temperature 70 °C, and carrot slice thickness of 3 mm. The third drying parameter that would have a significant impact on thin layer drying process was the drying time, which at 70 °C for a carrot slice thickness of 3 mm was 4.5 hours and a maximum DR ratio of 106.7 g/h.

References

[1] Sharma KD, Karki S, Thakur NS, and Attri S 2012 *J. Food Sci. Technol.* **49** 22-32

[2] Doymaz I 2004 *J. Food Eng.* **61** 359-364

[3] Veleşcu ID, Ţenu I, Cârlescu P, and Dobre V 2013 *Bull. Univ. Agric. Sci. Vet. Med. Cluj-Napoca, Food Sci. Technol.* **70** 129-136

[4] Haq R-u, Kumar P, and Prasad K 2015 *Cogent. Food Agric.* **1** 1096184 1-8

[5] Erbay Z, and Icier F 2010 *Crit. Rev. Food Sci. Nutr*. **50** 441-464

[6] Onwude DI, Hashim N, Janius RB, Nawi NM, and Abdan K 2016 *Compr. Rev. Food Sci. F.* **15** 599-618

[7] Kumar N, Sarkar BC, and Sharma HK 2012 *J. Food Sci. Technol.* **49** 33–41

[8] Markowski M, Stankiewicz I, Zapotoczny P, and Borowska 2006 *Dry. Technol.* **24** 1011-1018

[9] Gómez-Daza JC, and Ochoa-Martínez CI 2016 *DYNA* **83** 16-20

[10] Sonmete MH, Mengeş HO, Ertekin C, and Özcan MM 2017 *Food Measure* **11** 629-638

[11] Petković M, Đurović I, Miletić N and Radovanović J 2019 *Period. Polytech. Chem. Eng.* **63** 600-608

[12] Petković M, Đurović I, Miletić N, Lukyanov AD, Klyuchka EP, Radovanović J, and Donskoy DY 2020 *XXV Symposium on Biotechnology* **2** 563-569

[13] Origin8, Version 2007. OriginLab Corporation, Northampton, MA, USA

[14] Aghbashlo M, Kianmehr MH, Khani S, and Ghasemi M 2009 *Int. Agrophysics* **23** 313-317

[15] Aghbashlo M, Kianmehr MH, Arabhosseini A, and Nazghelichi T 2011 *Czech J. Food Sci.* **5** 528–538

[16] Filipović V, Petković M, Filipović J, Miletić N, Đurović I, Radovanović J, and Lukyanov A 2020 *EEESTS-2020* in press

Study of non-linear synergy control laws on the experimental stand of pneumatic actuators

E Obukhova

Department of Automation of Production Processes, Don State Technical University, Rostov-on-Don, Russia

Abstract. The purpose of this work is to synthesize the laws for controlling the position of the piston of a pneumatic cylinder using the synergetic method of analytical design of aggregated controllers (ACAR), which takes into account the nonlinear dynamics of the system under consideration.

The procedure for the synthesis of synergetic control is based on the introduction of a sequence of invariant manifolds, proceeding from the technological problem of positioning the pneumatic cylinder rod at the required position, and the subsequent step-by-step dynamic decomposition of the original dynamic system.

As a result, the synthesized nonlinear two-channel regulator moves the pneumatic actuator rod to a predetermined position while simultaneously stabilizing the pressure in the drain chamber. Simulation of the system with a regulator showed that the control law obtained in analytical form moves the pneumatic actuator rod to a given position while simultaneously stabilizing the pressure in the drain chamber.

The paper deals with practical research that was carried out at the educational and experimental stand of pneumatic drives for vertical and horizontal movement of the Camozzi company.

1. Introduction

The technological relevance of the task of controlling the pneumatic system is associated with the complexity of precise and smooth braking of the pneumatic drive piston in a given coordinate of its trajectory. This is justified by the fact that the working medium of the system is compressed air, which has the physical property of strong compressibility, as well as significant nonlinearity of the thermodynamic processes occurring in the system.

In the last century, the most used in the control of pneumatic systems were industrial regulators that implement typical linear control laws by adjusting the P, I, D components of the regulator. Linear control laws were distinguished by a simple algorithm for the functioning of regulators, a wide range of their use for most applied problems, and economically low costs for implementing control laws.

In this case, problems arose associated with the complexity of tuning the differential component of the regulator, an increase in the bandwidth and, as a result, the appearance of high-frequency interference, which affected the operation of the system and the appearance of errors [1, 2].

In work [3], studies of the synthesis of linear typical laws of regulation in a pneumatic servo drive were carried out in sufficient detail and clearly, where the disadvantages of the developed PI-controller are given, which are associated with the appearance of overshoot and the occurrence of low-frequency self-oscillations.

The active development of microprocessor technology in recent decades has led to the improvement of the algorithms for tuning PID regulators. At the moment, there are industrial regulators with automatic

tuning of parameters using adaptive algorithms, neural networks, fuzzy logic methods, as well as genetic algorithms [4].

Various modifications of PID controllers have appeared, for example, a controller that performs the task of tracking control based on Petri nets [5] or a controller with two degrees of freedom, which ensures the independence of the solution of two control problems [6]. In addition, additional functions of the controller have been added, namely: alarm functions, control of the rupture of the control loop, going beyond the boundaries of the dynamic range [7]. However, mostly fuzzy logic algorithms are used in systems that are difficult to formalize and mathematical description [8].

In this paper, it is proposed to consider the synthesis of nonlinear synergistic laws for controlling the position of the pneumatic actuator piston by changing the pressures in the filling and exhaust chambers. The synthesis of control laws is carried out using the method of analytical design of aggregated controllers (ACAR) of synergetic control theory [9-11].

2. Pneumatic system dynamics and mathematical model

Figure 1 shows a closed control loop of a pneumatic system including a pneumatic actuator (4), electro-pneumatic valves (3), a programmable logic controller (2) and a displacement sensor (1). The programmable logic controller issues discrete commands in the form of control voltages to the electro-pneumatic valves, which, in turn, change the cross-sectional area of the hole, while controlling the incoming and outgoing air flows.

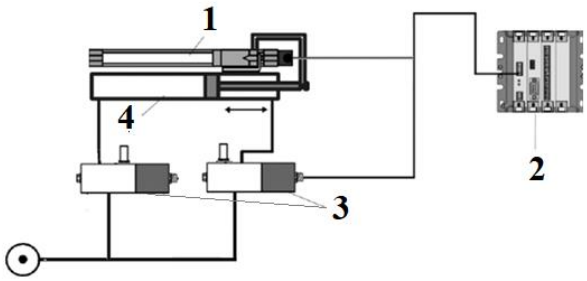

Figure 1. Closed loop control pneumatic system

A pneumatic valve (PR) with electromagnetic proportional control converts the input electrical signal - voltage U_i on the electromagnet of the *i*-th PR into the bore area U_{if}. Thus, the cross-sectional areas U_{1f} and U_{2f} PR are related to the control voltage by the following relationship [10]:

$$U_{if} = g \cdot U_i, \tag{1}$$

where g is the voltage gain $1{,}2 \cdot 10^{-6}$ m^2/V.

The mathematical model of a complex dynamic system, to which the EPS belongs, represents the relationship between the variables that characterize the behavior of the system, based on the equation of motion of the mechanical part of the device, as well as from the equations characterizing the thermodynamic and gas-dynamic processes occurring in the cylinder cavities [12-14]:

$$\begin{aligned}
\dot{x_1}(t) &= x_2;\\
\dot{x_2}(t) &= a_{21} \cdot x_3 - a_{22} \cdot x_4 - a_{23} \cdot x_2 - a_{24};\\
\dot{x_3}(t) &= \left[a_{31} \cdot (x_1 + l_{01})^{-1} \cdot U_{1f} \cdot \sqrt{p_{\text{м}}^2 - x_3^2}\right] - \frac{k x_3 x_2}{(x_1 + l_{01})};\\
\dot{x_4}(t) &= -\left[a_{41} \cdot (a_{42} - x_1)^{-1} \cdot U_{2f} \cdot \left(\frac{x_4}{p_a}\right)^{\frac{k-1}{2k}} \cdot \sqrt{x_4^2 - p_{\text{A}}^2}\right] + \frac{k x_4 x_2}{(a_{42} - x_1)}.
\end{aligned} \tag{2}$$

The following coefficients are introduced into the mathematical model (2) for a simplified representation and further analysis: $a_{21} = \frac{S_1}{M}$; $a_{22} = \frac{S_2}{M}$; $a_{23} = \frac{k_{\text{Втр}}}{M}$; $a_{24} = \frac{P_a(S_1 - S_2)}{M}$; $a_{31} = \frac{k\sqrt{RT_{\text{м}}}}{S_1\sqrt{\xi}}$; $a_{41} = \frac{k\sqrt{RT_{\text{м}}}}{S_2\sqrt{\xi}}$; $a_{42} = (L + l_{02})$.

In the model, the following parameters are designated as: x_1 – coordinate of the piston movement l (m); x_2 – speed of movement of moving masses $V(m/s)$; x_3 – pressure in the filling chamber p_1 $(P\text{a})$; x_4 – pressure in the exhaust chamber p_2 $(P\text{a})$; M – is the mass of the moving part of the piston and rod (0,5 kg); S_1 and S_2 – the effective areas of the piston and rod cavities of the pneumatic cylinder $(8 \cdot 10^{-4}\ m^2\ and\ 6 \cdot 10^{-4}\ m^2)$; $k_{\text{Втр}}$ – viscous friction coefficient $(100\ N \cdot s/m)$; $T_{\text{м}}$ – absolute gas temperature (293 K); k – is the adiabatic index for air (1,4); R – universal gas constant ((287 J)/(kg · K)); l_{01} and l_{02} – initial and final coordinates of the piston position (0.002 m); ξ – is the total resistance coefficient of the chokes included in the line (30); $p_{\text{м}}$ – pressure level at the inlet of the line $(5 \cdot 10^5 P\text{a})$; p_{a} – atmospheric pressure $(10^5 P\text{a})$.

3. Formulation of the control problem and methods of its implementation

One of the initial stages in the synthesis of control laws by the ACAR method is the selection of control objectives - invariants that are set based on the technological problem, taking into account the physical essence of the dynamics of the processes occurring in the system under study [15]. Since the considered electro-pneumatic system (EPS) is described by the equations of the dynamics of the piston motion and the equations of thermodynamic equilibrium, it is necessary to specify technological and thermodynamic invariants that will be the final goal of the state of the system.

According to the control task, pneumatic drives are divided into positional and tracking, thus the ultimate control goal - technological invariants can be: positioning the piston coordinate ℓ to a given position, as well as changing the piston speed V according to a given time law.

Thermodynamic invariants should reflect the "internal" balance of forces of the system, which will ensure the fulfillment of the final - technological control task. Similar forces in the system under study are: the pressure of compressed air in the filling chamber p_1, which is essentially the "working" pressure that affects the movement of the piston, as well as the pressure in the exhaust chamber p_2, a change in which affects the braking of the piston, and therefore its speed movement. Thus, a systemic control model is traced, in which the equilibrium of the system state variables will correspond to certain control objectives.

According to the ACAR method, the number of assigned objective functions must correspond to the number of control channels. The control in the electro-pneumatic system is carried out through two channels:

- control U_{1f} of the incoming mass air flow, forming the pressure p_1 in the filling chamber, is carried out by changing the sectional area f_1 of the PR1 valve;
- control U_{2f} of the mass flow of air leaving the chamber, which is physically reflected in the form of pressure p_2, is carried out by changing the cross-sectional area f_2 of the valve PR2.

In EPS, the created pressure p_1 in the filling chamber is responsible for the starting and further movement of the piston, and the increase in pressure p_2 in the exhaust chamber decelerates the piston.

In back pressure control, the piston is braked by increasing the pressure p_2 by forcing an air flow in the exhaust chamber of the pneumatic cylinder, which is carried out by connecting the pneumatic valve to a source with increased pressure.

Thus, the control task is that it is necessary to synthesize such control actions U_{1f} and U_{2f} providing certain pressure ratios p_1 and p_2, at which the piston of the pneumatic cylinder makes a smooth stop at a given position ℓ.

When the drive stops completely, the pressures in the inlet and outlet chambers will be equal to each other. Thus, during the movement of the stem, the pressure is equalized. It is possible to reflect this alignment by the corresponding invariant manifolds during the synergistic synthesis procedure.

According to the formulated technological problem of positioning the pneumatic cylinder rod at the required position, we introduce the first invariant corresponding to the control goal:

$$x_1 = x_1^*, \tag{3}$$

where x_1 is the current stem position, and x_1^* is the required value.

The second invariant of the system is the condition:

$$x_4 = x_3, \tag{4}$$

at which the pressures in the inlet and outlet chambers are equal to each other.

4. Synthesis of nonlinear synergistic laws of backpressure control

At the first stage of the synthesis, invariant (4) can be taken into account in the introduced set of invariant manifolds:

$$\begin{gathered}\psi_1 = x_4 - x_3 = 0,\\ \psi_2 = x_3 - \varphi_1(x_1, x_2) = 0\end{gathered} \tag{5}$$

In this case, the set of manifolds (5) must satisfy the solution of the system of functional equations:

$$\begin{cases}T_1\dot{\psi}_1(t) + \psi_1 = 0,\\ T_2\dot{\psi}_2(t) + \psi_2 = 0,\end{cases} \tag{6}$$

When the representing point of the system falls into the neighborhood of the intersection of manifolds (5) in the closed system, dynamic decomposition will occur [10] and the behavior of the system will be described by a reduced system of second-order differential equations:

$$\begin{cases}\dot{x}_1(t) = x_2;\\ \dot{x}_2(t) = (a_{21} - a_{22}) \cdot \varphi_1(x_1, x_2) - a_{23} \cdot x_2 - a_{24},\end{cases} \tag{7}$$

where $\varphi_1(x_1, x_2)$ is the so-called internal control of the decomposed system.

To find the internal control φ_1, a manifold is introduced, the structure of which corresponds to the invariant (3):

$$\psi_3 = x_2 - k(x_1 - x_1^*) = 0. \tag{8}$$

For asymptotically stable motion of the system on the attractor to the control goal $x_1 = x_1^*$ invariant manifold (8) must satisfy the solution of the functional equation:

$$T_3\dot{\psi}_3(t) + \psi_3 = 0, \tag{9}$$

The solution of the functional equation (9), taking into account the invariant manifold (8) and the model of the decomposed system (7), determines the structure of the internal control:

$$\varphi_1 = \frac{T_3(a_{23}x_2 + a_{24} + kx_2) - x_2 + k(x_1 - x_1^*)}{T_3(a_{21} - a_{22})}. \tag{10}$$

Expressions of control actions U_{1f} and U_{2f} are determined from the joint solution (5) and (6) taking into account the found internal control (10) and the mathematical model of the object (2). Thus, the control law for the flow area of the valve on PR1 has the form:

$$U_{1f} = \frac{T_2(\lambda_1 + \lambda_2 + \lambda_4) - x_3 + \lambda_5}{T_2\lambda_3}, \qquad U_{2f} = \frac{T_1(\lambda_3 U_1 + \lambda_4 + \lambda_7) - x_4 + x_3}{-T_1\lambda_6} \tag{11}$$

where $\lambda_1 = -\frac{kx_2}{T_3(a_{22}+a_{21})}$; $\lambda_2 = \frac{(T_3k+T_3a_{23}-1)(a_{21}x_3-a_{22}x_4-a_{23}x_2-a_{24})}{T_3(a_{22}+a_{21})}$;

$\lambda_3 = \frac{a_{31}\sqrt{p_{\text{M}}^2 - x_3^2}}{x_1 + l_{01}}$; $\lambda_4 = \frac{kx_3x_2}{(x_1 + l_{01})}$; $\lambda_5 = \frac{T_3(kx_2 + a_{23}x_2 + a_{24}) + k(x_1 - x_1^*) - x_2}{T_3(a_{21} - a_{22})}$;

$\lambda_6 = \frac{a_{41}(x_4/P_m)^{\frac{k-1}{2k}} \cdot \sqrt{(x_4^2 - p_{\text{A}}^2)}}{a_{42} - x_1}$; $\lambda_7 = \frac{kx_4x_2}{a_{42}-x_1}$.

5. Modeling a synergistic control system

Figures 2-3 show the results of modeling a system with the obtained nonlinear control laws (11). During the simulation, the following initial conditions of the system were set: $x_1 = 0\,m$; $x_2 = 0\,m/s$; $x_3 = 10^5\,Pa$; $x_4 = 10^5\,Pa$ and the desired values of piston displacement $x_1^* = 0{,}1m$ and pressure in the exhaust chamber $x_4 = x_3 = 10^5 Pa$. Controller parameter values: : $T_1 = T_2 = T_3 = 0{,}001\,s$, $k = -1$. The position of the rod x_1 reaches the desired displacement value in a time of 4 seconds (Fig. 2), which indicates the adequacy of the synthesized control law, as well as its asymptotic stability. The graph of the change in the speed of the rod x_2 of the pneumatic cylinder shows that the speed, increasing to the maximum at the beginning of the movement of the pneumatic cylinder, decreases, taking on a zero value when the specified displacement is reached. The pressure in the filling chamber x_3 at the end of the movement cycle coincides with the pressure in the exhaust chamber x_4 (Fig. 3), which was set when forming the invariant (4).

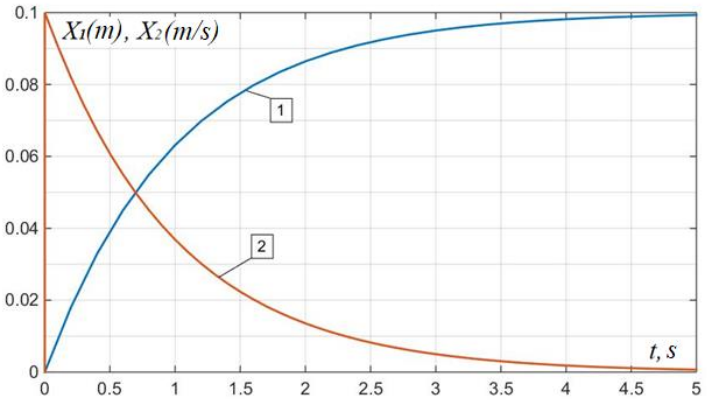

Figure 2. Graphs of changes in the phase variables of the EPS with coordinated control: 1) piston displacement (X_1, m); 2) piston speed ($X_2,\ m/s$)

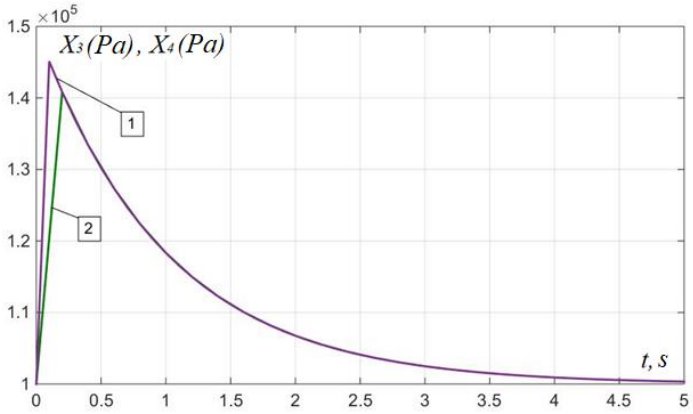

Figure 3. Graphs of changes in the phase variables of the EPS: 1) change in the pressure in the inlet chamber (X_3, Pa); 2) change in pressure in the exhaust chamber (X_4, Pa)

The analysis of the graphs of the transient processes presented in Figure 4 shows that when the back pressure is controlled, the opening area of the valve that admits the compressed air flow U_{1f} is larger, this leads to an increase in the working pressure X_3 (Figure 3). At the same time, due to a smooth decrease in the cross-sectional area of the exhaust valve U_{2f}, where air is supplied with excess pressure, the pressures in the filling chambers X_3 and exhaust X_4 are stabilized to the value of the atmosphere (Figure 3).

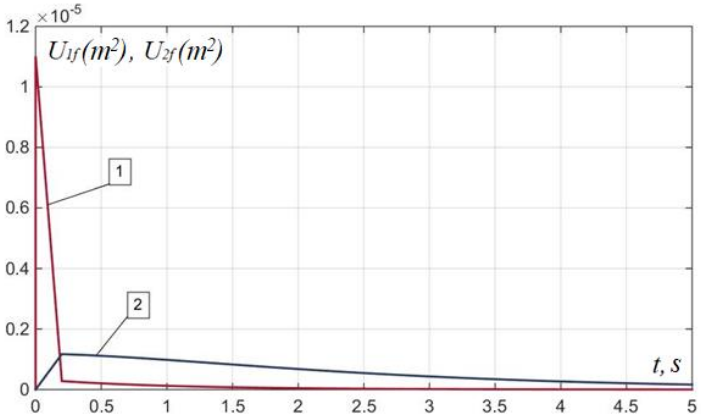

Figure 4. Graphs of transient processes with coordinated control:
1) cross-sectional area PR1 U_{1f}, m^2; 2) the cross-sectional area of the PR2 (U_{2f}, m^2)

Figure 5 shows the voltage graphs for PR1 and PR2. The value of the control voltage U_1 equal to ≈ 10 V corresponds to the full opening of the PR1 port and its connection to the compressed air supply line, this happens in a fraction of a second, then the port is completely closed. A positive voltage value U_2 corresponds to the connection of the PR2 port with a source of increased pressure, which can be either a power source or a special pneumatic device. In this case, the exhaust chamber is filled with compressed gas to a certain limit.

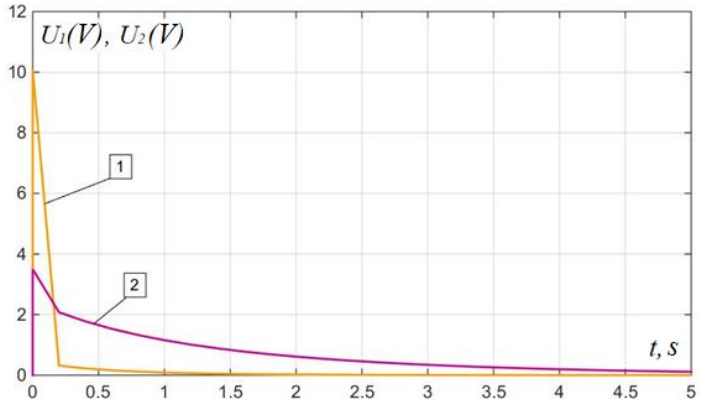

Figure 5. Graphs of voltages on PR with coordinated control: 1) voltage on PR1 (U_1, V); 2) voltage across PR2 (U_2, V)

This back pressure control is often used in pneumatic automation due to the possibility of smooth movement of the stem in real experimental conditions.

6. Experimental study of the obtained control laws on the bench of pneumatic drives of the Camozzi Company

The obtained control laws were empirically tested on the educational and experimental stand of the EPS, a photo of which is shown in Figure 6. Below are the main functional elements of the EPS stand:

- Pneumatic drives of horizontal and vertical movements Camozzi QCT2A032A200 series (1);
- LRWA2-36-2A00 series proportional pneumatic distributors of incoming and outgoing compressed air flows Camozzi (2);
- Programmable logic controller PLC Aries 150;
- MPS-128TSTP0 series magnetic piston position sensor.

This ERS stand is used for educational purposes to study the horizontal and vertical positioning of pneumatic drives, with proportional distributors of compressed air flows that provide braking and stopping of the drive at a given coordinate.

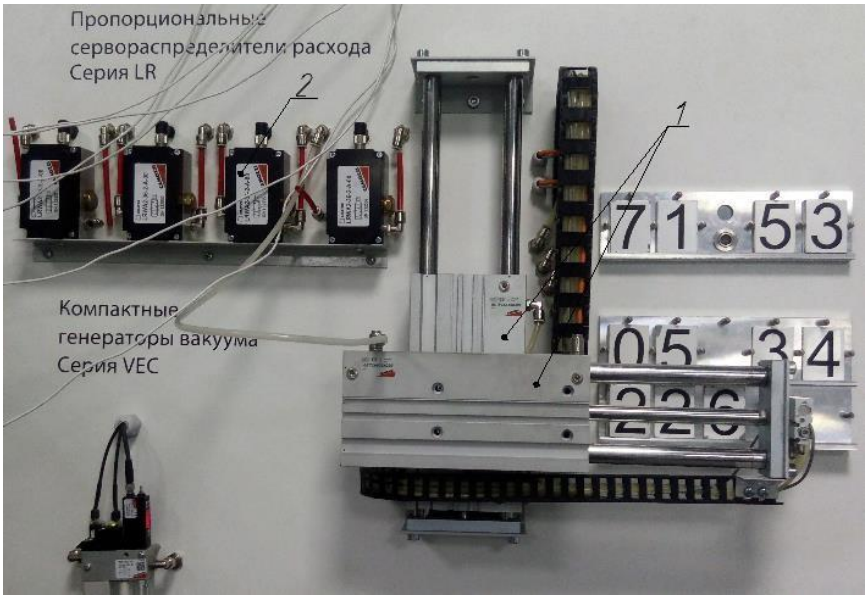

Figure 6. Educational and experimental stand for horizontal and vertical positioning of pneumatic drives

To graphically represent the electrical and pneumatic relationships between the functional elements included in the EPS, a schematic pneumatic diagram of the stand was implemented in the environment of the computer-aided design package "Compass", shown in Figure 7.

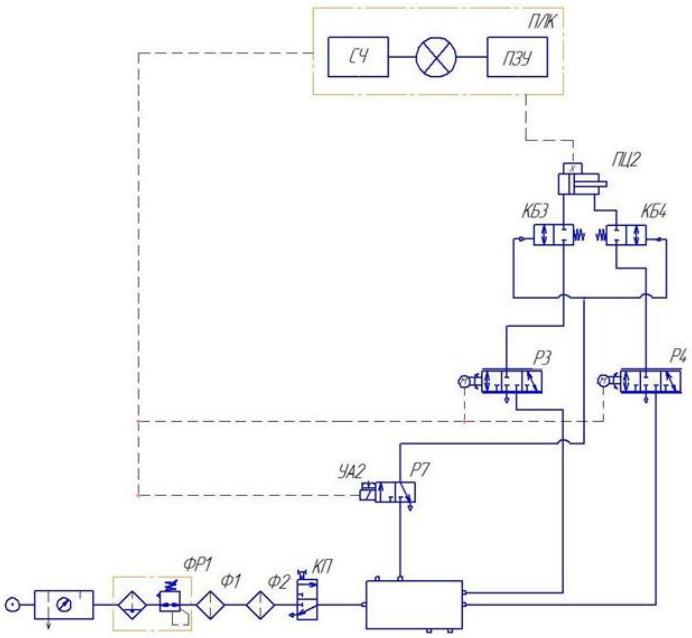

Figure 7. Schematic pneumatic diagram of the stand with horizontal positioning of the pneumatic drive

Designing, debugging and loading a program into a PLC is carried out in the CoDeSys industrial automation software development environment in one of five IEC 61131-3 programming languages. In this case, the graphical language of functional block diagrams FBD (Function Block Diagram) was chosen as the programming language, which allows for an accessible and visual representation of the processing and transmission of the control signal from the PLC to the PR, in the form of chains from certain elements-program components (POU).

Figure 8 shows the simultaneous digital tracing of two control signals - voltage U1 on PR1 (green graph) and voltage U2 on PR2 (red graph).The abscissa axes represent the cycles of the controller, while in the emulation mode in the CoDeSys software debugging environment, the PLC cycle is 55 milliseconds. Thus, 500 PLC cycles in terms of the operating time of the controller is 27.5 seconds. The ordinate axes represent the values of the output voltages - the unit is Volt.

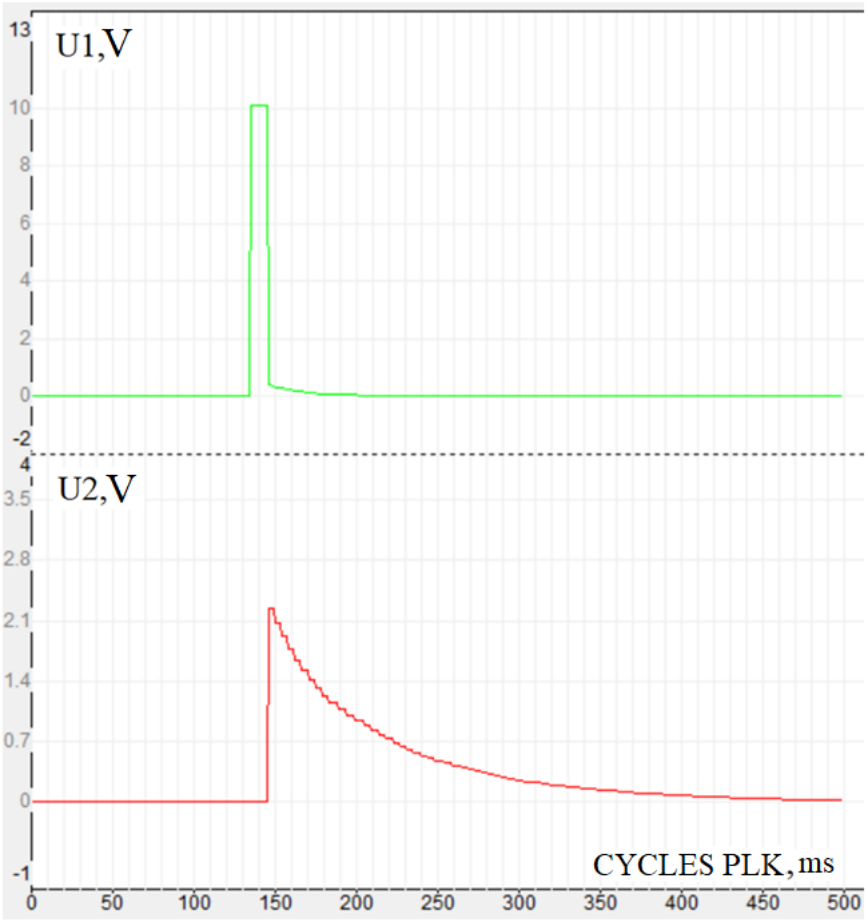

Figure 8. Graph of control voltages U1 on PR1 and U2 on PR2 for the case of back pressure control in the exhaust chamber

As seen from Fig. 8, the controller begins to generate a control signal voltage U1 at about 140 cycle, while the voltage signal U2 at about 150 cycle, which corresponds to a time of 8.25 seconds. This natural time delay of milliseconds is due to the fact that first the PR1 is triggered to the compressed air inlet into the filling chamber, and then the valve on the PR2 opens.

At the same time, the presence of initial controller cycles in which there are no values of control signals is due to the delay time, which includes: the operating system delay when the programming environment is connected to the controller, physical delays in the propagation of signals to the PLC inputs, as well as the delay in reproducing digital tracing in the controller emulation mode.

Judging by the voltage graph U2, (Fig. 5), the time during which the PR2 valve will completely close is 13.75 seconds, while, according to the graph obtained in the course of mathematical modeling in the Maple package, the time for the complete closing of PR2 is 6-8 seconds (Fig. 5). This is due to the mathematical idealization of obtaining analytical data, as well as the lack of accounting, when modeling processes, the time for receipt, processing and issuance of a control signal by the controller.

7. Conclusion

In general, comparing the graphs of control actions - voltages U1 and U2, obtained using the synergistic ACAR method and the graphs of signals of discrete outputs of the controller in Fig. 8, which are control actions on the valves PR1 and PR2, one can definitely state the identity of these graphs, which indicates the high accuracy of the analytically synthesized nonlinear synergistic control laws.

References

[1] Piavchenko T.A. Regulator without a differential component for managing complex industrial objects / Izvestia SFU. Technical science. 2012. № 2 (127). P. 135-141.

[2] Vostrikov A.S. The problem of synthesis of controllers for automation systems: state and prospects / Avtometriya. 2010. T. 46. № 2. *P*. 3-19.

[3] Kharchenko A.N. Improving the accuracy and speed of industrial mechatronic electro-pneumatic servo drives on the basis of hardware and software integration of mechatronic components: diss .. to-that tech. Sciences: 05.02.05 Moscow state. technologist. un-t. - Moscow, 2010.

[4] Tan K.K., Putra A.S. Drives and control for industrial automation. Part of the advances in industrial control: Servo hydraulic and pneumatic drive. – P.: Springer London. – 2011. – 386 p.

[5] Vázquez C.R., Gómez-Castellanos J.A., Ramírez-Treviño A. Petri Nets Tracking Control for Electro-pneumatic Systems Automation // Informatics in Control, Automation and Robotics. Lecture Notes in Electrical Engineering (2018), — Vol.613, p. 503-525, Springer, Cham.

[6] Jamian S., Salim S.N.S., Junoh S.C.K., Kamarudin M.N., Abdullah L. Nonlinear Proportional Integral (NPI) Double Hyperbolic Controller for Pneumatic Actuator System // Advances in Electronics Engineering. Lecture Notes in Electrical Engineering (2020), — Vol. 619, p. 221-229, Springer, Singapore.

[7] Yin Y. High Speed Pneumatic Theory and Technology. Control System and Energy System. P.: Springer Singapore, 2020. —386 p.

[8] Ren H., Fan J. Adaptive backstepping slide mode control of pneumatic position servo system // Chinese journal of mechanical engineering. – Vol. 29. – 2016. – P. 1003-1009.

[9] Kolesnikov A.A. Synergetic methods for managing complex systems: the theory of system synthesis. - Ed. 2nd. —M.: Librokom, 2012. - 237 p.

[10] Kolesnikov A.A., Introduction of synergetic control / Proceedings of the American Control Conference, 2014, pp. 3013-3016.

[11] Kolesnikov A. and etc., Modern Applied Control Theory: Synergetic Approach in Control Theory. Taganrog: Publishing house of TRTU, 2000.

[12] Popov D.N. Mechanics of hydraulic and pneumatic drives: Textbook. For universities. 2nd ed. stereotype. - M.: Publishing house of MSTU im. N.E. Bauman, 2002. 320 p.

[13] Obukhova E.N., Grishchenko V.I., Dolgov G.A. Formalization of dynamic model of pneumatic drive with variable structure / Conference Paper in MATEC Web of Conferences. 2018. C. 02022.

[14] Obukhova E. Synergistic method of pneumatic drive control / Conference Paper in AIP Conference Proceedings 2188(1):030004, December 2019.

[15] Veselov G.E., Popov A.N., Radionov I.A., Mushenko A.S. Adaptive power saving control for traction asynchronous electrical drive: Synergetic approach / ENERGYCON 2014 - IEEE International Energy Conference, pp. 1446-1453.

Influence of the structure of coolant flows on the temperature profile by phases in a water heating dryer

J E Safarov, Sh A Sultanova, G T Dadayev and Sh U Zulpanov

Food engineering laboratory, Tashkent state technical university,
Tashkent, Uzbekistan

Abstract. This research of the profiles of the temperature field of the process of convective drying of plant raw materials. Mathematical modeling of the temperature field on the basis of the three-phase flow structure was carried out. In a wide range of variation of design and operating parameters (from 50 to 150%) their nominal values are identified. A qualitatively new picture of the temperature field was found, which is expressed in the fact that, depending on the contact conditions of the gas and solid phases and the relative air flow, the temperature profile on the pallets can have both positive and negative slopes. The sensitivity of this relationship, formalized in the form of axonometric graphs and the corresponding families of isolines on the plane of variable factors, is shown. Criteria for non-uniformity of temperature profiles across pallets (dispersion of material temperature and angle of inclination of the approximating straight line with fixed values of the average temperature of the substance) are proposed. The procedure for solving the optimization problem on the conditions of the minimum criterion for the unevenness of the material profile is justified when the average temperature of the material specified in accordance with the conditions of the process schedule is restricted as equality. For the conditions of solving an optimization problem by the criterion of minimizing the square of the slope, minimization of the material temperature by the dispersion gives minor deviations:gotimal=0.3833, kmgoptimal=0.0124. For r=0 gives optimal, gotimal=1.2857, kmgoptimal=0.032, and for r=0.725, we get gotimal=0.3832, kmg=0.0126, which is in good agreement with the nomogram.

1. Introduction

In the world, 40% of medicinal raw materials are obtained from plants for the pharmaceutical industry. At the same time, today about 60% of medicines consist more or less of plant substances. In accordance with this, the process of manufacturing the necessary plant materials for the production of pharmaceuticals has the scientific and practical importance of introducing modern and intensive methods of technology as well as devices.

Drying is one of the most advanced and commonly used preservation methods. It consists of the removal of moisture from the product, resulting from the simultaneous process of heat and mass transfer through the use of heat. The drying process can affect (partially or completely) product quality in terms of sensory, nutritional and functional characteristics. For a successful drying operation, it becomes necessary to choose a suitable technique, especially for valuable products, including medicinal plants.

Scientists study determination of temperature and concentration of a vapor-gas mixture in a wake of water droplets moving through combustion products [1], hydrodynamics and mass-transfer characteristics analysis of vapor–liquid flow of dual-flow tray [2], mechanism of heat transfer in

heterogeneous droplets of water under intense radiant heating [3], a model of heat and mass transfer in gas phase in axial and turbulent dispersed annular flows [4].

In the work of A.B. Sukhotskii et al. [5], an experimental study and generalization of data on the intensified convective heat transfer of single-row finned tube bundles in air flow was investigated. The results of an experimental study of the intensified convective heat transfer of a single-row beam consisting of bimetallic finned tubes in a stream of heated air are presented as dependencies of the Nusselt number on the Grashof and Reynolds numbers.

In the work of V.A. Sychevsky et al. [6] investigates the aerodynamics of an experimental stand for drying the Institute for heat and mass transfer named after A.V. Lykov of the National Academy of Sciences of Belarus. The geometric structure of the wood drying bench is complex. Therefore, the calculation of the aerodynamics of the drying agent in the chamber is carried out on the basis of the ANSYS Fluent 14.5 software package. On the basis of the calculations performed, an analysis of the structure of the flow of the drying agent was carried out, and stagnant zones were revealed. It is established that the wood-drying bench does not work in the optimal aerodynamic mode. In [6-7] it was shown that vortices are formed at the front and rear edges of the boards arranged in a line in a stack, which adversely affect the aerodynamics of the flow and the processes of heat and mass transfer in the stack. In the drying chamber, the air flow overcomes a number of local resistances caused by the presence of a heat exchanger, a fan, a stack, and the geometry of the dryer (changing the direction of air flow).

Experimental investigation of bound and free water transport process during drying of hygroscopic food material [8]. It is interesting to highlight that the cell membranes rupture at different stages of drying rather than collapsing at one time. The membrane collapse depends predominantly on the penetration rate of heat energy and the pressure gradient between intracellular and intercellular environments. All test results suggest that most of the cell membranes rupture at the middle stage of drying where the moisture content is about 2-4 kg/kg (db.). Furthermore, the moisture distribution profile confirmed that some moisture remained around the centre of the dried sample although the surface of the sample became dry [8].

In the study mathematical simulation of convective drying: spatially distributed temperature and moisture in carrot slab [9], experimental study and analysis on heat transfer effect of far infrared convection combined drying [10], next generation drying technologies for pharmaceutical applications [11], heat and mass transfer parameters in the drying of cocoyam slice [12], mathematical modelling of convective drying of feijoa (Acca sellowiana Berg) slices [13], wheat convective drying: An analytical investigation via Galerkin-based integral method [14], research authentication of the medical plants by multispectral analysis [15], development of helio of a drying equipment based on theoretical researches of heat energy accumulation [16].

In the article [17] study, intensification of the plant products drying process by improving solar dryer design, as a result, graphical interpretations of isolines of drying agent flow are obtained and location of passive zones in the dryer chamber are identified. Uniformity of the temperature zones in the chamber is ensured by supplying additional drying agent into the passive zones. Temperature values at various levels of the drying chamber are experimentally obtained. Results for drying cut-up mass of vegetables and fruits are presented.

2. Methods

Development of a water-heating convective drying equipment for medicinal herbs with their medicinal properties at low temperatures without using electricity, providing the ability to predict changes in temperature and moisture content in the layer of dehydrated material, as well as knowledge of the time required to obtain the desired final values of temperature and moisture content. The solution of these problems determines the prospects of the drying process with obtaining a quality product at low cost and loss of raw materials.

The basis for obtaining a quality product is technological systems that have a complex structural and functional organization. As a rule, the control objects in these systems are specific technological processes.

High-quality drying of thermolabile products related to medicinal herbs should be carried out strictly controlling and regulating all process parameters, including the temperature of the dehydration objects. It is not experimentally possible to determine the temperature fields in the hovering fine particles with a significant intensity of the drying process. As a consequence, it is obvious that it is necessary to implement a mathematical model of heat and mass transfer in order to calculate temperatures at each spatial point of sputtered particles of dehydrated materials during the drying process in order to identify and implement rational modes and control product quality. When introducing rational modes and structures of drying apparatus, in the first place, it is necessary to ensure in practice the conditions for obtaining the required technological characteristics of the material being dried.

In Figure 1 the experimental values of the temperature profile along the height are presented, where medicinal plants were used as the test material.

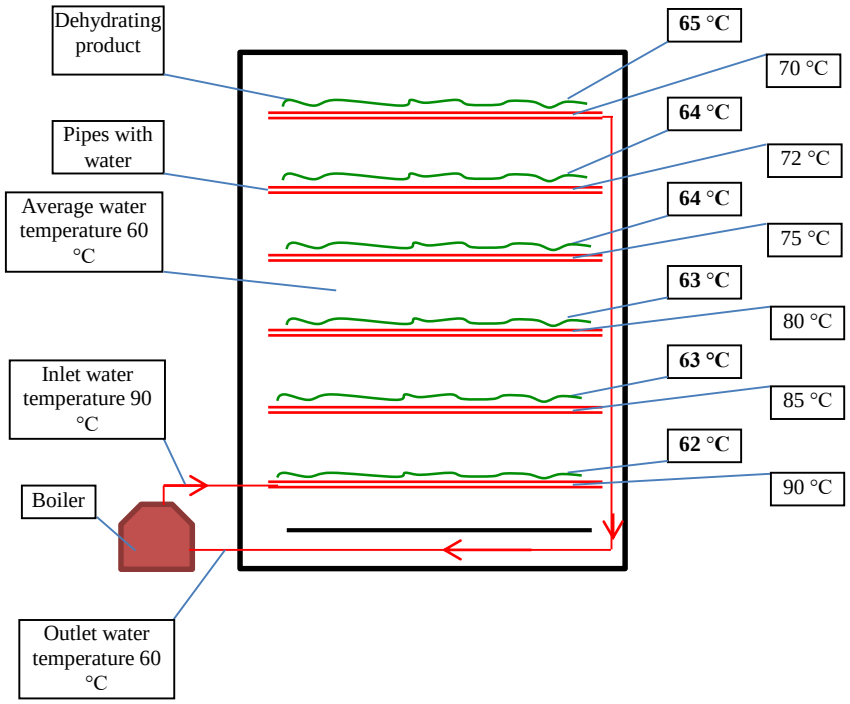

Figure 1. Scheme of the direct-flow movement of heat flows

Identification of the model on the experimental data shows that:

1. The model faithfully reflects a decrease in water temperature in height and an increase in air temperature approximately exponentially.

2. The distortion of the calculated and experimental curves even for the last stages of the process indicates the need to include in the model a parameter for the heat outflow from the section due to evaporation.

At this stage, the countercurrent flow and heat flow pattern is also checked (Figure 2).

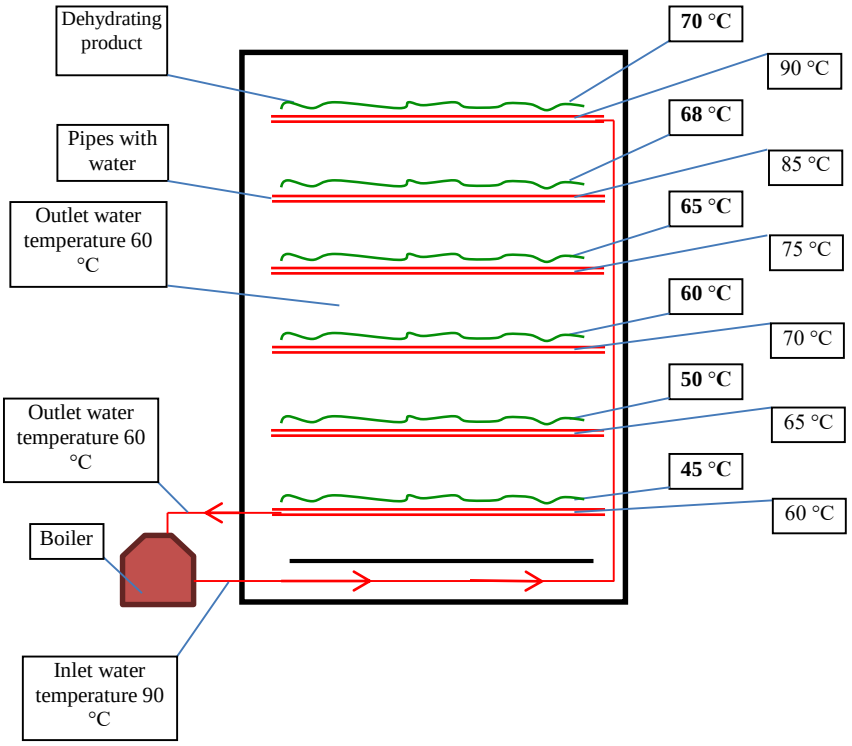

Figure 2. Organization of the circuit of the flow of heat flow

Based on the analysis of the technological situation conducted by the author, as variable factors, we choose the relative air flow through the drying unit and the coefficient expressing the intensity of heat exchange between the gas phase and the material being dried. At the same time, the remaining parameters expressing design and operational features are assumed to be unchanged. The range of variation is taken equal to 0.5 to 1.5 of their nominal values.

3. Results and discussion

Accepted nominal values of parameters:

gnom=.38;
Tn0=100;
Tg0nom=20;
knmnom=.025;
kmgnom=.0135;
kngnom=.1;

The individual results shown in Figure 3-4 show that the temperature profile of the material along the height can be both increasing and decreasing.

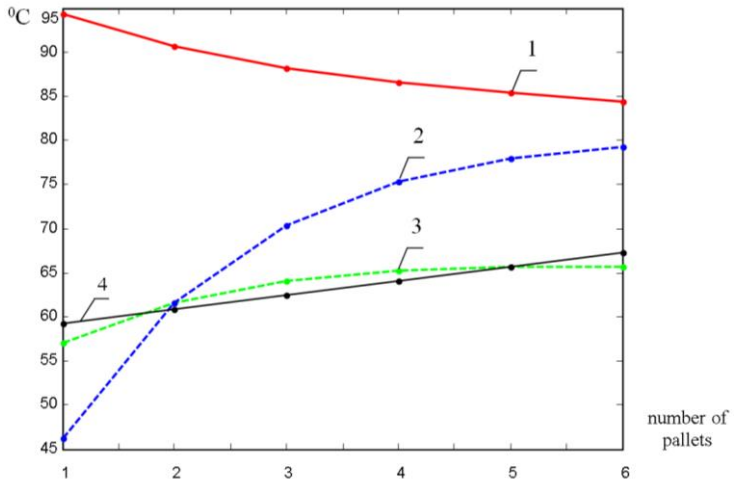

1 is the temperature of the coolant; 2-temperature gas phase; 3-temperature profile for the material; 4-results of theoretical studies.

Figure 3. Mode with a positive slope of the temperature profile

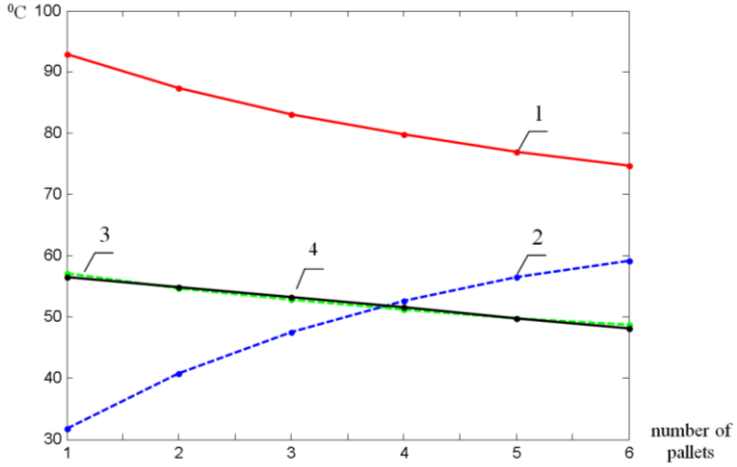

1-temperature of the coolant; 2-temperature gas phase; 3-temperature profile for the material; 4-results of theoretical studies.

Figure 4. Mode with a negative slope of the temperature profile

As a criterion for the uneven distribution of temperature across the pallets, along with the average temperature (tsr), we take the variance of the temperature tdisT and the proportionality coefficient in the linear approximation formula for the temperature profile.

The results of studies in these ranges are shown in Figure 5-8.

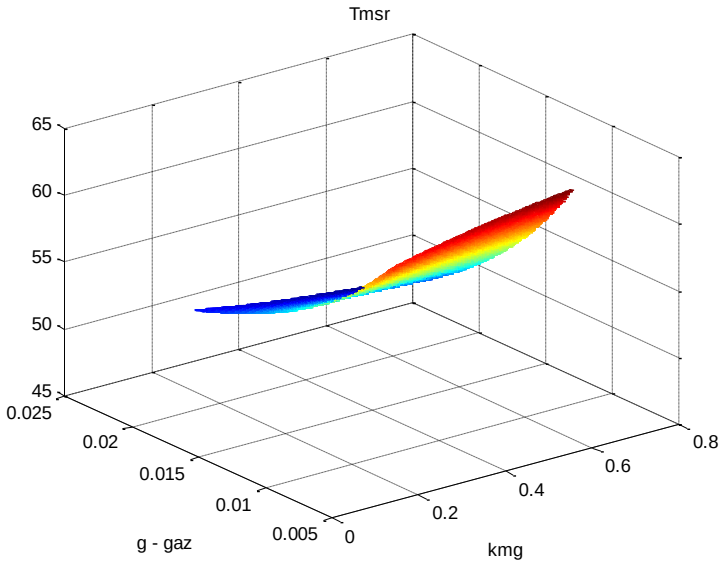

Figure 5. Average values of material temperature by pallet

As a result of the experiments, criteria were found for the non-uniformity of the temperature profiles across the pallets of the material temperature dispersion and the slope angle of the approximating straight line for fixed values of the average temperature of the substance.

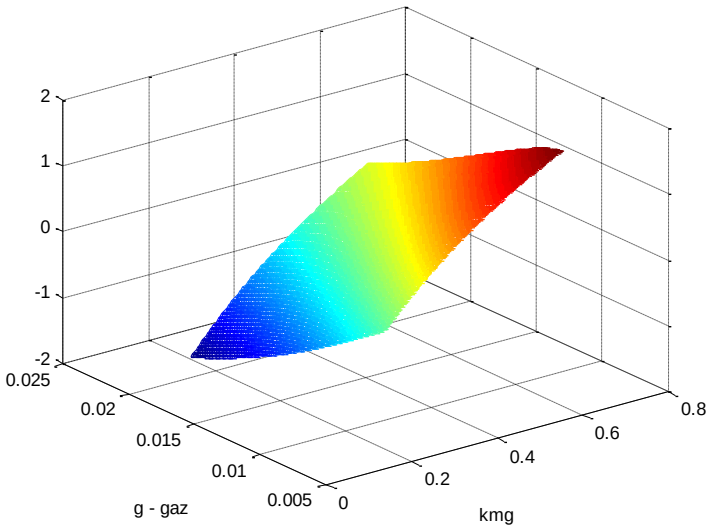

Figure 6. Surface expressing positive and negative values of the slope of the temperature profile

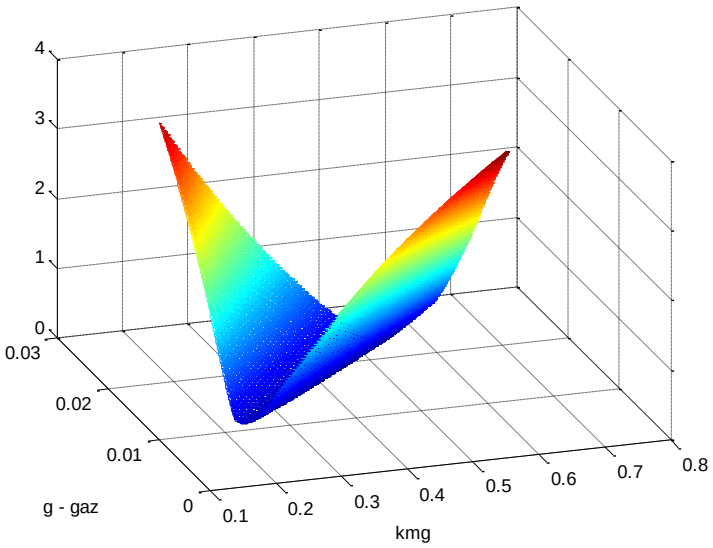

Figure 7. The surface of the criterion $T_{dispersiya}$

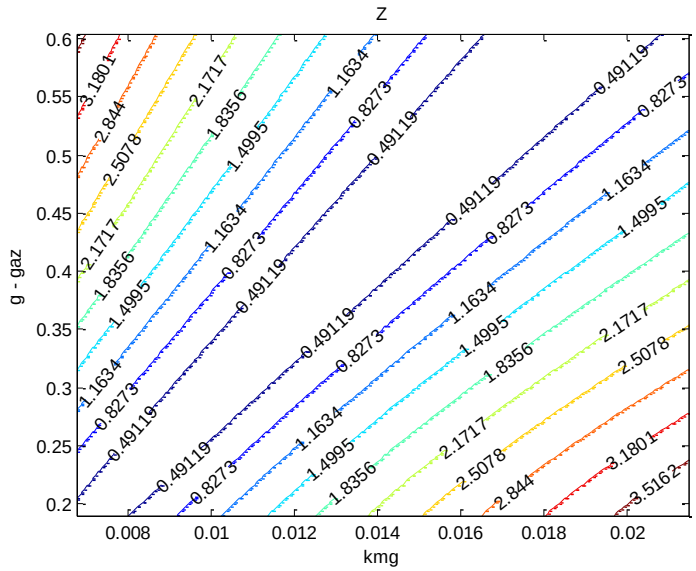

Figure 8. Isolation $T_{dispersiya}$

3.1. Development of recommendations for optimal process management

The relationship between the criteria for uneven profiles has a partial interdependence. In particular, the temperature dispersion and the angle of inclination of the aligned profile are almost correlated, but unlike the angle of inclination, which may be zero, which is ideal for drying, from the point of view of the same profile along the pallets, the dispersion has a certain hysteresis zone. This is consistent with the fact that there always remains some residual irregularity, which can be observed with an increase in the number of scans (Figure 9).

In practice, designing not only dryers, but also devices with interphase exchange, it becomes necessary to select variable optimizable variables, based on the requirements of equality of the average temperature to a certain value specified in accordance with the technological regulations and to ensure minimum slope.

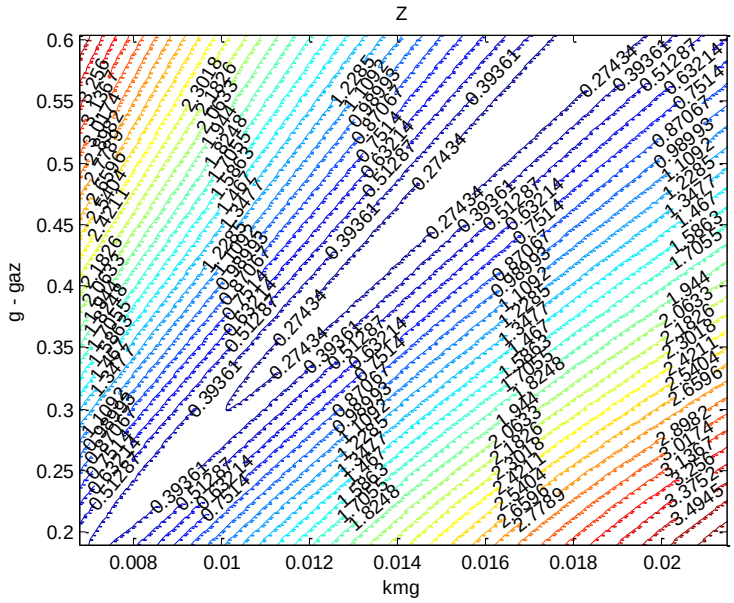

Figure 9. Zone with minimum bottom for dispersion values

Sometimes a situation arises of the need to provide some compromise between these indicators, in terms of energy efficiency. To solve these problems, the nomogram presented in Figure 2 is proposed as an engineering method. ten.

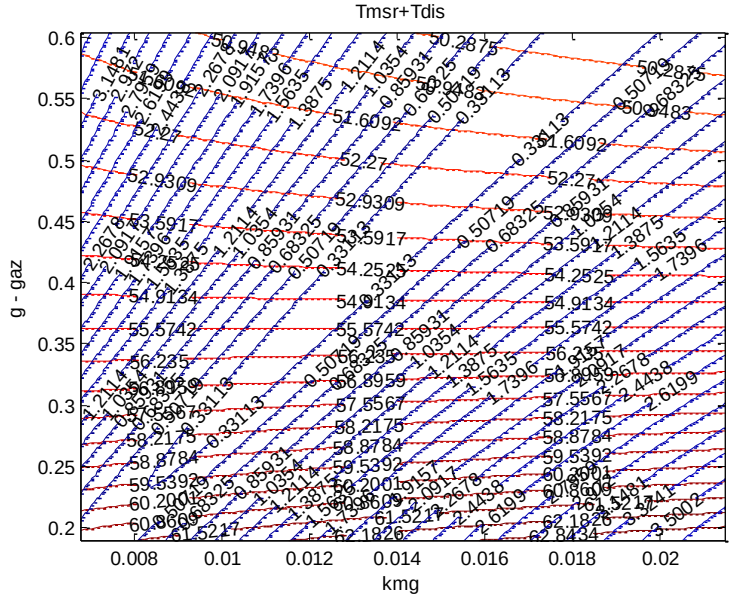

Figure 10. Nomogram for calculating a given temperature profile

In addition, the nomogram allows you to select the appropriate values of the parameters of the technological mode and the conditions of the contact phase (with increasing or decreasing nature) (Figure 11).

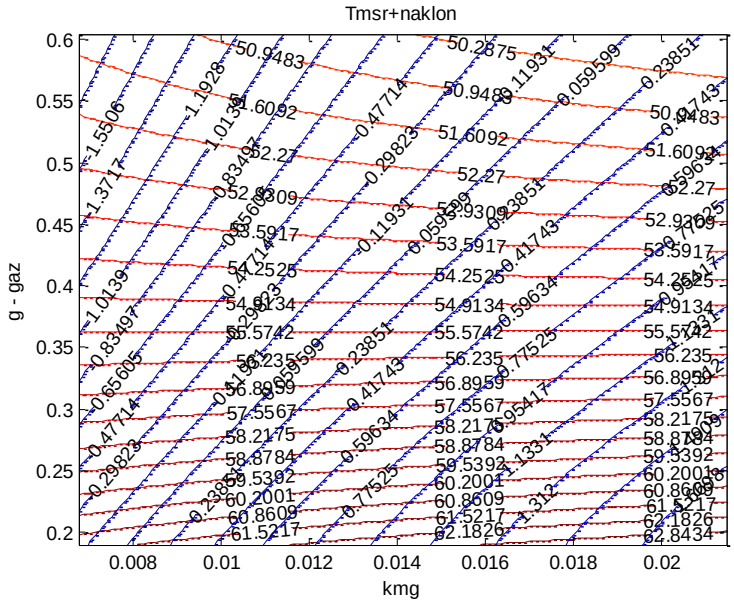

Figure 11. Nomogram to determine the optimal Tsr and slope (bmnk).

For a more accurate calculation of the optimal parameters, an algorithmic procedure was developed on Matlab:

```
global n Tn0 Tg0 knm kng r Tt
n=6;
gnom=.5;
Tn0=100;
Tg0=20;
knm=.025;
kmgnom=.015;
kng=.1;
r=0;
za0=[3.78 -.0182];
za2=fminsearch(@z170401L,za0,[0 1e-7 1e-7 5000])
za2=fminsearch(@z170401L,za2,[0 1e-7 1e-7 5000])
function FF=z170401L(aaa)
global n Tn0 Tg0 knmkng r Tt
g=aaa(1);
kmg=aaa(2);
parametri=[n Tn0 Tg0 g knmkmgkng r];
Tt=sushilka3f(parametri);
Tm=Tt(2,:);
Tmsr=mean(Tm);
disTm=std(Tm);
np=1:6;
pr=Tm;
np100(1:n)=ones;
      NP=[np' np100'];
bmnk=regress(pr',NP);
prmnk=NP*bmnk;
naklon=bmnk(1);
```

L=(naklon)^2+100*(Tmsr-85)^2;
FF=L;

The program implements the solution of the problem of finding the conditional extremum with the restriction in the form of equality to the average temperature given by the method of penalty functions.

The above procedure for r=0 gives optimal, gotimal=1.2857, kmgoptimal=0.032, and for r=0.725, we get gotimal=0.3832, kmg=0.0126, which is in good agreement with the above nomogram (Figure 10).

The above-mentioned relationship between the criteria of unevenness is clearly manifested when comparing optimization options according to different criteria. For the conditions of solving an optimization problem by the criterion of minimizing the square of the slope, minimization of the material temperature by the dispersion gives minor deviations:gotimal=0.3833, kmgoptimal=0.0124.

4. Conclusion

Mathematical modeling of the temperature field on the basis of the three-phase flow structure was carried out. In a wide range of variation of design and operating parameters (from 50 to 150%) their nominal values are identified.

A qualitatively new picture of the temperature field was found, which is expressed in the fact that, depending on the contact conditions of the gas and solid phases and the relative air flow, the temperature profile on the pallets can have both positive and negative slopes. The sensitivity of this relationship, formalized in the form of axonometric graphs and the corresponding families of isolines on the plane of variable factors, is shown.

Criteria for non-uniformity of temperature profiles across pallets (dispersion of material temperature and angle of inclination of the approximating straight line with fixed values of the average temperature of the substance) are proposed.

The procedure for solving the optimization problem on the conditions of the minimum criterion for the unevenness of the material profile is justified when the average temperature of the material specified in accordance with the conditions of the process schedule is restricted as equality.

References

[1] Antonov D V, Kuznetsov G V and Strizhak P A 2016 Determination of temperature and concentration of a vapor–gas mixture in a wake of water droplets moving through combustion products. *J. Engin. Therm.*, vol. 25, No 3, pp. 337–351.

[2] Zhang L, Li Z, Yang N, Jiang B, Pavlenko A N and Volodin O A 2016 Hydrodynamics and mass-transfer characteristics analysis of vapor–liquid flow of dual-flow tray. *J. Engin.Therm.*, vol. 25, No. 4, pp. 449–463.

[3] Vysokomornaya O V, Piskunov M V, Kuznetsov G V and Strizhak P A 2017 Mechanism of heat transfer in heterogeneous droplets of water under intense radiant heating. *J. Engin.Therm.*, vol. 26, No. 2, pp. 183–196.

[4] Laptev A G and Lapteva E A 2018 A model of heat and mass transfer in gas phase in axial and turbulent dispersed annular flows. *J. Engin. Therm.*, vol. 27, No. 1, pp. 45–50.

[5] Sukhotskii A B and Marshalova G S 2018 Intensified convection heat transfer of single-row bunch of finned tubes in an air stream: experimental study and generalization of the obtained data. *Energetika. Proc. CIS Higher Educ. Inst. and Power Eng. Assoc.*, vol. 61, No 6, pp. 552–563.

[6] Sychevsky V A, Chorny A D and Baranova T A 2016 Optimization of aerodynamic conditions of the chamber drier operation. *Energetika. Proc. CIS Higher Educ. Inst. and Power Eng. Assoc.*, vol. 59, No 3, pp. 260–271.

[7] Sun Z F 2001 Numerical simulation of flow in an array of in-line blunt boards: mass trans- fer and flow patterns. *Chem. Engin. Sci.*, vol. 56, No 3. pp. 1883–1896.

[8] Khan M I H, Mark W R, Szilvia A N, Joardder M U H and Karim M A 2017 Experimental investigation of bound and free water transport process during drying of hygroscopic food material. *Inter. J. Ther. Sci.*, vol. 117, pp. 266-273.
[9] Barati E and Esfahani J A 2012 Mathematical simulation of convective drying: spatially distributed temperature and moisture in carrot slab. *Int J Therm Sci.,* vol. 56, pp. 86-94.
[10] Liu Chunshan Sh T, Yang Sh, Wu W and Chen S 2017 Experimental study and analysis on heat transfer effect of far infrared convection combined drying. *2017 International Conference on Smart Grid and Electrical Automation (ICSGEA)*. China.
[11] Walters R H, Bhatnagar B, Tchessalov S, Izutsu K I, Tsumoto K and Ohtake S 2014 Next generation drying technologies for pharmaceutical applications. *J. Pharm. Sci.* vol.103, No. 9, pp. 2673-2695.
[12] Ndukwu M C, Dirioha C, Abam F I and Ihediwa V E 2017 Heat and mass transfer parameters in the drying of cocoyam slice. *Case Studies in Ther.Engin.,* vol. 9, pp. 62-71.
[13] Castro A M, Mayorga E Y and Moreno F L 2019 Mathematical modelling of convective drying of feijoa (Acca sellowiana Berg) slices. *J.Food Engin.,* vol. 252, pp. 44-52.
[14] Santos J P S, Santos I B, Pereira E M A, Silva J V, and Barbosa De Lima A G 2015 Wheat convective drying: An analytical investigation via Galerkin-based integral method. *Defect and Diffusion Forum.*, vol. 365, pp. 82-87.
[15] Safarov J E, Sultanova Sh A, Dadaev G T and Samandarov D I 2019 Method for drying fruits of rose hips. *International Journal of Innovative Technology and Exploring Engineering.* Volume-9, Issue-1, P.3765-3768.
[16] Safarov J E, Sultanova, Sh A and Dadaev G T 2020 Development of helio of a drying equipment based on theoretical researches of heat energy accumulation. *Energetika. Proc. CIS Higher Educ. Inst. and Power Eng. Assoc.*, vol. 63, No 2. Pp.174-192.
[17] Khazimov M Zh, Khazimov K M, Urmashev B A, Tazhibayev T S and Sagyndykova Zh B 2018 Intensification of the plant products drying process by improving solar dryer design. *J. Engin. Therm.*, vol. 27, No. 4, pp. 580–592.

Design embedded control system based controller of the quasi time optimization approach for a magnetic levitation system

C X Nguyen [1,*], T D Pham[2], A D Lukynov[3], P C Tran[1] and Q D Truong[4]

[1]Department of Automation and Computing Techniques, Le Quy Don Technical University,Hanoi, Vietnam
[2]Department of Technology, Equipment and Aerospace, Le Quy Don Technical University, Hanoi,Vietnam
[3]Department of Automation of production processes, Don State Technical University, Rostov-on-Don, Russia
[4]Department anti-aircraft missiles, Faculty of Control Engineering, Le Quy Don Technical University, Hanoi, Vietnam

*Corresponding author: nguyenxuanchiem83@gmail.com

Abstract. The magnetic levitation system is a typical system with many successful applications in practice. Due to the inherent instability and strong open-loop nonlinearity of the MLS, a controller is used to control the stability of the magnetic levitation system. With the rapid development of embedded systems, the intelligent digital control has begun to replace conventional analog control technology creating a new approach to the control MLS. This paper proposes a hardware module for the MLS based on a digital signal processor combined with a fast acting controller to ensure system stability even with incomplete mathematical models. The simulation and experimental results are compared with the linearized feedback control law. Finally, experiments are carried out to test the practical feasibility of the proposed control laws in the MLS embedded control system. The system, with the recommended controller, well responds to the tolerances allowing for stable system working. Both simulation and test results are included in this paper to show that the fast acting suboptimal controller has the advantage of being more durable and less complicated to perform in MLS control applications.

1. Introduction

Magnetic levitation systems are practical importance in many engineering systems such as high-speed magnetic cushion passenger trains, frictionless bearings, vibration isolation of sensitive machinery, lifting molten metal in furnaces Induction heating and lifting of metal plates during the manufacturing process. Maglev systems can be classified as suction or propulsion systems based on the magnetic force. These types of systems are often open-loop unstable and are described by highly nonlinear differential equations that make it difficult to control these systems. Therefore, designing the lifting position control system since the mathematical model is incomplete and the parameters are not defined is an important task.

In recent years, many works have been published, many studies on the control of MLS. In the work [3] shows the rules of controlling MLS using the PID controller. Control law of LQR on real model is realized in real system and published in the project [1]. The paper [2] presents the method of adaptive

sliding mode control based on a neural network for magnetic levitation systems. In [6], controller using stable neural network of nonlinear system for MLS system is presented. In addition, the adaptive controllers studied in [4,5] have fairly good results. In [7], optimal controllers based on dynamic adaptation are proposed and tested. Various methods for PI controller are designed and tested [8]. As far as we know, all of the above works are using a complete mathematical model to design control laws.

In this paper, a position stabilization embedded controller based on the AVR microcontroller for MLS is designed. The mathematical model of the system is set up, but when the current equation is removed, there is no current measuring sensor on the real model. The suboptimal nonlinear control law is designed by incomplete system math model and fast acting virtual system thanks to the microbial transformation. Finally, the simulation and testing results related to the actual efficiency and performance of the proposed method are examined. As far as we know, this is the first effective control method based on the fast-acting suboptimal algorithm and embedded hardware system for the MLS, delivering good results to achieve the desired location with allowed error for the system to work. The main contributions of this work are summarized as follows: (1) The proposed microcontroller based embedded system using state machine can significantly improve the system's processing speed; (2) Verified by the test results, the proposed fast-acting sub-optimal nonlinear controller could achieve better steady-state control performance while the system is not full sensor.

The remainder of the paper is organized as follows: Part 2 presents the design of a magnetic levitation system embedded control model. Part 3 presents the mathematical model of the magnetic levitation system. Part 4 presents the design of the fast acting suboptimal control rule for the magnetic levitation system when the mathematical model is incomplete. Section 5 presents simulation and experimental results and a related discussion. Finally, Section 6 gives the conclusions and further work of this paper.

2. Design of embedded levitation controller

The MLS embedded control system is a dedicated digital control system, able to meet stringent requirements for multifunctional, cost, volume, power consumption and other metrics. It can control, monitor and manage MLS with the features of small software code, high automation and fast response, especially suitable for real-time and multi-tasking systems. The embedded control system is divided into data acquisition, signal conditioning and output control. The embedded control system consists of sensors, power amplifiers and power circuits. In addition, the system is also connected to a computer via RS232 port to manage and monitor the system via software. Based on the analysis above, the overall design of the embedded magnetic control system based on the AVR microcontroller is illustrated in Figure 1.

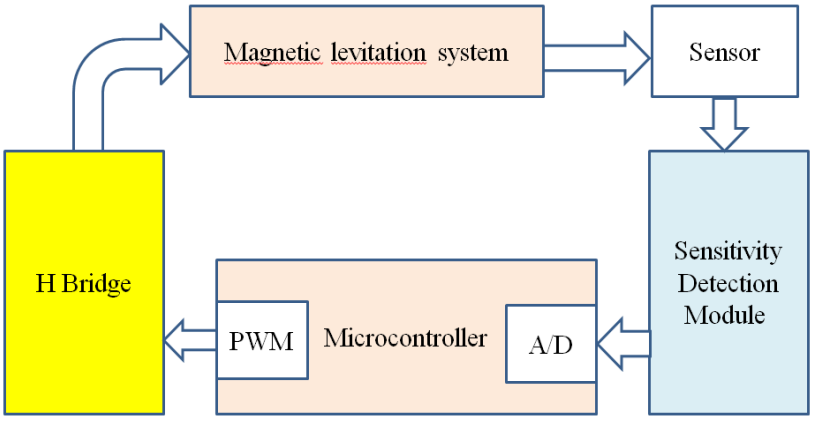

Figure 1. Overall structural block diagram of embedded control system for MLS

The basic control requirements are as follows: initial spacing is 20 mm and desired position 0 mm. The requirement for a stable suspension of the desired position is 0 ± 3 mm. Based on the above control requirements, the analysis and design of each modular circuit of the embedded controller are carried out as follows: Arduino Mega 2560 Embedded Board with ATmega2560 Chip, 256 KB flash memory, SRAM 8KB, 4 KB EEPROM and using quartz with 16 MHz oscillation frequency. The 49E Hall sensor is a linear magnetic field sensor for a small range of variation and the output voltage level is proportional to the strength of the magnetic field applied to its sensitive end.

3. Mathematical models of the MLS

The model of the object levitation system in the magnetic field is as shown in Figure 2. In which, u(t) is the object control input, changed to control the electromagnetic force F to raise or lower the ball compared to the electromagnet. The distance between the ball and the magnet is determined by the Hall distance sensor.

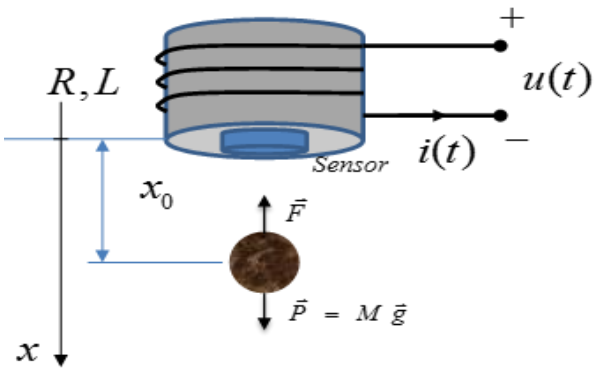

Figure 2. Model of magnetic levitation system

Based on [12, 13], the mathematical model of the levitation system in magnetic field has the following form:

$$\begin{cases} \dfrac{dx}{dt} = v \\ \dfrac{Mdv}{dt} = Mg - C\left(\dfrac{i}{x}\right)^2 \\ Ri + \dfrac{d\left(L(x)i\right)}{dt} = u \end{cases} \quad (1)$$

where, x is the position of the marble (m); v is the speed of the ball (m / s); i is the current through the coil (A); u is the supply voltage to the coil (V); R, L are the resistance and inductance of the electromagnet coil (Ω, H) respectively; C is the magnetic force constant (Nm2/A2); m is the mass of the marble (kg) and g is the acceleration of gravity (m /s2).

From the model of the magnetic levitation system, it is clear that the system has two mechanical and electrical systems, where the response of the electric system always has a higher frequency or time of inertia much less than that of the mechanical part. In the control model in the small range the oscillation velocity of the ball is low, so it can be considered that in the controllable range the voltage is proportional to the current, that means u (t) = K i(t). Where K is a constant determined by experiment. Therefore, when the real system has no current sensor, the mathematical model can be described of the system as follows:

$$\begin{cases} \dfrac{dx}{dt} = v \\ \dfrac{Mdv}{dt} = Mg - \dfrac{CK^2}{x^2}u^2 \end{cases} \tag{2}$$

From equation (2) see that the control signal is always positive. So the magnetic force is only directed upwards to ensure balance with the gravity of the ball. Set the state variable as follows: $x_1 = x, \quad x_2 = v.$

$$\begin{cases} x_1^{'} = x_2 \\ x_2^{'} = g - \dfrac{CK^2}{Mx_1^{\,2}}u^2 \end{cases} \tag{3}$$

The control goal is to keep stability around the desired position when there is variation of the model parameter, as well as the effect of noise.

4. Synthesis of controller based on a virtual system of the quasi time optimization approach

With this approach, it is possible to solve the problem of synthesizing control laws for the wide nonlinear object class, in which this control law brings many advantages to the system, such as optimal fast-approaching effect, asymptotic stability. and sustainable [9-11,14,15].

Synthesis of the fast-acting suboptimal control rule for the magnetic levitation system (3) for the position of the ball. The virtual system is selected as (7) then the steel ball position will be guaranteed to be placed in the preset position.

$$\begin{cases} \dot{y}_1 = -v_1 \dfrac{y_1 - y_{sp}}{\sqrt{\left(y_1 - y_{sp}\right)^2 + \varepsilon_1^{\,2}}} + y_2 \\ \dot{y}_2 = -\dfrac{y_2}{\varepsilon_2} \end{cases} \tag{4}$$

From the system of equations (4) conducting the micro-embryo transformation with y1 = x1, we get the sub-optimal fast-acting control according to the desired variable (5).

$$u(t) = \sqrt{\frac{M}{C}x_1^2\left(g + \frac{x_2}{\varepsilon_2} + v_1\left(\frac{1}{\varepsilon_2} + x_2\right)\frac{(x_1 - x_d)}{\left((x_1 - x_d)^2 + \varepsilon_1^{\,2}\right)^{0.5}} - 2v_1\frac{(x_1 - x_d)^2}{\left((x_1 - x_d)^2 + \varepsilon_1^{\,2}\right)^{1.5}}\right)} \tag{5}$$

5. Simulation and experimental results

5.1 Simulation results

Simulation was performed on Simulink-Matlab software. The model parameters are set as follows: weight of steel ball M = 0.001 (kg); coil resistance R = 2.4 (Ω); inductance L1 = 0.015 (H); magnetic force constant C = 1,4x10-4 (Nm2/A2); gravitational acceleration g = 9.8 (m/s2); and K = 0.05;

In Figure 3 and 4 shows the position response and velocity of the affected member when moving from initial position xb = 20 (mm) to position x = 10 (mm) and standing still. From the graph we see with the proposed control law having better response in terms of time and no overshoot in the position channel than with the linear feedback control law. But on the velocity channel, the period of change is smaller, but the response time is better.

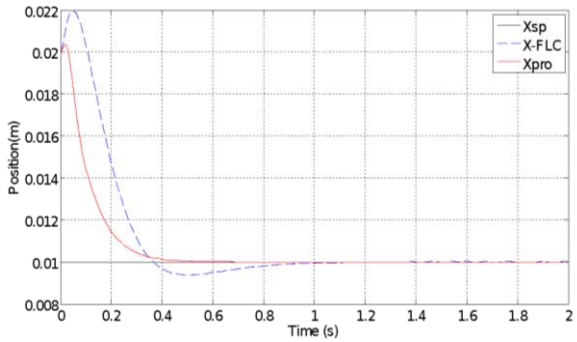

Figure 3. Response to the position of the ball

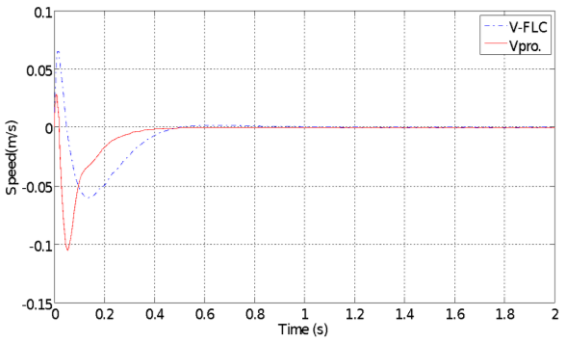

Figure 4. Response to the velocity of the ball

5.2 Experimental results

In order to demonstrate the physical performance of the control laws of the proposed method, experiments were conducted on the embedded control system of the magnetic levitation test system. The model has been independently developed at the "Control Systems" laboratory at Le Quy Don University by our team. The model of the magnetic levitation system covering the embedded controller, the power supply, the magnetic sensor, the H-bridge circuit, and the magnetic suspension system, as shown in Figure 5. The proposed control algorithm can be programmed in microcontroller of embedded system.

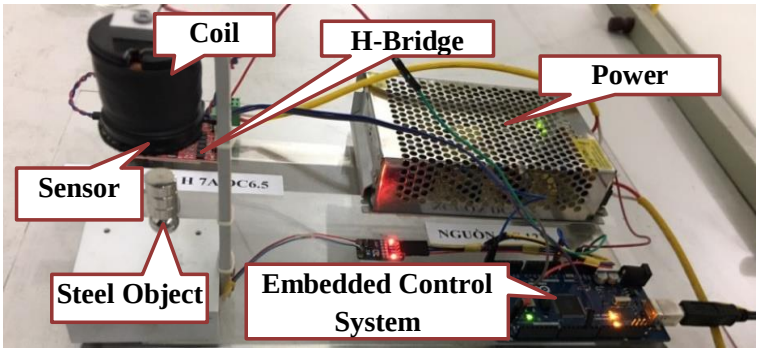

Figure 5. Magnetic levitation test with embedded control system.

To show the good control effect of this method, we proceeded the following method. Allow the magnetic carrier to shake from the desired position later during stabilization always have an impact on the carrier. Experimental results are shown in Figure. 6. From the experimental results, the system works stably. The system transition time is 0.25 (s) from 0.8 (cm) to the zero position. But with the control method using PWM pulses, during the stabilization process, the magnetic object always fluctuates around the original coordinates with very small amplitude 1(mm).

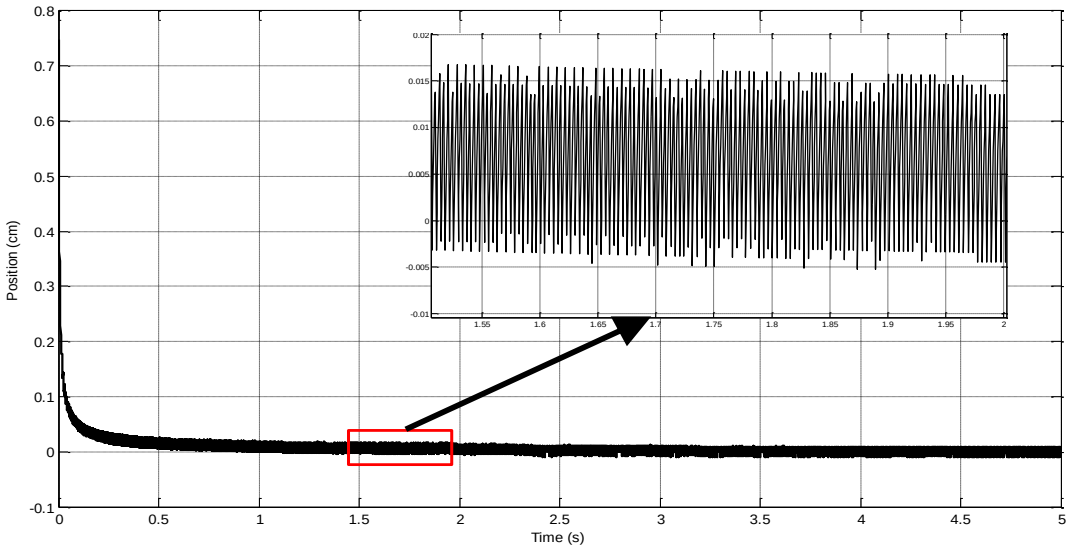

Figure 6. Response to the position of the ball on the experimental model

6. Conclusion

In the presented study, an embedded system based on microcontroller for magnetic levitation system. The fast-acting optimal proximal control algorithm ensures the system is asymptotic for some objects even when the mathematical model of the system is incomplete or the mathematical model parameter is incorrect. Specifically, an embedded magnetic lift control system is designed based on microcontroller AVR. According to the physical model, the mathematical equations of the system are then deduced. Fast-acting suboptimal response controller is designed. From the simulation results of the proposed controller and the conventional linear regression controller, shows the advantages of the proposed controller with inadequate mathematical model. In the experimental results show the controller performance on the embedded system built. The error and transient time well meet the real system requirements. In the next studies, the authors will offer solutions to build the suboptimal controller with fast impact when the mathematical model is complete.

References

[1] Mundher H.A. Yaseen, Haider J. Abd . Modeling and control for a magnetic levitation system based on SIMLAB platform in real time. Journals "Results in Physics". Volume 8, March 2018, Pages 153-159.

[2] Sun Y, Xu J, Qiang H, Chen C, Lin G (2019) Adaptive sliding mode control of maglev system based on RBF neural network minimum parameter learning method. Measurement 141:217–226.

[3] Zomorodian A, Menhaj MB, Daghooghi Z, Saboori I. A Real Time Digital Controller for Magnetic Levitation System. 2007 2nd IEEE Conference on Industrial Electronics and Applications. DOI: 10.1109/ICIEA.2007.4318561.

[4] Iglesias JA, Skrjanc I. Applications, results and future direction. Evol Syst 2014;5:1–2.

[5] Lughofer E, Sayed-Mouchaweh M. Adaptive and on-line learning in nonstationary environments. Evol Syst 2015;6:75–7.

[6] Meda-Campaña JA, Rodriguez-Valdez J, Hernandez-Cortes T, Tapia-Herrera R, Nosov V. Analysis of the fuzzy controllability property and stabilization for a class of T-S fuzzy models. IEEE Trans Fuzzy Syst 2015;23(2):291–301.

[7] Sayed-Mouchaweh M, Lughofer E. Decentralized fault diagnosis approach without a global model for fault diagnosis of discrete event systems. Int J Control 2015;88(11):2228–41.
[8] Iterative auto-calibration of digital controllers. Methodology and applications.Control Eng Pract 1998;6(3):345–58.
[9] Nguyen Xuan Chiem, Hai Nguyen Phan. Design controler of the quasitime optimization approach for stabilizing and trajectory tracking of inverted pendulum. MATEC Web of Conferences Volume 226, 2018 XIV International Scientific-Technical Conference "Dynamic of Technical Systems" (DTS-2018).
[10] Hai N. Phan, Chiem X. Nguyen. Building embedded quasi-time-optimal controller for two-wheeled self-balancing robot. MATEC Web Conf.Volume 132, 2017XIII International Scientific-Technical Conference "Dynamic of Technical Systems" (DTS-2017).
[11] Nguyen X.C. Phan N.H. Hoang D.L. Truong D.K. Kien L. M, Thuy X.P.. Building quasi-time-optimal control laws for ball and beam system. 2019 3rd International Conference on Recent Advances in Signal Processing, Telecommunications & Computing (SigTelCom).
[12] Al-Muthairi, N. F., Zribi, M., "Sliding mode control of a magnetic levitation system", Mathematical Problems in Engineering, 2, 2004, pp.93-107.
[13] Al-Muthairi, N. F., Zribi, M., "Sliding mode control of a magnetic levitation system", Mathematical Problems in Engineering, 2, 2004, pp.93-107.
[14] Barie, W., Chiasson, J., "Design of an embedded control system based on the quasi-time optimal control law when limiting the control signal for the ball and beam system", AIP Conference Proceedings 2188, 030007 (2019); https://doi.org/10.1063/1.5138400 Published Online: 17 December 2019.
[15] Al-Muthairi, N. F., Zribi, M., "Modeling and synthesizing quasi-time control laws for two degrees of freedom robotic arm ", Aip conference proceedings 2188, 030009 (2019); https://doi.org/10.1063/1.5138402 published online: 17 december 2019

Design of control laws for rotary inverted pendulum based on LQR and Lyapunov function

C X Nguyen[1,*], Th Tr Tran [2], Th X Pham[1] and K M Le[1]

[1]Department of Automation and Computing Techniques, Le Quy Don Technical University, Vietnam
[2]Control, Automation in Production and Improvement of Technology Institute, Hanoi, Vietnam.
[*]Corresponding author: nguyenxuanchiem83@gmail.com

Abstract. In this paper, a new technique for synthesizing control laws of stabilizing rotary inverted pendulum is proposed. The key of the proposed method is combination of linear quadratic regulator (LQR) method and Lyapunov function such that the control system can achieve higher performance. The Lyapunov function-based methods guarantee the globally approximate stability; however, they face to the difficulty of constructing an effective Lyapunov function. On the other hand, the LQR-based methods have been shown the ability to achieve high performance only if the control system has a weak nonlinearity and/or operate around equilibrium point. Combining them may partially deal with their limitations. The effectiveness of the proposed method is examined by experiments on the rotary inverted pendulum and compared with the LQR method. The results show that the proposed method has achieved a better performance.

1. Introduction

The Rotary Inverted Pendulum, which was first proposed by Furuka et al. [1], is a well-known test platform to verify the control theories due to its static instability. Designing controllers for many real-life applications such as aerospace vehicles and robotics [2-3] has shown that studying on the rotary inverted pendulum plays a key role to go further.

There are several methods, which have been proposed for the swing-up and stabilizing control of the rotary inverted pendulum in the literature. Akhtaruzzaman and Shafie [4] proposed a method that used proportional - integral – derivative (PID), fuzzy control and LQR techniques to balance the pendulum in its upright position. Chiem at al. [5] presented a method that uses quasi-time optimal control approach. Wen at al. [6] used Lyapunov control method to design control laws for stabilizing the rotary inverted pendulum. Rojas–Moreno at al. [7] designed a fractional order-based LQR controller for the system. However, many limitations of those methods such as complexity and strictly operated conditions are still presented and need to be solved.

Among many approaches, the Lyapunov method is an effective method, which can be applied to both linear and nonlinear systems. Especially, performance and characteristics of a complex system can be analysed by using analytic expression of designed control laws. In addition, the LQR method is an optimal control method, which was originally designed for linear systems and applied in many applications. To guarantee both stabilization and achieving high operating performance of the rotary inverted pendulum as illustrated in Figure 1 around equilibrium point, a method that combines the LQR and Lyapunov methods is proposed in this work.

The remaining of this paper is organized as follow. Section 2 introduces the mathematical model of the rotary inverted pendulum, in which the linear model is obtained. The control laws, which are designed by combining the LQR and Lyapunov methods, are presented in Section 3. Section 4 illustrates some simulation results as well as discussions. Finally, Section 5 concludes the paper.

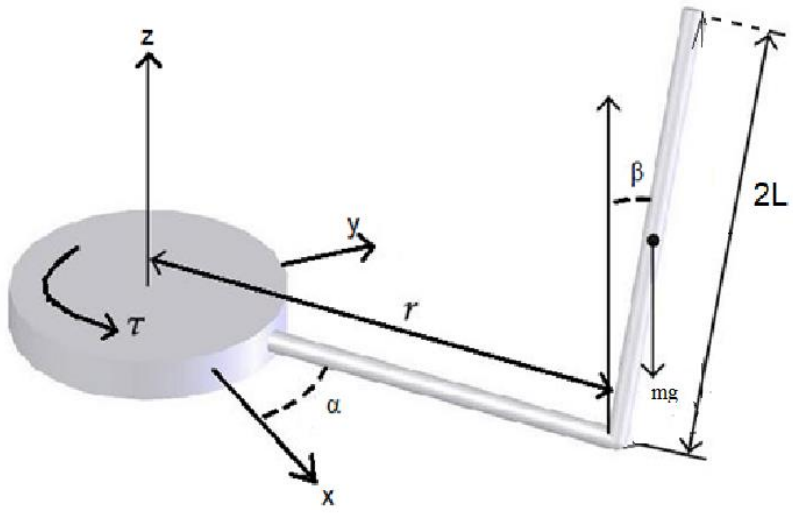

Figure 1. Schematic presentation of the rotary inverted pendulum

2. Mathematical model of rotary inverted pendulum

The rotary inverted pendulum illustrated in Figure 1, includes a rotating arm, which is driven by a motor, and a pendulum mounted on arm's rim. The pendulum moves as an inverted pendulum in a plane perpendicular to the rotating arm. α (angular displacement of the arm) and β (angular displacement of the pendulum) are used as the generalized coordinates to present the inverted pendulum system. Parameter settings for the system are set according to Table 1.

Table 1. Parameter settings for the open-source rotary inverted pendulum

Parameters	Values	Functions (unit)
L	0.2	Length of half pendulum (m)
M	0.1	Mass of pendulum (kg)
J_0	0.001	Moment of inertia at the load (kg.m^2)

Assuming that friction at all connected points is zero, applying Lagrange method, the mathematical model of the rotary inverted pendulum can be described as follows [8]:

$$\begin{cases} (J_0 + m\,r^2)\ddot{\alpha} - mLr\cos(\beta)\ddot{\beta} + mLr\sin(\beta)\dot{\beta}^2 = \tau \\ -mLr\cos(\beta)\ddot{\alpha} + \frac{4}{3}mL^2\ddot{\beta} - mgL\sin(\beta) = 0 \end{cases} \quad (1)$$

where, r is rotating arm length; g is gravitational constant; u is moment generated by motor.

Converting Eq. (1) into the state space from, we obtained:

$$\dot{x} = f(x) + B(x)\tau \quad (2)$$

where

$$f(x)=\begin{bmatrix} x_2 \\ \dfrac{mr\sin(x_3)[-4Lx_4{}^2+3gcos(x_3)]}{A(x_3)} \\ x_4 \\ \dfrac{3\sin(x_3)[Jg+mgr^2-Lmr^2x_4{}^2cos(x_3)]}{B(x_3)} \end{bmatrix}, \qquad B=\begin{bmatrix} 0 \\ \dfrac{4}{A(x_3)} \\ 0 \\ \dfrac{r\,cos(x_3)}{B(x_3)} \end{bmatrix}$$

with

$$\begin{cases} x=\begin{bmatrix} x_1 & x_2 & x_3 & x_4 \end{bmatrix}^T=\begin{bmatrix} \alpha & \dot{\alpha} & \beta & \dot{\beta} \end{bmatrix}^T \\ B(x_3)=4LJ+4Lmr^2-3Lmr^2cos^2(x_3) \\ A(x_3)=4J+4mr^2-3mr^2cos^2(x_3) \\ J=m(2L)^2/3 \end{cases} \tag{3}$$

Linearizing Eq. (2) at the equilibrium point, $x=\begin{bmatrix} 0 & 0 & 0 & 0 \end{bmatrix}^T$, it becomes

$$\dot{x}=\begin{bmatrix} \dot{x}_1 \\ \dot{x}_2 \\ \dot{x}_3 \\ \dot{x}_4 \end{bmatrix}=A_0x+B_0\tau=\begin{bmatrix} 0 & 1 & 0 & 0 \\ 0 & 0 & \dfrac{3mgr}{4J+4mr^2-3mr^2} & 0 \\ 0 & 0 & 0 & 1 \\ 0 & 0 & \dfrac{3(Jg+mgr^2)}{4LJ+4Lmr^2-3Lmr^2} & 0 \end{bmatrix}\begin{bmatrix} x_1 \\ x_2 \\ x_3 \\ x_4 \end{bmatrix}+\begin{bmatrix} 0 \\ \dfrac{4}{4J+4mr^2-3mr^2} \\ 0 \\ \dfrac{3r}{4LJ+4Lmr^2-3Lmr^2} \end{bmatrix}\tau \tag{4}$$

3. Design of control laws based on LQR method and Lyapunov function

3.1 Design of control laws using the LQR method

To regulate the system about the upright equilibrium point, control laws for the rotary inverted pendulum are designed by using the LQR method. Particularly, the control signal: $u(t)=-Kx(t)$ is designed such that objective function JLQR is minimum.

$$J_{LQR}=\int_0^\infty (x^TQx+u^TRu)dt \tag{5}$$

where Q and R are positive matrices. $K=R^{-1}B_0{}^TP$ is defined by solving algebraic Ricatti equation, in which P matrix has to be satisfied the following condition:

$$PA_0+A_0{}^TP+Q-PB_0R^{-1}B_0{}^TP=0 \tag{6}$$

By substituting the system parameters as given in Table 1, and A_0, B_0 in Eq. (4), we get P as follows:

$$P = \begin{bmatrix} 1.3528 & 0.4151 & -3.4828 & -0.5545 \\ 0.4151 & 0.4897 & -4.1572 & -0.6544 \\ -3.4828 & -4.1572 & 38.3713 & 5.5650 \\ -0.5545 & -0.6544 & 5.5650 & 0.8764 \end{bmatrix} \quad (7)$$

with Q and R are defined as follows:

$$Q = \begin{bmatrix} 1 & 0 & 0 & 0 \\ 0 & 1 & 0 & 0 \\ 0 & 0 & 2 & 0 \\ 0 & 0 & 0 & 1 \end{bmatrix}; \quad R = 1;$$

Hence, the control signal is presented by:

$$u_{LQR}(t) = -0.4142x_1(t) - 0.5607x_2(t) + 8.3021x_3(t) + 1.4376x_4(t) \quad (8)$$

3.2 The proposed method for designing control laws

Based on works from Le Tr Th. [9-10] for designing control laws using Lyapunov function, Eq. (2) for affine nonlinear systems can be rewritten as follows:

$$\dot{x} = f(x) + B(x)u_f \quad (9)$$

where *f(x)* is a differentiable and nonlinear function with *f(0) = 0.*

In this work, we propose to define *f(x), B(x)* and u_f with following forms:

$$f(x) = A_0 x + f_0(x)$$

$$B(x) = B_0 + \overline{B}(x) \quad (10)$$

$$u_f = u_{LQR} + u$$

By substituting Eq. (10) to Eq. (9), we obtained:

$$\dot{x} = (A_0 - B_0 K^T)x + \left[f_0(x) - \overline{B}(x) K^T x \right] + B(x)u = \left[A_1 x + f_1(x) \right] + B(x)u \quad (11)$$

The control laws derived from the Eq. (11) ensure the rotary inverted pendulum stable around the equilibrium point. In order to obtain high accuracy and fast convergence, Lyapunov function is selected by using quadractic function *V(x)* as follows:

$$V(x) = x^T P x \quad (12)$$

where *P* is a matrix obtained by solving Ricatti equation as in Eq. (6). Calculating the first derivative of *V(x),* we get:

$$\dot{V}(x) = x^T (A_0^T P + P A_0) x + 2[x^T P f(x) + x^T P B(x) u] \quad (13)$$

Since $A_0^T P + P A_0 = -Q + P B_0 B_0^T P$ is negative matrix, according to Lyapunov stability theorem [11] , the system is stable if and only if the selected *u(x)* make $\dot{V}(x) < 0$ in all system trajectories. Hence, the control law, u_f, is designed as the following form:

$$u_f = u_{LQR} + u = \begin{cases} 0, & \text{if} \quad x^T Pf(x) < \alpha x^T [Q - PB_0 B_0{}^T P]x \quad \text{or} \quad \left| x^T PB(x) \right| \le \varepsilon \\ -\dfrac{x^T Pf(x)}{x^T PB(x)}, & \text{if} \quad x^T Pf(x) \ge \alpha x^T [Q - PB_0 B_0{}^T P]x \quad \text{with} \quad x^T PB(x) \ne 0 \end{cases} \tag{14}$$

where ε is a small constant that making u does not go to infinity; α is a constant in [0, 0.5).

Note that, the detail of u is not presented here for the purpose of simplifying and compact.

4. Simulation results

In this section, the simulation results for two cases: the initial point of the pendulum is close to and far from the equilibrium point, will be represented. In each case, the system response will be estimated for both the LQR method and the proposed control law.

In the first case, the initial position of the pendulum is set with $x_0 = [0, 0, \pi/18, 0]$. Figure 2 and Figure 3 indicate that both methods can stabilize the rotary inverted pendulum with similar system responses. This is consistant with the theorical analysis in Section 3: around the equilibrium point, u_{LQR} will dominate in the control signal.

In the second case, the initial position of the pendulum is set with $x_0 = [0, 0, \pi/5, 0]$. Figure 4 and Figure 5 show the arm and pendulum responses for the considering methods. From the results, we can observe that the proposed method outperforms the LQR method in all performance criteria such as overshot, settling time. However, the figures also reveal that the switching step of the proposed control law has relay form. As a result, oscillation will be occured in the process that the system converges to the equilibrium point. This is an undesired phenomenon of mechanical systems.

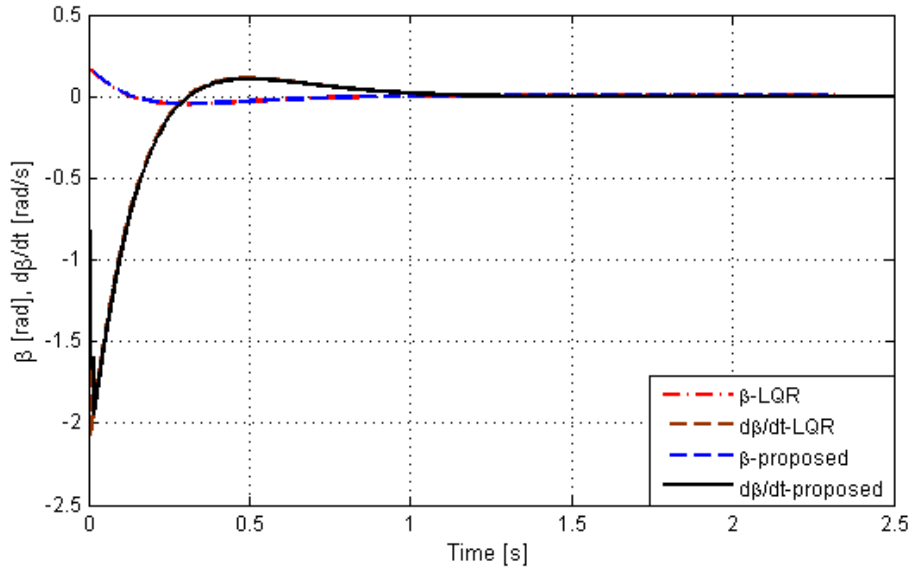

Figure 2. β and $\dot{\beta}$ responses for the LQR and proposed methods of the first case

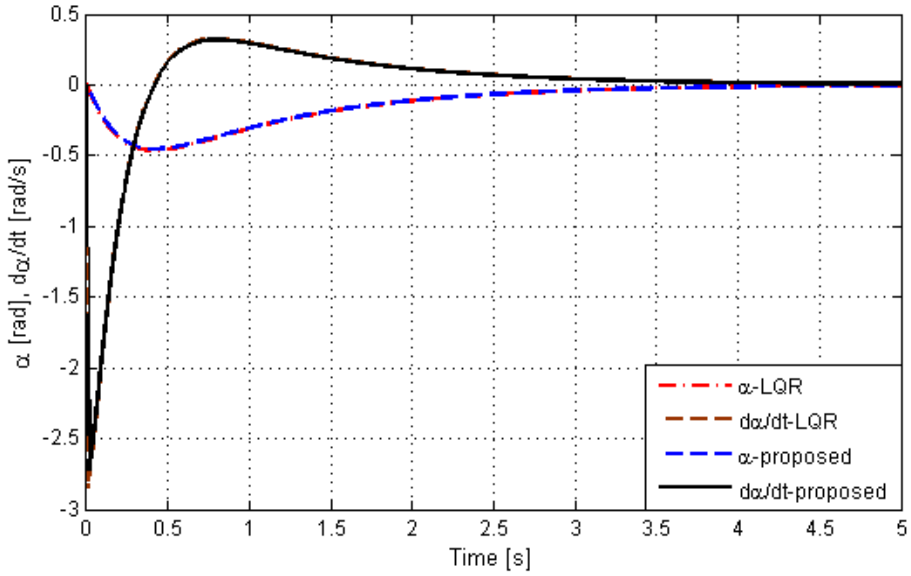

Figure 3. α and $\dot{\alpha}$ responses for the LQR and proposed methods of the first case

5. Conclusion

In this paper, a new method for designing control laws of stabilizing rotary inverted pendulum is represented. In essence, the proposed method is the combination of LQR method and Lyapunov function-based method such that the advantages of each method can be enhanced, simultaneously, their disadvantages may be eliminated. While the Lyapunov function-based method can guide the system to the equilibrium point effectively, the LQR method can help the system operating with high performance around the equilibrium point. The proposed control law has been theoretically analysed to prove the capability of globally approximate stabilization. The simulation results also reveal that the proposed method outperforms its counterpart. However, it still exist a limitation which is introducing oscillation when switching control signals. As a future work, we will consider solutions to get rid of the limitation. In addition, stability and robustness of the system will be examined in the presence of noise.

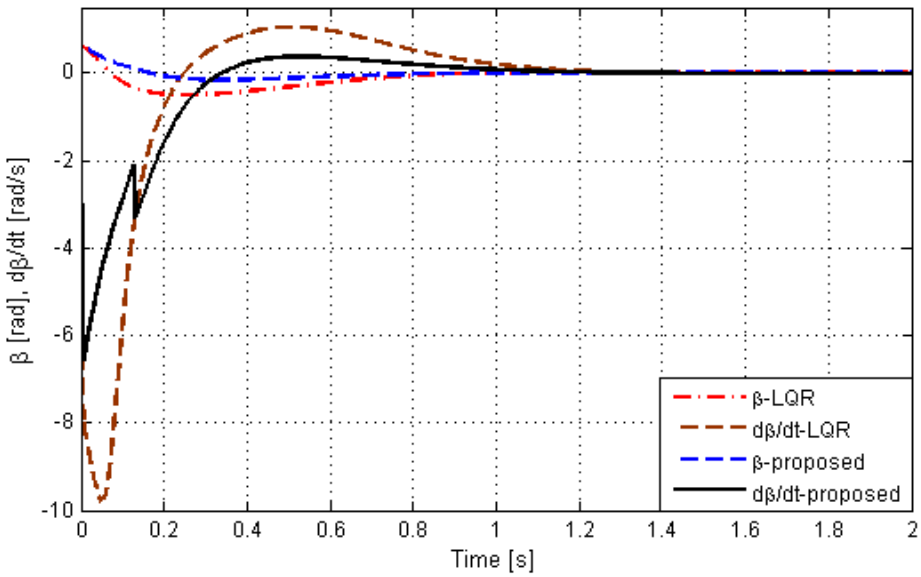

Figure 4. β and $\dot{\beta}$ responses for the LQR and proposed methods of the second case

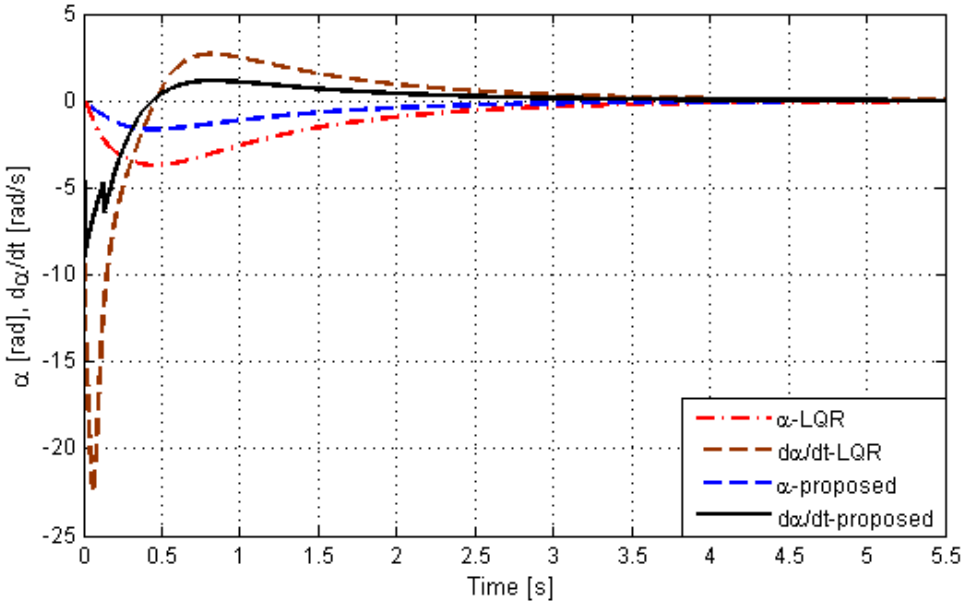

Figure 5. α and $\dot{\alpha}$ responses for the LQR and proposed methods of the second case

References

[1] K. Furuta, M. Yamakita and S. Kobayashi, Swing up control of inverted pendulum, International Conference on Industrial Electronics, Control and Instrumentation, 2193-2198, 1991.

[2] F. Grasser, A. D. Arrigo, S. Colombi, and A. C. Ruffer, JOE: a mobile, inverted pendulum, IEEE Transactions on Industrial Electronics, Vol. 49, No. 1, pp. 107-114, 2002.

[3] R. Ortega, M. W. Spong, E. Gomez-Estern, and G. Blankenstein, Stabilization of a class of under-actuated mechanical systems via interconnection and damping assignment, IEEE Transactions on Automatic Control, Vol. 47, No. 8, pp. 1218-1233, 2002.

[4] M. Akhtaruzzaman and A. A. Shafie, Modelling and control of a rotary inverted pendulum using various methods, comparative assessment and result analysis, in Proceedings of the IEEE International Conference on Machatronics and Automation (ICMA'10), pp. 1342-1347, IEEE Xian China, August 2010.

[5] Nguyen Xuan Chiem, Hai Nguyen Phan. Design controler of the quasitime optimization approach for stabilizing and trajectory tracking of inverted pendulum. MATEC Web of Conferences Volume 226, 2018 XIV International Scientific-Technical Conference "Dynamic of Technical Systems" (DTS-2018).

[6] Jie Wen, Yuanhao Shi, and Xiaonong Lu. Stabilizing a Rotary Inverted Pendulum Based on Logarithmic Lyapunov Function. Hindawi Publishing Corporation Journal of Control Science and Engineering Volume 2017, Article ID 4091302, 11 pages https://doi.org/10.1155/2017/4091302.

[7] Arturo Rojas–Moreno, Juan Hernandez–Garagatti, Oscar Pacheco–De la Vega, Luis Lopez–Lozano. FO Based–LQR Stabilization of the Rotary Inverted Pendulum. 2016 28th Chinese Control and Decision Conference (CCDC).

[8] V. Sirisha and A. S. Junghare, A comparative study of controllers for stabilizing a rotary inverted pendulum, International Journal of Chaos, Control, Modelling and Simulation, Vol. 3, No. ½, pp. 1-13, 2014.

[9] Le Tr. T Synthesis of nonlinear controllers of variable structure for one class of nonlinear object // Journal of DSTU 2007 T 7 No4 (35), - C 360-368.
[10] Le Tr. T., Gaiduk A.R., Synthesis of nonlinear control systems based on Lyapunov functions // Izvestiya TRTU. Special issue Technical Science Proceedings of the III scientific and technical conference of the faculty, graduate students and employees of TRTU - Taganrog Publishing house TRTU, 2006 No9 (64), - C 51 -56.
[11] V. I. Zubov Stability of motion (Lyapunov methods and their application). - M .: "High school", 1984.

The design of a quasi-time optimal cascade controller for ball and beam system

C X Nguyen[1], H Ng Phan[2] , L D Hoang[1] and H Ng Tran[1]

[1]Department of Automation and Computing Techniques, Le Quy Don Technical University, Vietnam
[2]Department of Software Engineering, Le Quy Don Technical University, Hanoi, Vietnam

Abstract. In this paper, a methodology for designing quasi-time optimal cascade controller for ball and beam system is presented and the result is compared with LQR method as well as implemented on real system. Ball and beam system is a highly non-linear system, its parameters are difficult to estimate accurately and easily affect by disturbance. In designed method, a mathematical model describing the system is built, including a motor that creates a rotation of beam and is divided into two subsystems when synthesizing the cascade controller for the system. The first floor is the beam subsystem with the output is the angle as the set value for the second floor, which is ball subsystem. The controller is synthesized for each subsystem based on the quasi-time optimal control. The advantage of this method is the synthesizing control law with non-linear system. The simulation results show the effectiveness of the proposed design.

1. Introduction

Ball and beam system is a typical system used in study of modern and intelligent control theory. It consists of a rigid beam rotating freely in a vertical plane around the axis while a Ball rolls along the beam. It can be categorized into two configurations. The first configuration is often called as “Ball and Beam Balancer”, in which the beam is supported in the middle, and it rotates against its central axis. The second configuration is built with the beam supported by two level arms on both sides. One of the level arms acted as the pivot, and the other is coupled to motor output gear. The purpose of ball and beam system is to hold the ball in a desired position on the beam, the ball position cannot be controlled directly but only through changing the angle of beam.

Among the studies on the first model, the study [10,11] uses the classic PID controller but the results are not good because the model is highly nonlinear, so the classical controller is not suitable for nonlinear control applications. The study [2] presents the approach based on Lyapunov method combined with the nonlinear observer showed positive results, but when designing the controller, the control quality is not really good. In the works [12] presenting LQR method for shading system and bar with good results. But this method is limited when using a linear model, it does not show all the dynamic nature of the system. Some studies using intelligent control methods such as [3-5] present the method of designing controllers using Neuron Network and Fuzzy Logic Type-2 that have been successful and have good simulated results, but not yet applied on real system. In the study [1,6], the

authors have used quasi-time optimal control laws for very good simulation results, but the control laws are too complicated.

The rest of the paper is organized as follows: Part II is for physical modelling of ball and beam system; part III is an overview of control structure diagram and the method to synthesis the quasi-time optimal cascade control for the ball and beam system; the simulation results are evaluated and compared with the LQR. Finally, the enforcement of quasi-time optimal cascade controller on actual ball and beam system is indicated in part IV.

2. Dynamical model of the ball and beam system

The first configuration is shown in Figure 1, the beam is supported in the middle, and it rotates against its central axis. Most ball and beam systems use this type of configuration. This type has the advantage of easiness of building and the simplicity of the mathematical model, but the motor need the high torque.

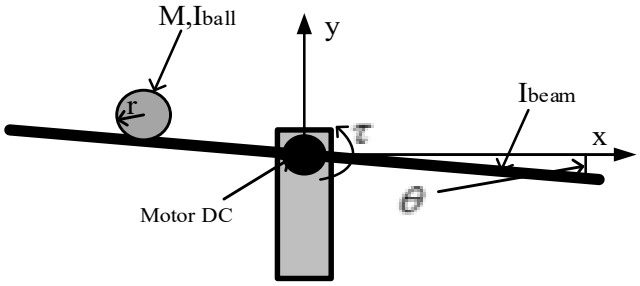

Figure 1. Ball and beam system

The parameters of system as follows: ball mass M = 0.05(kg); ball radius r = 0.002(m); moment of inertia of the ball Iball = 2.10-6(kg.m2); moment of inertia the beam Ibeam = 0.02(kg.m2); gravity g= 9.81(m/s2); moment of inertia of the motor Jm = 0.049.10−4(kg.m2); R=2.7 (Om)- armature resistance*;* motor's Torque constant Kt = 5.3.10-3(Nm/A); back EMF constant Ke = 5.10-3 (Vs/rad); gear ratio Kc = 27.

Assuming that friction at all connected points is zero, applying Lagrange method, the mathematical model of the ball and beam system can be described as follows [1,9]:

$$\begin{cases} \left(M + \dfrac{I_{ball}}{r^2}\right)\ddot{x} + Mg\sin(\theta) - Mx\dot{\theta}^2 = 0 \\ R\left(B_m + mx^2\right)\ddot{\theta} + 2mx\dot{x}\dot{\theta} + \left(K_c^2 K_t K_e + RK_c^2 b\right)\dot{\theta} + Rmg\cos(\theta)x = K_c K_t U \end{cases} \tag{1}$$

From equations (1), the state equation with the state variable $(x_1, x_2, x_3, x_4)^T = (x, \dot{x}, \theta, \dot{\theta})^T$ as follows.

$$\begin{bmatrix} \dot{x}_1 \\ \dot{x}_2 \\ \dot{x}_3 \\ \dot{x}_4 \end{bmatrix} = \begin{bmatrix} x_2 \\ \dfrac{M}{A}x_1 x_4^2 - \dfrac{Mg}{A}\sin(x_3) \\ x_4 \\ \dfrac{K_c K_t}{R\left(B + Mx_1^2\right)}U - \left(\dfrac{K_c^2 K_e K_t}{R\left(B + Mx_1^2\right)} + \dfrac{K_c^2 b}{\left(B + Mx_1^2\right)}\right)x_4 - \dfrac{2M}{\left(B + Mx_1^2\right)}x_1 x_2 x_4 - \dfrac{Mg}{\left(B + Mx_1^2\right)}x_1\cos(x_3) \end{bmatrix} \tag{2}$$

Where $A = M + \frac{I_{ball}}{r^2}; \quad B = I_{ball} + I_{beam} + K_c^2 J_m;$

3. The design of cascade controller with quasi-time optimization for ball and beam system

3.1 Control cascade structure diagram of ball and beam system

In the study [1,6-9], it is proposed the control law with quasi-time optimization, but the control law is too complicated to implement on embedded systems. In the ball and beam system, it is necessary to control the position of the ball and also to bring the beam to the horizontal position. Therefore, the authors propose the structure diagram of the ball and beam system with two controllers: the position of ball and the angle of beam. The control structure diagram of the ball and beam system is shown in Figure 2. The position controller based on the desired position value and current state to give the set value to the angular control of the ball and beam system. The angle controller based on the error between the set value and the state of the system gives the torque impacting on the ball and beam system.

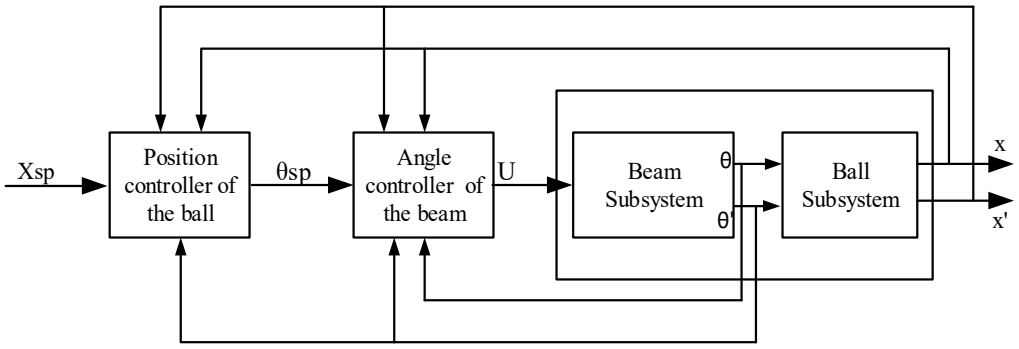

Figure 2. The control structure diagram of ball and beam system

3.2 The synthesis of quasi-time optimal cascade controller for ball and beam system

In order to synthesize the quasi-time optimal cascade control law on the embedded system and simplifies the control law, the authors propose to separate the original system into the two subsystems with the mathematical model of each subsystem after linearizing the equations (2) as follows.

The model of ball subsystem with state variable $(x_1, x_2)^T = (\theta, \dot{\theta})^T$:

$$\begin{cases} \dot{x}_1 = x_2 \\ \dot{x}_2 = -\dfrac{Mg}{A} U_1 \end{cases} \tag{3}$$

The model of beam subsystem with state variable $(z_1, z_2)^T = (\theta, \dot{\theta})^T$:

$$\begin{cases} \dot{z}_1 = z_2 \\ \dot{z}_2 = -\left(\dfrac{K_c^2 K_e K_t}{RB} + \dfrac{K_c^2 b}{B} \right) z_2 - \dfrac{Mg}{B} x + \dfrac{K_c K_t}{RB} U_2 \end{cases} \tag{4}$$

The direction of quasi-time optimal control is presented in the studies [1,6-9]. For subsystems (3), (4), the selected virtual equations has the form (5):

$$\begin{cases} \dot{y}_1 = -v_1 \dfrac{y_1}{\sqrt{y_1^2 + \varepsilon_1^2}} + y_2 \\ \dot{y}_2 = -\dfrac{y_2}{\varepsilon_2} \end{cases} \tag{5}$$

System (3) and (4) has a controlled Jordan form. The virtual system is selected as (5) then the ball position will be guaranteed to return to the preset position with quasi-time optimization. The quasi-time optimal control laws are found when solving equations (4) with $y_1 = x_1 - x_{sp}$ in equations (4) and $y_1 = z_1$ in equations (5). The formula of U_1 and U_2 have the form (6) and (7).

$$U_1 = \frac{A}{Mg}\left(v_1 \varepsilon_{11}^2 \frac{\dot{x} - \dot{x}_{sp}}{\left(\left(x - x_{sp} \right)^2 + \varepsilon_{11}^2 \right)^{1.5}} + \frac{1}{\varepsilon_{12}} \left(\dot{x} + v_1 \frac{x - x_{sp}}{\left(\left(x - x_{sp} \right)^2 + \varepsilon_{11}^2 \right)^{0.5}} \right) \right) \tag{6}$$

$$U_2 = \left(K_c K_e + \frac{RK_c b}{K_t} \right) \dot{\theta} + \frac{MgR}{K_c K_t} x - v_2 \varepsilon_{21}^2 \frac{\dot{\theta}}{\left(\theta^2 + \varepsilon_{21}^2 \right)^{1.5}} + \frac{1}{\varepsilon_{22}} \left(\dot{\theta} + v_1 \frac{\theta}{\left(\theta^2 + \varepsilon_{21}^2 \right)^{0.5}} \right) \tag{7}$$

4. Simulation and experiment results

4.1 Simulation results

By the method described above, the synthesized control laws U_1, U_2 provides the stable control over the ball and beam system. The simulation results with initial values are as follows: $x_{sp} = 0$, $x(0) = 0.5$, $\dot{x}(0) = 0$, $\theta(0) = 0.4$, $\dot{\theta}(0) = 0$. The parameters of quasi-time optimal controller with U_1, U_2: $v_1 = v_2 = 1$, $\varepsilon_{11} = 0.4; \varepsilon_{12} = 0.3; \varepsilon_{21} = 0.4; \varepsilon_{22} = 0.5$. Figure 3 shows the response of the ball position with the proposed method (CAS-KOB) and LQR is presented in the study [1]. It is clear that the position response of ball to proposed method is more stability than the LQR controller. Figure 4 shows the angle response of beam according to the proposed method for faster and more stable response than LQR, although the higher overshoot at the first time.

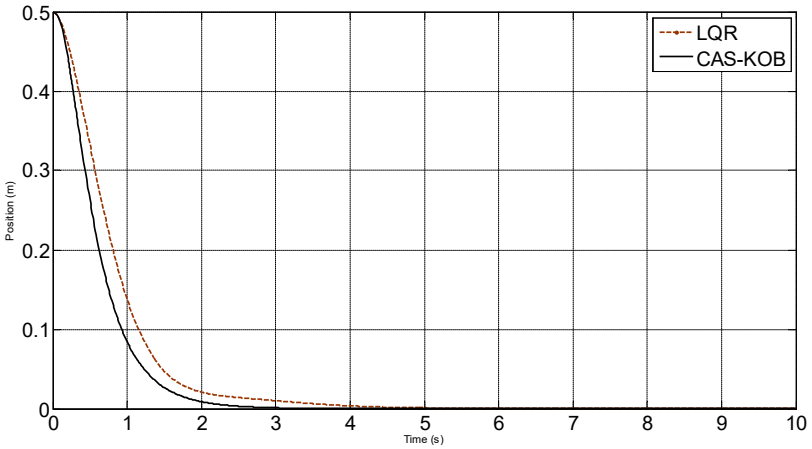

Figure 3. The position response of ball

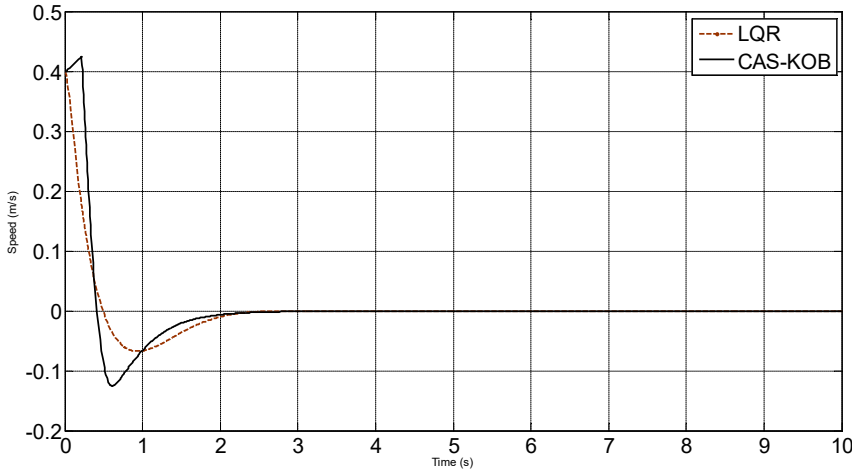

Figure 4. The angle response of beam

4.2 Experiment results

The quasi-time optimal cascade control law is implemented on real-time embedded system and the model made by the authors (Figure 5). The parameters are as follows: the travel distance of ball is 0.5 (m), the other parameters are the same as the simulation.

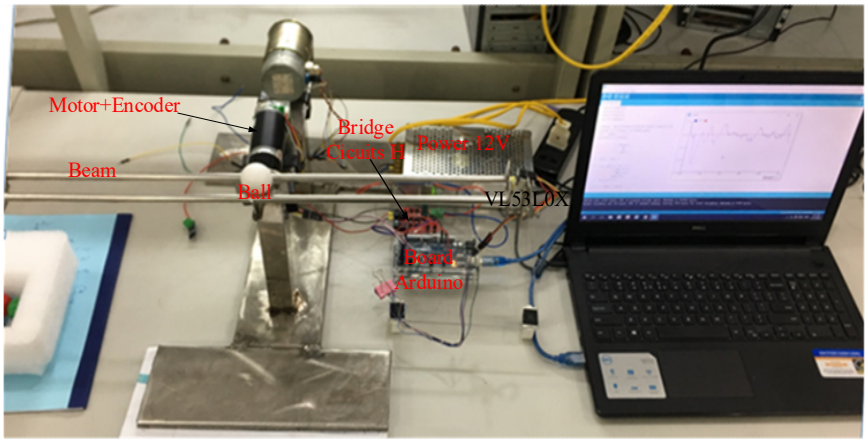

Figure 5. Experimental model of ball and stick systems.

Figures 6 and 7 show the angular and position response of the ball and beam system using the proposed controller, and we see that the optimal controller has worked with the designed ball and beam model. The ball is always guaranteed at the desired position and only fluctuates slightly around the equilibrium position. The fluctuations of the ball position around the set point tend to fade. At the same time, we also see that the response of the beam angle and the ball position sometimes fluctuate due to the mechanical errors of the gearbox, the measurement error when using the radar VL53L0X distance sensor. Another reason is that the control law is not optimal with the real model because υ, ε in the simulation are only approximate.

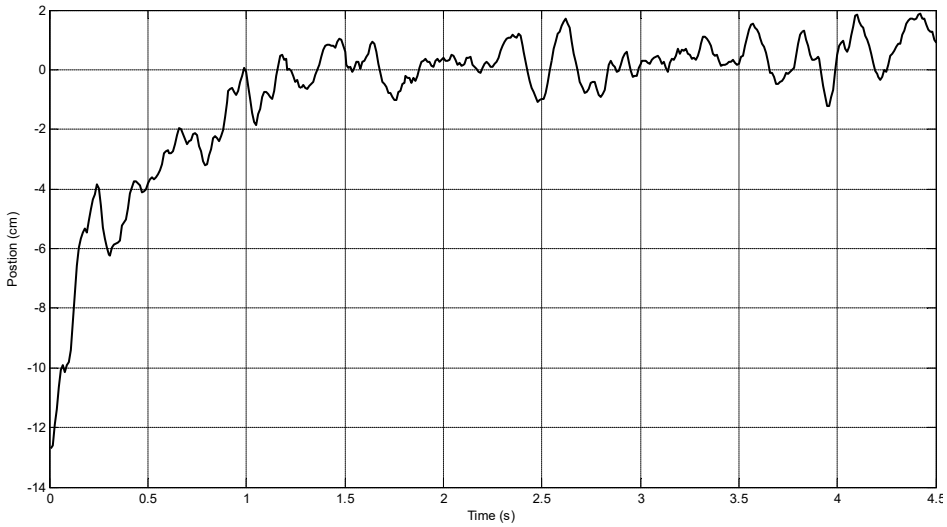

Figure 6. The position response of ball on embedded system.

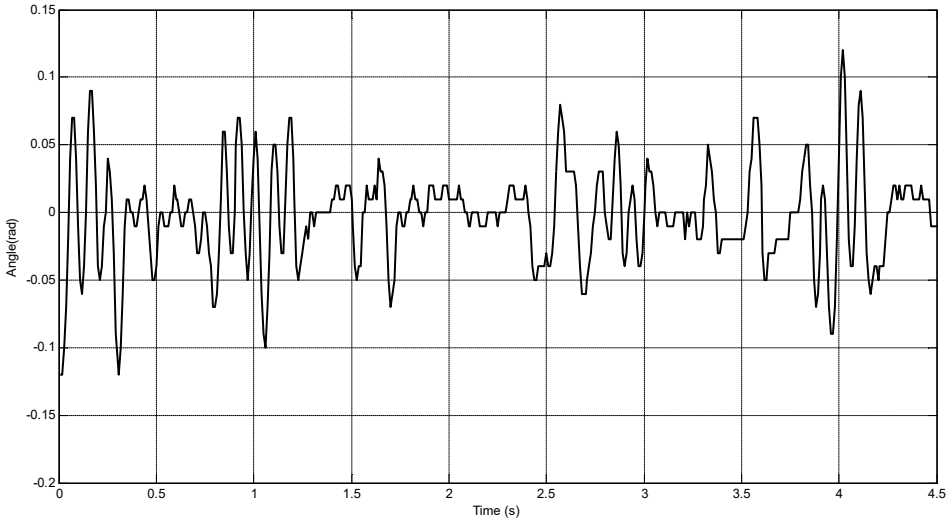

Figure 7. The angle response of beam on embedded system.

5. Conclusion

The results obtained when synthesizing control laws of the ball and beam system according to the proposed method show that the control law still remains the advantages of the quasitime optimal control for complex technical systems with high nonlinearity. In addition, the proposed method is much simpler than the quasi-time optimal control law when not separated into two subsystems. Therefore, the proposed method of this method are easily implemented on embedded systems. Comparison with the traditional LQR controller shows that the setting time when using the synthesized controller proposed in the paper is better. Future studies will supplement the research on sustainable controller and adaptive parameters of the control law when the object model is uncertain.

References

[1] Chiem Nguyen Xuan, Hai Phan Nguyen, Long Hoang Duc, Khoa Truong Dang, Le Minh Kien, Thuy Xuan Pham. “Building Quasi-Time-Optimal Control Laws For Ball And Beam

System". 2019 3rd International Conference on Recent Advances in Signal Processing, Telecommunications &Computing (SigTelCom).

[2] Philipp Rapp, Oliver Sawodny, and Cristina Tarın. "Stabilization of the Ball and Beam System by Dynamic Output Feedback using Incremental Measurements". Control Conference (ECC), 2013 European.

[3] Yeong-HwaChang, Chia-WenChang, Chin-WangTao, Hung-WeiLin, Jin-ShiuhTaur. "Fuzzy sliding-mode control for ball and beam system with fuzzy ant colony optimization". Expert Systems with Applications Volume 39, Issue 3, 15 February 2012, Pages 3624-3633.

[4] MahmoodianHamid, LotfizadehDehkordiElaheh. "Designing a Fuzzy Type-2 Model-based Robust Controller for Ball and Beam System". Procedia Computer Science Volume 105, 2017, Pages 125-130.

[5] J. Hauser, S. Sastry, and P. Kokotovic, "Nonlinear Control Via Approximate Input-Output Linearization: The Ball and Beam Example," IEEE Transactions on Automatic Control, vol. 37, no. 3, pp. 392–398, 1992.

[6] Hai N. Phan, Chiem X. Nguyen, "Building embedded quasi-time-optimal controller for twowheeled self-balancing robot," MATEC Web Conf.Volume 132, 2017 XIII International Scientific-Technical Conference"Dynamic of Technical Systems" (DTS-2017).

[7] Nguyen Xuan Chiem, Hai Nguyen Phan. "Design controler of the quasitime optimization approach for stabilizing and trajectory tracking of inverted pendulum". MATEC Web Conf. Volume 226, 2018 XIV International ScientiÒc-Technical Conference "Dynamic of Technical Systems" (DTS-2018).

[8] C. X. Nguyen, H. N. Phan, A. D. Lukianov, T. D. Pham, T. T. Nguyen, and H. T. Nguyen. Design of an embedded control system based on the quasi-time optimal control law when limiting the control signal for the ball and beam system. AIP Conference Proceedings 2188, 030007 (2019); https://doi.org/10.1063/1.5138400 Published Online: 17 December 2019.

[9] C. X. Nguyen, H. N. Phan, L. D. Hoang, H. T. Nguyen, KH. D. Truong, and N. H. V. Nguyen. Modeling and synthesizing quasi-time control laws for two degrees of freedom robotic arm. Aip conference proceedings 2188, 030009 (2019); https://doi.org/10.1063/1.5138402 published online: 17 december 2019.

[10] A. Taifour Ali*, Ahmed A. M., Almahdi H. A., Osama A. Taha, A. Naseraldeen A. Design and Implementation of Ball and Beam System Using PID Controller. Automatic Control and Information Sciences, 2017, Vol. 3, No. 1, 1-4.

[11] Mustafa Saad, Mohammad Khalallah. Design and Implementation of an Embedded Ball-beam Controller Using PID Algorithm. Universal Journal of Control and Automation 5(4): 63-70, 2017 . DOI: 10.13189/ujca.2017.050402.

[12] Rahul Soni ; Sathans. Optimal control of a ball and beam system through LQR and LQG. 2018 2nd International Conference on Inventive Systems and Control. DOI: 10.1109/ICISC.2018.8399060.

Two-dimensional plan source, vortex and vortex source

V N Kokhanenko, O A Burtseva* and M S Alexandrova

Department of General Engineering Disciplines Platov South-Russian State Polytechnic University (NPI), Novocherkassk, Russia

* e-mail kuzinaolga@yandex.ru

Abstract. Modern hydraulic structures require highly reliable water-supply channels, free-flow pipes and open spillways. Therefore, they must be built with considering dynamic properties of the affecting flow. The theory of one-dimensional open flows cannot answer many questions raised by the hydraulic engineering practice. Hence, this paper considers two- dimensional graphical open flows, with separate particular models following from the general theory, important for designing couplings, curves in more complex constructions (two different channels) required in hydraulic engineering (Hydraulics technical structures) (HTS). And the more such models are obtained, the more opportunities will appear for scientists and designers to synthesize more complex structures required in HTS.

This study identifies three elements, and three simplest models of two-dimensional graphic open water flows similar to flat models: a source, a vortex and a vortex source. The number of such individual models will continue to increase and expand the range of possibilities for designing more complex water technical objects (WTO).

The models are obtained analytically from solving the system of two-dimensional graphical open potential water flows in the plane of the velocity hodograph. The elementary construction of each model includes an analytical solution for the potential function and the stream function.

The paper considers the problem of determining the parameters of a two-dimensional graphical open water flow at any point in the flow: a source, a vortex, a vortex source. The practical significance of the models lies in the possibility to use the results by the designers of hydraulic structures both at the first stage of solving problems and at the subsequent ones, with flow resistance forces taken into account.

The study also represents the transition method from the plane of the flow velocity hodograph to the flow diagram by integrating the models in the plane of the velocity hodograph from the condition of the connection between the considered planes.

1. Introduction

The design of modern hydraulic structures is closely associated with comprehensive consideration of impacting dynamic properties of the flow. Continuously increasing dimensions and requirements for the reliability of water supply channels and free-flow pipes as well as open spillways require deep knowledge of the specific properties of open streams.

The classical one- dimensional flow theory cannot give answers to many questions raised by the hydraulic engineering practice. The two- dimensional graphical flow is a flow in an open channel, whose surface width is several times greater than the depth, the bottom relief is smooth and the current curvature in the graph is not great.

Scientists V.M. Makkaveev, N.M. Vernadsky, N.T. Meleschenko, G.I.Sukhomel, S.I. Numerov, A.T. Ippen, R. T. Knapp where the first developers of the 2D graphical open streams theory. Both Russian and foreign works mainly consider potential flows in a horizontal channel and this made it possible to use the well-known gas-hydraulic analogy and the method of characteristics associated with it. The results obtained in the works mentioned above are fundamental and retain their significance today.

The theory under consideration was later developed in the works of S.N. Numerov, who extended the calculation method based on characteristics to the case of vortex motion, and also for the first time took into account the friction forces and gave a numerical calculation method. In addition, S.N Numerov solved some problems of the two-dimensional theory in relation to slow graphical flows. A number of articles and a dissertation by I.A. Sherenkov are devoted to a detailed study of the problem of spreading a rapid current on the basis of the 2D theory. I.A. Sherenkov developed an original method for calculating a potential flow by characteristics as well as a numerical method that takes into account friction and bottom slope.

A number of foreign authors (A. Ippen, H. Rouse, D. Harleman, D. Dawson, R. Knapp) used the fundamentals of the theory of two-dimensional potential flows to construct calculating methods for transitional sections of rapid currents. They also carried out a number of experimental studies.

This study represents further research of previous studies of other authors [1-8]. Paper [9] gave solutions for plane problems of potential flow hydrodynamics which have both special theoretical and practical significance. However, similar problems can be solved for 2D graphical flows.

The aim of this work is to solve problems of spreading two-dimensional graphical, potential, open, stationary water flows. Namely, solving the problems of:

- two-dimensional graphical source;
- two-dimensional graphical vortex;
- a two-dimensional graphical vortex source.

The urgency of solving these problems is obvious, since their solution is to expand the capabilities of the two-dimensional plan flows' hydraulics [10-20].

2. Formulation of the problem

We proceed from the flow plane motion equations system of the velocity hodograph for the research. This system has the form [8, 19]:

$$\begin{cases} \dfrac{\partial\varphi}{\partial\tau}=\dfrac{h_0}{2H_0}\cdot\dfrac{(3\tau-1)}{\tau(1-\tau)^2}\cdot\dfrac{\partial\psi}{\partial\theta}; \\ \dfrac{\partial\varphi}{\partial\theta}=2\dfrac{h_0}{H_0}\cdot\dfrac{\tau}{1-\tau}\cdot\dfrac{\partial\psi}{\partial\tau}, \end{cases} \tag{1}$$

where τ,θ are the independent parameters: $\tau=\dfrac{V^2}{2gH_0}$ – defines the speed-dependent parameter; V – is the local flow rate; θ – is the angle characterizing the two-dimensional flow velocity vector direction; g – defines gravity acceleration; $\varphi=\varphi(\tau,\theta)$ – is the potential function; $\psi=\psi(\tau,\theta)$ – is the current function; $H_0=\dfrac{V_0^2}{2g}+h_0$ – is constant for the entire flow - hydrodynamic head; V_0,h_0 – are the local velocity and depth values at some characteristic point of the flow.

The system (1) is also complemented by D. Bernoulli's integral for two-dimensional flows:

$$\frac{V^2}{2g}+h=H_0, \tag{2}$$

moreover

$$V=\tau^{1/2}\sqrt{2gH_0};\quad h=H_0(1-\tau). \tag{3}$$

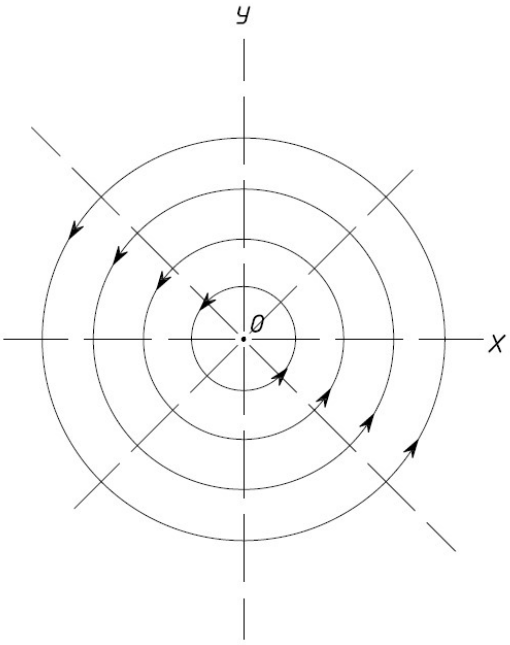

Figure 1. Flow diagram of a two-dimensional vortex

The system (1) has a whole range of analytical solutions [8, 19]. However, to solve the problems formulated in this article, we choose the following configuration from the spectrum of analytical solutions:

$$\begin{cases} \psi=\dfrac{C_2H_0}{2h_0}\left[\ln\tau-\tau\right]+C_1\theta; \\ \varphi=-\dfrac{C_1h_0}{2H_0}\left[\ln\dfrac{\tau}{1-\tau}-\dfrac{2}{1-\tau}\right]+C_2\theta. \end{cases} \tag{4}$$

It is possible to verify by direct verification that the equation (4) is a solution to the system (1). This design is basic for the following tasks: source, vortex, vortex source.

In case of a two-dimensional source from the configuration of analytical solutions (4), we single out the following:

$$\begin{cases} \psi=C_1\theta; \\ \varphi=-\dfrac{C_1h_0}{2H_0}\left[\ln\dfrac{\tau}{1-\tau}-\dfrac{2}{1-\tau}\right]. \end{cases} \tag{5}$$

Since the spreading of the flow is radial, the streamlines are rays emanating from the origin, see figure 1. This problem was solved and presented in [8, 9] for both quiet and turbulent flows.

The problem is solved from the general provisions of the two-dimensional potential plan flows theory for the first time for a two-dimensional vortex, and the configuration is singled out from (4):

$$\begin{cases} \psi = \dfrac{C_2 H_0}{2h_0}[\ln\tau - \tau]; \\ \varphi = C_2\theta, \end{cases} \tag{6}$$

where ψ = const – defines the streamlines; φ = const – defines the equipotential lines.

3. The solution of the problem

3.1. A two-dimensional vortex parameters' determination

For definiteness, the flow is assumed to be turbulent:

$$\frac{1}{3} \le \tau \le 1. \tag{7}$$

3.2. Flow spreading scheme in the physical domain

From the condition of the connection between the flow plan $\Phi(OXY)$ and the speed hodograph plane $\Gamma(\tau,\theta)$ we have [7, 8]:

$$d(x+iy) = \left(d\varphi + i\frac{h_0}{H_0(1-\tau)}d\psi\right)\cdot\frac{e^{i\theta}}{\tau^{1/2}\sqrt{2gH_0}}. \tag{8}$$

Since along the streamline $d\psi = 0$, the following comes from (8):

$$dx = \frac{d\varphi\cdot\cos\theta}{\tau^{1/2}\sqrt{2gH_0}}; \quad dy = \frac{d\varphi\cdot\sin\theta}{\tau^{1/2}\sqrt{2gH_0}}. \tag{9}$$

Having determined the differential from (6)

$$d\varphi = C_2 d\theta, \tag{10}$$

from (9) follows the system of equations

$$dx = \frac{C_2\cdot\cos\theta\cdot d\theta}{\tau^{1/2}\sqrt{2gH_0}}; \quad dy = \frac{C_2\cdot\sin\theta\cdot d\theta}{\tau^{1/2}\sqrt{2gH_0}}; \quad \frac{dy}{dx} = \mathrm{tg}\theta. \tag{11}$$

Integrating (11), we obtain:

$$x = \frac{C_2\cdot\sin\theta}{\tau^{1/2}\sqrt{2gH_0}}; \quad y = -\frac{C_2\cdot\cos\theta}{\tau^{1/2}\sqrt{2gH_0}}. \tag{12}$$

Raising both sides of the equalities in (12), adding them and using the main trigonometric identity, we obtain:

$$r^2 = x^2 + y^2 = \frac{C_2^2}{2gH_0\cdot\tau}. \tag{13}$$

3.3. The vortex streamline equation at a fixed τ – circle equation

We define the constant C_2 from the condition that for $r = r_0$:

$$V = V_0; \quad h = h_0; \quad \tau = \tau_0. \tag{14}$$

Therefore:

$$C_2^2 = 2gH_0\cdot\tau_0\cdot r_0^2. \tag{15}$$

It is possible to solve the problems of the constant with the found value from (13):

- setting the parameter τ, $\tau\in[\tau_0,1]$, the vortex trajectory radius is determined;
- setting the radius, it is possible determine τ and further local speed and depth:

$$\begin{cases} V = \tau^{1/2}\sqrt{2gH_0}; \\ h = H_0(1-\tau). \end{cases} \tag{16}$$

It is also seen from (13), (16), that for $\tau \to 1$

$$V \to V_{\max} = \sqrt{2gH_0}; \quad h \to 0; \quad r \to r_{\text{пр}} = \frac{C_2}{\sqrt{2gH_0}}.$$

Along the equipotential:

$$d\varphi = 0;$$

$$d\psi = \frac{C_2 H_0}{2h_0}\left(\frac{1-\tau}{\tau}\right)d\tau. \tag{17}$$

And it follows from (8):

$$\begin{cases} dx = -\frac{1}{2}\cdot\frac{\sin\theta}{\sqrt{2gH_0}}\cdot\frac{C_2}{\tau^{3/2}}d\tau; \\ dy = \frac{1}{2}\cdot\frac{\cos\theta}{\sqrt{2gH_0}}\cdot\frac{C_2}{\tau^{3/2}}d\tau. \end{cases} \tag{18}$$

It follows from (18):

$$\frac{dy}{dx} = -\text{ctg}\theta. \tag{19}$$

Comparing last equation (11) and (19) we see that streamlines and equipotential lines are mutually orthogonal, since the condition [21] is satisfied according to (11) and (19):

$$\text{tg}\theta\cdot(-\text{ctg}\theta) = -1. \tag{20}$$

Integrating the system (18) and setting the integration constants to zero, since the constant C_2 had already been defined earlier, we get the system:

$$\begin{cases} x = \frac{C_2\cdot\sin\theta}{\sqrt{2gH_0}}\cdot\frac{1}{\sqrt{\tau}}; \\ y = -\frac{C_2\cdot\cos\theta}{\sqrt{2gH_0}}\cdot\frac{1}{\sqrt{\tau}}; \end{cases} \tag{21}$$

$y = -\text{ctg}\theta\cdot x$ is the equipotential equation.

It becomes obvious from the comparison of (12) and (21) that the circle intersection points coincide with the rays themselves. Therefore, since $\tau_0 \le \tau \le 1$, then the system (21) describes the segments of rays emerging from the points on a circle with radius r_0 and up to a circle with limiting radius r_{lim}. Depths h on a circle of limiting radius r_{lim} tend to zero, the velocity tends to the maximum possible for turbulent flows:

$$V_{\max} = \sqrt{2gH_0}.$$

For a vortex source with the origin at the coordinates center, it is necessary to choose a structure (4) in the form of absorbing both the source and the vortex.

The procedure for solving the problem in principle coincides with the solution of the source and vortex problems.

4. Conclusions

The two-dimensional potential flows problems in terms of potential flows can be solved using the analytical solutions of the velocity hodograph plane system. It is quite simple to find a solution to the problems: a source, a vortex and a source.

The research started in this article, with a detailed study of turbulent and quiet flows and with further consideration of the flow resistance forces, can be presented within the framework of the dissertation work.

The convenient, simple algorithms for calculating two-dimensional plan flows in terms of source, vortex, vortex source have been shown in the presented work.

References

[1] Kokhanenko V N, Kelekhsaev D B, Kondratenko A I and Evtushenko S I 2019 *Two-dimensional motion equations in water flow zone* IOP Conf. Series: Materials Science and Engineering **698(6)** 066026 DOI:10.1088/1757-899X/698/6/066026

[2] Kokhanenko V N, Kelekhsaev D B, Kondratenko A I and Evtushenko S I 2019 *A System of Equations for Potential Two-Dimensional In-Plane Water Courses and Widening the Spectrum of Its Analytical Solutions* AIP Conference Proceedings **2188** 050017 DOI: 10.1063/1.5138444

[3] Kokhanenko V N, Kelekhsaev D B, Kondratenko A I and Evtushenko S I 2020 *Solution of equation of extreme streamline with free flowing of a torrential stream behind rectangular pipe* IOP Conf. Series: Materials Science and Engineering **775(1)** 012134 DOI:10.1088/1757-899X/775/1/012134

[4] Esin A I 2003 *Problems of technical fluid mechanics in natural coordinates* (Saratov: Publishing house of Saratov State Vavilov Agrarian University)

[5] Shiryaev V V, Mitsik M F, Duvanskaya E V 2007 *Development of the theory of two-dimensional open water flows* (Shakhty: Publishing house of Platov Suoth-Russian State Polytechnic University)

[6] Li J, Li D, Jiang B 2010 *Two & Three Dimensional Flow Numerical Simulation of Controlled Discharging Condition of Spillway Containing Processings* Frusta Asia-Pacific Power and Energy Engineering Conference 1 – 5

[7] Ghadirzad N, Mirmofidi S M, Zafarmand B 2011 *Numerical analysis of turbulent viscous flow around an elliptical airfoil and cylinder by potential flow patterns, vortices, sources & sinks: Random vortex method simulation* IEEE 3rd International Conference on Communication Software and Networks Processings 235 – 239

[8] Kokhanenko V N, Burtseva O A, Evtushenko S I, Kondratenko A I and Kelekhsaev D B 2019 Two-Dimensional in Plan Radial Flow (NonPressure Potential Source) *J. Construction and Architecture* vol **7**. Issue **4 (25)** p 74-78 DOI 10.29039/2308-0191-2019-7-4-74-78

[9] Loytsyansky L G 1978 *Mechanics of liquid and gas* (Moscow: Nauka Publ.) p 736

[10] Hyun B- S, Suh E J, Kim T Y 2006 *Turbulent Flow over Two-Dimensional Rectangular-Shaped Roughness Elements with Various Spacings* OCEANS-2006, Asia Pacific 1 – 6

[11] Bowman J C, Tran C V 2002 *Two-dimensional turbulent subgrid models* IEEE Conference Record - Abstracts. IEEE International Conference on Plasma Science Processings (Cat. No.02CH37340) 123

[12] Shiryaev V V, Mitsik M F et al. 2007 *Development of the theory of two-dimensional open water flows monography*, edited by Shiryaev V V (Shakhty: Publishing house of SRSUES)

[13] Fomin Yu G, Petrosov S P, Lemeshko M A, Kozhemyachenko AV, Donchenko I Ya 2016 *Mathematical model of heat leakage in camera of refrigerator* Izvestiya Vysshikh Uchebnykh Zavedenii, Seriya Teknologiya Tekstil'noi Promyshlennosti 1 158-161

[14] Lemeshko M A, Gornostaeva Z V, Duvanskaya E V, Danileko I N 2015 *Determination of the projections of the velocity vector of the cooled air from the refrigerating compartment with the door open* ARPN Journal of Engineering and Applied Sciences 10 (2) 954-958
[15] Kozhemyachenko A V, Lemeshko M A, Fomin Yu G, Tutskaya T P, Chertov Yu E, Romanov R P, Tuvin A A 2018 *To the question of modeling leakage in chamber of the refrigerating machine* Izvestiya Vysshikh Uchebnykh Zavedenii, Seriya Teknologiya Tekstil'noi Promyshlennosti 3 171-174
[16] Fomin Yu G, Petrosov S P, Lemeshko M A, Kozhemyachenko A V, Donchenko I Ya 2016 *Mathematical model of heat leakage in camera of refrigerator* Izvestiya Vysshikh Uchebnykh Zavedenii, Seriya Teknologiya Tekstil'noi Promyshlennosti 1 158-161
[17] Lemeshko M A, Gornostaeva Z V, Duvanskaya E V, Danileko I N 2015 *Determination of the projections of the velocity vector of the cooled air from the refrigerating compartment with the door open* ARPN Journal of Engineering and Applied Sciences 10 (2) 954-958
[18] Mitsik M F, Byrdina M V, Bekmurzaev L A 2017 *Modeling of developable surfaces of three-dimensional geometric objects* Proceedings of 2017 IEEE East-West Design and Test Symposium, EWDTS 2017, № 8110086 DOI: 10.1109/EWDTS.2017.8110086
[19] Kokhanenko V N, Burtseva O A, Evtushenko S I and Kondratenko A I 2020 *The Analytical Methods for Modelling the Two-Dimensional in the Open Water Circuits Development* IOP Conf. Series: Materials Science and Engineering **913(3)** 032068 DOI:10.1088/1757-899X/913/3/032068
[20] Duvanskaya E V 2003 *Calculation of the potential movement of two-dimensional stationary, quiet flows* (Author's abstract. diss. Cand. tech. sciences. – Shakhty) p 24
[21] Korn G and Korn T 1970 *Handbook of mathematics for scientists and engineers* (Moscow: Nauka Publ.) p 720

Nonlinear dynamics of liquid crystal: ultrasonic light modulator

O A Denisova

Department of Physics, Ufa State Petroleum Technological University, Ufa, Russia

Abstract. The article discusses the influence on the physical properties of a planar-oriented cholesteric liquid crystal (chlesterylpelargonate) with a thickness of 10-15 microns, the propagation of elastic waves in the ultrasonic range (exposure frequency 600 kHz). Changing the pitch of the crystal spiral leads to changes in its optical properties, which is shown in the modulation spectrum of light reflection from the cholesteric layer in the selective scattering region. It was found that a positive peak is observed at a light wavelength of 436 nm, and a negative peak at 427 nm. A technique of experimental measurements is proposed, which uses the principles of modulation spectroscopy, which makes it possible to record with a high degree of accuracy even insignificant changes in optical spectra, which are not possible to register with conventional optical spectrometers. By analyzing the reconstructed reflection spectrum, it can be concluded how the swirling of a liquid crystal affects the processes that occur in it during the propagation of ultrasonic waves. The considered nonlinear processes are interesting for creating ultrasonic light modulators based on liquid crystals.

1. Introduction

Interest in issues related to the influence of external factors on liquid crystals (LC) continues unabated. This is evidenced by the works of recent years, published by researchers from different countries [1-14]. The various properties of liquid crystals, which are very interesting for practical application, depend on the equilibrium in the distribution of molecules. Orientational rearrangement of molecules caused by the action of ultrasound, heating, electric and magnetic fields, the effect on the chemical composition of the liquid crystal, by doping, lead to significant changes in their physical properties. For example, the authors of [3], using the effect of ultrasound on the liquid crystal layer, propose a lens with variable focus. Thanks to the use of LC, the design has a small size. In [4], a new generation device for displaying information on a cholesteric liquid crystal (CLC) containing a chiral additive is considered. It reacts to a redox reaction, which improves the speed of the device and reduces its power consumption. The influence of sound waves on biological systems is still relevant for medical research. Cholesteric liquid crystals are used as models of living cells. And we can continue to give similar examples.

Below are the results of studying the optical properties of cholesteric liquid crystals under the action of ultrasound on them. To describe the propagation of an ultrasonic wave in a CLC, in addition to the functions of the density of sound energy, medium, angular momentum, a variable is introduced associated with the pitch and angle of inclination of the spiral. In the first case, the internal structure of a nematic liquid crystal has no significant effect on the propagation of an ultrasonic wave, and the speed of sound actually coincides with the speed of sound of the isotropic phase. In the second case, a sound appears for which the velocity c□ is determined by the wave vector qo of the spiral of the twist-structure of the NLC, and c□ □qo. Therefore, in the isotropic phase, c□=0. Since in this situation the

parameters of the spiral change, the optical properties of the NLC should change with the propagation of the ultrasonic wave.

2. Research objects and experimental technique

Let us consider an experimental situation in which the transverse wavelength is greater than the pitch of the spiral. An experimental study of the propagation of an ultrasonic wave in swirling liquid crystals is difficult due to a number of side factors associated with a change in the pitch of the CLC-coil. These factors include crystal heating, as well as significant orientation effects. In this regard, experimental studies of the propagation of an ultrasonic wave should be carried out at sufficiently low intensities of ultrasound acting on the CLC and with continuous heat removal. Taking this circumstance into account, a special registration technique was developed, which is based on the principles of modulation spectroscopy. This technique allows accurate measurements of subtle changes in spectra that are not recorded by conventional optical spectrometers.

The essence of the method is as follows: the action of an ultrasonic wave periodically changes the pitch of the CLC-coil and, accordingly, with selective scattering of light, the wavelength changes, and with monochromatic radiation, the intensity of the scattered light flux. These changes are recorded by the photodetector, separated from the noise and converted to a form convenient for measurements by the phase-sensitive detection system, and then are presented, for example, in the form of the ratio of the variable □I and constant I of the signal components.

The □I/I ratio can be measured in various ways. The simplest is to register only □I at constant I in the entire spectral range. To determine □I/I in this case, it is necessary to introduce a correction factor into the final result, which is determined by the value of I. This problem was solved by maintaining a constant signal level at the output of the photoelectric multiplier by changing the voltage across the diodes using a phase-sensitive amplifier, which through the feedback circuit in the source high voltage was controlled by a computer. After preliminary amplification, the alternating signal was fed to a selective amplifier, then to a voltage converter. A reference voltage with a frequency of 79 Hz was supplied to the voltage converter from a low-frequency generator, which was also used to modulate the high-frequency signal of the generator, which was carried out for the convenience of recording and isolating the useful signal against the background of noise.

Cholesteric liquid crystal (cholesteryl pelargonate) was placed in a flat capillary, where it formed a planar texture, and its state was monitored by a microscope. The thickness of the capillary was set by mica gaskets and was 10 - 15 μm. A longitudinal ultrasonic wave was excited using a shear transducer made of a bismuth selenite crystal with a resonance frequency of 600 kHz. Its acoustic contact with the cell was carried out by gluing it with a Canadian balsam. The experimental cell with a piezoelectric transducer was placed in a thermostated chamber, the temperature of which was set with an accuracy of 0.1° C and controlled using a chromel-alumel thermocouple. Data on temperature and □I/I value were output through two channels to a computer.

3. Research results and their discussion

The measurements performed made it possible to reveal modulation features in the reflection spectrum of CLC in the region of selective light reflection for this type of crystal. As an example, Figure 1 shows the differential spectrum of cholesteryl pelargonate.

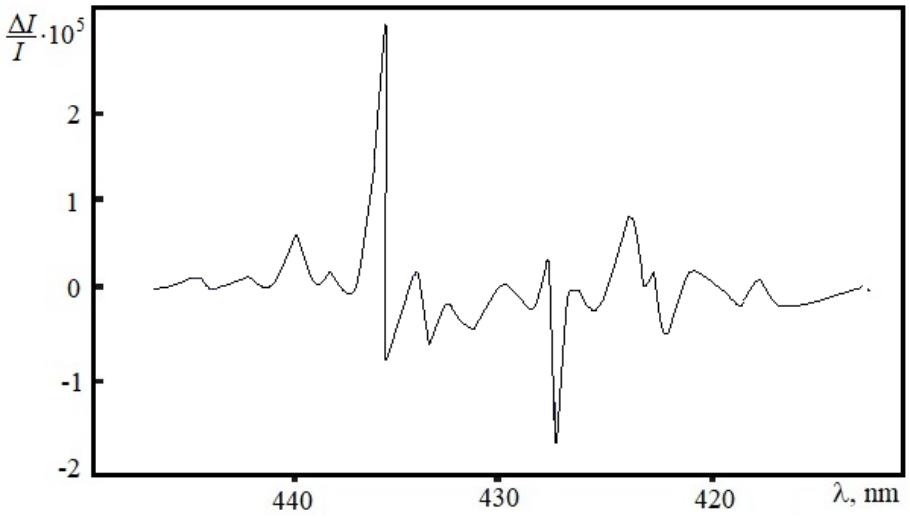

Figure 1. Modulation spectrum of light reflection from the CLC layer in the selective scattering region (T = 345 K)

A positive peak is observed at 436 nm and a negative peak at 427 nm. According to the experimental conditions, this is the differential spectrum of the first derivative of I, since the amplitude of the modulating field was small (pressure $P \approx 10^3$ dyn/cm^2) and the value of $\Delta I/I$ remained small. By restoring the original shape of the selective reflection line from this differential spectrum, one can determine the coefficient of the photoelastic effect. The reconstructed reflection spectrum showed complete coincidence with the shape of the selective scattering line, the form of which is shown in Figure 2.

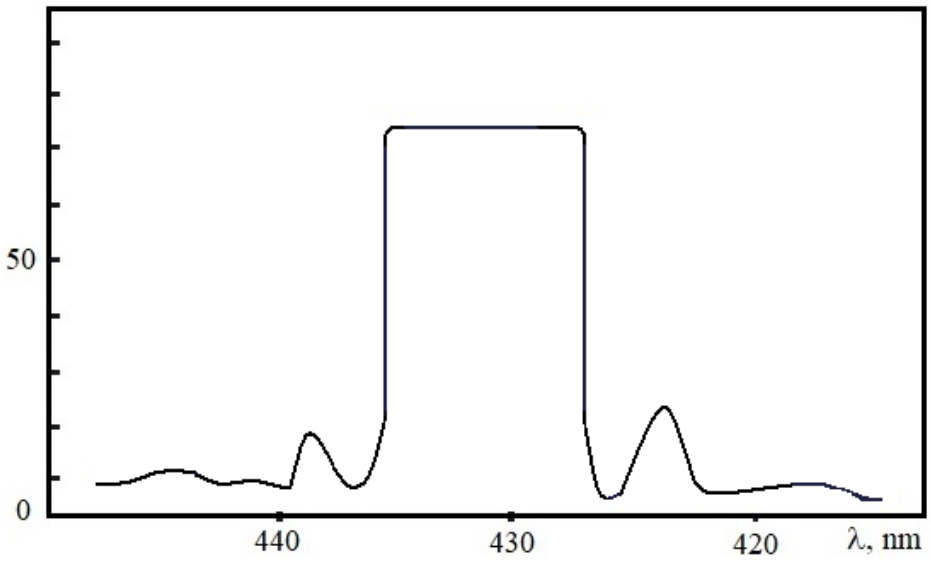

Figure 2. The reconstructed shape of the selective scattering line

To assess the photoelastic effect, it is first necessary to estimate the differential of the reflection coefficient of light from a CLC at angles of incidence close to normal [11]:

$$I \approx \frac{\sin^2(2\pi\ \delta\ h\ q_o)}{\beta^2 + \sin^2(2\pi\ \beta\ \delta\ h\ \alpha)},\ \text{где}\ \beta = \left[\left(\frac{k_o^2 - q_o^2}{\delta k_o^2}\right)^2 - 1\right]^{1/2}, \quad (1)$$

here α is the angle of light scattering, $\delta=(\varepsilon_1-\varepsilon_2)/(\varepsilon_1+\varepsilon_2)$, L is the crystal thickness, $\boldsymbol{q_o}$ is the wave vector of CLC structures, $\boldsymbol{k_o}$ is the wave vector of the incident light, ε_1 and ε_2 are dielectric permeability in the direction of the long and short axis of the molecules.

From (1) we have (for $k_o \approx q_o$)

$$\frac{\Delta I}{I} \approx \frac{ctg(2\pi\ \beta\ \delta\ q_o)}{\beta\omega}\frac{\partial q_o}{\partial t}, \quad (2)$$

which qualitatively characterizes the changes in the differential spectrum. In addition, expression (2) predicts, under the condition $2\pi\beta\delta q_o \sim 2m\pi$ the appearance of a number of additional features that appear in the experimentally recorded spectra (Figure 2). It should also be taken into account that formula (2) is applicable only in the ideal case; therefore, the finiteness of the $\Delta I/I$ value is explained by the imperfection of the real image representing the polycrystal.

4. Conclusion

In conclusion, it should be noted that using the described nonlinear processes observed in a cholesteric liquid crystal, increasing the number of reflections of a light wave from the surface of the LC layer, it is possible to create light modulators and deflectors with a sufficiently large modulation depth and a large deflection angle.

References

[1] Kapustina O 2015 *Akusticheskiy Zhurnal* **61** 49
[2] Kapustina O 2004 *Crystallography* **49(4)** 759
[3] Shimizu Y, Koyama D 2018 *Appl. Phys. Lett.* **112**, 161104
[4] Tokunaga S, Zeng M 2019 *JoVE Jouanal* doi:10.3791/59244
[5] Buka A, Eber N 2012 *Theory, Experiments and Applications* 300
[6] Sun J, Srivastava A, Zhang W, Wang L, Chigrinov V, Kwok H 2014 *Optics Letters* **39(21)** 6209
[7] Elamain O, Hegde G, Komitov L 2016 *Japanese Journal of Applied Physics* **55(7)** 115
[8] Kwon S, Huang W, Zhang S, Yuan F, Jiang X 2013 *Smart Materials and Structures* **22(11)** 115017
[9] Huang S, Huang W, Shu L 2018 *Journal of Advanced Dielectrics* **8(2)** 1830002-1
[10] Bahadur B 2014 *Handbook of liquid crystals. Liquid crystals: Applications and Uses* **1** 500
[11] Blinov L 2011 *Structure and properties of liquid crystals* (Springer) p 433
[12] Sokolova A, Pavlova E, Bagrov D, Klinov D, Shaitan K 2019 *Molecular Crystals and Liquid Crystals* **669(1)** 126
[13] Gahwiller C 2002 *Phys. Rev. Lett.* **28(24)** 1554
[14] Budagovsky I, Ochkin V, Shvetsov S, Bobrovsky A, Boiko N, Shibaev V 2017 *Molecular Crystals and Liquid Crystals* **647** 100

Theoretical studies of plain hinged linkage mechanisms movement in food processing robots-manipulators

S P Babenyshev [1], A A Bratsikhin[2], D S Mamay[2], E A Drofa[1] and O V Prikhodchenko[1,*]

[1]Technological Institute of Service - Stavropol, Don State Technical University, Stavropol, Russia
[2] Institute of Life Sciences, North Caucasus Federal University, Stavropol, Russia

e-mail: oksvo19@yandex.ru

Abstract. Significance of the studied problem is conducted due to the lack of simple and accessible engineering methods that allow predicting kinematic characteristics and selecting parameters of the main elements of modern robotic manipulators that include mechanisms of parallel structure in their design. The solution of such tasks allows determining the ranges of operational indicators of the designed technological equipment in advance, as well as to develop criteria for their analysis. An algorithm for applying the Lagrange II equations to determine the equations of plain hinged linkage mechanisms movement with four degrees of freedom is proposed.

1. Introduction

The modular method design of the basic mechanisms of technological equipment, such as robot manipulators used in food production, based on groups of normalized joint units has unmatched advantages in comparison with traditional design methods. The main of which are:

- the possibility to design the specialized standard units without redundant functions, i.e. designed to solve a specific technological problem;
- reducing of the design process complexity by predicting of kinematic characteristics and selecting needed parameters of the main elements of mechanisms;
- increasing of the unit reliability due to the complete compliance of the mechanism design with the function that is performed for;
- intensification of processes for the finish product obtaining [1-5, 7].

The main functional indicators of technological equipment, such as robot manipulators, are the load capacity, mobility, and, above all, its positioning error. One of the methods oriented for reducing the last indicator is the parallel structure mechanisms using.

However, the complexity of their design prevents the widespread use of such systems. In this regard, the development of an engineering method used for kinematic characteristics predicting and parameters of the main design elements of modern parallel structure mechanisms selecting at the early stages of their design is an urgent scientific and practical task [12,14,15].

2. Formulation of the problem

Figure 1 shows a general schematic diagram of a plain four-degree-of-freedom hinged linkage mechanism commonly used for the robotic arms development in food processing.

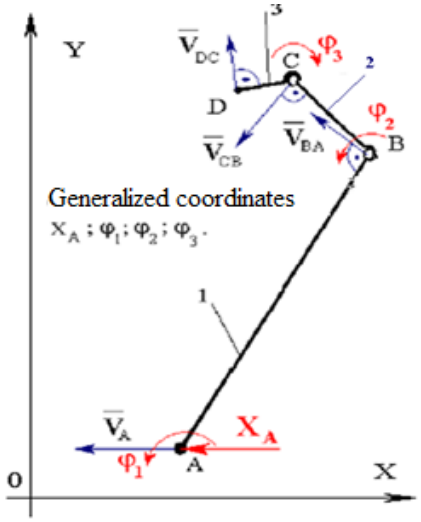

Figure 1. General diagram of a plain hinged linkage mechanism

The model of a plain hinged linkage mechanism, which has four degrees of freedom, in general form can be represented as a mechanical system consisting of:

- link 1, performing rotary movement in the horizontal plane relative to the point A, moving in a straight line;
- link 2 pin-connected to the link 1 in the point B performing translational movement with it and rotation relative to the point B;
- link 3, pin-connected to the link 2 in the point C, and performing translational movement with it and rotation relative to the point C.

The problem formulation is to determine the algorithm for any link position finding for the plain hinged linkage mechanism with four degrees of freedom, depending on the time of its movement from mechanism rest.

3. The proposed algorithm

It is necessary to equation obtain that allow to unambiguously determine the position of the mechanism as a time function. The following algorithm is proposed for that purpose:

- the independent kinematic parameters determination for every links of the mechanism;
- to draw up a system of equations containing a unified characteristic of the links system in the form of the mechanism kinetic energy[6,8-11];
- to compose a mathematical expression for the mechanism kinetic energy in general form, as a function of the joint coordinate system;
- to develop a mathematical model in the form of a system of differential equations describing the laws of movement of plain hinged linkage mechanisms with four freedom degrees;
- to find a solution to the obtained system of differential equations that is sufficiently accurate for engineering problems for preliminary design, which makes it possible to establish the laws of motion for individual links of the same kinds of mechanisms.

4. General solution to the problem

The position of link 3 at any time is determined by four independent parameters - coordinates x_A, φ_1, φ_2 и φ_3. Consequently, a mechanical system, for the first approximation subordinates to ideal, and confining and holonomic constraints, has four degrees of freedom and four Lagrange equations can be written for it in the following general form [3,11,16]:

$$\frac{d}{dt}\left(\frac{\partial T}{\partial \dot{X}_A}\right) - \left(\frac{\partial T}{\partial X_A}\right) = Q \quad (1)$$

$$\frac{d}{dt}\left(\frac{\partial T}{\partial \dot{\varphi}_1}\right) - \left(\frac{\partial T}{\partial \varphi_1}\right) = Q_1 \quad (2)$$

$$\frac{d}{dt}\left(\frac{\partial T}{\partial \dot{\varphi}_2}\right) - \left(\frac{\partial T}{\partial \varphi_2}\right) = Q_2 \quad (3)$$

$$\frac{d}{dt}\left(\frac{\partial T}{\partial \dot{\varphi}_3}\right) - \left(\frac{\partial T}{\partial \varphi_3}\right) = Q_3 \quad (4)$$

where: X_A, $\varphi_{1\text{-}3}$– joint system coordinates; $\dot{X}_A$, $\dot{\varphi}_{1-3}$ – time derivatives of joint coordinates (generalized velocities); T – kinetic energy of the system, expressed in terms of joint coordinates and generalized velocities; Q, $Q_{1\text{-}3}$ – generalized forces.

Let's write an expression for the system kinetic energy T, where all the variable quantities included in it are given in joint coordinates and generalized velocities. The kinetic energy of the entire system can be represented by the corresponding sum [1-5]:

$$T_{mech} = T_1+T_2+T_3 \quad (5)$$

where: T_1, T_2 and T_3– kinetic energies of the mechanical system links.

Link 1 moves at speed (portable) $\overrightarrow{V_A}$ and performs rotational (relative) movement in the horizontal plane (with an angular velocity ω_{BA}) relative to the point A. Consequently, the AB link makes a plane-parallel movement. Then the kinetic energy of link 1 in general form can be represented as:

$$T_1 = \frac{m_1 \cdot V_A^2}{2} + I_1 \cdot \frac{\omega_{BA}^2}{2} \quad (6)$$

$\vec{V}_A$ is the time derivative of the joint coordinate X_A and it is the generalized speed $\dot{X}_A = \frac{dX_A}{dt}$.

ω_{BA} - respectively, the time derivative of the joint coordinate φ_1, therefore, is the generalized velocity $\dot{\varphi_1} = \frac{d\varphi_1}{dt}$ (the angular velocity of the link 1). Thus:

$$T_1 = \frac{m_1 \cdot \dot{X}_A^2}{2} + I_1 \cdot \frac{\dot{\varphi}_1^2}{2}; \quad (7)$$

$$\text{assume that } I_1 = \frac{m_1 \cdot l_1^2}{3};$$

For the purposes of the mechanism kinematic study, the AB link can be considered as a homogeneous rod, then taking into account its moment of inertia, and the expression (6) can be rewritten in the following form:

$$T_1 = \frac{m_1}{2}\left(\dot{X}_A^2 + \frac{AB^2 \cdot \dot{\varphi}_1^2}{\mathbf{3}}\right) \quad (8)$$

Since the plane-parallel movement of a rigid body can be considered as the sum of its two simple motions: translational movement together with the pole and rotation around the pole [1,2,17,18], then,

based on this, link 2 moves together with link AB at a speed (portable) $\overrightarrow{V_B}$ and at the same time performs rotational (relative) motion in the horizontal plane (with an angular velocity ω_{BC}) relative to the point B. Consequently, the link BC makes a plane-parallel movement. Then the kinetic energy of link 2 in general form can be represented as:

$$T_2 = \frac{m_2 \cdot V_B^2}{2} + I_2 \cdot \frac{\omega_{BC}^2}{2}; \quad (9)$$

Point B, which belongs to the AB link, makes a complex movement (Figure 2).
Its absolute speed will be determined by the vector expression:

$$\vec{V}_B = \overrightarrow{V_A} + \overrightarrow{V_{BA}} \quad (10)$$

The velocity V_B is found from the algebraic equation:

$$V_B^2 = V_A^2 + V_{BA}^2 + 2 \cdot V_A \cdot V_{BA} cos(90 - \varphi_1) \quad (11)$$

since cos (90° — φ) = sin φ, then

$$V_B^2 = V_A^2 + V_{BA}^2 + 2 \cdot V_A \cdot V_{BA} sin\varphi_1 \quad (12)$$

where: φ_1 - the value of the joint coordinate at a given time.

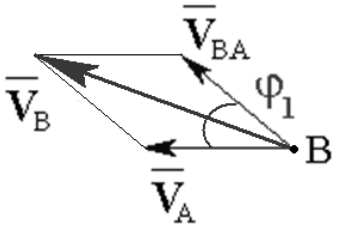

Figure 2. Diagram for the speed of point B determination

ω_{BC} it is a time derivative of the joint coordinate φ_2 and accordingly, it is the generalized speed $\acute{\varphi}_2 = \frac{d\varphi_2}{dt}$ (angular velocity of the link 2).
Thus:

$$T_2 = \frac{m_2 \cdot V_B^2}{2} + I_2 \cdot \frac{\acute{\varphi}_2^2}{2} \quad (13)$$

where it can be accepted that $I_2 = \frac{m_2 \cdot l_2^2}{12}$;

For the purposes of the kinematic study of the mechanism, the BC link can be considered a homogeneous rod, then taking into account the moment of inertia, the expression (13) can be rewritten in the following form:

$$T_2 = \frac{m_2}{2}(V_B^2 + \frac{BC^2 \cdot \acute{\varphi}_2^2}{12}); \quad (14)$$

By delivering (10) to (13) and taking into account that $V_{BA} = \omega_{BA} \cdot BA = \acute{\varphi}_1 \cdot BA$, it gets to the next form:

$$T_2 = \frac{m_2}{2}[\acute{X}_A^2 + (\acute{\varphi}_1 \cdot BA)^2 + 2 \cdot \acute{X}_A \cdot \acute{\varphi}_1 \cdot BA \cdot sin\varphi_1 + \frac{BC^2 \cdot \acute{\varphi}_2^2}{12}] \quad (15)$$

By the similar way, considering the movement of link 3 in the general case as complex, in accordance with [1,2,5,14,15] we can assume that the link 3 moves along with the aircraft link at a speed of

(portable) $\overrightarrow{V_C}$ and simultaneously performs a rotational (relative) movement in a horizontal plane (with angular velocity ω_{CD}) relative to the point C. Therefore, the CD link performs a plane-parallel movement. Then the kinetic energy of link 3 can be represented as:

$$T_3 = \frac{m_3 \cdot V_C^2}{2} + I_3 \cdot \frac{\omega_{CD}^2}{2} \quad (16)$$

assuming that $I_3 = \frac{m_3 \cdot l_3^2}{12}$; then

$$T_3 = \frac{m_3 \cdot V_C^2}{2} + \frac{m_3 \cdot l_3^2}{12} \cdot \frac{\omega_{CD}^2}{2}; \quad (17)$$

The point C belonging to the CB link performs a complex movement (figure 3).

Its absolute speed will be determined by the vector expression:

$$\vec{V}_C = \overrightarrow{V_B} + \overrightarrow{V_{CB}} \quad (18)$$

The value of the velocity V_C is found from the algebraic equation:

$$V_C^2 = V_B^2 + V_{CB}^2 + 2 \cdot V_B \cdot V_{CB} \cdot cos\varphi_2 \quad (19)$$

where: φ_3 - is the value of the joint coordinate at a given time.

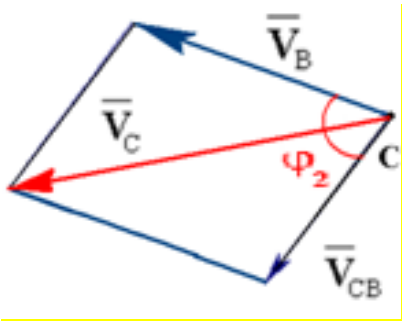

$$V_B^2 = V_A^2 + V_{BA}^2 + 2 \cdot V_A \cdot V_{BA} sin\varphi_1 ; \qquad V_C^2 = V_B^2 + V_{CB}^2 + 2 \cdot V_B \cdot V_{CB} \cdot cos\varphi_2$$

Figure 3. Diagram for the point C velocity determination

Taking into account (11) and taking into account that $V_{CB} = \omega_{BC} \cdot BC = \dot{\varphi}_2 \cdot BC$, gets an expression for determining the point C velocity:

$$V_C^2 = \dot{X}_A^2 + \dot{\varphi}_1^2 \cdot BA^2 + 2 \cdot \dot{X}_A \cdot \dot{\varphi}_1 \cdot BA \cdot sin\,\varphi_1 + \dot{\varphi}_2^2 \cdot BC^2 + 2 \cdot \left(\sqrt{\dot{X}_A^2 + \dot{\varphi}_1^2 \cdot BA^2 + 2 \cdot \dot{X}_A \cdot \dot{\varphi}_1 \cdot BA \cdot sin\,\varphi_1}\right) \cdot \dot{\varphi}_2 \cdot BC \cdot cos\varphi_2 \quad (20)$$

For the purposes of the mechanism kinematic study, the CD link can be considered as a homogeneous rod, then taking into account its moment of inertia, equation (20) can be rewritten as follows:

$$T_3 = \frac{m_3}{2}\left(V_C^2 + \frac{CD^2 \cdot \dot{\varphi}_3^2}{12}\right) \quad (21)$$

By delivering (20) to (21) and taking into account that $V_{CB} = \omega_{BC} \cdot BC = \dot{\varphi}_2 \cdot BC$, it gets to the next form:

$$T_3 = \frac{m_3}{2}[\dot{X}_A^2 + \dot{\varphi}_1^2 \cdot BA^2 + 2 \cdot \dot{X}_A \cdot \dot{\varphi}_1 \cdot BA \cdot sin\,\varphi_1 + \dot{\varphi}_2^2 \cdot BC^2 + 2 \cdot \left(\sqrt{\dot{X}_A^2 + \dot{\varphi}_1^2 \cdot BA^2 + 2 \cdot \dot{X}_A \cdot \dot{\varphi}_1 \cdot BA \cdot sin\,\varphi_1}\right) \cdot \dot{\varphi}_2 \cdot BC \cdot cos\varphi_2 + \frac{CD^2 \cdot \dot{\varphi}_3^2}{12}] \quad (22)$$

Taking into account the obtained results, the expression (5) for determining the mechanism kinetic energy takes the following form:

$$T_{мех} = \frac{m_1}{2}\left(\dot{X}_A^2 + \frac{AB^2\cdot\dot{\varphi}_1^2}{3}\right) + \frac{m_2}{2}\left[\dot{X}_A^2 + (\dot{\varphi}_1\cdot BA)^2 + 2\cdot\dot{X}_A\cdot\dot{\varphi}_1\cdot \mathrm{BA}\cdot sin\varphi_1 + \frac{BC^2\cdot\dot{\varphi}_2^2}{12}\right] + \frac{m_3}{2}\cdot\left[\dot{X}_A^2 + (\dot{\varphi}_1\cdot BA)^2 + 2\cdot\dot{X}_A\cdot\dot{\varphi}_1\cdot \mathrm{BA}\cdot sin\varphi_1 + \dot{\varphi}_2^2\cdot \mathrm{BC}^2 + 2\cdot\sqrt{\left(\dot{X}_A^2 + (\dot{\varphi}_1\cdot BA)^2 + 2\cdot\dot{X}_A\cdot\dot{\varphi}_1\cdot \mathrm{BA}\cdot sin\varphi_1\right)}\cdot\dot{\varphi}_2\cdot \mathrm{BC}\cdot cos\varphi_2 + \frac{CD^2\cdot\dot{\varphi}_3^2}{12}\right] \quad (23)$$

Find expressions for partial derivatives in equations (1-4):

$$\frac{\partial T}{\partial \dot{X}_A} = (m_1 + m_2 + m_3)\cdot\dot{X}_A + (m_2 + m_3)\cdot \mathrm{BA}\cdot\dot{\varphi}_1\cdot sin\varphi_1 + m_3\cdot\left(\frac{(\dot{X}_A + \dot{\varphi}_1\cdot \mathrm{BA}\cdot \boldsymbol{sin\varphi_1})\cdot\dot{\varphi}_2\cdot \mathrm{BC}\cdot cos\varphi_2}{\sqrt{\left(\dot{X}_A^2 + (\dot{\varphi}_1\cdot BA)^2 + 2\cdot\dot{X}_A\cdot\dot{\varphi}_1\cdot \mathrm{BA}\cdot sin\varphi_1\right)}}\right) \quad (24)$$

$$\frac{\partial T}{\partial \dot{\varphi}_1} = \left(\frac{m_1}{\mathbf{3}} + m_2 + m_3\right)\cdot\dot{\varphi}_1\cdot BA^2 + (m_2 + m_3)\cdot \mathrm{BA}\cdot\dot{X}_A\cdot sin\varphi_1 + m_3\cdot\left(\frac{(\dot{\varphi}_1\cdot BA^2 + \dot{X}_A\cdot \mathrm{BA}\cdot sin\varphi_1)\cdot\dot{\varphi}_2\cdot \mathrm{BC}\cdot cos\varphi_2}{\sqrt{\left(\dot{X}_A^2 + (\dot{\varphi}_1\cdot BA)^2 + 2\cdot\dot{X}_A\cdot\dot{\varphi}_1\cdot \mathrm{BA}\cdot sin\varphi_1\right)}}\right) \quad (25)$$

$$\frac{\partial T}{\partial \dot{\varphi}_2} = \left(\frac{m_2}{\mathbf{12}} + m_3\right)\cdot\dot{\varphi}_2\cdot BC^2 + m_3\cdot\left(\sqrt{\left(\dot{X}_A^2 + (\dot{\varphi}_1\cdot \mathrm{BA})^2 + 2\cdot\dot{X}_A\cdot\dot{\varphi}_1\cdot \mathrm{BA}\cdot sin\varphi_1\right)}\cdot \mathrm{BC}\cdot cos\varphi_2\right); \quad (26)$$

$$\frac{\partial T}{\partial \dot{\varphi}_3} = \frac{m_3\cdot CD^2\cdot\dot{\varphi}_3}{\mathbf{12}} \quad (27)$$

$$\frac{\partial T}{\partial X_A} = 0 \quad (28)$$

$$\frac{\partial T}{\partial \varphi_1} = (m_2 + m_3)\cdot \mathrm{BA}\cdot\dot{X}_A\cdot\dot{\varphi}_1\cdot cos\varphi_1 + m_3\cdot\left(\frac{\dot{X}_A\cdot\dot{\varphi}_1\cdot BA\cdot cos\varphi_1}{\sqrt{\left(\dot{X}_A^2 + (\dot{\varphi}_1\cdot BA)^2 + 2\cdot\dot{X}_A\cdot\dot{\varphi}_1\cdot \mathrm{BA}\cdot sin\varphi_1\right)}}\right) \quad (29)$$

$$\frac{\partial T}{\partial \varphi_2} = -m_3\cdot\left(\sqrt{\left(\dot{X}_A^2 + (\dot{\varphi}_1\cdot \mathrm{BA})^2 + 2\cdot\dot{X}_A\cdot\dot{\varphi}_1\cdot \mathrm{BA}\cdot \sin\varphi_1\right)}\cdot \mathrm{BC}\cdot \sin\varphi_2\right); \quad (30)$$

$$\frac{\partial T}{\partial \varphi_3} = 0 \quad (31)$$

Substituting (24-31) into equations (1-4) and notation making

K_1= (32)

$$\frac{\left[\frac{\left(\ddot{X}_A + \ddot{\varphi}_1\cdot \mathrm{BA}\cdot \cos\varphi_1 - \dot{\varphi}_1\cdot\dot{\varphi}_1\cdot \mathrm{BA}\cdot \sin\varphi_1\right)\cdot\dot{\varphi}_2\cdot \mathrm{BC}\cdot \cos\varphi_2}{1}\right] + \left[\frac{\left(\dot{X}_A + \dot{\varphi}_1\cdot \mathrm{BA}\cdot \cos\varphi_1\right)\cdot\ddot{\varphi}_2\cdot \mathrm{BC}\cdot \cos\varphi_2}{1}\right] -}{\sqrt{\left(\dot{X}_A^2 + (\dot{\varphi}_1\cdot BA)^2 + 2\cdot\dot{X}_A\cdot\dot{\varphi}_1\cdot \mathrm{BA}\cdot cos\varphi_1\right)}}$$

$$+\frac{\left[\frac{(\dot{X}_A+\dot{\varphi}_1\cdot BA\cdot\cos\varphi_1)\cdot\dot{\varphi}_2\cdot\dot{\varphi}_2\cdot BC\cdot\sin\varphi_2}{1}\right]\cdot}{\sqrt{\left(\dot{X}_A^2+(\dot{\varphi}_1\cdot BA)^2+2\cdot\dot{X}_A\cdot\dot{\varphi}_1\cdot BA\cdot cos\varphi_1\right)}}$$

$$\cdot\frac{\left[\frac{\sqrt{\left(\dot{X}_A^2+(\dot{\varphi}_1\cdot BA)^2+2\cdot\dot{X}_A\cdot\dot{\varphi}_1\cdot BA\cdot\cos\varphi_1\right)}}{1}\right]-}{\sqrt{\left(\dot{X}_A^2+(\dot{\varphi}_1\cdot BA)^2+2\cdot\dot{X}_A\cdot\dot{\varphi}_1\cdot BA\cdot cos\varphi_1\right)}}$$

$$\frac{\left(\frac{(\dot{X}_A\cdot\ddot{X}_A+\dot{\varphi}_1\cdot\ddot{\varphi}_1+\ddot{X}_A\cdot\dot{\varphi}_1\cdot BA\cdot cos\varphi_1+\dot{X}_A\cdot\ddot{\varphi}_1\cdot BA\cdot cos\varphi_1-\dot{X}_A\cdot\dot{\varphi}_1\cdot BA\cdot sin\varphi_1)}{\sqrt{\left(\dot{X}_A^2+(\dot{\varphi}_1\cdot BA)^2+2\cdot\dot{X}_A\cdot\dot{\varphi}_1\cdot BA\cdot cos\varphi_1\right)}}\right)}{\sqrt{\left(\dot{X}_A^2+(\dot{\varphi}_1\cdot BA)^2+2\cdot\dot{X}_A\cdot\dot{\varphi}_1\cdot BA\cdot cos\varphi_1\right)}}$$

$$\cdot\frac{(\dot{X}_A+\dot{\varphi}_1\cdot BA\cdot cos\varphi_1)\cdot\dot{\varphi}_2\cdot BC\cdot cos\varphi_2}{\sqrt{\left(\dot{X}_A^2+(\dot{\varphi}_1\cdot BA)^2+2\cdot\dot{X}_A\cdot\dot{\varphi}_1\cdot BA\cdot cos\varphi_1\right)}}$$

$K_2=$ (33)

$$\frac{\frac{(\ddot{\varphi}_1+\ddot{X}_A\cdot BA\cdot\cos\varphi_1-\dot{X}_A\cdot\dot{\varphi}_1\cdot BA\cdot\sin\varphi_1)}{1}\cdot}{\sqrt{\left(\dot{X}_A^2+(\dot{\varphi}_1\cdot BA)^2+2\cdot\dot{X}_A\cdot\dot{\varphi}_1\cdot BA\cdot cos\varphi_1\right)}}\cdot$$

$$\cdot\frac{\frac{\dot{\varphi}_2\cdot BC\cdot\cos\varphi_2+(\dot{\varphi}_1\cdot BA^2+\dot{X}_A\cdot BA\cdot\cos\varphi_1)\cdot\ddot{\varphi}_2\cdot BC\cdot\cos\varphi_2}{1}}{\sqrt{\left(\dot{X}_A^2+(\dot{\varphi}_1\cdot BA)^2+2\cdot\dot{X}_A\cdot\dot{\varphi}_1\cdot BA\cdot cos\varphi_1\right)}}-$$

$$+\frac{\frac{(\dot{\varphi}_1\cdot BA^2+\dot{X}_A\cdot BA\cdot\cos\varphi_1)\cdot\dot{\varphi}_2\cdot\dot{\varphi}_2\cdot BC\cdot\sin\varphi_2}{1}}{\sqrt{\left(\dot{X}_A^2+(\dot{\varphi}_1\cdot BA)^2+2\cdot\dot{X}_A\cdot\dot{\varphi}_1\cdot BA\cdot cos\varphi_1\right)}}\cdot$$

$$\frac{\frac{\sqrt{\left(\dot{X}_A^2+(\dot{\varphi}_1\cdot BA)^2+2\cdot\dot{X}_A\cdot\dot{\varphi}_1\cdot BA\cdot\cos\varphi_1\right)}}{1}}{\sqrt{\left(\dot{X}_A^2+(\dot{\varphi}_1\cdot BA)^2+2\cdot\dot{X}_A\cdot\dot{\varphi}_1\cdot BA\cdot cos\varphi_1\right)}}-$$

$$\frac{\left(\frac{(\dot{X}_A\cdot\ddot{X}_A+\dot{\varphi}_1\cdot\ddot{\varphi}_1+\ddot{X}_A\cdot\dot{\varphi}_1\cdot BA\cdot cos\varphi_1+\dot{X}_A\cdot\ddot{\varphi}_1\cdot BA\cdot cos\varphi_1-\dot{X}_A\cdot\dot{\varphi}_1\cdot\dot{\varphi}_1\cdot BA\cdot sin\varphi_1)}{\sqrt{\left(\dot{X}_A^2+(\dot{\varphi}_1\cdot BA)^2+2\cdot\dot{X}_A\cdot\dot{\varphi}_1\cdot BA\cdot cos\varphi_1\right)}}\right)}{\sqrt{\left(\dot{X}_A^2+(\dot{\varphi}_1\cdot BA)^2+2\cdot\dot{X}_A\cdot\dot{\varphi}_1\cdot BA\cdot cos\varphi_1\right)}}\cdot$$

$$\frac{(\dot{\varphi}_1\cdot BA^2+\dot{X}_A\cdot BA\cdot cos\varphi_1)\cdot\dot{\varphi}_2\cdot BC\cdot cos\varphi_2}{\sqrt{\left(\dot{X}_A^2+(\dot{\varphi}_1\cdot BA)^2+2\cdot\dot{X}_A\cdot\dot{\varphi}_1\cdot BA\cdot cos\varphi_1\right)}}$$

$$К_3=\left(\frac{(\dot{X}_A\cdot\ddot{X}_A+\dot{\varphi}_1\cdot\ddot{\varphi}_1\cdot BA^2+\ddot{X}_A\cdot\dot{\varphi}_1\cdot \text{BA}\cdot cos\varphi_1+\dot{X}_A\cdot\ddot{\varphi}_1\cdot \text{BA}\cdot cos\varphi_1-\dot{X}_A\cdot\dot{\varphi}_1\cdot\dot{\varphi}_1\cdot \text{BA}\cdot sin\varphi_1)\cdot \text{BC}\cdot cos\varphi_2}{\sqrt{(\dot{X}_A^2+(\dot{\varphi}_1\cdot BA)^2+2\cdot\dot{X}_A\cdot\dot{\varphi}_1\cdot \text{BA}\cdot cos\varphi_1)}}-\left(\sqrt{(\dot{X}_A^2+(\dot{\varphi}_1\cdot BA)^2+2\cdot\dot{X}_A\cdot\dot{\varphi}_1\cdot \text{BA}\cdot cos\varphi_1)}\right)\dot{\varphi}_2\cdot \text{BA}\cdot sin\varphi_2\right) \quad (34)$$

the final form can be given in the next view:

$$\frac{d}{dt}\left(\frac{\partial T}{\partial \dot{X}_A}\right)-\frac{\partial T}{\partial X_A}=(m_1+m_2+m_3)\cdot\ddot{X}_A+(m_2+m_3)\cdot BA\cdot(\ddot{\varphi}_1\cdot cos\varphi_1-\dot{\varphi}_1^2\cdot sin\varphi_1)+m_3\cdot К_1=\text{Q} \quad (35)$$

$$\frac{d}{dt}\left(\frac{\partial T}{\partial \dot{\varphi}_1}\right)-\frac{\partial T}{\partial \varphi_1}=(\frac{m_1}{12}+m_2+m_3)\cdot\ddot{\varphi}_1\cdot BA^2+(m_2+m_3)\cdot BA\cdot\left(\ddot{X}_A\cdot cos\varphi_1-\dot{X}_A\cdot\dot{\varphi}_1\cdot sin\varphi_1\right)+m_3\cdot К_2=\text{Q}_1 \quad (36)$$

$$\frac{d}{dt}\left(\frac{\partial T}{\partial \dot{\varphi}_2}\right)-\frac{\partial T}{\partial \varphi_2}=(m_2+m_3)\cdot\ddot{\varphi}_2\cdot BC^2+m_3\cdot К_3=\text{Q}_2 \quad (37)$$

$$\frac{d}{dt}\left(\frac{\partial T}{\partial \dot{\varphi}_3}\right)-\frac{\partial T}{\partial \varphi_3}=\frac{m_3\cdot CD^2\cdot\ddot{\varphi}_3}{3}=\text{Q}_3 \quad (38)$$

The established expressions (35-38) are the mathematical model that generally describes the laws of motion in the form of Lagrange equations of the second kind of plane hinged linkage mechanisms with four degrees of freedom. To simplify expressions (35-38), additional notation can be introduced:

$$m_1+m_2+m_3=\text{a} \quad (39)$$

$$(m_2+m_3)\cdot BA=\text{b} \quad (40)$$

$$(\frac{m_1}{12}+m_2+m_3)\cdot BA^2=\text{c} \quad (41)$$

$$(m_2+m_3)\cdot BC^2=\text{d}; \quad (42)$$

$$f=\frac{m_3\cdot l_3^2}{3} \quad (43)$$

Substituting (38-42) in (34-37), the following system of differential equations can be obtained:

$$a\cdot\ddot{X}_A+b\cdot(\ddot{\varphi}_1\cdot cos\varphi_1-\dot{\varphi}_1^2\cdot sin\varphi_1)+m_3\cdot К_1=\text{Q} \quad (44)$$

$$c\cdot\ddot{\varphi}_1+b\cdot\left(\ddot{X}_A\cdot cos\varphi_1-\dot{X}_A\cdot\dot{\varphi}_1\cdot sin\varphi_1\right)+m_3\cdot К_2=\text{Q}_1 \quad (45)$$

$$d\cdot\ddot{\varphi}_2+m_3\cdot К_3=\text{Q}_2 \quad (46)$$

$$\text{f}\cdot\ddot{\varphi}_3=\text{Q}_3 \quad (47)$$

The generalized forces Q must be defined at the next step. Doing that the possible and independent elementary displacements δq_i for every coordinates δx_A, $\delta\varphi_1$, $\delta\varphi_2$, $\delta\varphi_3$ must be set. Let's give the system

consecutive elementary moves $\delta x_A \neq 0$ by $\delta\varphi_i = 0$, and $\delta\varphi_i \neq 0$ by $\delta x_A = 0$ respectively. At that condition the following cases are possible when the forces acting on the mechanism will be reduced to one of its links (figure 4):

a) by $\delta xA \neq 0$ and $\delta\varphi 1\text{-}3 = 0$ forces are reduced to the resultant R = N, then Q1= N;
b) by $\delta\varphi 1 \neq 0$, $\delta\varphi 2,3 = 0$ and $\delta xA = 0$ forces are also reduced to a single resultant, similarly Q2= N;
c) if there are elastic forces in the system (Felas. = C·ΔS) and $\delta\varphi 2 \neq 0$, $\delta\varphi 1,3 = 0$ by $\delta xA = 0$ the value of the generalized force can be represented as Q2= R+ Felas.;
d) by $\delta\varphi 3 \neq 0$, $\delta\varphi 1,2 = 0$ and $\delta xA = 0$ forces are also reduced to a single resultant, which can be expressed as Q3=M as a moment of forces that is caused by the action Fres., attached at the point D.

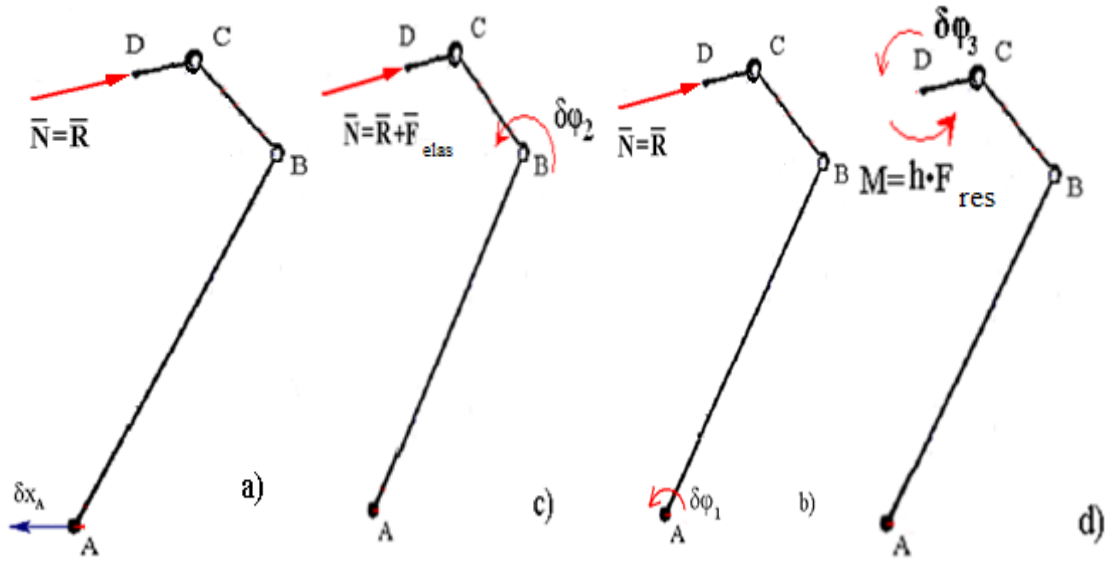

Figure 4. Scheme for generalized forces Q_i determination

The possible numerical values of the coefficients $K_{1\text{-}3}$ should be determined for the purposes of obtained system of differential equations (44-47) practical using. Let's introduced the new notations that do not affect the results of the study, but would simplify mathematical expressions:

$$K_1 = \frac{P-Q-G}{W},$$

where:

$$P = 2 \cdot AB \cdot BC \cdot x^2 \cdot y \cdot \cos\varphi_1 \cdot \cos\varphi_2 \cdot (z^2 + (x \cdot BA)^2 + 2 \cdot z \cdot x \cdot BA \cdot \cos\varphi_1) \quad (48)$$

$$Q = 2 \cdot (z + AB \cdot x \cdot \sin\varphi_1) \cdot y^2 \cdot BC \cdot \sin\varphi_2 \cdot (z^2 + (x \cdot BA)^2 + 2 \cdot z \cdot x \cdot BA \cdot \cos\varphi_1) \quad (49)$$

$$G = (z + AB \cdot x \cdot \sin\varphi_1) \cdot z \cdot y \cdot x^2 \cdot AB \cdot BC \cdot \cos\varphi_1 \cdot \sin\varphi_1 \quad (50)$$

$$W = (z^2 + (x \cdot BA)^2 + 2 \cdot z \cdot x \cdot BA \cdot \cos\varphi_1)^{1,5} \quad (51)$$

Substituting the numerical values of the mechanism geometric dimensions into expressions (48-51) and setting its initial kinematic parameters in the practically used ranges, it is clear that the last terms of the equations (44-46), in comparison with the rest in absolute value, represent values of a lower order. That is the case when the resulting differential equations (48-51) can be written in a simplified form:

$$a \cdot \ddot{X}_A + b \cdot (\ddot{\varphi}_1 \cdot cos\varphi_1 - \dot{\varphi}_1^2 \cdot sin\varphi_1) = \mathrm{N} \quad (52)$$

$$c \cdot \ddot{\varphi}_1 + b \cdot \left(\ddot{X}_A \cdot cos\varphi_1 - \dot{X}_A \cdot \dot{\varphi}_1 \cdot sin\varphi_1\right) = \mathrm{N} \quad (53)$$

$$d \cdot \ddot{\varphi}_2 = \mathrm{N} + \mathrm{C} \cdot l \cdot \varphi_2 \quad (54)$$

$$\mathrm{f} \cdot \ddot{\varphi}_3 = \mathrm{F}_{\mathrm{res.}} \quad (55)$$

where: l - the reduced linear size of the link 2; C is a reduced elasticity coefficient of the elements installed on the mechanism.

5. Discussion

To solve the resulting system of differential equations (52-55), the followed additional notation can be introduced:

$$\frac{b}{a} = A;\ \frac{b}{\mathrm{c}} = \mathrm{B};\ \frac{N}{a} = D;\ \frac{N}{\mathrm{c}} = R; \quad (56)$$

After substituting (56) in (52) and (53), the new view of equation system can be obtained:

$$\begin{cases} \ddot{X}_A + \mathrm{A} \cdot \ddot{\varphi}_1 \cdot cos\varphi_1 - \mathrm{A} \cdot \dot{\varphi}_1^2 \cdot sin\varphi_1 = D \\ \ddot{\varphi}_1 + \mathrm{B} \cdot \ddot{X}_A \cdot cos\varphi_1 - \mathrm{B} \cdot \dot{X}_A \cdot \dot{\varphi}_1 \cdot sin\varphi_1 = \mathrm{R} \end{cases} \quad (57)$$

Take into account that:

$$\frac{d(\dot{\varphi}_1 \cdot cos\varphi_1)}{dt} = \ddot{\varphi}_1 \cdot cos\varphi_1 - \dot{\varphi}_1^2 sin\varphi_1 \quad (58)$$

$$\frac{d(\dot{X}_A \cdot cos\varphi_1)}{dt} = \ddot{X}_A \cdot cos\varphi_1 - \dot{\varphi}_1^2 sin\varphi_1 \quad (59)$$

Then the system of differential equations (57) can be rewritten in the following form:

$$\ddot{X}_A + A \cdot \frac{d(\dot{\varphi}_1 \cdot cos\varphi_1)}{dt} = D \quad (60)$$

$$\ddot{\varphi}_1 + B \cdot \frac{d(\dot{X}_A \cdot cos\varphi_1)}{dt} = R \quad (61)$$

After integration, it will get into the next form:

$$\dot{X}_A + A \cdot \dot{\varphi}_1 \cdot cos\varphi_1 = D \cdot t + C_1 \quad (62)$$

$$\dot{\varphi}_1 + B \cdot \dot{X}_A \cdot cos\varphi_1 = R \cdot t + C_2 \quad (63)$$

Substituting the given initial conditions:

C_1=0 и C_2=0 ;

and multiply (63) by $A \cdot cos\varphi_1$ and the result is subtracted from (62). By the way, the equation (62) multiplied by $B \cdot cos\varphi_1$ and accordingly subtract from (63), and finally the following views will be obtained:

$$\dot{X}_A - A \cdot B \cdot \dot{X}_A \cdot cos^2\varphi_1 = D \cdot t - R \cdot t \cdot A \cdot cos\varphi_1 \quad (64)$$

$$\dot{\varphi}_1 - A \cdot B \cdot \dot{\varphi}_1 \cdot cos^2\varphi_1 = R \cdot t - D \cdot t \cdot B \cdot cos\varphi_1 \quad (65)$$

From (64, 65) it follows that:

$$\dot{X}_A = \frac{(D - R \cdot A \cdot cos\varphi_1) \cdot t}{1 - A \cdot B \cdot cos^2\varphi_1} \quad (66)$$

$$\dot{\varphi}_1 = \frac{(R - D \cdot B \cdot cos\varphi_1) \cdot t}{1 - A \cdot B \cdot cos^2\varphi_1} \quad (67)$$

at the same time let's assume that $cos^2\varphi_1 \neq \frac{1}{A \cdot B}$ и $0<|A \cdot B|<1$

It is obvious that the system (66,67) has a trivial solution when:

$$\begin{cases} \varphi_1 = 0 \\ D \cdot B = R \end{cases}$$

where from $\dot{X}_A = \frac{D - R \cdot A}{1 - A \cdot B} \cdot t$

To find the exact solution of the system (66,67), it is assumed that:

$$R - D \cdot B \cdot cos\varphi_1 \neq 0$$

The system (57) for t=0 under initial conditions can be written as follows:

$$\ddot{X}_A(0) + A \cdot \ddot{\varphi}_1(0) = D \quad (68)$$

$$\ddot{\varphi}_1(0) + B \cdot \ddot{X}_A(0) = R \quad (69)$$

where from $|A \cdot B|<1$:

$$\ddot{X}_A(0) = \frac{D - R \cdot A}{1 - A \cdot B} \quad (70)$$

$$\ddot{\varphi}_1(0) = \frac{R - D \cdot B}{1 - A \cdot B} \quad (71)$$

Let's integrate the equation (67) by separating of the variables:

$$\int_{\varphi_0}^{\varphi_1} \frac{d\varphi_1(1 - A \cdot B \cdot cos^2\varphi_1)}{R - D \cdot B \cdot cos\varphi_1} = \frac{t^2}{2} \quad (72)$$

and so on:

$$\int_{\varphi_0}^{\varphi_1} \frac{d\varphi_1}{R - D\ \cdot B \cdot cos\varphi_1} - A \cdot B \int_{\varphi_0}^{\varphi_1} \frac{(1 - sin^2\varphi_1)d\varphi_1}{R - D\ \cdot B \cdot cos\varphi_1} = \frac{t^2}{2} \tag{73}$$

then:

$$\left(\int_{\varphi_0}^{\varphi_1} \frac{d\varphi_1}{R - D\ \cdot B \cdot cos\varphi_1}\right)(1 - A \cdot B) - A \cdot B \int_{\varphi_0}^{\varphi_1} \frac{\sqrt{(1 - cos^2\varphi_1)}dcos\varphi_{1_1}}{R - D\ \cdot B \cdot cos\varphi_1} = \frac{t^2}{2} \tag{74}$$

The next notation for the integrals should be introduced:

$$I_1(\varphi_1) = \int_{\varphi_0}^{\varphi_1} \frac{d\varphi_1}{R - D\ \cdot B \cdot cos\varphi_1} \tag{75}$$

$$I_2(\varphi_1) = \int_{\varphi_0}^{\varphi_1} \frac{\sqrt{(1 - cos^2\varphi_1)}dcos\varphi_{1_1}}{R - D\ \cdot B \cdot cos\varphi_1} \tag{76}$$

Thus, the solution of equation (67) can be represented in the following compact form:

$$(1 - A \cdot B) \cdot I_1(\varphi_1) - A \cdot B \cdot I_2(\varphi_1) \tag{77}$$

In accordance with the recommendations [4] it can be written:

$$I_1(\varphi_1) = \frac{t^2}{2}, \tag{78}$$

$$I_2(\varphi_1) = -\frac{1}{D\ \cdot B} \int_1^{cos\varphi_1} \frac{\sqrt{(1 - X_A^2)}dX_A}{(X_A - \frac{\mathrm{R}}{D\ \cdot B})} = -\frac{1}{D\ \cdot B} \int_1^{cos\varphi_1} \frac{\sqrt{R}dX_A}{(X_A + p)} = \tag{79}$$

$$= -\frac{1}{D\ \cdot B}\left[-\int_1^{cos\varphi_1} \frac{X_A \cdot dX_A}{\sqrt{1 - X_A^2}} - \frac{\mathrm{R}}{D\ \cdot B} \cdot \int_1^{cos\varphi_1} \frac{dX_A}{\sqrt{1 - X_A^2}} + \left(1 - \frac{R^2}{D^2 \cdot B^2}\right) \cdot \int_1^{cos\varphi_1} \frac{dX_A}{(X_A + p)\sqrt{1 - X_A^2}} =\right]$$

$$= -\frac{1}{D\ \cdot B}\left[|sin\varphi_1| - \frac{\mathrm{R}}{D\ \cdot B} \cdot \varphi_1 + \left(\frac{R^2}{D^2 \cdot B^2} - 1\right) \cdot I_3\right]$$

where: $p = -\frac{R}{D \cdot B}, |p| > 1, R = 1 - X_A^2, \quad t = \frac{1}{X_A + p}$,

$$I_3 = \int_{(1+p)^{-1}}^{(cos\varphi_1 + \mathrm{p})^{-1}} \frac{dt}{\sqrt{-1 + 2 \cdot p \cdot t + (1 - p^2) \cdot t^2}} = \tag{80}$$

$$= \frac{1}{\sqrt{p^2 - 1}} \cdot arcsin\big((1 - p^2) \cdot t + p\big)\Big|_{(1+p)^{-1}}^{(coa\varphi_1 + \mathrm{p})^{-1}} =$$

$$= \frac{|D \cdot B|}{\sqrt{R^2 - D^2 \cdot B^2}} \cdot \left[\frac{\pi}{2} - arcsin \cdot \left(\frac{D^2 \cdot B^2 - R^2}{D \cdot B(D \cdot B \cdot cos\varphi_1 - R)} - \frac{R}{D \cdot B}\right)\right] =$$

$$= \frac{1}{\sqrt{p^2-1}} \cdot arcsin\big((1-p^2)\cdot t + p\big) \Big|_{(1+p)^{-1}}^{(coa\varphi_1 + \mathrm{p})^{-1}} =$$

$$= \frac{|D \cdot B|}{\sqrt{R^2 - D^2 \cdot B^2}} \left[\frac{\pi}{2} - arcsin \cdot \left(\frac{D^2 \cdot B^2 - R^2}{D \cdot B(D \cdot B \cdot cos\varphi_1 - R)} - \frac{R}{D \cdot B}\right)\right]$$

Thus, equation (68) under the next conditions: $A \cdot B \neq 1, D \cdot B \neq 0, (cos\varphi_1)^2 \neq \frac{1}{A \cdot B}$ (by A·B≠0) and R> D · B takes the new form:

$$(1 - A \cdot B) \cdot \frac{2}{\sqrt{R^2 - D^2 \cdot B^2}} \cdot arctg\left(\sqrt{R^2 - D^2 \cdot B^2} \cdot tg \cdot \frac{\frac{\varphi_1}{2}}{(R - D \cdot B)}\right) + \frac{A}{D} \cdot \cdot \left\{|sin\varphi_1| - \frac{R}{D \cdot B} \cdot \varphi_1 + \frac{\sqrt{R^2 - D^2 \cdot B^2}}{|D \cdot B|} \cdot \left[\frac{\pi}{2} - arcsin \cdot \left(\frac{D^2 \cdot B^2 - R^2}{D \cdot B(D \cdot B \cdot cos\varphi_1 - R)} - \frac{R}{D \cdot B}\right)\right]\right\} = {t^2}/{2} \quad (81)$$

The resulting expression is the desired dependence $\varphi_1(t)$, which describes the rotational movement of link 1 around point A.

Dividing (66) by (67) an equation of the form $X_A(\varphi_1)$ can be obtained:

$$X_A = \int_0^{\varphi_1} \frac{D \cdot R \cdot A \cdot cos\varphi_1}{R - D \cdot B \cdot cos\varphi_1} \cdot d\varphi_1 = \frac{R \cdot A}{D \cdot B} \cdot \varphi_1 + \frac{D^2 \cdot B - R^2 \cdot A}{D \cdot B} \cdot I_1 \quad (82)$$

Whence, taking into account (39-41), (56) and (78) it can be written as:

$$X_A = \varphi_1 + N \cdot t^2 \cdot \frac{(\frac{m_1}{12} + m_2 + m_3) \cdot BA^2 - m_1 + m_2 + m_3}{2 \cdot (m_1 + m_2 + m_3) \cdot (\frac{m_1}{12} + m_2 + m_3) \cdot BA^2} \quad (83)$$

which is the equation of the translational movement of link 1.

Then, let's turn to (54) and rewrite this expression in the following form:

$$\ddot{\varphi}_2 - \frac{\mathrm{C} \cdot l}{d}\varphi_2 = \frac{\mathrm{N}}{d} - const \quad \text{или} \quad \ddot{\varphi}_2 - k \cdot \varphi_2 = U \quad (84)$$

under the initial conditions ($\dot{\varphi}_{20} = 0$; $\varphi_{20} = 0$) the solution to the equation has the following form:

$$\varphi_2 = \frac{U}{2 \cdot \mathrm{k}} \cdot \mathrm{e}^{-\sqrt{\mathrm{k}}\tau} \cdot (\mathrm{e}^{\sqrt{\mathrm{k}}\tau} - 1)^2 \text{ or}$$

$$\varphi_2 = \frac{N}{2 \cdot \mathrm{C} \cdot l} \cdot \mathrm{e}^{-\sqrt{\frac{\mathrm{C} \cdot l}{d}}\tau} \cdot (\mathrm{e}^{\sqrt{\frac{\mathrm{C} \cdot l}{d}}\tau} - 1)^2 \quad (85)$$

which is the equation of link 2 movement around the point B.

The solution to equation (55) can be represented as:

$$\varphi_3 = 0.5 \cdot \frac{\mathrm{M}_{res}}{f} \cdot \tau^2 + C_1 \cdot \tau + C_2 \quad (86)$$

where C_1 and C_2 are integration constants determined from the initial conditions ($\dot{\varphi}_{30} = 0$; $\varphi_{30} = 0$) $\varphi_3 = 0.5 \cdot \frac{F_{res}}{f} \cdot \tau^2$ after substitution $f = \frac{m_3 \cdot l_3^2}{3}$ the equation of the link 3 movement can be obtained:

$$\varphi_3 = 1.5 \cdot \frac{F_{res}}{m_3 \cdot l_3^2} \cdot \tau^2 \quad (87)$$

6. Conclusion

As a result of theoretical research, it is established that the Lagrange equations of the second kind can be successfully used for a practical engineering method of the kinematic parameters predicting for designing of the three-link plain hinged linkage mechanisms of a parallel structure. That method does not require of cumbersome computing systems using, that are usually developed for every individual configuration of the technological machines components, including robots-manipulators used in food production.

References

[1] Kopchenkov, V. G. *Theory of mechanisms and machines: textbook* / V. G. Kopchenkov. - Stavropol : North Caucasus Federal University, 2018. — 187 c. — ISBN 2227-8397.

[2] G. A. Timofeev *Theory of mechanisms and mechanics of machines: textbook for universities* / [et al.]; under the editorship of G. A. Timofeeva. - 8th ed. and additional — Moscow: Bauman Moscow state technical University publishing House,2017. — 566 c.

[3] Yablonsky A. A., V. M. Nikiforova. *Course of theoretical mechanics/ Textbook for higher education Institutions*, 1976, " Higher school»

[4] Bristol, Dwight *Tables of integrals and other mathematical formulas / Herbert Dwight Bristol; translated by* N. V. levy. - Moscow, Izhevsk: Regular and chaotic dynamics, Institute for computer research, 2019. — 172 c. — ISBN 978-5-4344-0627-7.

[5] Babenyshev S. P., Bratsikhin A.A., Mamay D. S., Khoha D. S. (2017). *MECHANICS. PART 1. STATICS* TEXTBOOK for international students in OIL AND GAS ENGINEERING, CIVIL ENGINEERING and TECHNOLOGICAL MACHINES AND EQUIPMENT / Stavropol

[6] Yehorov, V., & Putnikov, D. (2017). *Using of robots-manipulators in laboratory works in higher education institutes*. Automation of Technological and Business Processes, 9(1). https://doi.org/10.15673/atbp.v9i1.504

[7] Záda and K. Belda (2016) *Mathematical modeling of industrial robots based on Hamiltonian mechanics.* 17th International Carpathian Control Conference (ICCC), Tatranska Lomnica, 2016, pp. 813-818, doi: 10.1109/CarpathianCC.2016.7501208.

[8] S. Ivanov, L. Ivanova and Z. Meleshkova (2020) *Calculation and Optimization of Industrial Robots Motion*, 2020 26th Conference of Open Innovations Association (FRUCT), Yaroslavl, Russia, 2020, pp. 115-123, doi: 10.23919/FRUCT48808.2020.9087376.

[9] K. Bai, M. Luo, T. Li and G. Jiang (2016) *Dynamics model and adaptive backstepping control on the 7-DOF manipulators of a humanoid robot*, IEEE International Conference on Information and Automation (ICIA), Ningbo, 2016, pp. 1032-1038, doi: 10.1109/ICInfA.2016.7831971.

[10] Li D., Hong H., Jiang X. (2017) *Dynamics Modeling, Control System Design and Simulation of Manipulator Based on Lagrange Equation*. In: Zhang X., Wang N., Huang Y. (eds) Mechanism and Machine Science. ASIAN MMS 2016, CCMMS 2016. Lecture Notes in Electrical Engineering, vol 408. Springer, Singapore. https://doi.org/10.1007/978-981-10-2875-5_91

[11] X. Li, Z. Xu, S. Li, H. Wu and X. Zhou (2020) *Cooperative Kinematic Control for Multiple Redundant Manipulators Under Partially Known Information Using Recurrent Neural Network*, in IEEE Access, vol. 8, pp. 40029-40038, doi: 10.1109/ACCESS.2020.2974248.

[12] F. Morabito, A. R. Teel and L. Zaccarian (2004) *Nonlinear antiwindup applied to Euler-Lagrange systems*, in IEEE Transactions on Robotics and Automation, vol. 20, no. 3, pp. 526-537, doi: 10.1109/TRA.2004.824933.

[13] H. Saadaouia, N. Manamannib, M. Djemaïa, J.P.Barbota, T. Floquetc (2006) *Exact differentiation and sliding mode observers for switched Lagrangian systems.* Nonlinear Analysis: Theory, Methods & Applications.Volume 65, Issue 5, 1 September, Pages 1050-1069. Nonlinear Analysis: Theory, Methods & Applications. https://doi.org/10.1016/j.na.2005.09.047

[14] N Van Khang (2004) *A contribution to the dynamic simulation of robot manipulator with the software Robot Dyn.* Vietnam Journal of Mechanics, Vol 26, No 4

[15] H. Temeltas, M. Gokasan, S. Bogosyan and A. Kilic (2002*) Hardware in the loop simulation of robot manipulators through Internet in mechatronics education*, IEEE 2002 28th Annual Conference of the Industrial Electronics Society. IECON 02, Sevilla, pp. 2617-2622 vol.4, doi: 10.1109/IECON.2002.1182806.

[16] J. D. English and A. A. Maciejewski (2000) *On the implementation of velocity control for kinematically redundant manipulators*, in IEEE Transactions on Systems, Man, and Cybernetics - Part A: Systems and Humans, vol. 30, no. 3, pp. 233-237, May 2000, doi: 10.1109/3468.844350.

[17] L. Huang, S. S. Ge and T. H. Lee (2004) *Adaptive position/force control of an uncertain constrained flexible joint robots - singular perturbation approach*, SICE 2004 Annual Conference, Sapporo, pp. 220-225 vol. 1.

[18] Meng-Pi Cheng and Ching-Chih Tsai (2003) *Dynamic modeling and tracking control of a nonholonomic wheeled mobile manipulator with two robotic arms*, 42nd IEEE International Conference on Decision and Control (IEEE Cat. No.03CH37475), Maui, HI, pp. 2932-2937 Vol.3, doi: 10.1109/CDC.2003.1273071.

Technological methods of improving mechanical and energy characteristics of sewing machines

E A Drofa, O V Prihodchenko, V S Yadykin, M F Goryainov

Technological Institute of Service - Stavropol, Don State Technical University, Stavropol, Russia

e-mail: kafedra_riss_tis@mail.ru

Abstract. Nowadays the segment of sewing services is packed with manual universal sewing machines. They need to be upgraded, that is why developing of energy-saving electro drive for sewing machines is actual. To improve energy datum, efficiency and expanding functional set of sewing machines usage of frequency-controlled drive is a solution. In this case frequency inverter is set by functional algorithm reproduced in frames of its logical macromodel. The model of frequency inverter reproduces instantaneous value of output voltage for modelling dynamic processes, whereas the current voltage applied to drive phase is the only thing to be known for confirmatory and steady-state analyses.

1. Introduction

Until recently developing of sewing machines were mainly devoted to their components, drives were usually based on universal electric drives. They did not rely on their functions as a part of a sewing machine. Exploiting conditions for the drive are severe. The drive has to provide steady functioning despite a lot of activations when acceleration speed is limited 524-630 s^{-1}, smooth speed control in a wide diapason, reduction of acceleration and run-down time when doing short strings, efficiency and quietness[11].

Nowadays the usage of a great amount of manual universal sewing machines, which need upgrading, has led to the relevant development issues of energy-saving electric drive for sewing machines[12].

International practice indicates that the level of sewing machinery for the last 10-15 years has dramatically increased, technical and technological opportunities as well as their multipurposeness have also improved. Firstly, it was achieved due to the wide usage of electronic items and microprocessor control systems and their cost reduction.

Leading engineering companies produce multipurpose lock-stitch machines only with electronic drive and a range of the electro-mechanical modules which not only enabled to automatize a number of functions, but also to equip multipurpose machines with additional machinery (material edge cutting, sheaves change, material adjustment to the needle, the stitch length adjustment etc.) and to offer sewing machinery consumers a diversity of new machines, where fundamentally new technical solutions and electronic control systems are applied. The usage of electronics enabled to increase technological capability of the equipment, videlicet its flexibility and mobility, joints solidity and accuracy, which also reduces the servicing time[9,20,21].

2. Formulation of the problem

Electric drive with friction coupler, which is installed in the sewing machines of 131 category, has rather huge electrical power expenses whilst the production of each item means 70% engine idle work [1].

Therefore, to improve the energetic index, to increase the efficiency and to expand the functional capacities of the sewing machine it is offered to use frequency-controlled drive [5,6].

According to the task, the most appropriate is a numerical computation of the runtime equations by means of software. The authors have implemented a runtime calculation program for the sewing machine «RTSSHM».

3. The proposed algorithm

The algorithm consists of following operations:

1) Entering initial data and conditions.

As initial conditions we enter:

Initial analysis time $t=0$

Initial rotor speed $\omega_1=\omega_0$ counter-drive speed $\omega_2=0$ and driving shaft speed $\omega_E=0$

Initial data can be mode-setting and architectonic.

Mode-setting indices, such as frictional moment M_{RB} and moment resistance M_{C1} and M_{C2}, can vary in dependence to selected mode.

Architectonic parameters only depend on construction of sewing machine and a type of electric drive. As architectonic initial data in the algorithm are used: inertia moment J_1 and J_2 and electric drive characteristics M_{KP} and S_{KP} for induction motor, U, $k\Phi$, R_a - for direct current motor.

Drive type is defined interactively for parameter A. Sample time *h* is also required.

2) Computation of current index of drive moment M_E depending on electric drive type.

Velocity calculation for drive control and driving shaft

$$\omega_2=\frac{M_{RB}-M_{C2}}{J_2}\cdot t \tag{1}$$

$$\omega_M=\omega_2\cdot i \tag{2}$$

3) Calculation of rotor speed derivative

$$\frac{d\omega_1}{dt}=\frac{M_E-M_{RB}}{J_1} \tag{3}$$

4) Calculation of current rotor speed at k-th integration step according to Euler method

$$\omega_{1k}=\omega_{1k-1}+h\cdot\frac{d\omega_1}{dt} \tag{4}$$

5) Extension of sample time at acceleration step

6) Current indices output t, ω_1, ω_2, ω_M.

7) Checking termination condition of acceleration step. Acceleration is over if $\omega_1<\omega_2$.

8) Calculation and output acceleration time

9) Calculation of speed for single-mass system and shaft at bite point according to Euler method.

10) Calculation of resulting system speed rate and defining time period to finish the bite point from $\omega_2\le\omega_{ET}$.

11) Calculation of run-down process for rotor shaft and counter-drive

12) Checking termination run-down condition $\omega_2 \leq 0$.

13) Results output

4. General solution to the problem

Frequency-controlled electric drive of a sewing machine is a complicated functionally interdependent system, which can be formalized by a system of differential, difference and algebraic equations[1].

Drive data-measuring system has to control following physical values:

1) Electrical (current, voltage, electromotive force, etc.)
2) Mechanical (moment, velocity, movement etc.)
3) Technological

Controller provides signal conversion from primary detectors, galvanic isolation, boost, integrating and semi-digital or pulse code conversion into microintegrated control system format. Operating speed of this element defines accuracy and operating speed of each control loop. It is based on chosen type of signal conversion, data exchange and hardware implementation.

Therefore, considered approach to optimal synthesis of automatically controlled induction motor drive elements enables to provide unitized energetic and dynamic capabilities of the whole system[16].

We have invented a working model for numerical computation, synthesis and mode and configuration optimization of frequency-controlled drive.

Modelling process consists of the following:

1) Drive usage mode selection

In dependence of consumer's requirements and exploitation conditions the drive can be used in different modes.

2) Organization of initial data base

Initial data can be entered into the model interactively by an operator with an appropriate software system, which implements math model. Initial data are passport drive data, mode parameters, algorithm of converter functioning and architecture of the sewing machine.

3) Modelling of confirmatory analysis of induction motor.

Confirmatory analysis means analyzing energetic, starting and working characteristics of the drive in static and when working simultaneously with frequency converter. The analyzing method relies on standard procedure of engineering serial machines. Meanwhile, exploitation the machine differently from design mode shows necessity to adapt this procedure to new conditions.

4) Dynamic processes modelling

This analyzes electromechanical (start and stop of drive) and electromagnetic (reset mode of power voltage) transient processes in system induction drive-frequency converter.

Model parameters required for completing modelling procedure can be divided into three groups

- Frequency converter parameters
- Empirical curve parameters, which are used in process of automatic modelling

Frequency converter parameters. Usually frequency converter is defined by its algorithm, reproduced within its logical macromodel. It is important that conversion model has to reproduce instant indices of its output voltage for modelling dynamic processes, whereas for confirmatory analysis current voltage applied on a drive phase is enough[3,8,10].

The following operations are to be completed

1) Initial data input. As initial data we consider extreme indices network $U_{mл}$ and phase $U_{mф}$ voltage, number of integration intervals M, converter frequency $f_{nч}$.

2) Analysis of instant indices of output voltage U_{SA}, U_{SB}, U_{SC} is made in accordance with the algorithm.

3) Calculation of current indices within the period of frequency converter output voltage.

To define analysis inaccuracy we complete analytical calculation of the frequency converter output voltage.

Inaccuracy is calculated according to:

$$\Delta = \frac{U_{AT} - U_{A\text{Ч}}}{U_{AT}} \cdot 100\% \quad (5)$$

U_{AT} - analytically calculated current voltage index

$U_{A\text{Ч}}$ – current voltage value calculated according to Simpson (Bode) method.

Table 1 indicates results of the research on how number of integration intervals M impact analysis accuracy of current value of frequency converter output value for following initial data: $U_{mф}$=220V; $U_{mл}$=380V; M=1, … , 10.

Table 1. Interval number impacts analysis accuracy

M	m. Simpson $U_{Aч}$,V	m. Bode $U_{Aч}$,V	Exact value, U_{AT},V	m. Simpson Δ,%	m. Bode Δ,%
1	180,22	187,265	187,163	3,85	0,05
2	186,833	187,164	187,163	0,18	0,0005
3	187,1	187,163	187,163	0,3	-
4	187,143	187,163	187,163	0,01	-

It can be concluded that satisfying results can reached with 3-4 integration intervals M.

This algorithm can be used to calculate current indices of frequency converter output voltage.

The analysis shows that usage of frequency-controlled electric drive in sewing machines will expand capabilities and increase efficiency of sewing machines, moreover, it will reduce the time needed for technological operations.

Simultaneous integration of soft- and hardware means of measuring, registration, information resources and control pilot unit have let automatize the research of inverter slowdown of induction drive when powered by frequency converter[17,18,19].

During the experiment value R_T changed from infinity to 50 Om. This stands for change $g_{Tэкв}$ from 0 to 0,02 cm. When R_T is off value $g_{Tэкв}$ is defined only by conduction. Filter volume changed within 5 to 500 mcF. Inertia of the shaft was $(1{,}2-4{,}2)J_{AД}$. Invertor carrier frequency was from 1 to 10 kHz. Frequency slowdown time was from 0,1 to 0,2s.

Picture 1,a shows speed diagram for 131-category machine, picture 1,b shows speed diagram for sewing machine with frequency-controlled electric drive.

Picture 1 shows that speed increase at machine accelerating differs for different types of electric drives. For example, machine produced by “Orsha” Ltd. is characterized by extended acceleration in the second period. This is because when skidding is over mass system increases dramatically compared to mass of rotor and balance wheel. Acceleration for machine with frequently-controlled electric drive is over much earlier. We suppose it depends on correlation of masses of machines and drives, which impacts the curving of acceleration speed.

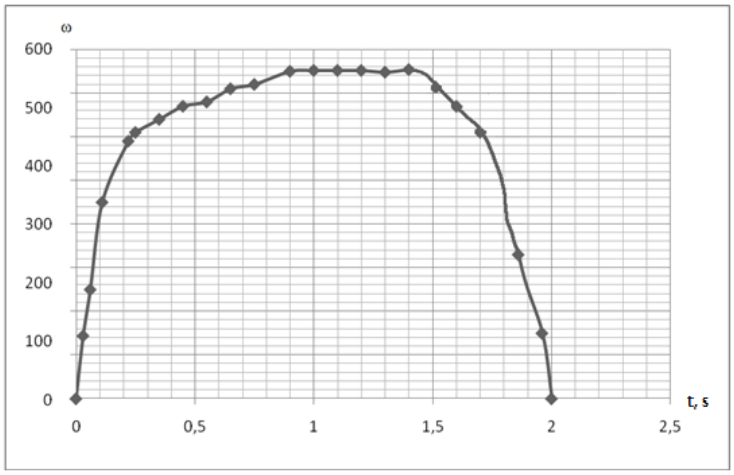

(a)

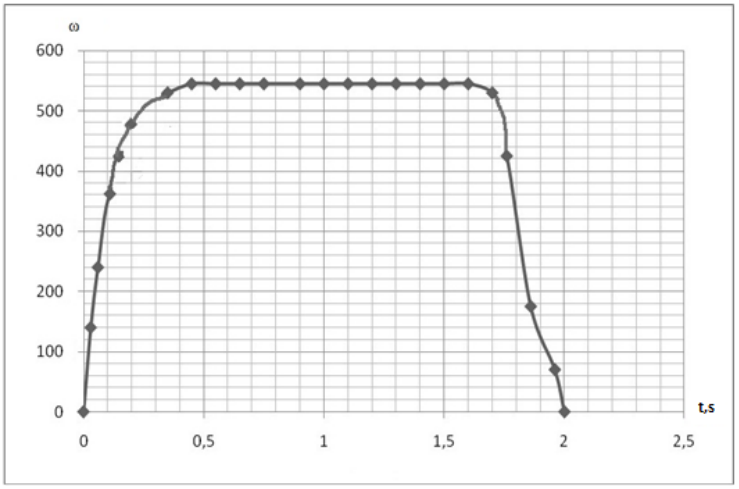

(b)

Figure 1. Speed diagrams of sewing machines:
a) – with frictional electric drive b) – with frequency-controlled electric drive

Slope of the velocity curve for 131 category machine at run-down is defined by clutch characteristic as it follows from pic. 1 (a). A bit more high-grade slope for the machine with frequency-controlled electric drive 1 (b).

Analysis of experimental data shows:

1) Acceleration time of machines and related losses at accelerating in terms of sudden on and off the clutch for most of the investigated machines surpass run-down time and related losses at run-down.

Russian machines are significantly inferior to frequency-controlled electric drives machines [15]. For example, for considered machines acceleration and rundown time is 0.7s and 0.4s with related losses 31.6 stitches, but for machine with frequency-controlled electric drive acceleration and rundown time is 0.25s and 0.35s. with related losses 18.8 stitches [4,13].

Russian machines with existing drives cannot be accelerated to the ultimate (nominal) speed when doing a range of operations at working conditions.

2) Acceleration time does not define the amount of related losses completely as they depend on how the speed increases.

Russian machines with frictional drives are less effective compared to frequency-controlled electric drive when working with short lines. When changing value m_1 (number of stitches) 1 cm. per line the limit of rational usage is in reverse proportion to m_1 change.

5. Conclusion

Therefore, characteristics of sewing machine drive limit its rational usage at operations, that is why the system of frequency control of induction drive was invented. It enabled to increase significantly speed capabilities of a sewing machine. As the result, time spent on auxiliary operation has reduced, labor effectiveness has risen, and, what is most important, energy consumption has also reduced [14].

When frictional electric drive is used, induction drive is always on and does idle work in period between technological operations. This leads to extra energy loss. Thus, energy consumption for sewing machine with friction drive is on average 24-28% higher than for frequently-controlled machines [2].

In modern conditions it is possible to create agile and cheap control system, which will let upgrade existing sewing machines with friction drive excluding only a friction coupler, without drive replace. It enabled to increase significantly speed capabilities of a sewing machine. As the result, time spent on auxiliary operation has reduced, labor effectiveness has risen, and, what is most important, energy consumption has also reduced.

References

[1] Goryainov M.F., *Upgrading electric drives for sewing machines, sewing industry*, Publisher: OOO "Arina" (Moscow)\ ISSN: 0132-0955

[2] Goryainov M.F., Yadykin V.S., Gunko V.A., *Reducing energy consumption of sewing machines at drive replace, don annals engineering*, Publisher: Russian non-governmental organization Rostov regional branch "Russian engineering academy" (Rostov-on-Don)\ eISNN: 2073-8633

[3] Goryainov M.F. Innovative approach *to energy saving issues for sewing machines, kant*, Publisher: Publisher "Stavrolit" (Stavropol)\ ISNN: 2222-243X

[4] Goryainov M.F., Yadykin V.S., *Innovative potential of regional service sphere: current condition and development vektors*, Publisher: OOO "Sekvoya" (Stavropol)\SBN: 978-5-9907432-6-7.

[5] Kopchenkov, V. G. *Theory of mechanisms and machines: textbook* / V. G. Kopchenkov. - Stavropol : North Caucasus Federal University, 2018. — 187 c. — ISBN 2227-8397.

[6] G. A. Timofeev *Theory of mechanisms and mechanics of machines: textbook for universities* / [et al.]; under the editorship of G. A. Timofeeva. - 8th ed. and additional — Moscow: Bauman Moscow state technical University publishing House,2017. — 566 c.

[7] Bristol, *Dwight Tables of integrals and other mathematical formulas* / Herbert Dwight Bristol; translated by N. V. levy. - Moscow, Izhevsk: Regular and chaotic dynamics, Institute for computer research, 2019. — 172 c. — ISBN 978-5-4344-0627-7.

[8] Li D., Hong H., Jiang X. (2017) *Dynamics Modeling, Control System Design and Simulation of Manipulator Based on Lagrange Equation*. In: Zhang X., Wang N., Huang Y. (eds) Mechanism and Machine Science. ASIAN MMS 2016, CCMMS 2016. Lecture Notes in Electrical Engineering, vol 408. Springer, Singapore. https://doi.org/10.1007/978-981-10-2875-5_91

[9] Sinyavets Tatyana Dmitrievna, Motherland Larisa Alexandrovna *Competitiveness of the garment industry based on the creation of an industry cluste*r//Economy of the region. 2016. №1. URL: https://cyberleninka.ru/article/n/konkurentosposobnost-shveynoy-promyshlennosti-na-osnove-sozdaniya-otraslevogo-klastera (дата обращения: 25.09.2020).

[10] Ryskulova B.R., Seidekhan A.E. *Improvement of methods for treatment of items of overalls with using sewing equipment textile technology*, Publishing House: Ivanovo State Polytechnic University (Ivanovo) ISSN: 0021-3497

[11] Isaeva R.A., Abduova A.A., Iztleuov G.M., Utebaev A.A., Baybatyrov B.U., Amerbekov E.U., Dayrabaev A.Z., *Harmful And Factors Textile Technology*, Publishing House: Ivanovo State Polytechnic University (Ivanovo), Issn: 0021-3497

[12] Y.A. Malenkov, Shishkin V.V., Kudryavtseva G.V., Shishkin V.I., *Strategic Guidelines Of Textile And Garment Industry Enterprises: Comparison Of Existing And New Industries, Journal: News Of Higher Educational Institutions. Textile Technology*, Publishing House: Ivanovo State Polytechnic University (Ivanovo), Issn: 0021-3497

[13] Kim I.S., Sabalakhova A.P., Saparbaeva E.M., Takibaev G.A., Baydibekova A.O., Adishova G.B., *Zharmakhanbetov F.K., Mathematical Models Textile Technology*, Publishing House: Ivanovo State Polytechnic University (Ivanovo), Issn: 0021-3497

[14] Murakhov-Pechenezhskaya, Ryabchikov N.L., Development Of *Dynamic Model Of Product Quality During Production, Journal: East European Journal Of Advanced Technologies*, Publishing House: Technological Center (Kharkov), Issn: 1729-3774eissn: 1729-4061

[15] Seites B.H., Usenbekov G., *Calculation Of Cross Oscillations Of Multi-Support Shaft Of Sewing Machine Taking Into Account Sleeve Deformations, Journal: News Of Higher Educational Institutions. Textile Technology*, Publishing House: Ivanovo State Polytechnic University (Ivanovo), Issn: 0021-3497

[16] Nosalchuk R.O., *Development Of Mobile Control System For Laboratory Stand For Study Of Fuzzy And Adaptive Positional Control Systems, Source: Education, Science, Production*, Belgorod State Technological University Named After V.G. Shukhov. 2015, Publishing House: Belgorod State Technological University Named After V.G. Shukhova (Belgorod)

[17] Zhiganov A.I., Kozhevnikov P.V., Afonin A.Y., *Software Development Of Highly Loaded Iot Device Control Systems For Embedded Systems With Scalable Control Logic, Source: Information Technology In Science And Education Problems And Perspectives*, A Collection Of Scientific Articles Of The Iv Annual Inter-University Научно-Практической Conference. 2017. Publishing House: Penza State University (Penza)

[18] Gavrilova S.V., Bairamov N.V., *Dual-Engine Electric Drive Control System, Source: Problems Of Improving Efficiency Of Electromechanical Converters In Electric Power Systems, Materials Of International Scientific And Technical Conference*. 2015, Publishing House: Federal State Autonomous Educational Institution Of Higher Education "Sevastopol State University" (Sevastopol)

[19] Carpenters A.A., Belyaev D.N., *Information Technologies In Textile Equipment Operation Control System, Journal: University Information Environment (See In Books)*, Publishing House: Ivanovo State Polytechnic University (Ivanovo)

[20] Ermakov A.A., Ryzhkova E.A., *Modernized Textile Density Management System, Source: Collection Of Scientific Works Of The Department Of Automation And Industrial Electronics*, Moscow, 2014, Publishing House: Federal State Budgetary Educational Institution Of Higher Education "Moscow State University Of Design And Technology" (Moscow)

[21] Smig Dmitry Nikolaevich, *Local Management Systems, Journal: Modern Scientific Research And Innovation*, Publishing House: International Science And Innovation Center (Moscow), Eissn: 2223-4888

Physical and mathematic N-option modeling and optimization of dynamically loaded nonlinear technical systems

I V Kolesnikov, V V Shapovalov, A L Ozyabkin, P V Kharlamov, M A Burakova*, R A Kornienko

Transport machinery and tribotechnology Department, Rostov State Transport University, Rostov-on-Don, Russia

*Corresponding author: ma.burakova@yandex.ru

Abstract. The development of modern industries significantly depends on the effective usage of innovative research methods and optimization of technological processes. Modeling methods are one of the science-intensive methods put into practice in research and diagnostics of both the current state of mechanical systems and predicting changes in the state of technological equipment during operation. The authors have developed and successfully adapted fundamental theoretical foundations of physical and mathematical modeling for solving problems of optimization and simulation of dynamically loaded nonlinear technical systems. A method for diagnosing tribo-couplings of helicopter tail drive couplings is proposed.

1. Introduction

The development of modern industries significantly depends on the effective application of innovative research methods, optimization of technological processes, application of advanced methods and processes for the production of structural and consumable materials, and usage of modern technological equipment.

Modeling methods are one of the science-intensive techniques exploited in research and diagnostics, both in the current state of mechanical systems and in predicting changes in the state of technological equipment during operation.

For solving problems of optimization and modeling of dynamically loaded nonlinear technical systems (NTS) the authors have developed and successfully adapted fundamental theoretical foundations of physical and mathematical modeling [1-5]. The methods of physical and mathematical modeling and dynamic monitoring are successfully used in solving tasks of optimizing loaded NTS.

The main advantage of these methods is that the cost of resources for their implementation is significantly less than for setting up and carrying out physical, laboratory, or even full-scale modeling. However, the measure of confidence in the results of a mathematical experiment is interrelated with the degree of resemblance of the model to the physical processes that it describes.

Based on available theoretical and experimental data in the field of friction dynamics, novel research methods have been developed, and innovative approaches have been applied to solve the problems of optimization of NTS and to improve their efficiency and competitiveness. In particular, the interaction and interrelation of dynamic processes in quasilinear and essentially nonlinear NTS subsystems were taken into account. The authors also took into consideration self-similarity of the dynamic processes that occur during the physical and mathematical modeling of NTS in frictional contacts, and provide the correct results due to significant overlapping of full-scale and model tests data.

2. Method for assessing the elastic-dissipative characteristics of the frictional interaction

The application of n-variant modeling allows drastic reduction of the time required for solving optimization problems by cutting down the volume of full-scale research of NTS. The creation of a physical and mathematical model of a full-scale system in 2, 3 and n-different scales lets us limit the results of volume of full-scale studies of the NTS to fixation of one or two leading parameters.

A new method has been developed for assessing the elastic-dissipative characteristics of the frictional interaction of the spline couplings of the tail transmission of the Mi-26 helicopter on the example of heavily loaded friction pairs of helicopters, in order to increase their reliability and durability when operating at low temperatures (Figure 1).

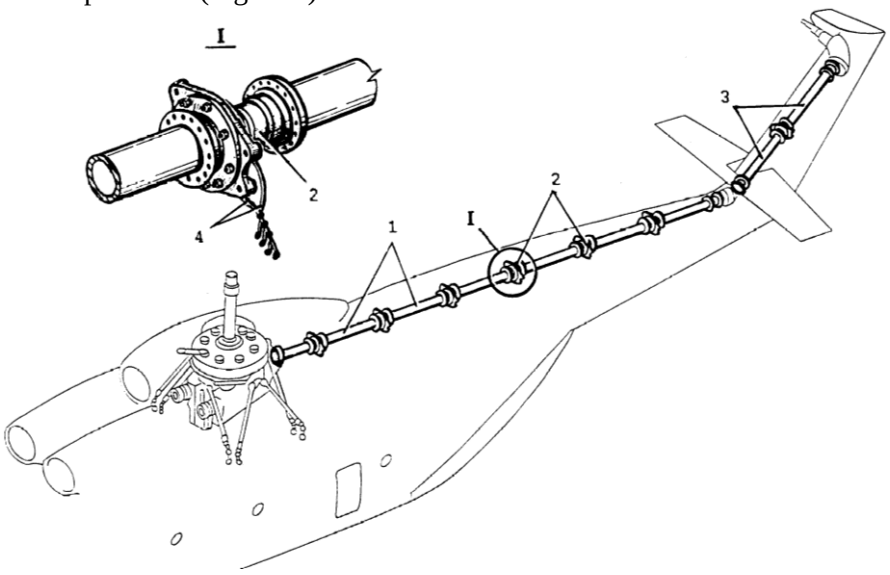

Figure 1. The tail shaft of the helicopter Mi-26:
I - splined coupling with flanges in the bearing; 1, 3 - hollow shafts;
2 - bearings of intermediate hearings; 4 - temperature sensors

The operational reliability and efficiency of heavily loaded helicopter couplers is determined not only by speed and load parameters, but also by physico-mechanical, physico-chemical, and tribological parameters of frictional processes in frictional subsystems.

The basic purpose of the tail shaft is to transfer the rotating moment from the main gearbox to the tail rotor by means of series-connected elastic elements having certain masses and moments of inertia. The splined coupling is designed in such a way that the annular thimble rotates in a bearing mounted on the frame (Figure 2).

The analysis of the research has shown that the main faults of the spline couplings of the helicopter transmission are the following:

- the formation of cracks and delamination of the rubber bearing cage;
- leakage of lubricant, which stimulates overheating of the coupling and its bearing;
- deformation and wear products generation of the coupling components;
- the formation of a sideways clearance in the coupling joints;
- misalignment of tail shaft bearings;
- increased outrun of the shaft tube, as well as axle fracture or shaft twisting.

During the launch of the helicopter transmission under extremely low temperatures conditions, the stationary temperature monitoring sensors 4 installed in the couplings (Fig. 1) are unable to inform the pilots in a timely manner about any emerging problems. A more advanced splined joint diagnostics technology is required in order to allow real-time identification of any emergency situations, which would improve the safety of long-distance piloting.

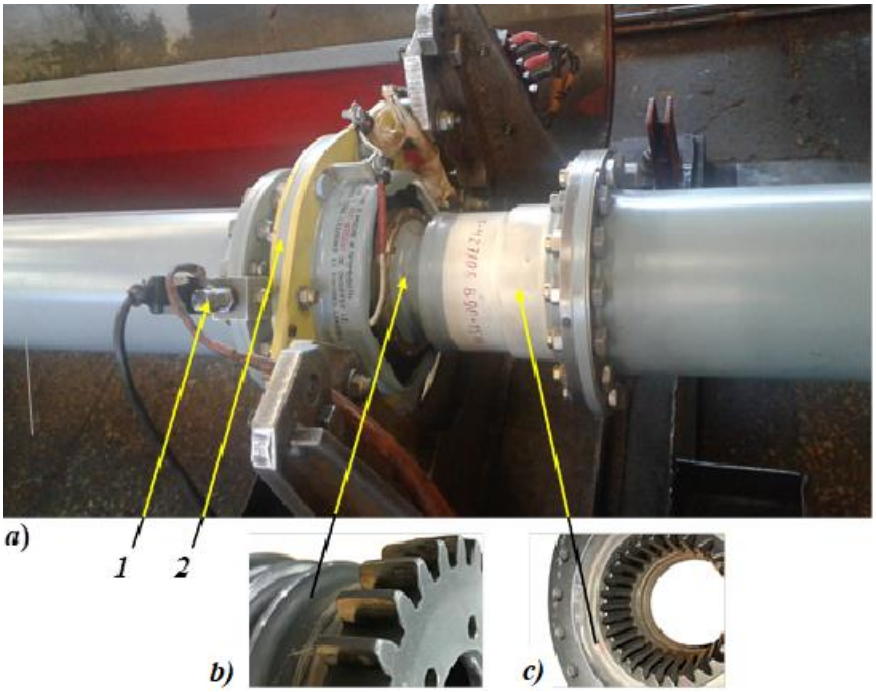

Figure 2. Experimental research complex splined coupling of the Mi-26 helicopter transmission: a) – coupling assembly at the stand; b) – barrel splines; c) – annular thimble splines; 1 – vibration acceleration sensors; 2 – fixed fuselage frame

3. Implementing the dynamic monitoring task

The tribological system of the spline joint of the transmission of the Mi-26 helicopter (Fig. 2) refers to systems that are characterized by nonlinear interconnected physico-mechanical, thermophysical, tribo-chemical, and load-velocity factors, as well as environmental ones. A feature of the coupling tribosystem operation spline joint is in the following. Its operation takes place under the influence of significant vibrations from the main engine and the entire helicopter as a whole. Therefore, modern technical means of measuring physical quantities, digital transmission and signal processing equipment should be used to achieve the goal. The most effective vibration measuring circuits include two measuring signals about oscillations in the input impact (engine thrust torque) and vibrations of the spline coupling itself. This allows using spectral analysis of data, estimating the ratio of the coherent spectrum to the spectrum of the input impact, and eliminating a significant part of random interference [6, 7].

To identify the processes of dynamic loading of couplings, we used the foundations of the automatic control theory [8] by analyzing the amplitude phase, time, and integral quality criteria. Based on the time-recorded measurement subsystem of the oscillations of the input impact (engine traction torque) and the output coordinates of the coupling movements, the complex transmission coefficient at each harmonic oscillation frequency is estimated as follows:

$$\mathbf{W(i\omega)} = \frac{\mathbf{S_N(i\omega)\cdot S_M(-i\omega)}}{\mathbf{|S_M(i\omega)|^2}} = \mathbf{A(\omega)\cdot e^{i\varphi(\omega)} = P(\omega) + iQ(\omega)}, \quad (1)$$

where $S_M(i\omega)$ is the power spectral density of the input impact, the traction moment M (t); $S_N(i\omega)$ is the power spectral density of the normal displacement force N (t); A (ω) is amplitude spectrum; φ (ω) is phase spectrum; P (ω) isreal spectrum; Q (ω) is an imaginary spectrum.

Expression (1) allows calculating the complex transfer coefficient [8] and the amplitude phase function that characterizes the ratio of elastic-inertial and dissipative components of the frictional interaction [6, 7]. Integrated estimates are known to allow estimating the amount of oscillation damping and deviations of the controlled value in aggregate, without determining them separately [8]. Therefore,

along with the well-known linear and quadratic integral quality criteria of the transient characteristics, we also proposed to evaluate the elastic-inertial and dissipative components by the amplitude phase characteristics for each time point in the given octave (1/3, 1/12 or 1/24-octave) frequency ranges [6, 7]. With a higher degree of reliability, it allows selecting the most informative ranges of natural frequencies, where you can find the influence of physical and mechanical characteristics of the lubricant (hypoid lubricant), as well as the wear of the surfaces of the splines of the coupling joint.

To identify the elastic-dissipative and dynamic characteristics of the couplings, the following integral estimates were used:

- elastic-inertial components of the interaction, conductive to the convergence of the contacting friction surfaces, as well as prompting an increase in contact stresses and temperatures:

$$\mathbf{I_C(t)} = \int_{\omega_i}^{\omega_j} \mathbf{P(\omega)d\omega}, \text{ given } P(\omega) \geq 0, \quad (2)$$

where t is registered operating time;

ωi, ωj are boundary frequencies for octave (fractional octave) spectral analysis;

P(ω) is real frequency response characterizing the elastic-inertial components of a complex quantity (1)

$$\mathbf{P(\omega)} = \mathbf{Re[W(i\omega)]} = \mathbf{A(\omega)} \cdot \mathbf{cos[\varphi(\omega)]}; \quad (3)$$

- inertial components of the interaction, contributing to the loss of stability of the friction bond:

$$\mathbf{I_M(t)} = \int_{\omega_i}^{\omega_j} \mathbf{P(\omega)d\omega}, \text{ given } P(\omega) < 0; \quad (4)$$

- dissipative components of the interaction, characterizing the resistance forces that are directed oppositely to the resultant sliding velocity vector:

$$\mathbf{I_{Fc}(t)} = \int_{\omega_i}^{\omega_j} \mathbf{Q(\omega)d\omega}, \qquad \text{given } Q(\omega) \leq 0, \quad (5)$$

where Q(ω) is imaginary frequency response of the complex quantity (1), characterizing the dissipation of energy during dynamic interaction:

$$Q(\omega) = Im[W(i\omega)] = A(\omega) \cdot \sin[\varphi(\omega)]; \quad (6)$$

- dissipative components of the interaction, characterizing the development in the frictional-mechanical subsystem of frictional self-oscillations, that is resistance forces with the vector co-directed with the sliding velocity vector:

$$I_A(t) = \int_{\omega_i}^{\omega_j} Q(\omega)d\omega, \text{ given } Q(\omega) > 0. \quad (7)$$

It is known that the damping properties of mechanical systems in the linear theory of oscillations are estimated by the dimensionless damping coefficient ξ, as the ratio of the exponent of the amplitude oscillations damping n to the frequency of free oscillations ω0. It is problematic to determine the coefficient in substantially nonlinear friction systems. The authors proposed an empirical expression for estimating the coefficient ξ in the form of a certain integral value Iξ (t) for the current time moment t, which makes it possible to identify the frequency ranges of nonlinear system oscillations where dissipative properties have the greatest influence on the dynamics of the system:

$$\xi = \frac{n}{\omega_0} = \frac{\beta}{\beta_0}; \quad I_\xi(t) \approx \frac{1}{\sqrt{1+\frac{1}{\left(\frac{I_{Fc}(t)+I_A(t)}{I_C(t)+I_M(t)}\right)}}}, \quad (8)$$

where n is the vibration damping coefficient, c–1;

ω0 is the frequency of natural vibrations, c–1;

β is coefficient of resistance to vibrations, N · s / m;

β0 is the critical value of the coefficient of resistance to oscillations, at which the oscillatory character is replaced by a monotonically decaying (aperiodic), N · s / m;

IFc, IA, IC, Im are integral assessment of quality [6, 7], calculated on the basis of the analysis of amplitude-phase characteristics and indirectly characterizing the ratio of resistance forces (5), frictional self-oscillations (7), elastic forces (2), and inertial forces (4).

Observing the expectation value, mean squared departure and peak-factor of estimates (2) - (8) in real time observation t, allows solving tasks of identification and time-to-time variation of elastic-dissipative characteristics.

It is more convenient to implement the task of dynamic monitoring of spline couplings using a single criterion that would allow analyzing the generalized characteristics of the friction-mechanical system and predicting, with a certain probability, changes in the trend of characteristics. We have proposed a dynamic quality criterion (9) to be such a characteristic. Its limiting value is equal to one, and corresponds to the "warning" threshold:

$$I_D(t) = \frac{1}{12}\sum_{k=1}^{12} I_k, \quad (9)$$

where Ik are integral estimates of the estimated parameters of the stationary transmission coefficient (1).

The lower the level of ID (t), the more stable and balanced the friction system of joint is. Values (9) exceeding 1 correspond to abnormal operating conditions in the form of outruns, resonance, and other forms of deviations from the stationary trajectory of motion. In accordance with the three sigma rule, the “danger” threshold was also set at the values of ID (t) ≥ 1.15.

Changes in load-speed operating conditions, ambient temperature and a significant number of side factors have a significant impact on the performance of the splined coupling. Such factors might include the following: high frequency oscillations in the formation of local metal links in the case of fretting-corrosion; a significant change in the rate of relative slip of friction surfaces; convergence or removal of contact surfaces of friction under the influence of inertia forces; deformation of active volumes of friction surfaces, increase of contact stresses. The combination of unfavorable factors, loads and sliding speeds can cause the change of the microgeometry of the friction surfaces, followed by the development of plastic deformations, friction auto fluctuations. All these can lead to increased instability of the tribosystem, athermic or thermal capture, high values of dynamic coefficient of friction (Tolstoi - Push effect).

One can estimate the residual supply of the couture according to the results of long-term tests or during the operation. For this purpose both the method of octave analysis of energy dissipation [sum of calculated estimates (5) and (7)], and the proposed method of dynamic quality criterion with established thresholds of "warning" and "danger" can be used. The nature of the octave spectrum changes is shown in Fig. 3, depending on the hourly operating time.

Observing the values of the amplitudes of the octave spectra during the operating time of the support coupling 5, it is possible to identify more reliably the periods of running-in (0–881 sec) and normal operation (992–1522 sec), when the dissipative energy losses for friction processes are maximum, and the fixed value of the damping coefficient ξ reaches minimum values of 0.11. In addition, monitoring several couplings simultaneously allows establishing statistical levels of the damping coefficient in each frequency range of the fractional octave spectrum: the base level (B), as well as warning (W) and danger (D) thresholds (Figure 3).

To simulate the main dynamic vibrations of the prongs of the spline connection of the tail shaft couplings of the Mi-26 helicopter when the nature of the loading effect changes, a laboratory stand was made to monitor the technical state of the spline model (Figure 4).

Thus, a technique for diagnostics of tribological couplings of the tail drive couplings of Mi-26 helicopters has been proposed. It allows identifying in real time the stability of elastic-inertial and dissipative characteristics of frictional interaction, periods of running-in, normal operation and catastrophic wear using the values of fractional octave spectra.

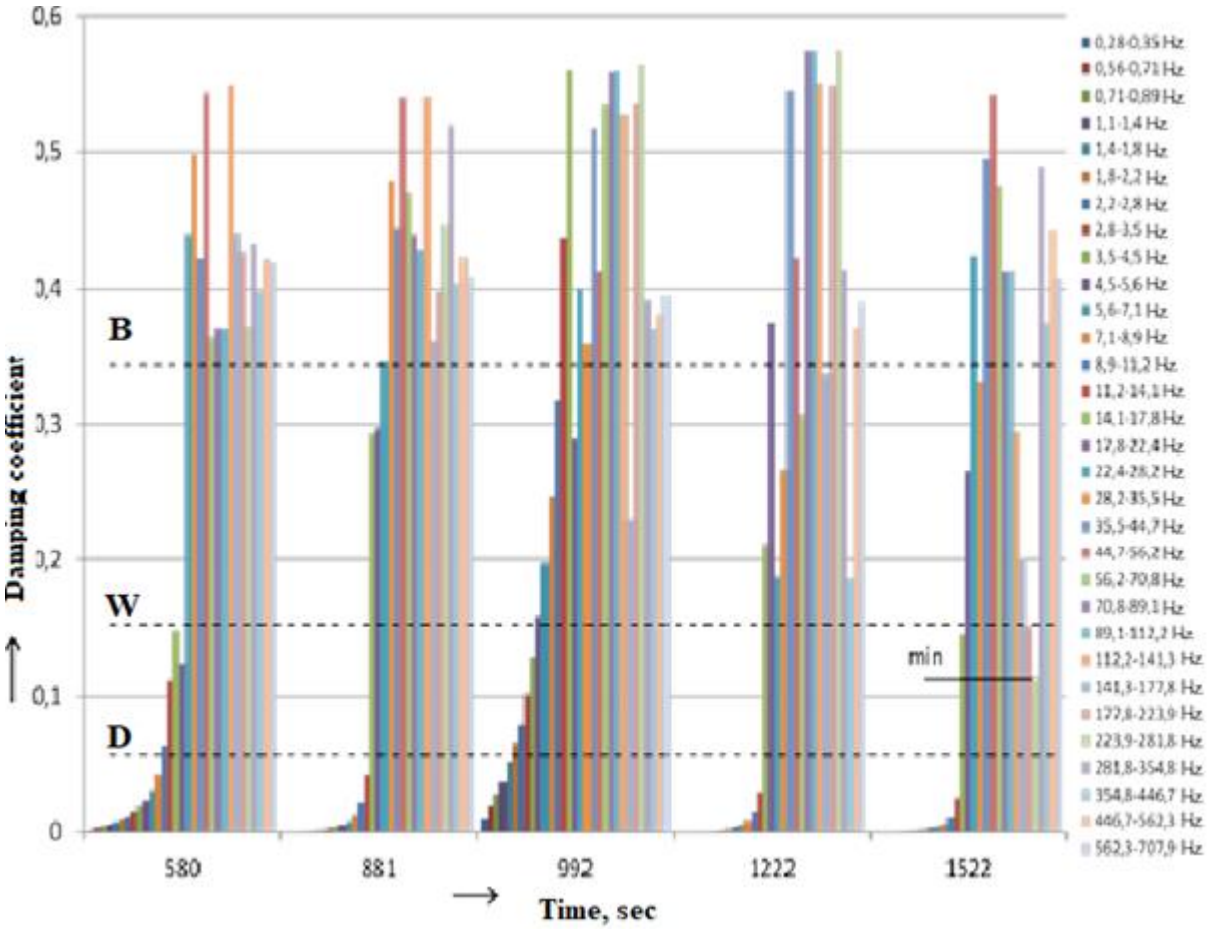

Figure 3. 1/3-octave spectrum analysis of the damping coefficient depending on the operating time of the splined coupling 5 of the frame support

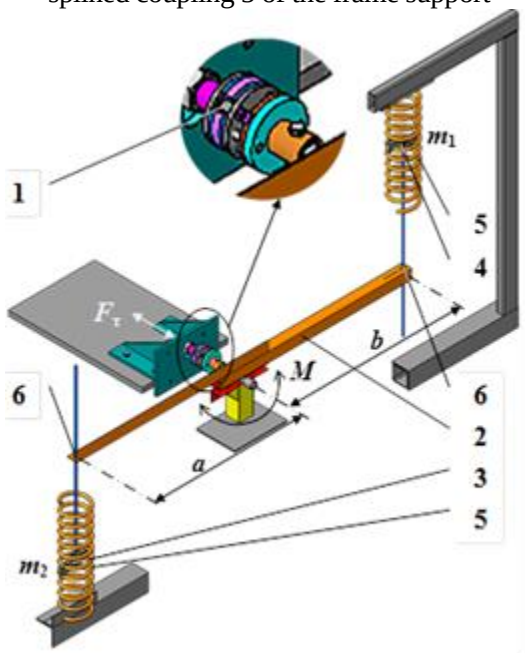

Figure 4. Stand for research of the spline connection:
1 - model node; 2 - double lever; 3 - bottom bar; 4 - top bar; 5 - loading springs; 6 - lock nuts

4. Conclusion

The use of the developed dynamic criterion simplifies the technological process of diagnostics, monitoring, and forecasting. It also allows optimization of significant changes in elastic-dissipative relationships, preventing the occurrence of abnormal operating conditions by informing the pilots about the fixed threshold values of "warning" or "danger".

The proposed technique for tribospectral identification of friction processes and dynamic monitoring of friction systems contributes to an increase in the safety of helicopter operation. It can also be applied to any friction units, which will make it possible to implement a short-term or long-term forecast in the change of the dynamic characteristics of loaded NTS.

Acknowledgments

This work was carried out within the federal target program "Research and Development in Priority Areas of Development of the Scientific and Technological Complex of Russia for 2014-2020" with financial support from the state represented by the Ministry of Science and Higher Education of Russia (project identifier RFMEFI60718X0203).

References

[1] Shapovalov, V.V. Application of methods of physical and mathematical modeling and tribospectral identification for monitoring friction mechanical systems [Primenenija metodov fiziko-matematicheskogo modelirovanija i tribospektral'noj identifikacii dlja monitoringa frikcionnyh mehanicheskih sistem] / V.V. Shapovalov, A.L. Ozyabkin, P.V. Kharlamov // Bulletin of mechanical engineering [Vestnik mashinostroenija]. – 2009. No. 5. – P. 49–57.

[2] Li H., Chao K., Duda J., and Klaus E. A Study of Wear Chemistry and Contact Temperature Using a Macrosample Four-Ball Wear Test/Tribology Transactions. -1999 (42), no. 3, 529-534.

[3] Filonenko S. F., Stadnychenko V. M., and Stahova A. P. Modelling of Acoustic Emission Signals at Friction of Materials' Surface Layers//Aviation. -2008 (12), no. 3, 87-94.

[4] Method for testing friction units. Pat. No. 2343450 RF, IPC G01N 3/56. / V.V. Shapovalov, A.V. Chelokhyan, A.M. Lubyagov [and others]. declared 06/13/2006; publ. 10.01.2009, Bul. No. 1; priority 13.06.2006, No. 2006121024/28.

[5] Maiba I.A. Friction materials for special purposes the contact zone «wheel-rail» / I.A. Maiba, D.V. Glazunov, A.M. Ananko – Rostov n/D: RSTU, 2017, 124 p.

[6] Fletcher D. I. and Lewis S. Creep Curve Measurement to Support Wear and Adhesion Modeling, Using a Continuously Variable Creep Twin Disc Machine//Wear. -2013 (298-299), 57-65

[7] Yang Y. C., Chu S. S., Chang W. J., and Wu T. S. Estimation of Heat Flux and Temperature Distributions in a Composite Strip and Homogeneous Foundation//Int. Commun. Heat Mass Tran. -2010 (37), no. 5, 495-500.

[8] Pupkov, K.A. Methods of classical and modern theory of automatic control [Metody klassicheskoj i sovremennoj teorii avtomaticheskogo upravlenija]: textbook. V. 1: Mathematical models, dynamic characteristics and analysis of automatic control systems [Matematicheskie modeli, dinamicheskie harakteristiki i analiz sistem avtomaticheskogo upravlenija] / K.A. Pupkov; ed. K.A. Pupkova, N. D. Egupova. 2nd ed., Rev. and add. Moscow.: Publishing house of MSTU im. N.E. Bauman, 2004 . – 656 p.

[9] Wolter, K.U. & Zacher, M. & Slovak, B. Correlation between track geometry quality and vehicle reactions in the virtual rolling stock homologation process. In: 9th World Congress on Railway Research, May 22-26, 2011.

Thermo-metal-cladding of working surfaces of closed friction units of mobile systems

V V Shapovalov, I V Kolesnikov, M A Burakova, P V Kharlamov, P N Scherbak

Transport machinery and tribotechnology Department, Rostov State Transport University, Rostov-on-Don, Russia

*Corresponding author: ma.burakova@yandex.ru

Abstract. Modeling methods play a significant role in the operation, diagnostics, and prediction of the current state of various mechanical systems. The authors have developed fundamentally new approaches to solving problems of optimization, increasing the efficiency and competitiveness of nonlinear technical systems. Test facility investigations of closed friction units of mobile systems using a lubricant with the aluminum powder insertion were carried out. Test bench allows simulating a reciprocating motion. The analysis of research demonstrates the stabilizing effect of such a lubricant on the tribothermodynamics of the friction unit.

1. Introduction

The usage of modern technological equipment, the application of cutting-edge methods and methods for the production of structural and consumables, as well as the optimization of technological processes, significantly affect the development of modern industries. Modeling methods play a significant role in the operation, diagnostics, and forecasting of the current state of various mechanical systems. The authors of the article used the basis of available theoretical and experimental data in the field of dynamics of friction processes and research methods. They have developed fundamentally new approaches to solving problems of optimization, increasing the efficiency and competitiveness of nonlinear technical systems [1-6].

Thus, samples of the spline joint of the tail rotor drive transmission coupling of the Mi-26 helicopter were investigated using a test bench that allows simulating the reciprocating motion with the given load and velocity parameters.

2. Examination of model samples of splined connection of transmission coupling

In accordance with the method of physical and mathematical modeling [5…10], the load-velocity conditions for carrying out a model experiment were determined with a simplex of diameters of a full-scale splined joint and its model Cd = 1.62 and a scale of the loading moment CM = 196.8. The load during the reciprocating motion of the spline joint model Nm = 2100 N and the frequency of the reciprocating motion ωm = 44.73 Hz, which corresponded to the tractive effort torque of the full-scale system.

For research of model samples of the spline joint of the helicopter tail rotor drive transmission coupling, a friction pair (full-scale pair) (Figure 1) was chosen. There was a cup made of 38Kh2MYuA steel (Figure 1, a) and a tip made of 12Kh2N4A (Figure 1, b). There was a model pair (Figure 2) with

an angular sample made of 38Kh2MYuA steel (Figure 2, c) 2 and 3) and a plate of 12Kh2N4A (Figure 2, c) 1). The samples of the model were undergone by full-cycle heat treatment, the angle sample was carburized, and the plate was nitrated.

Figure 1. Splined joint:
a) cup; b) tip; c) joint assembly

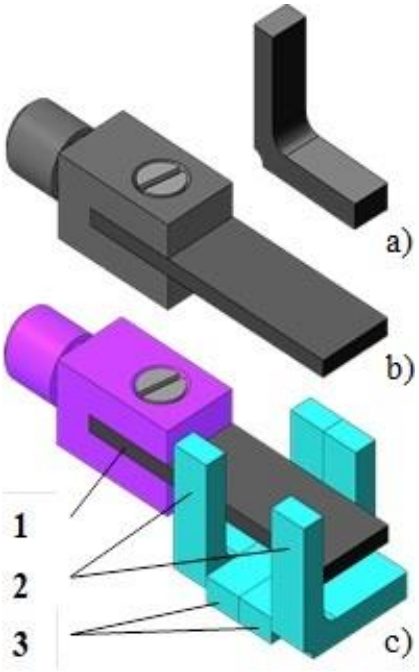

Figure 2. Model of spline joint:
a) sample; b) counter-sample;
c) joint assembly;
1 - plate; 2 and 3 - angle samples

When the frequency of the reciprocating motion and the load moment on the friction unit were changed, the dynamics of frictional interaction was modeled using a laboratory test bench with normal pressure of 100 MPa when working with different lubricants: in the oil bath with a standard HG oil lubricant and in the oil bath with a lubricant added to aluminum powder.

During the research, we recorded the values of the trends in the friction coefficient both in statics and in dynamics, as well as the energy losses of the dynamic friction coefficient, dissipative losses of the dynamic friction coefficient and the dimensionless value of the damping coefficient in the most significant octave frequency ranges, and the dynamic quality criterion of a nonlinear technical system.

Figure 3 shows the trends in the stationary (steady-state) value of the friction coefficient and its value during natural oscillations which occur under the influence of forced oscillations.

The most significant value is the dynamic friction coefficient of the elastic and inertial interaction 1 (Figure 3), since it takes into account additional inertial disturbances from the frictional mechanical system. The frictional mechanical system significantly affects the approach of the contacting friction surfaces to each other, as well as the increase in normal tension and temperature.

The dynamic friction coefficient of the inertial impact 2 (Figure 3) significantly affects stability of the frictional bonds, stability of the frictional mechanical system, and deviation of the characteristics transient in time from the stationary motion trajectory.

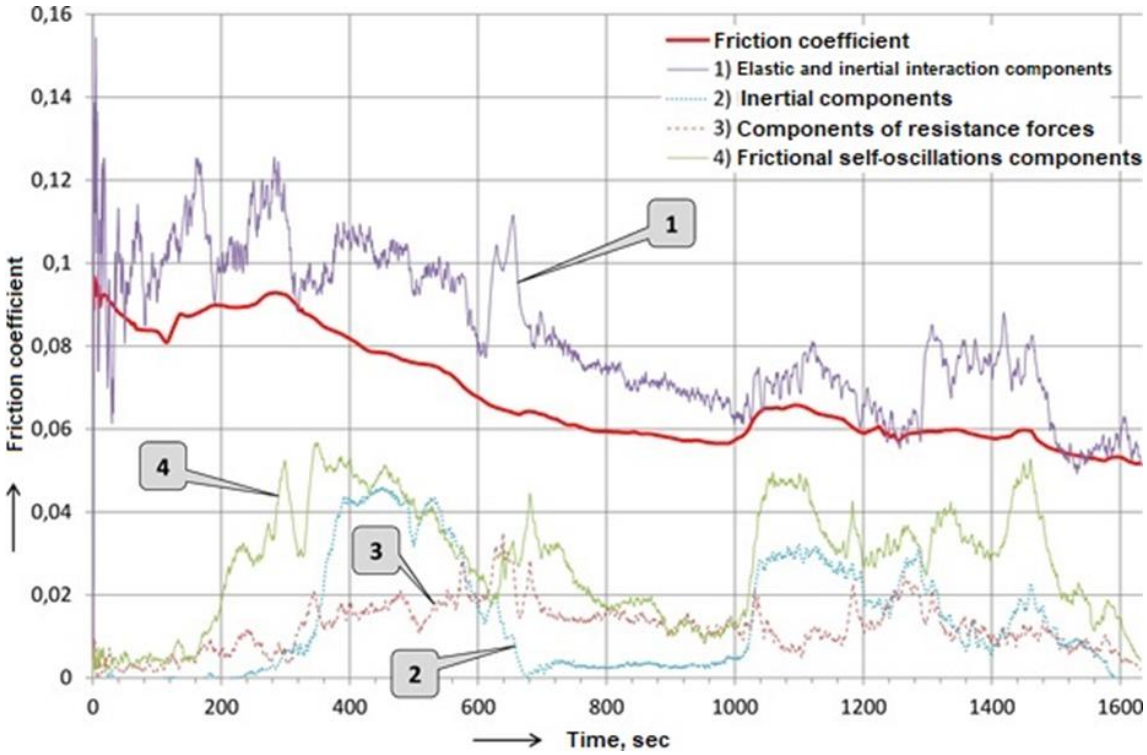

Figure 3. Comparative analysis of the friction coefficient in the statics and dynamics of the friction unit functioning with samples

The dynamic friction coefficient of resistance forces 3 (Figure 3) determines the speed of operation of the transient characteristics in time, when the vector of resistance forces is oppositely directed to the velocity vector of the relative sliding of the contacting friction surfaces.

The dynamic friction coefficient, caused by the frictional self-oscillations 4 formed in the friction contact (Figure 3), significantly affects both the stability of the frictional bonds, the stability of the frictional mechanical system, and the deviation of the characteristics transient in time from the stationary motion trajectory.

The test data show (see Figure 3) that with an increase in the relative sliding speed within 0 to 22.5 Hz at 1350 min – 1, the inertial components of the dynamic friction coefficient are absent, and the dissipative ones are insignificant. Due to frictional self-oscillations, the components of the dynamic friction coefficient increase significantly with a rise in the relative sliding speed to the nominal values. The inertial impacts on the friction unit significantly increase when reaching the rated load-speed operating mode and before the completion of transient oscillations in the range from 360 s till 680 s. From 680 s till 1000 s of observations, the stationary friction mode takes place, which is characterized by a decrease in all comprising values of both the dynamic friction coefficient and its value after the end of transient oscillations.

At 1020 s of observation period, aluminum powder is inserted into the oil bath with HG oil lubricant. At the same time, an increase in low-frequency vibration and a significant decrease in the volumetric temperature of the oil bath are noticed. In the range of experiment time from 1020 s till 1500 s, transient forced vibrations occur in the frictional mechanical system that are associated with the restructuring of the tribo-characteristics of the friction unit functioning. From 1500 s till 1590 s of the experiment, the stabilization of all components of the friction coefficient is recorded, and in the time range from 1590 s till 1630 s, braking and stopping are implemented.

Figure 4 shows the trends in energy losses of the dynamic friction coefficient. Indeed, in the ranges from 280 s till 600 s, and from 1020 s till 1480 s of observation periods during transient oscillations, we

record significant losses of the dynamic friction coefficient. The stationary friction mode is characterized by the coincidence of the gradients of change in both the friction coefficient in stationary motion and the integral estimate of the energy losses of the dynamic friction coefficient. Further, there is a change in the dissipative losses of the dynamic friction coefficient of the mechanical system in octave frequency ranges [4,8].

Figure 5 shows the trends of dissipative losses of the dynamic friction coefficient in the most significant octave frequency ranges. The significance of the frequency ranges was assessed by the value of the Pearson correlation coefficient and testing the null hypothesis using the Student's test. It was revealed that the frequency ranges with geometric mean frequencies of 36 Hz (Cxy = 0.77); 72 Hz (Cxy = 0.54) and 18 Hz (Cxy = 0.5) are the most significant in terms of the degree of impact on the tribo-characteristics of the system. The frequency range of dissipative energy losses with a geometric mean of 128 Hz has almost no correlation with the friction coefficient in stationary motion (Cxy = 0.19), but has a significant effect during free oscillations caused by external influences.

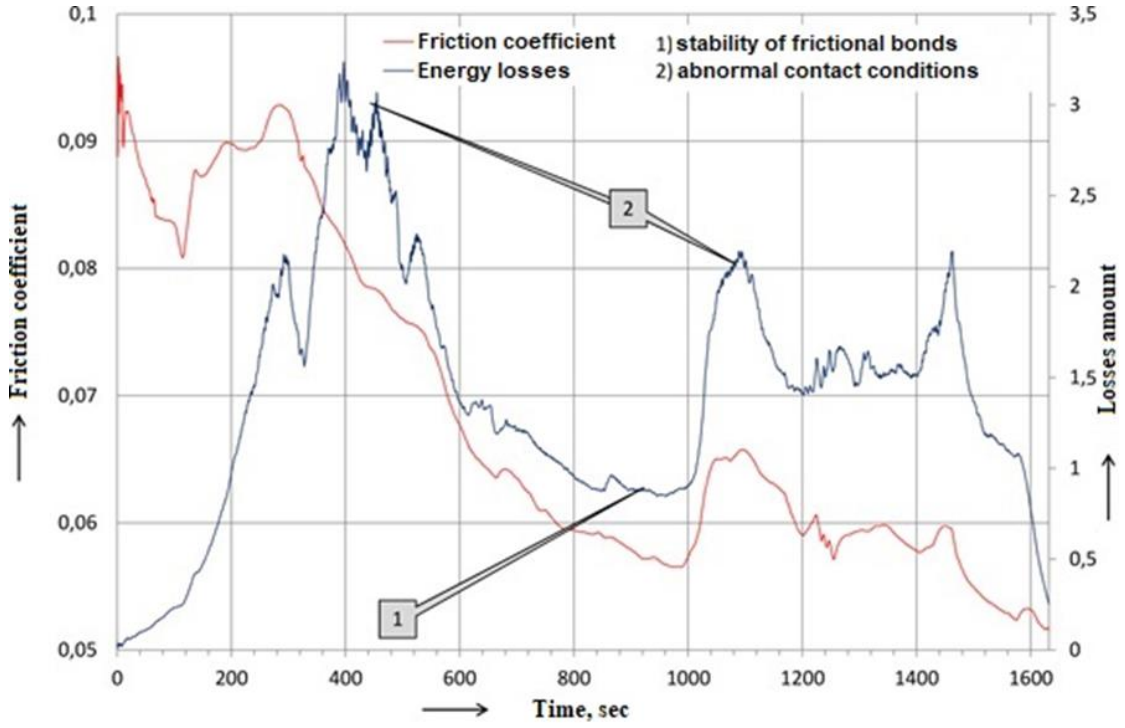

Figure 4. Comparative analysis of the friction coefficient f in static, and the integral value of energy losses fdyn

When reaching the nominal friction mode from 0 s till 360 s of observation time, dissipation energy losses in the frequency range 11.2 – 22.4 Hz (1) decrease, since equilibrium roughness is formed. In a wide frequency range of 22.4 – 177.8 Hz, on the contrary, dissipation losses increase as the relative slip speed goes up.

Upon reaching the rated load-speed operating conditions, dissipation losses are almost stationary in 11.2 – 22.4 Hz frequency range (1); in 22.4 – 177.8 Hz frequency range, they decrease monotonically, which indicates the stabilization of friction processes. According to the graph in Figure 5, the stationary friction regime is fixed in the time range from 760 s till 800 s of observation time, which correlates with the results of data analysis in Figure 3 and 4.

It should be noted that the insertion of aluminum powder into the oil reservoir for 800 s of the experiment stabilizes the dynamics of the frictional mechanical system in 11.2 – 22.4 Hz (1) and 22.4 – 44.7 Hz frequency ranges (2), and it is characterized by the values of dynamic friction coefficient

0.000125 ± 0.00003 (0.09 ± 0.015). In frequency ranges 44.7 – 89.1 Hz (3) and 89.1 – 177.8 Hz (4), we observe a decrease in dissipation energy losses.

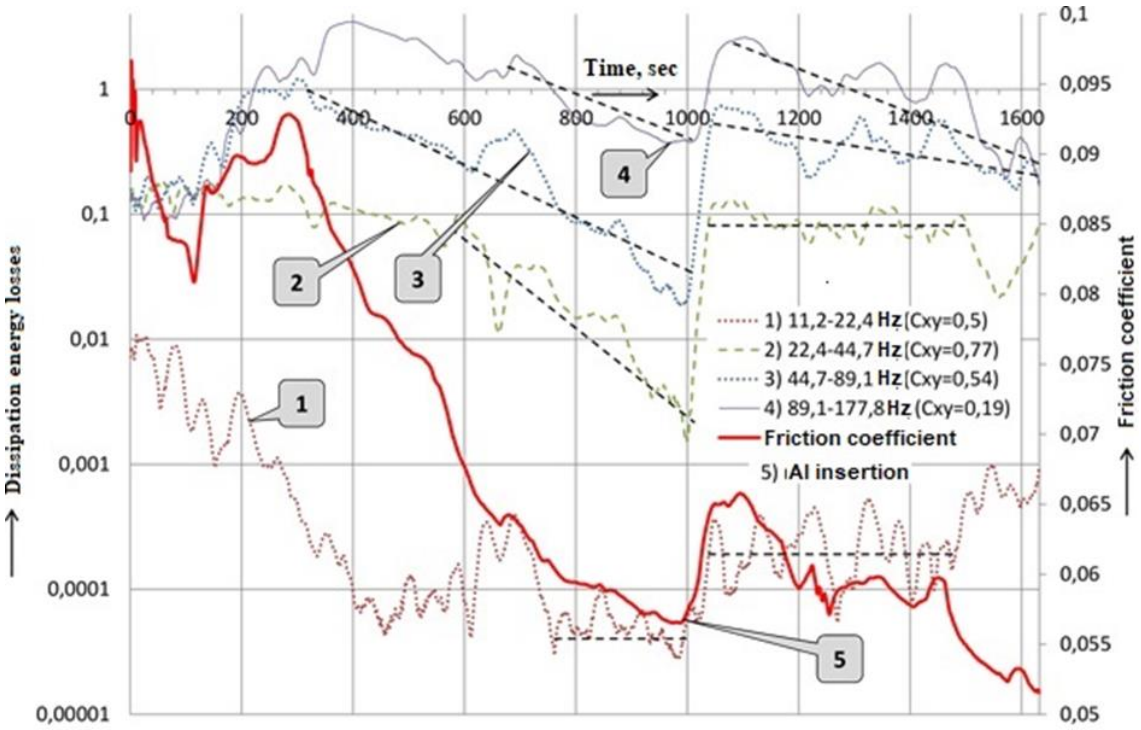

Figure 5. Comparative analysis of the friction coefficient f in static, and dissipative components of the dynamic coefficient of friction fdyn in octave frequency ranges

The analysis of the experiment shows that the insertion of aluminum powder into the HG oil lubricant improves the tribothermodynamics of the friction unit.

The results of determining the dimensionless value of the damping coefficient ξ are presented in the most significant octave frequency bands (Figure 6). The graphs display that upon completion of transient oscillations, the damping coefficient ξ is stationary in 0.71 - 22.4 Hz frequency ranges (1); in the frequency ranges 22.4 - 44.7 Hz (3) and 89.1 - 177, 8 Hz (41), it has a positive gradient of physical and mechanical properties, which indicates the stabilization of dynamic characteristics and an increase in the stability of the frictional mechanical system.

The insertion of aluminum powder into the HG oil lubricant reduces the speed of the system in 22.4 - 44.7 Hz frequency range (3). However, upon completion of transient oscillations, the value of the damping coefficient ξ in all frequency bands is characterized by more stationary values.

3. Organization of monitoring of friction-mechanical system functioning

It is more convenient to monitor the functioning of a frictional mechanical system on the basis of some dynamic quality criterion which characterizes the simultaneous change in frequency, time and integral quality criteria, as well as elastic-dissipative characteristics [6, 7,10]. Figure 7 shows the dependence of the dynamic quality criterion of the frictional mechanical system on the load-speed operating conditions, tribo characteristics and analyzed parameters of the system.

The maximum permissible values of the dynamic quality criterion correspond to one and are determined by the established load-speed modes – the so-called "warning" threshold 1 (Figure 7). If the values of the dynamic quality criterion are less than the "warning" threshold, the frictional mechanical system is operated in stationary-stable modes.

A dynamic quality criterion from 1 to 1.15 informs about the advent of critical operating modes, and the criterion above 1.15 signals about the danger of the formation of abnormal friction modes which can lead to a failure of the frictional mechanical system.

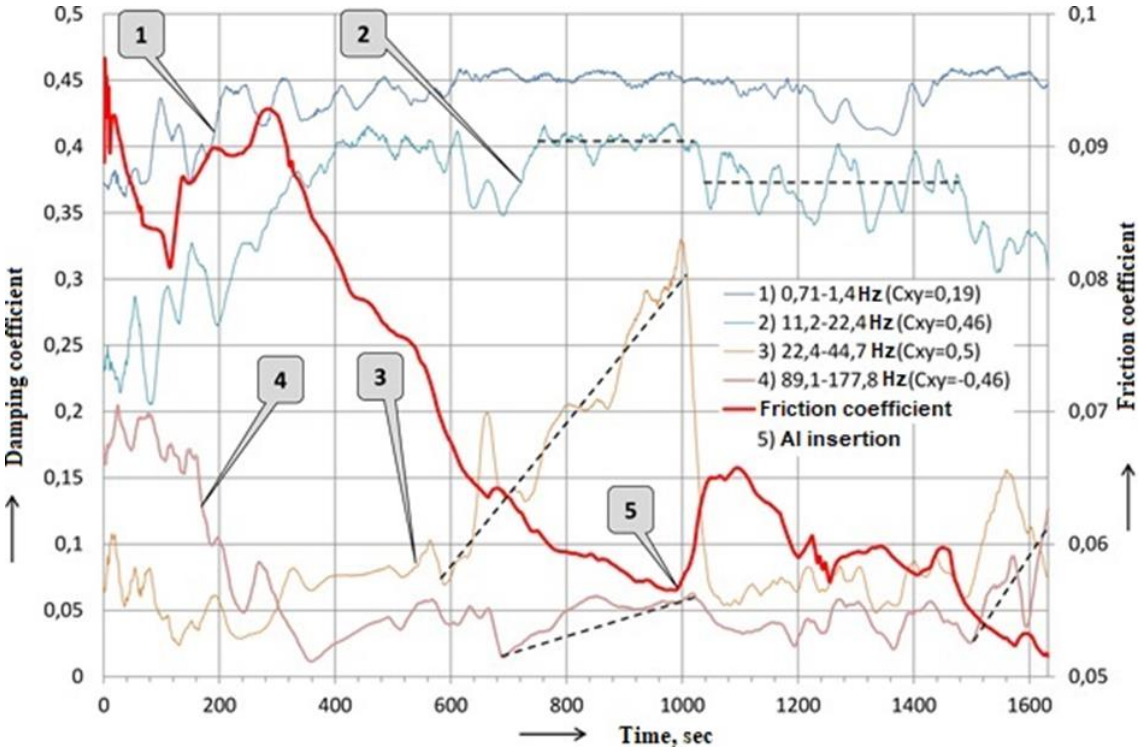

Figure 6. Comparative analysis of the friction coefficient f in statics and dimensionless damping coefficient ξ in octave frequency ranges

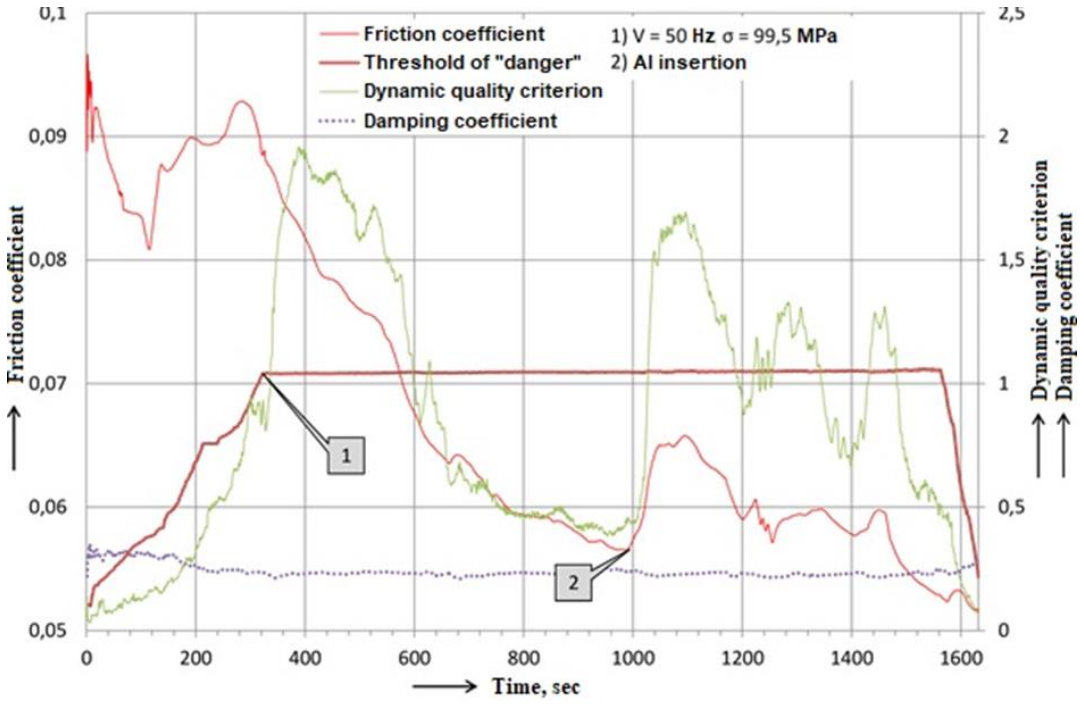

Figure 7. Trends of the dynamic criterion of system quality

A dynamic quality criterion from 1 to 1.15 informs about the advent of critical operating modes, and the criterion above 1.15 signals about the danger of the formation of abnormal friction modes which can lead to a failure of the frictional mechanical system.

In the interval from 0 s till 320 s, the nominal load-velocity friction mode is reached, which is characterized by low values of the dynamic quality criterion, and this determines the normal operating mode of the technical system. According to observations, transient friction regimes from 360 s till 600 s and from 1015 s till 1180 s are characterized by a significant value of the dynamic quality criterion, which exceeds the established threshold of "danger" by 1.15 times. Consequently, the investigated frictional mechanical system is subject to significant inertial and elastic-dissipative influences that exceed the permissible ones which may be due not only to the operation of the friction unit itself but also to additional dynamic influences from the drive.

It should be underlined that the stationary friction mode of the frictional mechanical system is characterized by the coincidence of the gradients of the friction coefficient and the dynamic quality criterion.

4. Conclusion

Thus, the use of the methods of tribospectral identification of friction processes and dynamic monitoring of changes during observation time of the parameters of the frictional mechanical system makes it possible to implement the problems of diagnostics of friction units and to reveal the influence of changing load-speed operating modes, wear, tribological characteristics of lubricants on the tribodynamic characteristics of the friction unit.

It should be noted that the introduction of aluminum powder into the HG oil lubricant has a stabilizing effect on the dynamic characteristics of the friction unit, reduces the speed of the system, shows more stationary values of the damping coefficient, reduces the bulk temperature of the lubricant in the friction unit by 20-30 ° C and, therefore, significantly improves tribothermodynamics of the friction unit.

5. Acknowledgments

This work was carried out within the federal target program "Research and Development in Priority Areas of Development of the Scientific and Technological Complex of Russia for 2014-2020" with financial support from the state represented by the Ministry of Science and Higher Education of Russia (project identifier RFMEFI60718X0203).

References

[1] Shapovalov, V.V. Application of methods of physical and mathematical modeling and tribospectral identification for monitoring friction mechanical systems [Primeneniya metodov fiziko-matematicheskogo modelirovaniya i tribospektral'noj identifikacii dlya monitoringa frikcionnyh mekhanicheskih sistem] / V.V. Shapovalov, A.L. Ozyabkin, P.V. Kharlamov // Bulletin of mechanical engineering [Vestnik mashinostroeniya]. - 2009. No. 5. - P. 49 - 57.

[2] Loktev, A.A. Simulation of the railway under dynamic loading. Part 1. Ray method for dynamic problem/A.A. Loktev, E.A. Gridasova, E.V. Zapolnova//Contemporary Engineering Sciences. -2015. -Vol. 8. -№ 18. -P. 799-807.

[3] Kolesnikov, V.I. Transport tribotechnics (tribomechanics): textbook. allowance. Vol. II [Transportnaya tribotekhnika (tribomekhanika): ucheb. posobie. T. II]/ V.I. Kolesnikov, V.L. Zakovorotny, V.V. Shapovalov; RSTU. – Rostov-na-Donu, 2006 .-- 478 p.

[4] Patent No. 2674899 RF Method of increasing the efficiency of the friction system [Sposob povysheniya effektivnosti frikcionnoj sistemy], publ. 13.12.2018, Bul. No. 35, V.V. Shapovalov, M.A. Burakova, V.A. Feyzov and others.

[5] Application of Methods Physical and Mathematical Modeling for a Research of Nonlinear Mechanical Systems on the Example of the Rolling Stock: XV International Scientific-Technical Conference "Dynamic of Technical Systems" (DTS-2019) / V. Shapovalov, P.

Kharlamov, A Ozyabkin, S. Gorin, V. Zinovev, R. Kornienko, A. Mihajluk. - New York: AIP Conference Proceedings, 2019. – Vol. 2188. - P. 020017-1 ... 020017-10. - ISBN: 978-0-7354-1935-3 ISSN: 0094-243X - Text: electronic // scitation.org/journal/apc: electronic journal. - URL: https://aip.scitation.org/doi/10.1063/1.5138391. - Date of publication: 12/16/2019.

[6] Evans, J. & Berg, M. Challenges in simulation of rail vehicle dynamics, Vehicle System Dynamics. 2009. Vol. 47. P. 1023-1048.

[7] Metal Plating of Friction Surfaces of the “Wheel – Rail” Pair / V. V. Shapovalov, Yu. F. Migal, A. L. Ozyabkin, I. V. Kolesnikov, R. A. Kornienko, E. S. Novikov, E. E. Feyzov & P. V. Kharlamov // Journal of Friction and Wear. - V. 41, P. 338 - 346. (Springer, 31.08.2020).

[8] Dumitriu, M. Modeling of railway vehicles for virtual homologation from dynamic behavior perspective. Applied Mechanics and Materials. 2013. Vol. 371. P. 647-651.

[9] Yang Y. C., Chu S. S., Chang W. J., and Wu T. S. Estimation of Heat Flux and Temperature Distributions in a Composite Strip and Homogeneous Foundation//Int. Commun. Heat Mass Tran. -2010 (37), no. 5, 495-500.

[10] Wolter, K.U. & Zacher, M. & Slovak, B. Correlation between track geometry quality and vehicle reactions in the virtual rolling stock homologation process. In: 9th World Congress on Railway Research, May 22-26, 2011.

Efficiency analysis using complex ultrasonic vibrations in electroacoustic spraying of axial cutting tools

S B Kudryshev, V A Naumenko, A A Zakalyuzhnyy

Don State Technical University, 344000, 1 Gagarin sq., Rostov-on-Don, Russia

Abstract. The article considers the electric spark intensification doping methods by using ultrasonic vibrations to obtain the method of electroacoustic deposition. The ultrasonic vibrations use in the deposition process is possible due to the use of an acoustic system at the end of which a naturally swirled waveguide is used. To analyze the waveguide oscillation amplitude dependence on the frequency, the article presents analytically obtained dependences of the longitudinal and torsional components of vibrations. The obtained results reliability of theoretical studies is confirmed by the good convergence of the theoretical and calculated frequency response resonant peaks. The electroacoustic deposition effectiveness method is confirmed by experimental studies of maintaining the hardened drills performance. The experimental data analysis showed a 2-4 fold increase in the total durability period of hardened drills.

1. Introduction

The wide and effective use of ultrasound in different processes largely depends on the type of oscillation. Application of ultrasonic vibrations in various processes found the use of longitudinal, torsional and integrated fluctuations. In connection with the ease of implementation, well-designed mathematical models and calculation bases, wide use in practice found longitudinal ultrasonic vibrations. Torsional ultrasonic vibrations have not found wide application due to the complex methods of implementation. Complex fluctuations include the coupling of longitudinal and torsional vibrations [11]. The implementation of such fluctuations does not differ from longitudinal, and their effectiveness and technological flexibility is much higher [14]. The expansion of effective use of energy in the technological practice of complex narrow can be associated with the development of the theory of transformation of this type of oscillations. The theory will allow to consider the dynamics of complex oscillations in a form convenient for engineering calculation, and, in addition to the basic formulas, to give a General method of calculation [12].

The formation of complex oscillations is possible through the use of a naturally twisted waveguide connected to the last stage of the concentrator of the longitudinal acoustic system. The consideration of the twisted waveguide as a naturally twisted rod [7, 8, 9], subject to the action of forces arising in the process or other type of processing leads to a certain dynamic three-dimensional problem.

2. The method of electro-acoustic spraying

The problem of rational use of material resources of modern Metalworking production can be solved by applying new methods of shaping and intensifying existing ones. One of the ways to solve this problem is to increase the wear cutting tool resistance by using various applying wear-resistant coatings methods to the cutting tool. Over the years and up to the present time, many different coating methods have been successfully applied, one of which is the method of electric spark doping [1, 2]. Each method has its

own advantages and disadvantages, but the main disadvantage of most methods is the special conditions for the environment in which the coating is applied. The method considered in the works differs in the complete absence of requirements for the coating environment [3, 4].

The essence of the method consists in transferring the electrode material melted by a pulsed current at the optimal gap between the tool and the electrode for an electric discharge. The gap is formed by performing ultrasonic longitudinal-torsional (complex) vibrations with the electrode. In addition, under the ultrasonic vibrations influence, plastic applied coating deformation is produced, which in turn increases the wear applied coating resistance. The ultrasonic vibrations use in the process of electric spark doping allowed us to obtain new properties of the known method. The effective ultrasonic vibrations use in various technological processes is largely due to the optimally selected acoustic system. Rod-type acoustic systems that form various types of ultrasonic vibrations are widely used in the practice of modern production [13]. Figure 1 shows an acoustic system that generates complex ultrasonic vibrations.

The figure shows: magnetostrictive converter-1, waveguide-2, amplitude graph in the acoustic system-3, plot of waveguide strain distribution-4. This type of oscillation can be obtained by using a waveguide in the form of a naturally twisted rod. The complex vibrations use in the coating process allows you to obtain a special type of impact on the surface to be hardened, which can be interpreted as a shear shock.

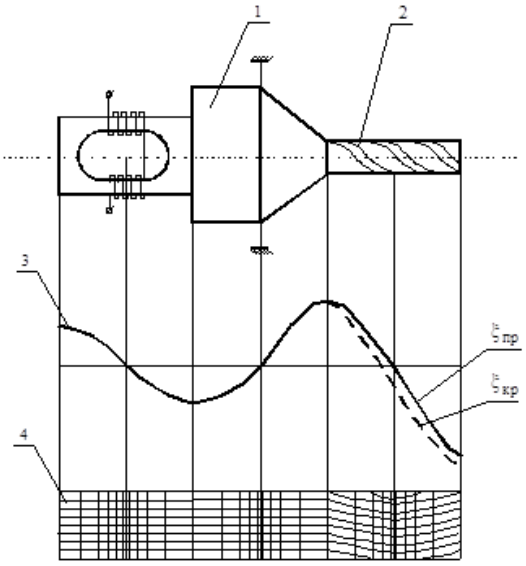

Figure 1. Complex speaker system

3. Amplitude-frequency characteristics of the waveguide

The results of theoretical studies were obtained depending on the amplitude and frequency for different types of naturally swirled waveguides [5].

The longitudinal and torsional components are determined by the formula (1)

$$U(x,t) = U_0(x) \cdot e^{i \cdot k \cdot t}, \quad \phi(x,t) = \phi_0(x) \cdot e^{i \cdot k \cdot t}, \tag{1}$$

where $U_0(x)$ and $\varphi_0(x)$ - longitudinal and torsional component amplitude multipliers.

At the end of the waveguide, the these multipliers values for x=l are equal.

$$U_0(l) = \frac{\alpha_{21} \cdot A}{Ro} \cdot \frac{a_1 \cdot cos\frac{k \cdot l}{c_2} - a_2 \cdot cos\frac{k \cdot l}{c_1}}{cos\frac{k \cdot l}{c_1} \cdot cos\frac{k \cdot l}{c_2}},$$

$$\phi_0(l) = \frac{\alpha_{21} \cdot A}{Ro} \cdot \frac{cos\frac{k \cdot l}{c_2} - cos\frac{k \cdot l}{c_1}}{cos\frac{k \cdot l}{c_1} \cdot cos\frac{k \cdot l}{c_2}}. \quad (2)$$

The received dependences analysis showed that by waveguide changing the geometrical parameters, such as groove width, angle of twist, it is possible to change the acoustic system resonance frequency and the ratio of the longitudinal and torsional component of the oscillations, up to change the direction of the complex vector. The theoretical dependence analysis of the amplitude on frequency changes, obtained in previous works [5], [6] showed that outside the resonant frequency, the longitudinal and torsional components of ultrasonic vibrations ratio changes, which in turn leads to a change in the vibration vector of the complex component. This phenomenon can be used when calculating a waveguide with a given ratio of complex vibrations components. Changing the waveguide geometric parameters allows you to influence both the value of the speaker system resonant frequency, and the direction and amplitude of complex vibrations.

Figure 2 shows the calculated and experimental frequency response of waveguides made of VT5 and steel 45.

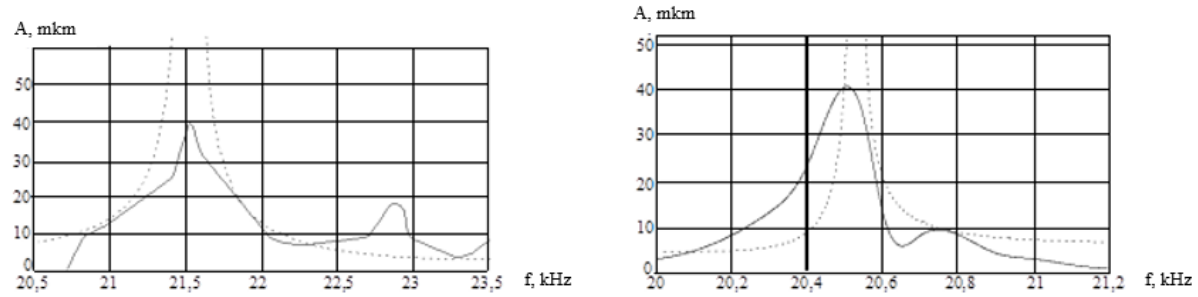

Figure 2. Frequency response of a twisted waveguide made of VT5 and steel 45

The characteristics analysis showed good convergence of the theoretical and experimental characteristics. The theoretical peak shift in both cases is probably due to the error in the experiment [10]. In addition, the experimental characteristic has a second rise in amplitude, which is not present in the calculated characteristic. This fact can be explained by the presence of reflected waves in the acoustic system, the influence of which was not taken into account in the theoretical calculations. The theoretical and experimental peaks deviation of the frequency response does not exceed the permissible values and is 4 percent.

4. Conclusion

The effectiveness of the applying wear-resistant coatings electroacoustic method is confirmed by studies on the example of drills, as one of the most common types of cutting tools. 2 batches of 27 P6M5 drills with a diameter of 12 mm were selected for the experiment. The first group was strengthened by applying a wear-resistant coating of hard alloy VT5. The second group was not strengthened. After drilling 50 holes in a plate made of 45 steel, the cutting capabilities of the drills were evaluated. In total, 500 holes were drilled. The experiment results in the form of a graph of the probability of preserving the cutting abilities of drills are shown in figure 3.

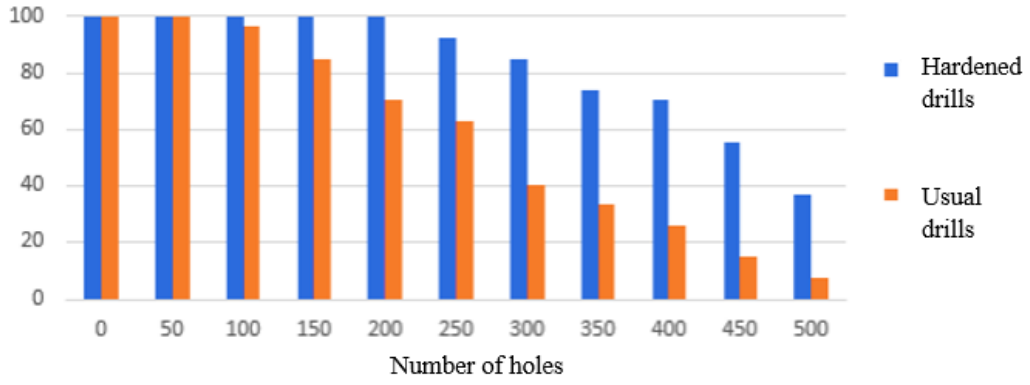

Figure 3. Probability graph of maintaining the cutting abilities of drills

As a result of hardening, 100% preservation of cutting abilities is observed after drilling 200 holes. This value was 70% for non-hardened patients. An even greater discrepancy in probability is observed when drilling 300 holes of 85% and 40%. In addition, it should be noted a significant increase in the probability of maintaining the cutting capacity of hardened tools throughout the entire working time. Thus, after 20 minutes of operation, the hardened drills had no failures, and after 30 minutes - 85% compared to 40% of non-hardened drills. After 40 minutes of operation, the non-hardened drills were almost completely exhausted, while 55% of the hardened drills were in working condition.
The efficiency of hardening 100 drills after 20 minutes of work will be expressed by an increase in the total period of durability by 1.43 times, after 30 minutes of work - by 2.02 times, and after 40 minutes by 4.7 times.

References

[1] Hasui A. the Technique of spraying: Translate with jap. Maslennikova, S. L., 1975, Moscow, Mashinostroenie, 264
[2] Gitlevich A. E., V. V. Mikhailov, N. Ya. Parkansky, etc. Electric spark alloying of metal surfaces, 1985, template synthesis of macrocyclic compounds, 604
[3] Minakov V. S. Development of complex mechanical and electrophysical processing processes based on the use of energy of transformable ultrasonic vibrations. dissertation of doctor of technical Sciences 1989, Rostov-on-don, 254
[4] Kudryashev S. B. Development of dynamics of longitudinal-torsional waveguides in relation to the process of electroacoustic deposition during hardening of cutting tools. Dissertation of the candidate of technical Sciences, 1998, Rostov-on-don, 187
[5] Borodulin I. D., Kudryashev S. B., Magomedov G. sh., Naumenko V. A. Analytical determination of the stiffness coefficient of a naturally twisted waveguide under electroacoustic sputtering. Fundamental foundations of mechanics, 2019, **4**, 177-180
[6] Kudryashev S. B. Solution of the problem of analysis and synthesis of a longitudinal-torsional ultrasonic waveguide. Young researcher of the don, 2018, **4**, 74-76
[7] A.K. Rukhadze Applied Mathematics and Mechanics. On deformation of naturally twisted rods, **11**, 5, 533-542 (1947)
[8] P.M. Reese Deformation of naturally twisted rods, DAN, USSR, **23**, 1, 18-21, 5, 441-444. (1939)
[9] I.A. Birger Strength, stability, oscillation, Moscow, Mechanical Engineering, **1**, 253-258. (1968)
[10] D. Stepanenko, V. T. Minchenya Modeling of flexible waveguides for ultrasonic vibrations transmission: Longitudinal and flexural vibrations of non-deformed waveguide, Ultrasonic, Elsevier, 50, 3, 424-430 (2009)

[11] Guangping Zhou Performance and design of ultrasonic vibration system for flexural mode, Ultrasonic, 38, **10**, 907-91, 2000
[12] G.P. Gavin, G.B. Mcguinness, F.B. Dolan, M.s.J. Hashmi Performance characteristics of a therapeutic ultrasound wire waveguide, International Journal of Mechanical Sciences, 49, 3, 298-305, 2007
[13] M.V. Golub, A.Eremin, A.N. Shpak Lamb wave scattering, conversion and resonances in an elastic layered wave- guide with a surface-bonded rectangular block, Applied Acoustics, **155**, 442-452, 2019
[14] Fernando Seco and Antonio R. Jiménez Modelling the Generation and Propagation of Ultrasonic Signals in Cylindrical Waveguides, Ultrasonic Waves, InTech, 282, 2012

Numerical solution of mathematical physics problems by the collocation method

E E Shcherbakova and S Yu Knyazev

Don State Technical University, Rostov-on-Don, Russia

Abstract. A modified collocation method for the numerical solving boundary value problems of mathematical physics is proposed. The irregular arrangement of collocation nodes in the problem solving domain can sharply increase the accuracy of the numerical solution by improving the quality of the linear algebraic equations system, to which the solved boundary value problem leads. Various basis functions systems are considered. The proposed method allows one to obtain an approximate solution of boundary value problems for a wide range of linear and nonlinear elliptic, parabolic and wave equations in an analytical form. This numerical method makes it possible to significantly expand the application field of traditional numerical methods when solving applied problems for modelling fields of various physical natures, described by linear and nonlinear equations of mathematical physics. The developed method is used to solve a quantum-mechanical problem for a hydrogen molecule ion. The results obtained in this work show the high potentialities of the complete collocation method, which are based on the universality of the method and high accuracy of numerical solutions. The energy of the ion ground state calculated with the minimum number of collocation nodes differs from the experimentally obtained value by 13%.

1. Introduction

Numerical modelling of different physical nature fields is one of the urgent physics problems. Currently the finite element method (FEM) and the finite difference method (FDM) [1-2] are the most frequently used to solve these problems. However, the using these methods in solving specific problems of mathematical physics, is not always justified.

High requirements for the numerical solution accuracy, the need to take into account the boundary conditions containing the normal derivative of the desired function on surfaces with a complex configuration, the difficulties in solving nonlinear problems force us to investigate and develop alternative numerical methods for solving boundary value problems.

The point-sources method (PSM) is a promising numerical method for solving problems of mathematical physics. PSM can be considered as one of the collocation method (CM) variants [3-8]. By PSM, an approximate solution is represented as a linear combination of basis functions that exactly satisfy the basic equation. However, in the collocation method, it is allowed to use other basic functions, which significantly expands the capabilities of the numerical method [9-10]. In this work, one of the collocation method variants is developed. It can be used to solve a fairly wide range of boundary value problems in mathematical physics, including nonlinear problems.

2. Method of complete collocations

Consider a domain Ω of a two-dimensional or three-dimensional space with a boundary $\partial\Omega$, in which a boundary value problem for the equation

$$L(\mathbf{r})U(\mathbf{r}) = f(\mathbf{r}),\ \mathbf{r} \in \Omega \tag{1}$$

is solved with conditions on the boundary $\partial\Omega$

$$\Lambda(\mathbf{r})U(\mathbf{r}) = g(\mathbf{r}),\ \mathbf{r} \in \partial\Omega, \tag{2}$$

where $L(\mathbf{r})$, $\Lambda(\mathbf{r})$ are linear operators in the domain Ω and on the boundary $\partial\Omega$; $f(\mathbf{r})$ and $g(\mathbf{r})$ are given functions in the domain Ω and on the boundary $\partial\Omega$. Let a system of linearly independent functions $\{\varphi_i(\mathbf{r})\}$ be given that have the completeness property in the domain Ω.

We represent the solution of problem (1), (2) in the form of a series

$$U(\mathbf{r}) = \sum_{i=0}^{\infty} C_i \varphi_i(\mathbf{r}).$$

Since finding an infinite number of expansion coefficients is practically impossible, we will seek an approximate solution to problem (1), (2) in the form of a finite sum

$$U_N(\mathbf{r}) = \sum_{i=0}^{N-1} c_i \varphi_i(\mathbf{r}). \tag{3}$$

To determine the unknown expansion coefficients in (3), we proceed as follows. We place nodal points N_v and N_G, collocation points in the domain Ω and on the boundary $\partial\Omega$, respectively. The total number of collocation points $N = N_v + N_G$ should correspond to the number of coefficients N in the expansion (3). The coordinates of the nodes, collocation points, in the domain Ω we denote as $\mathbf{r}_k$, $k = 1 \div N_v$, and on the boundary $\partial\Omega$ $\mathbf{r}_k$, $k = (N_v + 1) \div N$. To find the expansion coefficients c_i, we substitute (3) in equation (1) and in boundary condition (2) and require their exact fulfillment at the collocation points. The result is a system of linear algebraic equations

$$\sum_{i=0}^{N-1} c_i L(\mathbf{r}_k)\varphi_i(\mathbf{r}_k) = f(\mathbf{r}_k),\ k = 1 \div N_v, \tag{4}$$

$$\sum_{i=0}^{N-1} c_i \Lambda(\mathbf{r}_k)\varphi_i(\mathbf{r}_k) = g(\mathbf{r}_k),\ k = (N_v + 1) \div N. \tag{5}$$

We obtain the desired numerical solution in the form of a finite sum (3) after solving the system of linear algebraic equations (4) - (5). It should be noted that relation (3) gives an approximate analytical expression for the desired function $U(\mathbf{r})$. This means that the resulting solution $U(\mathbf{r})$ can be treated like any other analytical expression. It can be differentiated, other actions can be performed, and at the same time there is no additional numerical error.

The described here collocation method variant, which leads to a system of linear algebraic equations in the form of relations (4) - (5), will be called the **complete collocations method** (**CCM**), and system (4) - (5) will be called the **CCM** system. The word "complete" in the name of the CCM indicates that the collocation conditions must be satisfied not only at all internal nodal points of the solution domain Ω, but also at its boundary $\partial\Omega$.

The main problem that arises in finding an approximate solution to (3) is associated with the possibility of ill-conditioned system (4) - (5). For example, it was shown in [11] that when a function of two variables is interpolated by polynomials of degree n, the determinant of the system vanishes if the collocation nodes lie on the same curve of order n. A similar result takes place for functions of three variables. Therefore, with a regular, for example, with a uniform arrangement of collocation points, it is usually impossible to avoid bad conditioning. However, if you make adjustments in the location of the

collocation points, randomly making a small displacement of them, then the problem associated with the poor conditioning of the CCM system (4) - (5) can be eliminated.

Various variants of collocation methods differ from each other primarily in the system of used basis functions $\{\varphi_i(\mathbf{r})\}$. For example, solving two-dimensional problems, you can use functions of the form

$$\varphi_i(\mathbf{r}) = x^{i_x} y^{i_y}, \tag{6}$$

and solving three-dimensional boundary value problems, can use functions of the form

$$\varphi_i(\mathbf{r}) = x^{i_x} y^{i_y} z^{i_z}. \tag{7}$$

Each the number value i in (6), (7) must correspond to a certain set of numbers i_x, i_y, i_z.. In addition, the basis functions must be ordered thus, that with an increase in the ordinal number of the basis function i, the total degree of the basis function $n_i=i_x+ i_y+ i_z$ does not decrease, moreover $\varphi_0(\mathbf{r})=1$.

An approximate solution can also be searched in the form of a trigonometric sum (truncated Fourier series). Basic functions have certain attractiveness that taking a maximum, for example, a single value at the point of location of the corresponding collocation node and decrease with distance from this node. These can be, for example, functions of the following types:

$$\varphi_i(x,y) = \exp\left\{-k\left[(x-x_i)^2 + (y-y_i)^2\right]\right\}, \tag{8}$$

$$\varphi_i(x,y) = \left\{1+k\left[(x-x_i)^2 + (y-y_i)^2\right]\right\}^{-1}. \tag{9}$$

Here, the constants k are selected in such a way as to provide the smallest error in the numerical solution. The possibility of using other basic functions to obtain a solution to boundary value problems using the CCM is not excluded.

The CCM can be successfully used to solve various problems of mathematical physics, both linear and nonlinear [12-14]. The CCM is most naturally used to solve boundary value problems for linear equations of mathematical physics. However, it is possible to successfully apply the method under consideration when solving boundary value problems for an equation of parabolic type [12-14]. Below, as an example, we solve a quantum mechanical problem for a hydrogen molecule ion.

3. Hydrogen molecule ion model

The hydrogen molecule ion H_2^+ consists of two hydrogen nuclei and one electron. Let us denote the distance between two hydrogen nuclei (nucleus A and nucleus B) through a. We will assume that the value of a changes adiabatically and when solving the Schrödinger equation, it can be taken constant. This means that vibrations of nuclei around the equilibrium position, as well as rotation of nuclei around the center of gravity, will not be taken into account.

Let us consider the motion of an electron in a polar coordinate system (ρ, z, φ), placing nucleus A and nucleus B on the z axis at an equal distance from the origin. The potential energy of an electron in the Coulomb field of the nuclei of a molecule is determined by the expression

$$U(\rho,z) = -e^2(4\pi\varepsilon_0)^{-1}\left\{\left[\rho^2 + (z-a/2)^2\right]^{-1/2} + \left[\rho^2 + (z+a/2)^2\right]^{-1/2}\right\}.$$

The Schrödinger equation for an electron with zero orbital angular momentum has the form

$$-\hbar^2(2m)^{-1}\Delta\Psi - -e^2(4\pi\varepsilon_0)^{-1}\left\{\left[\rho^2 + (z-a/2)^2\right]^{-1/2} + \left[\rho^2 + (z+a/2)^2\right]^{-1/2}\right\}\Psi = E\Psi,$$

where E is the electron energy.

We will seek ax symmetric solutions for which $\Psi(\rho,z,\varphi)=\psi(\rho,z)$. Obviously, this solution corresponds, in particular, to the ground state of the ion.

Let's move on to atomic units of length $4\pi\varepsilon_0\hbar^2\left(me^2\right)^{-1}$ and energy $me^4\left(4\pi\varepsilon_0\hbar\right)^{-2}$. In these units, the Schrödinger equation has the form

$$\Delta\psi + 2\rho\left\{E + \left[\rho^2 + \left(z - a/2\right)^2\right]^{-1/2} + \left[\rho^2 + \left(z + a/2\right)^2\right]^{-1/2}\right\}\psi = 0. \qquad (10)$$

4. Results and discussion

Solving the problem numerically, it was first assumed that a = 2,1au, which corresponds to the known equilibrium distance between the nuclei of the hydrogen molecule ion [15]. The solution domain Ω was specified as a square with side L=8a. It was assumed that the wave function vanishes at the boundaries of the domain Ω. The correctness of this assumption was confirmed during subsequent testing the problem.

The CCM system (4) - (5) for the problem being solved is homogeneous and its solution is reduced to finding such energy values E for which the wave function $\psi(\rho, z)$ has a nontrivial solution that vanishes at the boundaries of the domain Ω. To obtain a nontrivial solution, a certain point M is set inside the domain Ω, for example, between the hydrogen nuclei, in which the value of the wave function is certainly not zero. At this point, the value of the wave function is assumed to be equal to unity: $\psi(M) = 1$. This condition can be regarded as a condition for normalizing the wave function. After obtaining the solution, the wave function can be easily renormalized.

As shown above, the numerical solution of boundary value problems using the CCM assumes to use of a certain system of basis functions. When solving the Schrödinger equation (10), the impossibility of using power functions (6) was found due to the instability of the numerical solution. Satisfactory results can be obtained using exponential (8) or hyperbolic (9) basis functions.

The problem is solved in accordance with the following algorithm. The initial value of the electron energy E_0 and the step of energy variation δε are set. It is desirable that this step be much less than the distance ΔE between the nearest energy eigenvalues, $\delta\varepsilon << \Delta E$. For each energy value E=E_0+kδε, therefore, at k = 0, 1, 2,…, the CCM system (4) - (5) is solved. The parameter is calculated as a criterion for the problem on the energy eigenvalues

$$K = \left[\sum_{k=1}^{N_S} \mathrm{abs}\left(\psi\left(\mathbf{r}_k\right)\right)\right]^{-1}. \qquad (11)$$

Here, the summation is performed over all points (not necessarily collocation nodes) located at random on the boundary of the domain Ω. The number of these points is equal to N_s. We will call parameter (11) the boundary criterion.

On the graph of the dependence of the criterion K on the energy E, the maxima should correspond to the eigenvalues of the electron energy. Figure 1 shows such a graph. The calculations were carried out with the total number of nodes N = 426, Ns = 100; the constants k in (8), (9) were set equal to k = 7. The electron energy varied from -40 eV to 0. The graph clearly shows three maxima corresponding to energies of -29.4 eV, -17.1 eV and -9.4 eV. Energy ε_0 = -29.4 eV corresponds to the ground state of an electron in a hydrogen ion. The total energy of the ion is the sum of the energy of the electron and the energy of the Coulomb interaction of nuclei, equal (at 2.1 au) U_0 = 13.0 eV, which adds up to the energy of the ground state W_0 = –16.4 eV. The deviation from the experimental value of the energy equal to -18.8 eV [15] is about 13%. For the simplest numerical model presented here, this accuracy is quite acceptable.

Then, the dependence of the ground state energy of the ion W_0 on the intern clear distance a was calculated. The distance a was varied from 0.5 au to 5.0 au. Using a numerical model based on the CCM, the energy of the ground state of the electron in the ion was found for each value of a, and then the energy of the ion W_0. Figure 2 shows a graph of the dependence $W_0 = W_0(a)$. This dependence has a

minimum at 1.8 au. The deviation from the experimental value a = 2.1 au is 14%, which also seems to be a quite acceptable error.

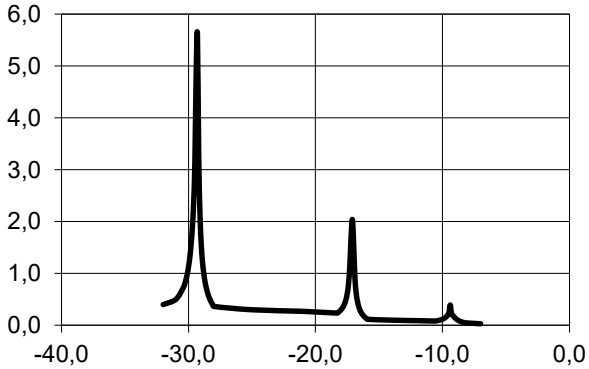

Figure 1. Dependence of the boundary criterion K on the electron energy

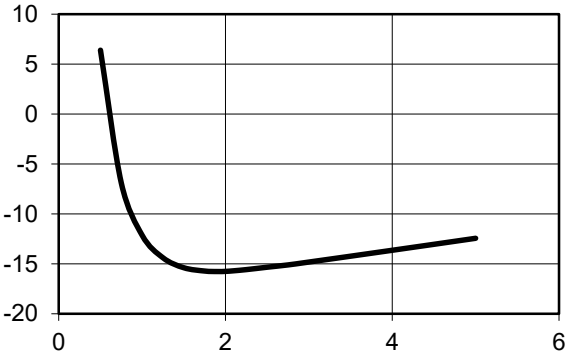

Figure 2. Dependence of the hydrogen ion ground state energy on the distance between the nuclei

5. Conclusion

The numerical solution of boundary value problems for elliptic and parabolic equations can become a difficult problem to solve, even if the sought solution is sufficiently smooth. Certain difficulties can arise if the original equation does not belong to the standard type of mathematical physics equations, or if the boundary conditions contain derivatives along the normal. In this case, the numerical solution of the boundary value problem using the finite element method (FEM) or the finite difference method (FDM) may have too slow convergence and not provide the required accuracy of the result. In these cases, as the results of the data presented here show, one can try to solve the boundary value problem using the CCM.

In these cases it is possible to solve the boundary value problem using the CCM. The results obtained confirm the possibility of using this method in solving not only two-dimensional, but also three-dimensional boundary value problems, including nonlinear ones. As in PSM, the solution using the CCM is obtained in an analytical form. Therefore, the obtained solution can be differentiated without loss of accuracy, and other mathematical operations can be performed with it.

Thus the presented methods compare favorably with FEM and FDM. It should also be noted the high accuracy of the results obtained using the CCM. All this makes the CCM a promising numerical method for modeling fields of various physical natures, using it in solving various physical problems, for example, quantum mechanical problems, an energy eigenvalues problems. Taking into account the extreme simplicity of the computer implementation of the CCM, further studies of this method possibilities should be considered promising.

References

[1] Carrera E, Pagani A and Zangallo F 2015 *Finite Elements in Analysis and Design* **95** 1-11
[2] Pandey1 P K and Jaboob S S A 2018 *Applied Mathematics and Nonlinear Sciences* **3**(1) 311–320
[3] Li Z C, Lu T T, Hu H Y and Cheng A H-D 2007 *Trefftz and collocation methods* (Southampton: MIT)
[4] Abbasbandy S, Roohani Ghehsareh H and Hashim I 2013 *Engineering Analysis with Boundary Elements* **37** 885-898
[5] HuiL V, Fang Hao, Yong Wang and Chen C S 2017 *Engineering Analysis with Boundary Elements* **83** 133-140
[6] Reinhard Piltner 2019 *Engineering Analysis with Boundary Elements* **101** 102-112
[7] Liu C-S, Wang F and Gu Y 2019 *Applied Mathematics Letters* **87** 87-92

[8] Shcherbakova E E and Knyazev S Yu 2019 *AIP Conference Proceedings. Proceedings of XV International scientific-technical conference "Dynamics of technical systems" (DTS-2019): electronic edition* 2019. P. 050035
[9] Wang D, Chen C and Fan C 2019 *Mathematics and Computers in Simulation* **159** 119-135
[10] Watson D W, Karageorghis A and Chen CSc2020 *Journal of Computational and Applied Mathematics* **363** 53-76
[11] Berezin I S and Zhidkov N P 1966 *Metody vychislenii* [*Calculation methods*] (Moscow: Nauka) vol. **1** 632 p.
[12] Knyazev S Yu and Shcherbakova EE 2016 *Russ. Phys. J.* **59**(10) 1616–22
[13] Knyazev S Yu and Shcherbakova E E 2017 *Russ. Phys. J.* **60**(7) 1124–32
[14] Knyazev S Yu, Shcherbakova E E and Shcherbakov A A 2016 *2nd International Conference on Industrial Engineering, Applications and Manufacturing, ICIEAM* 2016 - Proceedings. 2016. P. 7911559
[15] Flyugge Z 1974 *Zadachi po Kvantovoy Mekhanike* [*Problems in Quantum Mechanics*] (Moskva: Mir) vol. **1** 340

Improving the efficiency of technical means and methods for diagnostics of isolation of high-voltage distribution networks

A A Yurov[1,*], A S Voronov[2]

[1]Don State Technical University, Don Engineering Center,
Rostov-on-Don, Russia
[2]LLC «AC EnergyCom», Rostov-on-Don, Russia

[*]e-mail: yurov_npi@rambler.ru

Abstract. This work is aimed at developing and improving diagnostic equipment used in high-voltage distribution networks by modeling electromagnetic transients and expanding the functional part of devices. Presented are models of a three - phase distribution network and a high-voltage part of a test installation forming a technological system "diagnostic device-distribution network". Examples are shown of wave processes in the simulated system during insulation breakdowns, load characteristics of the test installation during operation of the device are shown, which makes it possible to optimize insulation control methods and technical diagnostic tools for electrical laboratories. Disclosed are examples of calculating the location of damage in case of insulation failures in different sections of the controlled network based on the analysis of wave processes in the line.

1. Introduction

Analysis of the operational properties of 6-10 kV distribution networks shows that the most common cases of insulation failure are: damage to cable lines, namely, breakdowns of the "core-core, "core-shell" type (this is both insulation aging and mechanical damage); damage to insulators on sections of overhead electric transmission lines (for example, its overlap). These examples indicate that isolation is the weakest element of the network and requires special solutions aimed at improving operational reliability. These solutions can be achieved through the development of computer models of power three-phase cable and overhead electric transmission lines, simulation models of high-voltage test installations that are part of electrical laboratories.

2. Main part

Low equipment of electrotechnical laboratories with inexpensive effective technical means of diagnostics of modern insulation materials of distribution networks reduces the reliability of power supply to the consumer and significantly complicates the work of operational personnel of the electric grid complex [1,2] during diagnostic work (fig. 1), this in turn can also lead to errors in assessing the isolation status of the monitored network.For example, when putting into operation electric power cable lines (CL) with crosslinked polyethylene insulation in the absence of ultra-low frequency installations, according to the guidance documents (OST 34.01-23.1-001-2017 "SCOPE AND STANDARDS OF TESTING OF ELECTRICAL EQUIPMENT") it is necessary to check the insulation of the electrical

cable line with the rated AC voltage of industrial frequency (operating voltage) within 24 hours, what is a work-intensive and energy-intensive task for a high-voltage laboratory and its personnel, in addition, it is almost impossible to monitor the leakage current in the cable every minute for 24 hours in the course of testing (24-hour on-line monitoring of parameters). The absence of devices for determining the location of damage by relative methods in electrical laboratories significantly complicates the search for the zone of insulation damage and increases the total time of the disconnected state of the cable line, which leads to economic losses. The development of a multifunctional high-voltage device of ultra-low frequency will significantly reduce the test time of the power cable line from 15 to 60 minutes (the time depends on the level of the output test voltage of the device), and significantly increase the efficiency of the electrical laboratory. Testing of CL with crosslinked polyethylene [3,4] insulation with high voltage of ultra-low frequency allows you to identify tree growth [5,6] in the insulation (microchannels in polyethylene insulation filled with water or other chemical compounds) that reduce its electrical strength. Defects in insulation lead to failures (electrical short) in the distribution network both during high-voltage insulation testing and during operation of the distribution network under load, therefore, determining the location of damage is an essential and important task in the complex of diagnostic work. To date, national manufacturers high-voltage test device of ultra-low frequency do not have technical solutions that allow combining the functions of high-voltage testing and determining the location of damage (DLD) of defective insulation in one device, it certainly affects the efficiency of the device. The high cost of foreign analogues and the complex management structure make it difficult to purchase and operate them. Today, the tasks of testing and DLD are solved in two steps with the use of a different fleet of devices, changing the schemes of work, and sometimes even by different ETL teams. The development of scientific and technical solutions that allow combining several functions in one device (high-voltage testing and determining the location of damage) without changing the scheme of work is particularly relevant and important for the country's power grid complex. A multifunctional diagnostic device (MFDD) for 10 kV distribution networks must meet the following requirements listed in table 1.

Table 1. ParametersMFDD

Parameter	Value
Maximum amplitude of the input voltage of the DLD organ in the power line diagnostics mode, kV	1-70
Range of measured distances of DLD, m	50-9999
Outputvoltagefrequency, Hz	0-0.1
The output voltage ULF, kV	30
Output rectified voltage of negative polarity, kV	70
Measurement range of the current consumed by the test object, mA	50
Additional parameterization via the human-machine interface	yes

Navigation in the menu should be clearly separated and understandable to operational personnel. A USB port must be provided in the installation to transmit data about searching for damage to power cables. When measuring the cable, all data is fully stored in the device's memory. Conclusions can be downloaded to a PC and reports can be processed using special software.

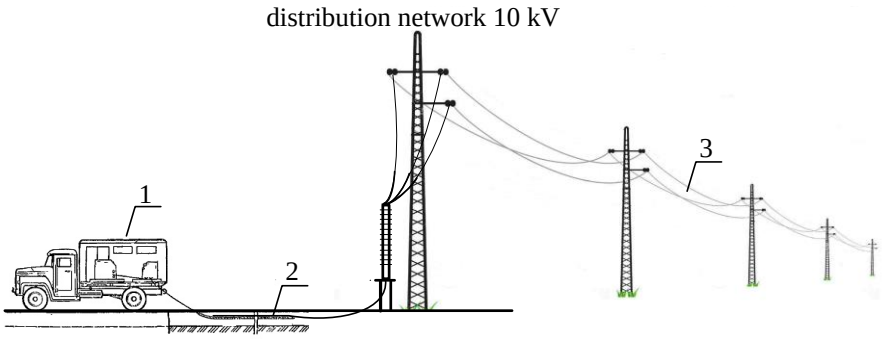

Figure 1. Diagnostic work in the distribution network 10 kV, where: 1-electrotechnical laboratory, 2-cable line, 3-overhead line

Such decisions can be made based on the analysis of computer modeling of electromagnetic transients in the technological system "test unit - distribution network" with experimental testing of the results of studies of wave processes in the controlled network in the diagnostic mode [7]. The simulation model of the technological system shown in fig. 1 can be obtained by combining models of the test facility [8] and the distribution network [9,10]. The most interesting are models of technological systems in three-phase design fig. 2, they should take into consider the distributed nature of the parameters of cable and overhead lines and take into consider the frequency of free oscillation. In the model fig.2 in each block of the CL and overhead line, a T-shaped replacement scheme for one element of the network length, , which takes into considering frequency-dependent specific parameters and mutual induction of current-carrying parts, allowing for a more established process of transient and steady-state processes in the 6-10 kV network, this provides an additional opportunity for developers to apply more effective isolation monitoring methods and improve the efficiency of damage location detection devices (DLD). The model also allows analyzing the wave processes that occur in it during insulation failures during line exploitation and in diagnostic modes, in order to study electromagnetic waves and improve the methods of DLD for various types of damage [14,19].

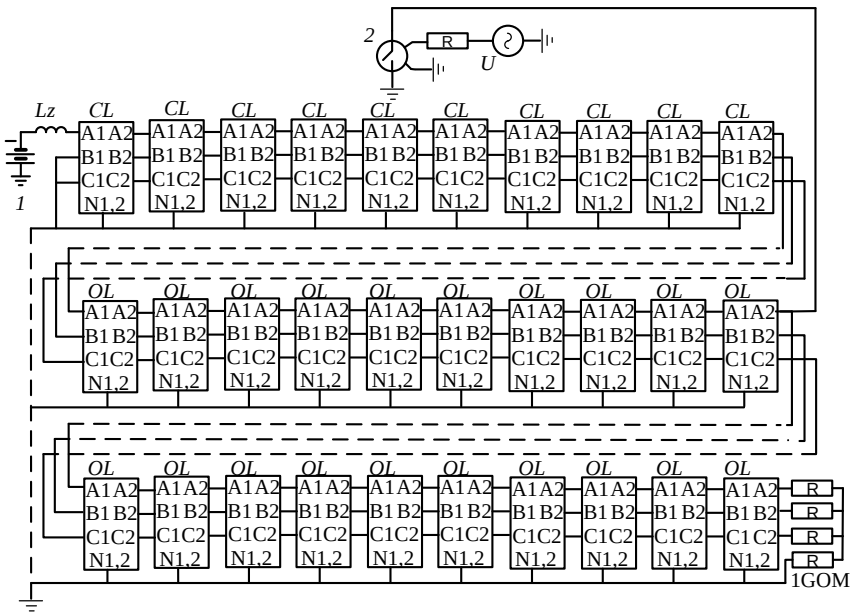

Figure 2. Computer model of a three-phase 10 kV distribution network in diagnostic mode presented in the form of hierarchical blocks, where: 1 – a high-voltage test source; 2-a key simulating a electrical short in the network; CL and OL 10 kV distribution network in the form of hierarchical blocks

The computational model of the bipolar rectifier circuit is shown in Fig.3. The same scheme can be used as part of a high-voltage unit of a multifunctional test facility for diagnostics of cables with crosslinked polyethylene insulation [11,12]. The proposed computational model allows us to study the external characteristics of the rectifier with voltage multiplication in any load range, which is applicable for any combination of parameters of circuit elements and the form of the supply voltage.

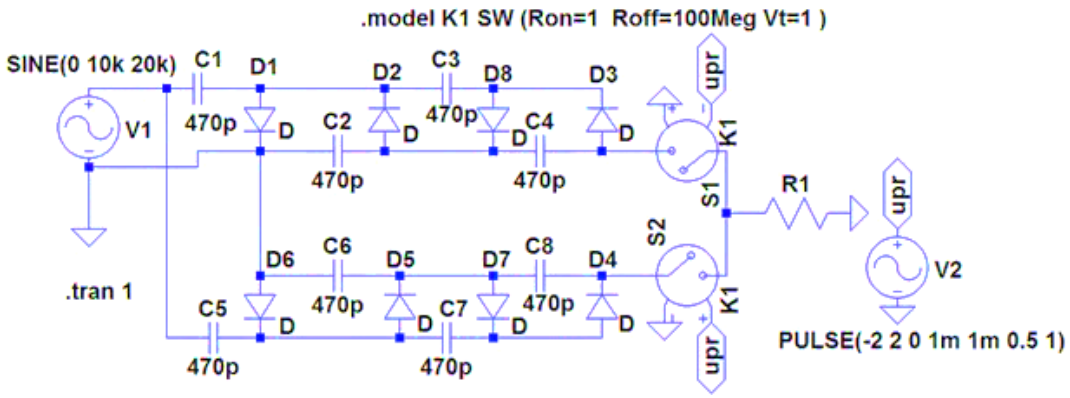

Figure 3. A computer model of a high-voltage source, where: V1 - is an ac voltage source with a frequency of 20 kHz and an amplitude of 10 kV; R1- is a load that changes the rectifier mode from idle to electrical short; Ci - is capacitances in the rectifier stages; Di - is diodes in the rectifier stages; K1 Si - are voltage-controlled alternately switched switches; V2 - is a voltage source controlled by a key.

Simulation computer model of the rectifier allows taking into consider the nonlinear dependence of the output voltage on the load current Fig. 4, table 2.

Table 2. Dependence of output voltage on leakage current

leakage current, *I,мА*	0,1	0,5	1,0	2,0	3,0	5,0	10	20	30	40	50
output voltage, *U,кВ*	39	38	38	37	36	35	30	22	15	9	2,6

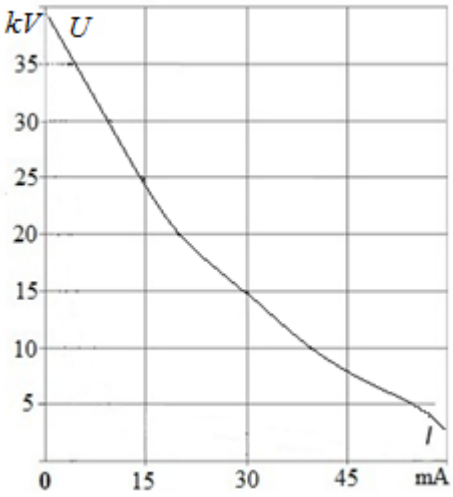

Figure 4. Load characteristics

In existing rectifier calculations, (for example, using the Balabukh method) this cannot be done, since this specified method allows to consider the load characteristic only on a linear section of the load characteristic, (that is until the moment insulation is broken or the rectifier operates with insignificant leakage currents). The proposed model allows us to study transient and established processes all points of the load characteristic (from the device no load to the electrical short mode), this solution allows developers of such equipment to improve their diagnostic devices, optimally select the parameters of the main installation elements, and develop more efficient network isolation monitoring equipment with increased operational reliability. Such models are made up of a set of elements that are located in the electronic library of the program (models Fig.2 and Fig. 3 are executed in the LTSpice program). Each element of the electronic model corresponds to nominal parameters, which in turn can be changed according to the specified criteria.

The wave process [13,16,18] obtained as a result of modeling during diagnostic work shown in fig. 5-6 allows operational personnel to determine the location of damage in the distribution network and select the optimal high-voltage test scheme based on the criterion of minimum shape distortion and free oscillation period [15,17].

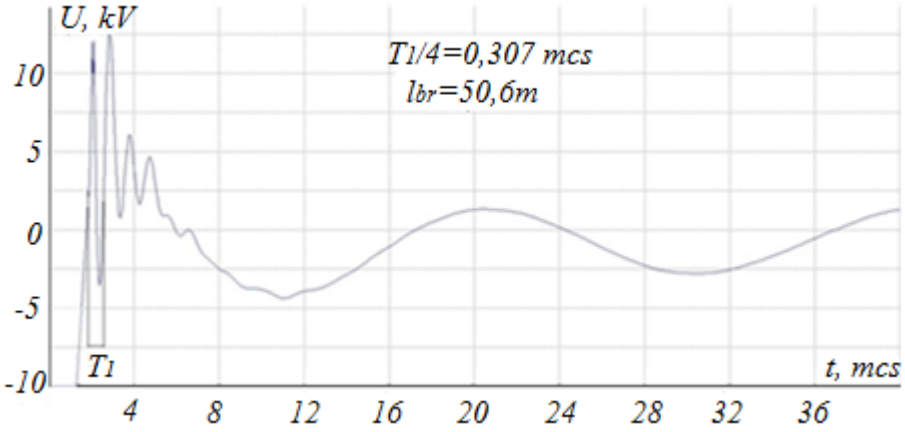

Figure 5. Waveform of the wave process at the beginning of the cable-air line at the breakdown of insulation (core-shell) ½ length of the power cable line section

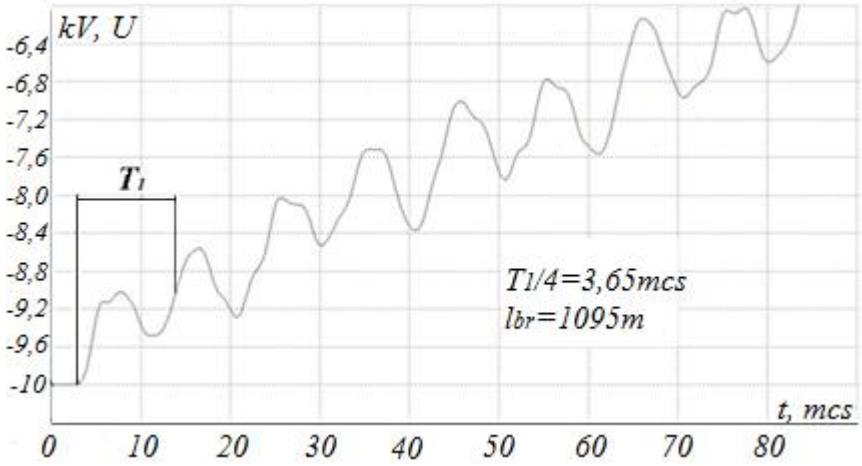

Figure 6. Waveform of the wave process at the beginning of the COL, when the suspension insulator the breakdown electric on a section of the overhead line of ¼ of the length of the OL

The period of free vibrations in a line closed on one side and open on the other is equal four times the range of the electromagnetic wave T1 = 4•tpr. The distance to the insulation breakdown can be determined by knowing the time and speed of the wave:

$$l = t_{\text{пр}} \cdot \upsilon = \frac{T_x}{4} \cdot \upsilon \quad (1)$$

where T1 - is the time of one full period of the wave path, and y is the propagation speed of the electromagnetic wave, for cable lines of this class makes up the value is 165 m/microseconds. Substituting the values of time T1 =1.28 microseconds (fig. 5) and speed υ=165 m/microseconds in the formula, we get the desired distance to the place of insulation damage in the controlled network equal to 50.6 m. On fig.6 shows an oscillogram voltage of the transition process in COL with a breakdown of the insulation on the cable line section. The period of the wave process (T_1=3.95 mcs) as a result of insulation failure in high voltage time test accurately indicates an accepted staff on the distance (formula 1) to the fault line (1095 m). On practice, operational personnel very often use burn-through installations to determine the location of a electric short CL with a high transient resistance at the point of damage, which is a time-consuming and complex operation that requires the engineer performing this work to change the test circuit and connect a new fleet of devices. The search time for such damages ranges from several hours to several days and is the most complex and expensive operation, while up to half of the costs in the diagnostic complex of works are spent on eliminating and determining the location of insulation damage in the distribution network. Availability of the ETL fleet of DLD devices that visualize the wave process using a relative method, or domestic test devices with the DLD function (MFDD) that meet the requirements of table 1, will significantly speed up and simplify repair work in the distribution network, as well as allow ETL personnel to avoid errors during repairing work [20-22].

3. Conclusion

With the development of software systems that allow modeling electromagnetic processes in complex electrical systems and diagnostic devices, it becomes possible to analyze wave processes in distribution networks. his analysis allows you to improve the main diagnostic equipment and methods for monitoring the state of isolation of the controlled network, make decisions that reduce the likelihood of errors by operational personnel when determining the location of damage, reduce the time of repair work in the network, which further increases the efficiency of electrotechnical laboratories. The three-phase model of the technological system "the testing device -distribution network" allows to optimize the area of the test site in conditions small areas, by making circuit decisions on connecting free cable cores during high-voltage testing of three-phase power lines and selecting the parameters of the circuit components. The existence of a fault location recorder built into the high-voltage device in automatic mode at the time of high-voltage testing will significantly simplify the complex of diagnostic work for the personnel servicing the distribution network, reduce the time of the consumer's disconnected state and reduce economic losses due to power interruption.

References

[1] Khaitan et al., «Design Techniques and Applications of Cyber Physical Systems: A Survey», IEEE SystemsJournal, 2014

[2] Dubyago M. N., Poluyanovich N. K., Estimation of Insulating Materials Depreciation and Forecasting the Residual Cable Resource Considering the Current Core Temperature // International Journal of Materials, Mechanics and Manufacturing. 2019. Vol. 7. № 1. Pp. 415–420

[3] Bustrom Y. O., Campus A., Hampton R. N., Heikala P., Jager K. M., and others. Copolymer compositions of crosslinked polyethylene (SuperCOPO) for high-voltage power cables of medium voltage / / Cables and wires. 2005 No. 5 (294). Pp. 7-2

[4] Mendelson, AERS M. world experience in working with Tr-insulation made of cross-linked polyethylene for a long useful life of MV cables. Presented at the Wire Russia exhibition. - Moscow, 2005
[5] N. Javerberg, H. Edin, "Applied Voltage Frequency Dependence of Partial Discharges in Electrical Trees" Proc. IR-EE-ETK, Stockholm, Sweden, 2009
[6] Aarts M., Kjellqvist J., Mendelsohn A.,Vaterrodt K. The Performance of XLPE Water Tree Resistant Insulation Systems Against The Requirements of DIN VDE 0276-60 5/A3 // 18th International Conference on electricity Distribution. – Turin, 2005
[7] Shuin V. A., Sarbeeva O. A. Shagurina E. S., Ganjaev D. I. Features of the use of electrical values of the transition process in earth fault protection of electric networks 6-10 kV // Vestnik IGEU, 2011 Issue 1-P. 32-41.
[8] Yurov A.A.,Pirozhnik A.A. "determination of equivalent parameters of a portable test installation for high-voltage testing of a power cable line" / / Izv.Vuz educational. Electromechanics. - 2008. P. 34-36.
[9] Yurov A. A., Pirozhnik A. A. "Modeling of power cable lines for determining the location of damage by the vibrational discharge method"//News of higher educational institutions. Electromechanics. 2014. No. 3. S. 149-151
[10] Yurov A. A., Pirozhnik A. A. "Analysis of the transition process in a simulated three-phase cable-overhead power transmission line of 10 kV", / Izv.Vuz educational. Electromechanics. 2019. Vol. 62. No. 2 P. 61-65
[11] Vanderson L. R., Raimundo C. S. F., Benedito A. L., Petrov C. L., Ewaldo S. Measuring the excitation current in transformers using hall effect sensors // Proc. IEEE Intern. Instrumentation and Measurement Technology Conf. (I2MTC), Montevideo, Uruguay. 2014. P. 960—963
[12] Nema P., Nema R.K., Rangnekar S.A. current and future state of art development of hybrid energy system using PV-solar: A review// Renewable and Sustainable Energy Reviews.2009. № 13(8) P.2096-2103. DOI:10.1016/jrser.2008.10.006
[13] Shu'in V. A., Sarbeeva O. A. Shagurina E. S., Ganjaev D. I. Features of the use of electrical values of the transition process in earth fault protection of electric networks 6-10 kV //messenger UGEU, 2011 Issue 1, Pp. 32-41.
[14] Faibisovich D. L., Karapetyan I. G.,Shapiro I. M., Handbook of electrical network design / edited by S. S. Rokotyan, I. M. Shapiro. –3rd ed., reprint. and add. M.: Phoenix, 2012. Pp. 376.
[15] Sabelnikov A. S. Modeling of transient processes when switching off a 10(6) kV overhead line using current quenching stages / A. S. Sabelnikov. — Text : direct // Young scientist. 2019. № 20 (258). p. 122-125.
[16] Dmitriev M. V. Neutral grounding in cable networks 6-35 kV // journal "Electric power: transmission and distribution", №5(38), 2016, pages 76-81.
[17] Dmitriev M. V. Damage to power transformers when switching cables 6 - 35 kV // journal "Electric power: transmission and distribution", №2(35), 2016, pp. 86-91.
[18] Dmitriev M. V. APV on air-cable lines // Electric power: transmission and distribution, No. 1, 2015, pp. 68-73.
[19] Nikonets L. A. et al. Modeling of electromagnetic processes in transformer windings under the influence of network overvoltages // Proceedings of Tomsk Polytechnic University, 2015, vol. 326, no. 4.
[20] Balabanov M. S., Baboshkina S. V., Khamitov R.N. Environmental aspects in energy-saving policy at the stage of creating intelligent power systems with an active adaptive network In Russia // Proceedings of Tomsk Polytechnic University. Engineering of geo-resources. 2015. Vol. 326. No 11. Pp. 141–152.
[21] Rysev P. V., Rysev D. V., Fedorov V. K., Shulga K. S., Pruss S. Yu. Identification and modeling of chaotic modes in electric power systems // Dynamics of systems,

mechanisms and machines:: Proceedings of the eleventh international IEEE scientific and technical conference. Omsk: Omstu, 2017. Vol. 5. No 3. Pp. 101-107.
[22] Vahdati P.M., Kazemi A. Bifurcations and chaos in nonlinear dynamics of power systems// 24th Iranian Conference on Electrical Engineering (ICEE). Shiraz, 2016. P. 1706–711.

Simulation of pneumatic actuator position system for long stroke mounting movements

V S Sidorenko, D A Korotych, V I Grishenko, A N Kharchenko

Don state technical university, Rostov-on-Don, Russia

Abstract. The creation of new equipment and technical means for the implementation of promising processes and technologies is largely determined by the level of development of mechanical engineering. The most important requirements for technological equipment are an increase in work processes, flexibility and adaptability, automation, implementation of complex algorithms of executive movements. The mechanisms of executive movements ensure the operation of transporting, fixing and other target mechanisms, this largely determines the quality and efficiency of processing processes. Positional actuators have existing technical solutions. However, to a greater extent they relate to linear movements realized by rod cylinders, this does not allow adapting the results of existing research to the development of long-stroke positional movements. In the course of this work, an assessment was made of the existing types of drives and a displacement and position measurement sensors. The proposed positional pneumatic scheme allows solving the problem of positioning long-stroke displacements, its mathematical and computer models were built, and dynamic analysis and conclusions were made.

1. **Assessment of the state of the issue**

In order to achieve the linear movement of the output link of the technological equipment, pneumatic, electromagnetic and hydraulic drives are usually used. The latter two types of engine are more widespread. An electromagnetic drive, on the other hand, is clean and reliable to operate, but often requires a mechanical transmission, the combination of which can be quite expensive.

Pneumatic units have a number of advantages: they are fast, cheap, have outstanding power per unit weight, and are easy to maintain. A big problem when using a pneumatic cylinder is the presence of piston friction and non-linear characteristics of the compressed gas flow. Therefore, with long-stroke movements, there is a deterioration in the dynamics and positioning of the drive [1-3].

The use of existing sensors for measuring displacement and position is not always possible in industries where special attention is paid to fire and explosion safety. The use of electrical elements is not permitted there. The use of sensors with long travel distances can affect their cost or require feedback, which can also increase the cost of the drive.

2. Development of a pneumatic positioning scheme

Positional pneumatic actuator consists of: air preparation device (APD); rodless pneumatic cylinder (PC1); short-running pneumatic cylinders (PC2, PC3); tandem pneumatic cylinder (PC4); nozzle apparatus (N) and rails; throttle (TH1, TH2), which are used to regulate the speed of movement of the cylinder piston; two-position two-way valves with electro-pneumatic control (PV1, PV2, PV4); three-position five-line distributor (PV3), mufflers (S1-S5).

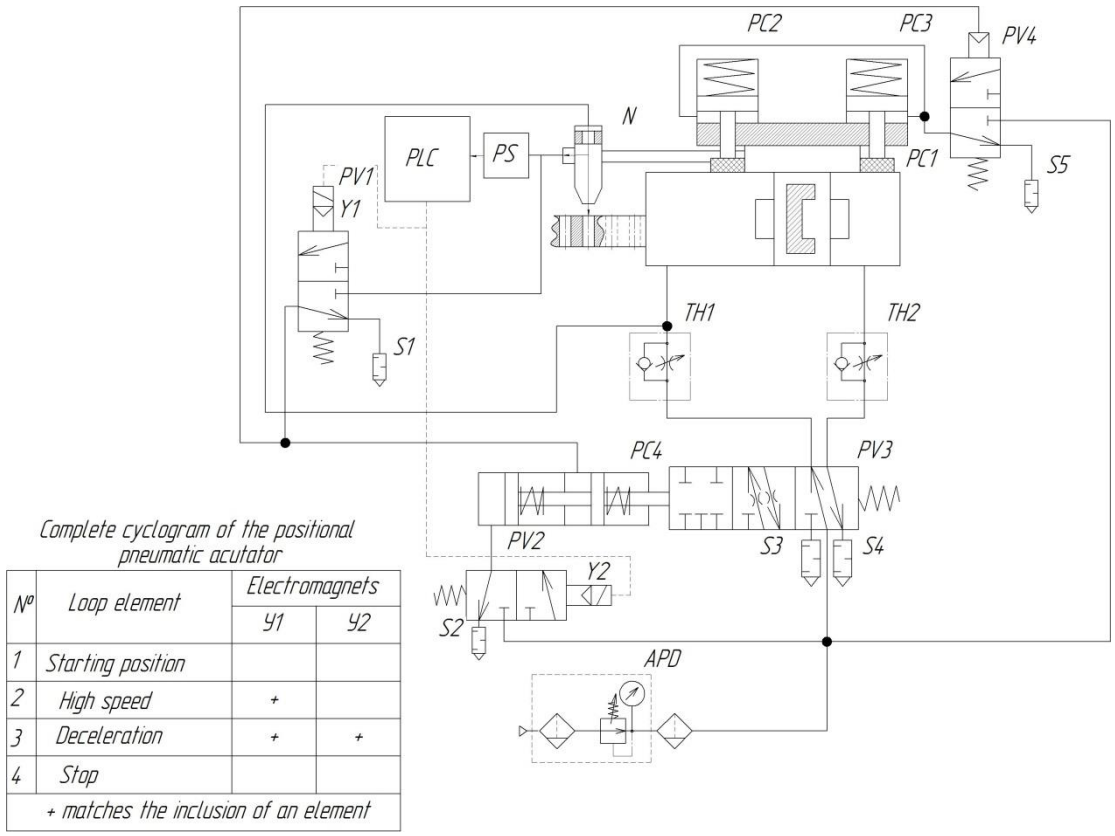

Complete cyclogram of the positional pneumatic acutator

№	Loop element	Electromagnets	
		Y1	Y2
1	Starting position		
2	High speed	+	
3	Deceleration	+	+
4	Stop		
+ matches the inclusion of an element			

Figure 1. Diagram of pneumatic positioning

3. Description of the principle of operation

The operator sets the required stop coordinate in the PLC, rapid traverse occurs. The pressure enters the nozzle N, then the pressure sensor PS. When the drive reaches the previously set coordinate, electromagnets Y1, Y2 are turned on. The cylinder rod PC4 switches the PV3 valve, the drive travel slows down. When the drive reaches the coordinate set by the operator through the N nozzle through the aligned hole, the pressure is supplied to the control line of the PV4 distributor and the PC4 tandem cylinder, and it switches the PV4, PV3 valves and blocks the inlet and outlet cavities, and activates the blocking brake.

4. Formation of a generalized mathematical model

The mathematical model of the pneumatic drive demonstrates a system of differential equations describing the movement of the working body and the change in pressure in the cavities of the actuator, the mathematical model of the pneumatic drive includes the following equations:

1. The equation of motion of the actuator of the pneumatic cylinder.
2. Equations of pressure change in the discharge cavity.
3. Equations of pressure change in the exhaust cavity.

The design diagram of the pneumatic drive is shown in Figure 2.

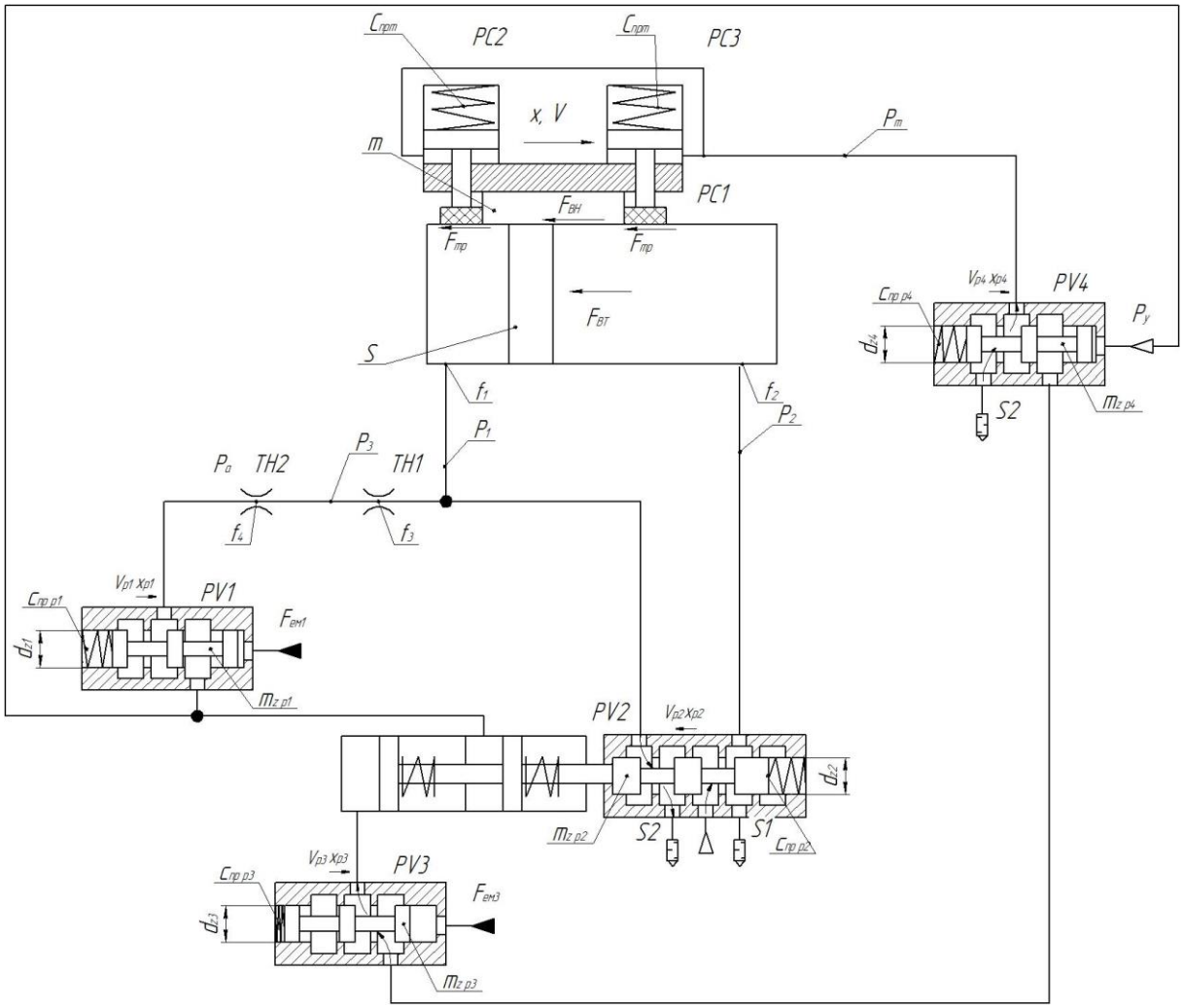

Figure 2. Design diagram of a pneumatic drive

When designing, one of the main conditions is to confirm the functionality of the developed drive, as well as to analyze the processes occurring in it when positioning the pneumatic cylinder.
When forming the mathematical model of the drive, the following assumptions were made:

- the pressure of the compressed air source is constant over time;
- the thermodynamic process of gas behavior in the pneumatic system is assumed to be adiabatic;
- in the description of pneumatic devices, the ideal gas model is used, since the pressure in the pneumatic system is below 10 bar;
- leaks are not taken into account;
- the force of viscous friction is proportional to the speed;
- the coefficients of expenses are taken as averaged;
- the mass of the moved parts is assumed constant;
- force Fc at the output link of the pneumatic drive is constant;
- relay control of pneumatic valves;
- the time of forming the control signal from the displacement sensor is not taken into account [4-5].

During the calculation of the pneumatic actuator, the initial data for the modeling were calculated and presented in Table 1.

Table 1. Initial data for modeling

Name	Identification	Mean.	Size
Drag coefficient	ks1	65	
	ks2	100	
	ks3	70	
	ks4	70	
Flow path diameter	d1	0.006	m
	d2	0.006	
	d3	0.001	
	d4	0.0012	
Compressor pressure	pm	600,000	Pa
Atmospheric pressure	pa	101325	Pa
Adiabatic coefficient	to	1.4	
Coordinates given	x01, x02	0.008	m
Mass of moving parts of PC	m	6	kg
Strength of external resistance	Fvn	20	N
Pipeline diameter	dtr	0.005	m
Pneumatic cylinder 1 piston diameter	D	0.04	m
Pneumatic cylinder 2,3 piston diameter	Dt	0.04	m
Viscous friction coefficient	kvt	400	N s/ m
Piston stroke	L	0.4	m
Friction coefficient	kt	0.4	

1.The equation of motion of the actuator of the pneumatic cylinder

$$m\frac{d^2x}{dt^2} = S \cdot (p_1 - p_2) - F_{\text{вн}} \cdot sign\left(\frac{dx}{dt}\right) - k_{\text{вт}} \cdot \left(\frac{dx}{dt}\right) - F_{\text{т}} \cdot sign\left(\frac{dx}{dt}\right) \quad (1)$$

2.Equation of motion of the actuator of the pneumatic brake cylinder

$$m\frac{d^2x_{\text{т}}}{dt^2} = S \cdot p_m - F_{\text{вн т}} \cdot sign\left(\frac{dx_{\text{т}}}{dt}\right) - k_{\text{вт т}} \cdot \left(\frac{dx_{\text{т}}}{dt}\right) - \text{c}_{\text{пр т}} \cdot (x_0 + x_{\text{т}}) \quad (2)$$

where S is the effective area of the cavities, m2;

P_1 , P_2- air pressure, respectively, in the discharge and exhaust cavities of the cylinders, Pa;

$\frac{dx}{dt}$ – speed of movement of moving masses, m / s;

$F_{\text{вн}}$ - the force of external forces, N;

$k_{\text{вт}}$ - coefficient of viscous friction;

m - mass of moving parts of the drive, kg.

$F_{\text{т}}$- braking force, N;

$$F_{\text{т}} = \mu \cdot N \quad (3)$$

$$N = P_m \cdot S_{\text{т}} \quad (4)$$

where μ is the coefficient of friction;

N- normal force, N;

P_m- supply pressure, Pa;

$S_{\text{т}}$- the area of the piston cavity in the pneumatic brake,.m^2

3. Equation of motion of the valve actuator 1

$$m_{z\,\text{р1}}\frac{d^2x_{z1}}{dt^2} = S_{\text{р1}} \cdot (p_3 - p_y) - \text{c}_{\text{пр р1}} \cdot x_{z1} - F_{c1} \cdot sign\left(\frac{dx_{z1}}{dt}\right) - F_{y1} \cdot \left(\frac{dx_{z1}}{dt}\right) - P_y \quad (5)$$

4. Equation of motion of the valve actuator 2

$$m_{z\,\text{р2}}\frac{d^2x_{z2}}{dt^2} = S_{\text{р2}} \cdot (p_{\text{м}} - p_1) - \text{c}_{\text{пр р2}} \cdot x_{z2} - F_{c2} \cdot sign\left(\frac{dx_{z2}}{dt}\right) - F_{y2} \cdot \left(\frac{dx_{z2}}{dt}\right) - F_{\text{ем2}} \quad (6)$$

5. Equation of motion of the valve actuator 3

$$m_{z\,\text{р3}}\frac{d^2x_{z3}}{dt^2} = S_{\text{р3}} \cdot (p_2 - p_a) - \text{c}_{\text{пр р3}} \cdot x_{z3} - F_{c3} \cdot sign\left(\frac{dx_{z3}}{dt}\right) - F_{y3} \cdot \left(\frac{dx_{z3}}{dt}\right) - F_{\text{ем3}} \quad (7)$$

6. Equation of motion of the valve actuator 4

$$m_{z\,\text{p4}}\,\frac{d^2x_{z4}}{dt^2} = S_{\text{p4}}\cdot(p_{\text{м}} - p_{\text{т}}) - \text{c}_{\text{пр p4}}\cdot x_{z4} - F_{c4}\cdot sign\left(\frac{dx_{z4}}{dt}\right) - F_{y4}\cdot\left(\frac{dx_{z4}}{dt}\right) - P_y \quad (8)$$

Where S_{p} is the effective area of the valve end of the distributor, m^2;

$P_{\text{м}}, P_1, P_{\text{т}}$ –Pressure at the inlet and outlet of the distributor, Pa;

P_y –Pressure in the control channel, Pa;

F_{c} - forces of resistance to movement of the distributor spool, N;

F_y- thrust reaction forces, N;

$F_{e\text{м}}$- force of action of the electromagnet on the valve spool, N;

$\text{c}_{\text{пр p}}$ - spring compression ratio, N / m;

$m_{z\,\text{p}}$ - mass of the distributor spool, kg.

7. Equation in the discharge cavity.

Based on the first law of thermodynamics, the amount of energy dQ_M supplied with the gas into the discharge cavity from the main goes to change the internal energy of the gas in the cavity dU_1 and to perform the work of the drive dL

$$dQ_M = dU_1 + dL; \quad (9)$$

$$dQ_M = q\cdot dm, \quad (10)$$

The specific energy of a gas is determined by its body content - enthalpy. Enthalpy is related to the specific and temperature of the gas in the pipeline by the dependence:

$$q = i = c_p\cdot T_M \quad (11)$$

Elementary mass of gas dm express it in terms of expense G_M:

$$dm = G_M\cdot dt \quad (12)$$

Substituting (11) and (12) into equation (10), we find the amount of energy that enters the piston cavity

$$dQ_M = c_p\cdot T_M\cdot G_M\cdot dt \quad (13)$$

After the transformation, we obtain the equation for the change in the internal energy of the gas:

$$dU_1 = d(c_v\cdot T_1\cdot m_1) = c_v\cdot d(T_1\cdot m_1) \quad (14)$$

Where $c_v -$ specific heat capacity of a gas at a constant volume;

$T_1 -$ gas temperature in the discharge cavity;

m_1 –mass of gas in the discharge cavity.

The mass of gas is determined in the size and volume of the cavity $\rho_1 V_1$:

$$m_1 = \rho_1\cdot V_1 \quad (15)$$

Next, we substitute (15) into formula (14) and obtain an expression for determining the change in the internal energy of the gas dU_1 in the cavity:

$$dU_1 = d(c_v\cdot T_1\cdot m_1) = c_v\cdot d(T_1\cdot m_1) \quad (16)$$

Next, we transform the equation (10)

According to the Mendeleev - Clapeyron equation $\frac{p_1}{\rho_1} = R\cdot T_1$

$$T_1\cdot\rho_1 = R\cdot T_1 \quad (17)$$

Then, substituting (17) into formula (16), we transform the equation:

$$dU = \frac{c_v\cdot d\cdot(p_1\cdot V_1)}{R} \quad (18)$$

After differentiation, we get the final expression

$$dU = \frac{c_v\cdot p_1\cdot dV_1}{R} + \frac{c_v\cdot V_1\cdot pV_1}{R} \quad (19)$$

Next, we get the work overcome by the gas:

$$dL_1 = p_1\cdot dV_1 \quad (20)$$

Next, we transform equations (13), (19), (20), we obtain

$$c_p\cdot T_M\cdot G_M\cdot dt = \frac{c_v}{R\cdot p_1\cdot dV_1} + \frac{c_v}{R\cdot V_1\cdot dp_1} + p_1\cdot dV_1$$

After that, we transform the expression and get:

$$c_p \cdot T_M \cdot G_M \cdot dt = p_1 \cdot \left(\frac{c_v}{R+1}\right) \cdot dV_1 + \frac{c_v}{R \cdot V_1 \cdot dp_1} \quad (21)$$

At constant pressure and constant volume, the specific heat capacities of the gas are interconnected by dependencies:

$$c_v + R = c_p \quad (22)$$

Substituting equation (18) into (17) we get: $c_p \cdot T_M \cdot G_M \cdot dt = \frac{c_p}{R \cdot p_1 \cdot dV_1} + \frac{c_v}{R \cdot V_1 \cdot dp_1}$

To simplify the expression, the adiabatic exponent for air, we multiply the entire equation by R and divide by, as a result we get:$\frac{c_p}{c_v} = k = 1.4$

$$k \cdot R \cdot T_M \cdot G_M \cdot dt = k \cdot p_1 \cdot \ dV_1 + V_1 \cdot dp_1 \quad (23)$$

Let us find expressions for the components of this equation. The volume of the discharge cavity V_1 consists of the working (variable) volume of the working cavity $V_{1P}$of the pneumatic cylinder and the initial (constant) volume V_{01} of the pneumatic drive:

$$V_1 = V_{1P} + V_{01} \quad (24)$$

The working volume of the discharge cavity V_{1P} is expressed through the area of the piston S_1 in the discharge cavity and the coordinate x:

$$V_{1P} = S_1 \cdot x \quad (25)$$

The initial volume V_{01} includes the structural volume of the discharge cavity in the extreme position of the piston and the volume of the supply line, which consists of the volumes of the pipeline and the connected pneumatic equipment.

The initial volume $V_{01}$of the supply line can be written, as is customary in some works [6-8], as follows:

$$V_{01} = S_1 \cdot x_{01} \quad (26)$$

where x_{01} is the reduced initial coordinate of the piston position.

Finally, substituting (25) and (26) into equation (24), we find the volume of the injection cavity V_1

$$V_1 = S_1(x + x_{01}) \quad (27)$$

Gas flow in pneumatic industrial drives. Coming into the discharge cavity depends on the nature of the process.

In pneumatic industrial drives, the gas flow is close to the isothermal process [7-9]. Therefore, the gas flow rate is determined from the equation which we write in the following form, bearing in mind that.$\sigma = \frac{p}{p_м}$

$$G_м = K_1 \cdot \sqrt{p_м^2 - p_1^2}, \quad (28)$$

where

$$K_1 = \frac{f_1}{\sqrt{R \cdot T_M \cdot \zeta_1}}; \quad (29)$$

Substituting the values and from (27) and (28) into the original equation, after transforming the equation (9), we obtain the equation for the change in pressure in the pressure cavity and emptying the pneumatic cylinder (30):

$$\frac{dp_1}{dt} = \frac{k \cdot f_1 \cdot \sqrt{R \cdot T_M}}{S(x+x_{01})\sqrt{\xi_1}} \cdot \sqrt{{p_M}^2 - {p_1}^2} - \frac{k \cdot f_3 \cdot \sqrt{R \cdot T_M}}{S(x+x_{01})\sqrt{\xi_2}} \cdot \left(\frac{p_3}{p_1}\right)^{\frac{k-1}{2k}} \cdot \sqrt{{p_1}^2 - {p_3}^2} - \frac{k \cdot p_1}{x+x_{01}} \cdot \frac{dx}{dt} \quad (30)$$

where is the adiabatic index; k

R - gas constant, J / $\kappa g \cdot K$;

$T_м$- temperature in the discharge line, K;
P_1 - air pressure in the discharge line, Pa;
P_3 - pressure in the sensor, Pa;
L - maximum piston stroke, m;
f_1 , f_3 - flow area of pipelines, m2;
x_{01}- the ratio of the initial ("passive") volumes V_{01} of the pneumatic drive to the useful area of the piston of the piston and rod cavity of the pneumatic cylinder, respectively, m;
$\frac{dx}{dt}$ −piston movement speed, m / s;
ξ_1, ξ_2- the coefficient of resistance of the supply and exhaust lines.

7. Equation of pressure in the exhaust cavity.

$$-dQ_2 = dU_2 + dL_2; \tag{31}$$

Similarly, we derive the equation in the drain cavity, the amount of energy leaving the exhaust cavity:

$$dQ_2 = c_p \cdot T_2 \cdot dm_2 = c_p \cdot T_2 \cdot G_2 \cdot dm_2 \tag{32}$$

After the transformation, we obtain the equation for the change in the internal energy of the gas:

$$dU_2 = d(c_v \cdot T_2 \cdot m_2) = c_v \cdot d(T_2 \cdot \rho_1 \cdot V_2) \tag{33}$$

According to the Mendeleev - Clapeyron equation $\frac{p_2}{\rho_2} = R \cdot T_2$

$$T_2 \cdot \rho_2 = \frac{p_2}{R} \tag{34}$$

Then, substituting (32) into formula (31), we transform the equation:

$$dU = \frac{c_v \cdot d \cdot (p_2 \cdot V_2)}{R} = \frac{c_v}{R \cdot p_2 \cdot dV_2} + \frac{c_v}{R \cdot V_2 \cdot dp_2} \tag{35}$$

Next, we get the work done by the gas in the exhaust cavity:

$$dL_2 = p_2 \cdot dV_2 \tag{36}$$

Next, we transform equations (32), (33), (34) into equation (31), we obtain

$$c_v + R = c_p;$$

$$-k \cdot R \cdot T_2 \cdot G_2 \cdot dt = k \cdot p_2 \cdot \ dV_2 + V_2 \cdot dp_2; \tag{37}$$

The volume of gas in the exhaust cavity, taking into account the volume of the outlet pipeline and pneumatic equipment, is:

$$V_2 = (S + x_2 - x) \cdot F_2 \tag{38}$$

The outflow of gas from the exhaust cavity through the pipeline is close to the isothermal process. Therefore, the flow rate is determined from the simplified equation corresponding to the isothermal gas outflow:

$$G_2 = K_2 \cdot \sqrt{p_2^2 - p_A^2} \tag{39}$$

Where

$$K_2 = \frac{f_2}{\sqrt{R \cdot T_2 \cdot \zeta_2}} \tag{40}$$

Substituting the values V_2 and G_2 from (38) and (39) into equation (37), we obtain the equation for the pressure change in the exhaust cavity:

$$\frac{dp_2}{dt} = -\frac{k \cdot f_2 \cdot \sqrt{R \cdot T_M}}{S(L - x + x_{02})\sqrt{\xi_2}} \cdot \left(\frac{p_2}{p_a}\right)^{\frac{k-1}{2k}} \cdot \sqrt{{p_2}^2 - {p_a}^2} + \frac{k \cdot p_2}{L - x + x_{02}} \cdot \frac{dx}{dt} \tag{41}$$

where is the adiabatic index; R - gas constant, J /$k\kappa g \cdot K$;
$T_м$, T - air temperature in the exhaust line, K;
P_2 - pressure in the exhaust line, Pa;
P_a - atmospheric pressure, Pa;

L - maximum piston stroke, m;
f_2 , - flow area of the drain pipeline, m2;
L - piston stroke, m;
x_{02} - the ratio of the initial ("passive") volume V_{02} of the pneumatic drive to the useful area of the rod cavity of the pneumatic cylinder, m;
$\frac{dx}{dt}$ −piston movement speed, m / s;
ξ_2 - the coefficient of resistance of the exhaust line.

5. Equation of pressure change in the sensor.

$$\frac{dp_3}{dt} = \frac{k \cdot f_3 \cdot \sqrt{R \cdot T_M}}{W_1 \cdot \sqrt{\xi_3}} \cdot \sqrt{{p_1}^2 - {p_3}^2} - \frac{k \cdot f_4 \cdot \sqrt{R \cdot T_M}}{W_2 \cdot \sqrt{\xi_4}} \cdot \left(\frac{p_3}{p_a}\right)^{\frac{k-1}{2k}} \cdot \sqrt{{p_3}^2 - {p_a}^2} \qquad (42)$$

where is the adiabatic index; R - gas constant, J /$k\kappa g \cdot K$;
- $T_м$ air temperature in the discharge line, K;
- P_a atmospheric pressure, Pa;
- P_1 , P_3 pressure in the flowing part of the pipeline, Pa;
W_1, W_2 - the volume of the flow parts, m^3/s
- ξ_3, ξ_4 the coefficient of resistance of the supply and exhaust lines.
f_3 , f_4 - pipeline section area, m2;
We obtain the system of equations of the mathematical model of this pneumatic system:

$$\begin{cases} m\frac{d^2x}{dt^2} = S \cdot (p_1 - p_2) - F_{вн} \cdot sign\left(\frac{dx}{dt}\right) - k_{вт} \cdot \left(\frac{dx}{dt}\right) - F_т \cdot sign\left(\frac{dx}{dt}\right) \\ m_{z\,p1}\ \frac{d^2x_{z1}}{dt^2} = S_{p1} \cdot (p_3 - p_y) - c_{пр\,p1}\ \cdot x_{z1}\ - F_{c1} \cdot sign\left(\frac{dx_{z1}}{dt}\right) - F_{y1} \cdot \left(\frac{dx_{z1}}{dt}\right) - P_y \\ m_{z\,p2}\ \frac{d^2x_{z2}}{dt^2} = S_{p2} \cdot (p_м - p_1) - c_{пр\,p2}\ \cdot x_{z2}\ - F_{c2} \cdot sign\left(\frac{dx_{z2}}{dt}\right) - F_{y2} \cdot \left(\frac{dx_{z2}}{dt}\right) - F_{ем2} \\ m_{z\,p3}\ \frac{d^2x_{z3}}{dt^2} = S_{p3} \cdot (p_2 - p_a) - c_{пр\,p3}\ \cdot x_{z3}\ - F_{c3} \cdot sign\left(\frac{dx_{z3}}{dt}\right) - F_{y3} \cdot \left(\frac{dx_{z3}}{dt}\right) - F_{ем3} \\ m_{z\,p4}\ \frac{d^2x_{z4}}{dt^2} = S_{p4} \cdot (p_м - p_т) - c_{пр\,p4}\ \cdot x_{z4}\ - F_{c4} \cdot sign\left(\frac{dx_{z4}}{dt}\right) - F_{y4} \cdot \left(\frac{dx_{z4}}{dt}\right) - P_y \\ \frac{dp_1}{dt} = \frac{k \cdot f_1 \cdot \sqrt{R \cdot T_M}}{S(x+x_{01})\sqrt{\xi_1}} \cdot \sqrt{{p_M}^2 - {p_1}^2} - \frac{k \cdot f_3 \cdot \sqrt{R \cdot T_M}}{S(x+x_{01})\sqrt{\xi_2}} \cdot \left(\frac{p_3}{p_1}\right)^{\frac{k-1}{2k}} \cdot \sqrt{{p_1}^2 - {p_3}^2} - \frac{k \cdot p_1}{x+x_{01}} \cdot \frac{dx}{dt} \\ \frac{dp_2}{dt} = -\frac{k \cdot f_2 \cdot \sqrt{R \cdot T_M}}{S(L-x+x_{02})\sqrt{\xi_2}} \cdot \left(\frac{p_2}{p_a}\right)^{\frac{k-1}{2k}} \cdot \sqrt{{p_2}^2 - {p_a}^2} + \frac{k \cdot p_2}{L-x+x_{02}} \cdot \frac{dx}{dt} \cdot \\ \frac{dp_3}{dt} = \frac{k \cdot f_3 \cdot \sqrt{R \cdot T_M}}{W_1 \cdot \sqrt{\xi_3}} \cdot \sqrt{{p_1}^2 - {p_3}^2} - \frac{k \cdot f_4 \cdot \sqrt{R \cdot T_M}}{W_2 \cdot \sqrt{\xi_4}} \cdot \left(\frac{p_3}{p_a}\right)^{\frac{k-1}{2k}} \cdot \sqrt{{p_3}^2 - {p_a}^2} \end{cases} \qquad (43)$$

The system of differential equations can be solved by various numerical methods (Euler, Runge-Kutta, etc.) for given initial conditions, drive parameters and control actions that functionally depend on the coordinate of the output link [10-13]. The study of the model was carried out in the SimIntech program by numerical methods.

5. Computer model

The computer model is shown in Figure 3.

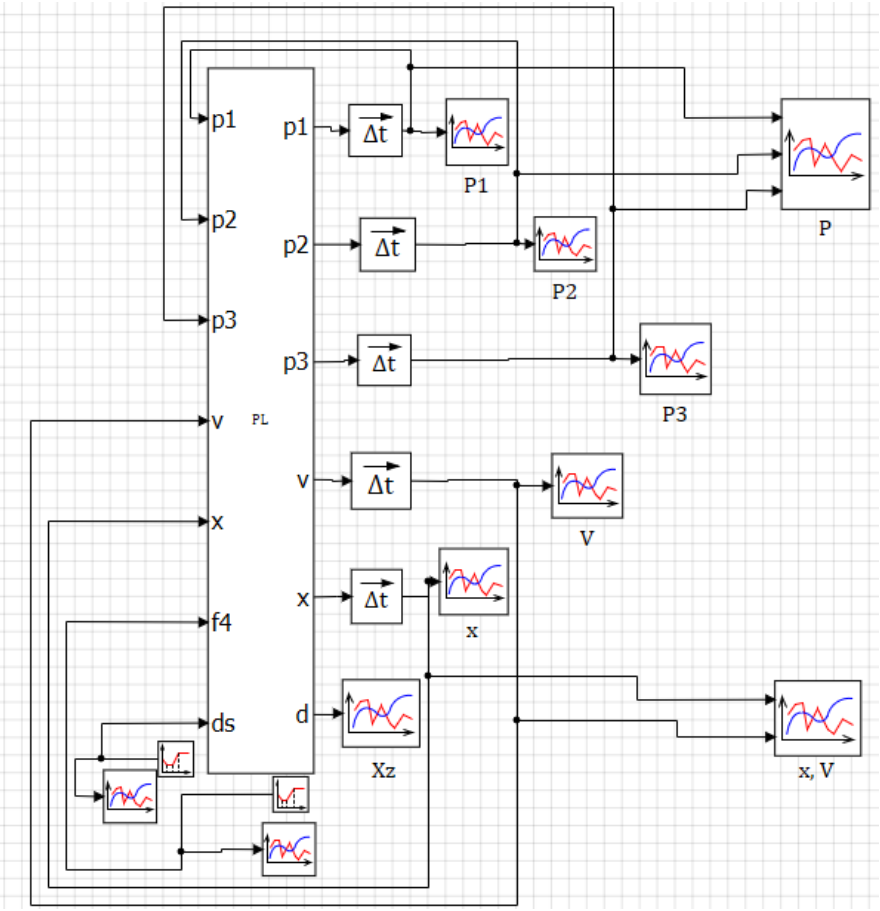

Figure 3. Block diagram of the mathematical model

```
input p1, p2, p3, V, x,f4,ds;
output p1, p2, p3, V, x, d;
init p1=100000,p2=100000, p3=100000, V=0, x=0;
xk=0.31  //The target coordinate
R=287;   //Universal gas constant
Tm=290;   //Ambient temperature
ks1=65;   //Drag coefficient
ks2=100;  //Drag coefficient
ks3=70;   //Drag coefficient
ks4=70;    //Drag coefficient
d3=0.001;   //Diameter of the passage section
d5=0.006;      //Diameter of the passage section
pm=6*10^5;          //Compressor pressure
pa=1.01325*10^5;        //The pressure of the atmosphere
k=1.4;             //The ratio of specific heats
x01=0.008;        //The given coordinate
x02=0.008;        //The given coordinate
m=6;          //Weight of moving parts of the pneumatic drive
Fvn=20;     //The force of external resistance
dtr1=0.005;   //Pipeline diameter
dtr2=0.005;    //Pipeline diameter
D=0.04;       //Cylinder piston diameter
Dt=0.04;      //Brake piston diameter
kvt=320;  //Diameter of the brake device piston
```

```
L=0.4;                  //Cylinder stroke
S=(pi*D^2)/4;      //Area of the cylinder piston cavity
St=(pi*Dt^2)/4;     //Area of the piston cavity of the brake device
kt=0.4              //Coefficient of friction
begin
if x<xk+0.0577 then
N=0
else
N=pm*St
end
Ft=kt*N; //Friction force
begin
if x<xk then
d2=0.008
else
d2=0.0004
end;
begin
if x<xk+0.0577 then
d=ds
else
d=d2=0
end;
```

Figure 4. Computer simulation of automatic positioning pneumatic actuator system (1)

```
begin
if x<xk then
f5=0
else
f5=(pi*d5^2)/4
end;
f1=(pi*d^2)/4;    //The area of the throttle
f2=(pi*d2^2)/4;   //The area of the throttle
f3=(pi*d3^2)/4;    //The area of the throttle
Ltr=0.01;          //Pipeline length
cpr=500000;        //The stiffness coefficient of the spring
W1=Ltr*((pi*dtr1^2)/4);    //The volume in the pipeline
W2=Ltr*((pi*dtr2^2)/4);     //The volume in the pipeline
begin
if L<x then Fy=(cpr*(x-L))
else
if (L>=x) or (x>=0) then Fy=0
else if x<0 then Fy=cpr*x
end
G11=(k*f1*sqrt(R*Tm)/(S*(x+x01)*sqrt(ks1)))*sqrt(abs(pm^2-p1^2));
G12=(k*f3*sqrt(R*Tm)/(S*(x+x01)*sqrt(ks2)))*(p3/p1)^((k-1)/(2*k))*
sqrt(abs(p1^2-p3^2));
G13=(k*p1/(x+x01))*V;
G21=(k*f2*sqrt(R*Tm)/(S*(L-x+x02)*sqrt(ks2)))*(p2/pa)^((k-1)/(2*k))*
sqrt(abs(p2^2-pa^2));
G22=(k*p2/(L-x+x02))*V;
G31=(k*f3*sqrt(R*Tm)/(W1*sqrt(ks3)))*sqrt(p1^2-p3^2);
G32=(k*f4*sqrt(R*Tm)/(W2*sqrt(ks4)))*((p3/pa)^((k-1)/(2*k)))*
sqrt(abs(p3^2-pa^2));
p1'=G11-G12-G13;
p2'=-G21+G22;
p3'=G31-G32;
x'=V;
V'=(S*(p1-p2)-Fvn*sign(V)-kvt*V-Fy-Ft*sign(V))/m;
```

Figure 5. Computer simulation of automatic positioning pneumatic actuator system (2)

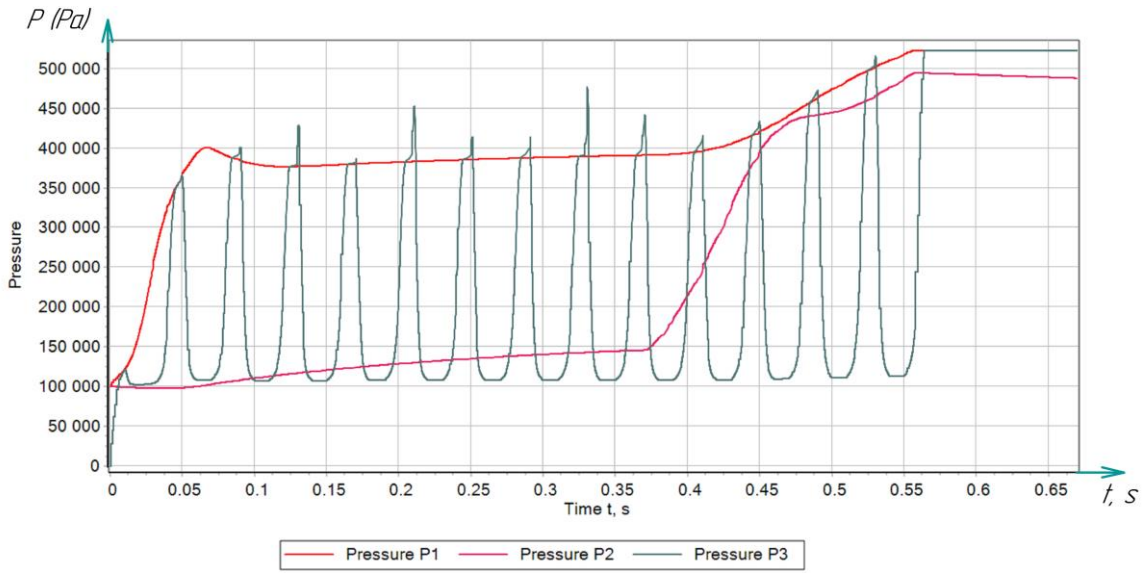

Figure 6. The resulting graph of pressure changes

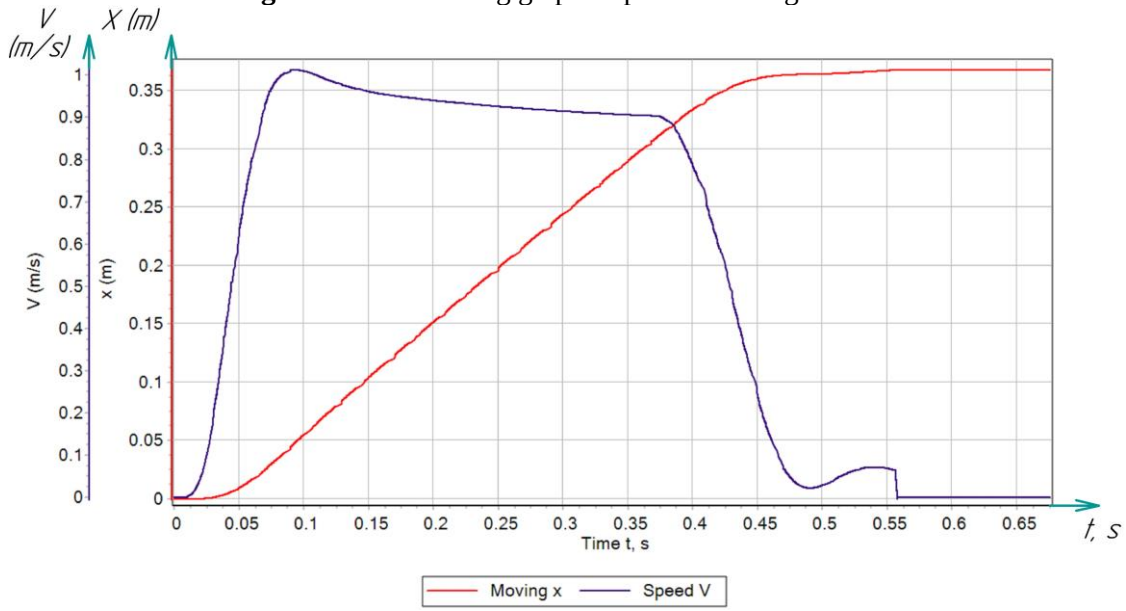

Figure 7. The resulting graph of displacement and speed

The results obtained confirm the functionality of the proposed drive and make it possible to evaluate the processes occurring in it during the positioning of the pneumatic cylinder piston. This drive model makes it possible to carry out a computational experiment for various positional cycles. The operator in the program sets positioning coordinates. The computer model can be modernized and corrected in order to introduce other control actions in other parameters after the experiment.

6. Discussion

The generalized mathematical model made it possible to analyze the functionality and characteristics of the developed positional actuator, to highlight and determine the assumptions necessary for further design. The developed computer model made it possible to evaluate the transient processes occurring in the drive. As a result of the computational experiment, the efficiency of the proposed technical solution was confirmed and the functionality of the positional pneumatic drive was determined.

Oscillographic analysis of the positioning process has established that the dynamic and control characteristics of the proposed drive are significantly improved when using a pneumatic brake. The drive run-out is significantly reduced, while providing a reliable fixation of the mechanism, which maintains accuracy under subsequent external influences [14-15].The speed of movement of the pneumatic cylinder has a decisive influence on the processes of deceleration, stopping and positioning of the control object [16-17]. So for a better stop, a deceleration was added at the penultimate coordinate.

References

[1] Sidorenko V.S., Grishchenko V.I., Rakulenko S.V., Poleshkin M.S., Dymochkin D.D. Study on oil pilot circuit of adaptive hydraulic drive of tool advance in mobile drilling machine. Vestnik of Don State Technical University. 2019;19(1):13-23. https://doi.org/10.23947/1992-5980-2019-19-1-13-23

[2] Sidorenko V.S., Grishchenko V.I., Rakulenko S.V., Poleshkin M.S. Adaptive hydraulic drive with delivery tool-feed control of production machine. Vestnik of Don State Technical University. 2017;17(2):88-98. (In Russ.) https://doi.org/10.23947/1992-5980-2017-17-2-88-98.

[3] Sirotenko A.N., Partko S.A., Saed B.A. Dependence of energy-speed characteristics of pneumatic drive on initial parameters of additional volume under counterpressure braking. Vestnik of Don State Technical University. 2017;17(4):69-76. (In Russian) https://doi.org/10.23947/1992-5980-2017-17-4-69-76

[4] Dao The An. Modeling of positioning processes of a high-speed pneumatic robot drive / Dao The An, V. S. Sidorenko, D. D. Dymochkin // Fundamental research. - 2015. -. Issue # 7. (part 2). pp. 285-292. https://fundamental-research.ru/ru/article/view?id=38687

[5] Obukhova E. N., Grishchenko V. I. Modeling of the dynamics of the positioning process of a two-way pneumatic actuator // Intelligent systems, control and mechatronics-2018 Proceedings of the all-Russian scientific and technical conference. 2018. Pp. 165-168.

[6] Dao The An. Research of positioning accuracy of an automated pneumatic drive with an external brake device / Dao The An, V. S. Sidorenko, D. D. Dymochkin // Bulletin of DSTU. - 2015. -. Issue No. 4(83). Pp. 46-53. https://www.vestnik-donstu.ru/jour/article/view/41

[7] Ozersky A.I. Modelirovanie dinamicheskih rezhimov raboty gidroprivodnyh sistem s teplovymi i elektricheskimi istochnikami `energii [Modelling of dynamic operating modes hydrodriven systems with thermal and electric energy sources]. Izvestiya vuzov.Severo-Kavkazskij region. Tehnicheskie nauki, 2013, no. 5, pp. 37 - 43.

[8] Gorin, A. & Tokmakov, N. & Kyznetsov, I.. (2020). Substantiation of Parameters of Machine with Volumetric Hydraulic Drive for Formation of Wells in Ground. 10.1007/978-3-030-22063-1_139.

[9] Sirotenko A.N., Partko S.A., Voinash S.A., Research of pneumodrive with energy recovery into additional volume. Lecture notes in mechanical engineering. 2020;9(1): 1325-1333. https://link.springer.com/chapter/10.1007%2F978-3-030-22063-1_140

[10] Tamarkin M.A., Tishchenko E.E., Gordiyenko A.V., Grebenkin R.V. Reliability control of final vibration strengthening of part processing in steel balls medium. Vestnik of Don State Technical University. 2017;17(3):38-45. (In Russ.) https://doi.org/10.23947/1992-5980-2017-17-3-38-45.

[11] Rybak A.T., Tsybriy I.K., Nosachev S.V., Zenin A.R. Theoretical background of hydraulic drive control system analysis for testing piston hydraulic cylinders. Vestnik of Don State Technical University. 2019;19(3):242-249. https://doi.org/10.23947/1992-5980-2019-19-3-242-249

[12] Sirotenko A.N., Partko S.A., Salloum W. Effect of recuperative volume parameters on dynamic characteristics of pneumatic drive underbraking. Vestnik of Don State Technical University. 2018;18(4):379-384. https://doi.org/10.23947/1992-5980-2018-18-4-379-384

[13] Dao The An. Multiparametric pneumomechanical sensor for positional pneumatic actuators / ao The An, V. S. Sidorenko, D. D. Dymochkin // Engineering Bulletin-Don. - 2015. -. Issue. № 2. Access mode: http://ivdon.ru/ru/magazine/archive/n2p2y2015/3055.

[14] Nekrashevich, K.Ya. Matematicheskaya model' gidrosistemy, realizovannoy s primeneniem kombinirovannogo printsipa adaptatsii k nagruzke. [Mathematical model of hydraulic system designed with using of combined principle of adaptation to load.] Mechanics of Machines, Mechanisms and Materials, 2014, no. 1 (26), pp. 21– 31 (in Russian).
[15] Vardhan, Alok & Dasgupta, Kaustubh & Mishra, Santosh. (2018). Dynamic analysis of a closed-circuit hydraulic drive system used in the rotary head of blasthole drilling machine using MATLAB–Simulink environment. Proceedings of the Institution of Mechanical Engineers, Part I: Journal of Systems and Control Engineering. 233. 095965181880887. 10.1177/0959651818808870.
[16] Mikhail Lemeshko, Mikhail Molev, and Igor Golovin Hydraulic technological machines with adaptive drive structure/ (ICMTMTE 2018) Sevastopol, Russia, September 10-14, 2018 MATEC Web of Conferences, Volume 224, 02087 (2018) DOI: https://doi.org/10.1051/matecconf/2018224020875.
[17] Pershin V.A., Khinikadze T.A. Technique of functional unification of adaptive hydraulic drive module capable of load stabilization on the working body of mobile machines. Vestnik of Don State Technical University. 2018;18(3):318-325. https://doi.org/10.23947/1992-5980-2018-18-3-318-325

Combined pneumatic drive of the rotary-dividing mechanism of the revolver head

G A Dolgov, V S Sidorenko, V I Grishenko and A N Kharchenko

Don state technical university, Rostov-on-Don, Russia

Abstract. Currently, the use of a positional combined drive in metal-cutting equipment must have a high-precision ability to process new materials, the design of workpieces and parts; ensure the technical and environmental safety of personnel, etc. All these requirements must be met by CNC machines to produce competitive products in the market criteria. Metal cutting equipment due to its high cost has led to the need to use a single power source for multiple work movements. To increase the productivity of the machine, it is necessary to use a combined two-motor positional pneumatic drive. This increases the total production time. reduce the main time (by automating two movements: rapid supply of the workpiece to the processing center, and reduce the auxiliary time (automating the installation of the workpiece and removing the part, reducing the path of movement of the tool), reduce the time for equipment changeover (using digital display and software control). The section "research results" presents the results of mathematical modeling based on a computer model implemented in the SimInTech software package. The graphs of pressure dependences in the piston and rod cavities of the pneumatic cylinder, speed and displacement of the pneumatic cylinder are obtained.

1. Introduction

The relevance of research

Multi-tool turrets are mainly equipped with an electric drive for performing pivoting and pivoting movements. But there are ways where it is not only possible to use, but also a pneumatic drive. For this, the actuator uses the principle of double positioning: pre-positioning, second precision positioning;

The novelty is as follows:

1. Variable drive structure during movement. (modular principle of variation of submodels in one working cycle, algorithms of block diagrams of the research model)

2. The complex dynamics of the entire pneumo-mechanical system, because mutual influence of drives: pneumatic cylinders PC1, PC2 and pneumatic accumulator PA [1-5].

3. Double positioning

I pre-positioning $\Delta\varphi \le \left[8-12^{I} \right]$;

II precision positioning $\Delta\varphi \le \left[5-8^{I} \right]$

$\Delta\varphi_I \downarrow$ due to double-sided stop;

$\Delta\varphi_I \to \Delta\varphi_{II}$

Reaching the goal: $T_c \to \min$

$$T_c = T_{rel} + T_r + T_{clam} + T_{clam} \quad (1)$$

T_c - Full cycle time of the drive, s;

T_{rel} - The time of the release actuator; s;

T_r - The time of rotation of the drive, s;

T_{clam} - Drive clamping time, s;

T_{loc} - Drive locking time, s;

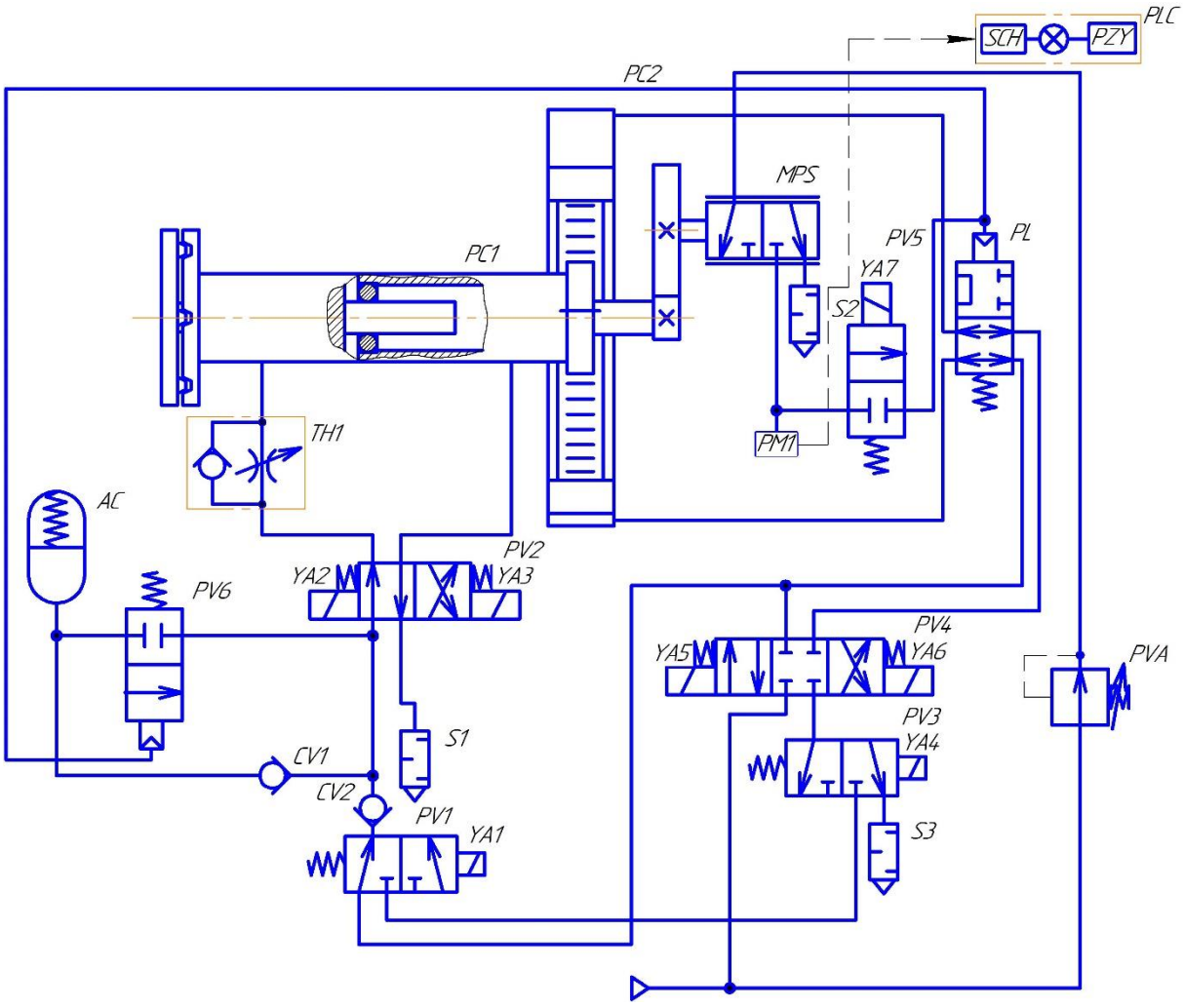

Figure 1. Pneumatic kinematic diagram of a combined positional pneumatic actuator
PL – pneumatic lock, PV1-PV6 – pneumatic valve, TH1 – throttle, PVA – pressure valve,
AC – accumulator, PC1 – PC2 – Pneumatic cylinder, PLC – programmable logic controller,
MPS – Mechanopneumatic sensor, YA1 – YA7 - Electromagnet. PM1 – Pressure meter, S – silencer,
CV1 – CV2 – Check Valve;

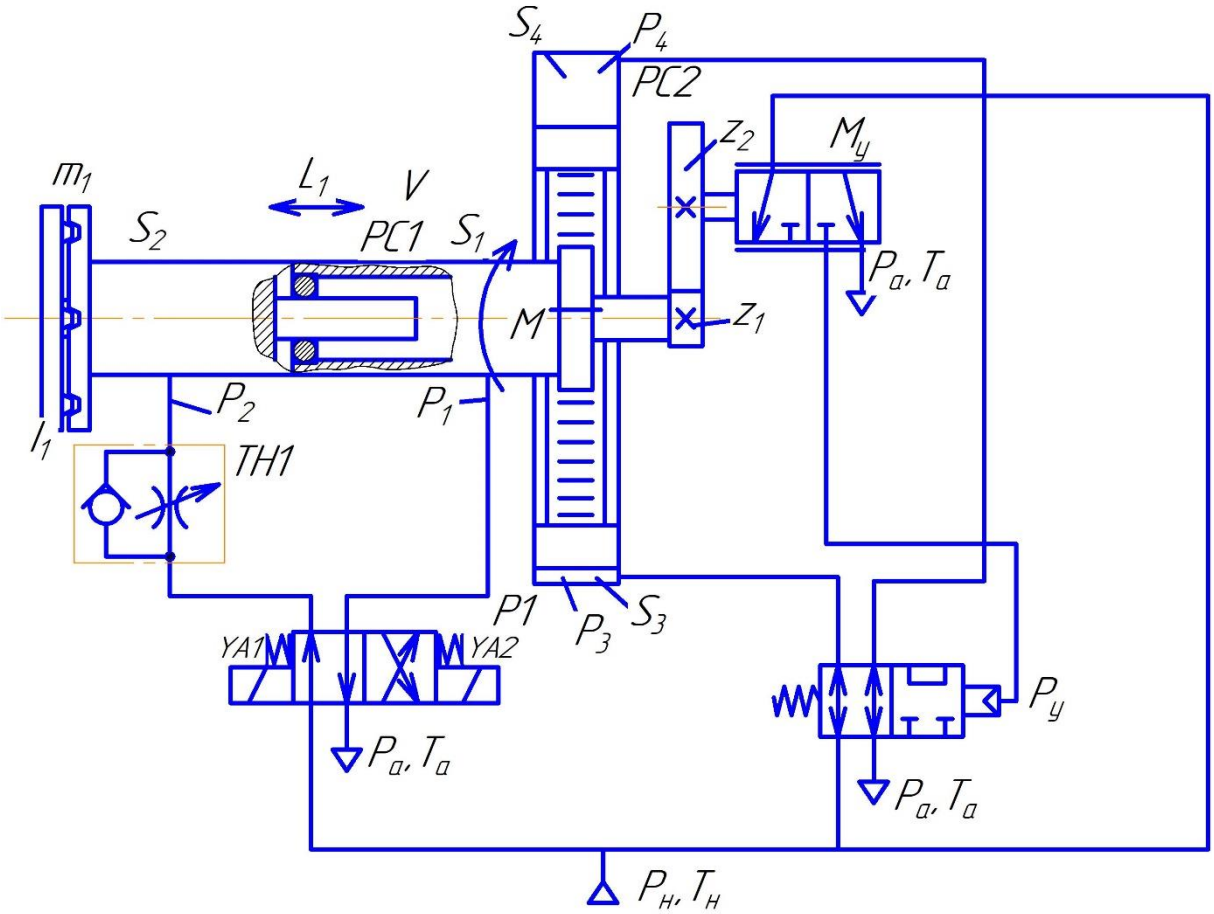

Figure 2. Design diagram of a positional pneumatic actuator

Mechanical subsystem:
Equation of motion of a linear motion positional pneumatic actuator

$$m_{pr} \cdot \frac{d^2 L}{dt^2} = (P_1 \cdot S_1 - P_2 \cdot S_2) - F_{v.f} - F_{d,f} \cdot sign(\frac{dl}{dt}) - \alpha \cdot F_{l.f}; \quad (2)$$

$$I_{pc1} \cdot \frac{d^2 \varphi}{dt^2} = S_3 \cdot (P_3 - P_4) - M_{f.d} - M_y + \alpha \cdot M_f; \quad (3)$$

m_{pr} - moving weight of the piston, kg;

S_1, S_2 - effective area of the discharge and exhaust cavities, m^2;

P_1, P_2 - air pressure, respectively, in the discharge and exhaust cavities of the cylinder PC 1, Pa;

S_3 - effective area of the rotary pneumatic cylinder m^2;

P_3, P_4 - air pressure, respectively, in the discharge and exhaust cavities of the cylinder PC 2, Pa;

$$m_{pr} = m_{pc1} + m_v + m_{pis}; \quad (4)$$

m_v - rotating mass, kg;

m_{pis} -the mass of the piston, kg;

m_{pc1} – workpiece weight, kg;

L - stroke of the PC1 piston (mechanical closure coupling), m;

$$F_c = F_{v.f} + F_{d.f} \tag{5}$$

$F_{v.f}$ -viscous friction force, N;

$F_{d,f}$ - dry friction force, N;

$F_{l.f}$ -Locking force, N;

$$F_{l.f} = P_2 \bullet S_2; \text{N}; \tag{6}$$

$\alpha = 0$ by $L \le L_{tz}$ and $\alpha = 1$ $L \ge L_{tz}$;

L - moving the power pneumatic cylinder rod, m;

L_{tz} - the target coordinate of the stop, m;

$$F_{v.f} = k_{v.f} \bullet V; \tag{7}$$

$k_{v.f}$ - coefficient of viscous friction, $N \bullet \frac{s}{m}$;

V - the speed of movement of the stock, m/s;

$$I_{rd} = I_{pc1} + I_{pc2} + I_c; \tag{8}$$

I_c - moment of inertia of the control device, $kg \bullet m^2$;

I_{rd} - Reduced moment of inertia, $kg \bullet m^2$;

α - a Boolean parameter

I_{pc1} - moment of inertia of the pneumatic cylinder 1, $kg \bullet m^2$;

I_{pc2} - moment of inertia of the pneumatic cylinder 2, $kg \bullet m^2$;

φ - angular displacement, rad/s;

R - Radius, m;

$$I_c = I_{\Delta T} \bullet i^2 \tag{9}$$

$i = 1/3$;

i - the ratio of gear set;

M_y - moment on the stop, N•m;

$M_{f.d}$ - moment of force of dry friction, N•m;

M_f - locking torque;

$$M_{f.d} = k_{v.f} \bullet \frac{d\varphi}{dt}; \tag{10}$$

$$M_f = F_0 \bullet R; \tag{11}$$

$$F_0 = F_f \bullet tg\alpha; \tag{12}$$

F_0 - drive stop power;

The kinematic equation of balance of mass flows on the pressure line of a pneumatic actuator

$$G_1 = G_{PC1} + G_{pis} + G_{1comp} + G_{PMS}; \quad (13)$$

$$G_1 = \mu_1 \cdot f_{d1} \cdot p_P \cdot \sqrt{\frac{2 \cdot k}{R \cdot T_p \cdot (k-1)}} \cdot \varphi(\sigma_1); \quad (14)$$

$$G_{1PC} = \frac{W_1 \cdot dp_1}{k \cdot R \cdot T_н}; \quad (15)$$

$$G_{pis1} = k_n \cdot (p_1 - p_2) \cdot sign(p_1 - p_2); \quad (16)$$

$$G_{1comp} = \frac{W_P}{E} \cdot \frac{p_1 \cdot dW_P}{R \cdot T_P}; \quad (17)$$

$$G_{PMS} = P_M \cdot \frac{\pi \cdot d^2}{4}; \quad (18)$$

G_1- flow through the pressure line distributor, $kg \cdot s^{-1}$;
G_{PC1} - flow rate in the Rodless cavity of the power pneumatic cylinder, $kg \cdot s^{-1}$;
G_{pis}- consumption caused by leaks in the piston, $kg \cdot s^{-1}$;
G_{1comp}- the cost of compressibility in the pressure line, $kg \cdot s^{-1}$;
k_n- the ratio of partecke;
G_{PMS}- flow rate flowing through the pneumatic-mechanical sensor, $kg \cdot s^{-1}$;
R– universal gas constant;
K - ratio of specific heats (for air k =1,4);
E - air volume elasticity modulus, Pa;
W1 - current volume of the piston cavity of the power pneumatic cylinder, m^3;
W_P- current volume in the pressure line of the pneumatic actuator, m^3;
T_P- air temperature in the discharge line, K;
pH, p1, p2 - supply pressure, in the piston cavity of the power pneumatic cylinder, in the rod cavity of the power pneumatic cylinder, PA.
After converting the formulas, the equation will take the following form:

$$\frac{dP_1}{dt} = \frac{k \cdot \mu_1 \cdot f_{d2} \cdot K \cdot p_p \cdot \sqrt{R \cdot T_p} \cdot \varphi(\sigma_1)}{S_1 \cdot (L_{11} + L)} - \frac{k \cdot p_1}{E \cdot (L_{11} + L)} \cdot \frac{dL}{dt} - \frac{k \cdot R \cdot T_p}{S_1 \cdot (L_{11} + L)} k_n \cdot (p_1 - p_2) \cdot sign(p_1 - p_2) - P_y \cdot \frac{\pi \cdot d^2}{4}; \quad (19)$$

Where L_{11} is the ratio of the initial ("passive") volumes Wn of the pneumatic actuator to the useful area of the pneumatic cylinder piston, respectively, m.

The current volume of air in the pressure line of the pneumatic actuator is determined by:

$$W_p = S \cdot L; \quad (20)$$

Where L is the length of the pressure pipeline, m; S is the cross-section area of the pipeline, m2;

Equation of mass flow balance of the pneumatic drive drain line

$$G_2 = -G_{pc2} + G_y + G_{2comp} + \beta \cdot G_p + G_{tr}; \quad (21)$$

$$G_2 = \mu_2 \cdot f_{d2} \cdot p_2 \cdot \sqrt{\frac{2 \cdot k}{R \cdot T_2 \cdot (k-1)}} \cdot \varphi(\frac{\sigma_a}{\sigma_2}); \quad (22)$$

$$G_{2pc} = \frac{W_2 \cdot dp_2}{k \cdot R \cdot T_2}; \quad (23)$$

$$G_y = k_y \cdot p_2; \quad (24)$$

$$G_{2comp} = \frac{W_{dr}}{E} \cdot \frac{p_2 \cdot dW_{dr}}{R \cdot T_2}; \quad (25)$$

$$G_{p1} = \mu_{p1} \cdot f_{p1} \cdot p_2 \cdot \sqrt{\frac{2 \cdot k}{R \cdot T_2 \cdot (k-1)}} \cdot \varphi(\sigma_a); \quad (26)$$

$$G_{tr2} = \mu_{tr2} \cdot f_{tr2} \cdot p_2 \cdot \sqrt{\frac{2 \cdot k}{R \cdot T_2 \cdot (k-1)}} \cdot \varphi(\sigma_a); \quad (27)$$

Where G_2 - drain line flow rate kg$\cdot s^{-1}$; G_{2pc} - flow rate in the rod cavity of the pneumatic cylinder kg$\cdot s^{-1}$; G_y - flow rate of working air leakage into the atmosphere kg$\cdot s^{-1}$; G_{2comp}- compressibility flow rate in the drain line kg$\cdot s^{-1}$; G_{p1} - flow through the pneumatic distributor P1; G_{2pc}- flow rate via

pneumatic throttle, kg; ; $\mu_2, \mu_{p1}, \mu_{tr2}$ - flow coefficients for the rod cavity of the power pneumatic cylinder, pneumatic distributor P1, and pneumatic throttle DDR2, respectively; $\beta -$ the Boolean parameter; (with β=1 when the distributor P1 is open during rapid feed, β=0 when the distributor P1 is closed during positioning);

$$\frac{dP_2}{dt} = \frac{k \cdot f_{d2} \cdot \mu_2 \cdot K \cdot p_2^{\frac{3k-1}{2k}} \cdot \sqrt{R \cdot T_a}}{S_2 \cdot (s + L_{12} - L) \cdot p_a^{\frac{k-1}{2k}}} \cdot \varphi\left(\frac{\sigma_a}{\sigma_2}\right) + \frac{k \cdot p_2}{E \cdot (s + L_{12} - L)} \cdot \frac{dL}{dt} + \beta \cdot \frac{\mu_{d1} \cdot f_{d1} \cdot p_2 \cdot \sqrt{R \cdot \left(\frac{p_a}{p_2}\right)^{\frac{k-1}{k}}}}{S_2 \cdot (s + L_{12} - L)} \varphi(\sigma_1) +$$

$$+ \frac{\mu_{tr2} \cdot f_{tr2} \cdot \sqrt{R \cdot \left(\frac{p_a}{p_2}\right)^{\frac{k-1}{k}} \cdot T_2 \cdot K}}{S_2 \cdot (s + L_{12} - L)}; \quad (28)$$

Where s is the stroke of the pneumatic cylinder; L_{12} is the ratio of the initial ("passive") volume W_{dr} of the pneumatic drive to the useful area of the piston and rod cavities of the pneumatic cylinder, respectively, m.

Control algorithm

Entry conditions

$t = 0;\ P_1 = P_2 = 0;\ P_2 = P_n;\ P_2 = P_\infty \downarrow = 0;$

1) t> 0; $P_2 \downarrow = 0;\ (P_{\phi} = P_{n0} \downarrow = 0);\ P_1 = P_3 = P_n;$

$V \uparrow\ (L = V \bullet t);\ w = V_{n4} \bullet \frac{d_k}{2};$

2) On diskret z=1 $\rightarrow PLC \rightarrow x_y$ to the Distributor . P_2 Drain $PC2 \rightarrow P_4 \rightarrow$ pressure PC1 consistent sequential, $\vec{V}\ w \downarrow$ deceleration is opened Distributor P3 P_y

3) In diskret z, when combining slots in the PMD of pneumatic locks. The second positioning is mechanical closure.

2. Discussion

Simulation program for transient processes of positional pneumatic mechanical drive in the simintech computer simulation system

When creating pneumatic actuators with positional control, it is required to ensure that the pneumatic actuator stops at any point along the stroke length. To ensure braking and stopping in these cases, a special pneumatic brake is used.

The mathematical model of a pneumatic drive demonstrates a system of differential equations describing the movement of the working body and the change in pressure in the cavities of the actuator. Thus, the mathematical model of the pneumatic drive includes the following equations.

1. Equation of motion of the actuator of the pneumatic cylinder.
2. Equations of pressure change in the discharge cavity.
3. Equations of pressure change in the exhaust cavity [6-11].

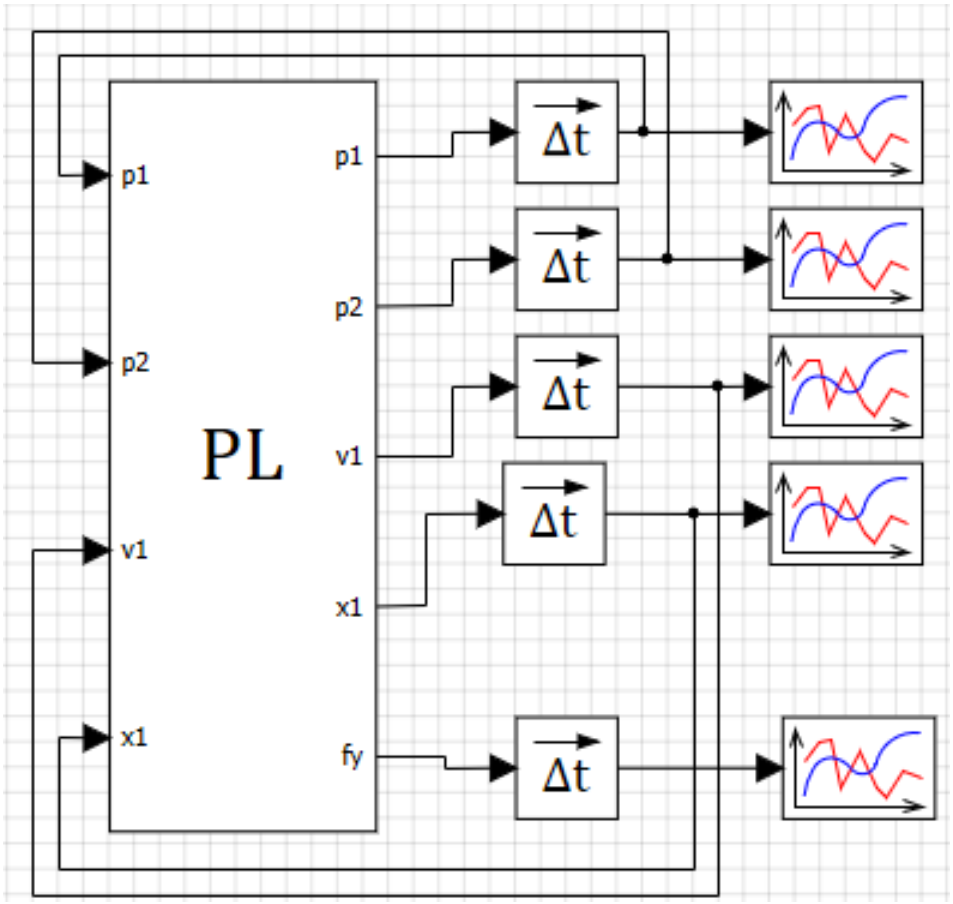

Figure 3. Computer model of a pneumatic cylinder created in the Simintech program

When designing, one of the main conditions is to confirm the functionality of the developed drive, as well as to analyze the processes occurring in it when positioning the pneumatic cylinder. The positioning process of a dynamic system, including mechanical and pneumatic subsystems, must be simulated, because the process is complicated by the non-stationarity of the compressed gas flow, the instability of the real effects on the pneumatic subsystem. Therefore, when forming the mathematical model of the drive (the design diagram is shown in Figure 2), the following assumptions were made: the pressure of the compressed air source is constant over time; the thermodynamic process of gas behavior in the pneumatic system is assumed to be adiabatic; in the description of pneumatic devices, the ideal gas model is used, since the pressure in the pneumatic system is below 10 bar; leaks are not counted; the force of viscous friction is proportional to the speed; the cost coefficients are taken as averaged; the mass of the moved parts is assumed constant; force Fc at the output link of the pneumatic drive is constant; relay control of pneumatic valves; the time of formation of the control signal from the displacement sensor is not taken into account [12-16].

```
input p1,p2,v1,x1;
output p1,p2,v1,x1,Fy;
init p1=600000,p2=100000,v1=0,x1=0;
//starting conditions
k=1.4; // the ratio of specific heats for air//
p11=600000;  // the inlet pressure into the cylinder, Pa//
pa=100000; // atmospheric pressure, Pa //
R=287; // gas constant //
dtr=0.008; // pipeline diameter, m //
f1=3.14*(dtr^2)/4; // cross-section area of the supply line //
f2=3.14*(dtr^2)/4; //cross-section area of the diverting line //
z1=65; // resistance coefficient of the supply line //
z2=100; // the resistance ratio of the exhaust line //
Tm=293; // gas temperature in the pipeline, K //
L=0.8; //cylinder stroke, m //
Ltr=0.1; // pipeline length, m //
W=L*((3.14*(dtr^2))/4); // the volume of the pipeline //
D=0.06; // air cylinder piston diameter //
Dst=0.04; // diameter of the pneumatic cylinder rod //
Mpr=5; // weight of moving parts of the pneumatic cylinder //
cpr=50000; // spring constant //
S1=((3.14*(D^2))/4); // air cylinder piston area //
S2=3.14*((D^2)-(Dst^2))/4; // air cylinder rod area //
x01=0.08; //the given coordinate //
x02=0.08; //the given coordinate //
Fvn=1200; // the force of external resistance //
kv=300; // coefficient of viscous friction of the piston //
begin
  if L<x1 then Fy=(cpr*(x1-L))
  else
  if (L>=x1) or (x1>=0) then Fy=0
  else if x1<0 then Fy=cpr*x1
end
p1'=k*f1*sqrt(R*Tm)/(S1*(x1+x01)*sqrt(z1))*sqrt(abs(p11^2-p1^2))-(k*p1*v1)/(x1+x01);
p2'=-k*f2*sqrt(R*Tm)/(S2*(L-x1+x02)*sqrt(z2))*sqrt(abs(p2^2-pa^2))*((p2/pa)^((k-1)/(2*k)))+((k*p2*v1)/(L-x1+x02));
v1'=((S1*p1)-(S2*p2)-Fvn*sign(x1')-kv*x1'-Fy)/Mpr;
x1'=v1;
```

Figure 4. Program for implementing mathematical modeling

The results of computer simulation

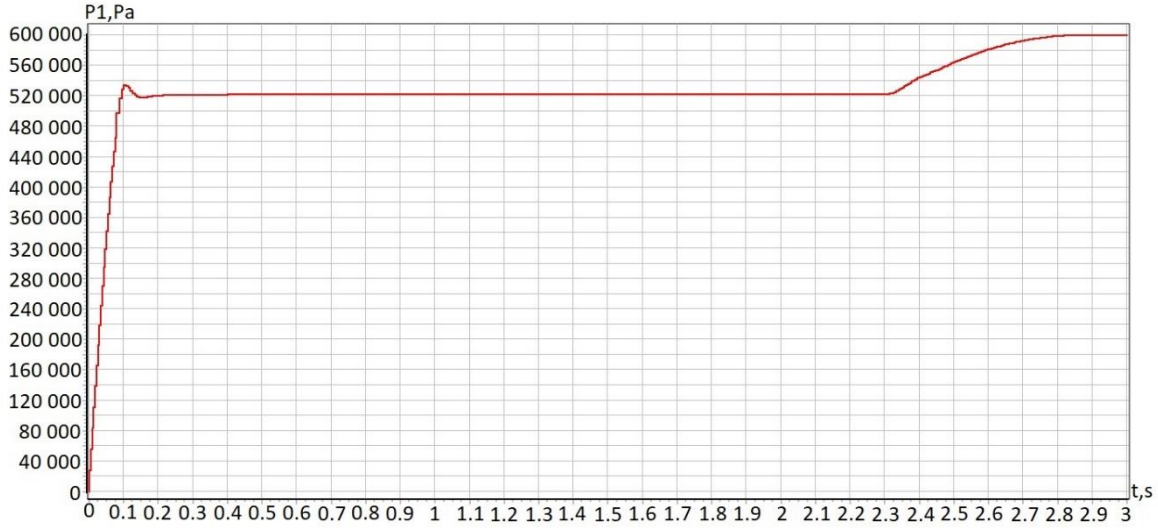

Figure 5. Graph of pressure changes in the pressure cavity of the PC

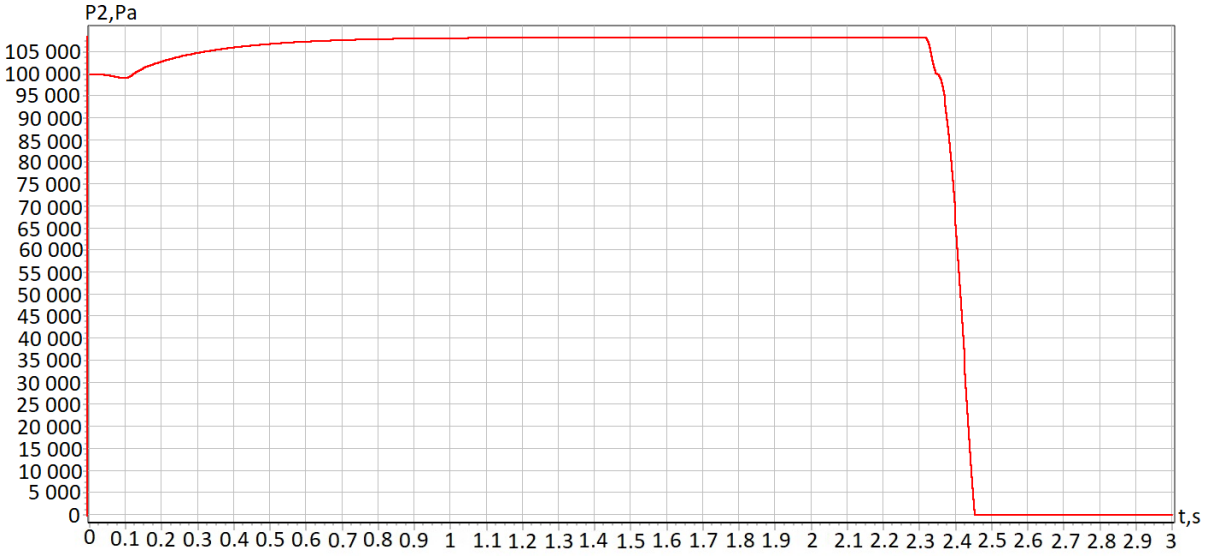

Figure 6. Graph of pressure changes in the exhaust cavity of the PC

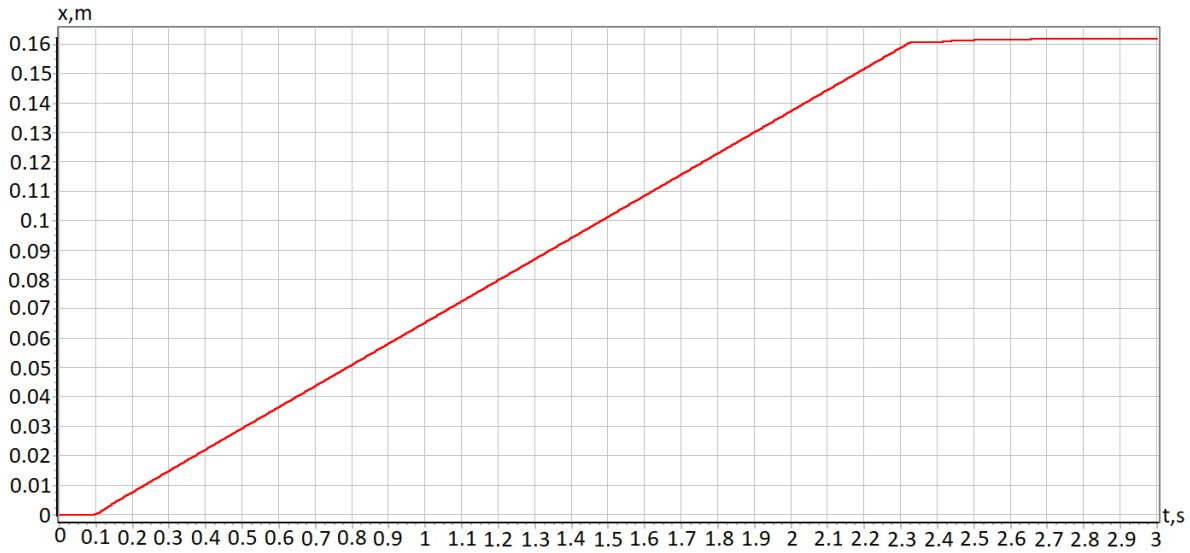

Figure 7. Graph of changes in movement from time to time

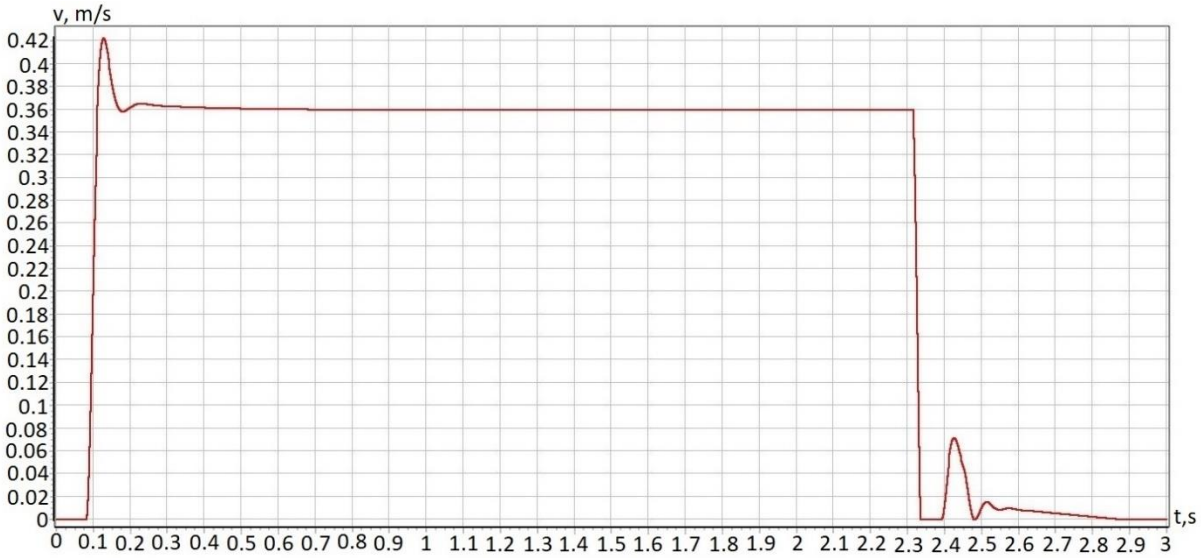

Figure 8. Graph of speed changes from time

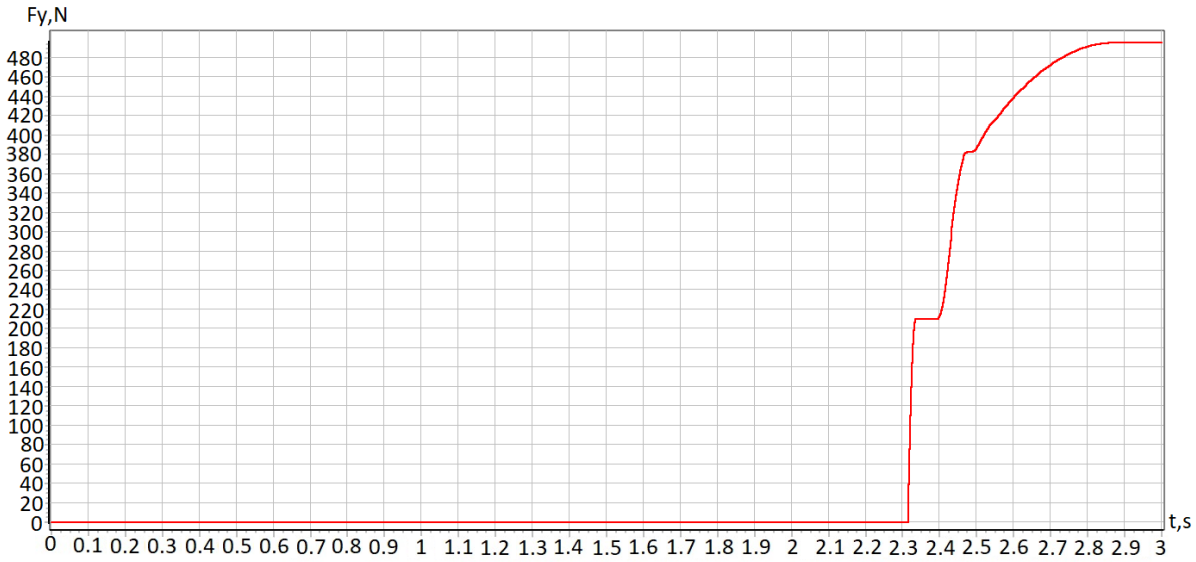

Figure 9. Graph of speed changes from time

Combining the obtained dependencies, we obtain a system of equations describing the process of positioning the output link of the pneumatic actuator. The system of differential equations can be solved by various numerical methods (Euler, Runge-Kutta, etc.) under given initial conditions, drive parameters, and control actions that functionally depend on the coordinate of the output link. The model was studied in the SimIntech program using numerical methods.

References

[1] Tamarkin M.A., Tishchenko E.E., Gordiyenko A.V., Grebenkin R.V. Reliability control of final vibration strengthening of part processing in steel balls medium. Vestnik of Don State Technical University. 2017;17(3):38-45. (In Russ.) https://doi.org/10.23947/1992-5980-2017-17-3-38-45.

[2] Pershin V.A., Khinikadze T.A. Technique of functional unification of adaptive hydraulic drive module capable of load stabilization on the working body of mobile machines. Vestnik of Don State Technical University. 2018;18(3):318-325. https://doi.org/10.23947/1992-5980-2018-18-3-318-325

[3] Sirotenko A.N., Partko S.A., Saed B.A. Dependence of energy-speed characteristics of pneumatic drive on initial parameters of additional volume under counterpressure braking. Vestnik of Don State Technical University. 2017;17(4):69-76. (In Russ.) https://doi.org/10.23947/1992-5980-2017-17-4-69-76

[4] Sirotenko A.N., Partko S.A., Salloum W. Effect of recuperative volume parameters on dynamic characteristics of pneumatic drive underbraking. Vestnik of Don State Technical University. 2018;18(4):379-384. https://doi.org/10.23947/1992-5980-2018-18-4-379-384

[5] Sidorenko V.S., Grishchenko V.I., Rakulenko S.V., Poleshkin M.S., Dymochkin D.D. Study on oil pilot circuit of adaptive hydraulic drive of tool advance in mobile drilling machine. Vestnik of Don State Technical University. 2019;19(1):13-23. https://doi.org/10.23947/1992-5980-2019-19-1-13-23

[6] Rybak A.T., Tsybriy I.K., Nosachev S.V., Zenin A.R. Theoretical background of hydraulic drive control system analysis for testing piston hydraulic cylinders. Vestnik of Don State Technical University. 2019;19(3):242-249. https://doi.org/10.23947/1992-5980-2019-19-3-242-249

[7] Dao The An. Modeling of positioning processes of a high-speed pneumatic robot drive / Dao The An, V. S. Sidorenko, D. D. Dymochkin // Fundamental research. - 2015. -. Issue # 7. (part 2). pp. 285-292. https://fundamental-research.ru/ru/article/view?id=38687

[8] Dao The An. Research of positioning accuracy of an automated pneumatic drive with an external brake device / Dao The An, V. S. Sidorenko, D. D. Dymochkin // Bulletin of DSTU. - 2015. -. Issue No. 4(83). Pp. 46-53. https://www.vestnik-donstu.ru/jour/article/view/41

[9] Obukhova E. N., Grishchenko V. I., Dolgov G. A. Formalization of a dynamic model of a pneumatic actuator with a variable structure. 14th international scientific-technical conference "dynamic of technical systems", DTS. 2018;226(51): 02022. https://elibrary.ru/item.asp?id=38626650

[10] Sirotenko A.N., Partko S.A., Voinash S.A., Research of pneumodrive with energy recovery into additional volume. Lecture notes in mechanical engineering. 2020;9(1): 1325-1333. https://link.springer.com/chapter/10.1007%2F978-3-030-22063-1_140

[11] Grishchenko V.I., Tumakov A.A., Poleshkin M.S., Kilina M.S., Dymochkin D.D. (2019) Modeling of automatic leveling system steep mobile machine with a hydraulic tilt sensor. Omsk Scientific Bulletin. - № 2 (164). P. 11-17..

[12] Vardhan, Alok & Dasgupta, Kaustubh & Mishra, Santosh. (2018). Dynamic analysis of a closed-circuit hydraulic drive system used in the rotary head of blasthole drilling machine using MATLAB–Simulink environment. Proceedings of the Institution of Mechanical Engineers, Part I: Journal of Systems and Control Engineering. 233. 095965181880887. 10.1177/0959651818808870.

[13] Mikhail Lemeshko, Mikhail Molev, and Igor Golovin Hydraulic technological machines with adaptive drive structure/ (ICMTMTE 2018) Sevastopol, Russia, September 10-14, 2018 MATEC Web of Conferences, Volume 224, 02087 (2018) DOI: https://doi.org/10.1051/matecconf/2018224020875.

[14] Ozersky A.I. Modelirovanie dinamicheskih rezhimov raboty gidroprivodnyh sistem s teplovymi i elektricheskimi istochnikami `energii [Modelling of dynamic operating modes hydrodriven systems with thermal and electric energy sources]. Izvestiya vuzov.Severo-Kavkazskij region. Tehnicheskie nauki, 2013, no. 5, pp. 37 - 43.

[15] Nekrashevich, K.Ya. Matematicheskaya model' gidrosistemy, realizovannoy s primeneniem kombinirovannogo printsipa adaptatsii k nagruzke. [Mathematical model of hydraulic system designed with using of combined principle of adaptation to load.] Mechanics of Machines, Mechanisms and Materials, 2014, no. 1 (26), pp. 21– 31.

[16] Gorin, A. & Tokmakov, N. & Kyznetsov, I.. (2020). Substantiation of Parameters of Machine with Volumetric Hydraulic Drive for Formation of Wells in Ground. 10.1007/978-3-030-22063-1_139.

Kids security on social networks by face blur technique

V Mladenovic[1], S Djukanovic[1], N Stefanovic[1], A Kar[2], M Jovanovic[3], S Makov[4]

[1]Faculty of Technical Sciences in Cacak,University of Kragujevac , Serbia
[2]Indian Institute of Information Technology, Design and Manufacturing, Kancheepuram, Chennai, India,
[3]Faculty of Electrical Engineering, University of Nis, Serbia
[4]Don State Technical University, Shakhty, Rostov region, Russia

Abstract. This article deals with increasing security and children protection under the age of 16 (underage) on social networks with photo content such as Facebook, Instagram, Twitter, and similar. Particularly, the emphasis is placed on the official sites of public institutions on Facebook, such as kindergartens, primary and secondary schools, and all institutions dealing with children. One of the source key issues is the ability to track these public pages by malicious visitors. The main point is the developed algorithm that analyzes any photo, recognizes kid(s), and blurs it during the upload photo onto the page of the social network. The complete procedure for processing is shown and performed testing, verification, and validation.

1. Introduction

Today, a large number of social networks exist where users can leave their photos without paying attention to where those photos may end up. Special attention is not paid to who can use these photos, and we can freely say - to misuse them. Typical examples of such social networks are 23snaps [1], Facebook [2], Instagram [3], Flickr [4], Fyuse [5], Tagged [6], Vingle [7], Virb [8]. Nowadays, many parents are too busy with jobs, and their children are left to the technologies that are available. Children still cannot distinguish between good and bad things, between good and bad intentions. Simply put, children are exposed to all the challenges on the Internet. On the way, children become like "digital natives" and begin to use the Internet at an early age and access it from various devices (computers, tablets, mobile phones). Usually, younger children use the Internet for entertainment (playing games, listening to music, watching videos, series, movies), while older children mostly use social networks [9]. Social networks have millions of users the number is increasing daily [10, 11]. Precise statistics on the number of children on the Internet have not yet been given precisely, but even that number is not negligible.

In the forest of social network users, one of the main dangers for children lurks from sexual predators. Their intentions are always with bad consequences for the children, and they use the methods that are various to get in touch with the child and turn him into a victim. For all activities that children perform on the Internet, such as surfing, chatting, using social networks, online games, child protection implies physical, mental, and moral safety of minors. This becomes one of the potential major threats to the child's identity, and perhaps to his life. In particular, this becomes more pronounced in a time of pandemic because few people pay attention to the activities of children who now spend much of their time in a closed environment. Despite ongoing commitments, it is easy to conclude that most of the time children spend in front of the computer.

This paper deals with one of the methods that can prevent child abuse on the Internet. The method involves preventing the possibility of a potential predator following a child through a social network through children's photos on the child's pages.

This paper is organized as follow. In section 2 the motivation for this paper is described. Section 3 provides what is problem statement and state-of-art. Complete algorithm, testing and results are presented in section 4.

2. Motivation

As already mentioned, the main goal of this paper is to develop a system that will increase the security of kids on social networks. The greatest aspiration of children on social networks is to be as visible as possible to the outside world, to present and popularize. Children do this by posting photos, videos, liking various information, and similarly. Getting in touch with other people is the next step in using social networks. Social networks allow you to connect with other people so that the child can get in touch even with an unknown person. There is a possibility that a malicious person or an internet predator is hiding behind that unknown person, who may have the profile of another child. By coming into contact with such a person, the child is introduced into a conversation, and ignorance of behavioral control mechanisms [12] can lead to challenges that can be fatal. On the other hand, an unknown person can make contact with the child on his/her own by making the first contact by praising the photos previously posted by the child, which makes the communication scenario similar. In this sense, this paper presents a model and algorithm to perform prevention for posting photos on social networks by a child by blurring photos. Then an unknown person will be able to see the photos, but the faces of children under the age of 16 will automatically be hidden (blurred). In order to see the full format of the photo, the algorithm identifies the location from which the child's profiles are accessed and asks the visitor to reveal their identity.

3. Problem statement and related work

3.1. How internet predators work?

There is no one and unique single method in which online predators work. But there are several methods that can have been identified as how online predators locate their victims and get them to do what they want, whether it is meeting them in person or simply engaging in some kind of online/on the phone sexual activity [13]. These are some typical methods online predators use: *Find kids* through social networking, blogs, chat rooms (even monitored, kids chat rooms), instant messaging, e-mail, and other Web sites, often using information in their targets' personal profiles. *Seduce* their targets through attention, flattery, affection, kindness, and even gifts. These types of manipulation will cause kids to lose their sense of awareness, and help the predators to get from bad intentions to sexual exploitation (this is called "grooming", and may continue over extended time periods). *Are familiar* with the latest music, hobbies, fashion, etc. that are likely to interest kids. Look for children that are *emotionally vulnerable* due to problems at school or home. *Listen to and sympathize* with kids' problems, while building a pseudo friendship, taking the kids side vis-à-vis their parents or teachers. *Gradually introduce sexual content* into conversations or show sexually explicit material that may even involve children engaging in sexual activity – in order to convince kids that this type of behavior is acceptable. If the victim tries to cut off communication, *predators scare the victim* into continuing the relationship by convincing them that they will tell their parents what they have been doing online and that they have viewed pornographic pictures, etc. *May impersonate other youths* in order to convince minors to meet with them [13].

3.2. Age recognition based on faces

One of the key phases of this algorithm is a method for identifying a person's age based on a photograph. There are currently several methods that give results with some accuracy. For each of them, a certain database of photographs is used in order to perform an age assessment. A longitudinal study of automatic face recognition uses two large databases of photos, PCSO LS with 147784 images of 18007 subjects, average 8 images per subject over average 8.5 years, and LEO LS with 31852 images of 5636 subjects,

average 6 images per subject over average 5.8 years). Each subject has at least four faces [14]. Paper [15] proposes a 3D facial aging model and simulation method for age-invariant face recognition. This method models from 2D to 3D domain and gives the additional capability of compensating for pose and, potentially, lighting variations. In paper [16] a wavelet transform is proposed to extract the face features and an Adaptive Resonance Theory for classifying age groups. The authors were trained neural networks with FG-NET images of different age groups and about 94.28% of images were grouped correctly. The study in [17] emphasis the signification of face recognition on social networks and addresses to development of techniques based on big data analytics, machine learning, etc.

In this paper, we use The Wolfram Neural Net Repository [18]. This is a public resource that can be used for evaluation, training, visualization, transfer learning, and more. More precision, we use the trained neural network in the model of "Age Estimation VGG-16 Trained on IMDB-WIKI Data". The neural network is trained using the concept of deep learning. The convolutional neural network (CNN) uses VGG-16 architecture and The IMDB-WIKI dataset is used with 460723 images in IMDb, and 62328 images in Wikipedia [19].

3.3. Face blur technique

Blur technique is an integral part of well-known commercial professional software packages such as Adobe Photoshop, Premiere or After Effects, YouTube's face blurring tool, Wondershare Filmora, Skitch, Blur and Mosaic, Movavi, KineMaster. The Blur Technique blurs the pixels so that the image begins to lose detail. In this way, the image becomes blurred and it is not possible to recognize details in the parts covered by blur. Some of the most famous blur techniques are Gaussian Blur, Lens Blur, Motion Blur, and Blur Filter. In this paper, we use the blur technique to blur children's faces.

4. The algorithm development, testing and results

The complete algorithm's roadmap is shown in Figure 1. In order to perform operations, it is necessary to fulfill the condition that there must be at least 3 people in each photo, one of whom must be younger than 16 years. On the other hand, the tested images are not of the same resolution, but the lowest resolution is 320×320. The algorithm starts by uploading a photo ⓐ. The next step is to detect faces in the picture and put them in a frame, ie. to separate from the photo ⓑ. After detecting and extracting faces, they are sent to an artificial neural network that has been pre-trained with a photo dataset where comparisons are made with other faces ⓒ. As a result of this phase ⓒ, an age is identified for each person sent. Thus, persons in the phase ⓓ were identified as having 45, 41, 7, and 10 years of age. U istoj fazi provera se vrsi koje je lice ima 16 godina ili je mladje. Kada se to uradi takvim licima se vrsi automatsko zamagljivanje lica. At the same phase, the check is performed on which person is 16 years old or younger. When this is done, such faces are automatically blurred ⓔ. Finally, the processed photo is automatically uploaded and placed on the user's page, ie the child's page.

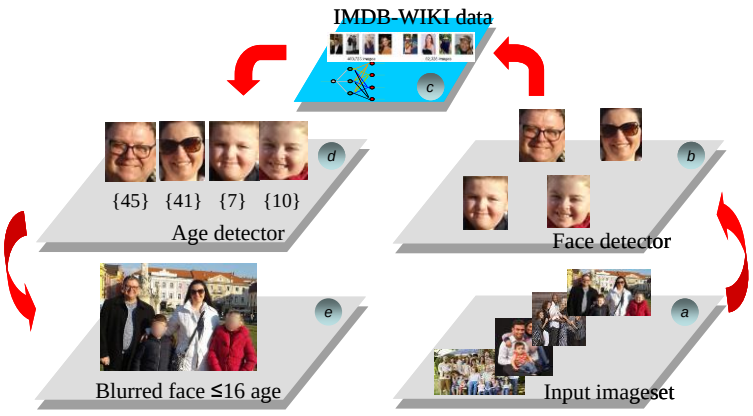

Figure 1. Algorithm's roadmap of face blur technique

Figure 2 shows the distributions with which the probability of age identification was performed for each person in the photo.

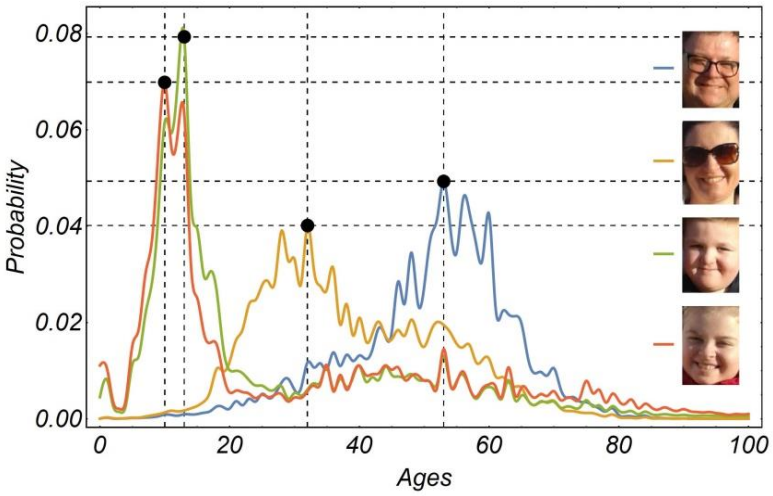

Figure 2. Distribution of age identification

5. Discussion

Many algorithms, developed as tools or toolboxes, aim to prevent children's activities by blocking their requests on the Internet. Basically, these add-ons are installed on user accounts, in this case these are kids, and block access to certain content or introduce parental controls. Such add-ons have been developed by companies such as Kaspersky [20]. For now, the world's greatest focus is to educate, which aims to guide children to all the challenges on the Internet and warn parents of the possible consequences [21]. With our method, we exclude the participation of parents, the child can work freely on the Internet, post their photos and content, and for that get protection from malicious visitors. Of course, all this includes mechanisms that record the attempt to access the content that children previously set, the content is protected automatically during upload, and in order to fully access the visitor must be personally identified and automatically revealed via the Internet location from which he accesses.

6. Conclusion

This paper deals with an algorithm that should prevent unwanted visitors from children and endanger their safety through social networks. This prevention is done by protecting the image, which the child places on his page, by blurring the faces of all persons aged 16 and younger. Modules that perform face isolation, face identification, and age assessment were tested.

References

[1] https://www.23snaps.com
[2] www.facebook.com
[3] https://www.instagram.com/
[4] https://www.flickr.com/
[5] http://fyu.se/
[6] https://secure.tagged.com/
[7] https://www.vingle.net/users/sign_up
[8] http://www.virb.com/
[9] M. Stevanović, A. Mitovski, D. Živković, S. Živković, A. Mladenović, S. Vasković, “Internet habits of school-age children in some villages of Bor municipality,” Sinteza 2014 - Impact of

the Internet on Business Activities in Serbia and Worldwide, Belgrade, Singidunum University, Serbia, 2014, pp. 351-355. doi:10.15308/sinteza-2014-351-355
[10] https://www.socialmediatoday.com/news/facebook-reaches-238-billion-users-beats-revenue-estimates-in-latest-upda/553403/
[11] https://www.statista.com/statistics/268136/top-15-countries-based-on-number-of-facebook-users/
[12] Li L. (2017) Behavior Analysis in Social Networks. In: Alhajj R., Rokne J. (eds) Encyclopedia of Social Network Analysis and Mining. Springer, New York, NY. https://doi.org/10.1007/978-1-4614-7163-9_110198-1
[13] https://www.puresight.com/Pedophiles/Online-Predators/how-do-online-predators-operate.html
[14] L. Best-Rowden and A. K. Jain, "Longitudinal Study of Automatic Face Recognition," in IEEE Transactions on Pattern Analysis and Machine Intelligence, vol. 40, no. 1, pp. 148-162, 1 Jan. 2018, doi: 10.1109/TPAMI.2017.2652466.
[15] U. Park, Y. Tong and A. K. Jain, "Age-Invariant Face Recognition," in IEEE Transactions on Pattern Analysis and Machine Intelligence, vol. 32, no. 5, pp. 947-954, May 2010, doi: 10.1109/TPAMI.2010.14.
[16] J. Nithyashri and G. Kulanthaivel, "Classification of human age based on Neural Network using FG-NET Aging database and Wavelets," 2012 Fourth International Conference on Advanced Computing (ICoAC), Chennai, 2012, pp. 1-5, doi: 10.1109/ICoAC.2012.6416855.
[17] Shahabadkar R., Sai Satyanarayana Reddy S. (2019) An Integrated Schema for Efficient Face Recognition in Social Networking Platforms. In: Silhavy R. (eds) Software Engineering and Algorithms in Intelligent Systems. CSOC2018 2018. Advances in Intelligent Systems and Computing, vol 763. Springer, Cham. https://doi.org/10.1007/978-3-319-91186-1_9
[18] https://resources.wolframcloud.com/NeuralNetRepository
[19] R. Rothe, R. Timofte, L.V. Gool, Deep expectation of real and apparent age from a single image without facial landmarks, International Journal of Computer Vision, Vol. 126, number 2-4, pages 144-157, 2018, Springer
[20] https://www.kaspersky.com/safe-kids
[21] https://www.cyberwise.org/online-security-hub

Optimization of dynamically loaded nonlinear technical systems

V V Shapovalov, P V Kharlamov*, S L Gorin, V B Mischinenko, R A Kornienko, V E Zinovev

Transport machinery and tribotechnology Department, Rostov State Transport University, Rostov-on-Don, Russia

*Corresponding author: kcharlamov@yandex.ru

Abstract. Modeling and simulation technologies play an important role in the operation, diagnosis of the current state and prediction of changes in various mechanical systems. The most effective approach for the study of nonlinear friction systems is the use of the method of physical and mathematical modeling, which is based on the construction of a mathematical model of a quasi-linear subsystem of a machine or mechanism and the creation of a physical model of a substantially nonlinear friction subsystem. Fundamentally new approaches have been developed to solve the problems of optimization, increasing the efficiency and competitiveness of non-linear technical systems using the example of the wheel-rail tribosystem. Proposed technology of metal cladding of locomotive wheel band and implementation of anisotropy of friction coupling provide significant increase of efficiency of "wheel-rail" tribosystem.

1. Introduction

Almost all technical systems use friction units, such as gearing, rolling and sliding bearings, brakes, frictional vibration dampers, friction gears of the wheel-rail, wheel-road surface, belt and chain drives, spline joints, etc. Comprising only 5–8% of the total weight of a technical system, friction units largely determine its main technical and economic characteristics, such as reliability, efficiency, economic indicators, etc. In turn, the output parameters of friction units (friction coefficient and its stability, wear and tear of working surfaces and their intensity, etc.) depend on more than forty interrelated parameters and factors in a complex and nonlinear way. There are the following ones among these factors: the temperature of the contacting bodies and their temperature gradients; temperature pattern displayed in a thin tribolayer; normal and tangential mechanical strains in contacting materials and their gradients; actual contact areas and coefficients of mutual overlap; relative sliding and rolling speeds; type of movement; environment; the nature of contacting lubricants; micro- and macrogeometry of the contacting surfaces; the nature of the film on the friction surfaces; design features of friction units; dynamic characteristics of quasilinear mechanical subsystems, including friction units, as well as tribospectral characteristics of frictional interaction, and many more.

Obtaining a mathematical model of a nonlinear friction system and nonlinear frictional processes in the form of regression equations leads to a violation of the principle of inapplicability of the superposition method for the nonlinear system study, as well as to an increase in the number of mathematical models. It might occur as a result of variation of just five factors out of 40 while the rest is “unaccounted”. It must be admitted that it is unrealistic to obtain such amount of information; as it

has been mentioned above, the models themselves would be incorrect due to the use of the superposition method[1-6].

2. Method for increasing the friction systems efficiency

The most effective approach for the study of nonlinear friction systems is the method of physical and mathematical modeling. It is based on the construction of a mathematical model of a quasilinear subsystem of a machine or mechanism in the form of an equivalent dynamic model performed at a selected scale (or scales when using n-variant modeling) . Further, a model (or models) of the friction unit is (are) attached to that dynamic model. At the same time, the model provides a given level of correlation coefficients of the main dynamic characteristics of the full-scale and model quasi-linear subsystems. Tribospectral characteristics of the full-scale and model friction subsystems are also provided .

This approach was used to solve a number of optimization problems for nonlinear technical systems. For example, by order of JSC Russian Railways, according to a business agreement, there was optimization of the geometric parameters of the railway track in small radius curves. The use of the method of physical and mathematical modeling and a unique model of the friction system “track – rolling stock” helped to reduce significantly the time of work performance and to develop recommendations for optimizing the geometry of the rail track. It allows obtaining an economic effect on the road network of JSC Russian Railways of about 3 billion rubles. A grant "Improving the wear resistance and durability of heavily loaded friction units of vehicles, machines and mechanisms by forming an antifriction layer of surface nanostructures on the tribocontact and providing dynamic control over the technical state of the tribosystem" was received for this purpose. In the process of solving the tasks of this grant, this approach has been chosen as the basis for creating a method for monitoring spline joints of the anti-torque rotor drive of the Mi-26 helicopter, as well as for obtaining options for studying the effectiveness of the developed measures to increase the reliability and durability of spline joint elements.

Technological progress is impossible without innovative developments, discoveries and inventions. One of such developments is a patent for invention RU No. 2674899 "Method for increasing the friction systems efficiency" [7]. This method is based on a fundamental research in the field of mechanics of contact frictional interaction and tribology, as well as contact interaction of solids.

One of the technical solutions made on the basis of the patent "Method for increasing the efficiency of friction systems" is the technology, technological equipment and consumables for increasing the tractive effort of the locomotive and the wheel sets resource. The theoretical basis of this technology is the anisotropy of frictional bonds formed by thermal metal cladding (TMC) of the working surfaces of the wheels (WSW) of locomotives (rolling circle surfaces and wheel flanges) [8].

As it is shown in multi-purpose studies of WSW thermal cladding with metals, their hardness is lower than the hardness of the WSW rim metal, the maximum effect of increasing the traction force of the locomotive (energy efficiency) and increasing the wheel sets resource is provided by the use of TMC technology where special aluminum alloys are used as consumables. Application of a thin aluminum layer on the traction surface of the rolling circle of a locomotive wheel provides 20–30% increase in the longitudinal friction forces (Figure 1). The increase in tractive effort is connected with a high rate formation of the aluminum adhesive component (in particular, the developed compounding of aluminum alloys), as well as a low level of limiting values of tangential [τ] and normal [σ] strain components [9-14]. The combination of these physical and mechanical characteristics is provided in the mode of rolling friction with slipping, at a sliding speed Vsl <3%, the mode of preliminary displacement with a friction coefficient (adhesion) equal to ffr.adhesion. $\geq$ 0.4, practically approaching the coefficient of static friction fstatic $\geq$ 0.5.

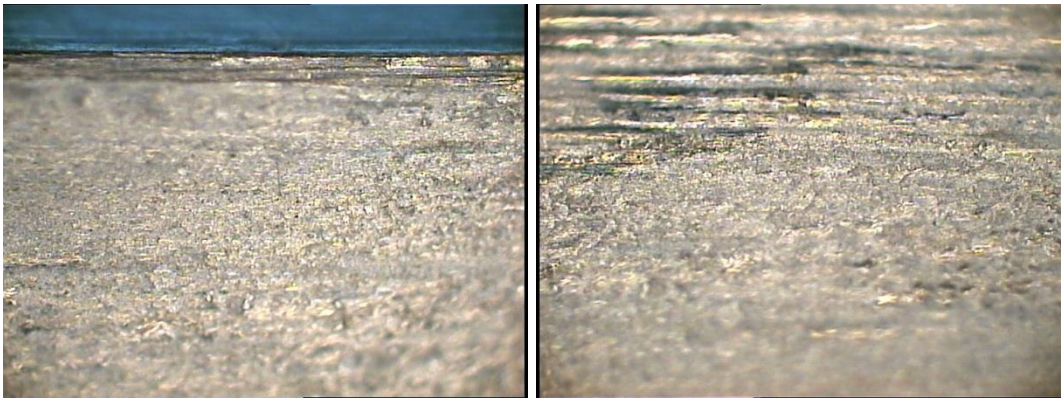

Figure 1. Surfaces after thermal metal cladding with an optimized aluminum alloy

The adhesion friction coefficient drops to 0.18–0.2 level in the following modes: in the mode of action of the forces of transverse creep (locomotive movement across the axis of the track); fitting into curved sections of the track, and movement along a sinusoid (lateral vibrations when overcoming a wind load, as well as while driving with a banking engine) if there is a layer of an aluminum alloy with an optimized formula (Al-M) on the surface of the wheel rolling circle. This decrease is explained by an increase in heat generation in proportion to an *n* times increase of the sliding speed approximately:

$$n = \frac{v_{lateral}}{v_{longitud}} = \frac{100\%}{2.5\%} = 40\%$$

Accordingly, the flash point at the tops of the contacting microroughnesses of the wheel and rail increases.

An increase in the flash point is connected with a *k*-fold increase in the energy released during friction, which is equal to the following:

$$N_{longitud} = F_{fr} \times V_{sl}^{longitud};$$
$$N_{lateral} = F_{fr} \times V_{sl}^{lateral};$$
$$k = \frac{F_{fr} \times V_{sl}^{lateral}}{F_{fr} \times V_{sl}^{longitud}} \approx n \approx 40.$$

A decrease in the level of the friction coefficient during the lateral movement of the locomotive is also connected with a 100% decrease in the adhesive component during sliding, and a decrease in the contact time of micro- and macro-irregularities. In this case, the rupture rate of single friction contacts is higher than the rate of formation of adhesive bonds between them. Thus, the use of the TMC of the wheel rolling circle surface makes it possible to increase the tractive effort of the locomotive by 20–30%, and to reduce the wear and tear (rolling) rate of the wheel by 5–7 times. In the case of using the TMC technology, the calculation of traction energy losses is also made according to the following formula:

$$\sum F_{long} = F_{long} + \Delta F_{long}$$
$$\Delta F_{long} = \sum F_{long} - F'_{long} \; or \; F_{long} = \sqrt{F'^2_{long}} + \sqrt{F^2_{lateral}} - F'_{long}$$
$$\Delta F_{long} = tg\left(45 - {}^{\alpha}/_{2}\right) \times F_{lateral} \approx 5\% \quad (1)$$

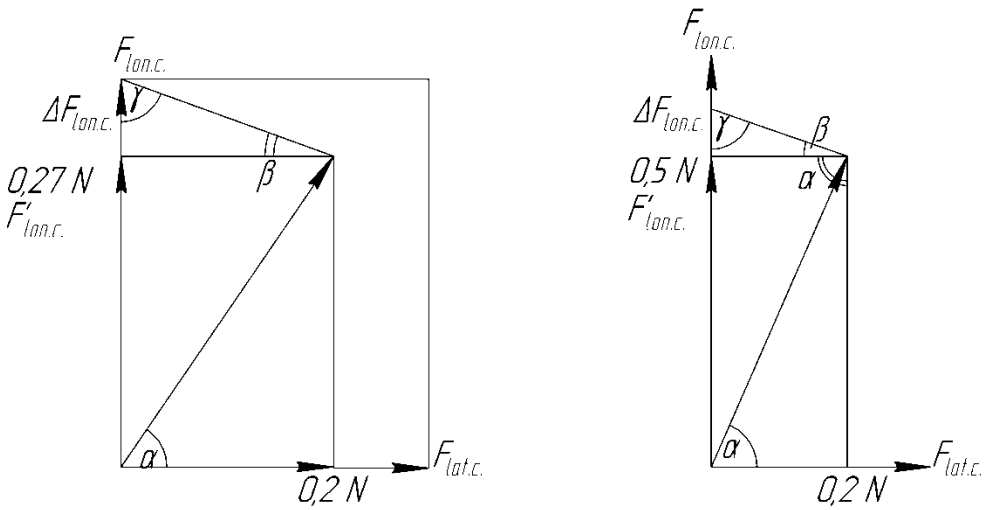

a) *b)*

Figure 2. Distribution of forces of lateral and longitudinal creep at frictional contact
a) Fe-Fe b) Fe-Al

Thus, the use of technology of thermal metal cladding reduces the level of traction energy losses in the presence of lateral creep forces by approximately several times. As it was mentioned above, when using the TMC for wear protection of the working surfaces of the flange, one can obtain additional tractive effort due to the frictional connection P of the surfaces of the flange and the side surface of the rail head. This two-point state of interaction of the locomotive wheel with the rail occurs when the locomotive fits into the curves, and when the required tractive effort increases significantly to compensate for the additional resistance of the trailed rolling stock when it moves in curved track sections. It also happens under wind load when moving with a banking engine. The traction force scheme is shown in Figure 2.

The possibility of existence of this traction two-point contact is associated with practically equal sliding speeds of the wheel relative to the rail at points 1; 2 and the absence of the output of the traction force curve at point 2 on the horizontal sections of the traction characteristic page Fig. 4.

3. Realization of traction force for point-to-point contact

Issues related to the wear and tear of the wheel sets flanges have always been and do remain relevant. Reducing the wear rate of the working surfaces of the wheels flanges to the level and below the level of the wear rate of the surfaces of the rolling circles makes it possible to reduce the number of wheel turning due to the "thin" flange and, accordingly, to increase the number of turns on the "rolling" of the tread . The latest technological scheme helps to reduce turning costs by 3–4 times and increase the resource of wheel sets by 4–5 times. Traditionally, the solution to problems associated with reducing the wear rate of the wheel sets flanges was carried out by supplying consistent antifriction lubricants to the contact zone of the wheel flange with the rail. However, the positive effect of lubrication of the wheel flanges is accompanied by negative consequences, such as oiling of the rolling stock and elements of the permanent way, getting of the rolling circle of the locomotive wheels into the contact zone and, as a consequence, the appearance of two-sided "flat wheels".

As a result of complex theoretical experimental studies, a technological scheme was developed to protect the working surfaces of the wheel flanges from wear by applying a protective metal film on them . This solution is based on a slight excess of the sliding speed of the working surface of the flange relative to the rail (no more than 0.2%) (Figure 3, point 2) compared to the sliding speed of the rolling surface of the tread.

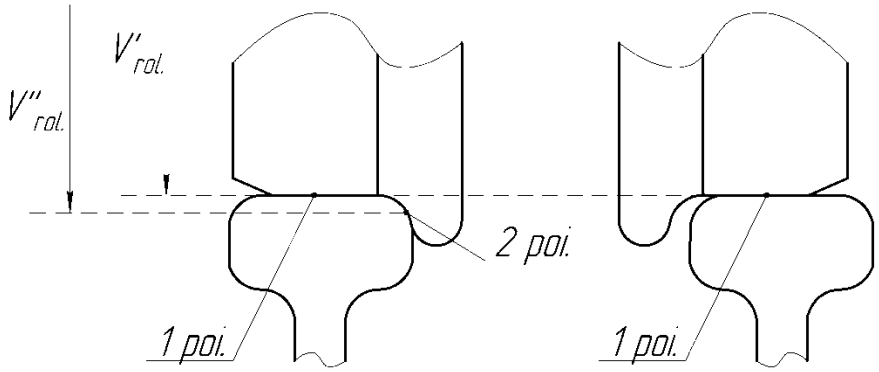

Figure 3. Scheme of contact of a railway wheel with a rail: a) one-point contact, b) two-point contact

Thus, in the two-point contact, an additional frictional connection is created, which helps to increase the tractive effort of the locomotive by 20–25% when driving in a traction mode (Figure 4).

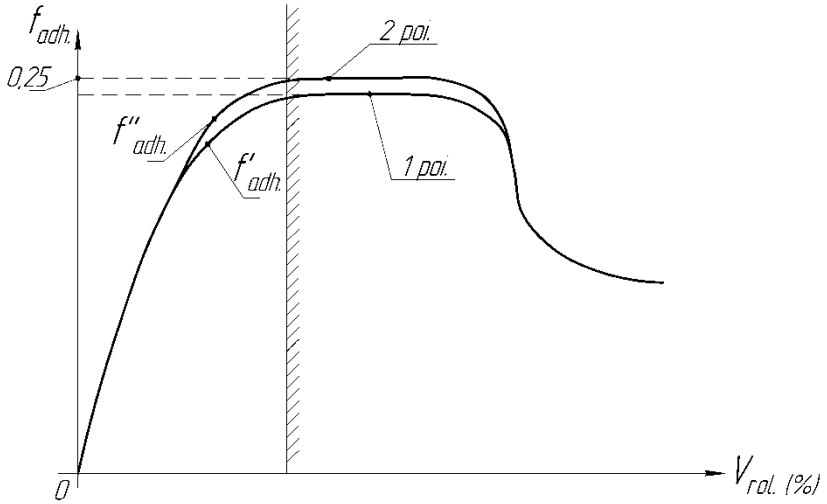

Figure 4. Dependence of the adhesion coefficient on the sliding speed for a two-point contact

Currently, there are two schemes for lubricating locomotive wheel set flanges with solid anti-friction materials: driven and non-driven.

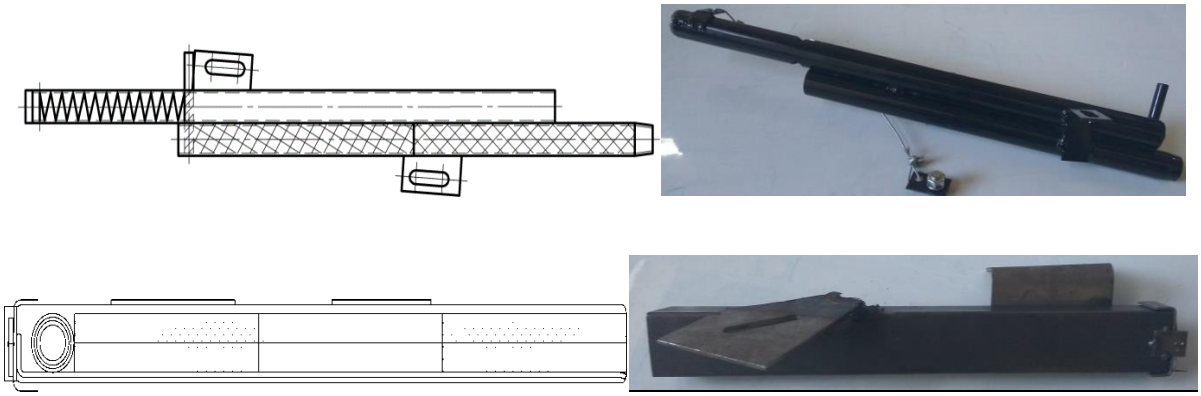

Figure 5. Shows diagrams and photos of drive lubricators

In some cases, for example, with limited geometrical spaces for the installation of flange lubrication systems (FLS) or grease rail lubrication systems (GRLS) or the need to provide a long service life with a single refueling, non-powered structures are the best option to protect against wear of flanges.

The scheme for calculating the values arising in the contact zone of lubricating rods (briquettes) or metal-clad rods is presented below.

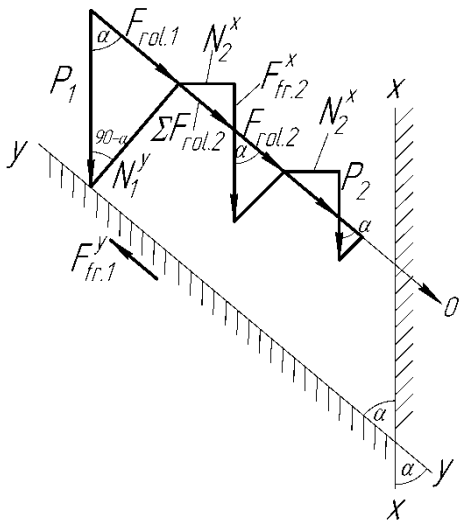

Figure 6. Scheme for calculating the action of forces in the contact zone of the lubricating rods

4. Conclusion

The considered technology, technological equipment and consumables (optimized aluminum alloy) can significantly improve the technical, economic and ecological characteristics of the friction subsystem "locomotive wheel – rail", as well as the entire system "track – rolling stock". Thermal metal cladding of the working surfaces of the wheel tread of the locomotive and use of the anisotropy of the Al-Fe friction bond allows the following:

- 5–6-fold reduction of the level of traction energy losses associated with the lateral creep forces when the locomotive moves in a pushing mode, when overcoming the wind load, and when moving in curved track sections;
- a possibility of turning locomotive wheel set treads due to such a defect as rolling along the rolling circle of a wheel set of a tread. Compared to turning due to a defect in the limiting value for the thickness of the flange, it ensures 3–4-fold reduction of the cost for the measures for turning locomotive wheel treads;
- thermal metal cladding of the rolling circle surface of the wheel tread of a locomotive wheel helps to increase the trailer load by 20–25% by increasing the adhesion coefficient from 0.27 in case of the frictional coupling of the wheel to the rail in the traditional form Fe-Fe to 0.45 – 0.5 when the Fe-Al friction bond is applied;
- thermal metal cladding with an optimized aluminum alloy of the working (frictional) surface of the wheel flange allows increasing the draw pull by 15–20% in the presence of unbalanced acceleration. It compensates for the resistance forces during the movement of the locomotive (for example, the forces of resistance to the movement of the rolling stock as a "carriage" in curved track sections);
- thermal metal cladding of the working surfaces of the wheel tread of the locomotive allows excluding (reduction) of using sand as an activator of the adhesion coefficient. It excludes the phenomenon of oversanding the ballast prism of the railway track and, as a result, 1.5–1.8-fold increase in the interrepair time; it also reduces the expenses of traction energy by 2–3%;

- the application of the technology of thermal metal cladding helps to increase the mileage of a locomotive from 1.5 thousand km with its one-time servicing to 8–10 thousand km when filling it with briquettes of the TMC modifier.

5. Acknowledgments

Researches are conducted within realization of a grant of JSC "Russian Railways" on development of scientific and pedagogical schools in the field of railway transport 2019-2021.

References

[1] Shapovalov V.V., Lubyagov A.M., Vyschepan A.L. [et al.] The Method of Dynamic Monitoring of Friction Mobile Systems // Russian Patent No. 2517946, 2014, Bulletin No. 16.

[2] Methods of the Classical and Modern Theory of Automatic Control: A Textbook. In 5 Vol. Vol. 1: Mathematical Models, Dynamic Characteristics and Analysis of Automatic Control Systems / K. A. Pupkov; eds. K. A. Pupkov, N. D. Egupov. 2nd ed., revised. and add. – Moscow: Bauman Moscow State Technical University. – 2004. – 656 p.

[3] Zinoviev, V.E. The Effect of Microcracks, Latent Defects and Residual Stresses of the Polymer Adhesive Layer On Its Destruction / Zinoviev V.E., Kharlamov P.V // Fundamentalnye Issledovaniya, 2015, No. 12. pages 37-42.

[4] Zakovorotniy V.L. The Study of the Complex Coefficient of Friction / V.L. Zakovorotniy, V.V. Shapovalov // Friction and Wear. – 1987. – Vol. 8. – pp. 22-24.

[5] Shapovalov V., Sladkovsky A., Erkenov A.Ch. Actual Problems of Modern Tribotechnics and Ways to Solve Them // Bulletin of Higher Educational Establishments. Mechanical Engineering. 2015. – No. 1 (658). – pp. 48–59.

[6] Loktev, A.A. Simulation of the railway under dynamic loading. Part 1. Ray method for dynamic problem/A.A. Loktev, E.A. Gridasova, E.V. Zapolnova//Contemporary Engineering Sciences. -2015. -Vol. 8. -№ 18. -P. 799-807.

[7] Patent for invention RU No. 2674899 "Method for increasing the efficiency of friction systems".

[8] Zadeh L., Desoer C. Theory of Linear Systems. – Moscow: Science. – 1979.

[9] Russian National Standard (GOST) 17168–82 Electronic Octave and Third Octave Filters. General Technical Requirements and Test Methods. – Moscow: Kaluga Printing House of Standards, 1982. – 19 p.

[10] Kolesnikov V.I. An Innovative Approach to the Study of Friction, Wear, and Monitoring of Heavily Loaded Tribosystems / V.I. Kolesnikov, A.L. Ozyabkin, E.S. Novikov // Friction and Wear. – 2019. – T. 40. – No. 4. – pp. 380–388.

[11] Evans, J. & Berg, M. Challenges in simulation of rail vehicle dynamics, Vehicle System Dynamics. 2009. Vol. 47. P. 1023-1048.

[12] Dumitriu, M. Modeling of railway vehicles for virtual homologation from dynamic behavior perspective. Applied Mechanics and Materials. 2013. Vol. 371. P. 647-651.

[13] Yang Y. C., Chu S. S., Chang W. J., and Wu T. S. Estimation of Heat Flux and Temperature Distributions in a Composite Strip and Homogeneous Foundation//Int. Commun. Heat Mass Tran. -2010 (37), no. 5, 495-500.

[14] Wolter, K.U. & Zacher, M. & Slovak, B. Correlation between track geometry quality and vehicle reactions in the virtual rolling stock homologation process. In: 9th World Congress on Railway Research, May 22-26, 2011.

Digital meter of frequency instability and phase noise of high stable oscillators

V P Fedosov*, Jacinto M B Nsue and A V Labyntsev

Department of Theoretical principles of radio engineering, Southern Federal University, Taganrog, Russia

*e-mail: vpfedosov@sfedu.ru

Abstract This paper discusses the measurement of frequency instability and phase noise of real oscillators. As part of this work, a device was developed in LabVIEW, which allows implementing the multiplier-conversion method (MCM), in the form of a subprogram for oscillations with a low level of frequency instability. Another device was developed, which allows the simulation of a signal with a given phase noise grade, for applying MCM to increase standard deviation as many times as is needed. The use of these devices confirmed the operability and efficiency of the MCM for increasing the oscillation instability by a given number of times. The research showed that in the case of oscillation with very high frequency stability, it is possible to increase this small instability by a concise number of times, using MCM, and thereby provide the possibility of measuring frequency and phase instability, by devices with a larger error than is required for the measurements of very small instability.

1. Introduction

Wherever radio engineering and telecommunications are used, the requirements towards the frequency stability of generated oscillations are increasing yearly [1-15]. This leads to the need of improving methods for measuring and monitoring the frequency and phase parameters of oscillations generated by highly stable oscillators. This paper is a logical continuation of publications [16, 17] and is devoted to the both numeric and graphic representation of the results obtained during the development of a digital meter of frequency and phase instability of real oscillators based upon the multiplier-conversion method (MCM) [18-20], thank to which the reference devices are useless. The modeling has been performed in LabVIEW environment using National Instruments technologies and MCM.

2. Instantaneous frequency of SFG-2110 oscillator

The realization of the instantaneous frequency of the SFG-2110 oscillator, with the frequency set at 10 MHz, which was measured by Ch3-85 frequency meter, is shown in figure 1(a). The data show, that in the observation interval of 45 seconds length the measurement of 450 instantaneous frequency values is performed and each value is obtained within 100 ms

The realization of the instantaneous frequency contains outstanding and fast fluctuations which represent Jitter and considerably slower and more systematic (less chaotic) changes, which characterize Wander. Each frequency value, e.g. f = 9999865.037543956 Hz, is measured with an accuracy of 1 nHz. Thus, the achievable high relative accuracy of the oscillation frequency is equal to $10^{-9}/10^{7} = 10^{-16}$. This is formally obtainable using the Ch3-85 frequency meter in the combined method of discrete

counting, which consists about dividing two values with the possibility of obtaining any number of decimals, which is limited only by the computer capacity.

In order to obtain the Allan deviation, the systematic component (Wander) is extracted from the instantaneous frequency signal (figure 1(a)) then, basing on the centered dependency of the components of frequency fluctuations (figure 1(b)), the Allan deviation (figure 1(c)) is calculated and the distribution histogram (figure 1(d)) is depicted.

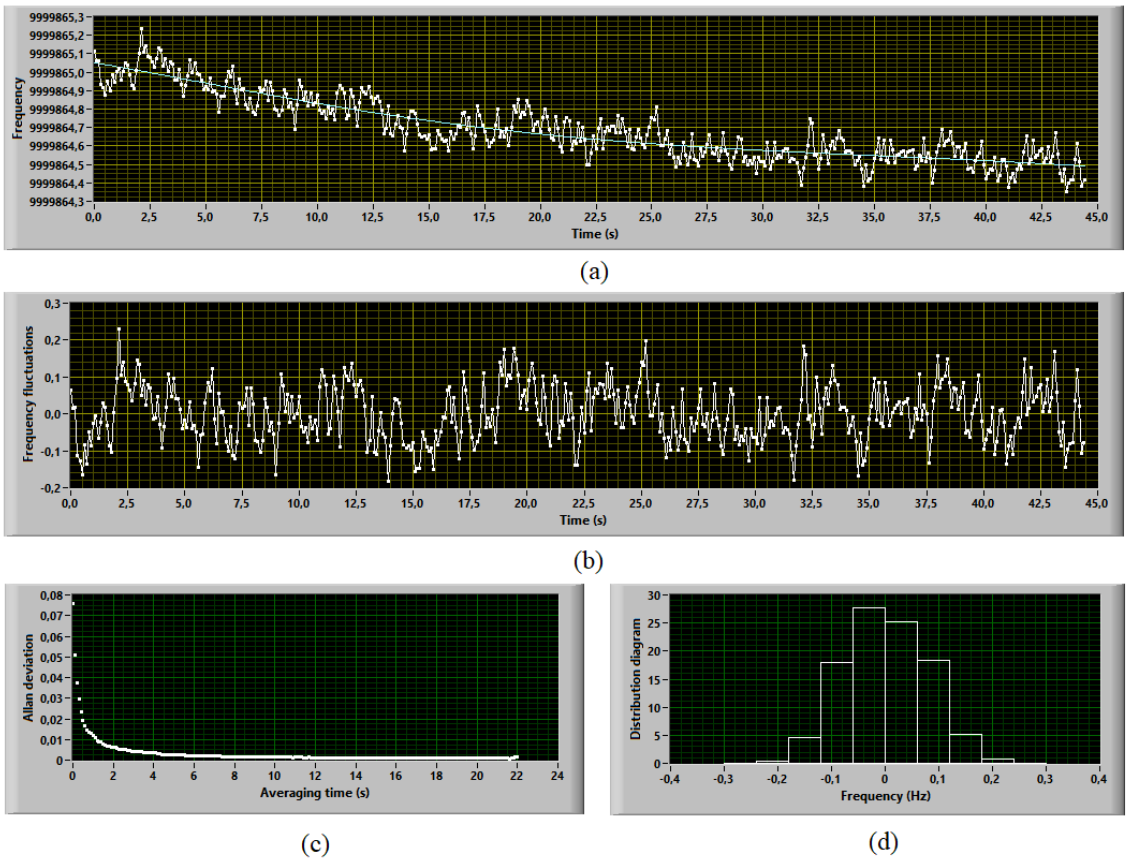

Figure1. The results of the oscillation frequency measurement of SFG-2110 oscillator

3. Jitter measurement by instantaneous frequency of the signal and by power spectral density of the instantaneous frequency

Focusing on the available data given by the mentioned combined discrete count method, and willing to simulate multiple instantaneous frequency oscillation signal of a real SFG-2110 oscillator, it was necessary to develop a LabVIEW virtual instrument (vi). Short-term frequency instability or Jitter is being quantitatively estimated basing on the realization of the instantaneous frequency, in other words, there should be the calculation of the standard deviation (SD) of frequency fluctuations σ_f within 2 sec. The figure 2(a) shows one of the realizations, obtained during the simulation of the instantaneous frequency of a signal provided by SFG-2110 oscillator. And the figure 2(b) shows the fluctuation component of the frequency df(t). It should be pointed out, that during the simulation; the initial frequency f_0, the initial SD σ_0, the maximum spectrum frequency f_m and the initial frequency relative instability δ_0 of the instantaneous frequency oscillation signal were set to:1 kHz, 1 mHz, 25 Hz and 10^{-6} respectively. After averaging the instantaneous frequency oscillation signal, the SD of the selected frequency fluctuation component σ_f resulted equal to 0.993 mHz almost equal to the input value 1 mHz. Thus, the high accuracy of the calculus is confirmed.

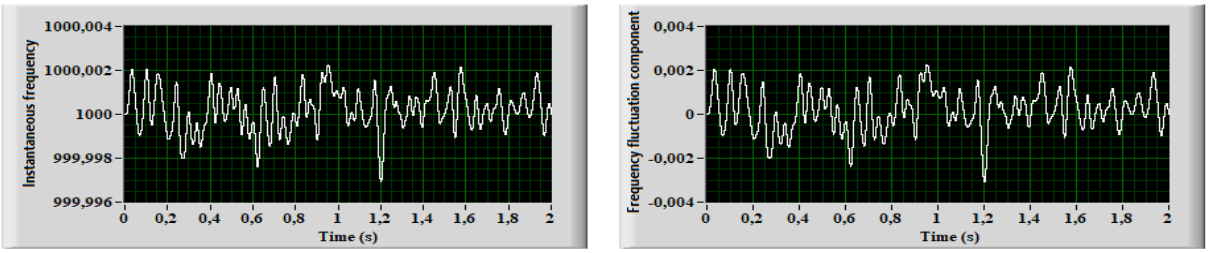

(a) (b)

Figure 2. The instantaneous frequency of the signal of SFG-2110

The following power spectral density (PSD), (figure 3) is the result of having applied the Fourier transform to the fluctuation component of the frequency df(t).

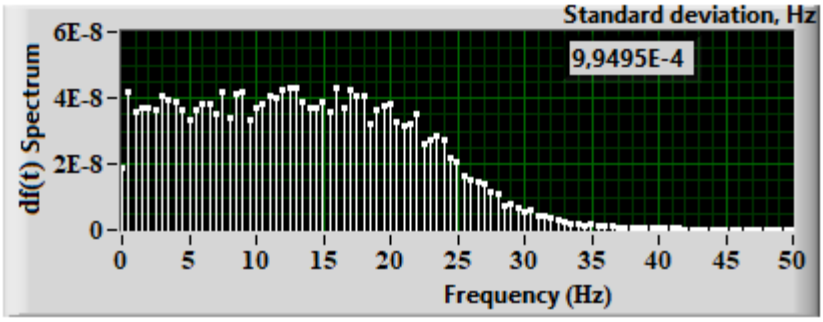

Figure 3. The PSD of the instantaneous frequency of the signal of SFG-2110

The averaging of the accumulated PSD of instantaneous frequency took place and the standard deviation of the average process happened to be 0.995 mHz.

Despite the strict interrelation between frequency instability and phase noise, this paper shows, that evaluating instability might be, in some cases done with higher efficacy using phase noise.

4. The measurement of phase noise using realization and PSD of the phase

The integration of the fluctuation component of the instantaneous frequency allows to switch to the fluctuation component of the instantaneous phase, and after that, it is possible to determine the phase noise from the timing diagram (figure 4(a)) or from the PSD of the instantaneous phase (figure 4(b)). There are respective standard deviations of the phase noise on the upper right corner of each of these figures. As well as the upper case; the displayed standard deviations correspond to the average phase fluctuation process, $\sigma_{\varphi,t} = 62.45 \mu rad$ and the average PSD process, $\sigma_{\varphi,f} = 62.33 \mu rad$ respectively. As you can see, the obtained values are quite close and fully correspond to the theory.

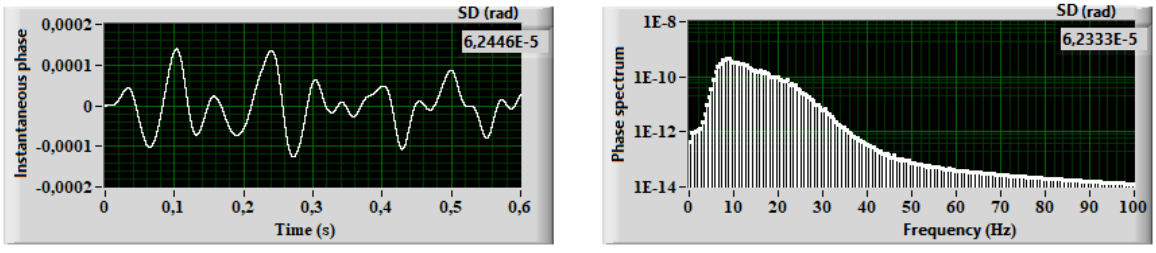

(a) (b)

Figure 4. Realization of the instantaneous phase and PSD of the phase of the signal, which is from SFG-2110

5. The measurement of SD of the phase noise via the PSD of the oscillation

The formation of the linear part of the argument of the oscillation, that simulates a harmonic signal from the SFG-2110 oscillator allows moving to the full instantaneous phase of the harmonic and form an s(t) oscillation with a given amplitude, frequency instability and the corresponding phase noise. After obtaining this oscillation, we proceed to solve two important tasks, that are related to obtaining an estimation of the phase noise, which is in the s(t) oscillation.

The first task is as follows. Using the Hilbert transform, switching from the s(t) oscillation to the analytical signal is possible. Now, the complex envelope is extracted from the analytical signal and, from complex envelope the instantaneous phase is extracted. A fragment of the block diagram for solving this task is shown in figure 5(a). The realization of the instantaneous phase, which is embedded in the model of the signal, is shown in the figure 5(b). This phase completely coincides with the phase noise (figure 5(c)), which is extracted from the signal argument s(t).

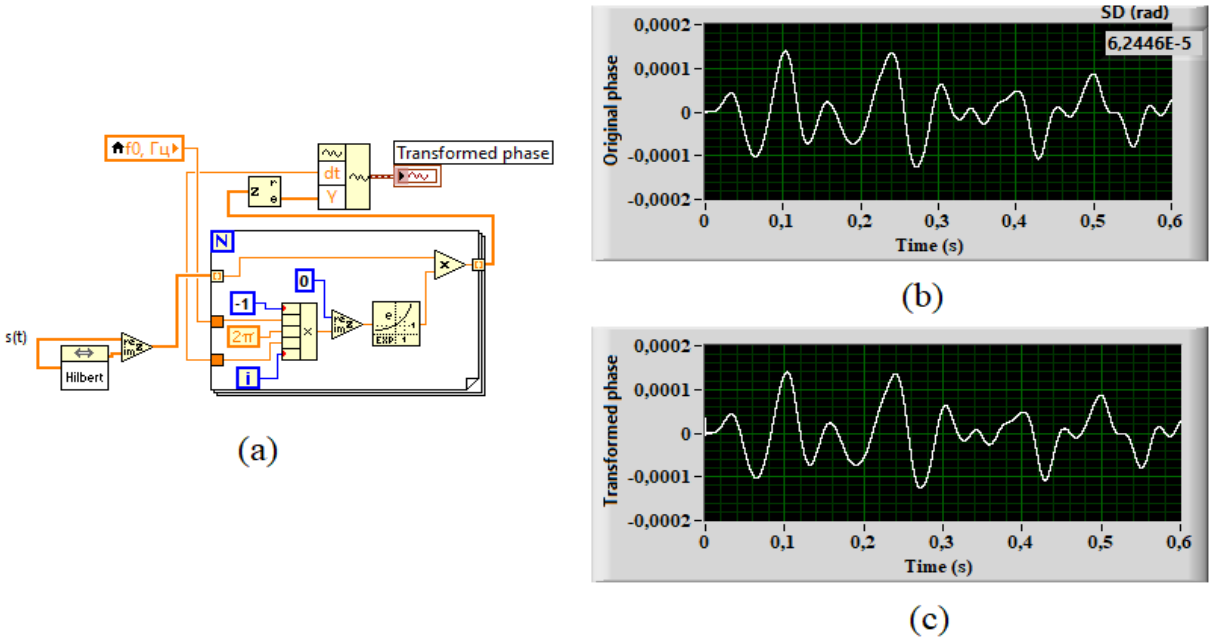

Figure 5. Extraction of the instantaneous phase from the s(t) oscillation

The second task is to find the PSD of the oscillation with the already known phase noise. Then once again evaluate this phase noise, finding SD of the phase noise $\sigma_{\varphi,s}$ using the PSD of the signal. PSD of the s(t) oscillation with a given phase noise is obtained by applying the corresponding Fourier transform. The result of this transformation is shown in figure 6.

To obtain an estimation SD of the phase noise is recommended to follow these steps. The P_0 harmonic on the carrier frequency is excluded from the PSD of the signal. All other P_n harmonics are summed and the sum is multiplied by two, after that the result is affected by the square root and the result is divided by the oscillation amplitude A, as it's shown in the equation:

$$\sigma_{\varphi,s} = \frac{1}{A}\sqrt{2\sum_{n=0}^{N} P_n} \quad , \tag{1}$$

where: $n = 0,1,2,\ldots,N$; P_n – all harmonics in the PSD, except the carrier frequency harmonic.

Eventually, the obtained value of SD of the phase noise $(\sigma_{\varphi,s})$ using the PSD of the signal is equal to $6.233\ 10^{-5}$ rad (figure 6) and this value coincides with the value of SD of the phase noise using the

realization of the instantaneous phase ($\sigma_{\varphi,t} = 6.245 \cdot 10^{-5}$rad). And this values coincide with the value of SD of the phase noise, using the PSD of the phase of the signal ($\sigma_{\varphi,f} = 6.233 \cdot 10^{-5}$ rad).

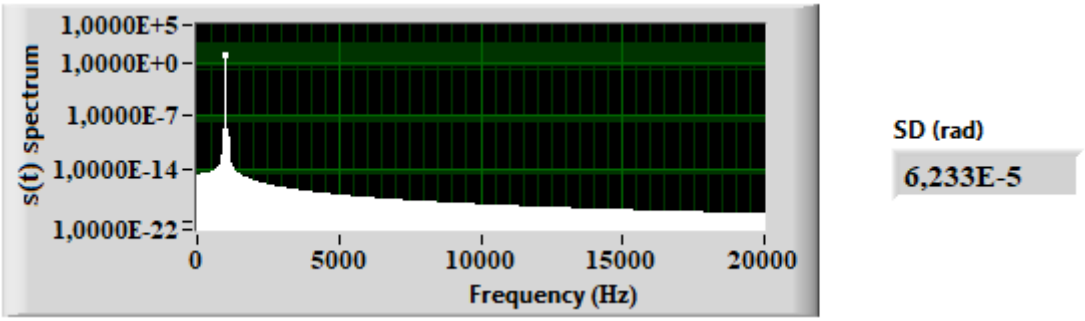

Figure 6. The power spectral density of the oscillation of SFG-2110 oscillator

6. Estimation of jitter of highly stable generators using MCM

It was earlier [18-20] shown, that in case of very insignificant frequency fluctuations, MCM can be efficiently used for measuring instability, relying on its property of transforming the oscillation, so that the frequency instability increases by several orders of magnitude and, then its measurement can be performed rather easily by known methods.

As part of this work, a device was developed in LabVIEW in the form of a subprogram, which allows implementing the MCM for oscillations with a low level of frequency instability.

Another device was also developed, which allows the simulation of a signal with a given phase noise grade and then use the MCM to increase of frequency instability as many times as is needed. The use of these devices fully confirms the operability and efficiency of the MCM for increasing the oscillation instability by a given number of times.

7. Conclusion

The paper deals with the measurement of frequency instability and phase noise of real oscillators. It is shown, that in the case of an oscillation with a very high frequency stability, it is possible to increase this small instability by a certain number of times, using the multiplier-conversion method and, thereby provide the possibility of obtaining an estimation of frequency instability and phase noise by devices that have a greater error than is required for direct measurements.

The article was recommended for publication by Doctor of Technical Sciences, Professor V.I. Marchuk

References

[1] Ochkov D, Silaev E and Formalnov I 2006 Methodology for estimating the coherence intervals of radar radio paths. *M.: Radio engineering (Journal in journal)* V **4** pp 36-38 https://rastr-radio.ru/pdf/coherence.pdf

[2] Ochkov D, Silaev E and Formalnov I 2007 The influence of the value of the frequency of the reference signal on the magnitude of the parasitic incursion of the phase of the quartz-based heterodyne. *M.: Radar location and communication* V **10** pp 94-99 https://rastr-radio.ru/pdf/coherence_2.pdf

[3] Belchikov S 2009 Phase Noise: How to Get Below –120 dBc / Hz at 10 kHz Offset in the Frequency Range up to 14 GHz, or The Decibel Struggle *Components and Technologies* V **5** pp 139-46

[4] Molchanov E, Ochkov D, Silaev E and Formalnov I 2007 Allan variation and its modifications in assessing the short-term instability of the heterodyne frequency of a coherent radar rastr-radio *M.: Radiotechnique* V **10** pp 108-110 rastr-radio.ru›pdf/allan.pdf
[5] Belloni M, Gioia M and Beretta S 2011 Space Mini Passive Hydrogen Maser - A Compact Passive Hydrogen Maser for Space Applications *Proc. IEEE Intern. Frequency Control Symposium and European Frequency and Time Forum, San Fransisco, USA* pp 906-910
[6] Vasilyev V and Kozlov S 2013 Figure of merit and limit of short-term stability in passive hydrogen maser *Proc. of the joint conference IFCS-EFTF, Praque, Czech Republic*, July 21-25 pp 768-770
[7] Vasilyev V 2014 Time and frequency measurements *M.: Measurement Techniques* V **2** pp 37-40 https://www.elibrary.ru/item.asp?id=21394529
[8] Vasilyev V 2016 Investigation of the limiting short-term instability of the output signal of a passive hydrogen frequency standard *M.: Measurement Techniques* V **9** pp 25-29 https://www.elibrary.ru/item.asp?id=27195360&
[9] Akulov V and Pashev G 2019 Analysis of the digital linear systems of automatic frequency adjustment of high-stability generators by radio signals of the global positioning system *M.: Measurement Techniques* V **3** pp 254-258 https://www.elibrary.ru/item.asp?id=37247987
[10] Verveyko A, Lappo I, Arkushenko P and Yusukhno S 2019 Frequency instability measurement device based on the pulse coincidence principle *Bulletin of National Technical University of Ukraine. Series Radiotechnique Radioapparatus building* V **76** pp 29-36 https://www.elibrary.ru/item.asp?id=37199649
[11] Kychak V. and Gavrasienko P. 2014 Device of Radio Frequency Instability Measurements *Visnyk NTUU KPI Seriia - Radiotekhnika Radioaparatobuduvannia* V **58** pp 83-89 https://doi.org/10.20535/RADAP.2014.58.83-89
[12] Mrachkovskiy O and Vishnevyy S 2008 Modelling of the multifunctional generator of video and radio signals in program application LabVIEW *National Technical University of Ukraine, Kyiv Politechnic Institute Kiev* V **36** pp 34-37 https://www.elibrary.ru/item.asp?id=22933878
[13] Goncharov A, Bonert A, Baraulya V, Tropnikov M, Kuznetsov S, Taichenachev A and Bagayev S 2018 Laser frequency stabilisation on narrow resonances of cold magnesium atoms at the $^1s_0$–$^3p_1$ transition *Quantum electronics* V **5** pp 410-414 https://www.elibrary.ru/item.asp?id=34940655
[14] Epikhin V, Baryshev V, Slyusarev S, Aprelev A and Blinov I 2019 Acousto-optic modulators for a controlled frequency shift of light beams in optical and microwave cold-atom frequency standards *Quantum electronics* V **9** pp 857-862 https://www.elibrary.ru/item.asp?id=41701544
[15] Goncharov A, Baraulya V, Bonert A and Tropnikov M 2020 457-nm radiation source based on a diode laser for precision spectroscopy of magnesium atoms *Quantum Electronics* V **3** pp 272-276 https://www.elibrary.ru/item.asp?id=42649746
[16] Nsue J, Fedosov V and Tereshkov V 2016 Evaluation of frequency instability using indicators in the time domain *Rostov Scientific Journal: Network Journal* V **4** I **6** pp 5-15
[17] Nsue J, Fedosov V and Tereshkov V 2016 Measurement of frequency instability of highly stable generators using indicators in the time domain *Rostov Scientific Journal: Network Journal* V**4** I **7** pp 63-70
[18] Nsue J and Fedosov V 2016 A digital algorithm for measuring the short-term frequency instability of highly stable generators by the multiply-converting method *Trends in the development of science and education: collection of articles scientific works, based on the materials of the XV International scientific conf. June 25, - The publishing house of the Research Center "L-Journal"* P **3** pp 16-18

[19] Nsue J, Fedosov V and Kucheryavenko S 2018 Measurement of short-term frequency instability of ultra-stable quasi-harmonic signals *Electronic scientific journal "Engineering Bulletin of the Don"* V **1** pp 24-28
[20] Nsue J, Fedosov V and Kucheryavenko S 2019 Experimental measurement of relative instability of frequency of oscillators by digital multiplier-converting method. *Izvestiya SFedU. Engineering Sciences* V **1** pp 69-70